

REPORT DOCUMENTATION PAGE				Form Approved OMB NO. 0704-0188	
<p>The public reporting burden for this collection of information is estimated to average 1 hour per response, including the time for reviewing instructions, searching existing data sources, gathering and maintaining the data needed, and completing and reviewing the collection of information. Send comments regarding this burden estimate or any other aspect of this collection of information, including suggestions for reducing this burden, to Washington Headquarters Services, Directorate for Information Operations and Reports, 1215 Jefferson Davis Highway, Suite 1204, Arlington VA, 22202-4302. Respondents should be aware that notwithstanding any other provision of law, no person shall be subject to any penalty for failing to comply with a collection of information if it does not display a currently valid OMB control number.</p> <p>PLEASE DO NOT RETURN YOUR FORM TO THE ABOVE ADDRESS.</p>					
1. REPORT DATE (DD-MM-YYYY) 05-10-2011		2. REPORT TYPE Final Report		3. DATES COVERED (From - To) 1-Jun-2005 - 31-May-2011	
4. TITLE AND SUBTITLE General, Unified, Multiscale Modeling to Predict the Sensitivity of Energetic Materials			5a. CONTRACT NUMBER W911NF-05-1-0265		
			5b. GRANT NUMBER		
			5c. PROGRAM ELEMENT NUMBER 611103		
6. AUTHORS Donald L. Thompson			5d. PROJECT NUMBER		
			5e. TASK NUMBER		
			5f. WORK UNIT NUMBER		
7. PERFORMING ORGANIZATION NAMES AND ADDRESSES University of Missouri - Columbia Office of Sponsored Programs The Curators of the University of Missouri Columbia, MO 65211 -			8. PERFORMING ORGANIZATION REPORT NUMBER		
9. SPONSORING/MONITORING AGENCY NAME(S) AND ADDRESS(ES) U.S. Army Research Office P.O. Box 12211 Research Triangle Park, NC 27709-2211			10. SPONSOR/MONITOR'S ACRONYM(S) ARO		
			11. SPONSOR/MONITOR'S REPORT NUMBER(S) 48101-EG-MUR.29		
12. DISTRIBUTION AVAILABILITY STATEMENT Approved for Public Release; Distribution Unlimited					
13. SUPPLEMENTARY NOTES The views, opinions and/or findings contained in this report are those of the author(s) and should not be construed as an official Department of the Army position, policy or decision, unless so designated by other documentation.					
14. ABSTRACT This report describes the accomplishments for the MURI grant "General, Unified, Multiscale Modeling to Predict the Sensitivity of Energetic Materials" (Grant No. 48101-EG-MUR). This was a comprehensive theoretical/computational research program to develop, validate, benchmark, and apply methods and models to provide predictive capabilities for energetic materials. The thrust of the work was the development of atomic-level models and ab initio quantum chemistry methods that are generally applicable to the chemical decomposition of					
15. SUBJECT TERMS Energetic materials, atomic-level models, molecular dynamics, reactive force fields, shock dynamics, sensitivity, hotspots					
16. SECURITY CLASSIFICATION OF:			17. LIMITATION OF ABSTRACT UU	18. NUMBER OF PAGES	19a. NAME OF RESPONSIBLE PERSON Donald Thompson
a. REPORT UU	b. ABSTRACT UU	c. THIS PAGE UU			19b. TELEPHONE NUMBER 573-882-0051

## Report Title

General, Unified, Multiscale Modeling to Predict the Sensitivity of Energetic Materials

### ABSTRACT

This report describes the accomplishments for the MURI grant “General, Unified, Multiscale Modeling to Predict the Sensitivity of Energetic Materials” (Grant No. 48101-EG-MUR). This was a comprehensive theoretical/computational research program to develop, validate, benchmark, and apply methods and models to provide predictive capabilities for energetic materials. The thrust of the work was the development of atomic-level models and ab initio quantum chemistry methods that are generally applicable to the chemical decomposition of condensed-phase energetic materials under extreme conditions. The approaches include quantum mechanics, molecular modeling, Monte Carlo, and molecular dynamics, to yield state-of-the-art methods specifically designed for and tailored to target DoD energetic materials research needs.

---

**Enter List of papers submitted or published that acknowledge ARO support from the start of the project to the date of this printing. List the papers, including journal references, in the following categories:**

**(a) Papers published in peer-reviewed journals (N/A for none)**

<u>Received</u>	<u>Paper</u>
2011/05/03 1: 28	L. He, T. Sewell, D. Thompson. Molecular dynamics simulations of shock waves in oriented nitromethane single crystals, <i>Journal of Chemical Physics</i> , ( ): . doi:
2010/11/18 1: 27	A. Siavosh-Haghighi, T. Sewell, D. Thompson. Molecular dynamics study of the crystallization of nitromethane from the melt, <i>Journal of Chemical Physics</i> , ( ): . doi:
2010/06/22 1: 26	S. Stuart, P. Krstic, T. Embry, C. Reinhold. Methane production by deuterium impact at carbon surfaces, <i>Nuclear Instruments and Methods in Physics Research B</i> , ( ): . doi:
2010/06/22 1: 25	C. Reinhold, P. Krstic, S. Stuart, H. Zhang, P. Harris, F. Meyer. Isotope dependence of chemical erosion of carbon, <i>Journal of Nuclear Materials</i> , ( ): . doi:
2010/06/22 1: 24	C. Reinhold, P. Krstic, S. Stuart. Time scales of chemical sputtering of carbon, <i>Nuclear Instruments and Methods in Physics Research B</i> , ( ): . doi:
2010/06/22 1: 23	A. Liu, S. Stuart. Empirical Bond-Order Potential for Hydrocarbons: Adaptive Treatment of van der Waals Interactions, <i>Journal of Computational Chemistry</i> , ( ): . doi:
2010/06/22 1: 22	P. Krstic, C. Reinhold, S. Stuart. Plasma-surface interactions of hydrogenated carbon, <i>Nuclear Instruments and Methods in Physics Research B</i> , ( ): . doi:
2010/06/22 1: 21	P. Krstic, E. Hollmann, C. Reinhold, S. Stuart, R. Doerner, D. Nishijima, A. Pigarov. Transfer of rovibrational energies in hydrogen plasma-carbon surface interactions, <i>Journal of Nuclear Materials</i> , ( ): . doi:
2010/06/04 0: 20	S. Stuart, M. Fallet, P. Krstic, C. Reinhold. Evolution of carbon surfaces under simulated bombardment by deuterium, <i>Journal of Physics</i> , ( ): . doi:
2010/06/03 1: 19	F. Meyer, P. Krstic, L. Vergaral, H. Krausel, C. Reinhold, S. Stuart. Low energy chemical sputtering of ATJ graphite by atomic and molecular deuterium ions, <i>Physica Scripta</i> , ( ): . doi:
2010/06/03 1: 18	E. Hollmann, P. Krstic, R. Doerner, D. Nishijima, A. Pigarov, C. Reinhold, S. Stuart. Measurement and modeling of hydrogen molecule ro-vibrational accommodation on E-294 polycrystalline graphite, <i>Plasma Physics and Controlled Fusion</i> , ( ): . doi:
2010/06/02 0: 17	P. Krstic, C. Reinhold, S. Stuart. Chemical sputtering from amorphous carbon under bombardment by deuterium atoms and molecules, <i>New Journal of Physics</i> , ( ): . doi:
2010/06/02 0: 16	C. Reinhold, P. Krstic, S. Stuart. Hydrogen reflection in low-energy collisions with amorphous carbon, <i>Nuclear Instruments and Methods in Physics Research</i> , ( ): . doi:
2010/05/28 0: 15	P. Krstic, S. Stuart, C. Reinhold. Chemical Sputtering of Fusion Plasma-Facing Carbon Surfaces, <i>American Institute of Physics</i> , ( ): . doi:
2010/05/28 0: 14	P. Krstic, C. Reinhold, S. Stuart. Energy and angle spectra of sputtered particles for low-energy deuterium impact of deuterated amorphous carbon, <i>Journal of Applied Physics</i> , ( ): . doi:
2010/05/28 0: 13	P. Krstic, C. Reinhold, S. Stuart. Chemical sputtering by impact of excited molecules, , ( ): . doi:
2010/04/14 1: 12	Y. Shi, D. Brenner. Jetting and Detonation Initiation in Shock Induced Collapse of Nanometer-Scale Voids, <i>Journal of Physical Chemistry C</i> , ( ): . doi:
2010/04/14 1: 11	Y. Shi, D. Brenner. Molecular Simulation of the Influence of Interface Faceting on the Shock Sensitivity of a Model Plastic Bonded Explosive, , ( ): . doi:
2010/04/14 1: 10	Y. Shi, D. Brenner. Hotspot formation in shock-induced void collapse, , ( ): . doi:
2010/04/14 1: 9	Y. shi, D. Brenner. Simulated thermal decomposition and detonation of nitrogen cubane by molecular dynamics, , ( ): . doi:

2010/04/06 1: 8	D. Bedrov, J. Hooper, G. Smith, T. Sewell. Shock-induced transformations in crystalline RDX: A uniaxial constant-stress Hugoniot molecular dynamics simulation study, Journal of Chemical Physics, ( ): . doi:
2010/04/06 0: 7	A. Bolesta, L. Zheng, D. Thompson, T. Sewell. Molecular dynamics simulations of shock waves using the absorbing boundary condition: A case study of methane, Physical Review B, ( ): . doi:
2010/04/06 0: 6	A. Metropoulos, D. Thompson. A quantum chemistry study of the dissociation and isomerization reactions of methylene amidogene, Theochem, ( ): . doi:
2010/04/06 0: 5	J. Coe, T. Sewell, M. Shaw. Optimal sampling efficiency in Monte Carlo simulation with an approximate potential, Journal of Chemical Physics, ( ): . doi:
2010/04/06 0: 4	J. Coe, T. Sewell, M. Shaw. Nested Markov chain Monte Carlo sampling of a density functional theory potential: Equilibrium thermodynamics of dense fluid nitrogen, Journal of Chemical Physics, ( ): . doi:
2010/04/01 1: 3	M. Cawkwell, T. Sewell. Shock-induced shear bands in an energetic molecular crystal: Application of shock-front absorbing boundary conditions to molecular dynamics simulations, Physical Review B, ( ): . doi:
2010/04/01 1: 2	A. Siavosh-Haghighi, R. Dawes, T. Sewell, D. Thompson. Shock-induced melting of (100)-oriented nitromethane: Structural relaxation, Journal of Chemical Physics, ( ): . doi:
2010/04/01 1: 1	R. Dawes, A. Siavosh-Haghighi, T. Sewell, D. Thompson. Shock-induced melting of „100...-oriented nitromethane: Energy partitioning and vibrational mode heating , Journal of Chemical Physics, ( ): . doi:

**TOTAL: 28**

**Number of Papers published in peer-reviewed journals:**

---

**(b) Papers published in non-peer-reviewed journals (N/A for none)**

<u>Received</u>	<u>Paper</u>
-----------------	--------------

**TOTAL:**

**Number of Papers published in non peer-reviewed journals:**

---

**(c) Presentations**



Donald W. Brenner, North Carolina State University:

1. "Role of Theory and Modeling in the Development of New Materials and Structures", Department of Mechanical and Materials Engineering, Duke University, January 2011. (invited)
2. 'New Insights into Nanometer-Scale Structure and Dynamics from Atomic and Multi-Scale Modeling', Plenary Lecture, Computational Engineering and Science/HPP: Enabling New Discoveries, Lehigh University, October 2009. (invited)
3. 'Using Atomic and Multiscale Modeling to Advance New Technologies: Simulations of Au Contacts in RF-MEMS and Shock Sensitivity of Energetic Materials, University of North Texas, Denton Tx, February 20, 2009. (invited)
4. 'Molecular Simulations of the Influence of Morphology on Initiation Sensitivity', 4th Advanced Energetics Technical Exchange, Fort Belvoir, Alexandria, Va, January 22, 2008. (invited)
5. 'A Molecular Dynamics Study of Model Energetic Crystals under Shock Loading', Y. Shi and D. Brenner, MRS National Meeting, Boston, Nov. 26, 2007.
6. 'Detonation Sensitivity of Defected Energetic Crystals under Shock Loading', Y. Shi and D. Brenner, Gordon Research Conference on Energetic Materials, Tilton, N.H. June 15-20, 2008.

Steven J. Stuart, Clemson University:

7. Stuart, S.J., "Recent Developments in Bond-Order Potentials", Workshop on Next-Generation Force Fields for Nanoscience, Oak Ridge National Laboratory, Oak Ridge, TN (September 15, 2010).
8. Stuart, S.J., "Recent Developments in Bond-Order Potentials, and Parallel Parameterization Methods", 5th Meeting on Reactive Potential Development, Penn State, State College, PA (October 13, 2010).
9. Stuart, S.J., "Parallel Parameterization of Models with Noisy Simulation Data", TMS 2011 Annual Meeting, San Diego, CA (February 28, 2011).
10. Stuart, S.J., "Empirical Bond-Order Potentials for Covalent Materials", High Fidelity 3D Multiscale Materials Modeling and Experimental Analysis Workshop, Engineer Research and Development Center, Vicksburg, MS (August 2, 2011).

Thomas D. Sewell, University of Missouri:

11. Keynote Speaker, Plasticity '11, Symposium on Phase Transformations and Mechanochemistry; Puerto Vallarta, Mexico; 3-8 January 2011
12. Invited Speaker, Pacificchem 2010; Symposium on Chemistry and Material Science at High Pressure; 16-20 December 2010
13. Colloquium Speaker, Institute for Shock Physics; Washington State University; Pullman, WA; 15 September 2010

**Number of Presentations:** 13.00

---

**Non Peer-Reviewed Conference Proceeding publications (other than abstracts):**

Received                      Paper

**TOTAL:**

**Number of Non Peer-Reviewed Conference Proceeding publications (other than abstracts):**

---

**Peer-Reviewed Conference Proceeding publications (other than abstracts):**

Received                      Paper

**TOTAL:**

**Number of Peer-Reviewed Conference Proceeding publications (other than abstracts):**

---

**(d) Manuscripts**

Received                      Paper

**TOTAL:**

Number of Manuscripts:

---

**Books**

Received

Paper

**TOTAL:**

**Patents Submitted**

---

**Patents Awarded**

---

**Awards**

Awards, Honors and Appointments:

---

Tahir Cagin, Texas A & M University:

1. College of Engineering William Keeler Faculty Fellow, 2010
  2. Federal Demonstration Partnership, TAMU Faculty Representative, 2008-present
  3. Chair, Materials Science and Engineering Program, September 2007 - December 2009.
- 

**Graduate Students**

<u>NAME</u>	<u>PERCENT SUPPORTED</u>	Discipline
Oscar U. Ojeda	1.00	
Bedri Arman	0.25	
Dheeraj Chahal	0.38	
Marcel Fallet	0.04	
Jaewoong Hur	0.04	
Mustafa Kucukkal	0.41	
Tugba Kucukkal	0.60	
Dulma Nugawela	0.00	
<b>FTE Equivalent:</b>	<b>2.72</b>	
<b>Total Number:</b>	<b>8</b>	

---

**Names of Post Doctorates**

<u>NAME</u>	<u>PERCENT SUPPORTED</u>
Yanhong Hu	1.00
Ali Siavosh-Haghighi	0.79
<b>FTE Equivalent:</b>	<b>1.79</b>
<b>Total Number:</b>	<b>2</b>

---

**Names of Faculty Supported**

<u>NAME</u>	<u>PERCENT SUPPORTED</u>	National Academy Member
Donald Brenner	0.50	No
Tahir Cagin	0.33	
Steven J. Stuart	0.17	
<b>FTE Equivalent:</b>	<b>1.00</b>	
<b>Total Number:</b>	<b>3</b>	

---

### Names of Under Graduate students supported

<u>NAME</u>	<u>PERCENT SUPPORTED</u>	Discipline
Daniel Dewer	0.50	
<b>FTE Equivalent:</b>	<b>0.50</b>	
<b>Total Number:</b>	<b>1</b>	

### Student Metrics

This section only applies to graduating undergraduates supported by this agreement in this reporting period

The number of undergraduates funded by this agreement who graduated during this period: .....	0.00
The number of undergraduates funded by this agreement who graduated during this period with a degree in science, mathematics, engineering, or technology fields:.....	0.00
The number of undergraduates funded by your agreement who graduated during this period and will continue to pursue a graduate or Ph.D. degree in science, mathematics, engineering, or technology fields:.....	0.00
Number of graduating undergraduates who achieved a 3.5 GPA to 4.0 (4.0 max scale):.....	0.00
Number of graduating undergraduates funded by a DoD funded Center of Excellence grant for Education, Research and Engineering:.....	0.00
The number of undergraduates funded by your agreement who graduated during this period and intend to work for the Department of Defense .....	0.00
The number of undergraduates funded by your agreement who graduated during this period and will receive scholarships or fellowships for further studies in science, mathematics, engineering or technology fields: .....	0.00

---

### Names of Personnel receiving masters degrees

<u>NAME</u>
<b>Total Number:</b>

---

### Names of personnel receiving PHDs

<u>NAME</u>	
Oscar U. Ojeda	
Bedri Arman	
Dheeraj Chahal	
<b>Total Number:</b>	<b>3</b>

---

### Names of other research staff

<u>NAME</u>	<u>PERCENT SUPPORTED</u>
Win Grace	0.78
<b>FTE Equivalent:</b>	<b>0.78</b>
<b>Total Number:</b>	<b>1</b>

---

### Sub Contractors (DD882)

1 a. North Carolina State University

1 b. Office of Contract and Grants

Leazar Hall Lower Level - MC

Raleigh NC 27695-7214

**Sub Contractor Numbers (c):**

**Patent Clause Number (d-1):**

**Patent Date (d-2):**

**Work Description (e):** General, Unified, Multiscale Modeling to Predict the Sensitivity of Energetic Materials

**Sub Contract Award Date (f-1):** 6/1/2005 12:00:00AM

**Sub Contract Est Completion Date(f-2):** 5/31/2011 12:00:00AM

---

1 a. Clemson University

1 b. Office of Sponsored Programs

Clemson SC 29634

**Sub Contractor Numbers (c):**

**Patent Clause Number (d-1):**

**Patent Date (d-2):**

**Work Description (e):**

**Sub Contract Award Date (f-1):** 6/1/2005 12:00:00AM

**Sub Contract Est Completion Date(f-2):** 5/31/2011 12:00:00AM

---

1 a. Texas A & M University

1 b. Department of Chemical Engineering

College Station TX 77842

**Sub Contractor Numbers (c):**

**Patent Clause Number (d-1):**

**Patent Date (d-2):**

**Work Description (e):**

**Sub Contract Award Date (f-1):**

**Sub Contract Est Completion Date(f-2):** 5/31/2011 12:00:00AM

---

**Inventions (DD882)**

## Scientific Progress

Donald W. Brenner, North Carolina State University:

### Accomplishments for Reporting Period

- Demonstrated atomic three-dimensional homogeneous detonation from hotspots spontaneously formed during cook-off.
- These are the first reported atomic simulations of detonation that is not induced by shock stimulus.
- Simulations showed multiple hot spots that self-extinguish unless they reach a critical radius above which they grow to a full detonation. This is the first clear demonstration of critical radii for detonation.
- The critical radius for hotspot growth gleaned from the simulations matches Frank-Kamenetskii classical initiation theory.
- This is the first connection between atomic simulations of detonation and classical initiation theory.
- The rate of product formation shows Arrhenius behavior with respect to the annealing temperature with an activation energy of about 0.5 eV. This is roughly half of that determined previously for thermal decomposition. The origin of the different values is not yet understood.
- New equations were proposed for the extent of detonation based on a combination of Johnson-Mehl-Avrami-Kolmogorov phase transformation equations and an Eyring chemical dynamics expression.
- In nucleation theory applied to phase transitions, parameters in the Johnson-Mehl-Avrami-Kolmogorov expression can be related to the nucleation mechanism; e.g. homogeneous random nucleation or nucleation from non-random defects such as grain boundaries. The new mathematical expression introduced in this work has the potential to yield similar insight into the dynamics of detonation initiation.

Tahir Cagin, Texas A&M University:

### Accomplishments for Reporting Period

- Ab initio quantum chemistry level determination of potential energy surfaces for rotational degrees of freedom in selected energetic materials for phase behavior
- Density Functional Theory level determination of phase behavior and Equations of State for NM, PETN, TATB, HMX, FOX-7
- Electronic band structures and charge distributions from DFT as a function of applied pressure
- Adiabatic isotropic/anisotropic compression behavior NM, PETN, TATB, HMX
- Vibrational spectra (IR-Raman) of selected systems
- Anisotropic elastic properties and their pressure dependence for NM, TATB, PETN, and HMX
- Influence of van der Waals corrections on structure and properties of munitions
- Effects of extended defects in high explosive crystals
- Ab initio molecular dynamics simulations of NM using Car Parrinello Method

Steven J. Stuart, Clemson University:

### Accomplishments for Reporting Period

- Extension of multicomponent models to additional atom types, now including H,C,N,O,F,Si
- Development of new simplex optimization strategies to accommodate stochastic data
  - o One new method applies the previous pairwise comparison only for specific types of simplex operations, rather than all of them. This method is even less prone to premature collapse of the simplex than prior methods.
  - o One new method applies both the “max noise” method that compares the internal standard deviation of the vertices to the noise estimate at each vertex, along with pairwise comparison of individual vertices at a specific confidence level.

- Detailed analysis and comparison of simplex optimization strategies. The combined max noise + pairwise comparison strategy was found to be the most efficient for the trial optimization problems studied.
- Deployment of the automated, parallel, stochastic simplex optimization for bond-order potential parameterization.
- Parameterization of the electrostatic terms in the bond-charge CHO model
- Parameterization of the covalent bonding terms in the CHO model
- Parameterization of the angular terms in the CHO model
- Validation of the bond-order AIREBO model in the LAMMPS large-scale parallel molecular dynamics code.
- Extension of the LAMMPS implementation of AIREBO to multiple atom types.

Donald L. Thompson and Thomas D. Sewell, University of Missouri:

#### Scientific Progress and Accomplishments during Reporting Period

- Developed and published methods for simulating and analyzing crystallization of nitromethane from the melt in contact with various crystal faces.
- Developed and published methods for the analysis of shock-induced phase changes in molecular crystals, with specific application to the study of shock waves shocks along [100], [010], [001], [110], [011], [101], and [111] directions in crystalline nitromethane.
- Developed and published methods for calculations of pressure-dependent vibrational spectra at 0 K and at finite temperatures, with specific application to the hydrostatic compression of nitromethane crystal.
- Reported on combined theoretical and experimental studies of anomalous shock compression response in (021)-oriented RDX single crystals.
- Completed an invited book chapter on simulating deformation processes in energetic materials.

#### **Technology Transfer**

## **Final Performance Report**

### **General, Unified, Multiscale Modeling to Predict the Sensitivity of Energetic Materials (Grant # 48101-EG-MUR)**

#### **Report Period:**

June 1, 2005 – May 31, 2011

#### **Principal Investigator:**

Donald L. Thompson

#### **Research Team:**

**Thomas D. Sewell** (co-PI), University of Missouri-Columbia

**Donald Brenner** (subcontractor), North Carolina State University

**Steven J. Stuart** (subcontractor), Clemson University

**Tahir Cagin** (subcontractor) Texas A&M

## Objective

The goal of this theoretical/computational research program was to develop practical methods for predicting fundamental properties and processes in energetic materials and to gain a better understanding of how those processes affect initiation sensitivity of energetic materials subjected to mechanical and thermal loading. The aim was to establish a unified framework within which to understand and predict the underlying physical-chemical mechanisms and controlling parameters that dictate material responses to stimuli over broad spatial and temporal scales. Conventional and novel materials for insensitive munitions were studied, with emphasis placed on the intra- and inter- molecular interactions in organic energetic materials.

## Summary of Research Accomplishments

The overall project, although substantially integrated, can be viewed as comprising the following main topics:

- Medium- and Large-Scale Atomic Simulations of Non-Reactive Dynamical Phenomena
- Atomic and Multiscale Modeling of Thermal and Shock-Induced Initiation;
- Accurate Reactive Potentials for Simulating Energetic Materials
- Anisotropic Equation of State Properties for HE Crystals using Quantum Mechanical and Classical Mechanical Methods

A wide range of theoretical and computational approaches was used in an overlapping and integrated fashion to achieve the goals of the project. Among these methods used, phenomena studied, and results obtained are:

- A multi-scale modeling method was developed based on a bridging scale decomposition scheme for simulating coupled continuum-level hotspot formation and chemical dynamics.
- Molecular dynamics (MD) methods were extended to sufficient temporal and spatial scales to simulate energy localization and initiation of chemistry under practical conditions of thermo-mechanical load.
- Equation of state, anisotropic response, and properties of energetic materials were determined to establish a relationship to sensitivity.
- *Ab initio* DFT methods – both plane wave and Gaussian basis set approaches – were used for studying isotropic and anisotropic EOS of energetic materials.
- *Ab initio* results obtained at 0 K were corrected to account for entropic (*i.e.*, finite temperature) effects through the use of phonon/vibrational density of states.



- Classical MD was used to include the effect of anharmonicity through the use of equilibrium fluctuation formulas derived from classical statistical mechanics, finite elasticity theory, and statistical thermodynamics.
- Careful analysis of chemical shock dynamics and threshold shock strengths for inelastic deformation and onset of chemistry was performed to understand sub-continuum factors that contribute to sensitivity, and to aid in the development of analytic models that can be scaled to the micron/microsecond scales.
- Using MD simulation data, a new quasi-thermodynamic theory was developed based on existing nucleation and phase transition concepts that connects homogenous hot spot formation and the transition to detonation to atomic-scale chemical processes.
- New temporal and spatial scaling relations were developed based on kinetic Monte Carlo concepts that connect picosecond/nanometer detonation from a MD simulation to microsecond/micrometer hotspot initiation.
- Computationally efficient many-body reactive potentials were developed for modeling shock-induced molecular dissociation and detonation initiation.
- Improvements were made to bond-order models to account for changes in chemical environment.
- A bond-order model was developed that includes charge transfer *via* adaptive bond charges.
- Assessment of three different methods (local descriptors, Huckel methods, and equations of state) for describing the charge-transfer characteristics of a simulated material was performed.
- Addition of covalent bond screening methods to next-generation bond-order models was accomplished.
- Automated, parallel force field parameterization methods were developed.
- Molecular dynamics simulations of shock waves propagating in oriented single crystals were analyzed in detail to extract information concerning:
  - Mechanisms by which such materials relax when mechanically or thermally shocked to states above the elastic or chemical stability limit;
  - Spatio-temporal evolution of local thermodynamic conditions (e.g., temperature, density, phase) in the shocked material; and
  - Fundamental timescales for energy transfer from a shock wave into the vibrational degrees of freedom of the system.
- Calculations of pressure-dependent spectral properties of molecular crystals were performed to provide validation of force field models and to interpret experimental data.
- Simulations of crystallization of oriented nitromethane crystals in contact with the pure melt of the same substance were performed to understand the processes by which the crystallization disorder-order transition occurs.

## **Relevance to Army**

This project contributed to long-term goal to provide reliable predictive computational tools to aid in the search for new and safer energetic materials and to predict the safety and reliability of existing ones under both normal and abnormal conditions. Our specific aim was to provide the basis for formulating, for complicated, mechanically anisotropic molecular materials, improved thermal-mechanical-chemical constitutive models. Our work, in collaboration with the Caltech and UNLV MURI projects, has provided an improved understanding of the essential factors that control initiation sensitivity. This project provides DoD with the basis for formulating, for complicated, mechanically anisotropic molecular materials, improved thermal-mechanical-chemical constitutive models that can employ realistic thermal chemical reaction rates based on understanding of processes that occur on sub-grid spatial scales rather than the empirically fitted “effective” rates that are only valid on millimeter or larger spatial scales and within relatively narrow calibration intervals in the parameter space for a given formulation. This improved knowledge is especially important for predictions of initiation for a material that has evolved, whether by slow physical or chemical aging processes or by sub-critical mechanical insult (to cite two examples), to a state that differs significantly from the one for which a homogenized model parameterization would have been calibrated originally for use in engineering simulations of the response of nominal material.

The models and modeling techniques developed in this project are applicable to the condensed phases of a wide range of materials of current and potential interest in the discovery and design of more insensitive munitions. An important contribution to DoD interests is an improved understanding of the essential factors that determine sensitivity. The information can be, and is being, upscaled into the continuum-model for energetic material response under development by Professor Ortiz at Caltech. Those multiscale modeling techniques will be applicable to condensed phases of a wide range of materials of current and potential future interest to DoD. This project makes available to DoD the full power of computational modeling that is possible given the current state of theory, experiments, and computer speeds and capacity. This is expected to result in significant savings in manpower and related costs in the synthesis, formulating, testing, and other practical labor involved in the exploration for new materials of acceptable sensitivity and power.

## **Summary List and Reprints of Publications Supported by the MURI**

Below is a complete list of published or in-press peer-reviewed journal articles and book chapters that were supported by this MURI project. The report concludes with reprints of each of the publications included in the list.

### **2007:**

- Y. Shi and D. W. Brenner, *Simulated thermal decomposition and detonation of*

*nitrogen cubane by molecular dynamics*, J. Chem. Phys. **127**, 134503 (2007).

- V. Bolesta, L. Zheng, D. L. Thompson, and T. D. Sewell, *Molecular Dynamics Simulations of Shock Waves Using the Absorbing Boundary Condition: A Case Study of Methane*, Phys. Rev. B **76**, 224108 (2007).

#### **2008:**

- Y. Shi and D. W. Brenner, *Jetting and Detonation Initiation in Shock-induced Collapse of Nanometer Scale Voids*, J. Phys. Chem. C **112**, 6263 (2008).

- M. J. Cawkwell, T. D. Sewell, L. Zheng, and D. L. Thompson, *Shock-induced Shear Bands in an Energetic Molecular Crystal: Application of Shock-front Absorbing Boundary Conditions to Molecular Dynamics Simulations*, Phys. Rev. B **78**, 014107 (2008).

- A. Liu and S. J. Stuart, *Empirical Bond-order Potential for Hydrocarbons: Adaptive Treatment of van der Waals Interactions*, J. Comput. Chem., **29**, 601 (2008).

- Y. Shi and D. W. Brenner, *Hotspot Formation in Shock-Induced Void Collapse*, Solid State Phenom. **139**, 77 (2008).

- Y. Shi and D. W. Brenner, *Molecular Simulation of the Influence of Interface Faceting on the Shock Sensitivity of a Model Plastic Bonded Explosive*, J. Phys. Chem. B **112**, 14898 (2008).

#### **2009:**

- A. Siavosh-Haghighi, R. Dawes, T. D. Sewell, and D. L. Thompson, *Shock-induced melting of (100)-oriented nitromethane: Structural relaxation*, J. Chem. Phys. **131**, 064503 (2009).

- R. Dawes, A. Siavosh-Haghighi, T. D. Sewell, and D. L. Thompson, *Shock-induced melting of (100)-oriented nitromethane: Energy partitioning and vibrational mode heating*, J. Chem. Phys. **131**, 224513 (2009).

- D. Bedrov, J. Hooper, G. D. Smith, and T. D. Sewell, *Shock-induced transformations in crystalline RDX: A uniaxial constant-stress Hugoniotat molecular dynamics simulation study*, J. Chem. Phys. **131**, 034712 (2009).

- J. D. Coe, M. S. Shaw, and T. D. Sewell, *Optimal sampling efficiency in Monte Carlo simulation with an approximate potential*, J. Chem. Phys. **130**, 164104 (2009).

- J. D. Coe, T. D. Sewell, and M. S. Shaw, *Nested Markov chain Monte Carlo sampling of a density functional theory potential: Equilibrium thermodynamics of dense fluid nitrogen*, J. Chem. Phys. **131**, 074105 (2009).

#### **2010:**

- A. Siavosh-Haghighi, T. D. Sewell, and D. L. Thompson, *Molecular dynamics study of the crystallization of nitromethane from the melt*, J. Chem. Phys. **133**, 194501 (2010).

- A. Siavosh-Haghighi, R. Dawes, T. D. Sewell, and D. L. Thompson, *A molecular dynamics study of classical vibrational spectra in hydrostatically compressed crystalline nitromethane*, J. Phys. Chem. B **114**, 17177 (2010).
- K. J. Ramos, D. E. Hooks, T. D. Sewell, and M. J. Cawkwell, *Anomalous hardening under shock compression in (021)-oriented cyclotrimethylene trinitramine single crystals*, J. Appl. Phys. **108**, 066105 (2010).

#### **2011:**

- L. He, T. D. Sewell, and D. L. Thompson, *Molecular dynamics simulations of shock waves in oriented nitromethane single crystals*, J. Chem. Phys. **134**, 124506 (2011).
- O. U. O. Mota and T. Cagin, *Anisotropic behavior of energetic materials at elevated pressure and temperature*, Journal of Loss Prevention in the Process Industries **24**, 805 (2011).
- O. U. Ojeda and T. Cagin, *Hydrogen bonding and molecular rearrangement in 1,3,5-triamino-2,4,6-trinitrobenzene under compression*, J. Phys. Chem. B (in press, September 2011).
- L. He, T. D. Sewell, and D. L. Thompson, *Molecular dynamics simulations of shock waves in oriented nitromethane single crystals: Plane-specific effects*, J. Chem. Phys. (submitted).

#### **Book Chapters**

- O. U. Ojeda and T. Cagin, *Multiscale modeling of crystalline energetic materials*, in “Computers, Materials, and Continua,” S. Kalidindi, N. Ramakrishnan, R. Rolfes, V. Tewary, and S. N. Atluri Eds. (Tech Science Press, 2010) Vol. 16, p. 127.
- R. H. B. Bouma, A. E. D. M. van der Heijden, T. D. Sewell, and D. L. Thompson, *Simulations of deformation processes in energetic materials*, in “Numerical Simulations of Physical and Engineering Processes,” Jan Awrejcewicz, Ed. (InTech Open Access Publisher, Croatia, 2011).

# Simulated thermal decomposition and detonation of nitrogen cubane by molecular dynamics

Yunfeng Shi<sup>a)</sup> and Donald W. Brenner

*Department of Materials Science and Engineering, North Carolina State University,  
Raleigh, North Carolina 27587-7907, USA*

(Received 11 July 2007; accepted 14 August 2007; published online 2 October 2007)

We present simulations of a model molecular solid of nitrogen cubane subject to thermal agitation and mechanical shock. A new approach, a reactive state summation potential, has been used to model nitrogen cubane dissociation. At elevated temperatures, the system decomposes to  $N_2$  mixed with a small amount of oligomeric nitrogen. When subject to shock loading the system detonates above some critical threshold after which a shock front is self-sustained by the energy release from chemical reactions at a constant intrinsic speed. This is the first example of a fully three-dimensional atomic simulation of a chemically-sustained detonation. The spatial confinement of the shock front results in longer chain intermediates than in the case of thermal decomposition, suggesting that shock intermediates can be structurally very different from the same material subject to comparable temperatures and pressures. © 2007 American Institute of Physics. [DOI: 10.1063/1.2779877]

## I. INTRODUCTION

Solids under shock loading can exhibit various phenomena such as phase transformation,<sup>1</sup> plastic deformation,<sup>2</sup> and chemical reaction,<sup>3</sup> which are crucial in discovering new phases, studying dynamical mechanical responses, and understanding condensed phase chemistry. However, it is very difficult to achieve those extreme conditions experimentally and measuring various physical values is even harder. In particular, the motion of detonation fronts in solid explosives occurs on the spatial scale of tens of nanometers within a time scale of picoseconds. Although advances in experimental techniques such as high resolution transmission electron microscopy and time-resolved molecular spectroscopy are providing the capability to probe subnanometer features or physical processes with nanosecond resolution,<sup>4</sup> it is still impractical to achieve both spatial and temporal resolutions simultaneously. Theoretical frameworks such as the classic Zel'dovich, von-Neumann, and Doering continuum theory concerns the conservation of mass, balance of momentum, and energy in the case of planar shocks, but contains no description of atomic-scale defects or anisotropy of the molecular crystal. More importantly, the material inside the reaction zone is far from equilibrium; thus the assumption that thermodynamic variables (other than chemical composition) are in equilibrium may not hold.

While the spatial and temporal scales associated with shock dynamics are difficult to probe experimentally, these scales are ideal for molecular dynamics (MD) simulations.<sup>5</sup> One of the challenges to using MD simulation in modeling physical processes involving chemical reactions is the design of an appropriate interatomic potential.<sup>6</sup> A range of interatomic potential forms have been developed over the last 20 yrs that have incorporated chemical reactivity into simulations of shock and related phenomena, including chemically-

sustained detonations. Examples include predissociative models,<sup>7</sup> a London-Eyring-Polanyi-Sato (LEPS) potential,<sup>8</sup> bond-order based potentials,<sup>9-15</sup> tight binding Hamiltonians,<sup>16-18</sup> and first principles methods.<sup>19-21</sup> The first potentials to demonstrate intrinsic detonation velocities in an atomic simulation in one and two dimensions were the LEPS (Ref. 8) and the "A-B" model,<sup>9</sup> respectively. The latter model, which is based on a bond-order formalism,<sup>22</sup> is computationally efficient such that large-scale two- and three-dimensional simulations can be carried out, yet still captures generic but essential features of chemical reactivity. Other related analytic potentials have been developed since, most notably the ReaxFF potentials developed by Goddard *et al.*,<sup>12,14,15</sup> that attempt to model the details of specific systems rather than generic chemistry, but at the cost of computational efficiency.

Each of these approaches to modeling interatomic forces for shock simulations have their relative merits, and in some cases severe limitations. In predissociative models, for example, chemical energy is released through bond breakage, instead of bond formation. This can lead to the nonphysical partitioning of the energy such that no energy goes initially into intramolecular vibration.<sup>23</sup> Generic studies such as the A-B model, which emphasize computational efficiency, have focused primarily on energetic materials of small molecules where all energy release comes from bond formation. These small molecule simulations, while providing critical examples of self-sustaining shock chemistry, may have behavior that is very different from energetic materials composed of relatively large molecules. For example, vibrational relaxation in large molecules will be significantly different from small molecules, and for large molecules a high fraction of the energy release can come from dissociation into fragments. It should also be noted that a simulated atomic-scale

<sup>a)</sup>Electronic mail: YSHI2@NCSU.EDU

shock front sustained by chemical reaction with an intrinsic velocity has only been demonstrated in one and two dimensions.<sup>8,9</sup>

Reported in this article are the results of simulations of a model molecular solid of nitrogen cubane subject to thermal agitation and mechanical shock. These simulations use a new approach to modeling large-scale reactivity in a covalent system that retains computational efficiency while still allowing a physical treatment of chemical reactions and intermediate states. This relatively simple potential used to describe condensed phase reaction of a large molecule is intended to provide a bridge between generic treatments such as the “A-B” model and the detailed but more complicated descriptive potentials such as ReaxFF. As discussed below the simulations show the formation of N<sub>2</sub> and short-chain nitrogen clusters as products of both thermal and shock decomposition. In the case of shocks, decomposition of multiple molecules is spatially confined to the shock front as opposed to thermal decomposition that occurs randomly throughout the simulation. The former conditions result in longer chain intermediates than in the case of thermal decomposition, suggesting that shock intermediates can be structurally very different from the same material subject to the comparable temperatures and pressures.

## II. REACTIVE STATE SUMMATION POTENTIAL

The reactive state summation potential is an extension of a concept that was originally implemented to control angular

terms in modeling silica<sup>24</sup> and boron oxide.<sup>25</sup> During a chemical reaction, the system starts from the state of the reactant in the potential energy landscape. Driven by thermal agitation at high temperature or mechanical agitation under shock, the system evolves over the chemical reaction barrier toward a product state. The state of the reactant, the final products, and other possible intermediates, which we refer to as reactive states, determines the thermodynamics and kinetics of the chemical reaction. Each of these reactive states can be quantified and distinguished by a reaction coordinate. The central idea of this formulation is to model each state separately, then combine them together through a reaction-coordinate-dependent weighting function. Therefore, individual force fields can be turned on or off depending on the reaction coordinate. If each reactive state is modeled by a conventional two-body interatomic potential, the total potential energy is the sum of those potentials modulated by a weighting function

$$PE = \frac{1}{2} \sum_{i \in N} \sum_{j \in N} \sum_s w_i^s E^s(r_{ij}), \quad (1)$$

where  $i, j$  loops over  $N$  atoms,  $s$  loops over a number of reactive states including any number of reactants, products and intermediates and  $E^s(r_{ij})$  is the pair potential for reactive state  $s$ . The weighting function  $w_i$  is written as

$$w_i = e^{-A(CN_i - \overline{CN})^2}, \quad (2)$$

$$CN_i = \sum_{j=N} f_{CN}(r_{ij}), \quad (3)$$

$$f_{CN}(r_{ij}) = \begin{cases} 1 & r_{ij} < r_{ij}^c - 2w \\ \frac{1}{2} + \frac{1}{2} \cos \left[ \frac{\pi}{2} \left( \frac{r_{ij} - r_{ij}^c + w}{w} + 1 \right) \right] & r_{ij}^c - 2w < r_{ij} < r_{ij}^c \\ 0 & r_{ij} > r_{ij}^c \end{cases}. \quad (4)$$

The parameter  $A$  controls the width of the weighting function.  $CN$  is the coordination number, which is the sum of a neighbor-counting function  $f_{CN}$ .  $f_{CN}$  is a smooth function changing from 1 to 0 in a transition region of width  $2w$  from  $r_{ij}^c - 2w$  to  $r_{ij}^c$  as the interatomic distance increases.  $\overline{CN}$  is the coordination number for a specific reactive state that has to be unique among all states. Therefore, the reaction coordinate is represented by the coordination number for its simplicity computationally, although there are many alternative ways to define such a quantity.

Here a nitrogen RSS force field is given that considers the chemical reaction of N<sub>8</sub> nitrogen cubane as it decomposes in the solid state into N<sub>2</sub> molecules. Therefore the reactant ( $r$ ) is chosen to be N<sub>8</sub> nitrogen cubane and the prod-

ucts ( $p$ ) are N<sub>2</sub> nitrogen molecules. The total energy is the weighted sum of two reactive states plus a Van der Waals (VDW) term as well as a hard sphere (HS) repulsion term

$$PE = \frac{1}{2} \sum_{i \in N} \sum_{j \in N} (w_r E^r(r_{ij}) + w_p E^p(r_{ij}) + E^{HS}(r_{ij}) + E^{VDW}(r_{ij})). \quad (5)$$

It should be noted that there is no explicit angular constraints for N<sub>8</sub>. Instead, the constraint on the coordination ensures the cubic shape of the molecule. To accurately describe the energetics of other threefold-coordinated phases such as the black phosphorous or cubic gauche structures, angular constraints would have to be included. Inclusion of these terms,

TABLE I. Parameters for the RSS potential for nitrogen.

	CN	A	B	$r_{ij}^c$ (Å)	$w$ (Å)	$\varepsilon$ (eV)	$\sigma$ (Å)	$\rho$ (Å <sup>-1</sup> )	Cutoff (Å)
Reactant	3	1.15	1.15	2.05	0.1	1.6	1.5	0.90	2.05
Product	1	1.30	1.30	2.05	0.1	9.8	1.1	3.82	2.05
VDW				2.05	0.1	0.0005	2.55		3.75
HS		0.1				20	0.95		0.95

however, would reduce the computational efficiency of the model. As stated above, because our intent is to produce a potential that is intermediate in complexity between the  $A$ - $B$  and more descriptive potentials, these terms are neglected. Both reactive states are modeled by a pair-wise Morse-type potential

$$E(r_{ij}) = \varepsilon(e^{2\rho(\sigma-r_{ij})} - 2e^{\rho(\sigma-r_{ij})})f_{\text{cutoff}}(r_{ij}), \quad (6)$$

$$f_{\text{cutoff}}(r_{ij}) = f_{\text{CN}}(r_{ij})^B, \quad (7)$$

$$E^{\text{HS}}(r_{ij}) = \begin{cases} \varepsilon \cdot e^{A/(r_{ij}-\sigma)} & r_{ij} < \sigma, \\ 0 & r_{ij} \geq \sigma, \end{cases} \quad (8)$$

$$E^{\text{VDW}}(r_{ij}) = 4\varepsilon \left( \left( \frac{\sigma}{r_{ij}} \right)^{12} - \left( \frac{\sigma}{r_{ij}} \right)^6 \right) \cdot (1 - f_{\text{CN}}(r_{ij})). \quad (9)$$

The cutoff function ensures the finite range of the covalent bonding as well as the computational efficiency. The potential parameters can be readily obtained from the bond length, bond strength, and bond vibration frequency from experiments or first principles calculations, which are listed in Table I.<sup>26,27</sup> The hard sphere repulsion term is to ensure that no atoms overlap for coordination states other than those two reactive states considered in this simple potential model. The intermolecular interaction is a conventional 12–6 Lennard-Jones potential. Because the inter- or intra-molecular interactions are calculated for all atoms in this RSS formalism, the short covalent bond distance between atoms within one molecule would result in a large positive potential energy due to the repulsive regime of the Lennard-Jones interaction. Therefore, the Lennard-Jones potential is modulated to zero within the covalent bonding distance as in Eq. (9). This approach is similar to the treatments of other reactive force fields.<sup>28</sup> Because no data is available for the nitrogen cubane-cubane Van der Waals interaction experimentally or computationally, a relatively weak potential energy depth has been chosen to keep the dominance of the intramolecular force in the cubane-cubane interaction. The equilibrium distance of this Van der Waals interaction is also

set to be small for computational efficiency. There are also no reports on the crystalline state of nitrogen cubane. Similar cubic shaped molecules, such as C<sub>8</sub>H<sub>8</sub> cubane,<sup>29</sup> normally have a rhombohedral crystalline state. However, the ratio of cube-cube distance over the cube size for C<sub>8</sub>H<sub>8</sub> cubane is about 3.5, which is larger than the ratio (2.9) for the current model nitrogen cubane. It is conceivable that as the cube-cube separation decreases, simple cubic will eventually become the choice for the densest packing. Therefore, we choose an apparent simple cubic packing to construct the nitrogen cubane crystal. The lattice constant is 0.4313 nm. This yields a density of 2.32 g/cm<sup>3</sup> that is within the range of 2.29–2.65 g/cm<sup>3</sup> estimated from empirical methods.<sup>30</sup> The physical values for N<sub>8</sub> and N<sub>2</sub> are given in Table II for this model along with comparable literature values.

The advantage of this RSS formalism is its simplicity and flexibility. Due to the absence of long-range interactions and a simple switching between inter- and intra-molecular interactions, the computing time for the force calculation for RSS nitrogen potential scales linearly with system size. It is also straight forward to include multiple species, angular dependency and multiple products. Furthermore, it is also possible to combine two sets of parameters for the same potential or totally different force fields in a multiscale simulation approach.

### III. THERMAL DECOMPOSITION

A series of thermal decomposition simulations were performed using the RSS potential. Simulations were carried out with N<sub>8</sub> cubane crystals within an NVT ensemble. The initial system consists of 216 N<sub>8</sub> cubane molecules or 1728 nitrogen atoms with a fixed density of 2.32 g/cm<sup>3</sup>.

For a reactive system that has a single reactant and one possible product, the chemical reaction is accomplished by individual molecules going through a thermally activated reaction path. The extent of the reaction can be monitored by the average potential energy

TABLE II. Physical values for N<sub>8</sub> and N<sub>2</sub>.

	Bond length (Å)		Bond angle (°)	Vibration period (fs)	Atomization energy per atom (eV)	
	N <sub>8</sub>	N <sub>2</sub>			N <sub>8</sub>	N <sub>2</sub>
RSS model	1.52	1.10	90.0	14.14	−2.41	−4.91
Literature values	1.52	1.10	90.0	14.13	−2.38	−4.90
	26	27	26	26	26	27



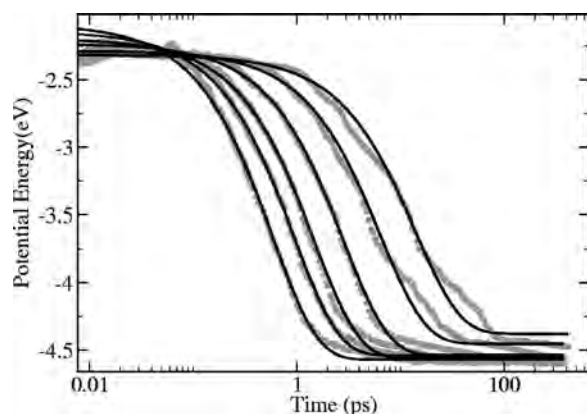


FIG. 1. Average potential energy evolution (gray dots) as a function of time at temperatures 2030, 2320, 2901, 3481, 4062, and 4642 K, from right to left. Solid lines are nonlinear fitting to Eq. (10) assuming a constant reaction rate for each temperature.

$$\overline{PE} = PE_p + (PE_r - PE_p)e^{-Rt}, \quad (10)$$

where  $\overline{PE}$  is the average potential energy per atom,  $PE_r$  and  $PE_p$  are the potential energy for the reactant and product respectively,  $R$  is the reaction rate at the given temperature, and  $t$  is the time. By monitoring the average potential energy evolution of the system,  $R$ ,  $PE_r$ , and  $PE_p$  can be obtained at various temperatures through nonlinear fitting procedures as plotted in Fig. 1. The reaction rate follows the Arrhenius rate law, as demonstrated by Fig. 2, which is characterized by an activation energy barrier of 1.0 eV. We found that there is no need to include an equilibration-induction time in Eq. (10), as was done in Ref. 15, because the reaction rate is well behaved without the addition of a fitting parameter.

The product at the end of the reaction is composed of mostly  $N_2$  nitrogen molecules (onfold coordinated) with a small percentage of nitrogen oligomers (twofold coordinated). The nitrogen chains are quasi-one-dimensional with a maximum cluster size of 6 as shown in Fig. 3(a). The product after reacting at 2030 K for 380 ps consists of about 56%  $N_2$  and 44% oligomeric nitrogen in terms of atomic percentage as shown in Fig. 4. As the cookoff temperature increases, there is less oligomeric nitrogen in the final product. The average potential energy per atom for twofold-coordinated

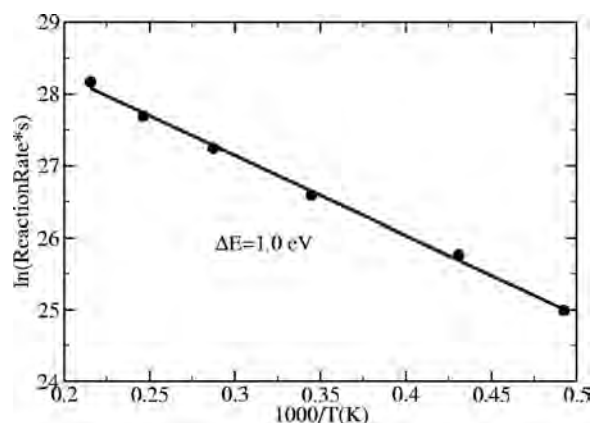


FIG. 2. Reaction rates from nonlinear fitting of the average potential energy evolution according to Eq. (10) as a function of reaction temperature from 2030 to 4642 K. The slope of this Arrhenius plot is 1.0 eV.

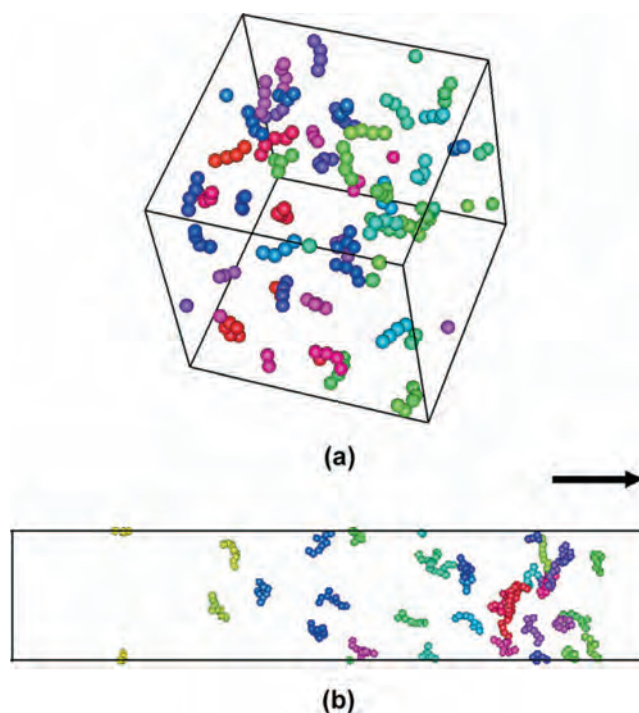


FIG. 3. (Color) Cluster analyses for the reaction product (a) a nitrogen cubane system at 2030 K after 380 ps. Clusters with four or more nitrogen atoms are shown; (b) a nitrogen cubane system that is subject to a shock initiated by a flyer plate (10.5 km/s) after 5 ps. Clusters with eight or more nitrogen atoms are shown. For both figures, two atoms are considered connected if the separation distance is smaller than 0.135 nm, which is the upper bound of the first peak of the pair correlation function. Atoms in the same cluster have the same color. The size of the box in (a) and the height of the box in (b) are both approximately 2.6 nm. The right end of the box in (b) indicates the shock front position. The shock propagates from left to right as shown by the arrow.

nitrogen is approximately  $-3.0$  eV, which is much higher than the onfold-coordinated nitrogen which is about  $-4.9$  eV. Therefore, chainlike polymer clusters are metastable energetically and tend to overcome the dissociation barrier and turn into smaller segments at higher temperature.

Although there is no explicit term for twofold-coordinated oligomeric nitrogen in Eq. (5), its energetics is determined by the weighted sum of one- and threefold-coordinated states. Moreover, the twofold-coordinated state is a

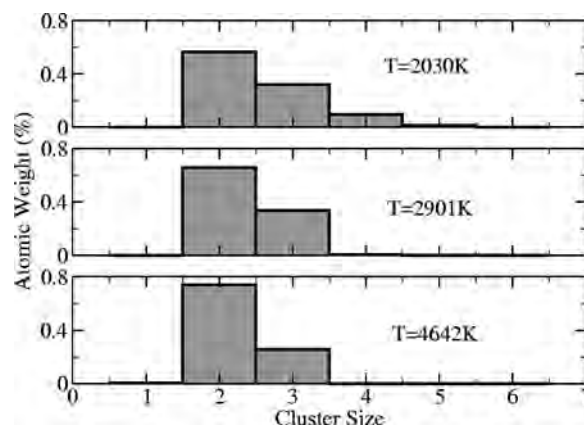


FIG. 4. Cluster size distributions in terms of atomic weight for thermal decomposition simulations at different temperatures for 380 ps. Clusters with cluster size 2 are diatomic nitrogen  $N_2$ .



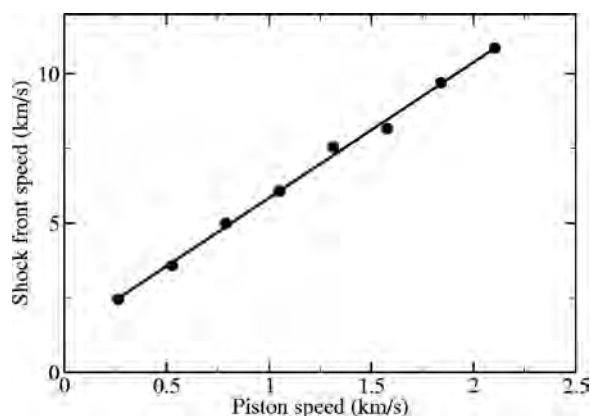


FIG. 5. Shock front speeds plotted as a function of piston speeds. The sound velocity is about 1.3 km/s, which is extrapolated as the shock front speed at zero piston speed. A smaller system that spans  $2.6 \times 2.6 \times 52$  nm<sup>3</sup> is used to obtain this data.

natural intermediate state in the transition from threefold-coordinated to onefold-coordinated state, given that simultaneous bond breaking is less likely than bond breaking one by one. Such metastable polymeric form for nitrogen has also been predicted previously by first principles methods.<sup>31</sup> The presence of oligomeric nitrogen may also be due to the short time scale of the system with such a high temperature and high pressure. We note that the fit in Fig. 1 deviates from the function at low temperatures and long times, which suggests that there may be multiple reaction barriers. Nonetheless, the overall chemical reaction can be characterized by a single reaction barrier as shown in Fig. 2. This may be because: (1) the secondary reaction from N<sub>8</sub> cubane to oligomeric nitrogen has a similar reaction barrier; (2) the amount of twofold-coordinated nitrogen is small, especially in the high temperature regime.

#### IV. SHOCK SIMULATIONS OF NITROGEN CUBANE

To simulate chemical reactions caused by mechanical shock waves, both moving pistons and flyer plates are used to initiate shock waves. A simple cubic N<sub>8</sub> cubane crystal with 4320 molecules (34560 atoms) in a box of  $2.6 \times 2.6 \times 52$  nm<sup>3</sup> is subject to shock. The system is periodic in the two directions perpendicular to the shock propagation direction (Z direction). The initial system rests at 0 K. There is no thermostat or barostat coupled to the shock simulations. To simulate shocks formed by a moving piston, the left (negative Z direction) most layer of material consisting of 36 molecules are held rigid while moving to the right (positive Z direction) with a constant piston speed. To simulate shocks formed by a flyer plate, the same left most layer is given an initial velocity without restricting their dynamics thereafter.

The shock velocity scales approximately linearly with the piston velocity as plotted in Fig. 5. The longitudinal sound velocity is about 1.3 km/s as determined by extrapolating the shock velocity to a zero piston velocity. For a piston velocity less than 1.58 km/s, no chemical reaction is observed during the course of the simulation (3.8 ps). For piston velocities greater than about 1.84 km/s, chemical reaction occurs behind the shock front and propagates quickly,

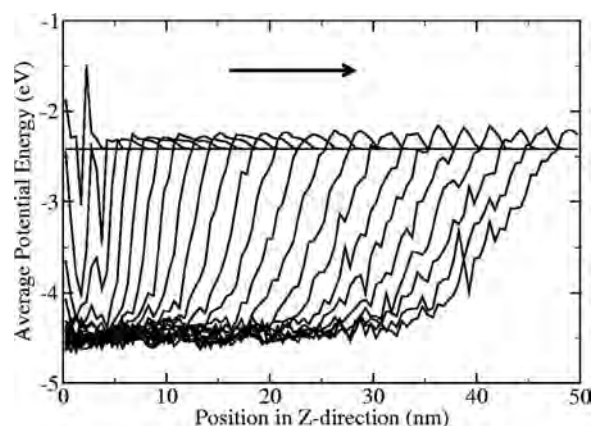


FIG. 6. Average potential energy profiles at different times for a shock simulation initiated by a 10.5 km/s flyer plate. The horizontal line corresponds to 0 ps and the right-most line corresponds to 5.3 ps. The time interval between adjacent lines is 0.23 ps. The shock propagates from left to right.

eventually overtaking the preceding shock front. Similarly, shocks by flyer plate will not initiate chemical reactions for flyer plate speeds lower than a threshold value. Figure 6 shows the average potential energy along the shock direction at different times, which demonstrates that the shock front moves at a constant speed and is followed by a very narrow reaction zone about 2 nm at the beginning of the shock and about 15 nm at the end of the simulation. The reaction products at the end of the simulation are a mixture of N<sub>2</sub>, chain-like nitrogen and single nitrogen atoms. For example, with a flyer plate speed of 10.5 km/s, the product at 5 ps after the shock consists of 63% N<sub>2</sub> molecules, 23% chainlike nitrogen and about 14% isolated nitrogen atoms, all in terms of weight percentage. A connectivity analysis (Fig. 7) shows that the dominant oligomeric nitrogen is N<sub>3</sub> trimer, which is similar to the product of thermal decomposition at high temperatures. However, as depicted in Fig. 7, the difference is that the size of the oligomeric nitrogen clusters can well exceed 10 with the maximum size of 24. These large clusters are metastable energetically and quickly dissociate to smaller segments, thus they are only concentrated in the reaction zone immediately trailing the shock front as shown in Fig. 3(b). This is in clear contrast to the maximum nitrogen clus-

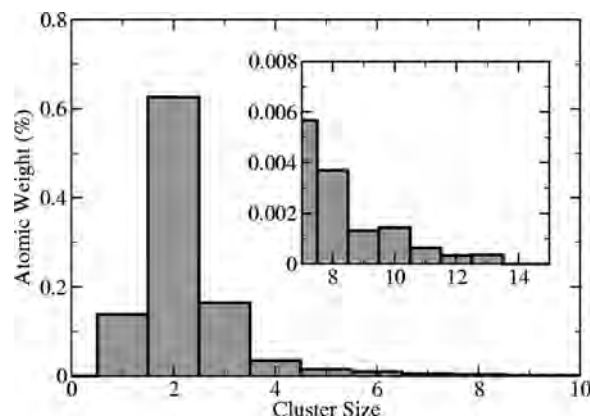


FIG. 7. The cluster size distribution for the shock simulation product, same as Fig. 3(b), in terms of atomic weight.

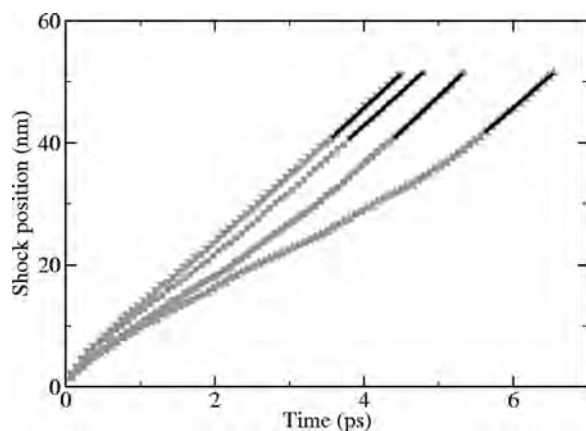


FIG. 8. Shock front positions as a function of time for various flyer plate speeds: 9.2 (triangle up), 10.5 (circle), and 15.8 (square) and 21.0 km/s (triangle down). The black lines are a linear fit to obtain a steady shock propagation speed that is sustained by chemical reaction.

ter, which is 6, during the whole simulation process for thermal decomposition. This is because at the shock front the chemical reaction occurs almost simultaneously in neighboring nitrogen cubane molecules; thus smaller chains can be linked together before being further decomposed into  $N_2$  molecules. In the case of thermal decomposition, the chemical reaction occurs randomly both spatially and temporally so that large polymeric clusters are less likely to form.

Plotted in Fig. 8 are the positions of the shock front as a function of time as determined by the position of the right most atom that deviates from the initial crystal structure. For four different flyer plate speeds, the final shock fronts propagate at a common detonation speed of about 11.0 km/s, as indicated by Fig. 9. For flyer plate speeds higher than the final detonation speed, the shock front slows down, while for flyer plate speeds lower than the final detonation speed, the shock front speeds up. For even lower flyer plate speeds, no reaction occurs. Therefore, a threshold flyer plate speed to initiate chemical reaction can be identified. Note that this value can be affected by the thickness of the flyer plate, the duration of the simulation, and the presence of defects in the lattice. For the current simulation with one layer of nitrogen

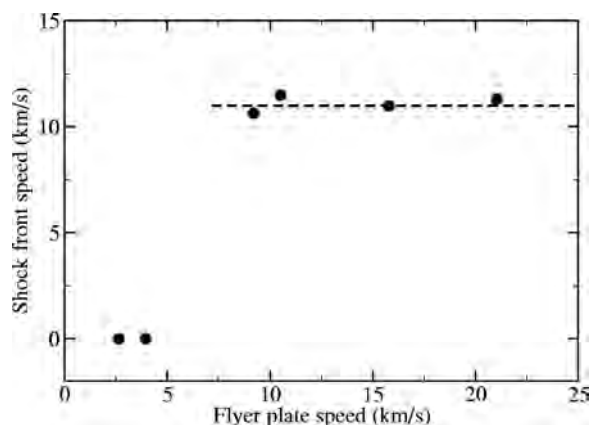


FIG. 9. Steady shock propagation speeds for shocks that initiate chemical reaction as a function of flyer plate speed. The shock front speed is set to zero to represent shocks that do not initiate chemical reaction.

cubane molecules as a flyer plate and a shock simulation for 7.6 ps, this threshold value resides between 4.0–5.3 km/s.

## V. CONCLUSIONS

The thermal decomposition and shock loading of an energetic molecular solid of nitrogen cubane has been simulated at the atomic scale. The interatomic interactions are modeled with a new RSS formalism that yields an activation energy barrier for thermal decomposition of 1.0 eV. Under shock loading with a rigid piston, the simulations show a threshold piston velocity above which a fully three-dimensional chemically sustained detonation with an intrinsic velocity of 11.0 km/s is initiated. Structural analysis shows that chainlike nitrogen forms during reaction, and that the maximum chain length in the shock simulations is much larger than that in thermal decomposition simulations. This observation is mainly due to the fact that, unlike thermal cook-off conditions, reactions occur instantaneously in a cooperative manner in shocks. Therefore, the shocked material is structurally different from the system subject to similar temperatures and pressures.

## ACKNOWLEDGMENTS

We thank stimulating discussions with L. P. Huang for potential development and D. Thompson, T. Sewell, Y. Hu, L. Sun, and B. Broom regarding shock simulations. Molecular dynamics simulations were carried out in LAMMPS.<sup>32–34</sup> The North Carolina State University High-Performance Computing Facility is also thanked for providing computational resources. This work was supported by a Multi-University Research Initiative from the U.S. Army Research Office.

- <sup>1</sup>C. S. Yoo and W. J. Nellis, *Science* **254**, 1489 (1991).
- <sup>2</sup>M. W. Chen, J. W. McCauley, D. P. Dandekar, and N. K. Bourne, *Nat. Mater.* **5**, 614 (2006).
- <sup>3</sup>W. Fickett and W. C. Davis, *Detonation* (University of California Press, Berkeley, 1979).
- <sup>4</sup>D. D. Dlott, *Annu. Rev. Phys. Chem.* **50**, 251 (1999).
- <sup>5</sup>B. L. Holian, *Shock Waves* **13**, 489 (2004).
- <sup>6</sup>D. W. Brenner, O. A. Shenderova, and D. A. Areshkin, in *Quantum-Based Analytic Interatomic Forces and Materials Simulation, Reviews in Computational Chemistry*, edited by K. B. Lipkowitz and D. B. Boyd (VCH Publishers, New York, 1998), pp. 213–245.
- <sup>7</sup>M. Peyrard, S. Odier, E. Lavenir, and J. M. Schnur, *J. Appl. Phys.* **57**, 2626 (1985).
- <sup>8</sup>M. L. Elert, D. M. Deaven, D. W. Brenner, and C. T. White, *Phys. Rev. B* **39**, 1453 (1989).
- <sup>9</sup>D. W. Brenner, D. H. Robertson, M. L. Elert, and C. T. White, *Phys. Rev. Lett.* **70**, 2174 (1993).
- <sup>10</sup>D. H. Robertson, D. W. Brenner, and C. T. White, *Phys. Rev. Lett.* **67**, 3132 (1991).
- <sup>11</sup>J. J. C. Barrett, D. H. Robertson, and C. T. White, *Chem. Phys. Rep.* **18**, 1969 (2000).
- <sup>12</sup>B. M. Rice, W. Mattson, and S. F. Trevino, *Phys. Rev. E* **57**, 5106 (1998).
- <sup>13</sup>A. Strachan, A. C. T. van Duin, D. Chakraborty, S. Dasgupta, and W. A. Goddard, *Phys. Rev. Lett.* **91**, 098301 (2003).
- <sup>14</sup>A. C. T. van Duin, Y. Zeiri, F. Dubnikova, R. Kosloff, and W. A. Goddard, *J. Am. Chem. Soc.* **127**, 11053 (2005).
- <sup>15</sup>A. Strachan, E. M. Kober, A. C. T. van Duin, J. Ongaard, and W. A. Goddard, *J. Chem. Phys.* **122**, 054502 (2005).
- <sup>16</sup>J. D. Kress, S. R. Bickham, L. A. Collins, B. L. Holian, and S. Goedecker, *Phys. Rev. Lett.* **83**, 3896 (1999).
- <sup>17</sup>S. R. Bickham, J. D. Kress, and L. A. Collins, *J. Chem. Phys.* **112**, 9695 (2000).

- <sup>18</sup>M. R. Manaa, L. E. Fried, C. F. Melius, M. Elstner, and T. Frauenheim, *J. Phys. Chem. A* **106**, 9024 (2002).
- <sup>19</sup>M. Riad Manaa, E. J. Reed, L. E. Fried, G. Galli, and F. Gygi, *J. Chem. Phys.* **120**, 10146 (2004).
- <sup>20</sup>H. Liu, J. J. Zhao, and D. Q. Wei, and Z. Z. Gong, *J. Chem. Phys.* **124**, 124501 (2006).
- <sup>21</sup>S. Mazevet, P. Blottiau, J. D. Kress, and L. A. Collins, *Phys. Rev. B* **69**, 224207 (2004).
- <sup>22</sup>D. W. Brenner, *Mater. Res. Bull.* **21**, 36 (1996).
- <sup>23</sup>D. W. Brenner, in *Shock Compression of Condensed Matter*, edited by S. C. Schmidt, R. D. Dick, J. W. Forbes, and D. G. Tasker (North-Holland, Amsterdam, 1992), p. 115.
- <sup>24</sup>L. P. Huang, M. Durandurdu, and J. Kieffer, *Nat. Mater.* **5**, 977 (2006).
- <sup>25</sup>L. P. Huang and J. Kieffer, *Phys. Rev. B* **74**, 224107 (2006).
- <sup>26</sup>W. J. Lauderdale, J. F. Stanton, and R. J. Bartlett, *J. Phys. Chem.* **96**, 1173 (1992).
- <sup>27</sup>R. D. Johnson, *NIST Computational Chemistry Comparison and Benchmark Database* (2005) (<http://srdata.nist.gov/cccbdb>).
- <sup>28</sup>S. J. Stuart, A. B. Tutein, and J. A. Harrison, *J. Chem. Phys.* **112**, 6472 (2000).
- <sup>29</sup>E. B. Fleischer, *J. Am. Chem. Soc.* **86**, 3889 (1964).
- <sup>30</sup>R. Engelke and J. R. Stine, *J. Phys. Chem.* **94**, 5689 (1990).
- <sup>31</sup>C. Mailhot, L. H. Yang, and A. K. McMahan, *Phys. Rev. B* **46**, 14419 (1992).
- <sup>32</sup>L. A. M. M. P. S. Molecular Dynamics Simulator (<http://lammmps.sandia.gov>).
- <sup>33</sup>S. J. Plimpton and J. Comp. Physica **117**, 1 (1995).
- <sup>34</sup>S. J. Plimpton, R. Pollock, and M. Stevens, Proceedings of the Eighth SIAM Conference on Parallel Processing for Scientific Computing, Minneapolis, MN (1997).

# Molecular dynamics simulations of shock waves using the absorbing boundary condition: A case study of methane

Alexey V. Bolesta,<sup>\*</sup> Lianqing Zheng,<sup>†</sup> and Donald L. Thompson<sup>\*</sup>

*Department of Chemistry, University of Missouri-Columbia, Columbia, Missouri 65211, USA*

Thomas D. Sewell<sup>§</sup>

*Theoretical Division, Los Alamos National Laboratory, Los Alamos, New Mexico 87545, USA*

(Received 5 April 2007; revised manuscript received 19 September 2007; published 14 December 2007)

We report a method that enables long-time molecular dynamics (MD) simulations of shock wave loading. The goal is to mitigate the severe interference effects that arise at interfaces or free boundaries when using standard nonequilibrium MD shock wave approaches. The essence of the method is to capture between two fixed pistons the material state at the precise instant in time when the shock front, initiated by a piston with velocity  $u_p$  at one end of the target sample, traverses the contiguous boundary between the target and a second, stationary piston located at the opposite end of the sample, at which point the second piston is also assigned velocity  $u_p$  and the simulation is continued. Thus, the target material is captured in the energy-volume Hugoniot state resulting from the initial shock wave, and can be propagated forward in time to monitor any subsequent chemistry, plastic deformation, or other time-dependent phenomena compatible with the spatial scale of the simulation. For demonstration purposes, we apply the method to shock-induced chemistry in methane based on the adaptive intermolecular reactive empirical bond order force field [S. J. Stuart *et al.*, *J. Chem. Phys.* **112**, 6472 (2000)].

DOI: [10.1103/PhysRevB.76.224108](https://doi.org/10.1103/PhysRevB.76.224108)

PACS number(s): 62.50.+p, 82.20.Wt, 82.40.Fp

## I. INTRODUCTION

Dynamic material response to shock wave loading has been studied for decades for both practical and fundamental reasons.<sup>1</sup> Molecular dynamics (MD) is the most widely used method for theoretical studies of physical and chemical processes in condensed materials on submicron scales. Since the 1970s, nonequilibrium molecular dynamics (NEMD) has been applied to studies of shock-induced phenomena such as defect generation,<sup>2</sup> phase transitions,<sup>3</sup> and chemistry.<sup>4,5</sup> Although current computer capabilities allow shock wave simulations for systems containing even billions of atoms interacting via comparatively simple potentials (for instance, the embedded-atom model),<sup>6</sup> it is computationally expensive to use NEMD to study shock waves in complicated, polyatomic molecular crystals characterized by many-body interactions and electrostatic contributions to the potential energy.<sup>7</sup> This is particularly true since many of the phenomena of interest occur on time scales significantly larger than those required for the passage of a shock wave through a typical MD simulation cell.

Various equilibrium MD methods, sometimes called Hugoniot methods, have been developed in the past decade to reproduce the final states of shocked materials by way of extended equations of motion that act on the system to drive it toward a prescribed Hugoniot state.<sup>8–12</sup> (The Hugoniot is the locus of states accessible by shock wave loading.) This allows long-time sampling of shock states without the need to simulate a system that is large enough to sustain the compressed state for a long enough time to arrive at those states. In cases where the shock wave dynamics is of interest, however, the Hugoniot methods are of limited use. Zhakhovskii *et al.*<sup>13</sup> developed a “moving window” method that allows the study of the detailed dynamics in the

vicinity of a shock front by systematically adding new material to the unshocked end of the simulation cell and removing shocked material from the other end so that the simulation size remains constant and the simulation frame remains centered on the shock front. However, even this method becomes difficult to apply to simulations with nonprompt chemistry or mechanical deformation, since adding and removing material from the simulation will certainly introduce artifacts for practically accessible simulation domains. Most recently, Zhao *et al.*<sup>14</sup> developed a NEMD method to study shock-induced alloying reactions in Ni/Al nanolaminates. In their method, shock waves are first generated by colliding two identical slabs with equal but opposite center-of-mass velocities. The periodic boundaries along the shock direction shrink consistently with the mass velocity. Once the shock waves reach the periodic boundaries, however, the cell parameters are fixed, and the simulation is continued in the usual three-dimensional periodic, constant energy–constant volume (*NVE*) ensemble to allow the alloying reactions to approach equilibrium.

Here, we report a NEMD method that allows the dynamics behind a shock wave to evolve with minimal interference from the free surface of the simulation cell. We demonstrate the method in a study of shock-induced chemistry in condensed-phase methane based on the adaptive intermolecular reactive empirical bond order (AIREBO) force field.<sup>15</sup>

## II. COMPUTATIONAL DETAILS

### A. Absorbing boundary condition

A schematic diagram of how the absorbing boundary condition is applied in a simulation of a shock wave is presented



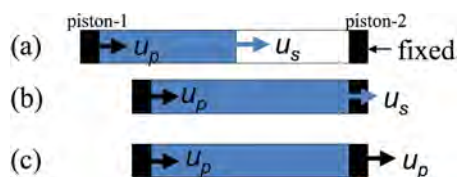
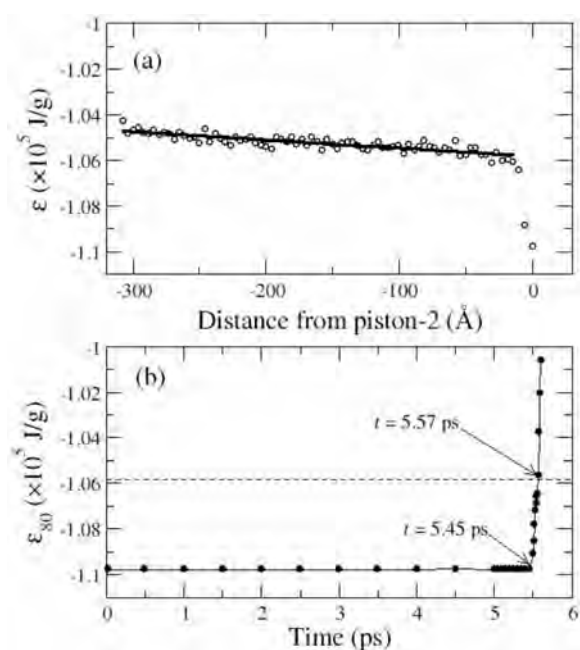


FIG. 1.<sup>16</sup> By moving a rigid piston (piston-1) at constant velocity  $u_p$ , a shock wave is generated that moves with velocity  $u_s$  through the target material [see Fig. 1(a)]. On the opposite end of the simulation cell is a second rigid piston (piston-2), contiguous with the target and assigned zero velocity. When the shock wave reaches piston-2 [Fig. 1(b)], it is instantaneously assigned the same constant velocity as piston-1 ( $u_p$ ) [see Fig. 1(c)]. From that point onward, the simulation is microcanonical and maintains the initial Hugoniot state associated with the passage of the shock front. Chemical reactions or other dynamical processes can be followed until they reach equilibrium. These processes can result in significant changes in temperature, pressure, and composition in the confined region.

A critical issue is exactly when and how to apply the velocity  $u_p$  to the second piston. Although various criteria can be imagined, the initial transfer of internal energy is a reasonable one for defining the instant of shock wave passage across a given dividing surface in configuration space since shock wave propagation is essentially energy transfer from the moving piston to lattice degrees of freedom in the target material. We show in Fig. 2 how we use the internal energy to determine the time at which the second piston begins to move. In this case, the piston velocity  $u_p = 3.0$  km/s is below the threshold for shock-induced chemistry in methane. The simulation cell is arbitrarily divided into 80 bins, each one unit cell wide; these bins deform affinely as the shock wave compresses the sample. Figure 2(a) contains the internal energy profile in the material along the shock direction at  $t = 5.45$  ps, which is just before the internal energy of the bin immediately adjacent to piston-2 begins to rise rapidly [denoted as bin 80, corresponding to zero displacement along the abscissa in Fig. 2(a); the internal energy of this bin is denoted as  $\varepsilon_{80}$  in Fig. 2(b)]. The internal energy profile of the shocked material in Fig. 2(a) is fitted to a straight line, which is extrapolated to predict the internal energy  $\varepsilon_{80}$  at the moment when the shock front just reaches its outer edge (that is, the contiguous boundary with the second piston). Monitoring the internal energy  $\varepsilon_{80}$  as the trajectory continues, we find that the extrapolated value is achieved at  $t = 5.57$  ps [see Fig. 2(b)]; the dashed horizontal line in Fig. 2(b) shows the extrapolated value for the internal energy corresponding to the moment when the shock wave reaches piston-2. It is at this time that the second piston begins to move with the same fixed velocity  $u_p$  as the first one.

There is a significant disparity in the time scales for shock wave traversal of the sample in most NEMD simulations and subsequent establishment of chemical or thermo-mechanical equilibrium. In the simplest sense, the maximum time accessible to the former is the shock transit time across the sample,  $t_{\max} = l_{\text{sample}}/u_s$ . However, this only applies to material in the immediate vicinity of the first piston; material on the free boundary is under compression for essentially zero time. (The time required for a backscattered wave to re-traverse the compressed system sets the true upper limit on the time that any region in such a simulation can be sustained in the shocked state.) The proposed *absorbing boundary condition* described here minimizes in a practical way the effects of wave reflection from a free surface, effectively providing a near-perfect impedance match<sup>17</sup> between the target material and the two pistons, and thus, allows simulation of the sample in a shock-compressed state for an interval of time whose limit is determined by the stability of the numerical integration scheme.



**B. Model system and details of simulation procedure**

For demonstration purposes, we have chosen to study shock-induced chemistry in methane as predicted by the AIREBO potential due to Stuart *et al.*<sup>15</sup> AIREBO is an extension of the reactive empirical bond order potential.<sup>18</sup>

AIREBO was designed to optimally describe liquid-state hydrocarbon properties at ambient pressure, while perturbing as little as possible predictions for the solid-state polymorphs of pure carbon. AIREBO has been used previously in MD studies of thermal dissociation in methane, ethylene, and benzene,<sup>19</sup> and of shock-induced chemistry in solid acetylene,<sup>20,21</sup> ethylene,<sup>20</sup> methane,<sup>20,21</sup> and anthracene.<sup>21</sup> The MD simulations presented here were performed using a computer code developed for AIREBO by Stuart *et al.* Trajectories were integrated using the velocity Verlet algorithm, with step sizes in the interval from 0.1 to 0.25 fs depending on the temperature and pressure.

The simulation cell for the shock wave simulations consists of  $82 \times 3 \times 3$  unit cells of methane phase I, a face-centered-cubic (fcc) unit cell with rotating molecules at the lattice sites.<sup>22</sup> Initially, all atoms were positioned on the perfect fcc lattice with no orientational disorder. Next, the system was equilibrated in the *NVT* ensemble, with periodic boundary conditions applied in the directions transverse to the direction of subsequent shock loading, and cell parameters adjusted to yield zero pressure at a given temperature; a gap of 11.722 Å (two unit cell widths) was introduced between the first and second layers of unit cells along the shock direction. Atoms in the first and last layers of unit cells along the shock direction, which comprise piston-1 and piston-2, respectively, were held fixed during this equilibration period, which was continued until the system reached steady-fluctuating values about the prescribed temperature. Shock waves were generated by driving piston-1 into the target sample with constant velocity  $u_p$ . Piston-2, on the opposite end of the sample, was initially assigned zero velocity. Both pistons were perfectly rigid.

### III. RESULTS AND DISCUSSION

#### A. Comparison of adaptive intermolecular reactive empirical bond order predictions to experimental results

We provide details of the validation of the absorbing boundary condition in Sec. III B. In this section, we present a comparison between AIREBO predictions obtained using the absorbing boundary condition and experimental shock wave data<sup>23,24</sup> for liquid methane at initial temperature 111 K and density  $0.42 \text{ g/cm}^3$ ; the results are summarized in Fig. 3. The shock temperature predicted for AIREBO is in good agreement with experiment [Fig. 3(a)]. Figure 3(b) indicates that the AIREBO potential overestimates the shock speed by  $\sim 25\%$  for  $u_p = 8.3 \text{ km/s}$ , whereas the compression ratio  $\rho/\rho_0$  in Fig. 3(c) is underestimated by  $\sim 30\%$  at that same piston velocity. Finally, the component of stress along the shock direction  $P_{xx}$  (hereafter referred to as shock pressure) behind the shock front is overestimated by about 25% at the highest piston velocity considered [see Fig. 3(d)]; this discrepancy tends to zero with decreasing piston velocity. Since temperature is the dominant thermodynamic variable for chemistry, the agreement in Fig. 3(a) suggests that shock-induced reactions predicted for methane by AIREBO may be reasonable, and are certainly sufficient for the present goal of methods development.

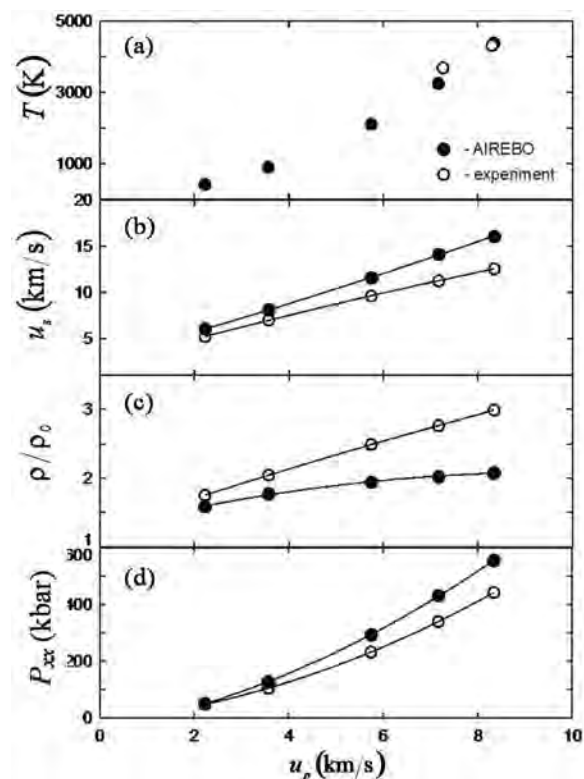


FIG. 3. Shock strength dependence of (a) temperature, (b) shock speed, (c) compression ratio, and (d) shock pressure in liquid methane. The initial temperature and density are 111 K and  $0.42 \text{ g/cm}^3$ , respectively. Solid symbols, simulation predictions, open symbols, experiment. Data for pressure, compression ratio, and shock velocity are from Nellis *et al.* (Ref. 23); temperature measurement is from Radousky *et al.* (Ref. 24).

#### B. Validation of the absorbing boundary condition

Figure 4 contains plots of density, material velocity, internal energy, and temperature profiles for subvolumes of the simulation cell along the shock direction, at times before and after the second piston begins to move. The results, eight snapshots in time, are for a  $u_p = 3.0 \text{ km/s}$  shock in crystalline methane equilibrated at 50 K and zero pressure. Traces for successive times are shifted vertically along the ordinate as an aid to the eye. In this case, the shock wave reaches the second piston at  $t \sim 5.57 \text{ ps}$  (bold trace in Fig. 4), at which time piston-2 is assigned a velocity  $u_p$ . Whereas this would be the maximum time (or, at best, half the maximum time) accessible by other NEMD shock methods, with the exception of that of Zhao *et al.*,<sup>14</sup> in the present case, the simulation was continued for an additional 30 ps. One can see from Fig. 4 that spatial distributions of the density, local mass velocity, and temperature are essentially constant over the entire time interval after the second piston starts to move. The profiles of internal energy—which are the basis for determining when the shock wave traverses the sample boundary into the second piston—have a negative slope across the simulation cell during shock wave passage. In this case, the slope is approximately preserved immediately after the second piston begins to move, but disappears within 5 ps. There is no evidence in any of the results shown in Fig. 4 for

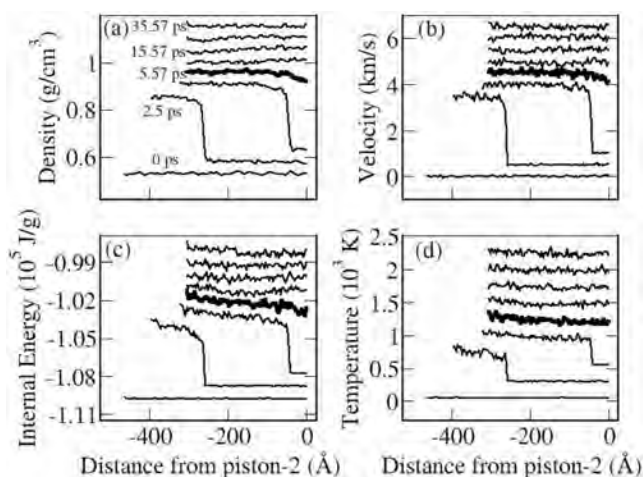


FIG. 4. Spatial profiles of (a) density, (b) local velocity, (c) internal energy, and (d) temperature along the shock direction, for eight time snapshots before and after the absorbing boundary condition is applied to shocked solid methane. The piston velocity is 3 km/s and the initial temperature is 50 K. The absorbing boundary condition is applied at  $t=5.57$  ps (bold trace in the figures). Traces for successive snapshots are shifted vertically for clarity.

significant reflections or buildup of energy at either piston-sample boundary.

In Fig. 5, we compare results obtained using the absorbing boundary condition to those obtained using a standard<sup>1</sup> NEMD shock simulation. The only difference between the simulations is that the sample length in the latter case is twice as long as in the former. Both sets of results correspond to  $t=10.0$  ps, which is just prior to the point of maximum compression in the longer cell (black lines) and 4.43 ps

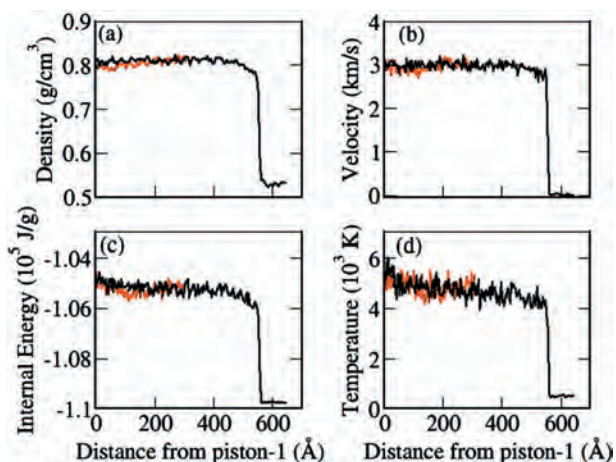


FIG. 5. (Color) Spatial profiles of (a) density, (b) local velocity, (c) internal energy, and (d) temperature along the shock direction at time  $t=10.0$  ps for two simulations of shocked methane crystal differing only in the initial sample length. Red lines correspond to the simulation discussed in connection with Fig. 4, for which the absorbing boundary condition was applied at  $t=5.57$  ps; black lines correspond to a system twice as long in the shock direction, which has not reached maximum compression by the end of the simulation. The piston velocity is 3 km/s and the initial temperature is 50 K.

after piston-2 was applied in the smaller one (red lines). Thus, this comparison provides a direct test of the absorbing boundary condition approach. While there are observable deviations for density, local mass velocity, internal energy, and temperature in the regions of Fig. 5 for which computational domains overlap, they are small and insignificant considering their magnitude in light of the pre- and postshock states of the material.

One can estimate the length of system that would be required, using a standard NEMD simulation, to obtain results comparable to those shown in Fig. 4; that is, one in which a shocked state is sustained for 30 ps. For  $u_p=3.0$  km/s,  $\sim 5.5$  ps is required for the shock wave to traverse the  $\sim 47.5$  nm sample length, which means that a simulation cell of length  $\sim 260$  nm would be needed. Simulation of a system of this size using a complicated reactive potential-energy function is impractical with current computing capabilities even for a single shock-passage time, let alone for the long times required to approach chemical equilibrium (e.g.,  $\sim 150$  ps in the following example, and in many cases, much longer).

### C. Chemically reactive waves in methane

Analyses of shock-induced chemical transformations were performed for the cases  $u_p=8.3$  and 11.0 km/s for shocked liquid and solid methane, respectively, based on an *ad hoc* geometric definition of molecular connectivity. Specifically, it was assumed that carbon atoms are chemically bonded when their separation is within the cutoff distance for the intramolecular interactions in the AIREBO potential function.<sup>15</sup> Thus, a molecule is defined as the set of carbon atoms for which any two members of that set can be linked to all other members through an unbroken sequence of bonds. Within this framework, we define isolated carbon monomers, dimers, trimers, etc., as having molecular sizes 1, 2, 3, etc.

Examination of molecular sizes after shock wave propagation through liquid methane for  $u_p=8.3$  km/s indicates that initial ethane production occurs with a latency of  $\sim 3$  ps after shock wave passage. (Recall that the shock wave traversal time for the entire sample is only about 5.5 ps.) The study of several specific reaction events reveals a propensity for ethane formation to occur by two unimolecular dissociation events:  $2\text{CH}_4 \rightarrow 2\text{CH}_3 + 2\text{H}$  followed by recombination to yield  $\text{C}_2\text{H}_6 + \text{H}_2$ . This result is in agreement with tight-binding MD simulations<sup>25</sup> and experimental measurements of temperature<sup>24</sup> and conductivity<sup>26</sup> behind the shock front. Given that molecular dissociation is thermally activated, it is not surprising that moderate differences between the calculated and experimental pressures have comparatively small effects on the predicted reaction thresholds and chemistry.

The decomposition threshold for solid methane using AIREBO is  $u_p=9$  km/s, for which the shock temperature is  $\sim 4600$  K. This temperature is close to the value observed in liquid methane shock propagation, 4400 K [see Fig. 4(a)]. Elert *et al.*<sup>20</sup> carried out MD simulations of shock wave propagation in solid methane and reported a somewhat higher value, 10 km/s, for the decomposition threshold ve-



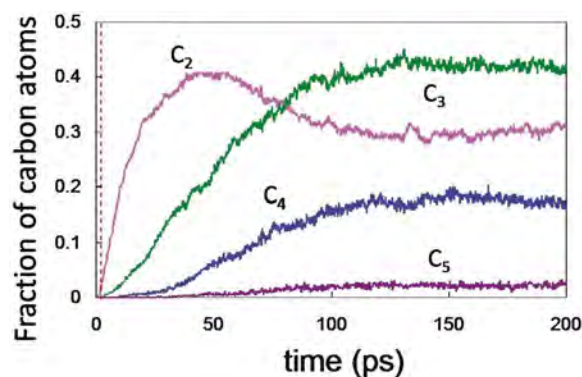


FIG. 6. (Color online) Time dependence of molecular carbon cluster size in solid methane shocked with a piston velocity  $u_p = 11$  km/s. The initial temperature and density were 50 K and  $0.53$  g/cm<sup>3</sup>, respectively. Curves  $C_2$ ,  $C_3$ ,  $C_4$ , and  $C_5$  correspond nominally to ethane, propane, isomers of butane, and isomers of pentane, respectively. The vertical dashed line at  $t = 2.2$  ps indicates the time at which the second piston began to move.

locity. This discrepancy is likely caused by the different approach used for shock wave initiation in those simulations: a finite flyer plate of several unit cells thickness was used, which resulted in rarefaction waves entering the compressed region and, thus, decreasing the time available for reaction to occur in the fully compressed state, whereas the initiating piston used here emulates a macroscopic striker.

In Fig. 6, we show the time evolution of carbon molecular sizes for solid methane shocked at  $u_p = 11$  km/s. The shock wave traversal time is only about 2.2 ps (denoted by the vertical line in the figure). Though most of the carbon atoms in the system are members of three-atom molecules (i.e., propanelike chains,  $C_3$ ), about 20% are involved in clusters containing four or more atoms and about 25% of all carbon atoms belong to clusters consisting of more than 50 carbon atoms. Diamond anvil cell experiments in which infrared absorption, Raman spectroscopy, and x-ray diffraction were measured indicate that diamond and hydrogen, as well as hydrocarbon polymer chains, are formed from methane upon static compression in the interval of 10–50 GPa and laser heating to 2000–3000 K.<sup>27</sup> It is likely that the system studied here at  $t = 200$  ps represents an early stage on the transformation path toward diamond+H<sub>2</sub>, an overall process characterized by diffusion-limited rates with time constants and spatial scales that exceed those of the present simulation.

#### IV. SUMMARY AND CONCLUSIONS

We have developed a practical approach for nonequilibrium molecular dynamics simulations of shock waves that allows the study of shocked states for time scales far larger than the shock wave traversal time of the MD simulation

cell. A shock wave is generated by driving a rigid piston into a sample at constant piston velocity. A second rigid piston is located at the opposite end of the simulation cell, contiguous to and equilibrated with the material. When the shock wave reaches the end of the simulation cell, the second piston begins to move at the same velocity as the first and, thus, provides an “impedance match” for the shock wave across the sample-piston interface. With both pistons moving at the same velocity, the Hugoniot state of the shocked material is sustained, while the sample continues to evolve. This allows a significantly longer simulation without significant interference from reflected waves that arise at interfaces. The principal distinction between the present method and the one due to Zhao *et al.*<sup>14</sup> is the extent to which the present one should be extendable to treat split wave structures, for instance, an elastic precursor followed by a plastic wave, or to accommodate inhomogeneous wave profiles that might require finite piston acceleration profiles, which themselves might vary across the surface of the piston (e.g., a shock wave propagating along the longitudinal axis of a hexagonal-cylindrical microphase segregated copolymer morphology).

We applied this absorbing boundary condition approach to shock waves in methane, modeled using the AIREBO force field.<sup>15</sup> We demonstrated that the method does not introduce significant fluctuations in density or local velocity across the simulation cell or at the piston-sample interfaces, and that the internal energy (which is the criterion upon which the time to start the second piston moving is based) is equilibrated on a several picosecond time scale. We illustrated the practical usefulness of the method by simulating shock-induced chemistry in methane on a 200 ps time scale, for a simulation cell with a shock wave traversal time of only 2.2 ps. While the simple implementation of the absorbing boundary condition described here involves infinite acceleration of the second piston, adaptations to provide more sophisticated “soft catches” should be straightforward. We expect this general approach to be useful for simulations of shock-induced dynamics including chemistry in various materials, with numerical integration stability and, of course, the validity of the classical approximation being the limiting factors.

#### ACKNOWLEDGMENTS

We are grateful to Don Brenner, Steve Stuart, Marc Cawkwell, Ed Kober, Sam Shaw, Ali Siavosh-Haghighi, and Jenel Vatamanu for several fruitful discussions. We are especially grateful to Steve Stuart for providing a copy of his code along with personal instructions for using it. L.Z. is grateful for Wei Yang’s support. This work was supported by a DOD MURI grant managed by the Army Research Office. T.D.S. was supported by the U.S. Department of Energy under Contract No. DE-AC52-06NA25396 with Los Alamos National Security, LLC.



\*Present address: Institute of Theoretical and Applied Mechanics, Institutskaja Strasse 4/1, Novosibirsk 630090, Russia.

†Present address: School of Computational Science, Florida State University, Tallahassee, FL 32306.

‡thompsondon@missouri.edu

§sewell@lanl.gov

<sup>1</sup>B. L. Holian, *Shock Waves* **5**, 149 (1995); **13**, 489 (2004).

<sup>2</sup>E. M. Bringa, K. Rosolankova, R. E. Rudd, B. A. Remington, J. S. Wark, M. Duchaineau, D. H. Kalantar, J. Hawreliak, and J. Belak, *Nat. Mater.* **5**, 805 (2006).

<sup>3</sup>K. Kadau, T. C. Germann, P. S. Lomdahl, and B. L. Holian, *Science* **296**, 1681 (2002).

<sup>4</sup>B. L. Holian, T. C. Germann, J.-B. Maillet, and C. T. White, *Phys. Rev. Lett.* **89**, 285501 (2002).

<sup>5</sup>A. J. Heim, N. Gronbech-Jensen, T. C. Germann, E. M. Kober, B. L. Holian, and P. S. Lomdahl, *Phys. Rev. E* **76**, 026318 (2007).

<sup>6</sup>T. C. Germann, B. L. Holian, K. Kadau, and P. S. Lomdahl, *Lecture Series in Computer and Computational Sciences* (VSP BV, AH Zeist, Netherlands, 2005), Vol. 4A-4B, p. 1138.

<sup>7</sup>A. Strachan, A. C. T. van Duin, D. Chakraborty, S. Dasgupta, and W. A. Goddard III, *Phys. Rev. Lett.* **91**, 098301 (2003).

<sup>8</sup>J.-B. Maillet, M. Mareschal, L. Soulard, R. Ravelo, P. S. Lomdahl, T. C. Germann, and B. L. Holian, *Phys. Rev. E* **63**, 016121 (2000).

<sup>9</sup>E. J. Reed, L. E. Fried, and J. D. Joannopoulos, *Phys. Rev. Lett.* **90**, 235503 (2003).

<sup>10</sup>E. J. Reed, L. E. Fried, M. R. Manaa, and J. D. Joannopoulos, in *Chemistry at Extreme Conditions*, edited by M. R. Manaa (Elsevier, New York, 2005), pp. 297–328.

<sup>11</sup>R. Ravelo, B. L. Holian, T. C. Germann, and P. S. Lomdahl, *Phys. Rev. B* **70**, 014103 (2004).

<sup>12</sup>F. Barmes, L. Soulard, and M. Mareschal, *Phys. Rev. B* **73**, 224108 (2006).

<sup>13</sup>V. V. Zhakhovskii, S. V. Zybin, K. Nishihara, and S. I. Anisimov, *Phys. Rev. Lett.* **83**, 1175 (1999).

<sup>14</sup>S. Zhao, T. C. Germann, and A. Strachan, *J. Chem. Phys.* **125**,

164707 (2006).

<sup>15</sup>S. J. Stuart, A. B. Tutein, and J. A. Harrison, *J. Chem. Phys.* **112**, 6472 (2000).

<sup>16</sup>The absorbing boundary condition approach presented in this paper should not be confused with other approaches in the computational physics literature, wherein artificial zones are introduced at the boundaries of a computational domain to damp out waves at the simulation boundary; for example, the use of negative imaginary potentials at the edges of the grid in simulations of quantum wave packets.

<sup>17</sup>Mathematically, acoustic impedance is defined as  $k=\rho c$ , where  $\rho$  is density and  $c$  is sound speed. The difference between acoustic impedances at a material interface determines the amount of energy transmitted and reflected at that interface. Our use of “near perfect impedance match” in the present context refers to the absence of significant reflected waves due to the presence of the second piston and its infinite acceleration from zero to  $u_p$ .

<sup>18</sup>D. W. Brenner, *Phys. Rev. B* **42**, 9458 (1990).

<sup>19</sup>J. A. Viecelli and J. N. Glosli, *J. Chem. Phys.* **117**, 11352 (2002).

<sup>20</sup>M. L. Elert, S. V. Zybin, and C. T. White, *J. Chem. Phys.* **118**, 9795 (2003).

<sup>21</sup>M. L. Elert, S. V. Zybin, and C. T. White, in *Chemistry at Extreme Conditions*, edited by M. R. Manaa (Elsevier, New York, 2005), pp. 351–368.

<sup>22</sup>R. M. Hazen, H. K. Mao, L. W. Finger, and P. M. Bell, *Appl. Phys. Lett.* **37**, 288 (1980).

<sup>23</sup>W. J. Nellis, F. H. Ree, M. van Thiel, and A. C. Mitchell, *J. Chem. Phys.* **75**, 3055 (1981).

<sup>24</sup>H. B. Radousky, A. C. Mitchell, and W. J. Nellis, *J. Chem. Phys.* **93**, 8235 (1990).

<sup>25</sup>J. D. Kress, S. R. Bickham, L. A. Collins, B. L. Holian, and S. Goedecker, *Phys. Rev. Lett.* **83**, 3896 (1999).

<sup>26</sup>W. J. Nellis, D. C. Hamilton, and A. C. Mitchell, *J. Chem. Phys.* **115**, 1015 (2001).

<sup>27</sup>L. R. Benedetti, J. H. Nguyen, W. A. Caldwell, H. Liu, M. Kruger, and R. Jeanloz, *Science* **286**, 100 (1999).

# Jetting and Detonation Initiation in Shock Induced Collapse of Nanometer-Scale Voids

Yunfeng Shi\* and Donald W. Brenner

Department of Materials Science and Engineering, North Carolina State University,  
Raleigh, North Carolina 27587-7907

Received: December 20, 2007; In Final Form: February 7, 2008

Molecular dynamics simulations have been used to characterize the dynamics of the shock-induced asymmetric collapse of nanometer-scale voids in cubane nitrogen and to characterize how this dynamics couples with local chemistry to increase the shock sensitivity relative to homogeneous initiation. Mesoscopic-scale features of the void collapse correspond well to experimentally observed features of micrometer-scale bubble collapse, including a transition from single to double jetting with an increasing transverse void length. An analytic model is developed for the enhanced shock sensitivity as a function of void size and shape that reproduces the simulation results. At the atomic level, the simulations show vibrational up-pumping of molecules in the jet front because of collisions with the downstream wall followed by bi-molecular reactive dynamics from continued jet impact that triggers the onset of initiation. These results provide important new insights into the coupling of hydrodynamic void collapse and the enhanced shock sensitivity of energetic materials.

## I. Introduction

The sensitivity of solid explosives is enhanced by the presence of voids which, when shocked, lead to hotspots via void collapse.<sup>1,2</sup> The specific mechanism by which void collapse leads to local heating depends on several factors, including the initial size of the void, the strength of the applied shock, and the yield strength and viscosity of the shocked solid.<sup>3</sup> Under conditions where the shock travels faster than the characteristic time for void collapse, symmetric collapse occurs, and heating comes mainly from visco-plastic dynamics. As the collapse time approaches the time needed for the shock to traverse the void, void collapse becomes asymmetric, and the collapse dynamics evolves from a viscous to a hydrodynamic regime. The collapse in a fully hydrodynamic regime is characterized by the formation of a jet that emerges from the upstream wall of the void.<sup>4,5</sup> This jetting leads to an enhanced focusing of kinetic energy onto the downstream side of the collapsing void. In both the viscous and the hydrodynamic regimes, there is also a contribution from adiabatic heating of gas trapped in the collapsing void, although the magnitude of this contribution is typically small. Enhanced shear banding in the vicinity of a collapsing void may also contribute to hot spot formation and the enhanced sensitivity observed for energetic materials with increasing porosity.

Jetting during shock-induced collapse of millimeter-size voids in gels has been experimentally characterized by Bourne and Field and co-workers using high-speed photography.<sup>1,2,4,5</sup> In these studies, luminescence was observed from the point at which a jet initially impacts the cavity side wall, as well as from two “lobes” that form on either side of the jet after impact. On the basis of the temperature inferred from the intensity of the luminescence and the time scale of the collapse, they suggest that ignition in energetic materials within the hydrodynamic regime results from the high-speed jet impact on the downstream wall and not from the high temperatures in the lobes that form after impact. They also observed the formation of dual jets

during the shock collapse of a void within which the upstream wall is initially a flat surface.

Jetting also plays a critical role in other important processes. The Munroe effect in solids, for example, is exploited in the development of shaped charges,<sup>6</sup> and jetting due to bubble collapse near a solid boundary leads to cavitation erosion.<sup>7</sup>

Several molecular dynamics simulations have provided important insights into the interaction of shocks with nanometer-scale voids in solids that have implications for hotspot formation and shock sensitivity. Mintmire et al. modeled the collapse of a cylindrical void with a 2 nm diameter in a shocked molecular solid composed of harmonic diatomic molecules bound into a solid by pair additive Morse potentials.<sup>8</sup> They reported a transition from symmetric to asymmetric void collapse with increasing speed of the supported shock. For asymmetric collapse, turbulent ejection of molecules into the void followed by collisions with the downstream side of the void was reported which leads to formation of a hotspot. Jetting dynamics, however, was not noted, and because of the nonreactive nature of the interatomic potential, chemical reactivity and shock sensitivity could not be quantified. In subsequent work, White and co-workers modeled the interaction of a driven planar shock with an infinite gap (created via periodic boundary conditions) within a model two-dimensional reactive system.<sup>9</sup> For a gap width of 15 nm, they found that a driven shock would initiate detonation at a front velocity that was 20% below that needed to initiate detonation in a defect-free system. For the detonating system, initiation was not observed at the point at which molecules that were ejected into the void impacted the far side of the gap, but rather initiation occurred as the gap collapsed under the influence of the supported shock. To explain this result, Holian et al. developed a model that considers PV work coming from recompression of the ejected particles.<sup>10</sup> This model predicts size-dependent sub-threshold detonation with chemical reactions initiating in the compressed region, consistent with the White et al. simulations as well as with comparable simulations using a nonreactive Lennard-Jones potential.

\* Corresponding author.

Molecular dynamics simulations by Germann et al. used the same model as White and co-workers to characterize shock dynamics and initiation in a two-dimensional system containing circular and elliptical voids.<sup>11</sup> They reported hydrodynamic jet formation and detonation initiation from supported shock fronts that have speeds below that needed to initiate a defect-free system. For elliptical voids, structures having the long axis along the direction of the shock were found to have lower threshold shock pressures than voids with the same shape but with the long axis oriented perpendicular to the shock front. For all cases, initiation was reportedly not a result of the initial jet collision with the downstream wall, but rather chemical reactivity leading to initiation occurred in the high temperatures and pressures during void collapse after the initial jet impact. The lower threshold for elliptical voids with the long axis along the shock direction was attributed to the longer transit time for the jet and therefore the higher PV work available to induce reactivity.

Hatano used molecular dynamics simulations and a nonreactive Lennard-Jones potential to model collapse of nanometer-scale rectangular voids in a solid due to a supported shock.<sup>12</sup> The voids had dimensions from 4 to 40 unit cells. He reported an elevated kinetic energy and an increased number of energetic collisions during collapse. The kinetic energy enhancement was reportedly due to momentum and energy focusing from the two void walls that were along the direction of the supported shock, although no jetting was reported.

Nomura et al. used molecular dynamics simulations and the ReaxFF many-body reactive potential energy expression to model the collapse of a spherical void in an RDX crystal.<sup>13</sup> Because of the computational demands of the potential energy expression and the required system sizes, only two piston speeds were used, 1 km/s and 3 km/s. They observed the formation of a jet that was accelerated through the void due to focusing from the void walls. For the higher piston speed, they report the formation of molecular NO<sub>2</sub> fragments at the jet-sidewall interface as the jet traverses the void. Upon impact of the jet, different products form, most notably N<sub>2</sub>, H<sub>2</sub>O, and HONO, from mechanisms that included molecular dissociation and recombination. Hence, these simulations provide clear evidence that jetting in a nanometer-scale void can have a large influence on the shock chemistry of energetic materials. However, simulations of RDX using this force field have yet to demonstrate a transition from reactive chemistry to a chemically sustained detonation, and therefore it is difficult to draw further conclusions regarding the role of voids in determining the sensitivity of RDX and related systems from these simulations.

For continuum level analyses, the choice of spherical voids is due to both the ease of computation and the minimum energy shapes assuming isotropic surface free energies. At the nanometer scale, however, faceting that reflects the relative stabilities of discrete surfaces can, in principle, produce voids with relatively abrupt features. The experimental observation of dual jetting during the collapse of macroscopic voids with a flat surface together with the work of Hatano at the atomic scale suggests that such features may play an important role in energy focusing during hydrodynamic collapse. To further explore this issue within the context of detonation initiation, we have carried out an extensive set of molecular dynamics simulations of a supported shock traveling through a reactive system containing nanometer-scale rectangular voids of different sizes and aspect ratios. As described in more detail below, these simulations display characteristics that mimic those observed at the macroscopic scale, including enhanced sensitivity relative to homogeneous detonation, asymmetric collapse and jetting, for-

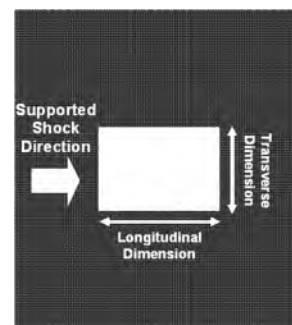


**Figure 1.** Illustration of the initial simulation system.

mation of hot regions of material surrounding the jet impact site, a transition from single to double jetting with increasing transverse void size, and initiation from the point where the jet impacts the downstream void wall. By using these results as a guide, an analytic model is developed that reproduces the influence of void shape on the detonation sensitivity of the material. The simulations are also characterized in terms of reactive chemistry at the atomic scale. The simulations show vibrational up-pumping of spalled molecules due to collision with the downstream wall, followed by a bimolecular reaction with additional spalled molecules that leads to product formation and detonation initiation.

## II. Simulation

The energetic material used in these simulations was a model nitrogen cubane crystal. A recently developed reactive state summation (RSS) potential was used to model the nitrogen–nitrogen interactions.<sup>14</sup> This potential is designed to model the exothermic dissociation of nitrogen cubane molecules into diatomic nitrogen molecules, and it has been tested in thermal decomposition and mechanical shock simulations in three-dimensional systems.<sup>14</sup> It has been demonstrated that this model has a well-defined threshold for homogeneous detonation via mechanical loading, and steady-state detonation fronts have been observed to propagate at an intrinsic speed. Both of these attributes are critical for studying shock sensitivity via molecular simulation. This energetic material model has also been used to simulate a plastic bonded explosive.<sup>15</sup> The initial configuration of the system used in the current study was a thin slab geometry in which nitrogen cubane molecules were packed in a simple cubic structure in a simulation box of  $46 \times 52 \times 0.9$  nm<sup>3</sup>. The system was periodic in the *Y* and *Z* directions and shocks propagated along the positive *X* direction. The classical dynamics were calculated using a standard numerical integrator without temperature or pressure control using a time step of 0.08 fs. This relatively small time step was essential to ensure integration stability under the high temperatures associated with detonation process. For all systems, the initial temperature was 0 K (although the system is mechanically stable at finite temperatures).

Rectangular voids were created by removing nitrogen cubane molecules from a perfect crystal (Figure 1). The relevant characteristics of the void are a longitudinal length (*X* direction) and a transverse length (*Y* direction). The void dimension in the *Z* direction was infinite due to the periodic boundary condition. The onset of detonation within a simulation is defined to occur when the total potential energy of the system as it is being shock-compressed starts to decrease relative to the initial state because of the formation of reaction products. Previous studies have demonstrated that these conditions lead to a steady-state detonation in this model. The reaction products include

oligomeric intermediates,  $N_2$ , and a very small amount of single nitrogen atoms. For the discussion below, a reaction product is defined as an atom with a potential energy less than  $-3.0$  eV (for reference,  $N_2$  has a potential energy of  $-4.91$  eV/atom and  $N_8$  cubane has a potential energy of  $-2.41$  eV/atom with this potential). A supported shock was generated by keeping the relative positions of the molecules in a single layer rigid and incrementing their positions by a constant amount in the shock direction. To determine relative sensitivities, a series of simulations for each atomic configuration were carried out where each consecutive simulation uses a higher piston velocity until the configuration detonates.

Two series of simulations were conducted, one in which the transverse length of the void was varied while keeping a constant longitudinal length, and one in which the longitudinal length was varied while keeping a constant transverse length (see Figure 1). To evaluate the influence of the placement of the void in the direction of the supported shock, three types of voids within the former series were initially evaluated, a void aligned within 10 nm of the piston, a void aligned within 10 nm of the end of the simulation cell, and a void in the center of the system. The detonation thresholds for the centered void and the void nearest the end of the simulation away from the shock overlap within the uncertainty of the simulation. For longitudinal lengths less than about 15 nm, voids aligned near the piston exhibit a lower detonation threshold than the other systems. For this alignment, as the ejected energetic molecules hit the downstream wall, a compressive re-shock wave is reflected back, and detonation occurs when this re-shock wave reaches the rigid piston. This type of sub-threshold detonation is a result of the finite thickness of the upstream-wall and is thus an artifact of the simulation size. If simulations where the detonation starts at the piston are excluded, the detonation thresholds become independent of the placement of the voids in the direction of the piston motion. Therefore, the remainder of the results are based on center aligned voids. The influence of the system size in the Z direction on the threshold piston velocity for detonation was also explored by doubling the thickness of a system containing a void 14 nm in the longitudinal direction and 20 nm in the transverse direction. The threshold velocity was only 2% less than that of the smaller system size, which is within the numerical uncertainty inherent to the simulations of the piston threshold estimates for each void dimension.

### III. Results

The discussion of the simulation results is divided into two subsections, one in which void collapse and jetting is discussed, and one in which reactive chemical dynamics is discussed. Because it is established from other studies (see above) that jetting can occur across multiple length scales, the void collapse and jetting observed in these simulations is referred to as mesoscopic-scale dynamics (although the simulations are strictly atomistic). The reactive dynamics, in contrast, is characterized on a molecular level and is therefore referred to as atomic-scale dynamics. The initiation of the detonation wave depends on the coupled dynamics of both scales and is therefore discussed in both of the subsections below.

**III.i. Mesoscopic-Scale Dynamics.** Plotted as the points (with error bars) in the top panel of Figure 2 are the threshold piston velocities obtained from the molecular dynamics simulations as a function of the transverse length of the void with a constant longitudinal length of 20 nm. The upper bound of the error bar denotes the lowest attempted piston velocity for which the system detonated. The lower bound to the error bar denotes the

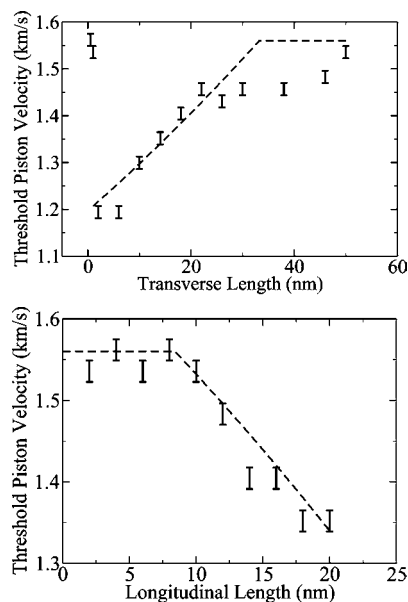


**Figure 2.** Threshold piston velocities as a function of void dimension. Top panel: data for a constant longitudinal dimension of 20 nm with a varying transverse dimension. Bottom panel: data for a constant transverse dimension of 14 nm and a varying longitudinal dimension. The bottom and top of the error bars denote the highest piston velocity where detonation did not occur and the lowest piston velocity that initiated detonation, respectively. The dashed line is the fit of equations 5a,b to the simulation results.

highest attempted piston velocity that did not detonate the system. For reference, the piston velocity needed for homogeneous detonation of this system is 1.56 km/s. For voids with a longitudinal dimension of 1 nm or less, which are 1 to 2 molecules wide, there is no appreciable reduction in the threshold piston velocity compared with the homogeneous case. In contrast, starting at about 2 nm, there is an approximately 25% reduction in the threshold piston velocity. The threshold velocity increases monotonically for transverse lengths between about 6 and 20 nm, after which the reduction in the threshold piston velocity becomes independent of the transverse length. The points in the bottom panel of Figure 2 are the threshold piston velocities obtained from the molecular simulations as a function of the longitudinal length of the void with a constant transverse length of 14 nm. This transverse length corresponds to the value of the transverse void dimension where the threshold piston velocity begins to increase monotonically with increasing transverse length. As the longitudinal length decreases from 20 nm, the threshold piston velocity increases monotonically until about 8 nm, where there is no longer any appreciable reduction in the threshold piston velocity compared with a homogeneous detonation.

Illustrated in Figure 3 are a series of snapshots from simulated void collapses for transverse and longitudinal void dimensions of 14 and 20 nm, respectively. The atoms are shaded according to the local effective temperature, and the times are given relative to the time at which the leading edge of the supported shock first reaches the void. The local effective temperature is calculated from the internal kinetic energy of each cubane molecule. Consistent with a hydrodynamic regime, the collapse of the void occurs on the time scale of the passage of the supported shock. Material is ejected into the void as the supported shock front reaches the upstream wall of the void. After a delay, a single jet of material forms that moves through the void until it collides with the downstream wall. After collision, two "lobes" containing a hot gas form on either side



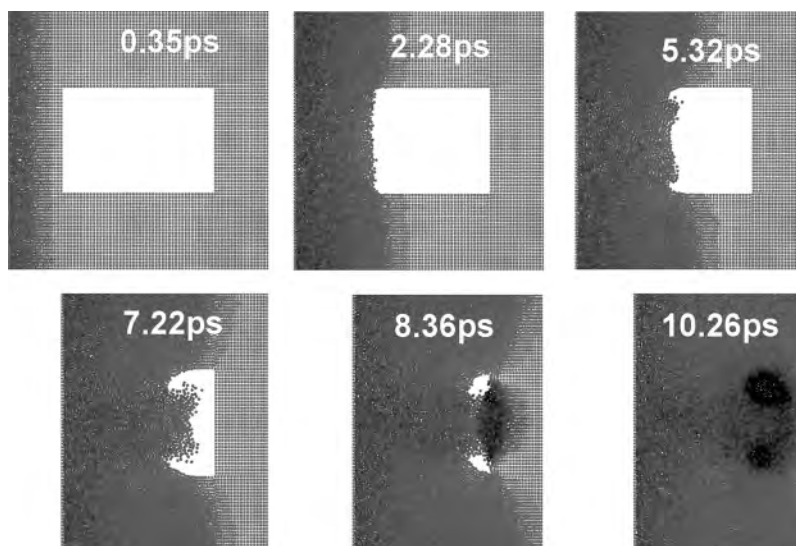


**Figure 3.** Illustration from a simulation of the hydrodynamic collapse of a void of 20 nm in the longitudinal direction and 14 nm in the transverse direction. The supported shock, which travels from left to right, has a piston velocity just above that needed for initiation. The gray scale corresponds to the internal kinetic energy of each nitrogen cubane. Gray represents 0 eV/atom, and black represents 0.4 eV/atom. The times are relative to that at which the supported shock first reaches the void.

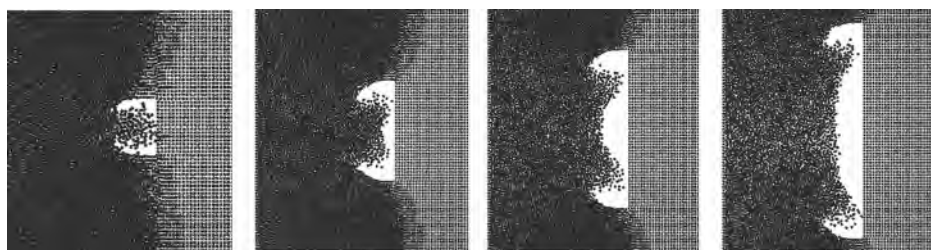


**Figure 4.** Snapshots from simulations as the jet impacts the downstream void wall for different transverse void lengths with the same longitudinal length (20 nm). The transverse lengths are 6, 14, 22, and 30 nm from left to right.

of the jet impact point. The formation of these lobes is consistent with the experimental high-speed photography images and luminescence studies of the hydrodynamic collapse of millimeter-size cylindrical voids in gels by Bourne and Field and co-workers discussed above.<sup>1,2,4,5</sup> Hence, the shape and heating profile in these atomic-scale simulations are qualitatively consistent with those observed experimentally at the macroscopic scale.

The increase in the threshold piston velocity with respect to the transverse void size apparent from the bottom panel of Figure 2 can be qualitatively understood by further examining the mesoscopic-scale dynamics of the void collapse. Illustrated in Figure 4 are snapshots of systems just prior to the impact of material onto the downstream portion of the void for different transverse void lengths that correspond to those in the top panel of Figure 2. In the region with the lowest threshold piston velocity, there is a single jet that is focused by both walls of the void. As the transverse length increases with a constant longitudinal length, the focusing effect of the two walls is diminished, and the jet is correspondingly more diffuse. With further increase in the transverse void dimension, the hydrodynamic collapse evolves to two jets, each of which is focused by only one wall. Once these two jets become sufficiently isolated from one another, the threshold piston velocity for detonation becomes independent of transverse length. The production of dual jets from two corners of a collapsing void is consistent with the macroscopic-scale experiments by Bourne and Field and co-workers discussed above.

In the final stages of the hydrodynamic void collapse illustrated in Figure 3, material flows into the two lobes on either

side of the jet both from the region of the jet impact and from the collapsing walls of the initial void. Hence, the entire void collapse process can be considered as a primary collapse from jetting and secondary collapsing of the lobes. Because of the geometry of the system, material flows into the lobes from the direction of the jet impact and from the direction of the void walls; hence, this secondary collapse is more symmetric than the primary collapse that is accompanied by jetting. In the case of double jetting, there is also a secondary void collapse into lobes formed between the jets and the initial void walls, as well as an additional secondary void collapse in the region between the two jet impact points. This is visible in the double jetting snapshot in Figure 4. For the simulation conditions used here, the material that enters the void formed between the jets comes from the upstream direction, and hence, the secondary collapse in the center of the system is asymmetric, although an additional jetting is not observed.

Plotted in the top panel of Figure 5 is the average velocity of 10 molecules that define the leading edge of the material ejected into the void as a function of time for the system corresponding to the dynamics illustrated in Figure 3. The time in the plot is relative to the time at which the supported shock first reaches the upstream void wall. Plotted as the solid line in the bottom panel of Figure 5 is the position of the same 10 molecules as a function of time during the collapse of the void for the same system. The ejected material undergoes a rapid acceleration over approximately 0.5 ps to a constant velocity of  $\sim 1.2$  km/s, which roughly matches the piston velocity of 1.36 km/s. During this time, the material in the void has ejected en masse in a compressed state reminiscent of the bulk material

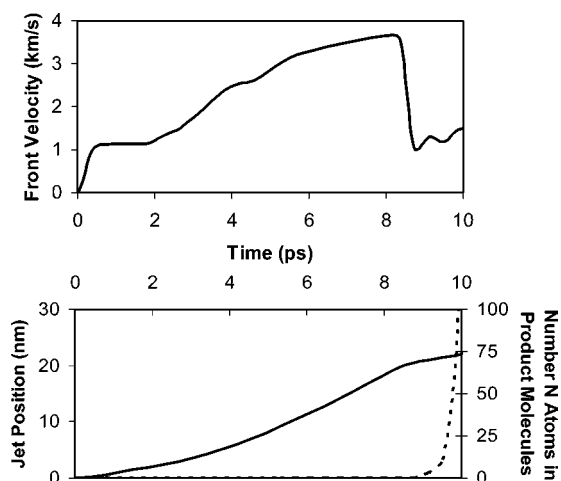


**Figure 5.** Data from the simulation illustrated in Figure 3. Top Panel: jet front velocity as a function of time. Bottom Panel: jet front position (solid line) and number of nitrogen atoms in the products in the system (dashed line) as a function of time. The time in both panels are relative to that at which the shock front first reaches the upstream void wall. The jet front position is relative to the upstream edge of the void.

in the front of the supported shock. Starting at about 2 ps, the ejected material decompresses, which results in a further acceleration to roughly twice the piston velocity at about  $\sim 4$  ps. This primary acceleration is consistent with the observations of Holian and co-workers in their simulations of shocked material containing a void. For times greater than  $\sim 4$  ps, the ejected material undergoes an additional acceleration that is concurrent with the formation of the jet (see Figure 3). This secondary acceleration, which results from focusing from the walls, is responsible for the reduced threshold piston velocity in the bottom panel of Figure 2 for longitudinal voids greater than  $\sim 9$  nm. A similar acceleration due to wall focusing was also noted in recent simulations by Numora et al.<sup>13</sup>

By using the concepts gleaned from Figures 2–5, an analytic expression can be derived that reproduces the dependence of the threshold piston velocity on the longitudinal and transverse void lengths as indicated in Figure 2. For simplicity, the primary acceleration is ignored, and it is assumed that the spalled material prior to jet formation has a velocity of  $2V_p$  where  $V_p$  is the piston speed. This approximation is justified by the behavior indicated in the bottom panel of Figure 2, which demonstrates that during the period over which the ejected material is decompressing the threshold piston velocity is constant. Apparently, the total energy of the ejected material, not just the kinetic energy, contributes to detonation initiation. It is further assumed that, after focusing, the jet front undergoes an additional accelerated  $a$  due to focusing by the void walls, but this acceleration is delayed because of the time needed for the decompression wave in the leading edge of the void to propagate to the side walls. The delay time  $t_d$  can be estimated as the transverse length  $W$  divided by the propagation velocity of the decompression wave  $V_d$

$$t_d = \frac{W}{V_d} \quad (1)$$

With these assumptions the jet front velocity as a function of time  $t$  (the time origin being the moment the shock reaches the void) is

$$V_j = 2V_p, \quad t < t_d \quad (2a)$$

$$V_j = 2V_p + a(t - t_d), \quad t \geq t_d \quad (2b)$$

and the jet front position  $x_j$  with respect to the upstream edge of the void is

$$x_j = 2V_p t, \quad t < t_d \quad (3a)$$

$$x_j = 2V_p t + \frac{a}{2}(t - t_d)^2, \quad t \geq t_d \quad (3b)$$

Solving equation 3 for  $t$  when  $x_j = L$  and substituting in equation 2 gives the jet front velocity when the jet collides with the downstream wall as

$$V_j = 2V_p, \quad \frac{L}{2V_p} < t_d \quad (4a)$$

$$V_j = \sqrt{4V_p^2 + 2a(L - 2t_d V_p)}, \quad \frac{L}{2V_p} \geq t_d \quad (4b)$$

Within this model, the threshold piston velocity for detonation of a void  $V_p^{\text{det}}$  corresponds to the conditions at which the velocity of the ejected material just before reaching the downstream wall of the void equals twice the threshold piston velocity for a perfect crystal  $V_p^{\text{crystal}}$ . Therefore, the threshold piston speed for the voids is

$$V_p^{\text{det}} = V_p^{\text{crystal}}, \quad \frac{L}{2V_p^{\text{crystal}}} < \frac{W}{V_d} \quad (5a)$$

$$V_p^{\text{det}} = \frac{1}{2} \left( \frac{aW}{V_d} + \sqrt{-2aL + a^2 \left( \frac{W}{V_d} \right)^2 + 4(V_p^{\text{crystal}})^2} \right), \quad \frac{L}{2V_p^{\text{crystal}}} \geq \frac{W}{V_d} \quad (5b)$$

Indicated by the dashed lines in Figures 2 are the relations given by equations 5a,b. The quantity  $V_p^{\text{crystal}}$  was measured to be 1.56 km/s, leaving two fitting parameters, the jet acceleration  $a$  due to focusing from the void walls and the speed for the decompression wave  $V_d$ . The best fit to the simulation data corresponds to  $a = 0.1 \times 10^{15} \text{ m/s}^2$  and  $V_d = 5.18 \text{ km/s}$ . The velocity of the decompressive wave is close to the range of the velocity (6.8 to 8.4 km/s) of the shock created by the piston. The analytic expressions equations 5a,b provide an excellent fit to the data in the bottom of Figure 2. However, there are noticeable deviations between the analytic model and the simulation results for the top panel of Figure 2. Equation 2b in the above model only considers the acceleration of ejected material as a whole and does not account for the jet formation nor for the transition from single jet to double jets. Therefore, the delay time  $t_d$  is an overestimate because the true acceleration is more localized. This leads to an overestimate of the detonation threshold. This effect is more pronounced for voids with large transverse lengths.

To characterize the possible contribution of recompression to initiation sensitivity for this system, simulations were also carried out for planar voids without sidewalls with gap widths up to 20 nm. In contrast to the simulation results reported in ref 9, no reduction in detonation threshold was found, suggesting that gas recompression without jetting does not make a significant contribution to enhanced sensitivity for this system.

**III.ii. Atomic-Scale Dynamics.** Plotted in the bottom panel of Figure 5 as the dashed line is the number of nitrogen atoms in products in the system as a function of time during void

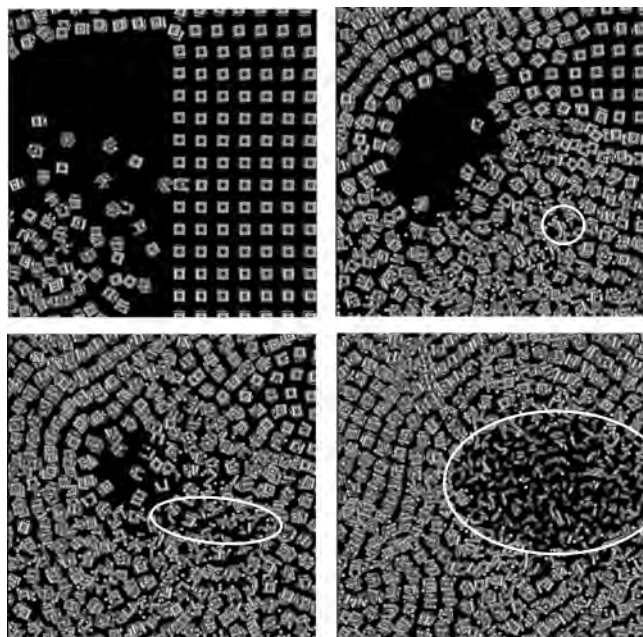


**Figure 6.** Close-up snapshots of the same system discussed in Figure 3 and Figure 4 near the region where the jet first impacts the void downstream wall.

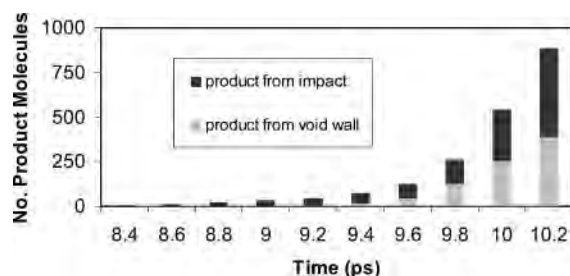


**Figure 7.** Number of product species arising from different spatial regions of the simulation at different times for the system illustrated in Figure 6.

collapse. No product molecules are formed during the time period over which the jet forms and accelerates through the void. After the jet collides with the downstream wall, products begin to form, with the number of products rising sharply starting at about 9.5 ps or about 1 ps after the jet first collides with the downstream void wall. Illustrated in Figure 6 are snapshots from the simulation corresponding to Figure 5 where only the local region near the initial jet collision with the downstream wall is shown. The products are indicated by circles superimposed over the snapshots. Reactions leading to product molecules initially occur in the condensed region where the jet first impacts the void wall. As the simulation progresses, material expands into the lobes from both the impact region and from the walls of the void, leading to the heating observed on the mesoscopic scale.

Plotted in Figure 7 are the number of product molecules at different times for the simulation illustrated in Figure 6. The dark portion of the bars correspond to product species that originated from cubane molecules that were initially part of the jet or part of the downstream void wall near the jet impact point. The lighter portion of the bars correspond to product species that originated from cubane molecules that were initially part of the void wall that expanded in the hot lobes. Prior to 9 ps, all of the product species (a total of 31) originated from the impact dynamics. As the system evolves in time, products start to form in the hot lobes, and by about 9.8 ps, the amount of

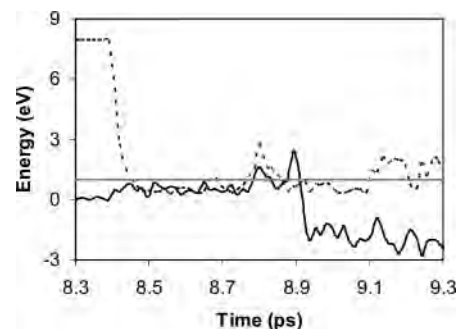


**Figure 8.** Total center-of-mass kinetic energy (dotted line) and the total potential energy (relative to that at 0 K of an isolated molecule) for a molecule at the jet front from the simulation illustrated in left-most simulation of Figure 4. The horizontal shaded line is the potential energy barrier for thermal reaction (1 eV).

product originating from the side wall molecules match that from the impact. For reference, by using the criteria given above, the onset of detonation occurs at  $\sim 9.7$  ps. From this data, it is apparent that the exothermic reactions that transition to detonation originate initially from the impact point. Taken together with the ability of the model described above to reproduce the dependence of the threshold piston velocity on void dimensions using only the velocity of the jet front as it traverses the void, this observation suggests that the expansion and subsequent recompression in the lobes is not the primary mechanism that initiates detonation for this system. This conclusion is consistent with the conclusions based on macroscopic-scale experimental studies of void collapse discussed above where initiation arises from the jet impact and not from the hot regions associated with the lobes.

The jet front velocity needed for detonation initiation is  $\sim 3.12$  km/s, which corresponds to a total center-of-mass kinetic energy of  $\sim 8$  eV for each cubane molecule. This kinetic energy is significantly larger than the thermal barrier of 1 eV for the formation of  $N_2$  from cubane for the potential model used here,<sup>14</sup> which implies a relatively inefficient transfer of center-of-mass kinetic energy directly to the reaction coordinate during collisions with the downstream void wall. Plotted as the dotted line in Figure 8 is the total center-of-mass kinetic energy for a molecule at the jet front for the simulation illustrated in Figure 6. Plotted as the solid line in Figure 8 is the total potential energy relative to that at 0 K of the same molecule, while the horizontal line indicates the potential barrier of 1 eV for dissociation. The molecule rapidly loses center-of-mass kinetic energy when it hits the downstream void wall at about 8.4 ps. The internal potential energy rises up to about 0.8 eV (which is just below the reaction barrier) at about 8.45 ps, and again at about 8.65 ps. At 8.8 ps, the internal potential energy rises to 1.64 eV, decreases to below 1 eV, and then rises again to 2.45 eV at 8.9 ps after which the potential energy decreases because of the reaction that leads to the formation of  $N_2$ .

Plotted in the top panel of Figure 9 is a close-up of the data in Figure 8. To better analyze the dynamics associated with this plot, the data is divided into six regions that are denoted by Roman numerals. In region I, which is before the initial collision with the downstream wall, there is a small oscillation in the potential energy that arises from a vibrational symmetric breathing mode of the molecule. In region II, the molecule in the jet first collides with the downstream wall. The translational kinetic energy declines sharply with a corresponding increase in the internal potential energy. In region III, the molecule continues to vibrate with a greater amplitude. For reference, the gray line from about 8.5 to 8.65 ps corresponds to a squared



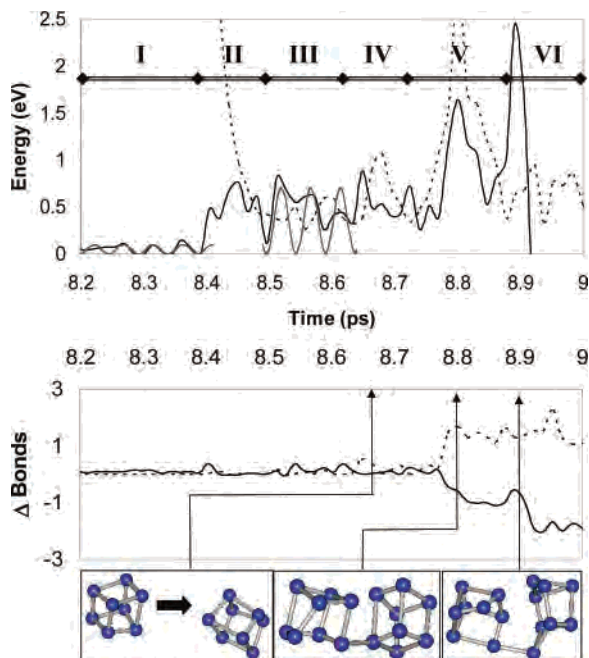


**Figure 9.** Data from the same simulations discussed in Figure 8. Top Panel: close-up of data in Figure 8. The dotted line, solid line, and gray lines represent the center-of-mass kinetic energy, relative potential energy, and squared sine wave functions, respectively. The Roman numerals correspond to different reaction dynamics. Bottom Panel: the change in the number of bonds within the molecule (solid line) and the number of bonds to the molecule (dotted line). The illustrations at the bottom are for two colliding molecules, and the times are indicated by the arrows.

sine wave with the same frequency as the molecular breathing mode, and that has an amplitude and phase shift that best matches the peaks in the molecular potential energy. This molecular dynamics appears to be an “up-pumping” of the breathing mode due to the collision with the downstream wall. There are second and third collisions of the jet molecule in regions IV and V. The former corresponds to an additional collision with a molecule that was initially in the void wall, while the collision in region V is with a molecule that was further back in the jet that collided with the void wall in the vicinity of the initial jet impact. The latter collision transfers a significant amount of kinetic energy into the molecule that was already vibrationally excited due to the initial jet impact. This combination of impacts is apparently sufficient to initiate the production of  $N_2$  molecules that signal the start of the chemically sustained detonation.

Plotted at the bottom of Figure 9 is the change in the number of bonds associated with the molecule whose energy is tracked in the upper plot as determined by the bond counting function used in the potential energy expression.<sup>14</sup> The solid line corresponds to the change in intramolecular bonds, while the dashed line corresponds to changes in the intermolecular bonds. The images at the bottom of Figure 9 illustrate the dynamics of the molecules of interest at the times indicated by the arrows. In these illustrations, the molecule to the right is the molecule that was initially at the front of the jet, while the molecule at the left of each panel is the molecule that is responsible for the collision in region V in the upper plot. The collisions in regions II and IV in the upper plot do not result in significant changes in the bonding topology. In contrast, the collision with the second molecule in the jet in region V results in the formation of first one and then two intermolecular bonds and the corresponding breaking of one and then two intramolecular

bonds. The concerted dynamics leads to the formation of the  $N_2$  products, which release energy with further reaction transitions to the detonation. From this analysis, which is representative of the reactive chemistry in this simulation, the reactive dynamics appear to involve vibrational up-pumping from the initial jet collision followed by a bi-molecular reaction.

The details of reactions such as these will obviously depend very sensitively on the molecular species and the features of the potential energy surface,<sup>13</sup> and therefore, appropriate caution is warranted with respect to drawing general conclusions regarding reaction mechanisms. Nonetheless, this analysis, together with the mesoscopic-scale analysis in the prior section, illustrates the inherent complex interplay between reactive chemistry, hydrodynamic void collapse and jetting, and the initiation dynamics of an energetic crystal.

#### IV. Conclusions

Molecular dynamics simulations have been used to characterize the dynamics of shock-induced collapse of nanometer-scale voids in cubane nitrogen with different aspect ratios and to characterize how this dynamics couples with local chemistry that transitions to a chemically sustained shock front. Mesoscopic-scale features of the void collapse correspond well to experimentally observed features of micrometer-scale bubble collapse characterized by high-speed photography. These features include asymmetric collapse and jetting with a transition from single to dual jets with increasing transverse dimensions of the void and the formation of hot lobes of material on either side of initial jet impact. The simulations demonstrate initiation from the initial impact rather than from the hot lobes, also in agreement with conclusions made on the basis of prior macroscopic-scale studies. An analytic model is developed for the reduction in the initiation piston threshold as a function of void size and shape that reproduces the simulation results. At the atomic level, the simulations show up-pumping of molecules in the jet front because of collisions with the downstream wall, followed by bi-molecular reactive dynamics from continued jet impact that triggers the onset of detonation. While the system studied here is relatively simple compared with energetic materials of practical interest, these results provide important new insights into the coupling of asymmetric void collapse dynamics and the enhanced sensitivity of energetic materials.

**Acknowledgment.** We thank D. Thompson, T. Sewell, Y. Hu, and B. Broom for stimulating discussions. This research was supported in part by the National Science Foundation through TeraGrid resources provided by the NCSA. The North Carolina State University High-Performance Computing Facility is also thanked for providing computational resources. The simulations were performed using LAMMPS molecular dynamics software (<http://lammps.sandia.gov>) with a customized force field. This work was supported by a Multi-University Research Initiative from the U.S. Army Research Office.

#### References and Notes

- (1) Bourne, N. K.; Field, J. E. *Proc. R. Soc. London A* **1999**, 455, 2411.
- (2) Field, J. E. *Acc. Chem. Res.* **1992**, 25, 489.
- (3) Kang, J.; Butler, P. B.; Baer, M. R. *Combust. Flame* **1992**, 89, 117.
- (4) Dear, J. P.; Field, J. E.; Walton, A. J. *Nature* **1988**, 332, 505.
- (5) Bourne, N. K.; Field, J. E. *J. Fluid Mech.* **1992**, 244, 225.
- (6) Waters, W. P.; Zukas, J. A. *Fundamentals of shaped charges*; John Wiley & Sons: New York, 1989.
- (7) Kornfield, M.; Suvorov, L. *J. Appl. Phys.* **1944**, 15, 495.
- (8) Mintmire, J. W.; Robertson, D. H.; White, C. T. *Phys. Rev. B* **1994**, 49, 14859.



- (9) White, C. T.; Swanson, D. R.; Robertson, D. H. In *Chemical Dynamics in Extreme Environments*; Dressler, R., Ed.; World Scientific: Singapore, 2001; p 547.
- (10) Holian, B. L.; Germann, T. C.; Maillet, J. B.; White, C. T. *Phys. Rev. Lett.* **2002**, 89, 285501. Holian, B. L.; Germann, T. C.; Maillet, J. B.; White, C. T. *Phys. Rev. Lett.* **2003**, 90, 069902.
- (11) Germann, T. C.; Holian, B. L.; Lomdahl, P. S.; Heom, A. J.; Gronbech-Jensen, N.; Maillet, J.-B. *Molecular Dynamics Simulations of Detonation in Defective Explosive Crystals*; Symposium of Detonation, 2002.
- (12) Hatano, T. *Phys. Rev. Lett.* **2004**, 92, 015503.
- (13) Nomura, K.; Kali, R. K.; Nakano, A.; Vashishta, P. *Appl. Phys. Lett.* **2007**, 91, 183109.
- (14) Shi, Y. F.; Brenner, D. W. *J. Chem. Phys.* **2007**, 127, 134503.
- (15) Shi, Y. F.; Brenner, D. W. *Appl. Phys. Lett.* **2008**, submitted.

# Shock-induced shear bands in an energetic molecular crystal: Application of shock-front absorbing boundary conditions to molecular dynamics simulations

M. J. Cawkwell\* and Thomas D. Sewell†

*Theoretical Division, Los Alamos National Laboratory, Los Alamos, New Mexico 87545, USA*

Lianqing Zheng‡ and Donald L. Thompson§

*Department of Chemistry, University of Missouri-Columbia, Columbia, Missouri 65211, USA*

(Received 16 November 2007; revised manuscript received 13 June 2008; published 17 July 2008)

The response of the energetic molecular crystal cyclotrimethylene trinitramine (RDX) to the propagation of planar shock waves normal to (100) has been studied using large-scale molecular dynamics simulations that employ an accurate and transferable nonreactive potential. The propagation of the shock waves was simulated using nonequilibrium molecular dynamics. Shear bands were nucleated during shocks with a particle velocity of  $1.0 \text{ km s}^{-1}$  and corresponding Rankine-Hugoniot shock pressure of 9.7 GPa. These defects propagate into the compressed material at  $45^\circ$  to [100] in the [010] zone. The shear bands evolve slowly compared to the time scales routinely accessible to nonequilibrium molecular dynamics toward a liquidlike state as a result of viscous heating. A recently developed shock-front absorbing boundary condition [A. V. Bolesta *et al.*, Phys. Rev. B **76**, 224108 (2007)] was applied to the simulation cells at the moment of maximum compression to sustain the shock-compressed state. Molecular dynamics simulations were then employed to study the temporal and structural evolution of the shock-induced shear bands toward a steady-fluctuating state. Owing to the intense, viscous flow-driven heating within the shear bands, these defects can be considered to be homogeneously nucleated hot spots.

DOI: [10.1103/PhysRevB.78.014107](https://doi.org/10.1103/PhysRevB.78.014107)

PACS number(s): 62.50.-p, 62.20.F-, 61.72.Bb, 61.20.Ja

## I. INTRODUCTION

Defects in solid and crystalline energetic materials are known to exert a significant influence on impact and initiation sensitivity.<sup>1</sup> Mesoscopic and macroscopic defects lead to the spatial localization of the translational energy from a shock through, for example, the formation of jets during the collapse of voids<sup>2,3</sup> or interfacial friction at cracks or particle boundaries.<sup>4,5</sup> Events of this kind result in hot spots where temperature and/or stress may exceed significantly values in the bulk and hence promote molecular decomposition. The formation of hot spots through these mechanisms is well understood, at least on a qualitative level,<sup>6</sup> and apply in general to all solid energetic materials.

The impact sensitivity of defect-free single crystals of the energetic molecular crystal pentaerythritol tetranitrate (PETN) was found to depend strongly on the crystallographic orientation of the shock propagation direction.<sup>7-9</sup> In this case, dislocation-mediated plastic deformation was proposed as an explanation for the observed orientation dependencies. Slip systems were identified in single crystals using x-ray topography and by the analysis of slip traces after surface indentation.<sup>10</sup> Those orientations of the shock propagation direction for which there was no resolved shear stress on any slip system were found to have a high Hugoniot elastic limit and high impact sensitivity. Similarly, those orientations for which a shear stress was resolved on all of the slip systems identified experimentally were found to have low Hugoniot elastic limit and low impact sensitivity. Hence, in the absence of mesoscopic and macroscopic defects, extended crystal defects at the atomic or molecular scale were found to play a role in determining impact sensitivity. This work led to the formulation of the steric-hindrance

model,<sup>7,8,11</sup> wherein an absence of dislocation-mediated plasticity for a given crystallographic orientation of the shock propagation direction promotes initiation since shear stresses cannot be relaxed easily and molecules deform severely, inducing bond-breaking events.

We have studied the response of single crystals of the widely used energetic molecular crystal cyclotrimethylene trinitramine,  $\text{C}_3\text{H}_6\text{N}_6\text{O}_6$  (RDX), to the propagation of shock waves normal to (100) by means of large-scale molecular dynamics (MD) simulations, with particular focus on the shock-induced nucleation of extended defects. Under ambient pressure and temperature, RDX adopts an orthorhombic unit cell in space group *Pbca* that contains eight molecules ( $\alpha$ -polymorph).<sup>12</sup> An RDX molecule is depicted in Fig. 1(a) and a projection of the  $\alpha$ -RDX unit cell along [001] in Fig. 1(b). Three slip systems were identified in RDX single crystals by the analysis of slip traces after surface indentation: (010)[001], (021)[100], and (02 $\bar{1}$ )[100].<sup>10</sup> Hence, the [100] shock propagation direction is special since there is no resolved shear stress on any of the slip systems identified un-

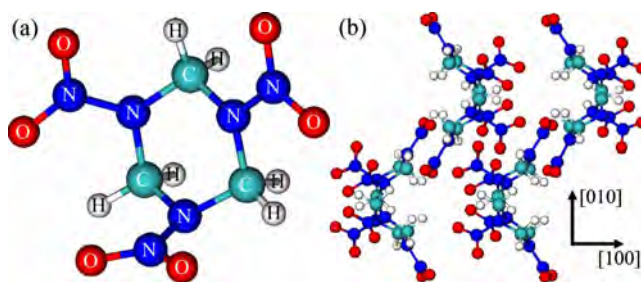


FIG. 1. (Color online) (a) An RDX molecule and (b) projection of the  $\alpha$ -RDX unit cell along [001].

der quasistatic loading.<sup>13</sup> Thus, on the basis of the steric-hindrance model, we expect this orientation to be of high impact sensitivity. However, earlier work on (111)-oriented RDX single crystals revealed an abrupt change in the mechanism of plastic deformation above a certain shock pressure that could not have been anticipated based on either crystallographic arguments or the results of quasistatic loading experiments.<sup>13,14</sup> This work led us to the conclusion that extrapolating the mechanisms for plastic deformation identified in energetic molecular crystals under quasistatic loading over many orders of magnitude in strain rate can be rather unreliable, particularly for complicated, low-symmetry crystal structures. In fact, PETN can be considered as a special case in this regard since it adopts a relatively high-symmetry tetragonal unit cell comprising only two molecules.

Nonequilibrium molecular dynamics (NEMD) simulations<sup>15–20</sup> of the propagation of planar shock waves normal to (100) were performed for particle velocities  $U_p = 0.63$  and  $1.0 \text{ km s}^{-1}$ , corresponding to shock pressures,  $P_{RH}$ , calculated using the Rankine-Hugoniot jump conditions<sup>21</sup> of 5.7 and 9.7 GPa, respectively. At  $P_{RH} = 5.7 \text{ GPa}$ , we found no evidence for the nucleation of crystal defects. However, at  $P_{RH} = 9.7 \text{ GPa}$ , liquidlike shear bands (SBs) were nucleated which propagate at  $45^\circ$  to the compression axis. The remainder of this paper is devoted to the characterization of these defects.

A popular method for generating planar shock waves in NEMD simulations is to either drive a rigid piston at a specified particle velocity onto a stationary simulation cell or impact a simulation cell onto a fixed, rigid piston at a specified particle velocity. In this paper we have employed the latter approach. Both of these methods limit the time interval over which material remains on the Hugoniot locus since once the shock wave reaches the free surface of the simulation cell, a rarefaction wave propagates rapidly back into the shock-compressed material. Hence, material near the free surface is on the Hugoniot locus for a very limited time. Simulations of this type typically employ simulation cells that are relatively long parallel to the shock propagation direction in order to maximize the time interval over which material in the vicinity of the piston is sustained in the shocked state. This approach is often not practical computationally, particularly in the simulation of slow processes such as plasticity or chemistry. In the present work, this limitation of NEMD simulation techniques is particularly pronounced since the internal structure of the shock-induced shear bands evolves relatively slowly, compared to typical NEMD time scales, by a viscous heating mechanism.

We have employed, with modifications, a simple and robust method for extending time scales in molecular dynamics simulations of shock loading that was first developed by Bolesta *et al.*<sup>22</sup> The shock-front absorbing boundary condition (SFABC) (Ref. 23) enables a seamless transition from a NEMD simulation of the propagation of a shock front to the simulation of shock-induced defects during their evolution toward a steady-fluctuating state. SFABCs capture the simulation cell at the point of maximum compression in a NEMD simulation and prevent the emission of rarefaction waves from the free surface. Furthermore, the SFABC approach obviates the requirement for simulation cells that are “long”

parallel to the direction of shock propagation, does not introduce any incoherent interfaces into the system, and leaves unaffected the microcanonical equations of motion. The SFABC method and its application to a crystalline solid are described in detail in Sec. III.

Other methods for the absorption of waves incident at boundaries in MD simulations have been developed in recent years. For example, Namilae *et al.*<sup>24</sup> implemented a differential equation-based absorbing boundary condition (ABC) to match the impedance of a semi-infinite continuum space to that of an atomistic region. However, ABCs of this type are based on the linear wave equation and for this reason are not suited to the absorption of shock waves.

## II. NONEQUILIBRIUM MOLECULAR DYNAMICS SIMULATIONS

The nonreactive, fully flexible molecular potential for nitramines developed by Smith and co-workers<sup>25,26</sup> was employed in all of the MD simulations. The Smith-Bharadwaj potential<sup>25</sup> describes bond stretches, bond angles, and out-of-plane bends using harmonic springs. Torsions are represented by anharmonic terms that display extrema at the torsion angles that correspond to stationary points on the conformational energy surface. The intramolecular terms were parametrized to quantum chemistry calculations of the structure, vibrational frequencies, and barriers to conformational change in a model compound, 1,3-dimethyl-1,3-dinitro methylidiamine. Intermolecular interactions are represented by a sum of Buckingham potentials parametrized to standard literature values. Electrostatic interactions are included explicitly and employ partial charges that were increased for all species by 25% compared to quantum chemistry-calculated values to account for the effects of polarization in condensed phases. The Smith-Bharadwaj potential,<sup>25</sup> while not parametrized to reproduce any particular property of condensed phase nitramines, was shown to provide excellent descriptions of crystalline cyclotetramethylene tetranitramine (HMX) (Refs. 26 and 27) and RDX. In the case of RDX the Smith-Bharadwaj potential<sup>25</sup> not only predicts the orthorhombic *Pbca* space group to be the crystal structure with the lowest free energy at zero pressure and 300 K but it also provides remarkably accurate predictions for its lattice parameters,<sup>12</sup> single-crystal elastic constants,<sup>28</sup> coefficient of thermal expansion,<sup>29</sup> and isothermal compression curve up to the  $\alpha$ -to- $\gamma$  phase transformation.<sup>30</sup> Furthermore, it predicts the  $P$  versus  $U_p$  Hugoniot of RDX crystals shock loaded normal to (111) to within 0.5 GPa of experiment.<sup>31</sup>

The lattice parameters of  $\alpha$ -RDX calculated using the Smith-Bharadwaj potential<sup>25</sup> at 300 K and zero pressure are  $a = 13.400 \text{ \AA}$ ,  $b = 11.517 \text{ \AA}$ , and  $c = 10.623 \text{ \AA}$ , each of which is within 1.7% of experiment.<sup>12</sup> These calculated lattice parameters were used for all the simulations reported here. NEMD simulations of the propagation of planar shock waves normal to (100) employed an oblong simulation cell measuring  $120a \times 20b \times 20c$ , containing  $8.064 \times 10^6$  atoms. A shorter simulation cell measuring  $60a \times 20b \times 20c$  was also used to study the effect of SFABCs on the structure of shock-induced defects. These cells are hereafter referred to

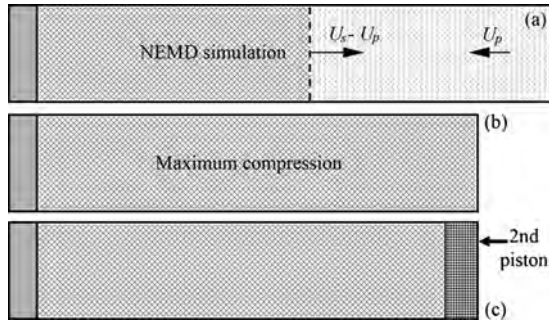


FIG. 2. (a) Schematic illustration of a NEMD shock loading simulation. The vertical broken line represents the position of the shock front which is traveling from left to right. (b) Simulation cell at maximum compression. (c) Application of the second piston in the shock-front absorbing boundary condition (SFABC) method.

as the long and short cells, respectively. Finally, we also created a quasi-two-dimensional (quasi-2D) simulation cell to assess and mitigate any finite-size effects on the defect structures generated during the simulations. The quasi-2D cell measured  $149a \times 3b \times 141c$  and contained  $10.6 \times 10^6$  atoms. An additional 200 Å thick vacuum region was included in the simulation cells along [100] to minimize electrostatic interactions between free surfaces upon the application of three-dimensional periodic boundary conditions. The simulation cells were thermalized until intermolecular and intramolecular temperatures equilibrated to 300 K prior to shock loading. The propagation of supported planar shock waves was simulated in the microcanonical ensemble by impacting the cells onto a fixed piston of thickness  $3a$  consisting of rigid RDX molecules in the same crystallographic orientation as the simulation cell by adding to all atoms a particle velocity  $U_p$  parallel to [100]. This generates a shock wave propagating at velocity  $U_w = U_s - U_p$  relative to the stationary piston, where  $U_s$  is the shock wave velocity; this is illustrated schematically in Fig. 2(a). All simulations were performed using the LAMMPS code.<sup>32</sup> Long-range electrostatic interactions were calculated using the PPPM method<sup>33</sup> and all C-H bonds were constrained to equilibrium length using the SHAKE algorithm. One NEMD simulation was performed at  $U_p = 0.63 \text{ km s}^{-1}$  using the long cell and three at  $U_p = 1.0 \text{ km s}^{-1}$  using the long, short, and quasi-2D cells. A 0.4 fs time step for the integration of the equations of motion was employed in each case.

### III. SHOCK-FRONT ABSORBING BOUNDARY CONDITIONS

The SFABC method facilitates a seamless transition from a NEMD simulation of the propagation of a shock wave through a medium to a MD simulation of the evolution of any defects created by the shock wave. SFABCs were originally implemented and applied to MD studies of shock waves in reactive methane.<sup>22</sup> In the present work on crystalline RDX, we used a modest simplification of the original method for absorbing the shock front which we expect to be more robust in its implementation. The SFABC method is illustrated schematically in Fig. 2.

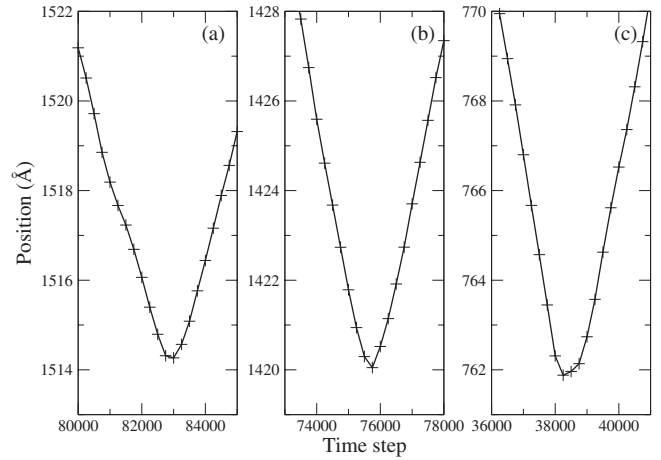


FIG. 3. Plots of the  $x$  coordinate of the last molecule as a function of the time step from the NEMD simulations of (a) the long cell,  $U_p = 0.63 \text{ km s}^{-1}$ , (b) long cell,  $U_p = 1.0 \text{ km s}^{-1}$ , and (c) short cell,  $U_p = 1.0 \text{ km s}^{-1}$ .

The starting point for the application of SFABCs is a NEMD simulation of shock loading as described in Sec. II. The shock wave is allowed to propagate until the simulation cell reaches the point of maximum compression. The point of maximum compression can be identified to a high level of accuracy by monitoring as a function of time the  $x$  coordinate of the center of mass of the “last” molecule in the simulation cell. The last molecule, the one with the largest  $x$  coordinate, can be identified easily by postprocessing analysis of the NEMD simulation. The simulation cells were captured at maximum compression to within a tolerance of 1 Å in the three NEMD simulations described in Sec. II. Plots of the  $x$  coordinate of the last molecule as a function of the time step are presented in Fig. 3.

Once the point of maximum compression was identified in the NEMD simulations, the force and velocity vectors of all atoms within the last 30 Å of the cell were set equal to zero. In this manner, those molecules at the end of the simulation cell are treated as a second piston that, together with the first stationary rigid piston, serve to constrain the shock-compressed material at constant volume. In principle, it would also be possible to capture the simulation cell at maximum compression by removing from the system the vacuum region and applying periodic boundary conditions along the shock propagation direction. However, the approach adopted here ensures that the interface between the simulation cell and second piston is structurally coherent, unlike the interface that would be created upon the application of periodic boundary conditions. Furthermore, since the second piston can be made arbitrarily thick, the SFABC method is not affected adversely by the finite width of the shock front.

In the original implementation of the SFABC method,<sup>22</sup> the point of maximum compression was determined by monitoring as a function of time the specific energy content of layers of molecules perpendicular to the direction of shock propagation. The profile of specific energy versus position was fit to a straight line which was extrapolated to predict the time at which the second piston, which in this case was rigid and at rest, was assigned velocity  $U_p$ .



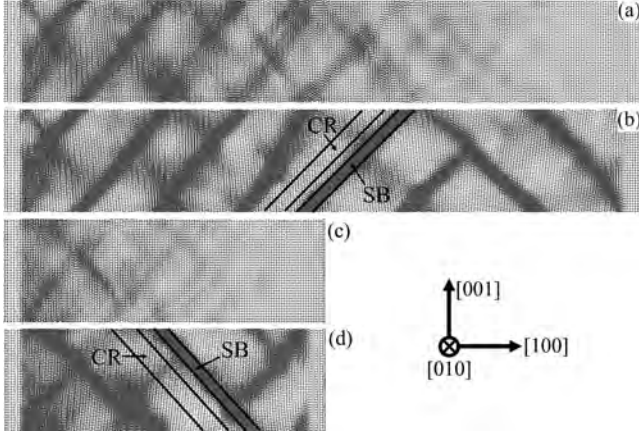


FIG. 4. Projections along  $[010]$  of the molecular centers of mass after shock loading at  $U_p = 1.0 \text{ km s}^{-1}$ . (a) Long cell at maximum compression (Ref. 34), (b) long cell after 121 ps MD simulation under SFABCs (Ref. 34), (c) short cell at maximum compression, and (d) short cell after 110 ps MD simulation under SFABCs. The crystalline regions (CRs) and shear bands (SBs) used for subsequent analysis are indicated in (b) and (d).

## IV. RESULTS

### A. Shock-induced defects

#### 1. NEMD simulations

The NEMD simulation of the propagation of a planar shock wave along  $[100]$  in the long cell at  $U_p = 0.63 \text{ km s}^{-1}$  ( $P_{RH} = 5.7 \text{ GPa}$ ) did not result in the nucleation of crystal defects. As noted in Sec. I, at this orientation of the shock propagation direction, none of the dislocation slip systems identified under quasistatic loading conditions<sup>10</sup> are subject to a resolved shear stress.

Shock loading at  $U_p = 1.0 \text{ km s}^{-1}$  ( $P_{RH} = 9.7 \text{ GPa}$ ) led to the formation of shear bands during NEMD simulations employing both the long and short cells. Projections of the molecular centers of mass along  $[010]$  of the long and short cells at maximum compression are presented in Figs. 4(a) and 4(c), respectively.<sup>35</sup> In both cases, the shock wave propagated from left to right and it is apparent that the shear bands are structurally more developed in the vicinity of the piston since their growth rate is relatively slow compared to the time scale of the simulations. The shear bands propagate at approximately  $45^\circ$  to  $[100]$  and the plane of the bands lies in the  $[010]$  zone. There appears to be no preference as to whether the shear bands propagate at positive or negative  $45^\circ$  to  $[100]$ ; the bands are not aligned with any crystallographic orientation of the underlying structure and are driven only by shear stresses which are a maximum at these orientations. However, there is a distinct preference for the plane of the bands to lie in the  $[010]$  zone. The shear bands are not appreciably higher in density than the surrounding crystalline regions (CRs); the latter appear to be of low density since in this projection columns of molecules are viewed “end on,” while the former comprise amorphous material.

#### 2. SFABC simulations

The SFABC was applied to the simulation cells as described in Sec. III. The long cell shock loaded at  $U_p$

$= 0.63 \text{ km s}^{-1}$  was simulated in the microcanonical ensemble for 42 ps after the application of SFABCs. The long and short cells shock loaded at  $U_p = 1.0 \text{ km s}^{-1}$  were simulated in the microcanonical ensemble under SFABCs for 121 and 110 ps, respectively. Snapshots of the long and short cells shock loaded at  $U_p = 1.0 \text{ km s}^{-1}$  taken at the conclusion of the SFABC simulations are presented in Figs. 4(b) and 4(d), respectively. The SFABCs enable simulation times sufficient for the shear bands to propagate throughout the entire system, and, more importantly, for their internal structure to evolve to a steady-fluctuating state. Detailed analyses of the internal structure of the shear bands are provided in Sec. IV B.

Upon the application of SFABCs, shear bands propagate into the shock-compressed material from the second piston in the opposite orientation to those formed at the first piston. From the moment that the second piston is applied and both ends of the cell are fixed, the total plastic strain mediated by the shear bands in the directions normal to  $[100]$  must equal to zero. Hence, growth of the shear bands nucleated in the NEMD simulation is compensated by shear in the opposite sense provided by shear bands growing from the opposite end of the cell. While this may at first seem to be an unphysical artifact associated with SFABCs, it is, in fact, physically correct. We previously observed an abrupt change in the orientation of shear bands in NEMD simulations of systems with very high aspect ratio (15:1 rather than 8:1) owing to the constraints on lateral motion imposed by the unshocked material ahead of the shock front.<sup>36</sup> Hence, in this respect, SFABCs mimic a NEMD simulation using a cell of very high aspect ratio.

Simulations using the long and short cells at  $P_{RH} = 9.7 \text{ GPa}$  ( $U_p = 1 \text{ km s}^{-1}$ ) exhibit pronounced finite-size effects whereby one shear band propagates a significant distance through the simulation cell owing to application of periodic boundary conditions. While such finite-size effects are generally undesirable, they in no way affect our conclusions. In Fig. 5 we present a snapshot of the quasi-2D cell after shock loading to 9.7 GPa using NEMD and 56.8 ps of MD simulation after the application of the SFABC. The orientation and dimensions of the quasi-2D cell were selected both to lead to the formation of shear bands (the shortest axis of the cell is parallel to  $[010]$ ) and to minimize the role of finite-size effects on their subsequent growth. It is clear from Fig. 5 that many shear bands have nucleated randomly both at the pistons and in the bulk. Furthermore, the shear bands have grown at  $\pm 45^\circ$  to  $[100]$  in roughly equal amounts. Since only a small fraction of the shear bands cross the  $(001)$  periodic boundaries, we propose that the simulated spatial distribution of defects corresponds closely to that which would be observed in a mesoscopic specimen.

### B. Structural and thermodynamic analysis

The simulations at  $U_p = 0.63$  and  $1.0 \text{ km s}^{-1}$  were examined to quantify shock-induced changes in molecular conformation, the internal structure of the shear bands, and the temperature rise caused by viscous heating during their nucleation and growth. We studied these quantities both for

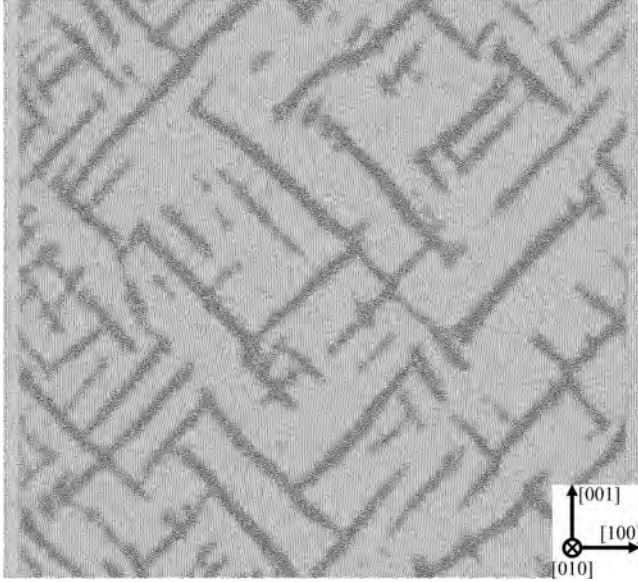


FIG. 5. A projection of the molecular centers of mass of the quasi-2D simulation cell following shock loading to 9.7 GPa using NEMD and a 56.8 ps MD simulation after the application of the SFABC (Ref. 34). At maximum compression, the cell measures  $1638.5 \times 34.55 \times 1497.9 \text{ \AA}^3$  parallel to  $[100]$ ,  $[010]$ , and  $[001]$ , respectively.

crystalline regions and shear bands adjacent to these regions in our simulations at  $U_p = 1.0 \text{ km s}^{-1}$ . The sampled CRs and SBs are indicated in Figs. 4(b) and 4(d).

### 1. Radial distribution functions

Radial distribution functions (RDFs) for molecular centers of mass were calculated to determine whether the shear bands comprise a liquidlike structure that is consistent with melting and/or amorphization. The RDF is defined as  $g(R) = n(R) / 4\pi\rho R^2 \Delta R$ , where  $n(R)$  is the number of particles in a spherical shell of radius  $R$  and thickness  $\Delta R$  and  $\rho$  the particle number density. We used  $\Delta R = 0.2 \text{ \AA}$  in all calculations and  $\rho$  was determined uniquely for each system. All RDFs were averaged over at least 7900 molecules.

We plot the RDFs for an unshocked RDX crystal at 300 K and a crystalline region at the point of maximum compression from a NEMD simulation at  $U_p = 1.0 \text{ km s}^{-1}$  in Figs. 6(a) and 6(b), respectively. Comparing Figs. 6(a) and 6(b), we find only a small change in the RDFs at first nearest neighbors but notable changes at second-nearest neighbors and beyond. The most relevant feature is the decreased gap between first- and second-nearest neighbors. This is expected due to the large uniaxial compression imparted by shock loading. The RDF of the shock-compressed system becomes relatively smooth at  $R > 16 \text{ \AA}$  which suggests some loss in long-range order, although the system is still clearly crystalline.

The RDFs calculated for a crystalline region and an adjacent shear band after a 121 ps MD simulation under SFABCs are presented in Figs. 7(a) and 7(b), respectively. The RDF for the crystalline region shows a recovery of the gap between the first- and second-nearest-neighbor shells that was

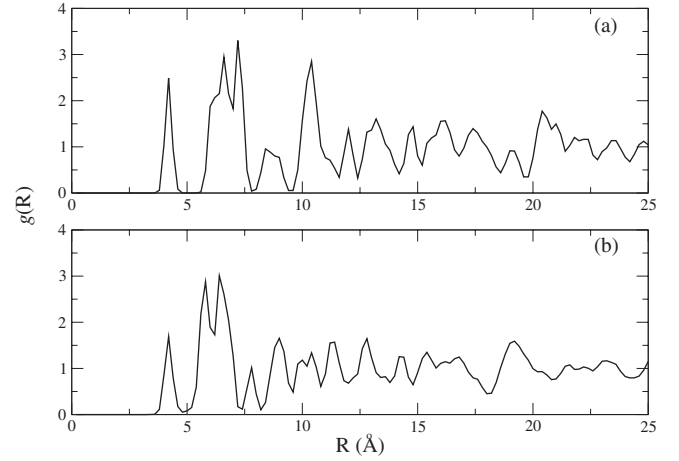


FIG. 6. Center-of-mass radial distribution functions. (a) Unshocked  $\alpha$ -RDX crystal at 300 K and (b) crystalline region from the long simulation cell at maximum compression after shock loading at  $U_p = 1.0 \text{ km s}^{-1}$ .

reduced during the NEMD phase of the simulation [Fig. 6(b)]. This suggests that SFABCs facilitate the evolution of the system from a metastable configuration after shock loading to geometries more similar to those in the unshocked crystal. The RDF for the shear band corresponds unambiguously to that of a liquidlike state and shows that the shear bands are regions of localized, shear stress-driven amorphization.

### 2. Heating via viscous flow

The intermolecular and intramolecular temperatures of a crystalline region and adjacent shear band were calculated as a function of time during equilibrium MD simulations employing SFABCs. Plots of the temperatures calculated in the long and short cells are shown in Figs. 8 and 9, respectively. In both the long and short cells, the onset of shear band formation can be discerned clearly by the rapid increase in the intermolecular and intramolecular temperatures that is

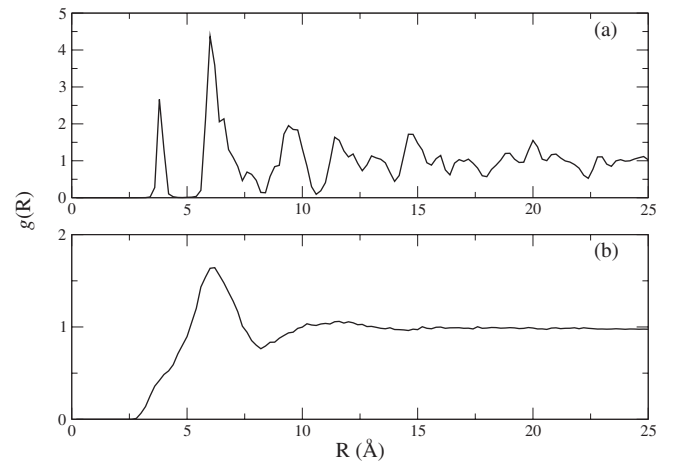


FIG. 7. Center-of-mass radial distribution functions after 121 ps MD simulation under SFABCs. (a) Crystalline region and (b) shear band.

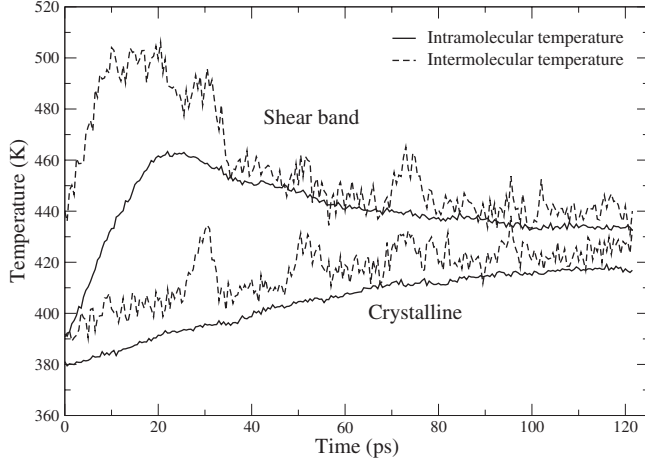


FIG. 8. Intermolecular and intramolecular temperatures of a crystalline region and adjacent shear band during an MD simulation employing SFABCs and the long cell. Zero time corresponds to the start of the SFABC simulation.

driven by viscous flow.<sup>34</sup> In both simulations, the intramolecular temperature within the shear band increases from around 390 to a maximum of 460 K. The passage of the shock wave is responsible for the 90 K increase in intramolecular temperature compared to that in the unshocked RDX crystal. The heating rate within the shear band is about  $3.5 \times 10^{12} \text{ K s}^{-1}$  during the initial stage of growth in the long cell and about  $5.8 \times 10^{12} \text{ K s}^{-1}$  in the short cell.

The intense direct heating of material in the shear bands during viscous flow drives the indirect heating of the surrounding crystalline regions. After the initial growth of the shear bands, the intermolecular and intramolecular temperatures equilibrate throughout the crystal. Both simulations suggest that temperatures of the shear bands and bulk will equilibrate to about 430 K. Here we are using a nonreactive potential, but in reality the intense heating and viscous flow associated with the formation of shear bands would cause some RDX molecules to decompose via a strongly exother-

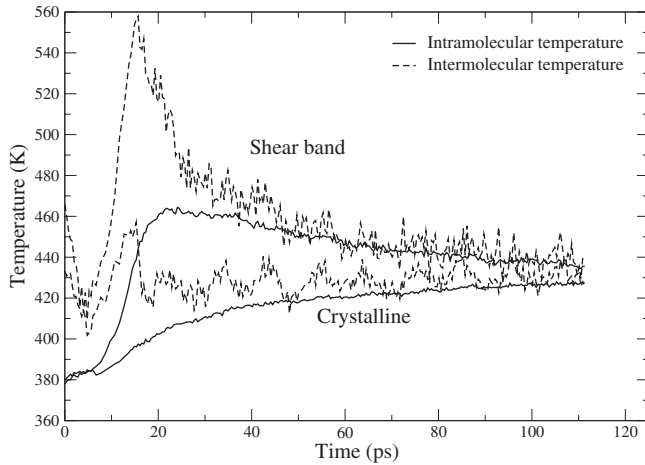


FIG. 9. Intermolecular and intramolecular temperatures of a crystalline region and adjacent shear band during an MD simulation employing SFABCs and the short cell. Zero time corresponds to the start of the SFABC simulation.

mic path. Assuming that this chemistry progresses to the exothermic steps in the decomposition mechanism, the heating would be enhanced by the processes. Nevertheless, the release of stored elastic strain energy that the formation of shear bands facilitates increases the temperature of the entire crystal by 40–50 K over that due to the passage of the shock wave alone.

It is important to note that the levels of shock heating we calculate from our classical MD simulations underestimate those that would take place in a real organic molecular crystal. Within classical MD, each degree of vibrational freedom is associated with a thermal energy  $k_B T/2$ . However, the Debye temperatures of the intramolecular vibrational modes in RDX are known to be significantly higher than room temperature (see, for example, Ref. 37). Thus, the true heat capacity of RDX under ambient conditions is significantly less than the classical limit.

The shock compression determined from our NEMD simulations of shock loading to  $P_{RH}=9.7 \text{ GPa}$  is  $V/V_0=0.82$ . This can be considered a weak shock since  $P_{RH}$  is less than the bulk modulus of the material. Using experimental and experimentally derived values for material properties, we can estimate the shock heating that takes place in real RDX under the same loading conditions by summing contributions from the heating upon isentropic compression from specific volume  $V_0$  to  $V$ ,  $\Delta T_S$ , and from the additional heating that arises from the passage of the shock front,  $\Delta T_H$ , i.e.,<sup>37</sup>

$$\Delta T = \Delta T_S + \Delta T_H, \quad (1)$$

where

$$\Delta T_S = T_0 \left[ \exp \left( - \int_{V_0}^V \frac{\Gamma}{V} dV \right) - 1 \right] \quad (2)$$

and

$$\Delta T_H = \int_{e_S(V)}^{e_H} \frac{de}{c_v}. \quad (3)$$

Here,  $\Gamma$  is the Grüneisen coefficient,  $T_0$  the initial temperature,  $c_v$  the heat capacity at constant volume,  $e_S(V)$  the specific energy on the initial isentrope, and  $e_H$  the specific energy on the Hugoniot. We calculated  $c_v=1077.0 \text{ J kg}^{-1} \text{ K}^{-1}$  and  $\Gamma=1.103$  using published room-temperature values for the heat capacity at constant pressure,  $c_p$ ,<sup>30</sup> the coefficient of volumetric thermal expansion,<sup>38</sup> isentropic bulk modulus,  $K_S$ ,<sup>28</sup> and ideal equilibrium density,  $\rho_0$ .<sup>12</sup> These values yield  $\Delta T_S=74 \text{ K}$ . The pressure on the isentrope expanded to leading order about the equilibrium specific volume,  $V_0$ , is

$$P_S(V) = K_S \left[ \left( 1 - \frac{V}{V_0} \right) + \mathcal{G} \left( \frac{V}{V_0} - 1 \right)^2 \right], \quad (4)$$

where  $\mathcal{G}$  is the fundamental derivative.<sup>39</sup> The energy on the initial isentrope can be expressed analytically as



$$e_S(V) = - \int_{V_0}^V P_S(V) dV, \quad (5)$$

$$= \frac{K_S}{\rho_0} \left\{ (1 + \mathcal{G}) \left( 1 - \frac{V}{V_0} \right) - \left( \mathcal{G} + \frac{1}{2} \right) \left[ 1 - \left( \frac{V}{V_0} \right)^2 \right] + \frac{\mathcal{G}}{3} \left[ 1 - \left( \frac{V}{V_0} \right)^3 \right] \right\}. \quad (6)$$

An experimental value for fundamental derivative was obtained from the gradient of the Hugoniot in the  $U_s$ - $U_p$  plane determined from isentropic compression experiments on RDX (100), namely,  $\mathcal{G}=5.6$ .<sup>39,40</sup> The energy on the Hugoniot is given simply by the Hugoniot equation,<sup>21,39</sup>

$$e_H = \frac{P_{RH}}{2\rho_0} \left( 1 - \frac{V}{V_0} \right). \quad (7)$$

Combining the values of  $P_{RH}$  and  $V/V_0$  from our NEMD simulations and the calculated values of  $e_S(V)$ ,  $e_H$ , and  $c_v$  with Eq. (3), we estimate the additional heating arising only from the passage of the shock front,  $\Delta T_H=289$  K. Hence, the total temperature increase in real RDX during shock loading is about  $\Delta T=363$  K. Thus, our classical MD simulations underestimate the true shock heating by factor of about 4, although this should be considered to be an upper limit owing to the temperature dependence of the experimental heat capacities and  $\Gamma$ .

### 3. Rotational order

A rotational order parameter,  $P_2$ , was used to determine the onset of shear band formation and characterize their internal structure.  $P_2$  characterizes the relative orientation between a given vector within each molecule, in this case the vector connecting carbon and nitrogen atoms on opposite sides of the six-membered ring, at time  $t=0$  and that same vector at subsequent time.  $P_2$  is defined as

$$P_2(t) = \frac{1}{N} \sum_{i=1}^N \frac{1}{2} [3(\hat{\mathbf{n}}_i(0) \cdot \hat{\mathbf{n}}_i(t))^2 - 1], \quad (8)$$

where  $N$  is the number of molecules and  $\hat{\mathbf{n}}_i(t)$  the unit vector between specified atoms in molecule  $i$  at time  $t$  and  $P_2$  equals unity in a system with perfect rotational order and  $1/4$  when there is no rotational order.

Plots of  $P_2$  for a crystalline region and an adjacent shear band in the long and short cells shock loaded at  $U_p=1.0$  km s<sup>-1</sup> are shown in Figs. 10(a) and 10(b), respectively. The rotational order parameters calculated during the NEMD and SFABC simulations have been merged so that they are plotted as a function of the total simulation time. All plots are continuous in value and gradient across the vertical lines which denote the time at which the SFABC was applied, providing convincing evidence that applying SFABCs, in this case, does not introduce unphysical artifacts in the simulations.

Owing to thermal motion,  $P_2 \approx 0.96$  in the perfect crystal at 300 K. We do not observe a significant change in the value of  $P_2$  after the passage of a shock wave although Fig. 7

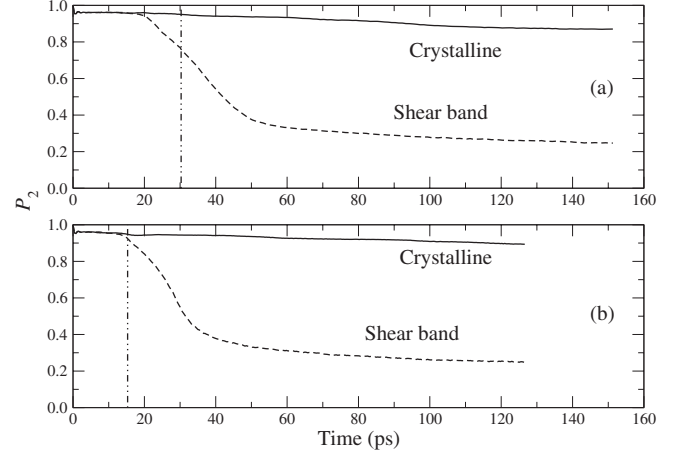


FIG. 10. Rotational order parameter in a crystalline region and shear band after shock loading at  $U_p=1.0$  km s<sup>-1</sup>. The vertical line denotes the time at which SFABCs were applied. (a) Long cell and (b) short cell.

shows notable differences in the RDFs of the shocked and unshocked systems. Hence, shock loading changes significantly the crystal structure on a center-of-mass level but individual molecules largely retain their original orientation.

The rotational order parameter reveals clearly the onset of shear band formation and its subsequent structural evolution. In both the long and short cells,  $P_2$  decreases rapidly from about 0.96 to about 0.35 during the initial stage of growth where the rate of viscous heating is high and amorphization progresses rapidly. The initial stage of growth takes about 20–30 ps. The shear bands subsequently evolve relatively slowly to a state of rotational disorder over a time period of about 100 ps. This secondary stage of growth is associated with the equilibration of the thermal gradients generated during the initial growth stage, as described in Sec. IV B 2. The rotational order parameter for the crystalline regions decreases slowly during shear band formation from about 0.96 to about 0.88. We attribute this decrease to both the 40–50 K rise in temperature in the crystalline regions that results from the intense heating in the shear bands and the misorientation of the crystalline regions with respect to their original axes due to the shear strains mediated by viscous flow (see Fig. 4).

We computed the autocorrelation function, averaged over all time origins, of the rotational order parameter for eight representative molecules randomly dispersed within a shear band. By fitting the initial decay of the autocorrelation function to  $C(t)=A \exp(-t/\tau)$ , where  $A$  is a constant, we estimate that the molecules within the shear bands lose memory of their initial orientation and amorphize within a characteristic time interval of  $\tau^*=9.7$  ps.

### 4. Molecular conformation

At ambient temperature and pressure, the point group of molecules in the  $\alpha$ -RDX crystal structure is  $C_s$ . The six-membered ring is in a chair conformation with two nitramine group N-N bonds oriented axially (A) to the ring and one equatorially (E); this molecular conformation is commonly



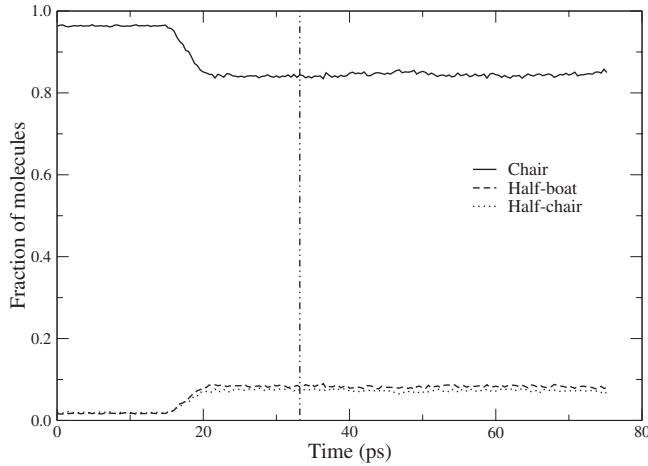


FIG. 11. Fraction of molecules in a given ring conformation after shock loading at  $U_p=0.63$  km s $^{-1}$ . The vertical line denotes the time at which SFABCs were applied.

denoted as AAE. Shock compression or melting/amorphization may change the ring conformation and/or the orientations of the three nitro groups with respect to the ring. To characterize the geometry of the molecular ring we calculated ring-puckering coordinates using the formalism of Cremer and Pople.<sup>41</sup> The orientation of the three nitro groups with respect to the ring was determined by calculating the angles between the three N-N bonds and the vector normal to the ring.

In Fig. 11 we plot the fraction of molecules in a given ring conformation as a function of the total NEMD plus SFABC simulation time during shock loading at  $U_p=0.63$  km s $^{-1}$  ( $P_{RH}=5.7$  GPa). Before the arrival of the shock wave in the examined region of the simulation cell, 96% of the molecular rings are in the chair conformation and 2% are in each of the half-boat and half-chair conformations. The passage of the shock wave through the sampled volume induces a change in the relative populations of the three conformations, namely, the fraction of molecular rings identified as being in the chair conformation falls to 85%, while those in the half-boat and half-chair conformations increase to 8% and 7% of the total, respectively. The fraction of molecular rings in the boat and twist-boat conformations is negligible both before and after the passage of the shock front. Furthermore, we did not detect nitro-group conformations other than AAE. Since no deformation mechanisms are active to relieve the uniaxial shock compression at this  $U_p$ , the relative populations of molecules in these three ring conformations remain constant.

The same analysis was performed for a crystalline region and adjacent shear band in the long and short cells shock loaded at  $U_p=1.0$  km s $^{-1}$ . The fractions of molecules in a given ring conformation as a function of total simulation time in crystalline regions in the long and short cells are plotted in Figs. 12(a) and 12(b), respectively. Behavior similar to that observed under shock loading at  $U_p=0.63$  km s $^{-1}$  was found but with some important differences. First, the passage of the shock front through the sampled regions mediates a greater shift in the relative populations of the ring conformations. In both the long and short simulation cells, immediately after the passage of the shock

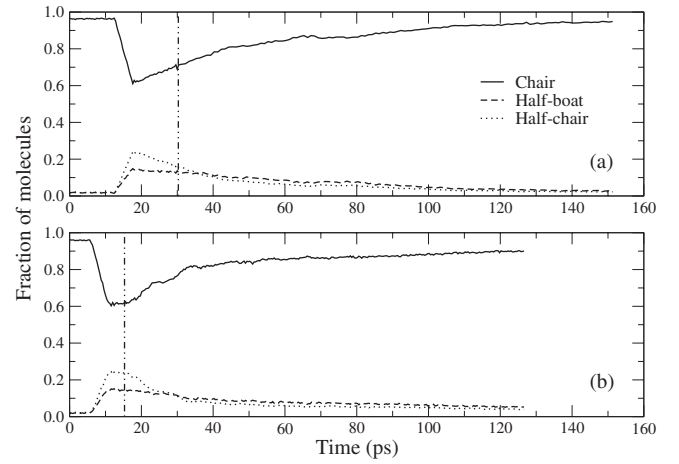


FIG. 12. Fraction of molecules in a given ring conformation in a crystalline region after shock loading at  $U_p=1.0$  km s $^{-1}$ . The vertical lines denote the time at which SFABCs were applied. (a) Long cell and (b) short cell.

front, only 60% of the molecular rings are identified as chair conformers. The fractions of half-boat and half-chair conformations do not increase in equal amounts; initially 25% of molecules adopt the half-chair conformation and 15% the half-boat conformation. As before, in the crystalline regions we observe negligible fractions of the boat or twist-boat conformations or nitro groups in orientations other than AAE. However, since in these simulations at  $U_p=1.0$  km s $^{-1}$  shear bands form that relax the large shock-induced shear stresses, the crystalline regions are able to relax to a state in which the average molecular conformation is more similar to that in a perfect  $\alpha$ -RDX crystal. Hence, as shear bands grow throughout the system, the fraction of molecular rings identified as being in the chair conformation in the crystalline regions increases to around 90% over 100 ps, while the fraction of molecular rings in the half-boat and half-chair conformations decay accordingly. Thus, we propose that plastic deformation via the formation and growth of shear bands under shock loading in (100)-oriented RDX single crystals is largely driven by the free energy released upon relaxation of the shock-induced ring conformations to relative populations that are more consistent with the  $\alpha$ -RDX crystal structure.

Analyses of molecular ring conformations in the shear bands in the long and short cells are presented in Figs. 13(a) and 13(b), respectively. As for the crystalline regions, immediately following the passage of the shock front around 60% of molecular rings are in the chair conformation with 25% and 15% in the half-chair and half-boat conformations, respectively. These populations begin to relax initially due to the growth of shear bands elsewhere in the cells. However, once shear bands start to propagate into these volumes and melting commences, the populations of the five possible ring conformations evolve to distributions more consistent with the liquid state. In both the long and short cells, the fractions of molecular rings in the chair, half-boat, and half-chair conformations decrease over 100 ps to 34%, 13%, and 12%, respectively. In contrast to the crystalline regions discussed in the preceding paragraph, 20% and 21% of the molecular rings in the shear bands are in the boat and twist-boat con-

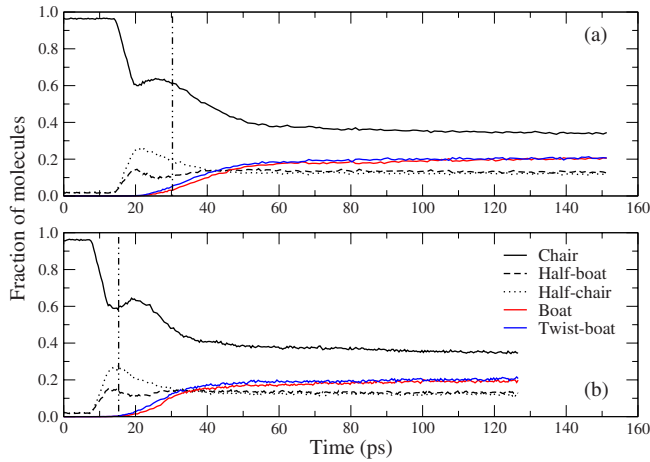


FIG. 13. (Color online) Fraction of molecules in a given ring conformation in a shear band after shock loading at  $U_p = 1.0 \text{ km s}^{-1}$ . The vertical lines denote the time at which SFABCs were applied. (a) Long cell and (b) short cell.

formations, respectively. Hence, the appearance of molecules in these conformations signals the onset of melting since they serve as an indicator of the increase in conformational disorder facilitated by the liquid state. Furthermore, at the same simulation times that increase in the populations of boat and twist-boat conformations are observed, we also find notable increases in the fraction of molecules identified as not being in the AAE conformation. The fractions of molecules within the shear bands in the long and short simulation cells identified as not possessing the AAE conformation—that is, those molecules whose nitro groups are in an AEE or EEE conformation—are plotted as a function of total simulation time in Figs. 14(a) and 14(b), respectively. In both the long and short cells, around 30% of the molecules in the shear bands are not in the AAE conformation once a steady-fluctuating state is achieved. Although the AAA conformation is suggested to be favored in the gas phase,<sup>42,43</sup> we detect only a negligible number of molecules in this conformation in the condensed phase.

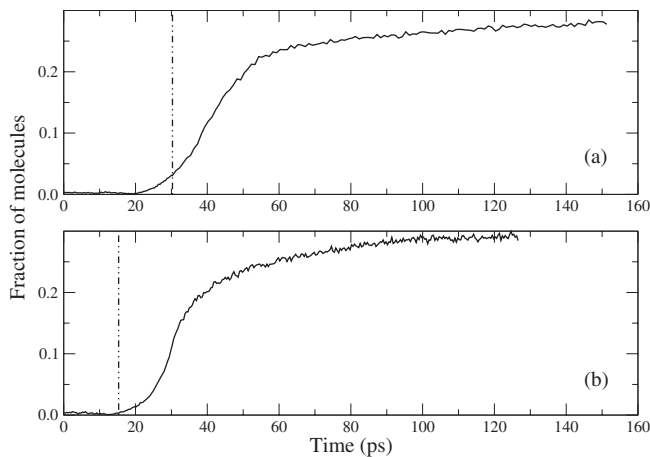


FIG. 14. Fraction of molecules in a shear band with nitro groups not in the AAE conformation after shock loading at  $U_p = 1.0 \text{ km s}^{-1}$ . The vertical lines denote the time at which SFABCs were applied. (a) Long cell and (b) short cell.

## V. DISCUSSION AND CONCLUSIONS

### A. Efficacy of the SFABC method

The use of SFABCs allowed us to extend simulation times to the extent that shock-induced shear bands, which evolve slowly on the time scale of a typical NEMD simulation, could be studied over their complete evolution to a steady-fluctuating state. This is demonstrated with greatest clarity in Figs. 13 and 14 where relative abundances of the ring and nitro-group conformations at the point of maximum compression in the respective NEMD simulations, as denoted by the vertical broken lines, differ significantly from those once a steady state is reached. More generally, the absence in Figs. 10–14 of perturbations associated with the application of the SFABC at the moment of maximum compression further supports the validity of the approach.

There are certain situations where the application of SFABCs may not be appropriate. For example, it would be difficult to apply this method in the study of shock waves in ductile metals where, in the two-wave regime, an elastic precursor may lead a strong plastic wave by tens of nanometers. In this case, if SFABCs are applied when the elastic precursor reaches the free surface, the slower plastic wave may reflect off the second piston, setting up undesirable density waves in the material. However, this problem could be overcome within the SFABC framework by applying the second piston within the simulation cell at a point that has been passed by both the elastic and plastic waves rather than at the end of simulation cell. This approach would still require a computationally expensive NEMD simulation, but subsequent MD simulations could be performed using a smaller number of atoms. In the case of shock waves in RDX, we do not find strong plastic waves that lag significantly behind the elastic precursor; hence the SFABC method is particularly adept at capturing the simulation cell at maximum compression.

Hugoniot methods have been developed that allow shock loading to be simulated within the framework of MD and which are less computationally demanding than large-scale NEMD simulations.<sup>19,44–47</sup> These methods modify the equation of motions of atoms to drive a system toward a prescribed state on the Hugoniot locus. It is not obvious that Hugoniot methods are appropriate tools for use in the simulation of molecular crystals since phenomena at the shock front in these materials are extremely complex owing to their relatively low symmetry and many intramolecular degrees of freedom. Explicit simulation of the shock front using NEMD will provide a more accurate description of, for example, the initial overshoot in intermolecular temperature and its equilibration with the intramolecular vibrational modes in the nanometers behind the shock front.<sup>14,27</sup> Previous work showed that these phenomena are of fundamental importance to the homogeneous nucleation of dislocations in (111)-oriented RDX single crystals.<sup>14</sup> However, Hugoniot methods do provide certain advantages over SFABCs; for example, the former ensures that the system remains on the Hugoniot locus, while the latter, in general, does not. SFABCs capture the simulation cell at a constant volume that corresponds only to the system after the passage of the leading shock wave(s).

Shock-induced phase transformations or plastic deformation that lags the elastic wave will reduce the diagonal component of the stress tensor parallel to the direction of shock propagation and the system under SFABCs will depart from the Hugoniot locus. Hugoniot methods enforce a constant pressure rather than a constant volume simulation. This limitation of the SFABC method may be acceptable in certain circumstances, for example, if one wishes to extend simulation times to identify events that occur at a rate too low to be observed directly in NEMD simulations, such as the homogeneous nucleation of dislocations, second phases, or the initiation of slow, complex chemical reactions. Hence, the SFABC method may be of particular advantage in cases where the description of interatomic bonding is sufficiently expensive that large-scale NEMD simulations are not feasible but an accurate treatment of the dynamics associated with the shock front is required. The principal advantages of SFABCs over Hugoniot methods are that the former are extremely simple to implement, robust, do not affect the equations of motion of atoms artificially, and provide an essentially exact treatment of phenomena at the shock front.

In order to reach the same total NEMD plus SFABC simulation time for the material subvolumes sampled here in a normal NEMD simulation, a simulation cell of length  $604a$ , containing over  $40 \times 10^6$  atoms, would be required. Such simulations would be computationally challenging at present (the simulation reported here using the quasi-2D cell required 8.8 CPU years). Thus, the SFABC method facilitates simulations that otherwise may be prohibitively expensive. Furthermore, the results reported in Sec. IV B for the long and short cells, the latter containing half the number of atoms of the former, concur in every regard once a steady-fluctuating state is achieved (these simulations appear to differ only in the rate of shear band formation). Thus, SFABCs not only enable simulation times to be extended for a given cell size but also facilitate simulations with significantly fewer atoms with no loss in the accuracy of the description of the final state. Finally, in comparison with Hugoniot methods, use of the SFABC provides an exact treatment of the dynamics during shock loading and is far more simple and robust in its implementation.

### B. Implications for initiation sensitivity

Dislocation-mediated plasticity was not observed during shock loading at either  $U_p = 0.63 \text{ km s}^{-1}$  ( $P_{RH} = 5.7 \text{ GPa}$ ) or  $U_p = 1.0 \text{ km s}^{-1}$  ( $P_{RH} = 9.7 \text{ GPa}$ ). This result was expected for this orientation of the shock propagation direction since none of the slip systems identified under quasistatic loading are subject to a resolved shear stress.<sup>13</sup> Furthermore, we can eliminate the possibility that for this orientation of the shock propagation direction, other previously unknown slip systems are activated by the passage of the shock wave; that is, phenomena such as those observed during shock loading on (111) (Ref. 14) do not occur for this orientation. Thus, based on the steric-hindrance model, we expect high sensitivity for impacts on (100), in accord with Ref. 13.

An unanticipated deformation mechanism was identified during shock loading on (100) at  $U_p = 1.0 \text{ km s}^{-1}$ , namely,

the formation and growth of shear bands. While the steric-hindrance model suggests that deformation mechanisms which serve to relax shear stresses promote low impact sensitivity, the intense heating caused by viscous flow within the shear bands will certainly promote thermal molecular decomposition. Moreover, viscous flow may promote the mechanical rupture of intramolecular bonds, further enhancing the rate of molecular decomposition. Thus, in a sense, shear bands can be considered to be homogeneously nucleated hot spots since the potential energy stored in the shock compressed material is partly released in spatially localized material subvolumes.

One might expect that if dislocation slip systems could be activated at relatively low values of  $P_{RH}$  at this orientation of the shock propagation direction, then shear stresses would not build to the level where deformation via shear bands is inevitable. However, NEMD studies of shock waves in  $\alpha$ -HMX by Jaramillo *et al.*<sup>27</sup> revealed a gradual transition from dislocation-mediated plasticity to deformation mediated by the growth of liquidlike shear bands with increasing  $P_{RH}$ . Hence, the deformation of energetic molecular crystals via the nucleation and growth of shear bands appears to be related to intrinsic instabilities of the crystal structure.

### C. Comments on the effects of nonclassical phenomena in simulations of nonequilibrium processes in molecular crystals

It is well known that in the temperature range of interest in this study, the heat capacity of a system of classical oscillators with a frequency distribution representative of a molecular crystal is significantly larger than the value in the corresponding quantum-mechanical system; thus, for the weak-to-moderate shock strengths considered here, the shock temperature predicted on the basis of classical MD will be lower than the “real” value, as was shown in Sec. IV B 2. Nevertheless, this underestimate, which is inherent to the use of classical mechanics, does not affect our underlying theses, namely, that the homogeneous nucleation of liquidlike shear bands occurs in [100]-oriented RDX crystals under sufficiently strong shock loading and the viscous flow of material within these defects leads to an *additional*, non-negligible localized heating. Since our simulations underestimate the magnitude of the shock heating, it is a reasonable assumption that experimentally these defects will nucleate at significantly lower shock pressures. Furthermore, the magnitude of the heating in the shear bands will be higher than the 70–90 K we calculate since the “error” in the heat capacity of material due to classical mechanics is equally present within these subvolumes. Thus, while our calculated shock and defect temperatures are low compared to those in real, quantum dynamical RDX, they are almost directly proportional; that is, based on specific heat alone, classical MD simulations will also underestimate the additional heating within the shear bands by roughly the same factor of 4 as was predicted for the shock heating.

Fundamentally, the “specific-heat problem” of interest here for the case of a condensed phase molecular system and the “zero-point energy problem” that arises for the case of

gas-phase polyatomic molecules are manifestations of quantum effects and have no classical analog. At present there is no satisfactory method for performing large-scale MD simulations with a quantum-mechanically accurate treatment of the zero-point energy problem (for gas-phase species) or the specific-heat problem (for condensed molecular phases). Nevertheless, our simulations were designed to mitigate in a physically sensible way the overestimation error in the specific heat of RDX by freezing out via geometric constraints, the contributions to the heat capacity from vibronic degrees of freedom with the highest modal Debye temperature, namely, the C-H bond stretches. Attempts to go beyond this type of strategy are problematic: Thompson and co-workers<sup>48,49</sup> demonstrated that for model Hamiltonians with small numbers of degrees of freedom that both “active” and “passive,” quantum-inspired corrections to classical dynamic trajectories may result in severely unphysical behavior. Specifically, even for systems containing only zero-point vibrational energy, observables obtained from uncorrected classical MD trajectories resembled more closely the true quantum-mechanical ones than those obtained for trajectories that included quantum-corrected classical dynamics.

Another option, essentially a generalization of the idea of freezing out the high-frequency degrees of freedom employed in the current study, is to introduce a Debye-type dependence of the heat capacity on temperature using the mesoparticle dynamics of Strachan and Holian.<sup>50</sup> In this approach, a reduced-dimension representation of the potential-energy function results in a significant decrease in the classical heat capacity of the system. This is balanced by introducing into the equations of motion for the system “implicit degrees of freedom” that correspond to local heat reservoirs within the mesoparticles. These internal degrees of freedom can be populated using either classical or quantum statistical descriptions of their behavior. While this approach is attractive, it is rather empirical and mesopotentials presently do not demonstrate the levels of sophistication needed to describe accurately a system as complex as an RDX crystal under extreme loading conditions. Thus, although simulations based on classical MD display certain well-known and well-understood limitations, at present there exists no better tool for the study of shock-induced phenomena in organic molecular crystals.

#### ACKNOWLEDGMENTS

M.J.C. and T.D.S. thank Eugenio Jaramillo for assistance with LAMMPS and Sam Shaw, Ralph Menikoff, Dan Hooks, and Kyle Ramos for many fruitful discussions. L.Z. is grateful for Wei Yang’s support. This work was supported by the National Nuclear Security Administration of the U.S. Department of Energy under Contract No. DE-AC52-06NA25396 with Los Alamos National Security, LLC (M.J.C. and T.D.S.) and a U.S. Department of Defense MURI grant managed by the Army Research Office (L.Z. and D.L.T.).

#### APPENDIX: CONSERVATION OF ENERGY IN SFABC SIMULATIONS

As discussed briefly in Sec. I, shock waves can be generated in NEMD simulations by driving a piston at a specified

$U_p$  into a stationary simulation cell as in Ref. 22 or by impacting a simulation cell onto a fixed rigid piston at a specified  $U_p$ . For convenience and clarity, we refer hereafter to these approaches as the moving-piston and moving-cell methods, respectively. These methods are Galilean invariant, thus it is largely a matter of personal preference which is employed. However, we found unexpected differences between these formally equivalent methods upon the application of SFABCs.

If the moving-piston method is used to generate the shock wave in a NEMD simulation, SFABCs can be applied in much the same way as described in Sec. III. The time at which the simulation cell reaches maximum compression can be determined with high accuracy by again plotting as a function of time the  $x$  coordinate of the center of mass of the last molecule and identifying when the curvature becomes nonzero. The second piston is then applied by setting the force and velocity vectors of all atoms within a specified distance from the end cell to zero and  $(U_p, 0, 0)$ , respectively. In this manner, the volume of the cell is fixed to that corresponding to maximum compression and the entire system translates with a velocity  $(U_p, 0, 0)$ .

When a shock wave was generated in (100)-oriented RDX using the moving-cell method at  $U_p = 1.0 \text{ km s}^{-1}$  and SFABCs were applied as in Sec. III, during equilibrium MD simulations in the microcanonical ensemble, total energy was conserved to a tolerance of 1.2 ppm. However, when the moving-piston method was employed we found that the total energy was conserved to only 2.2 parts per thousand using otherwise identical computational protocols. Despite the thousandfold decrease in energy conservation in the latter simulation, we found that the relative particle trajectories in the two simulations were identical until numerical divergences arose due to chaotic dynamics.

The origin of the apparent poor conservation of the total energy when the simulation cell translates is determined entirely by the contribution from the kinetic energy,  $T$ , to the total energy. We can write the kinetic energy of an ensemble of  $N$  thermalized particles of mass  $m_i$  in a system whose center of mass translates with constant velocity  $\mathbf{U} = (U_p, 0, 0)$  as

$$T(\mathbf{U}) = \frac{1}{2} \sum_{i=1}^N [m_i \mathbf{v}_i \cdot \mathbf{v}_i + m_i \mathbf{U} \cdot \mathbf{U} + 2m_i \mathbf{v}_i \cdot \mathbf{U}], \quad (\text{A1})$$

where  $\mathbf{v}_i = (v_i^x, v_i^y, v_i^z)$  is the velocity of particles with respect to a coordinate system translating with velocity  $\mathbf{U}$ . The first term is related to the temperature of the ensemble and the second term is a constant. The third term,  $T'$ , is a contribution to the kinetic energy arising from the momentum of the system parallel to  $\mathbf{U}$ ,

$$T' = U_p \sum_{i=1}^N m_i v_i^x. \quad (\text{A2})$$

Hence, the apparent poor conservation of the total energy of simulation cells under SFABCs translating with velocity  $U_p$  is explained by fluctuations of the total momentum,  $\sum_{i=1}^N m_i v_i^x$ . Hence, in the microcanonical ensemble, MD configuration



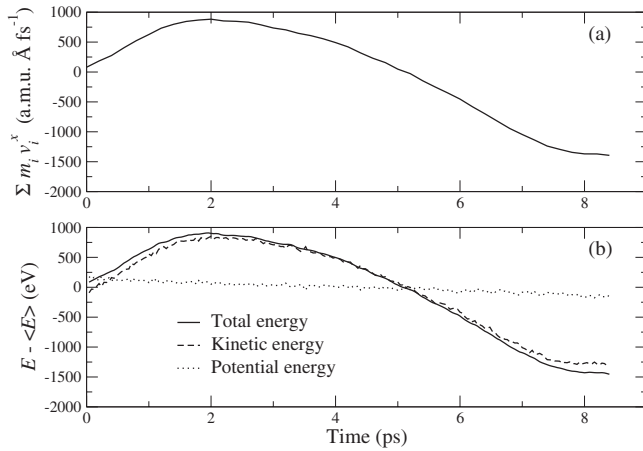


FIG. 15. (a) Oscillation of the total momentum in a system under SFABCs translating with velocity at  $U_p = 1.0 \text{ km s}^{-1}$  and (b) deviations of the total, kinetic, and potential energies of the system from their mean values.

trajectories are independent of  $\mathbf{U}$  (i.e., they are Galilean invariant in configuration space), but the kinetic energy of the system depends on the scalar product of the total momentum with  $\mathbf{U}$ .

To illustrate the contribution from the nonconserved linear momentum to the kinetic energy in a translating system we plot in Fig. 15(a) the quantity  $\Sigma_{i=1}^N m_i v_i^x$  as a function of simulation time for an RDX crystal under SFABCs. The simulation cell was shock loaded using the moving-piston method and is translating with velocity  $U_p = 1.0 \text{ km s}^{-1}$ . In Fig. 15(b) we plot as a function of simulation time the deviation of the total, kinetic, and potential energies of the system from their mean values time averaged over the simulation. Comparing Figs. 15(a) and 15(b) it is evident that the kinetic and total energies track oscillations of the total momentum, while the potential energy, which reflects the relative particle trajectories of the system, is independent of the total momentum. The slow decrease in the potential energy in Fig. 15(b) arises from the nucleation and growth of shear bands in the system.

\*cawkwell@lanl.gov

†sewell@lanl.gov

‡Present address: School of Computational Science, Florida State University, Tallahassee, Florida 32306, USA.

§thompsondon@missouri.edu

<sup>1</sup>A. E. D. M. van der Heijden, R. H. B. Bouma, and A. C. van der Steen, *Propellants, Explos., Pyrotech.* **29**, 304 (2004).

<sup>2</sup>R. Menikoff, in *Shock Compression of Condensed Matter—2003*, edited by M. D. Furnish, Y. M. Gupta, and J. W. Forbes (American Institute of Physics, Melville, NY, 2004), p. 393.

<sup>3</sup>S. M. Chitanvis, *Shock Compression of Condensed Matter—2003* (Ref. 2), p. 319.

<sup>4</sup>H. W. Sandusky, B. C. Glancy, D. W. Carlson, W. L. Elban, and R. W. Armstrong, *J. Propul. Power* **7**, 518 (1991).

<sup>5</sup>J. K. Dienes, Q. H. Zuo, and J. D. Kershner, *J. Mech. Phys. Solids* **54**, 1237 (2006).

<sup>6</sup>T. Boddington, P. Gray, and G. C. Wake, *Proc. R. Soc. London, Ser. A* **357**, 403 (1977).

<sup>7</sup>J. J. Dick, *Appl. Phys. Lett.* **44**, 859 (1984).

<sup>8</sup>J. J. Dick, R. N. Mulford, W. J. Spencer, D. R. Pettit, E. Garcia, and D. C. Shaw, *J. Appl. Phys.* **70**, 3572 (1991).

<sup>9</sup>J. J. Dick, *J. Appl. Phys.* **81**, 601 (1997).

<sup>10</sup>H. G. Gallagher, P. J. Halfpenny, J. C. Miller, and J. N. Sherwood, *Philos. Trans. R. Soc. London* **339**, 293 (1992).

<sup>11</sup>J. J. Dick and J. P. Ritchie, *J. Appl. Phys.* **76**, 2726 (1994).

<sup>12</sup>C. S. Choi and E. Prince, *Acta Crystallogr., Sect. B: Struct. Crystallogr. Cryst. Chem.* **28**, 2857 (1972).

<sup>13</sup>D. E. Hooks, K. J. Ramos, and A. R. Martinez, *J. Appl. Phys.* **100**, 024908 (2006).

<sup>14</sup>M. J. Cawkwell, T. D. Sewell, K. J. Ramos, and D. E. Hooks (unpublished).

<sup>15</sup>All of the simulations described in this work were performed in the microcanonical (*NVE*) ensemble using Newton's equations without modification or coupling to external fields. In order to maintain consistency with the prior literature on molecular dy-

namics simulations of shock waves, we use the nomenclature “NEMD” nonequilibrium molecular dynamics to describe the microcanonical evolution of a system of particles with a highly nonequilibrium distribution of momenta at the beginning of the simulation. This use of NEMD should not be confused with explicitly non-Newtonian methods used by others; See, for example, S. S. Sarman, D. J. Evans, and P. T. Cummings, *Phys. Rep.* **305**, 1 (1998).

<sup>16</sup>B. L. Holian and P. S. Lomdahl, *Science* **280**, 2085 (1998).

<sup>17</sup>B. L. Holian, *Shock Waves* **5**, 149 (1995).

<sup>18</sup>B. L. Holian, *Shock Waves* **13**, 489 (2004).

<sup>19</sup>F. Barmes, L. Souillard, and M. Mareschal, *Phys. Rev. B* **73**, 224108 (2006).

<sup>20</sup>E. M. Bringa, A. Caro, M. Victoria, and N. Park, *JOM* **57**, 67 (2005).

<sup>21</sup>Y. B. Zel'dovich and Y. P. Raizer, *Physics of Shock Waves and High-Temperature Hydrodynamic Phenomena* (Academic, San Diego, 1966), Vol. I.

<sup>22</sup>A. V. Bolesta, L. Zheng, D. L. Thompson, and T. D. Sewell, *Phys. Rev. B* **76**, 224108 (2007).

<sup>23</sup>In order to distinguish our method for absorbing the shock front in molecular dynamics simulations from the extensive literature on absorbing boundary condition (ABC) methods for acoustic waves, we hereafter refer to the approach first described by Bolesta *et al.* (Ref. 22) as the shock-front absorbing boundary condition method (SFABC).

<sup>24</sup>S. Namila, D. M. Nicholson, P. K. V. V. Nukala, C. Y. Gao, Y. N. Osetsky, and D. J. Keffer, *Phys. Rev. B* **76**, 144111 (2007).

<sup>25</sup>G. D. Smith and R. K. Bharadwaj, *J. Phys. Chem. B* **103**, 3570 (1999).

<sup>26</sup>D. Bedrov, C. Ayyagari, G. D. Smith, T. D. Sewell, R. Menikoff, and J. M. Zaug, *J. Comput.-Aided Mater. Des.* **8**, 77 (2001).

<sup>27</sup>E. Jaramillo, T. D. Sewell, and A. Strachan, *Phys. Rev. B* **76**, 064112 (2007).

<sup>28</sup>R. B. Schwarz, D. E. Hooks, J. J. Dick, J. I. Archuleta, and A. R.

- Martinez, J. Appl. Phys. **98**, 056106 (2005).
- <sup>29</sup> *LASL Explosive Property Data*, edited by T. R. Gibbs and A. Popolato (University of California, Berkeley, 1980).
- <sup>30</sup> B. Olinger, B. Roof, and H. Cady, *Comportement des Milieux Denses sous Hautes Pressions Dynamiques* (Commissariat à l'Energie Atomique, Paris, 1978), p. 4.
- <sup>31</sup> E. Jaramillo and T. D. Sewell (unpublished).
- <sup>32</sup> S. J. Plimpton, J. Comput. Phys. **117**, 1 (1995).
- <sup>33</sup> S. J. Plimpton, R. Pollack, and M. Stevens, Proceedings of the Eighth SIAM Conference on Parallel Processing for Scientific Computing (SIAM, Philadelphia, 1997).
- <sup>34</sup> See EPAPS Document No. E-PRBMDO-78-060825 for movies of the formation of shear bands under shock loading to 9.7 GPa and their evolution upon the application of the SFABC. For more information on EPAPS, see <http://www.aip.org/pubservs/epaps.html>.
- <sup>35</sup> Figures 4 and 5 were rendered using the AtomEye atomistic configuration viewer: J. Li, Modell. Simul. Mater. Sci. Eng. **11**, 173 (2003).
- <sup>36</sup> M. J. Cawkwell and T. D. Sewell (unpublished).
- <sup>37</sup> R. Menikoff, Combust. Theory Modell. **12**, 73 (2008).
- <sup>38</sup> H. H. Cady, J. Chem. Eng. Data **17**, 369 (1972).
- <sup>39</sup> R. Menikoff, in *Shock Wave Science and Technology Reference Library*, edited by Y. Horie (Springer, New York, 2007), Vol. 2, p. 143.
- <sup>40</sup> M. R. Baer, M. L. Hobbs, C. A. Hall, D. E. Hooks, R. L. Gustavsen, D. M. Dattelbaum, and S. A. Sheffield, in *Shock Compression of Condensed Matter—2007*, edited by M. D. Furnish, M. L. Elert, R. Chau, N. C. Holmes, and J. Nguyen (American Institute of Physics, Melville, NY, 2008), p. 1165.
- <sup>41</sup> D. Cremer and J. A. Pople, J. Am. Chem. Soc. **97**, 1354 (1975).
- <sup>42</sup> I. F. Shishkov, L. V. Vilkov, M. Kolonits, and B. Rozsondai, Struct. Chem. **2**, 57 (1991).
- <sup>43</sup> N. J. Harris and K. Lammertsma, J. Am. Chem. Soc. **119**, 6583 (1997).
- <sup>44</sup> J. B. Maillet, M. Mareschal, L. Soulard, R. Ravelo, P. S. Lomdahl, T. C. Germann, and B. L. Holian, Phys. Rev. E **63**, 016121 (2000).
- <sup>45</sup> E. J. Reed, L. E. Fried, and J. D. Joannopoulos, Phys. Rev. Lett. **90**, 235503 (2003).
- <sup>46</sup> R. Ravelo, B. L. Holian, T. C. Germann, and P. S. Lomdahl, Phys. Rev. B **70**, 014103 (2004).
- <sup>47</sup> E. J. Reed, M. R. Manaa, L. E. Fried, K. R. Glaesemann, and J. D. Joannopoulos, Nat. Phys. **4**, 72 (2008).
- <sup>48</sup> T. D. Sewell, D. L. Thompson, J. D. Gezelter, and W. H. Miller, Chem. Phys. Lett. **193**, 512 (1992).
- <sup>49</sup> Y. Guo, D. L. Thompson, and T. D. Sewell, J. Chem. Phys. **104**, 576 (1996).
- <sup>50</sup> A. Strachan and B. L. Holian, Phys. Rev. Lett. **94**, 014301 (2005).

# Empirical Bond-Order Potential for Hydrocarbons: Adaptive Treatment of van der Waals Interactions

AIBING LIU, STEVEN J. STUART

Department of Chemistry, Clemson University, Clemson, South Carolina 29634

Received 16 May 2007; Revised 11 July 2007; Accepted 12 July 2007

DOI 10.1002/jcc.20817

Published online 4 September 2007 in Wiley InterScience (www.interscience.wiley.com).

**Abstract:** Bond-order potentials provide a powerful class of models for simulating chemically reactive systems with classical potentials. In these models, the covalent bonding interactions adapt to the environment, allowing bond strength to change in response to local chemical changes. However, the non-bonded interactions should also adapt in response to chemical changes, an effect which is neglected in current bond-order potentials. Here the AIREBO potential is extended to include adaptive Lennard-Jones terms, allowing the van der Waals interactions to vary adaptively with the chemical environment. The resulting potential energy surface and its gradient remain continuous, allowing it to be used for dynamics simulations. This new potential is parameterized for hydrocarbons, and is fit to the energetics and densities of a variety of condensed phase molecular hydrocarbons. The resulting model is more accurate for modeling aromatic and other unsaturated hydrocarbon species, for which the original AIREBO potential had some deficiencies. Testing on compounds not used in the fitting procedure shows that the new model performs substantially better in predicting heats of vaporization and pressures (or densities) of condensed-phase molecular hydrocarbons.

© 2007 Wiley Periodicals, Inc. J Comput Chem 29: 601–611, 2008

**Key words:** bond-order potential; hydrocarbon; AIREBO; van der Waals interactions; reactive potential

## Introduction

The bond-order potential, originally proposed by Tersoff,<sup>1,2</sup> provides a classical model for interactions in covalently reactive systems, such as silicon and carbon. In these potentials, the interaction between two atoms is represented as the combination of a repulsive and an attractive interaction,

$$V_{ij}(r) = V_{ij}^R + b_{ij}V_{ij}^A, \quad (1)$$

where the relative contribution of these two terms is controlled by the bond order,  $b_{ij}$ . The bond order is a many-body term that depends on the local chemical environment, including coordination numbers and bond angles, and enables the strength of the covalent bond between atoms  $i$  and  $j$  to vary adaptively in response to changes in the bonding environment. As with embedded-atom models,<sup>3</sup> each individual bond weakens as the atoms participating in the bond acquire more neighbors, since their valence electrons are divided among more bonding interactions. However, the bond-order potentials also treat the dependence of the bond energy upon the angular distribution of neighbors—a term that is crucial for the directional bonding found in covalent materials.

This approach has been particularly fruitful for modeling carbon and hydrocarbons, and there have been a number of

parameterizations of bond-order potentials for hydrocarbon systems. Following the original Tersoff model,<sup>4</sup> Brenner developed the REBO model,<sup>5</sup> which has been widely used. Pettifor has shown that the potential energy expressions used in these empirical bond-order models are equivalent to one that can be derived from orthogonal tight-binding models in the second-moment approximation,<sup>6</sup> and has developed analytical bond-order potentials that go beyond this approximation.<sup>7</sup> The AIREBO model extends the REBO model to include nonbonded interactions, including van der Waals terms.<sup>8</sup> These intermolecular interactions are crucial for modeling condensed-phase molecular systems, or the non-covalent interactions between layers in graphitic materials. The Reax force field is another model that is motivated by bond order concepts, and includes both van der Waals and electrostatic interactions.<sup>9</sup>

The van der Waals interactions are treated adaptively in the AIREBO potential, allowing the interaction to be switched off smoothly as the chemical environment changes and a non-bonded

**Correspondence to:** S. J. Stuart; e-mail: ss@clemson.edu

Contract/grant sponsor: US DoE; contract/grant number: DE-FG02-01ER43889

Contract/grant sponsor: NSF; contract/grant number: CHE-239448

Contract/grant sponsor: DoD MURI (administered by ARO)



pair becomes bonded. But although the strength of the van der Waals interactions responds adaptively to the local environment, the form of that interaction does not. That is, the van der Waals radius and magnitude of the dispersion interaction do not vary with changes in hybridization to reflect changes to the size or polarizability of the electrons, which give rise to the van der Waals interaction; a single parameterization of the van der Waals energy expression is used for all interactions. Consequently, the van der Waals interactions in the original AIREBO potential are not as transferable across different hydrocarbon hybridizations as would be desired. Here we describe an extension of the AIREBO potential to allow the parameterization of the van der Waals interaction to change adaptively with the chemical environment of the interacting atoms. This is done by having the coefficients of the Lennard-Jones 12-6 expression for the van der Waals interaction depend parametrically on the coordination number of the interacting atoms.

The rest of paper is organized as follows. First we present the modifications to the AIREBO potential that allow the van der Waals interactions to change adaptively in response to bonding changes. We then describe the details of the fitting procedure used to reparameterize the model. Next, we describe the application of this new model to a variety of hydrocarbons not included in the fitting procedure, and discuss the results.

## Model

Van der Waals interactions represent the combination of attractive dispersion interactions and repulsive Pauli exclusion interactions. There are many functional forms used to represent these van der Waals interactions in molecular simulations; the form used in the AIREBO potential is the Lennard-Jones (LJ) 12-6 form,

$$V_{ij}^{\text{LJ}}(r_{ij}) = 4\epsilon_{ij} \left[ \left( \frac{\sigma_{ij}}{r_{ij}} \right)^{12} - \left( \frac{\sigma_{ij}}{r_{ij}} \right)^6 \right] \quad (2)$$

where  $r_{ij}$  is the distance between atoms  $i$  and  $j$ , and  $V_{ij}$  is the potential energy of their interaction. The computational advantages of using this form (only two parameters, no unphysical turnover, computational efficiency) outweighed the increased accuracy that can be obtained from different functional forms.<sup>10</sup> The infinitely repulsive  $r^{-12}$  core is treated adaptively in the AIREBO potential, so that the repulsive interactions are diminished between reactive or covalently bound atoms, but is undiminished for chemically saturated atoms. The total van der Waals interaction included in the potential is thus

$$E_{ij} = \alpha V_{ij}^{\text{LJ}}(r) \quad (3)$$

where the many-body term  $\alpha$  is a function not only of the bond distance  $r$ , but also the bond order between  $i$  and  $j$ , as well as the position of all atoms bonded to  $i$  and  $j$ .<sup>8</sup> Neither the LJ 12-6 functional form nor the means of making the repulsive interactions adaptive is modified in the current work. Rather, we confine our attention to the variability of the LJ  $\epsilon$  and  $\sigma$  parameters (due to changes in the underlying polarization and radius of the electron cloud) with chemical environment.

The  $\sigma_{ij}$  and  $\epsilon_{ij}$  parameters characterize the van der Waals interaction between atom types  $i$  and  $j$ . These determine many of the material properties for soft, molecular systems, such as their cohesive energy, boiling point, and density. They also depend on the local coordination environment of the atom in question. Consequently, most nonreactive force fields, such as CHARMM,<sup>11</sup> UFF,<sup>12</sup> AMBER,<sup>13</sup> MM3,<sup>14</sup> and COMPASS,<sup>15,16</sup> utilize different  $\epsilon$  and  $\sigma$  values for different “types” of carbon atoms. These atom types can be distinguished by their hybridization state ( $sp^2$  vs.  $sp^3$  carbon) or by their bonding environment (a carbonyl carbon or an olefinic carbon or a carbon in a conjugated system), and can extend to dozens of different atom types for a single atomic number. The physical basis for distinguishing between atoms in different chemical environments is, of course, that the chemical environment influences the electronic distribution on the atom, and both the size and polarizability of this electron cloud affect the exchange and dispersion interactions.

In a reactive potential such as AIREBO, however, hybridization state and bonding environment are free to change, and all carbon atoms must be treated with the same potential. Consequently, the original AIREBO potential used only a single  $\sigma$  and  $\epsilon$  value for each atom, neglecting any variation in the shape of the van der Waals potential with bonding environment. In the original AIREBO potential, the  $\sigma_{\text{CC}}$  and  $\epsilon_{\text{CC}}$  parameters were obtained by fitting to the interlayer spacing and elastic properties of graphite, while  $\sigma_{\text{HH}}$  and  $\epsilon_{\text{HH}}$  were determined by fitting to the pair correlation function of liquid-state methane and ethane. (The heterogeneous parameters,  $\sigma_{\text{HC}}$  and  $\epsilon_{\text{HC}}$ , are determined from the Lorentz-Berthelot combining rules.<sup>17</sup>) One result of this fitting procedure has been that the AIREBO potential provides a better description for the saturated molecular hydrocarbons to which it was directly fit than it does for unsaturated species. For example, the fine detail in the liquid structure of ethylene is not reproduced well by the AIREBO model (see Fig. 1).

If the performance of the AIREBO potential is to be improved in this regard, it is necessary to allow the shape of the van der Waals potential to adapt in response to changes in the local bonding

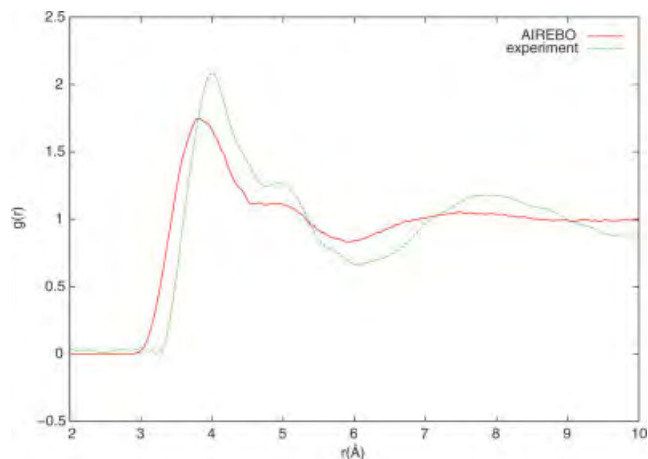


**Figure 1.** Carbon-carbon pair correlation function for liquid ethylene at 106 K. Experimental result from ref. 18. [Color figure can be viewed in the online issue, which is available at [www.interscience.wiley.com](http://www.interscience.wiley.com).]

environment. The approach taken here is to treat the  $\sigma_{ij}$  and  $\epsilon_{ij}$  terms as functionally dependent on the bonding environment, rather than as unvarying constants. At a minimum, the LJ parameters for an atom should depend on the atom's hybridization state, which determines to a large degree the size and character of its electron distribution. In addition, these parameters should also depend on the type of covalent bonds in which the atom participates; bonds of different polarity and different length will give rise to different nonbonded interactions. Although both C–C and C–H bonds are nonpolar, they have very different lengths. Thus, since the bond order potentials use coordination number as a proxy for hybridization state, we allow the  $\sigma$  and  $\epsilon$  values for a given atom to depend on the number of carbon and hydrogen neighbors of the atom in question. That is, the van der Waals parameters for carbon are now  $\sigma_C(N^C, N^H)$  and  $\epsilon_C(N^C, N^H)$ , rather than constant values that are independent of their bonding environment. In this framework, the van der Waals parameters of hydrogen atoms are nominally allowed to depend on their coordination number as well, but since hydrogen atoms in hydrocarbons always have  $N^C = 1$  and  $N^H = 0$ , this results in only a single set of parameters for hydrogen. This assumption for hydrogen is not unreasonable; in the nonpolar, hydrocarbon systems for which AIREBO has been parameterized, the electron distribution on the  $s$ -valent hydrogen atom can be assumed not to change substantially in different environments, and so the  $\sigma_{HH}$  and  $\epsilon_{HH}$  values remain constant. It would presumably be more accurate to include more flexibility in the van der Waals parameters for hydrogen, to account for the difference in electron-withdrawing character of aromatic and aliphatic carbons, for example. Other force fields, for example, have distinct hydrogen atom types for aliphatic, aromatic, and olefinic hydrogens.<sup>11,13</sup> While these hydrogen parameters differ less dramatically than do the carbon parameters to be determined below, such flexibility would certainly result in improved description of the nonbonded properties of hydrocarbons. However, the current model based on first-neighbor coordination numbers does not offer sufficient flexibility to allow more than a single set of hydrogen parameters.

A physical basis could also be provided for even more complex features of the chemical environment, such as the number and identity of second neighbors. This approach may prove to be necessary with the introduction of heteroatoms, as is the case with many classical, nonreactive force fields.<sup>11,13,14</sup> However, these effects are neglected in the current model. It might be expected that the LJ parameters should also depend on the degree of local conjugation; the  $\pi$ -bonding electrons on an unsaturated carbon may give rise to very different van der Waals interactions depending on whether they are localized and relatively nonpolarizable, as in an olefin, or delocalized and more polarizable, as in benzene or graphite. Such a dependence of the LJ parameters on local conjugation was considered, but was found not to be necessary. The parameters for conjugated and nonconjugated  $sp^2$  carbons were found to be quite similar, as described below, so the extra complexity of this additional environmental dependence was abandoned.

In a reactive, bond-order potential, the coordination numbers  $N^C$  and  $N^H$  are not integer quantities, as in a nonreactive potential, but take on fractional values, varying smoothly over the course of a reaction.<sup>5,8</sup> Consequently, the functions  $\sigma_C(N^C, N^H)$  and  $\epsilon_C(N^C, N^H)$  must be defined for non-integer arguments. It is highly impractical to fit such a function for LJ parameter values at noninteger values of

$N^C$  and  $N^H$ , both because there is no unambiguous method of assigning noninteger coordination numbers to a partially dissociated bond, and because there are no appropriate experimental or even *ab initio* data, which can be used to fit the van der Waals interactions for such transient and unstable systems. Consequently, we have chosen to implement the functional dependence of the Lennard-Jones parameters on coordination number via a bicubic spline,<sup>19</sup> in which a knowledge of the function (and some of its derivatives) at integer knot points can be used to generate a smooth function that can be interpolated for noninteger arguments. The integer knot points correspond to stable molecular species, for which the function can be parameterized with experimental data.

Thus we take

$$\sigma_C(N^C, N^H) = \sum_{k=0}^3 \sum_{l=0}^3 c_{kl}^{\sigma} (N^C)^k (N^H)^l \quad (4)$$

and

$$\epsilon_C(N^C, N^H) = \sum_{k=0}^3 \sum_{l=0}^3 c_{kl}^{\epsilon} (N^C)^k (N^H)^l. \quad (5)$$

where the  $\{c_{kl}^{\sigma}\}$  and  $\{c_{kl}^{\epsilon}\}$  coefficients are defined within a rectangular region in which  $N_{\min}^C \leq N^C \leq N_{\max}^C$  and  $N_{\min}^H \leq N^H \leq N_{\max}^H$ ; i.e., within a region bounded by four spline knot points at  $(N^C, N^H) = (N_{\min}^C, N_{\min}^H)$ ,  $(N_{\min}^C, N_{\max}^H)$ ,  $(N_{\max}^C, N_{\min}^H)$ , and  $(N_{\max}^C, N_{\max}^H)$ . The sixteen coefficients  $\{c_{kl}\}$  in eqs. (4) and (5) can thus be determined by specifying the value of the function and three of its derivatives at each of the four knot points. In a different region, the function  $\sigma_C$  or  $\epsilon_C$  is determined similarly, but with a different set of coefficients. The continuity of the function and its gradient are ensured at the boundary through the shared spline knot points at that boundary. Here we use integer values of  $N^C$  and  $N^H$  as the knot points, and require that

$$\frac{\partial \sigma_C}{\partial N^C} = \frac{\partial \sigma_C}{\partial N^H} = \frac{\partial^2 \sigma_C}{\partial N^C \partial N^H} = 0 \quad (6)$$

and

$$\frac{\partial \epsilon_C}{\partial N^C} = \frac{\partial \epsilon_C}{\partial N^H} = \frac{\partial^2 \epsilon_C}{\partial N^C \partial N^H} = 0 \quad (7)$$

at each of the knot points. These derivatives are assumed to be 0 for simplicity, and because of a lack of experimental information that correlates to these derivatives. The values of  $\sigma_C$  and  $\epsilon_C$  at the knot points (i.e., for integer number of bonded neighbors) are obtained by fitting to the cohesive energies and density for liquids of small molecular hydrocarbons, as described in the following section. To do this fitting, we make use of the fact that for a stable, nonreactive system (such as a hydrocarbon liquid at sub-pyrolytic temperatures) the coordination number for each atom is an integer, and the van der Waals interactions in the liquids are determined only by the  $\sigma$  and  $\epsilon$  values at the knot points. Thus these simulations can be performed without knowledge of all of the coefficients in eqs. (4) and (5), and

thus before the  $\sigma_C$  and  $\epsilon_C$  values have been obtained at all knot points.

The strength of the reactive bond-order potentials, however, lies in their ability to simulate chemical reactions. During these reactions, the coordination numbers will be non-integer and the bicubic splines will be evaluated away from the knot points. Thus the full Lennard-Jones interaction is evaluated as in eq. (2), where the interatomic  $\sigma_{ij}$  and  $\epsilon_{ij}$  parameters are obtained from the single-atom values using the Lorentz-Berthelot combining rules,<sup>17</sup>

$$\sigma_{ij} = \frac{1}{2}(\sigma_i + \sigma_j) \quad (8)$$

and

$$\epsilon_{ij} = \sqrt{\epsilon_i \epsilon_j}, \quad (9)$$

and  $\sigma_C$  and  $\epsilon_C$  are now calculated from eqs. (4) and (5) for the case where  $i$  or  $j$  is a carbon atom. Equations (4) and (5) thus represent the only modification to the AIREBO potential in the current work, and the coefficients needed to parameterize this equation are obtained in the following section.

It is worth commenting also on how this minor change affects the calculation of forces and long-range corrections under the new potential. The forces are calculated from the negative gradient of the potential in the usual manner, so that the force on atom  $i$  in the Cartesian direction  $\beta$  ( $= x, y$ , or  $z$ ) is

$$F_{i\beta}^{\text{LJ}} = -\frac{\partial}{\partial \beta_i} \sum_m \sum_{n < m} V_{mn}^{\text{LJ}}, \quad (10)$$

where  $V_{mn}^{\text{LJ}}$  is given by eq. (2) and we are ignoring all of the contributions to the force from non-van der Waals terms in the potential. The Lennard-Jones potential as traditionally implemented is a function only of the interatomic distance, so the Lennard-Jones contribution to the force is evaluated simply as

$$F_{i\beta}^{\text{LJ}} = -\sum_{j \neq i} \frac{\partial V_{ij}^{\text{LJ}}}{\partial r_{ij}} \frac{\partial r_{ij}}{\partial \beta_i}. \quad (11)$$

In the new model, however, the van der Waals potential depends on the atomic positions not only explicitly through the  $i$ - $j$  bond length, but also implicitly via the  $\epsilon$  and  $\sigma$  parameters. Thus the force becomes

$$F_{i\beta}^{\text{LJ}} = -\sum_m \sum_{n < m} \left[ \frac{\partial V_{mn}^{\text{LJ}}}{\partial r_{mn}} \frac{\partial r_{mn}}{\partial \beta_i} + \frac{\partial V_{mn}^{\text{LJ}}}{\partial \sigma_{mn}} \frac{\partial \sigma_{mn}}{\partial \beta_i} + \frac{\partial V_{mn}^{\text{LJ}}}{\partial \epsilon_{mn}} \frac{\partial \epsilon_{mn}}{\partial \beta_i} \right]. \quad (12)$$

Now, because of the dependence of  $\sigma_{mn}$  and  $\epsilon_{mn}$  on the coordination numbers of atoms  $m$  and  $n$ , the double sum must run not only over all pairs of atoms involving the atom  $i$  in question, but also over all pairs where one atom is at least partially bonded to  $i$  (such that displacing  $i$  will change the coordination number of  $m$  or  $n$  and thus alter  $\sigma_{mn}$  and  $\epsilon_{mn}$ ).

As with any simulation involving spherical cutoffs on the LJ interactions, it is necessary to apply long-range corrections<sup>20</sup> to account for the interactions beyond the cutoff distance that have been neglected. For a system interacting with a 12-6 LJ potential, where the LJ interactions are neglected beyond a cutoff  $r_c = \lambda\sigma$  that is some multiple of the LJ  $\sigma$  parameter, the interactions can be evaluated analytically, assuming a uniform density at distances beyond  $r_c$ , leading to corrections

$$E_{\text{LRC}} = \frac{8}{3}\pi V \left( \frac{1}{3}\lambda^{-9} - \lambda^{-3} \right) \rho^2 \epsilon \sigma^3 \quad (13)$$

for a monatomic system of number density  $\rho$  and volume  $V$ . When the system is composed of multiple atom types with different LJ parameters, the long-range correction to the energy can be written

$$E_{\text{LRC}} = \frac{8}{3}\pi V \left( \frac{1}{3}\lambda^{-9} - \lambda^{-3} \right) \sum_j \sum_k \rho_j \rho_k \epsilon_{jk} \sigma_{jk}^3, \quad (14)$$

where  $\rho_k$  represents the density of a particular atom type  $k$ , and the LJ parameters  $\sigma_{jk}$  and  $\epsilon_{jk}$  depend on the interacting atom types. The equivalent expression for the long-range correction to the pressure is

$$P_{\text{LRC}} = \frac{16}{3}\pi \left( \frac{2}{3}\lambda^{-9} - \lambda^{-3} \right) \sum_j \sum_k \rho_j \rho_k \epsilon_{jk} \sigma_{jk}^3. \quad (15)$$

In a constant-volume simulation with conventional LJ interactions, these corrections are evaluated only once, and do not change during the course of the simulation. In the model presented here, however, the LJ parameters can vary in time, and the number densities  $\rho_k$  change with each chemical reaction. Thus eqs. (14) and (15) must be evaluated every time an atom's coordination number changes. This represents a modest increase in computational cost for highly reactive systems. This extra cost could be avoided by using a fixed-length cutoff (rather than a multiple of the variable LJ  $\sigma$  parameter). However, this would have the disadvantage that a greater fraction of the long-range cohesive energy would be included within the cutoff for some bonding environments than for others. The resulting potential would not be conservative unless efforts were made to include the (rather cumbersome) forces due to the variation of the long-range corrections with changes in coordination number. In all of the simulations described below, the LJ cutoffs were applied at a multiple of  $\lambda = 3$  times the LJ  $\sigma$  parameter, and eqs. (14) and (15) were evaluated at every timestep.

## Parameterization

### Simulation Details

To parameterize this new potential for hydrocarbons, molecular dynamics simulations were performed for a variety of small molecular hydrocarbons in the liquid state. These compounds ranged from one to four carbons in size, and included both saturated hydrocarbons, as well as unsaturated carbon atoms with  $sp$  and  $sp^2$  hybridization, including both conjugated and nonconjugated

**Table 1.** Heats of Vaporization ( $\text{kJ mol}^{-1}$ ) and Pressures (bar) at the Specified Temperature and Density, from Experiment, as Calculated with the Original AIREBO Potential,<sup>8</sup> and as Calculated with the New Potential.

Compound	$T$ (K)	$\rho$ ( $\text{g cm}^{-3}$ )	Experiment	AIREBO <sup>8</sup>			This work		
			$\Delta_{\text{vap}}H$	$\Delta_{\text{vap}}H$	err (%)	$P$	$\Delta_{\text{vap}}H$	err (%)	$P$
Benzene	298	0.874 <sup>21</sup>	33.93 <sup>21</sup>	28.84	−15.0	1070	33.64	−0.9	0
Methane	111.7	0.423 <sup>22</sup>	8.17 <sup>21</sup>	9.55	16.9	−380	8.15	−0.3	−20
Ethane	184.6	0.545 <sup>23</sup>	14.69 <sup>22</sup>	16.26	10.7	480	14.70	0.1	20
Ethylene	169.5	0.570 <sup>24</sup>	13.54 <sup>22</sup>	12.50	−7.7	400	13.54	0.0	20
Acetylene	189.6	0.613 <sup>21</sup>	16.95 <sup>21</sup>	8.90	−47.5	850	16.90	−0.3	30
Propane	231.1	0.584 <sup>21</sup>	19.04 <sup>25</sup>	19.45	2.2	450	18.99	−0.3	60
Allene	240	0.658 <sup>22</sup>	18.62 <sup>22</sup>	17.52	−5.9	420	18.46	−0.9	0
Isobutane	262	0.593 <sup>22</sup>	21.30 <sup>22</sup>	22.32	4.8	200	21.31	0.1	0
MAD					13.8	530		0.3	20

The experimental pressure of each system at the specified state point is 1 bar. The mean absolute deviation (MAD) from experiment is provided for both properties.

molecules. A complete list of the eight molecules used in the fitting procedure is provided in Table 1. Each molecular dynamics simulation consisted of 128 molecules in a periodic simulation cell at the experimental density, except for one case (methane) where 256 molecules were used in order that the side length of the periodic cell would exceed twice the LJ cutoff of  $3\sigma_{\text{CC}}$ . When experimental data for the enthalpy of vaporization were available, the simulations were performed at the experimental boiling point of the system,  $T_b$  (or 298 K, if  $T_b > 298$  K, as for benzene). If  $\Delta_{\text{vap}}H$  was not available at  $T_b$ , the simulation was performed at 298 K. The specific temperatures used for each compound, along with the experimental density and  $\Delta_{\text{vap}}H$ , are provided in Table 1. The simulations were performed in the canonical ensemble, using the Langevin thermostat.<sup>26</sup> Long-range corrections<sup>20</sup> were used to account for the van der Waals energy contributions beyond the LJ cutoff of  $3\sigma$ . The simulations were run for a minimum of 100 ps after equilibration at the desired temperature, although frequently for as long as 200 ps in order to obtain adequate statistical averaging of the system pressure.

The simulated properties used to fit the LJ potential are the pressure ( $P$ ) and the enthalpy of vaporization ( $\Delta_{\text{vap}}H$ ). Because the systems are simulated at the experimental density measured at ambient pressure, a well-parameterized potential should give a pressure of 1 bar, while the target value for  $\Delta_{\text{vap}}H$  is obtained from experiment. The pressure is calculated using the internal virial, with long-range corrections, while  $\Delta_{\text{vap}}H$  is calculated from the equilibrium energies of separate simulations of a single gas-phase molecule and an  $N$ -molecule simulation of the liquid at the same temperature,

$$\Delta_{\text{vap}}H = NU(g) - U(l) + RT \quad (16)$$

where it has been assumed that the gas is ideal and the molar volume of the liquid is negligible compared to that of the gas.

### Parameterization

In the original AIREBO potential, the LJ parameters for carbon were obtained from the properties of graphite. Thus we take these

values, unmodified, as the LJ parameters for graphitic carbon, with  $(N^C, N^H) = (3, 0)$ , as well as for  $\text{sp}^2$  carbon in a benzene-like environment of  $(N^C, N^H) = (2, 1)$ . At this point the only two remaining parameters needed in an unreactive simulation of liquid benzene are the values of  $\sigma_H$  and  $\epsilon_H$ . These two parameters were modified to obtain the best fit to the experimental values of  $\Delta_{\text{vap}}H$  and  $P$  for benzene. Because the strong and monotonic dependence of energetic properties such as  $\Delta_{\text{vap}}H$  on  $\epsilon$  and  $PV$  properties such as the pressure (or density) on  $\sigma$ , this optimization is relatively straightforward and results in an unambiguous pair of  $(\sigma_H, \epsilon_H)$  values. The values of  $\sigma$  and  $\epsilon$  for hydrogen are 2.538 Å and 28.8 K, respectively. These values are assumed to apply for H atoms in any chemical environment.

Next, the values of  $(\sigma_C, \epsilon_C)$  were determined in a like fashion, for one type of stable bonding environment at a time. This was done first for molecules containing carbon in only a single bonding environment: methane, ethane, ethylene, and acetylene. Next, with  $(\sigma_C, \epsilon_C)$  values in hand for the specific spline knots corresponding to these bonding environments, these values could be used in order to parameterize  $(\sigma_C, \epsilon_C)$  values for additional spline knots using molecules such as propane or isobutane, which contain carbon in more than one different bonding environment. In all cases, each pair of experimental values of  $\Delta_{\text{vap}}H$  and  $P$  for a specific liquid was used to fit only a single pair of  $(\sigma_C, \epsilon_C)$  values at one knot point. The resulting parameter values are tabulated in Table 2.

The values of the heat of vaporization and pressure (at the experimental density) obtained during the parameterization procedure for the compounds used in the fitting process are presented in Table 1, along with the results obtained using the published AIREBO potential.<sup>8</sup> Because these properties were explicitly used during the fitting procedure, it is no surprise that they are well reproduced by the new model, with a mean absolute deviation (MAD) of 0.3% in the heat of vaporization and 20 bar in the pressure. The AIREBO values are presented merely as an illustration of the accuracy of the potential when not using adaptive LJ parameters, with a MAD of 13% in the heat of vaporization and over 500 bar in the pressure.

Although the parameterization using the compounds in Table 1 was straightforward, there are some difficulties at other spline knots. One of these is that not all of the desired spline knot points can be

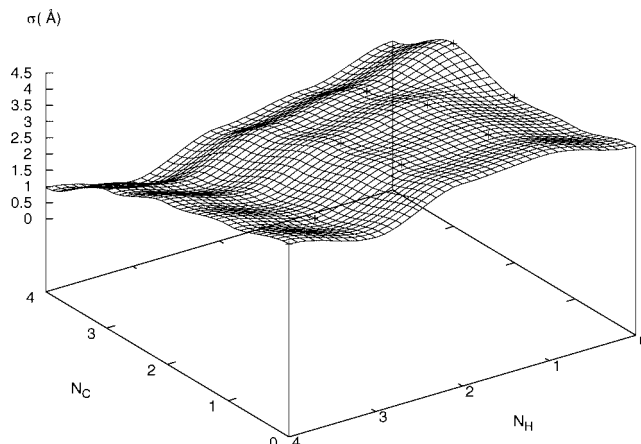
**Table 2.** Knot Values Characterizing the Bicubic Spline for  $\epsilon_C$  and  $\sigma_C$  at Integer Values of  $N^C$  and  $N^H$ .

$N^C$	$N^H$	$\sigma(\text{\AA})$	$\epsilon(K)$	Fitting compound
0	0	3.58	167.7	
0	1	4.13	75.1	
0	2	3.99	34.8	
0	3	3.12	15.6	
0	4	3.70	5.1	Methane
1	0	3.05	157.1	
1	1	3.60	64.5	Acetylene
1	2	3.46	24.3	Ethylene
1	3	2.59	50.8	Ethane
1	4	3.17	40.3	
2	0	2.85	125.6	Allene
2	1	3.40	33.0	Benzene
2	2	3.00	48.7	Propane
2	3	2.13	75.2	
2	4	2.71	64.7	
3	0	3.40	33.0	Graphite
3	1	2.70	82.7	Isobutane
3	2	2.30	98.4	
3	3	1.43	124.9	
3	4	2.01	114.4	
4	0	2.35	104.5	
4	1	1.65	154.2	
4	2	1.25	169.9	
4	3	0.38	196.4	
4	4	0.96	185.9	

All derivatives of  $\epsilon_C$  and  $\sigma_C$  with respect to  $N^C$  and  $N^H$  are zero at these knot points. The values were obtained by fitting to energetics and *PV* properties of the specified compound, if identified, or by extrapolation from nearby parameter values.

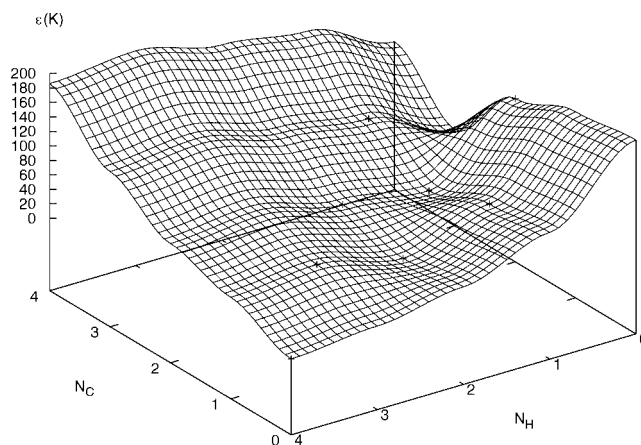
easily parameterized from existing data. In some cases, the bonding environment corresponding to the knot point may be physically meaningful, but the experimental or *ab initio* data may be hard to obtain. Such is the case for  $N^C = 1$  and  $N^H = 0$ , corresponding to a  $C_2$  dimer. This species exists, and is an important component in many reactive systems, such as in simulations of sputtering,<sup>27</sup> but it is too reactive to exist in a condensed phase from which the van der Waals parameters could be inferred. It is possible to imagine a series of *ab initio* calculations on a pair of  $C_2$  dimers from which their van der Waals interaction potential could be obtained, although it would not be trivial to decouple this interaction from the covalent bonding interaction. The simpler approach used here is to arbitrarily specify values of  $\sigma_C$  and  $\epsilon_C$  that preserve the general contour of the bicubic spline surface. Thus the parameters for the carbon dimer ( $N^C, N^H$ ) = (1,0) were obtained by linear extrapolation from the values for acetylene (1,1), allene (2,0), and benzene (2,1).

In other cases, the bonding environment corresponding to one of the desired spline knots may not be physically realistic. Such is the case for overcoordinated forms of carbon, such as ( $N^C, N^H$ ) = (2,3). Although there are no stable molecular species with this bonding configuration, such geometries may appear as transient states during energetic collisions. Furthermore, the parameter values at five-coordinate knot points may

**Figure 2.** Graphical depiction of the  $\sigma(N^C, N^H)$  surface. Crosses represent the values determined by fitting directly to condensed phase properties.

be needed to obtain values at noninteger coordination numbers, e.g. during an  $S_N2$  reaction, even if the total coordination number never exceeds four during the reaction. Here it is difficult even to conceive of a realistic *ab initio* calculation that could provide realistic LJ parameters for such species. In this case also, the approach taken is to extrapolate from nearby parameter values. All extrapolated values chosen in this manner are specified in Table 2. It should be emphasized that although the LJ parameters obtained in this manner are somewhat arbitrary, they have little effect on any realistic simulations. They control the van der Waals interactions only for highly reactive or transient species, for which the interactions are primarily determined by covalent bonding.

Finally, one additional case that presented difficulties during the parameterization was ( $N^C, N^H$ ) = (4,0). Although this case could in principle have been parameterized using neopentane (together with knowledge of the ( $N^C, N^H$ ) = (1,3) parameters derived from

**Figure 3.** Graphical depiction of the  $\epsilon(N^C, N^H)$  surface. Crosses represent the values determined by fitting directly to condensed phase properties.



ethane), we were unable to find parameters that exactly reproduced the pressure and  $\Delta_{\text{vap}}H$  for this system. This is presumably because the density and cohesive energy of liquid neopentane depend very little on the van der Waals interactions of the buried central carbon. But for this same reason, the properties of any simulation will be likewise very insensitive to the values of the LJ parameters chosen at this knot point. The parameter value at  $(N^{\text{C}}, N^{\text{H}}) = (4, 0)$  is extrapolated from the parameter values at (0,4), (1,3), (2,2), and (3,1).

Once the values of  $\sigma_{\text{C}}$  and  $\epsilon_{\text{C}}$  are determined at all the knot points, and the derivatives at these knot points are specified using eqs. (6) and (7), it is straightforward to invert eqs. (4) and (5) in order

to obtain the coefficients  $c_{kl}^{\sigma}$  and  $c_{kl}^{\epsilon}$  in each domain of the spline. The result of this procedure is shown in Figures 2 and 3, which show the variation of  $\sigma$  and  $\epsilon$  with changes in the local coordination number.

## Results and Discussion

To test the performance of the new LJ parameters, simulations were performed for a variety of compounds not used in the fitting

**Table 3.** Pressures for 27 Compounds Not Used in Fitting, as Calculated with the New Potential and with the Original AIREBO Potential.<sup>8</sup>

			P (bar)	
	Compound	<i>T</i> (K)	$\rho$ (g cm <sup>-3</sup> )	
Alkanes	Butane	272.7	0.6011 <sup>21</sup>	489
	Cyclohexane	298	0.7739 <sup>25</sup>	1447
	Hexane	298	0.6606 <sup>25</sup>	706
	Octane	298	0.6986 <sup>25</sup>	918
	MAD			890
	RMSD			980
Alkenes	<i>Z</i> -Butene	276.84	0.6213 <sup>21</sup>	538.6
	Propene	225.46	0.6100 <sup>25</sup>	−495
	<i>E</i> -Butene	274.2	0.6041 <sup>21</sup>	372
	<i>Z</i> -2-Pentene	309.8	0.6503 <sup>21</sup>	−277
	1,2-Butadiene	284	0.6760 <sup>25</sup>	1426
	1,3-Butadiene	269	0.6506 <sup>25</sup>	704
	Toluene	298	0.8668 <sup>21</sup>	1133
	MAD			707
	RMSD			823
Branched alkanes	2,3-Dimethylpentane	298	0.6908 <sup>25</sup>	692
	2,3-Dimethylbutane	298	0.6616 <sup>25</sup>	503
	3-Methylpentane	298	0.6598 <sup>25</sup>	617
	2-Methylhexane	298	0.6787 <sup>25</sup>	696
	2-Methylheptane	298	0.698 <sup>25</sup>	790
	Isopentane	301.1	0.6201 <sup>25</sup>	418
	3-Methylhexane	298	0.687 <sup>25</sup>	771
	MAD			641
	RMSD			655.7
Branched alkenes	2-Methyl-1,3-butadiene	298	0.679 <sup>25</sup>	794
	2,3-Dimethyl-2-butene	293	0.708 <sup>25</sup>	768
	<i>trans</i> -1-Propenylbenzene	293	0.9023 <sup>25</sup>	1596
	Styrene	298	0.9016 <sup>25</sup>	1266
	2-Methyl-2-pentene	298	0.6863 <sup>25</sup>	760
	Isobutene	298	0.6242 <sup>21</sup>	824
	MAD			1001
	RMSD			1061
Alkynes	1-Butyne	281.23	0.6783 <sup>25</sup>	1356
	2-Butyne	298	0.691 <sup>25</sup>	1994
	1-Pentyne	298	0.6901 <sup>25</sup>	1295
	MAD			1548
	RMSD			1596
Total	MAD			850
	RMSD			963

The experimental pressure of each system at the specified state point is 1 bar. The mean absolute deviation (MAD) and root mean square deviation (RMSD) from experiment are provided separately for several categories of compounds.

**Table 4.** Enthalpies of Vaporization ( $\text{kJ mol}^{-1}$ ) for 27 Hydrocarbons Not Used in Fitting, as Calculated with the New Potential, with the Original AIREBO potential,<sup>8</sup> and as Reported Experimentally.

Compounds		Expt $\Delta_{\text{vap}}H$	AIREBO <sup>8</sup>			This work		
			$\Delta_{\text{vap}}H$	$\Delta(\Delta H_{\text{vap}})$	%	$\Delta_{\text{vap}}H$	$\Delta(\Delta H_{\text{vap}})$	%
Alkanes	Butane	22.44 <sup>25</sup>	22.95	0.51	2.27	23.34	0.90	4.00
	Cyclohexane	33.01 <sup>25</sup>	33.81	0.80	2.42	34.78	1.77	5.36
	Hexane	31.56 <sup>25</sup>	34.39	2.83	8.96	35.98	4.42	14.0
	Octane	41.49 <sup>25</sup>	47.06	5.57	13.42	50.72	9.23	22.3
	MAD			2.42	6.77		4.08	11.40
	RMSD			3.37	8.67		5.54	14.21
Alkenes	Z-Butene	23.34 <sup>25</sup>	20.83	−2.51	−10.7	22.18	−1.16	−4.94
	Propene	18.42 <sup>25</sup>	21.57	3.15	17.1	18.64	0.22	1.20
	E-Butene	22.72 <sup>28</sup>	22.04	−0.68	−2.98	22.10	−0.62	−2.73
	Z-2-Pentene	26.1 <sup>28</sup>	32.09	5.99	22.9	26.81	0.71	2.73
	1,2-Butadiene	24.02 <sup>25</sup>	21.48	−2.54	−10.6	24.38	0.36	1.50
	1,3-Butadiene	22.47 <sup>25</sup>	19.44	−3.03	−13.5	22.18	−0.29	−1.27
	Toluene	38.01 <sup>25</sup>	34.01	−4.00	−10.5	38.09	0.08	0.21
	MAD			3.12	12.63		0.49	2.08
	RMSD			3.52	14.08		0.61	2.59
	2,3-Dimethylpentane	34.26 <sup>25</sup>	25.48	−8.78	−25.6	33.96	−0.30	−0.89
Branched alkanes	2,3-Dimethylbutane	29.12 <sup>25</sup>	23.55	−5.57	−19.1	28.52	−0.60	−2.04
	3-Methylpentane	30.28 <sup>25</sup>	27.07	−3.21	−10.6	30.71	0.43	1.42
	2-Methylhexane	34.87 <sup>25</sup>	36.94	2.07	5.93	39.91	5.04	14.4
	2-Methylheptane	39.67 <sup>25</sup>	37.97	−1.70	−4.27	41.16	1.49	3.76
	Isopentane	24.79 <sup>28</sup>	30.43	5.64	22.75	31.54	6.75	27.2
	3-Methylhexane	35.1 <sup>29</sup>	31.56	−3.55	−10.1	35.97	0.87	2.47
	MAD			4.35	14.06		2.21	7.46
	RMSD			5.01	16.38		3.40	12.39
	2-Methyl-1,3-butadiene	26.8 <sup>29</sup>	24.11	−2.69	−10.04	27.81	1.41	5.34
	2,3-Dimethyl-2-butene	32.51 <sup>25</sup>	24.37	−8.14	−25.1	30.75	−1.76	−5.41
Branched alkenes	trans-1-Propenylbenzene	46.4 <sup>29</sup>	45.23	−1.17	−2.51	49.38	2.98	6.42
	Styrene	43.9 <sup>29</sup>	33.62	−5.08	−13.1	43.70	−0.2	−0.45
	2-Methyl-2-pentene	31.6 <sup>29</sup>	28.86	−2.74	−8.68	31.88	0.28	0.88
	Isobutene	22.13 <sup>25</sup>	19.81	−2.32	−10.60	18.52	−3.61	−16.31
	MAD			4.49	13.1		1.71	3.70
	RMSD			5.85	15.9		2.20	4.64
	1-Butyne	24.52 <sup>25</sup>	20.38	−4.14	−16.9	27.22	2.70	11.0
	2-Butyne	26.7 <sup>29</sup>	22.69	−4.26	−15.8	27.28	0.33	1.24
	1-Pentyne	28.4 <sup>29</sup>	22.18	−6.22	−21.9	30.80	2.40	8.46
	MAD			4.79	17.9		1.89	7.22
Alkynes	RMSD			4.94	18.3		2.22	8.54
	MAD			3.86	12.8		1.96	6.45
	RMSD			4.62	14.8		2.98	9.55
Total								

The mean absolute deviation (MAD) and root mean square deviation (RMSD) from experiment are provided separately for several categories of compounds.

procedure. There are 27 of these test species, consisting of straight-chain, branched, and ring compounds with between three and nine carbon atoms, both saturated and unsaturated, with the latter including both conjugated and aromatic species. The full list of 27 test species appears in Tables 3 and 4. As with the compounds used in the parameterization procedure, the heat of vaporization and pressure are calculated at a specified temperature (typically the lower of the boiling point or 298 K) and the experimental density at that temperature. The results for the new potential, as well as the predecessor AIREBO potential, are tabulated in Tables 3 and 4.

The pressures tabulated in Table 3 demonstrate that the *PV* performance of the current potential is much better than with the previous (nonadaptive) LJ parameterization. For each class of compounds (linear and branched (or ring) alkanes and alkenes, and linear alkynes) the new model shows a substantial improvement over the previous AIREBO parameterization. The MAD from the expected experimental pressure is only  $\sim 210$  bar with the new model, rather than 850 bar with AIREBO. The improvement is particularly good for alkynes, where the mean absolute error in the pressure has been reduced to about 7% of its previous value. Note that because of

the relative incompressibility of the liquid phases being studied, the pressure at equilibrium density is much more sensitive to errors in the potential than is the density error at equilibrium pressure. For hydrocarbon liquids with an isothermal compressibility of  $\sim 10^{-4} \text{ bar}^{-1}$  and a density of  $\sim 0.6 \text{ g cm}^{-3}$  (both typical for small hydrocarbons), a pressure error of  $\sim 200 \text{ bar}$  corresponds to an error in the density of about  $0.01 \text{ g cm}^{-3}$ , or 2%.

A distribution of errors in the pressure is presented in Figure 4. This distribution shows that both potentials tend to overestimate the pressure for hydrocarbons in the liquid state near the normal boiling point, but both the mean and the variance of this error are lower with the new potential. Whereas pressure errors of 0.5 to 2 kbar are common with AIREBO, the largest pressure error observed with the new model on the 27-species test set was 500 bar.

The cohesive energies of liquid molecular hydrocarbons are also improved with the new potential, as can be seen from the heat of vaporization data presented in Table 4. The only class of compounds for which the new potential is not improved is the linear alkanes, where the mean absolute deviation (MAD) in the heat of vaporization increased from  $2.42 \text{ kJ mol}^{-1}$  with the AIREBO potential to  $4.08 \text{ kJ mol}^{-1}$  with the new potential. This is perhaps not surprising, as saturated alkanes are the class of compounds for which the AIREBO potential was explicitly parameterized. For all other classes of compounds examined, the new potential provides an improved description of the cohesive energy in the liquid. The improvement is dramatic for linear alkenes, with the MAD decreasing from  $3.13 \text{ kJ mol}^{-1}$  to  $0.49 \text{ kJ mol}^{-1}$ . For the set of test molecules taken as a whole, the MAD has improved from  $3.86 \text{ kJ mol}^{-1}$  to  $1.96 \text{ kJ mol}^{-1}$ , and now indicates a mean absolute error of less than 7% in the heat of vaporization. Because no data from this test set were included in the parameterization, and efforts have been made to ensure that the test set represents a variety of different types of small hydrocarbon molecules, these errors can be expected to be typical for additional small-molecule hydrocarbon species not analyzed here. Figure 5 shows the distribution of error values in the heat of vaporization with the AIREBO and new potential. From this figure it is evident that the errors in the modeled enthalpies of vaporization are much more tightly clustered, although

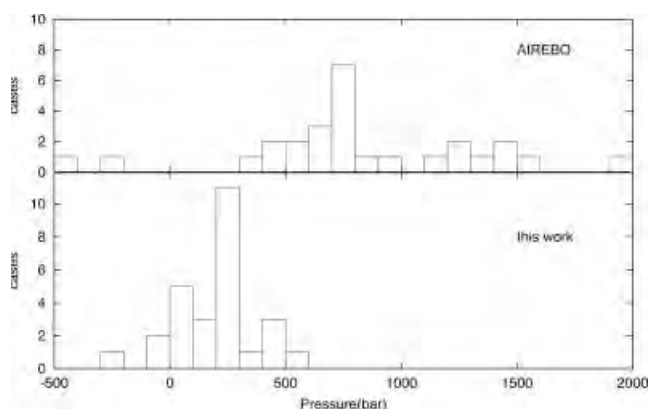


**Figure 4.** Distribution of errors in the pressure for 27 liquid hydrocarbons not included in the fitting procedure, as calculated with AIREBO (upper panel) and the current model (lower panel).

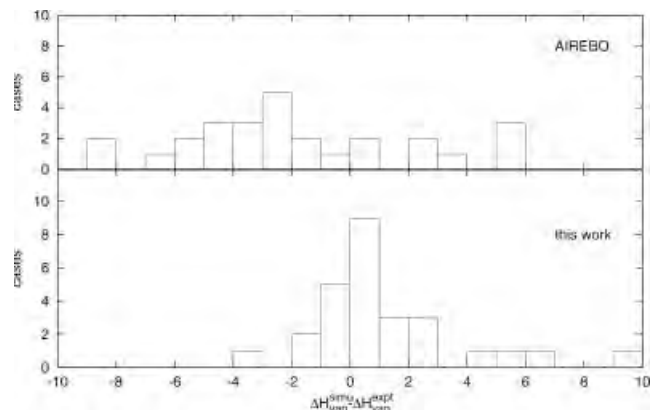


**Figure 5.** Distribution of errors in the enthalpy of vaporization ( $\text{kJ mol}^{-1}$ ) for 27 hydrocarbons not included in the fitting procedure, as calculated with AIREBO (upper panel) and the current model (lower panel).

a slight bias towards overly positive heats of vaporization has been introduced.

The carbon-carbon pair correlation function,  $g_{CC}(r)$ , provides an additional, highly sensitive test of the van der Waals interactions in the liquid. The positions of the peaks are highly sensitive to the density of the fluid and the atomic radii, while the peak heights are sensitive to the strength of the nonbonded interactions. In contrast to the parameterization of the original AIREBO potential, no structural data were utilized here in the parameterization of the new potential. Thus a comparison of pair correlation functions with experiment provides additional evidence of the success of the new potential, relative to the previous AIREBO potential. Figures 6–9 show the pair correlation functions for methane, benzene, ethylene, and ethane. In all cases, there is a good agreement between the experimental pair correlation function and that calculated with the current potential. In most cases, the liquid structure shows clear improvement over the AIREBO model. For example, in the first peak in methane (Fig. 6) and the weak structure in benzene (Fig. 7). The agreement is particularly good for ethylene (Fig. 8), which was poorly described by AIREBO. Only for ethane (Fig. 9) does the model not provide a better description of liquid structure than the AIREBO model. This result is not surprising, because the pair correlation function data for ethane were explicitly used in the parameterization of the AIREBO model.<sup>8</sup> The quantitative and near-quantitative description of liquid structure with the present model is particularly remarkable given that this model was parameterized solely with energies and pressures, without using structural data explicitly.

## Summary

A new potential has been developed and implemented, which enables the van der Waals interactions in a reactive bond-order potential to vary with the chemical environment. This is done by having the parameters characterizing the van der Waals interaction

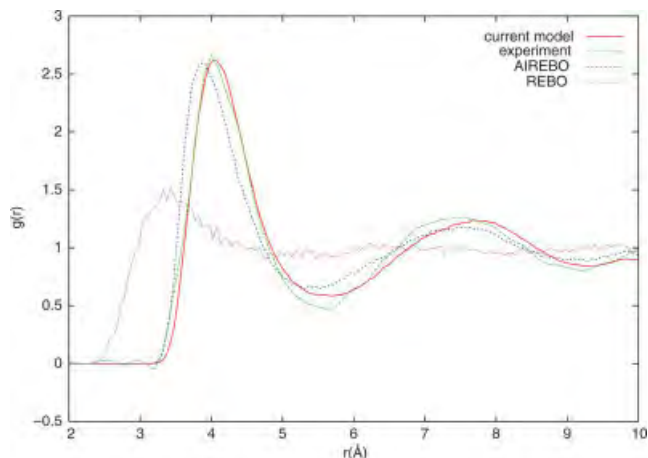


**Figure 6.** Carbon–carbon pair correlation function  $g_{CC}$  for liquid methane at 92 K as calculated by AIREBO and the current model, and from experiment.<sup>18</sup> The result as calculated by the REBO potential (which lacks van der Waals interactions) is also shown for comparison. [Color figure can be viewed in the online issue, which is available at [www.interscience.wiley.com](http://www.interscience.wiley.com).]

( $\sigma$  and  $\epsilon$  in the Lennard-Jones equation) vary smoothly and continuously with the coordination number and chemical identity of the neighbors of each atom.

This model has been parameterized using the energetics and  $PV$  behavior of a set of eight hydrocarbon molecules. When used to simulate a set of 27 molecules that were not included in the parameterization procedure, this potential provides substantially improved results over the AIREBO potential, which does not allow for adaptive changes in the van der Waals interactions. For stable molecular species, the errors in the pressure near the boiling point were reduced

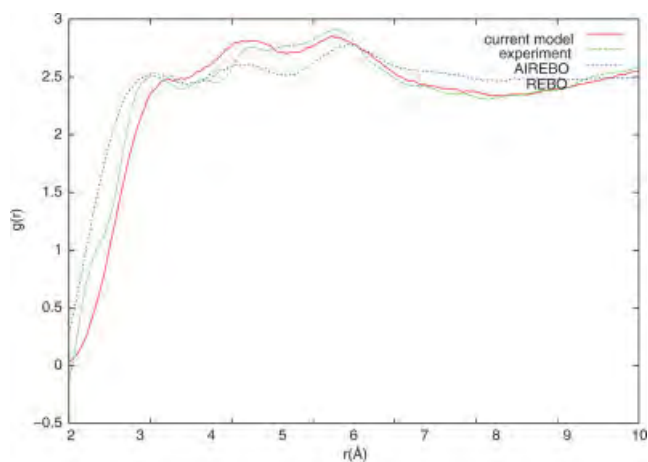


**Figure 7.** Carbon–carbon pair correlation function  $g_{CC}$  for liquid benzene at 298 K as calculated by AIREBO and the current model, and from experiment.<sup>30</sup> [Color figure can be viewed in the online issue, which is available at [www.interscience.wiley.com](http://www.interscience.wiley.com).]

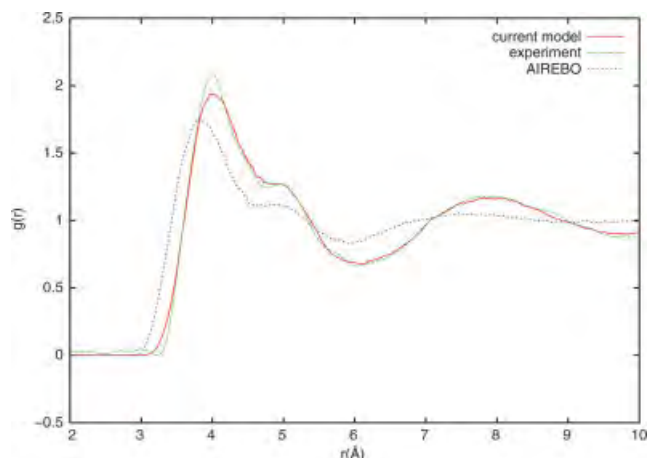


**Figure 8.** Carbon–carbon pair correlation function  $g_{CC}$  for liquid ethylene at 106 K as calculated by AIREBO and the current model, and from experiment.<sup>18</sup> [Color figure can be viewed in the online issue, which is available at [www.interscience.wiley.com](http://www.interscience.wiley.com).]

from 850 under AIREBO to 207 bar with the new model. The errors in predicted heats of vaporization are reduced by approximately 30%, to below 3 kJ mol<sup>−1</sup>.

While a number of additional parameters have been introduced into the model (one pair of Lennard-Jones parameters for each coordination state of carbon), this is done to capture the physically realistic variation of atomic size and dispersion with changes in electronic bonding environment. The substantially improved agreement with experimental energetics,  $PV$  properties, and liquid structure, even for compounds not used in the fitting procedure, indicate that the new model should be transferable to other hydrocarbon systems.

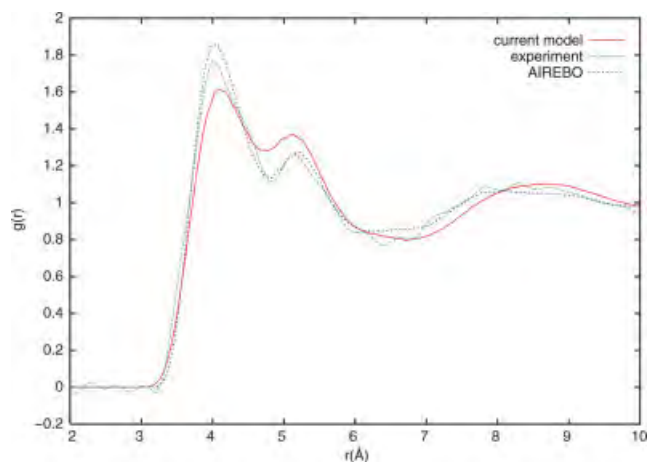


**Figure 9.** Carbon–carbon pair correlation function  $g_{CC}$  for liquid ethane at 105 K as calculated by AIREBO and the current model, and from experiment.<sup>31</sup> [Color figure can be viewed in the online issue, which is available at [www.interscience.wiley.com](http://www.interscience.wiley.com).]

## References

1. Tersoff, J. *Phys Rev B* 1988, 37, 6991.
2. Tersoff, J. *Phys Rev B* 1989, 39, 5566.
3. Daw, M. S.; Baskes, M. I. *Phys Rev B* 1984, 29, 6443.
4. Tersoff, J. *Phys Rev Lett* 1988, 61, 2879.
5. Brenner, D. W.; Shenderova, O. A.; Harrison, J. A.; Stuart, S. J.; Ni, B.; Sinnott, S. *J Phys Condens Matter* 2002, 14, 783.
6. Pettifor, D. G.; Oleinik, I. I. *Phys Rev B* 1999, 59, 8487.
7. Oleinik, I. I.; Pettifor, D. G. *Phys Rev B* 1999, 59, 8500.
8. Stuart, S. J.; Tutein, A. B.; Harrison, J. A. *J Chem Phys* 2000, 112, 6472.
9. van Duin, A. C. T.; Dasgupta, S.; Lorant, F.; Goddard, I. W. A. *J Phys Chem A* 2001, 105, 9396.
10. Halgren, T. A. *J Comput Chem* 1996, 17, 520.
11. Brooks, B. R.; Bruccoleri, R. E.; Olafson, B. D.; States, D. J.; Swaminathan, S.; Karplus, M. *J Comput Chem* 1983, 4, 187.
12. Rappe, A. K.; Casewit, C. J.; Colwell, K. S.; Goddard, W. A.; Skiff, W. M. *J Am Chem Soc* 1992, 114, 10024.
13. Cornell, W. D.; Cieplak, P.; Bayly, C. I.; Gould, I. R.; Merz, K. M. Jr.; Ferguson, D. M.; Spellmeyer, D. C.; Fox, T.; Caldwell, J. W.; Kollman, P. A. *J Am Chem Soc* 1995, 117, 5179.
14. Allinger, N. L.; Yuh, Y. H.; Lii, J.-H. *J Am Chem Soc* 1989, 111, 8551C8566.
15. Sun, H.; Rigby, D. *Spectrochim Acta A* 1997, 53, 1301.
16. Sun, H. *J Phys Chem B* 1998, 102, 7338.
17. Hudson, G. H.; McCoubrey, J. C. *Trans Faraday Soc* 1959, 56, 761.
18. Habenschuss, A.; Johnson, E.; Narten, A. H. *J Chem Phys* 1981, 74, 5234.
19. Press, W. H.; Flannery, B. P.; Teukolsky, S. A.; Vetterling, W. T. *Numerical Recipes*; Cambridge University Press: Cambridge, 1986.
20. Allen, M. P.; Tildesley, D. J. *Computer Simulation of Liquids*; Oxford University Press: London, 1987.
21. Dean, J. Ed.; *Lange's Handbook of Chemistry*; McGraw-Hill: New York, 1999.
22. *L'Air Liquide, Division Scientifique, Gas Encyclopaedia*; Elsevier: Amsterdam, 1976.
23. Lide, D. R. Ed.; *CRC Handbook of Chemistry and Physics*; Chemical Rubber: Boca Raton, 2006.
24. Maass, O.; Wright, C. H. *J Am Chem Soc* 1921, 43, 1098.
25. Lide, D. R. Ed.; *CRC Handbook of Chemistry and Physics*; Chemical Rubber: Boca Raton, 2004.
26. Adelman, S. A.; Doll, J. D. *J Chem Phys* 1976, 64, 2375.
27. Krstic, P. S.; Reinhold, C. O.; Stuart, S. J. *Europhys Lett* 2007, 77, 33002.
28. Majer, V.; Svoboda, V. *Enthalpies of Vaporization of Organic Compounds: A Critical Review and Data Compilation*; Blackwell Scientific Publications: Oxford, 1985.
29. Chickos, J. S.; Acree, W. E. *J Phys Chem Ref Data* 2003, 32, 519.
30. Narten, A. H. *J Chem Phys* 1977, 67, 2102.
31. Sandler, S. I.; Lombardo, M. G.; Wong, D. S.-H.; Habenschuss, A.; Narten, A. H. *J Chem Phys* 1982, 77, 2144.



# Hotspot formation in shock-induced void collapse

Yunfeng Shi<sup>1, a</sup> and Donald W. Brenner<sup>1, b</sup>

<sup>1</sup> Department of Materials Science and Engineering  
North Carolina State University, Raleigh, NC 27695-7907, USA

<sup>a</sup>yshi2@ncsu.edu, <sup>b</sup>brenner@ncsu.edu

**Keywords:** energetic materials, shock, detonation, void defect, hotspot, jetting.

**Abstract.** We present results from molecular dynamics simulations of shock-induced hydrodynamic void collapse in a model energetic crystal. During void collapse, hotspot formation is observed that leads to subsequent detonation. The hotspot formation mechanism is identified as shock energy focusing via jetting. There is another initiation mechanism that arises from the interaction of reflected shock waves with the rigid piston, which is considered to be an artifact. Such artifact can be eliminated by altering the location of the void. The detonation threshold as a function of the velocity of the driven piston is determined for various void geometries. It is found that a system containing a void has a lower detonation threshold than that of a perfect energetic crystal. The amount of reduction of the detonation threshold depends on the geometry of the void. For square voids, there exists a minimum size above which reduction of the detonation threshold occurs. Among voids that have an equal volume, the void that is elongated along the shock direction gives the lowest detonation threshold.

## Introduction

It is well established that detonation in solid explosives can be facilitated by void collapse and that initial chemical reactions occur at so-called “hotspots” [1-3]. However, the hotspot formation mechanism, i.e. why chemistry is localized, has not been fully established at the atomic level. Jetting occurs in many high speed phenomena and serves as an important means to concentrate energy that causes, for example, the Munroe effect [4] and cavitation erosion [5, 6]. The Munroe effect in shaped charges can be quantitatively described by liner collapsing models [4, 7]. However, the application of these models to general void collapse is not obvious because the assumption that the jetting material is an inviscid/incompressible fluid may not hold. Unlike shaped charges, void collapse in water is closely related to void collapse in energetic material. Thus it is reasonable to link jetting to hotspot formation, as supported by both numerical and experimental results. Mader studied shock collapse of a spherical void using reactive hydrodynamics [8]. It was found that a high temperature liquid jet emerges during void closure due to energy convergence. More recently, jetting has been observed in studying the shock collapse mm-size voids in gel, in which case high speed jet impact on the downstream wall is the main mechanism for ignition [2, 9, 10]. However, it is not clear whether those macroscopic observations can be extended to nanometer-scale voids. At the atomic scale, where the transient nature of these processes limit experimental studies, molecular dynamics simulations have provided many useful insights into detonation as well as hotspot formation [11-15]. Hatano has reported an elevated temperature and an increased number of energetic collisions during collapsing of a rectangular void. Such shock chemistry enhancement is due to momentum/energy focusing although no jetting was observed [15]. A planar gap defect, which precludes any convergence of the spallated material, has also been shown to reduce the detonation threshold by as much as 20% in model system [13]. A recompaction model has been used to explain the hotspot formation mechanism for such defects; this model considers heating from recompression of the ejected particles at the down-stream wall [14]. This model predicts that size-dependent sub-threshold detonation with chemical reaction initiates in the compressed gas instead of the down-stream wall. Molecular dynamics simulations by Germann *et al.* investigated

two-dimensional energetic materials containing circular or elliptical voids. They observed jet formation and void shape-dependent detonation behavior [16]. Nomura *et al.* used molecular dynamics simulations and the ReaxFF many-body reactive potential energy expression to model the collapse of a spherical void in an RDX crystal [17]. They observed the formation of a jet that was accelerated through the void due to focusing from the void walls.

We have simulated shock collapsing of rectangular voids [18] and identified the detonation mechanism at both the mesoscale and the atomic scale. At the mesoscale, jetting is the primary feature that appears during void collapsing that leads to hotspot formation. At the atomic scale, vibrational up-pumping which is followed by bi-molecular reaction triggers the onset of detonation. In this work, we address two important issues that have not been sufficiently covered in our previous report. The first one is the effect of the location of the void on the detonation threshold from which we identified an undesirable detonation mechanism that arises from the finite system size. The second issue is to investigate the effect of the void shape on detonation sensitivity in terms of size and aspect ratio. These results provide useful insights in understanding shape-dependent shock chemistry during void collapsing.

## Simulation System

**The reactive force field.** The energetic material used in this study is a model nitrogen cubane crystal. A recently developed reactive state summation (RSS) potential is used to model nitrogen-nitrogen interactions [19]. This potential is designed to model the exothermic dissociation of nitrogen cubane molecules into diatomic nitrogen molecules. This potential has been tested in thermal decomposition and mechanical shock simulations in three-dimensional systems [19]. Steady detonation has been observed to propagate at an intrinsic speed. In addition, this energetic material model has been used to simulate a plastic bonded explosive (PBX) [20] and shock collapsing of rectangular voids [18].

**Model explosive containing voids.** The initial configuration of the system is a thin slab geometry. Nitrogen cubane molecules are packed in simple cubic structure in a simulation box of  $46 \times 52 \times 0.9$  nm<sup>3</sup>. The system is periodic in Y and Z-directions, and shocks propagate along positive X-direction. Rectangular voids are created by removing nitrogen cubane molecules from a perfect crystal. The relevant characteristics of the void are a longitudinal length (in the X-direction) and a transverse length (in the Y-direction). The void dimension in the Z-direction is infinite due to the periodic boundary condition. Three types of voids with different locations along the X-direction were created: (L, left aligned) the left boundary of the void is fixed so that the thickness of the upstream wall (the material between the piston and the void) is 10 nm; (R, right aligned) the right boundary of the void is fixed so that the thickness of the downstream wall (the material between the far-end of the explosive and the void) is 10 nm; (C, center aligned) the center of the void is fixed at the center of the system. This is to investigate how the location of the void effects detonation behavior in a finite system. Three series of voids were investigated: (I) varying the transverse length while keeping a constant longitudinal length; (II) varying the size of the void while keeping a square shape; (III) varying the aspect ratio of the void while keeping the volume (especially the project area in the X-Y plane) constant. A shock is generated by a moving rigid piston. The detonation threshold was obtained by systematically varying the piston velocity to determine when the system detonates.

## Results and Discussion

**The effect of void locations.** Plotted in Figure 1 are the detonation thresholds for series I. Three types of voids (L, R and C void) are included. The detonation thresholds of R voids and C voids almost overlap. For voids with a small longitudinal dimension, there is no reduction of detonation threshold. Above a critical length, the detonation threshold decreases monotonically with increasing longitudinal length. For L voids, the detonation thresholds deviate from R voids and C voids at small longitudinal lengths. In those cases, it was found that the initiation occurs not in the vicinity

of the void, but near the piston. As the ejected energetic molecules hit the downstream wall, a compressive reshock wave is reflected back. When this reshock wave reaches the rigid piston, detonation occurs. This type of sub-threshold detonation is a result of the finite thickness of the upstream-wall and is thus considered an artifact. Fortunately, it is straight forward to exclude such artifacts by examining the location of initial chemical reactions. Figure 2 illustrates the two types of detonation initiation for a L void. The initiation due to the artifact discussed above is located adjacent to the rigid piston. After removing these initiations from the data, the detonation threshold curve for L voids overlaps very well with the other two curves. Therefore, the location of the voids along the X-direction, or the thickness of the upstream/downstream wall, does not affect the detonation behavior. S

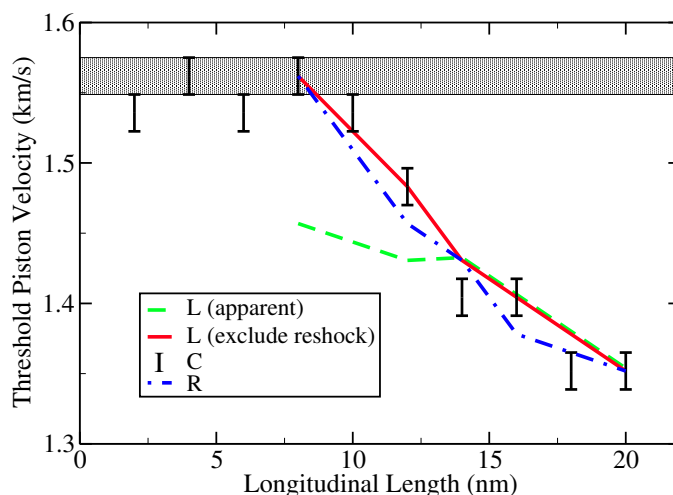


**Figure 1** Detonation thresholds are shown for voids (series I) with different longitudinal lengths but keeping the transverse length constant (14 nm).

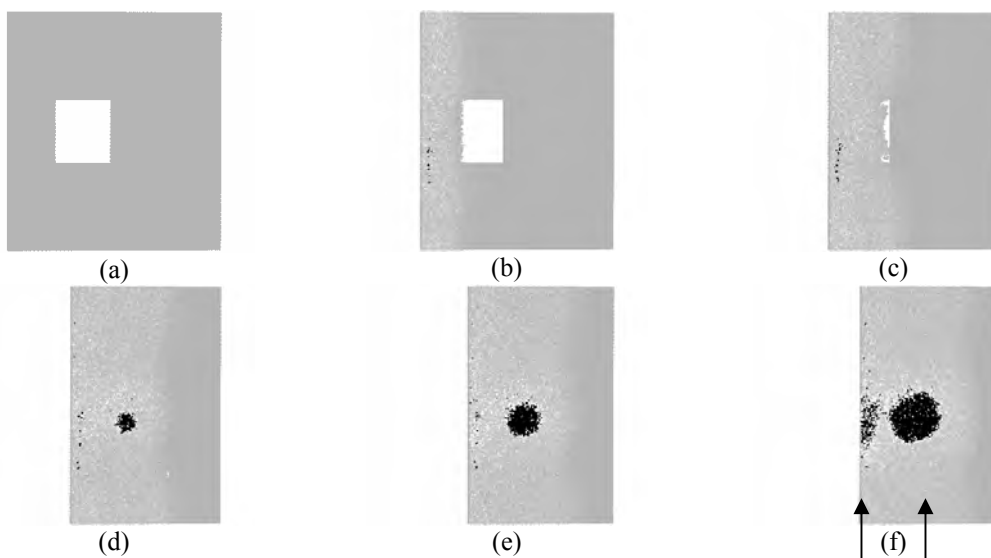


**Figure 2** The sequence of void collapse for an L void (12 nm by 14 nm). The piston speed is above the true detonation threshold so that the hotspots from void collapsing as well as from the artifact appear. Gray represents the potential energy of nitrogen in the perfect nitrogen cubane. Black represents low potential energy of nitrogen in detonation products including diatomic and small amount of oligomeric nitrogen molecules. Therefore, the growing black region is the detonation region. Note that there are two detonation initiation locations that are marked by the arrows in pane (f). The left one is an artifact from the interaction of the reflected shock wave and the rigid piston. The right one is from void collapsing.

**Shape evolution of the jet.** The observed sub-threshold detonation behavior is due to jet formation as illustrated in Figure 2. As the shock wave reaches the upstream wall of the void, material is ejected and begins to fly toward the downstream wall. This causes the material of the upstream wall to be compressed vertically by adjacent regions above and below. This can be seen by the shape change of the upstream wall and also the curving side walls. Consequently, the material in the upstream wall expands in the shock direction and a jet is formed. Illustrated in Figure 2(a) is the shape evolution of the jet. First, the flying molecules maintain an almost flat front. At this stage, the detonation threshold remains the same as the perfect crystal. Then due to the compression from the side walls, two corner-jets emerge near the side walls and move towards the centerline, which resembles experimental observations [9]. Those corner-jets are energetic enough to reduce the detonation threshold. Therefore, it is the formation of the corner-jets that sets the critical length in the longitudinal direction as shown in Figure 1. Finally, the two corner-jets combine to form an even more energetic single jet. The jet does not travel at a constant speed. Instead, its front is accelerating as evidence by the increased spacing between each profile in Figure 3.

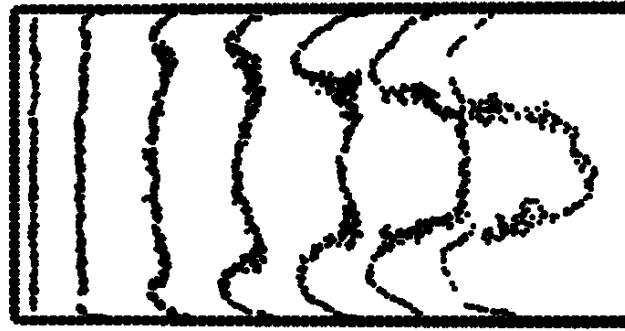


**Figure 3** Shape evolution of a jet with equal time intervals. Only the edge of the jet and the boundary of the voids are shown. The downstream wall is removed.

**Size-dependent shock sensitivity of squared void.** Figure 4 shows the detonation thresholds for square voids with different sizes (series II). Similar to Figure 1, there exists a critical void size to initiate sub-threshold detonation. The threshold piston speed decreases with increasing void size that is larger than 8 nr

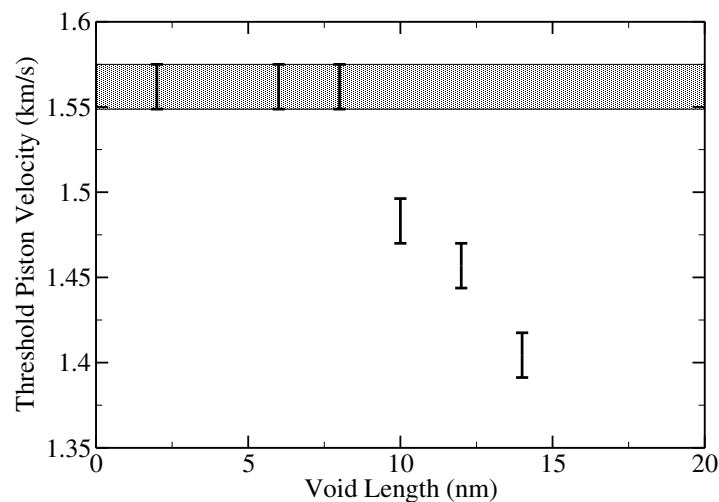


**Figure 4** Detonation thresholds for square voids (series II) with different sizes.

**Aspect ratio-dependent shock sensitivity.** To further illustrate the effect of the void shape, plotted in Figure 5 are the detonation thresholds of series III. It is clear that elongated voids along the shock direction are the most effective to sensitize explosives.

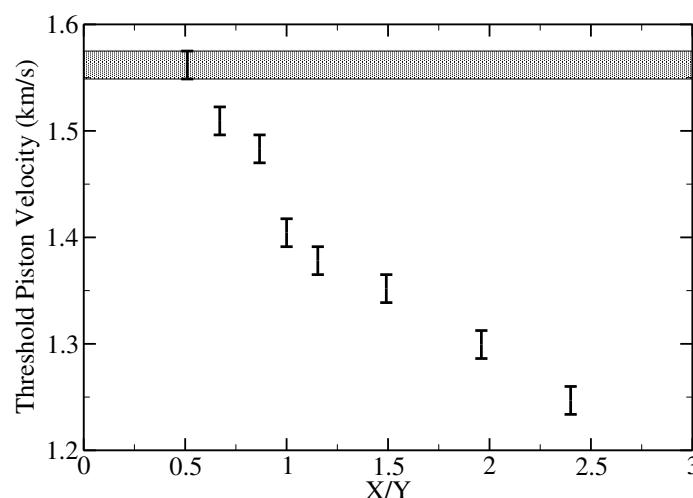


**Figure 5** Detonation thresholds for a void (series III) with a constant volume (a constant projected area in X-Y plane of  $200 \text{ nm}^2$ ) but different aspect ratio.

**Hotspot formation mechanisms.** As illustrated in Figure 3, the shock energy localizes mainly via jetting. The degree of localization, which determines the intensity of the hotspot formation, depends sensitively on the shape of the voids. Upon shock, the materials in the up-stream wall are ejected and subject to continuous accelerating from behind and by the side wall. Therefore, the impact velocity of the ejected material on the down-stream wall increases as the void length in the shock direction increases. This explains the main feature in Figure 1, 4 and 5 that larger voids lead to a lower detonation thresholds. The hotspot formation mechanism in this study agrees with the momentum and energy focusing [15]. The shape dependency observed here is similar to a temperature representation reported in Ref. [14]. Contrary to a previous report [13], we observe no reduction in detonation threshold for systems with planar gaps (up to 20 nm in width) for C and R voids. This is because jetting is impossible for a planar gap. However, systems with gaps (L voids) show reduced detonation thresholds. This is again due to the artifact that the reshock wave reaches the piston.

## Summary

We observed void collapsing in a model energetic crystal that leads to hotspot formation through jetting. This causes a reduction of the detonation threshold of an energetic crystal containing a void. The strength of jetting depends on the geometry of the void. An artifact of detonation initiation, which is caused by the reflection of a shock wave, is identified. Such an artifact can be avoided by changing the position of the void. A critical length of the void in the shock direction exists for sub-threshold detonation.

## Acknowledgements

We thank D. Thompson, T. Sewell, Y. Hu and B. Broom for stimulating discussions. The North Carolina State University High-Performance Computing Facility is also thanked for providing computational resources. The simulations were performed using LAMMPS molecular dynamics software (<http://lammps.sandia.gov>) with a customized force field. This work was supported by a Multi-University Research Initiative from the U.S. Army Research Office.



## References

- [1] F. P. Bowden and A. D. Yoffe, *Fast Reactions in Solids* (Butterworths Scientific Publications, London, 1958).
- [2] J. P. Dear, J. E. Field, and A. J. Walton, *Nature* Vol. 332, (1988), p.505.
- [3] J. E. Field, *Accounts Chem Res* Vol. 25, (1992), p.489.
- [4] W. P. Walters and J. A. Zukas, *Fundamentals of shaped charges*, 1989).
- [5] M. Kornfeld and L. Suvorov, *J Appl Phys* Vol. 15, (1944), p.495.
- [6] J. I. Katz, *P Roy Soc Lond a Mat* Vol. 455, (1999), p.323.
- [7] G. Birkhoff, D. P. Macdougall, E. M. Pugh, et al., *J Appl Phys* Vol. 19, (1948), p.563.
- [8] C. L. Mader, *Phys Fluids* Vol. 8, (1965), p.1811.
- [9] N. K. Bourne and J. E. Field, *J Fluid Mech* Vol. 244, (1992), p.225.
- [10] N. K. Bourne and A. M. Milne, *P Roy Soc Lond a Mat* Vol. 459, (2003), p.1851.
- [11] D. W. Brenner, D. H. Robertson, M. L. Elert, et al., *Phys Rev Lett* Vol. 70, (1993), p.2174.
- [12] D. W. Brenner, in *Shock compression of condensed matter*, edited by S. C. Schmidt, R. D. Dick, J. W. Forbes and D. G. Tasker, 1992), p. 115.
- [13] C. T. White, D. R. Swanson, and D. H. Robertson, in *Chemical Dynamics in Extreme Environments*, edited by R. A. Dressler (World Scientific, Singapore, 2001), p. 547.
- [14] B. L. Holian, T. C. Germann, J. B. Maillet, et al., *Phys Rev Lett* Vol. 89, (2002), p.285501.
- [15] T. Hatano, *Phys Rev Lett* Vol. 92, (2004), p.015503.
- [16] T. C. Germann, B. L. Holian, P. S. Lomdahl, et al., in *12th International Detonation Symposium*, San Diego, (2002).
- [17] K. I. Nomura, R. K. Kalia, A. Nakano, et al., *Appl Phys Lett* Vol. 91 (2007).
- [18] Y. F. Shi and D. W. Brenner, *Journal of Physical Chemistry C*, submitted (2008).
- [19] Y. F. Shi and D. W. Brenner, *J Chem Phys* Vol. 127, (2007), p.134503.
- [20] Y. F. Shi and D. W. Brenner, *Phys Rev Lett*, submitted (2007).

## **Theory, Modeling and Numerical Simulation**

doi:10.4028/www.scientific.net/SSP.139

## **Hotspot Formation in Shock-Induced Void Collapse**

doi:10.4028/www.scientific.net/SSP.139.77

# Molecular Simulation of the Influence of Interface Faceting on the Shock Sensitivity of a Model Plastic Bonded Explosive

Yunfeng Shi\* and Donald W. Brenner

Department of Materials Science and Engineering, North Carolina State University, Raleigh, North Carolina 27587-7907

Received: June 28, 2008; Revised Manuscript Received: September 5, 2008

Molecular dynamics simulations are used to model the shock loading of an interface with various degrees of nanometer scale faceting between an inert binder and an energetic crystal. The facets create regions of local compression that induce exothermic reaction that leads to local hotspots and an increased shock sensitivity to detonation. Two mechanisms for compression and hotspot formation are identified that depend on the shock impedance mismatch between the binder and energetic crystal, namely shock focusing and local compression of the facets. These results provide a possible explanation for why spherical RDX crystals in cast polymer-bonded explosives appear less shock sensitive than RDX with more faceted morphologies.

## I. Introduction

Despite decades of intensive research, understanding and ultimately controlling the shock sensitivity of high explosives remains one of the most challenging unsolved issues facing the energetic materials community. It is now well established that initiation originates from “hotspots” that can arise from the interaction of shocks with defects such as shear bands, heterogeneous interfaces, voids, and occlusions.<sup>1</sup> The details of this interaction, however, are not completely established and can differ widely from system to system. Chemical impurities, for example, can play a large role in hotspot formation and initiation, as can void collapse accompanied by adiabatic heating or jetting. The size of energetic crystals is also known to influence sensitivity, where small crystals are generally less sensitive than larger crystals.

The role of morphology and chemical purity in determining the sensitivity of so-called “reduced sensitivity” (RS) 1,3,5-trinitro-1,3,5-*s*-triazine (RDX) has been of continuing interest over the past two decades. van der Steen et al. initially reported that the shape of RDX crystals bound into a plastic bonded explosive (PBX) can have a large influence on sensitivity, with rounder crystals producing less sensitive materials.<sup>2</sup> Researchers at the French company Sociéte Nationale des Poudres et Explosifs subsequently reported the discovery of an RDX that when incorporated into a cast PBX significantly lowers the shock sensitivity.<sup>3</sup> The French researchers reported that their RS RDX, which is created by a recrystallization process, cannot be differentiated from conventional RDX by particle size, physical or chemical considerations, or the impact sensitivity of the neat crystals.<sup>4</sup> Follow-up studies by Australian researchers appear to confirm this result and also demonstrate that other RDX forms produced by other manufacturers can also lead to RS when cast into a PBX.<sup>4</sup> On the basis of examination of scanning electron micrographs, it appears that the crystals of all of the RS RDX tend to be more rounded than the other non-RS RDX forms.<sup>4,5</sup>

More recently, Doherty and Watt reported results from an extensive interlaboratory study of the chemical and physical properties (including impact and shock sensitivity) of seven types of RDX from five manufacturers.<sup>6</sup> These studies indicated

that the impact sensitivity of neat samples of the various forms of RDX do not vary to a significant extent but that when cast into a PBX there are measurable differences in shock sensitivity between RS RDX and other forms of RDX. They also noted that the amount of HMX in each sample, which is a common impurity arising from the production of RDX, can have a profound influence on shock sensitivity. Most of the RS forms of RDX have a low HMX content, but this is not sufficient to guarantee RS. The role of crystal morphology was not explicitly addressed in this study.

Baer has used the CTH shock physics code to model the mesoscopic scale shock dynamics of packed neat HMX crystals and HMX crystals incorporated into a PBX.<sup>7,8</sup> He noted the formation of hotspots in the simulations from plastic flow and jetting into voids as well as from shock focusing due to differences in shock impedances in the material. For the packed crystal simulations, flow into the intercrystal regions was the dominant mechanism for hotspot formation. To probe the influence of crystal shape on shock properties, simulations of the shock loading of a regular array of spherical and cubic HMX crystals within a PBX were carried out, where the latter had a random rotational orientation. Larger pressure fluctuations were noted for the spherical crystals that arise from resonances in shock reflections due to the regular arrangement of crystals that are suppressed by the random rotations of the cubic crystals. A reactive model in which chemistry is initiated by a pressure threshold was also incorporated into a simulation of the shock compression of packed neat HMX crystals. A comparable study in a PBX, however, was not reported, and no further studies of the influence of crystal morphology or shock focusing on hotspot formation were noted.

Baer’s modeling provides an explanation for why there is no difference in the impact sensitivity of neat crystals of RS and other RDX forms as reported by Doherty and Watt; hotspot formation and subsequent initiation is determined by material expansion in intercrystalline voids, which is largely unaffected by the purity or crystal morphology (for the same range of crystal sizes). However, it does not explain why the RS is manifest in the cast PBXs.

To further probe the possible role of crystal morphology on the sensitivity of cast PBXs, we have carried out molecular

\* To whom correspondence should be addressed. E-mail: shiy2@rpi.edu.

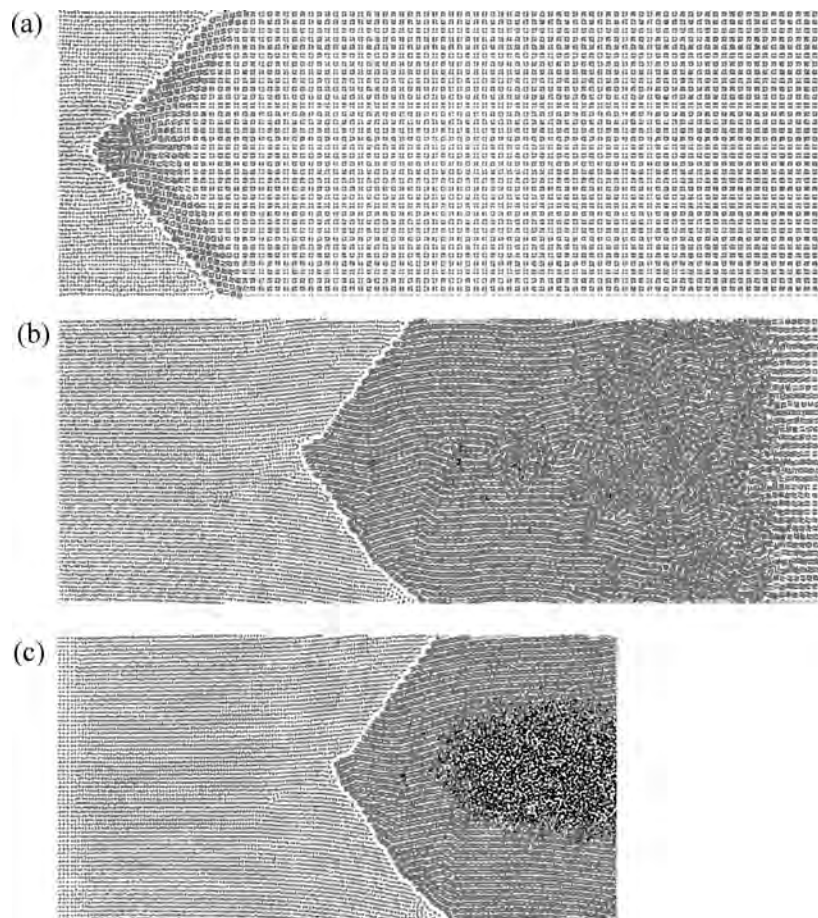


**Figure 1.** Illustrations of atomic configurations from a simulation of the shock loading of system I. The velocity of the driven piston is just above that needed for detonation. The atoms are colored according to their potential energy so that atoms with low potential energy appear darker. Time from frames (a)–(c) are 2.28, 8.36, and 14.44 ps, respectively.

dynamics simulations of the shock loading of interfaces with different degrees of nanometer-scale faceting between an inert binder and a model energetic crystal. Our simulations suggest that interface faceting can induce hotspots at specific locations, and for our model these hotspots can reduce the detonation threshold by as much as 24%. Two effects contribute to the mechanism of hotspot formation and enhanced sensitivity at a faceted interface depending on the shock impedance mismatch. When the velocity of a driven shock is larger in the binder than that in the energetic crystal, a planar shock front is refracted and focused toward the region between facets in the energetic crystal. This focusing is analogous to that reported by Baer in his mesoscopic scale modeling. In the second effect, the interface becomes flattened such that the tips of the facets that protrude into the binder are preferentially compressed. Unlike systems with a flat interface where detonation initiates randomly, the location of the hotspot for systems with a faceted interface is determined by the above mechanisms.

## II. Computational Model

The simulated binder–crystal interface used in this study is composed of a model nitrogen cubane crystal and a single-component inert binder. For nitrogen, a recently developed reactive state summation (RSS) potential is used.<sup>9</sup> This potential is designed to model the exothermic dissociation of nitrogen cubane molecules into diatomic nitrogen molecules. This potential has been tested in thermal decomposition, mechanical shock, and void collapsing simulations in three-dimensional

systems.<sup>9,10</sup> Steady detonation has been observed to propagate at an intrinsic speed. A pair-additive Morse potential was used for the binder–binder interactions.

$$E_{B-B}(r_{ij}) = \varepsilon_{B-B}(e^{2\rho_{B-B}(\sigma_{B-B}-r_{ij})} - 2e^{\rho_{B-B}(\sigma_{B-B}-r_{ij})}) + \varepsilon_{B-B}^{\text{shift}} \quad (1)$$

where  $\varepsilon_{B-B}$  is 0.0003 eV,  $\rho_{B-B}$  is 8.0 Å<sup>-1</sup>,  $\sigma_{B-B}$  is 3.0498 Å, and  $\varepsilon_{B-B}^{\text{shift}}$  is  $2.21 \times 10^{-6}$  eV. The cutoff is 3.75 Å. The interaction between nitrogen and binder atoms is modeled by a truncated and shifted Lennard-Jones potential

$$E_{B-N}(r_{ij}) = 4\varepsilon_{B-N}((\sigma_{B-N}/r_{ij})^{12} - (\sigma_{B-N}/r_{ij})^6) + \varepsilon_{B-N}^{\text{shift}} \quad (2)$$

where  $\varepsilon_{B-N}$  is 1.0 eV,  $\sigma_{B-N}$  is 3.3409 Å, and  $\varepsilon_{B-N}^{\text{shift}}$  is 1.0 eV. The cutoff is 3.75 Å, which is the interatomic distance corresponding to the energy minimum. Therefore, this interaction is purely repulsive.

A thin slab geometry was used for the composite. The system contains about 40 000 binder atoms and 200 000 nitrogen atoms and has initial dimensions of  $93.2 \times 35.5 \times 0.86$  nm<sup>3</sup>. The system is periodic in the *Y* and *Z* directions, with the *X* direction being the shock direction. The nitrogen cubane molecules and the binder atoms are both in their energy minima and were initially packed with a lattice constant 0.4313 nm<sup>9</sup> in a simple cubic and a face-centered cubic lattice, respectively. This



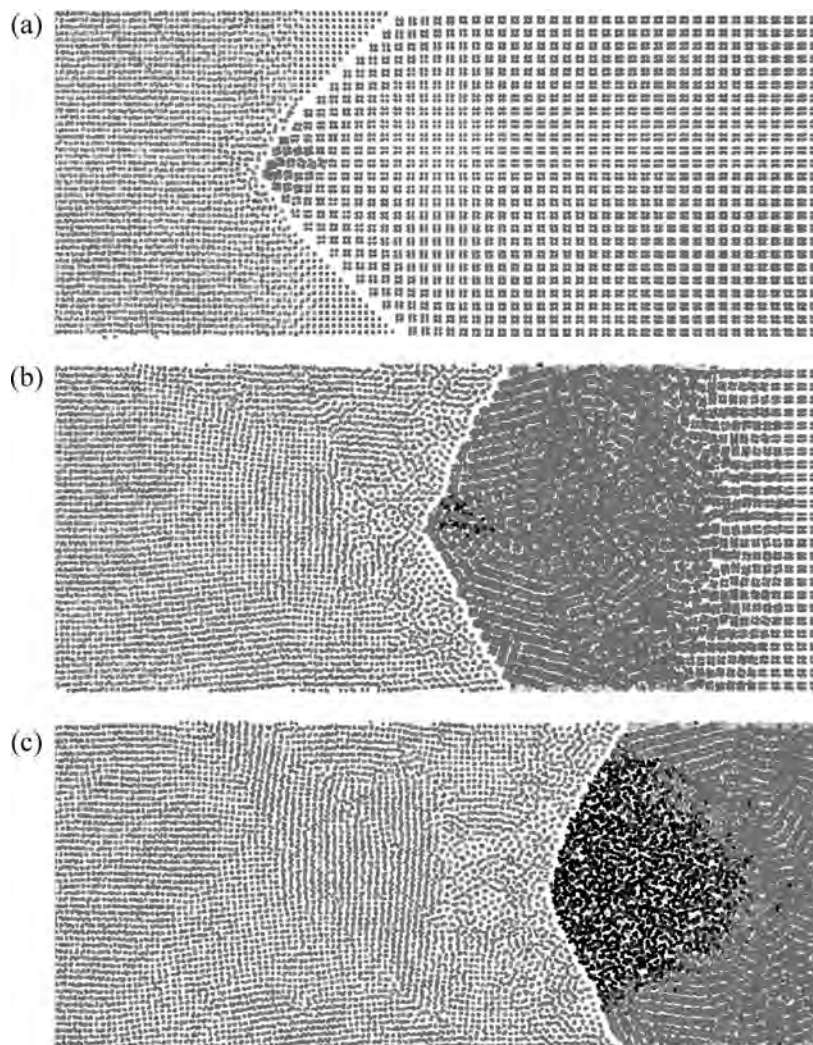


**Figure 2.** Illustrations of atomic configurations from a simulation of the shock loading of system III. The velocity of the driven piston is just above that needed for detonation. The atoms are colored according to their potential energy so that atoms with low potential energy appear darker. Time from frames (a)–(c) are 3.80, 6.84, and 9.12 ps, respectively.

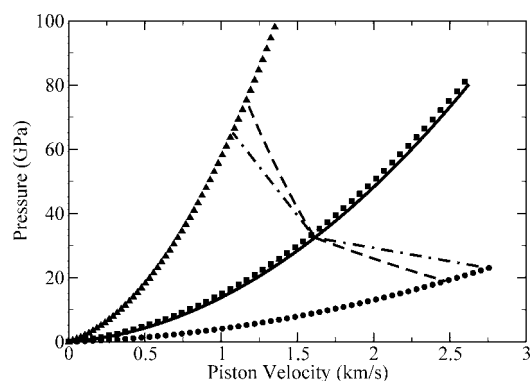


**Figure 3.** Shock Hugoniot for the binders in system I (circles), II (squares), and III (triangles) and the energetic crystal (solid line). The Hugoniot are parabola fits assuming shock velocity scales linearly with piston velocity. On the basis of the mirror-reflection Hugoniot approximation, the reshock (lower-right dashed line for system I) and decompressive isentrope lines (upper-left dashed line for system III) are drawn from the detonation threshold for the pure explosive. The dot-dashed straight lines have a slope of the negative of the initial binder density times the shock velocity according to the acoustic approximation. The detonation threshold is the intersection point of those lines with the binder's Hugoniot.

produces a mechanically stable configuration and creates a coherent interface between the binder and energetic crystal. The

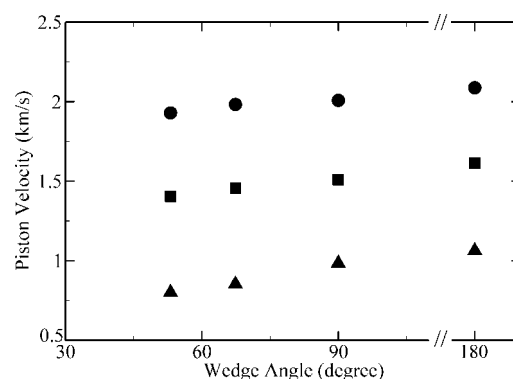


**Figure 4.** Threshold piston velocities as a function of interface angle for system I (circles), II (squares), and III (triangles). A flat interface has an angle of 180°. The measured threshold values have an accuracy of  $\pm 0.013$  km/s.

$\langle 100 \rangle$ ,  $\langle 010 \rangle$ , and  $\langle 001 \rangle$  directions of both the binder and the energetic crystal are parallel to the  $X$ ,  $Y$ , and  $Z$  directions of the simulation box, respectively. Shock simulations on composite systems with binder's and explosive's  $\langle 110 \rangle$  and  $\langle 111 \rangle$  directions parallel to the  $X$  direction (the shock direction) as well as systems that are twice as large in the  $Z$  direction have shown the same results regarding the location of the hotspots and reduced detonation threshold due to interface geometries.



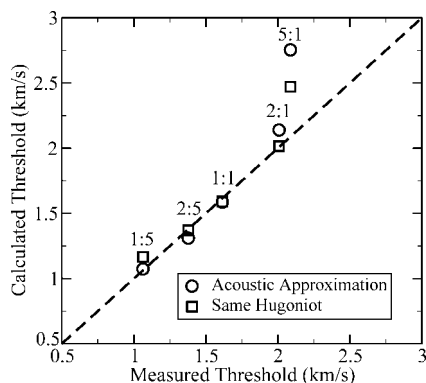


**Figure 5.** Threshold piston velocities calculated from eqs 3 and 4 plotted against threshold velocities determined from the simulations for five density ratio ( $\rho_X/\rho_B$ ) as labeled in the plot.

Both the binder and energetic crystal were first cut to matching shapes and then brought to close contact to form either infinite flat interfaces (analogous to a PBX with spherical explosive particles) or zigzag interfaces (analogous to a PBX with faceted particles), as illustrated in Figures 1a and 2a. The average thickness of the binder is approximately the same for all interface shapes. The system starts at 0 K, and there is no temperature or pressure control in the subsequent MD simulations. A supported shock is created by displacing the first layer of the binder atoms at a constant rate toward the composite interface. The system is considered to detonate when the potential energy of the energetic crystal, which continuously increases due to shock compression, reaches a maximum and starts to decrease as a result of extensive exothermic reactions. Prior studies have shown that once this criterion is met, further dynamics with this potential will lead to a steady-state detonation. Minimum piston velocities needed to initiate detonation were determined by performing multiple simulations with different piston velocities which is similar to ref 10.

Three composite systems with different masses for the binder particles (and hence different densities) but identical atomic interactions were used to study how shock impedance matching affects the detonation threshold. The density ratio of binder over energetic crystal is 1/5, 1, and 5 for systems I, II, and III, respectively. The parameters for the binder–binder interaction were chosen so that the shock velocity of the binder in system II and the energetic crystal is identical within the range of piston speeds investigated here. Therefore, the shock velocity of the binder in system I (III) is always higher (lower) than that of the explosive given the same piston speed. Consequently, as shown in Figure 3, the pressure–piston velocity Hugoniot curves of the binders in system I, II, and III are below, on top of, and above that of the energetic crystal, respectively.

### III. Results

Snapshots from simulations of systems I and III are illustrated in Figures 1 and 2, respectively, for a faceted interface with a facet angle of 90°. In both cases the piston velocity is above that needed to initiate detonation. As the rigid piston compresses the binder, an initially planar shock front is generated in the binder that propagates along the *X* direction. As the shock front propagates through the binder, extensive plastic damage is generated (cf. Figure 2c). For system I, where the shock impedance of the energetic crystal is larger than that of the binder, compressive reshock waves reflect back into the binder. In contrast, for system III, where the impedance of the energetic crystal is larger than that of the binder, decompression waves

reflect back into the binder. For system II, where the shock impedance of the binder and crystal match, there are no reflection waves, and all of shock is transmitted from the binder to the crystal. Thus, the transmitted pressure inside the energetic crystal is greater, equal to, or smaller than the pressure of the compressed binder for system I, II, and III, respectively.

Detonation of the energetic crystal after the shock travels through the interface depends on the velocity of the driven piston. Plotted in Figure 4 is the minimum piston velocity needed to initiate detonation as a function of the wedge angle of the interface for the three systems. There are two important features to this data. First, the threshold piston velocity decreases with increasing density (mass) of the binder. Second, for each system the threshold piston velocity decreases monotonically with decreasing facet angle. To quantitatively understand the first feature, we focus on systems with flat interfaces. The full derivation of the two equations below will be given in the Appendix.

It can be assumed that the interface between the binder and the energetic crystal acts as a piston, and at the threshold detonation conditions the interface velocities and the pressure at the interface for different composites are identical and should be equal to that required to initiate detonation of the pure energetic system (measured in prior studies to be 1.61 km/s and 32.5 GPa). If the shock speed *D* of the binder and the explosive is linearly related to the piston speed *U* such that  $D = a + bU$ , the threshold piston velocity can be calculated under an acoustic approximation as<sup>11,12</sup>

$$U_B^{\text{Th}} = \frac{-2a_B + b_B U_X^{\text{Th}} + \sqrt{(2a_B + b_B U_X^{\text{Th}})^2 + \frac{8b_B(a_X + b_X U_X^{\text{Th}})\rho_X^0/\rho_B^0 U_X^{\text{Th}}}{4b_B}}}{4b_B} \quad (3)$$

where  $U_B^{\text{Th}}$  is the threshold piston velocity for a composite system and  $U_X^{\text{Th}}$  is that of the pure explosive, and  $\rho_X^0$  and  $\rho_B^0$  are the initial densities of the explosive and the binder, respectively. Alternatively, the piston velocity and pressure of the binder can be related to those of the interface by the reshock Hugoniot (in the case of system I) or the decompression isentrope (in the case of system III). Assuming those curves are mirror reflections of the principal Hugoniot of the binder (see ref 13), the detonation threshold in terms of binder piston velocity can be calculated as

$$U_B^{\text{Th}} = \frac{-a_B + 2b_B U_X^{\text{Th}} + \sqrt{a_B^2 + 4b_B(a_X + b_X U_X^{\text{Th}})\rho_X^0/\rho_B^0 U_X^{\text{Th}}}}{4b_B} \quad (4)$$

Given in Figure 5 are threshold piston velocities for systems with the flat interfaces calculated from eqs 3 and 4 plotted against the values determined from the simulations. Data are given for systems I, II, and III together with two additional binder/energetic crystal combinations with intermediate density ratios. Except for the composite with the lightest binder, both equations predict the threshold values within 10% of that determined from the simulations. This level of agreement is sufficient to establish that the difference in threshold piston

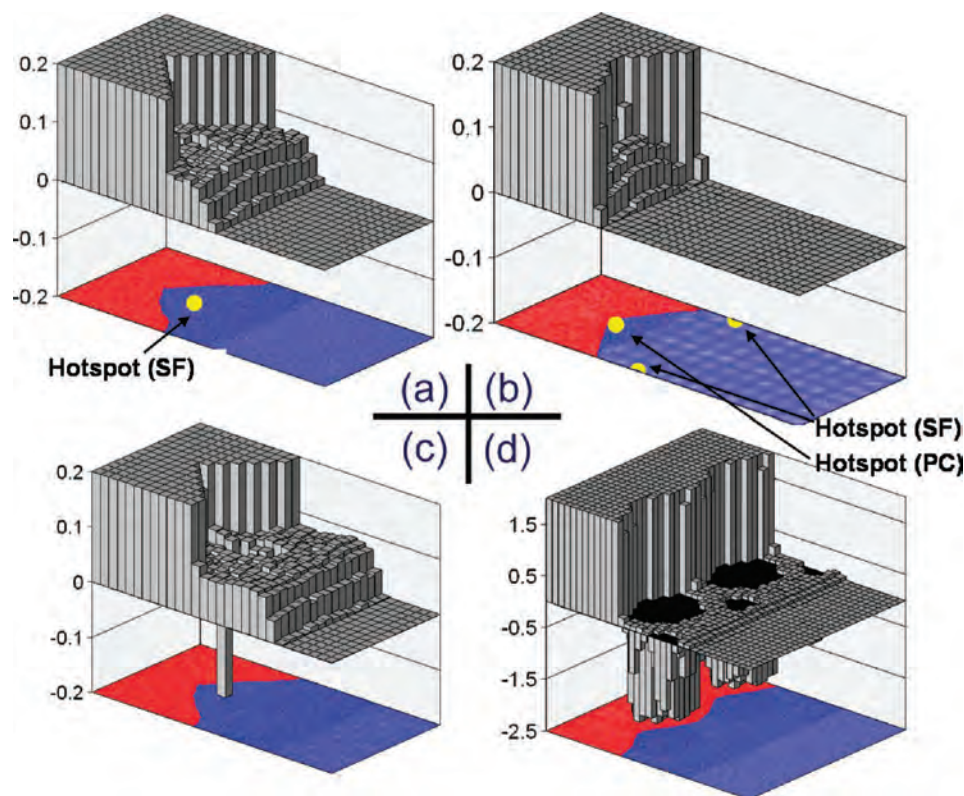


**Figure 6.** Coarse-grained potential energy (relative to the unperturbed explosive in units of eV/atom) and illustrated snapshots for an initial 90° facet for system I (panes a–c) and system III (panes b–d). Panes (a, b) are before and (c, d) are after the onset of detonation. The entire simulation cell is illustrated except for pane (d), where the system is doubled in the *Y* direction for better illustration of the hotspot. Yellow dots in panes (a, b) indicate the locations of the hotspots from shock focusing (SF) and preferential compression (PC). The piston speeds are just above the detonation threshold for each system (2.021 and 0.998 km/s for systems I and III, respectively). Binder atoms are red and nitrogen atoms are blue.

velocities for the flat interfaces is due mainly to shock impedance mismatch.

Detailed analysis of the simulation dynamics revealed two mechanisms that are responsible for the dependence of the threshold piston velocity on the facet angle. For system I, the effective piston speed for compression of the energetic crystal (the interface speed) is slower than the piston speed of the binder, and hence the shock front slows down as it propagates from the binder to the energetic crystal. This causes bending of the shock front and focusing of the shock pressure into the region of the energetic crystal between the facets. The degree of bending of the shock front away from the original shock direction, and hence the amount of focusing, increases for sharper interfaces. Illustrated along the bottom of the box in Figure 6a are the atomic coordinates for system I projected onto a single plane just after a shock front passes a faceted interface. The velocity of the piston driving the shock is just above the threshold velocity for detonation. The atoms in the binder and energetic crystal are red and blue, respectively, and the yellow dot indicates the position at which the hot spot will form. The three-dimensional bar graph above the atom positions indicates the corresponding coarse-grained potential energy of the atoms. There is a local increase in the potential energy due to shock focusing at the point where the hotspot will form. Figure 6c illustrates the same system a little further in the trajectory. The shock front, which is visible as the sudden increase in the potential energy bar graph, has moved further into the energetic crystal. The increase in potential energy between the facets in the energetic crystal due to focusing was sufficient to overcome the barrier for reaction, and the potential energy has dropped at this local point as exothermic reaction is initiated. This drop in

potential energy results in a corresponding increase in local kinetic energy—the hotspot—that grows and transitions into the detonation.

Panels b and d in Figure 6 illustrate the same quantities for system III as those considered for panels a and c for system I. The yellow dots in panel b indicate two places where hotspots will form (one of the dots skirts the periodic boundaries). The dots labeled SF arise from shock focusing as in system I. However, because the effective piston speed for compression of the energetic crystal (the interface speed) is *faster* than the piston speed of the binder, the focusing occurs at points in the energetic crystal near where the tips of the binder protrude into the energetic crystal. As in system I, this focusing locally raises the potential energy. The second hotspot for this system occurs between the facets as in system I but is located closer to the interface than in system I. This second hot spot is due to a flattening of the interface and hence preferential compression of the facets. It is apparent from the localized drop in the potential energy visible in the bar graph in panel d in Figure 6 that both the shock focusing and facet compression are sufficient to induce exothermic reactions. For this system, however, the hotspot and subsequent initiation of detonation occur more readily from the latter.

#### IV. Summary

The simulations reported herein were motivated by the recent interest in understanding the origin of the RS reported for several grades of RDX and specifically to explore how a smoother crystal embedded within an inert matrix might reduce the sensitivity of a PBX. Our simulations demonstrate that a nanometer-scale faceted interface structure between a binder and

energetic crystal can influence sensitivity via two mechanisms: shock focusing and facet compression. How these two mechanisms translate to larger scales is unclear; however, based on the shock focusing noted by Baer the former mechanism likely operates at the grain scale.

**Acknowledgment.** We thank D. Thompson, T. Sewell, Y. Hu, and B. Broom for stimulating discussions. Molecular dynamics simulations were carried out in LAMMPS.<sup>14,15</sup> Computational resources are provided by HPC-NCSU. This work was supported by a MURI project from the U.S. Army Research Office.

#### Appendix. Derivations of Detonation Thresholds for PBXs with Flat Interfaces.

The detonation thresholds for energetic composites with flat interfaces are given in eqs 3 and 4 in the main text. In a PBX system, the detonation threshold, as characterized by the piston velocity that drives the binder, is different than that for the pure explosive. This is due to impedance mismatch between the binder and the explosive. From the continuity conditions across the binder and explosive interface, one can calculate the detonation threshold values for the PBXs based on the threshold values for the pure explosive as well as the material properties of the binder. The derivation will be given here.

We assume a linear relationship between the piston speed  $U$  and the shock speed  $D$ , so that

$$D_B = a_B + b_B U_B \quad (\text{A1})$$

$$D_X = a_X + b_X U_X \quad (\text{A2})$$

Here  $a$  and  $b$  are materials constants that can be obtained via a linear fitting from our simulation data. Subscript B denotes the binder and X denotes the explosive. From mass conservation and momentum balance

$$P_B = \rho_B^0 U_B D_B \quad (\text{A3})$$

$$P_X = \rho_X^0 U_X D_X \quad (\text{A4})$$

Here  $P_B$  and  $P_X$  are pressures of the compressed state inside the binder and explosive being driven by a piston. Note that eqs A3 and A4 describe the behavior of isolated binder and explosive. In a PBX composite, since the binder is driven directly by the piston, eq A3 remains valid.  $\rho_B^0$  and  $\rho_X^0$  are initial densities for the binder and the explosive.

Based on the assumption that, at threshold detonation, the interface pressure/velocity equals the threshold detonation pressure/piston speed for a pure explosive, the PBX interface is essentially a piston driving the explosive. Thus

$$P_I = P_X^{\text{Th}} = \rho_X^0 U_X^{\text{Th}} D_X^{\text{Th}} = \rho_X^0 U_X^{\text{Th}} (a_X + b_X U_X^{\text{Th}}) \quad (\text{A5})$$

$$U_I = U_X^{\text{Th}} \quad (\text{A6})$$

Here  $P_I$  and  $U_I$  are the interface pressure and velocity in a PBX setting.  $U_X^{\text{Th}}$  is the threshold piston speed for a pure explosive to detonate.

Now we need one additional relation from one of the following approximations that originate from continuity across the binder–explosive interface. Please note that these two approximations give very close results that agree with the molecular dynamics simulation results reasonably well, as shown in Figure 5.

**Acoustic Approximation.** Based on the acoustic approximation (refs 11 and 12)

$$\frac{P_B - P_I}{U_B - U_I} = -\rho_B^0 D_B \quad (\text{A7})$$

Substituting  $P_B$ ,  $P_I$ ,  $D_B$ , and  $U_I$  using eqs A3, A5, A1, and A6, eq A7 becomes

$$\frac{\rho_B^0 U_B (a_B + b_B U_B) - \rho_X^0 U_X^{\text{Th}} (a_X + b_X U_X^{\text{Th}})}{U_B - U_X^{\text{Th}}} = -\rho_B^0 (a_B + b_B U_B) \quad (\text{A8})$$

Solving the above quadratic equation for  $U_B$  and two solutions can be obtained. It can be shown that these two solutions have opposite signs therefore the negative solution is discarded. Thus, the threshold piston speed for the energetic composite is (same as eq 3 in the main text)

$$U_B^{\text{Th}} = \frac{-2a_B + b_B U_X^{\text{Th}} + \sqrt{(2a_B + b_B U_X^{\text{Th}})^2 + 8b_B(a_X + b_X U_X^{\text{Th}})\rho_X^0/\rho_B^0 U_X^{\text{Th}}}}{4b_B} \quad (\text{A9})$$

**Mirror-Reflection Hugoniot Approximation.** Based on the mirror-reflection Hugoniot approximation (ref 13), the reshock or the decompressive isentrope for the binder is the mirror reflection (around  $U = U_B$ ) of the primary Hugoniot of the binder (eq A3). Therefore, it has the following functional form in the pressure vs piston speed domain:

$$P = \rho_B^0 (2U_B - U)(a_B + b_B(2U_B - U)) \quad (\text{A10})$$

This reshock/decompressive curve intersects with the Hugoniot of the explosive at  $(U_I, P_I)$ . Therefore,  $(U_I, P_I)$  satisfies eq A10

$$P_I = \rho_B^0 (2U_B - U_I)(a_B + b_B(2U_B - U_I)) \quad (\text{A11})$$

Again substituting  $P_I$  and  $U_I$  using eqs A5 and A6

$$\rho_X^0 U_X^{\text{Th}} (a_X + b_X U_X^{\text{Th}}) = \rho_B^0 (2U_B - U_X^{\text{Th}})(a_B + b_B(2U_B - U_X^{\text{Th}})) \quad (\text{A12})$$

Solving the above equation for  $U_B$  and two solutions can be obtained. One of them is negative for the parameters from molecular dynamics simulations. Thus, the threshold piston speed for the energetic composite is (the same as eq 4 in the main text)

$$U_B^{\text{Th}} = \frac{-a_B + 2b_B U_X^{\text{Th}} + \sqrt{a_B^2 + 4b_B(a_X + b_X U_X^{\text{Th}})\rho_X^0/\rho_B^0 U_X^{\text{Th}}}}{4b_B} \quad (\text{A13})$$

## References and Notes

- (1) Field, J. E. *Acc. Chem. Res.* **1992**, 25, 489.
- (2) van der Steen, A. C.; Verbeek, H. J.; Meulenbrugge, J. J. *9th Symposium (International) on Detonation*; OCNr: Arlington, VA, 1989; p 83.
- (3) Lecume, S.; Chabin, P.; Brunet, P. 2001 Insensitive Munitions and Energetic Materials Symposium, Bordeaux, 2002.
- (4) Lochert, I. J.; Franson, M. D.; Hamshire, B. L. Defence Science and Technology Report DSTO-TR-1447, DSTO Science Systems Laboratory, **2003**.
- (5) van der Heijden, A. E. D. M.; Bouma, R. H. B. *Cryst. Growth Des.* **2004**, 4, 999.
- (6) Doherty, R. M.; Watt, D. S. *Propellants, Explos., Pyrotech.* **2008**, 33, 4.
- (7) Baer, M. R. *Thermochim. Acta* **2002**, 384, 351.
- (8) Baer, M.; Sewell, T. *Molecular Dynamics Simulations of Detonation Phenomena*; ITRI Press: Laurel, MD, 2004; Chapter 5.
- (9) Shi, Y. F.; Brenner, D. W. *J. Chem. Phys.* **2007**, 127, 134503.
- (10) Shi, Y. F.; Brenner, D. W. *J. Phys. Chem. C* **2008**, 112, 6263.
- (11) Duff, R. E.; Houston, E. *J. Chem. Phys.* **1955**, 23, 1268.
- (12) Deal, W. E. *J. Chem. Phys.* **1957**, 27, 796.
- (13) Davison, L.; Graham, R. A. *Phys. Rep.* **1979**, 55, 255.
- (14) Plimpton, S. J. L.A.M.M.P.S. Molecular Dynamics Simulator (<http://lammmps.sandia.gov>).
- (15) Plimpton, S. J. *J. Comput. Phys.* **1995**, 117, 1–19.

JP805690W



# Shock-induced melting of (100)-oriented nitromethane: Structural relaxation

Ali Siavosh-Haghighi, Richard Dawes,<sup>a)</sup> Thomas D. Sewell, and Donald L. Thompson<sup>b)</sup>  
*Department of Chemistry, University of Missouri-Columbia, Columbia, Missouri 65211-7600, USA*

(Received 6 May 2009; accepted 21 July 2009; published online 11 August 2009)

Molecules subjected to shock waves will, in general, undergo significant intramolecular distortion and exhibit large amplitude orientational and translational displacements relative to the unshocked material. The analysis of molecular dynamics simulations of strongly perturbed materials is complicated, particularly when the goal is to express time-dependent molecular-scale properties in terms of structural or geometric descriptors/properties defined for molecules in the equilibrium geometry. We illustrate the use of the Eckart–Sayvetz condition in a molecular dynamics study of the response of crystalline nitromethane subjected to supported shock waves propagating normal to (100). The simulations were performed with the nonreactive but vibrationally accurate force field due to Sorescu *et al.* [J. Phys. Chem. B **104**, 8406 (2000)]. Shocks were initiated with impact velocities of  $U_p=0.5, 1.0, 2.0$ , and  $3.0 \text{ km s}^{-1}$  in crystals at initial temperatures of  $T_0=50$  and  $200 \text{ K}$ . Statistical precision in the analysis was enhanced through the use of a spatiotemporal reference frame centered on the advancing shock front, which was located as a function of time using the gradient of the kinetic energy along the shock direction. The Eckart–Sayvetz condition provides a rigorous approach by which the alignment can be obtained between a coordinate frame for a perturbed molecule and one in a convenient reference frame (e.g., one based on the equilibrium crystal structure) for analyses of the molecules in the material as the system evolves toward equilibrium. Structural and dynamic properties of the material corresponding to orientation in the lattice, translational symmetry, and mass transport (orientational order parameters, two dimensional radial distribution functions, and self-diffusion coefficients, respectively) were computed as functions of time with  $4 \text{ fs}$  resolution. The results provide clear evidence of melting for shocks initiated by impacts of at least  $U_p=2.0 \text{ km s}^{-1}$  and provide insights into the evolution of changes at the molecular-mode level associated with the onset of the melting instability in shocked crystal.

© 2009 American Institute of Physics. [DOI: [10.1063/1.3202441](https://doi.org/10.1063/1.3202441)]

## I. INTRODUCTION

The passage of a shock wave through a material results in rapid increases in temperature and pressure.<sup>1</sup> Thus, in general, material immediately behind a shock front is in a highly nonequilibrium thermodynamic state—characterized by large spatial gradients of local physical properties as well as non-thermal modal distributions of internal energy—that, if it exceeds the mechanical or chemical stability limits of the material, may relax irreversibly via kinetically limited pathways such as phase transitions<sup>2,3</sup> or chemical transformations.<sup>4–6</sup> Although recent experimental advances<sup>7–9</sup> have provided valuable information concerning energy transfer rates and pathways, phase transitions, and *in situ* chemistry on small time and space scales, it is still extremely difficult if not impossible to obtain from experiment complete information concerning the detailed molecular dynamics (MD) of mechanical instabilities or chemistry in shocked materials. However, MD simulations can be used to study such phenomena and are ideally suited for doing so due to the short times and spatially localized nature of many of the processes

of interest.<sup>10</sup> The principal concerns in any MD simulation are the accuracy of the force field and, of course, the validity of the classical approximation. Of particular concern in simulations of shocked materials is the need to simulate pieces of material sufficiently large and for times sufficiently long to capture the dominant physical relaxation or chemical transformation processes that occur for the dynamic load regime of interest. For short time-scale (subnanosecond) simulations using an analytic force field, fully atomic simulations can be performed for systems containing tens of millions of atoms for organic materials<sup>11</sup> and hundreds of billions of atoms in the case of metals.<sup>12</sup> Although theoretical models for the basic mechanisms of energy redistribution in shocked materials exist,<sup>13–16</sup> a clear picture of the detailed dynamics on short time scales is lacking.

From the time dependence of the phase-space coordinates obtained from a MD simulation it is easy to extract the total energy deposited in a molecular material due to shock loading, but information about the time dependence of the partitioning of energy among the molecular modes is essential for a complete understanding of what physical or chemical changes may occur and on what time scales. Thus, it is of interest to identify and characterize the fundamental processes that underlie these changes in microscopic state in

<sup>a)</sup>Present address: Combustion Research Facility, Sandia National Laboratories, P.O. Box 969, Livermore, CA 94551.

<sup>b)</sup>Electronic mail: [thompsondon@missouri.edu](mailto:thompsondon@missouri.edu).



material subjected to a particular set of shock parameters starting from a given initial thermodynamic condition.

One requirement for optimal analysis of information obtained from MD simulations of relaxation following an extreme thermal or mechanical perturbation of a molecularly complex material is to define a suitable frame of reference. In the case of shock wave simulations it is also useful to know precisely where the shock front is at a given instant in time, since passage of the shock provides a well-defined time marker in the material relative to which subsequent analyses can be performed. Given a supported, nondispersive, planar shock wave propagating through a sample, as the shock wave moves through a given volume element it produces a near-instantaneous change in the total content and distribution of energy in that volume element. The more accurately the instant of excitation is known, the greater the precision with which data analysis can be performed. Moreover, if the shock advances with constant velocity, all such instants of shock passage across some set of symmetry-equivalent planes in the material normal to the direction of shock propagation define equivalent time origins suitable for averaging, thereby increasing drastically the precision with which structural or dynamical processes can be determined.

Condensed-phase nitromethane has been the subject of numerous experimental<sup>17–25</sup> and theoretical<sup>26–46</sup> studies. The neat liquid is known to detonate via a homogeneous initiation mechanism in response to a shock with sufficient energy.<sup>25</sup> For weak to moderately strong shocks, there is a significant induction time between shock wave passage and the transition to detonation.<sup>25</sup> Nitromethane is a liquid at room temperature and atmospheric pressure, which may account for the fact that no experimental measurements of the shock Hugoniot for the solid have, to our knowledge, been reported. Here, we report the results of a study using MD simulations with a vibrationally accurate but nonreactive force field<sup>34,35</sup> to investigate the molecular-scale mechanism for shock-induced melting of nitromethane. In particular, we track the time-dependent orientational and spatial orders of the molecules as well as molecular mobility prior to and after shock passage and thereby gain insight into the mechanism and characteristics of the shock-induced melting transition.

The rest of the paper is arranged as follows. In Sec. II details of the simulations will be described. This includes a description of the force field as well as the computational method used for introducing and analyzing shocks. Section III contains results obtained for two initial temperatures and four different impact velocities that span the Hugoniot elastic limit (HEL) for the (100) crystal orientation. Section IV contains a summary and the conclusions.

## II. METHODS

### A. Force field

All of the simulations were performed using the DL\_POLY code, version 3.06.<sup>47</sup> The vibrationally accurate but nonreactive flexible-molecule force field due to Sorescu *et al.*<sup>34,35</sup> was used without modification. The Sorescu–Rice–Thompson (SRT) force field has been tested extensively against equilibrium data and produces good agreement with

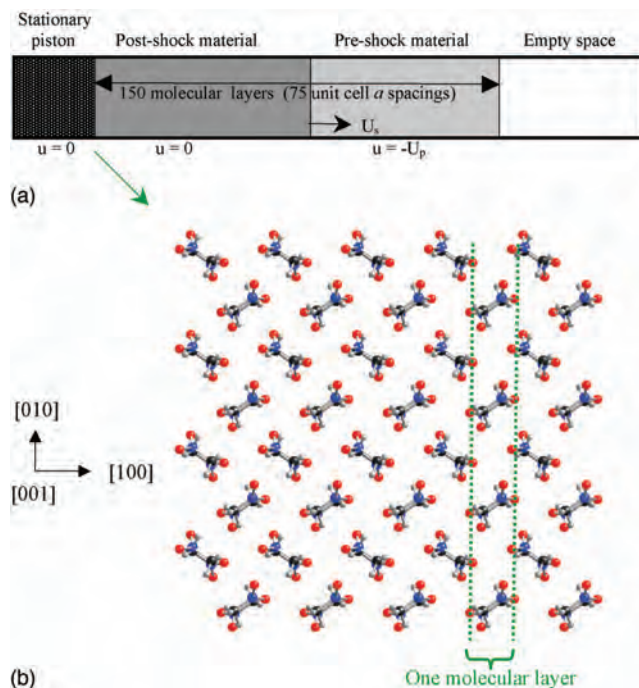


FIG. 1. (a) Illustration of the approach used to generate shock waves. A slab of thermalized flexible molecules 150 layers (75 unit cells) thick impacts from the right onto an infinitely massive slab of rigid molecules ten molecular layers (five unit cells) thick. This leads to a shock wave propagating from left to right through the flexible slab. (b) Zoom-in on the nitromethane crystal structure.

bulk properties such as melting point, thermal expansion, and pressure dependent lattice parameters.<sup>34–39</sup> As shown in Ref. 34, computed normal-mode frequencies and eigenvectors for the SRT force field are in quite good agreement with B3LYP/6-31G\* gas-phase predictions which are, in turn, in reasonable agreement with experimental data.

### B. Simulations

Nitromethane crystallizes in the orthorhombic space group  $P2_12_12_1$  in a unit cell containing four molecules; the asymmetric unit is a single nitromethane molecule.<sup>48</sup> The measured lattice parameters at 298 K are  $a=5.270$  Å,  $b=6.375$  Å, and  $c=8.832$  Å.<sup>49</sup> Thus, a nearly cubic block of material can be obtained by constructing a supercell with lattice repeats of 5, 4, and 3 along the  $a$ ,  $b$ , and  $c$  directions, respectively. However, explicit simulation of a shock wave in the microcanonical ensemble requires the use of a supercell that is long parallel to the direction of shock loading. For the current study of shocks directed along [100], lattice repeat factors of  $80a$ ,  $4b$ , and  $3c$  were used in conjunction with three-dimensional (3D) periodic boundary conditions, leading to primary simulation blocks containing 3840 molecules. As shown in Fig. 1, this results in 160 layers of molecules along the [100] direction (which corresponds to the  $x$ -axis in our chosen laboratory frame); each layer contains 24 molecules, which are arranged as an assembly of 12 head-to-tail molecular dimer pairs.

The simulations were performed in two stages: Equilibration and shock simulation. Prior to equilibration a large gap was introduced at one end of the system, such that the

TABLE I. Stress tensor (top entry) and rms fluctuation (bottom entry) of stress tensor during the final 30 ps *NVT* equilibration using the Nose–Hoover thermostat. Units are kbar.

$T$ (K)	$\sigma_{11}$	$\sigma_{22}$	$\sigma_{33}$	$\sigma_{23}$	$\sigma_{13}$	$\sigma_{12}$
50	$-1.441 \times 10^{-01}$	$4.686 \times 10^{-01}$	$4.376 \times 10^{-01}$	$-1.831 \times 10^{-03}$	$-1.244 \times 10^{-03}$	$-3.163 \times 10^{-04}$
	$1.131 \times 10^{+00}$	$5.439 \times 10^{-01}$	$3.516 \times 10^{-01}$	$3.831 \times 10^{-02}$	$5.317 \times 10^{-02}$	$3.915 \times 10^{-02}$
200	$-5.996 \times 10^{-02}$	$1.119 \times 10^{+00}$	$1.407 \times 10^{+00}$	$-1.296 \times 10^{-04}$	$2.026 \times 10^{-03}$	$3.499 \times 10^{-03}$
	$2.998 \times 10^{-01}$	$1.920 \times 10^{-01}$	$2.732 \times 10^{-01}$	$1.029 \times 10^{-01}$	$1.061 \times 10^{-01}$	$7.118 \times 10^{-02}$

total length of the primary simulation cell along the [100] direction was 1000 Å; this vacant space was included to minimize interactions between the two free surfaces in the shock simulation setup. This was followed by isochoric-isothermal (*NVT*) equilibration at either  $T_0=50$  or 200 K for 50 000 time steps. The lattice parameters measured at 298 K were used to define cell dimensions for the transverse directions. During the first 10 000 steps of equilibration the velocities were rescaled every ten time steps, after which the Nosé–Hoover thermostat was used with a relaxation constant of 1.00 ps.<sup>50</sup> The resulting average stress tensors are given in Table I. All diagonal components of stress are less than 1.5 kbars while the shear components are essentially zero.

Simulations of shock loading were performed in the isochoric-isoergic (*NVE*) ensemble in order to accurately compute the microcanonical dynamics. Starting from the final phase-space point of the *NVT* equilibrations, shocks were initiated as follows. First, the velocities of all atoms in the first ten molecular layers (a  $5 \times 4 \times 3$  slab) at the left-hand end of the simulation cell were set to zero and were constrained to zero for the remainder of the simulation. At the same time,  $-U_p$  was added instantaneously to the  $x$ -component of velocity for all remaining atoms in the system. The result of this procedure is an initial condition from which a block of thermalized flexible molecules will impact from the right onto a rigid, infinitely massive piston comprised of molecules that are structurally commensurate with the flexible slab. Integrating the microcanonical equations of motion (i.e., Newton's equations with no extra terms), a shock wave propagates along the [100] crystal direction (i.e., from left to right as depicted in Fig. 1). The shock wave will propagate with constant velocity until it reaches the right-hand end of the simulation cell, at which time trajectory integration is discontinued (total *NVE* simulation times of  $\sim 4$ – $7$  ps depending on  $U_p$ ). Values of the impact velocity  $U_p=0.5$ , 1.0, 2.0, and 3.0 km s<sup>-1</sup> were considered for initial temperatures of  $T_0=50$  and 200 K. These initial temperatures are well below the experimental normal melting point of 244.73 K (Ref. 51) and predictions based on various MD simulations<sup>35,37–39</sup> using the SRT force field, which fall in the range of 238–266 K.

The standard Ewald summation technique was used for the Coulomb interactions.<sup>50</sup> A cutoff distance of 11.0 Å was used for repulsion and dispersion and for the real-space portion of the Ewald sum. The equations of motion were integrated using the velocity-Verlet algorithm.<sup>50</sup> A fixed time step of 0.75 fs was used during the *NVT* equilibration; accurate resolution of the H-atom motion during the *NVE* simulations required the use of a 0.1 fs time step.

### C. Moving reference frame

Prior to initiation of the shock, the molecules were indexed according to layer in the crystal. Atomic positions, velocities, and forces were recorded at 4 fs intervals for all of the molecules in the system. As described below, some shock strengths led to liquefaction and significant mass transport. The index assigned to each molecule prior to initiation of the shock was retained at all later times so that even if a particular molecule diffused through neighboring layer postshock, it was analyzed as a member of the set of molecules that formed a given molecular layer in the unshocked crystal. This was done so that detailed properties for each molecule were always recorded relative to the shock event for that molecule.

The shock front position at a given time was determined based on the gradient of the kinetic energy, with layer-by-layer resolution along the direction of shock propagation. This is a common approach that has also been extended to nonplanar shocks.<sup>52</sup> As shown in Fig. 2(a) the gradient of the kinetic energy forms a sharp peak that provides resolution of the shock front assignment with a full width at half maximum (FWHM) of approximately four molecular layers or two  $a$ -spacings (i.e., approximately 10.5 Å in the unshocked crystal). The layer having maximum gradient in kinetic energy is plotted as a function of time in Fig. 2(b). Clearly this procedure determines with high accuracy and precision the motion of the shock front as it progresses at constant velocity through the crystal; and thus, with knowledge of the lattice parameters at a given initial temperature, provides accurate values for the shock velocity corresponding to each combination of impact velocity and initial temperature.

The efficiency of the data analysis can be enhanced significantly by considering a moving reference frame centered on the shock front.<sup>53,54</sup> Specifically, as the shock passes through the 150 layers of the flexible slab, dynamical quantities at some given location in the material can be analyzed using a time origin defined as the moment of shock passage across that point. Further, since the shock wave does not spread significantly over time, all points in the material are equivalent in this transformed reference frame and therefore averaging can be performed over all of them to improve the statistical precision of the results. The shocks spent on average between 31.8 fs ( $U_p=3.0$  km s<sup>-1</sup>,  $T_0=50$  K) and 59.3 fs ( $U_p=0.5$  km s<sup>-1</sup>,  $T_0=200$  K) in each layer. While it is possible to shift the data recorded for each layer by the nearest integer step of 4 fs, and thus maintain 4 fs resolution in the averaged data (this will be done in a study of modal excitations, to be published separately), in this work the analysis

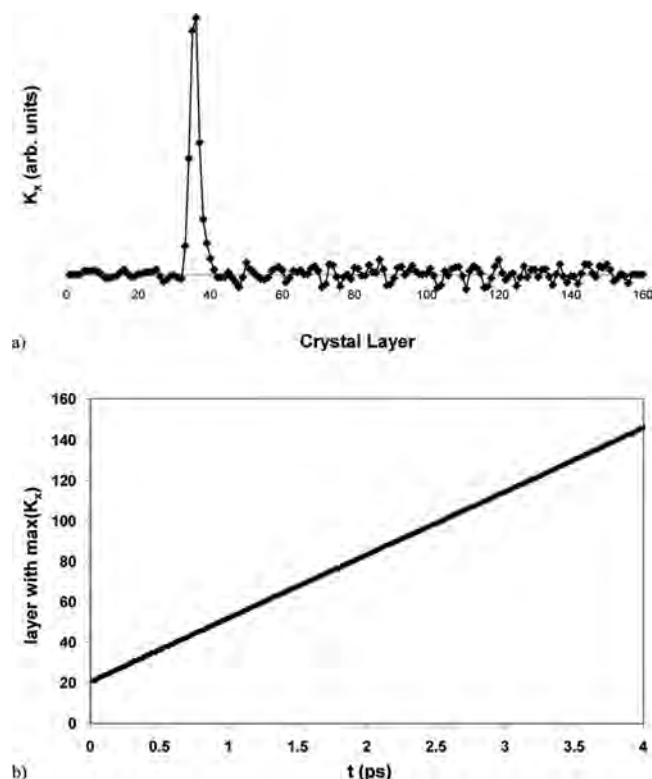


FIG. 2. (a) Component of the gradient of kinetic energy  $K_x$  parallel to  $[100]$  plotted as a function of the molecular layer at an arbitrarily chosen time. The maximum in this plot is sharply peaked over an area comprising approximately two unit cells (FWHM) and serves to locate with high precision the position of the shock front as a function of time. (b) Position of the shock front as a function of time based on the analysis depicted in panel (a). As expected for the supported shocks simulated in this work, the shock front moves through the material with a constant velocity. Results shown correspond to an initial temperature of  $T_0=50$  K and impact velocity of  $U_p=3.0$  km s $^{-1}$ .

was done by layers since the dynamical quantities studied varied relatively slowly with respect to the data collection rate. This means that data from each 4 fs snapshot contribute to average quantities for the layer relative to the shock front; given the regularity of the data, the assignment of snapshots to particular layers can be accomplished using an easily automated procedure. For example, for  $U_p=2.0$  km s $^{-1}$  and  $T_0=200$  K, the shock spends an average of 40.06 fs in each layer. For these conditions, when the shock is first assigned to a particular layer in the crystal, data collected for that layer will continue to contribute to averaged properties in the shock front layer for the next ten 4 fs snapshots. Thus the total data recorded at the shock front layer represent averages over 150 layers  $\times$  24 molecules/layer  $\times$  10 snapshots = 36 000 molecules. Once the shock front has moved on to the next layer, for the next ten 4 fs snapshots that same (previously considered) layer will now contribute to properties one layer behind the shock.

### III. RESULTS

#### A. General features of the shocked states

The calculated shock velocities, shock pressures, temperatures, and uniaxial compression ratios are summarized in Table II for each combination of initial temperature and im-

TABLE II. Shock pressure, final bulk temperature, and uniaxial compression ratio for the two initial temperatures and four impact velocities considered.

$T_0$ (K)	$U_p$ (km s $^{-1}$ )	$U_s$ (km s $^{-1}$ )	$P=\rho_0 U_s U_p$ (GPa) <sup>a</sup>	$T_f$ (K) <sup>b</sup>	$a/a_0$ <sup>c</sup>
50	0.5	4.84	3.1	66	0.879
	1.0	5.79	7.4	111	0.813
	2.0	6.84	17.5	310	0.712
	3.0	8.17	31.4	814	0.639
200	0.5	4.46	2.9	238	0.891
	1.0	5.47	7.0	302	0.822
	2.0	6.61	16.9	524	0.703
	3.0	7.98	30.6	1036	0.630

<sup>a</sup>The initial density  $\rho_0$  was taken to be 1280 kg m $^{-3}$  for both initial temperatures.

<sup>b</sup>Determined for volume elements located 2 ps behind the shock front.

<sup>c</sup>Determined from slab dimensions between crystal layers 20 and 140 immediately postshock.

pect velocity considered. The shock pressures calculated using the Rankine–Hugoniot relation  $P=\rho_0 U_s U_p$ ,<sup>1</sup> where  $\rho_0$  is the initial density, range from 2.9 to 31.4 GPa. Corresponding temperature rises ( $T_f-T_0$ ), determined by time averaging over 100 fs intervals starting at times  $t=2$  ps after shock passage through a given layer, range from 16 to 836 K. In general, lower initial temperature yields higher shock pressure and smaller temperature rise for a given impact velocity  $U_p$ . The shock speeds  $U_s$  in Table II are considerably larger than those recorded for liquid nitromethane in the LASL Shock Hugoniot Data Volume (Fig. 3),<sup>55</sup> we estimate a ratio between the two of approximately 1.7 for  $U_p=1.0$  km s $^{-1}$ . The first, and presumably most important, reason for this difference is that here we are studying shock propagation through an ordered crystal lattice rather than a liquid; concomitant with this are the facts that the initial density is higher ( $\rho_0 \sim 1280$  kg m $^{-3}$  here versus  $\rho_0 \sim 1125$  kg m $^{-3}$  in the experiments on the liquid) and the initial temperature considerably lower ( $T_0 \leq 200$  K here versus  $T_0 \sim 295$  K in the experiments), both of which will also yield higher shock velocities all other factors being equal.

#### B. Orientational order based on Eckart frame alignment

A molecular orientational order parameter was computed as a function of time relative to shock front passage for  $T_0$

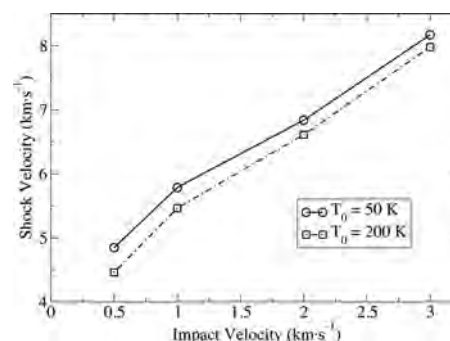


FIG. 3. Shock Hugoniot loci in the  $U_s$ - $U_p$  plane for initial temperatures  $T_0=50$  K and 200 K. The lines connect the points and are simply guides for the eye.



=50 and 200 K and the four impact velocities  $U_p=0.5, 1.0, 2.0$ , and  $3.0 \text{ km s}^{-1}$ . The orientational order parameter for a given molecule is defined using the rotation matrix required to align the Eckart frame<sup>56,57</sup> of that molecule with the Eckart frame of a reference molecule that corresponds to the orientation and intramolecular geometry of the molecules in a perfect crystal as predicted by the SRT force field at  $T=0 \text{ K}$  and  $P=1 \text{ atm}$ . The Eckart frame is widely used in studies of the chemical dynamics of small, gas-phase molecules.<sup>58</sup> In general, shock excitation of a molecule introduces significant intramolecular distortion as well as molecular rotations and translations. Thus, the Eckart axis condition [see Eq. (1)] is particularly useful since it defines a rigorous separation of orientation from the internal degrees of freedom,

$$\sum_{i=1}^N m_i \mathbf{r}'_i \times (\mathbf{U} \mathbf{r}_i) = 0, \quad (1)$$

where  $m$  is atomic mass,  $\mathbf{r}$  and  $\mathbf{r}'$  are, respectively, reference and instantaneous structures with coincident centers of mass but different intramolecular geometries and orientations in the laboratory frame, and  $\mathbf{U} \in SO(3)$  is the particular rotation matrix required to satisfy the identity. It can be shown<sup>59</sup> that this is equivalent to minimizing the mass-weighted mean squared displacement,

$$\min_{\mathbf{U} \in SO(3)} \sum_{i=1}^N m_i |\mathbf{r}'_i - (\mathbf{U} \mathbf{r}_i)|^2. \quad (2)$$

We used a quaternion-based algorithm to solve for the rotation matrix  $\mathbf{U}$ .<sup>60</sup> Application of the  $3 \times 3$  rotation matrix  $\mathbf{U}$  to the coordinates of a particular analysis molecule  $\mathbf{r}'$  aligns its Eckart frame with that of the reference molecule  $\mathbf{r}$ . We define an orientational order parameter  $S$  as one-third of the trace of  $\mathbf{U}$ , averaged over the  $M$  molecules in the sample,

$$\langle S \rangle = \frac{1}{M} \sum_{j=1}^M \frac{1}{3} \sum_{i=1}^3 U_{ii}(j), \quad (3)$$

where  $U_{ii}(j)$  are the diagonal elements of  $\mathbf{U}$  for the  $j$ th molecule. If a molecule and its reference structure are in perfect alignment, then  $\mathbf{U}$  is simply the identity matrix  $\mathbf{I}$  and thus  $S_j$  equals unity. Here the laboratory frame reference structure for a given molecule was taken to be its symmetry equivalent in the ( $T=0 \text{ K}$ ,  $P=1 \text{ atm}$ ) SRT crystal structure. Using the moving reference frame procedure described above, the value of the orientational order parameter (as well as other structural metrics discussed below) at each time is actually an average over thousands of molecules.

The results of the orientational order parameter  $S$  analysis are shown in Fig. 4. At finite temperature even in a well-ordered crystal the value of  $S$  is slightly less than 1.0 due to thermal fluctuations. The preshock values of  $S$  are 0.98 and 0.89 for  $T_0=50$  and 200 K, respectively. The postshock behavior of  $S$  depends on whether, or to what extent, melting occurs. In the absence of melting (as seen for impact velocities of  $U_p=0.5$  and  $1.0 \text{ km s}^{-1}$ ; top four traces in Fig. 4 for  $t > 1000 \text{ fs}$ ) there are two competing effects. Larger initial temperature results in larger thermal fluctuations (decreasing

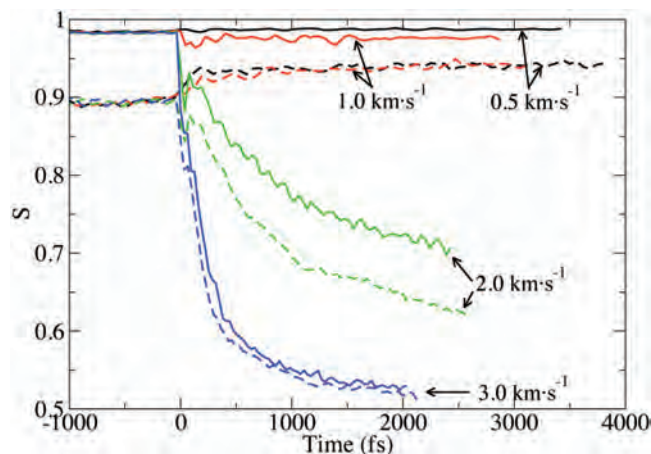


FIG. 4. Orientational order parameter [see Eq. (3)] vs time for various impact velocities and initial temperatures. Solid lines:  $T_0=50 \text{ K}$ ; dashed lines:  $T_0=200 \text{ K}$ . Black:  $U_p=0.5 \text{ km s}^{-1}$ ; red:  $U_p=1.0 \text{ km s}^{-1}$ ; green:  $U_p=2.0 \text{ km s}^{-1}$ ; blue:  $U_p=3.0 \text{ km s}^{-1}$ . Negative values of time correspond to unshocked material.

$S$ ), while increased pressure in the shocked material dampens thermal fluctuations (increasing  $S$ ). The effect of a shock due to  $U_p=0.5 \text{ km s}^{-1}$  impact is an increased value of  $S$  for both initial temperatures, signifying increased geometric order in the crystal; the effect is much more pronounced for the  $T_0=200 \text{ K}$  crystal. The  $U_p=1.0 \text{ km s}^{-1}$  impact produces mixed results due to the larger amount of heat generated by the shock. For  $T_0=50 \text{ K}$ , the increased temperature due to the shock dominates over the increased pressure, slightly lowering the value of  $S$ ; by contrast, the initially lower value of  $S$  for an initial temperature of  $T_0=200 \text{ K}$  is increased significantly postshock due to the increased pressure.

The two higher velocity impacts ( $U_p=2.0$  and  $3.0 \text{ km s}^{-1}$ ) resulted in melting for crystals at both initial temperatures (the four lower traces in Fig. 4). When melting occurs the limiting value of  $S$  and the rate at which it is achieved depend on the temperature and pressure of the system. In general, the equilibrium value of  $S$  in an associated liquid will depend also on molecular shape and intermolecular forces. Dipole-dipole interactions are important in nitromethane and would be expected to lead to significant deviations from a purely random orientational distribution. The time dependence of the decay of  $S$  in the case of a melting instability was well fitted by an exponential function. Shocks due to  $U_p=2.0 \text{ km s}^{-1}$  impacts produced decay constants of 836 and 827 fs and final values of  $S$  of 0.69 and 0.62 at the ends of the respective simulations, for initial temperatures of  $T_0=50$  and 200 K, respectively. Thus, in light of the considerations mentioned above it is not possible, based on the results of the  $S$ -analysis alone, to discriminate between associated liquid behavior versus vitrification for the  $U_p=2.0 \text{ km s}^{-1}$  impacts. The stronger shocks resulting from  $U_p=3.0 \text{ km s}^{-1}$  impacts caused a more rapid loss of orientational order, producing decay constants of 286 and 277 fs, and limiting values of  $S$  of  $\sim 0.5$ , for the two initial temperatures. In the next sections these time constants for loss of orientational order upon melting will be compared with changes in two-dimensional center-of-mass mean square displacement (2D MSD) and 2D radial distribution functions

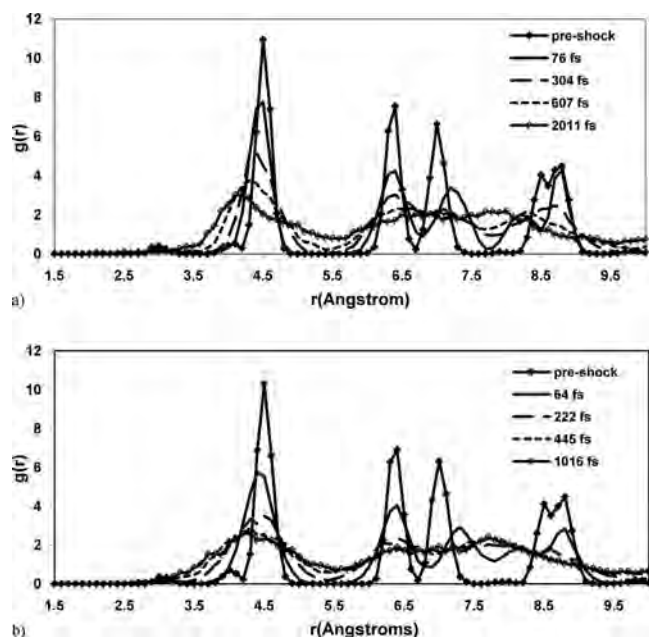


FIG. 5. 2D center-of-mass RDFs for an initial temperature of  $T_0=50$  K [Eq. (4)]. (a) Impact velocity  $U_p=2.0$  km s $^{-1}$ ; (b) impact velocity  $U_p=3.0$  km s $^{-1}$ .

(RDFs). These additional complementary analyses will help distinguish between melting and vitrification for the  $U_p=2.0$  km s $^{-1}$  impacts.

### C. 2D RDF

A 2D RDF for molecular centers of mass in each layer of the crystal was evaluated as a function of time (pre- and postshock). The RDF defined by Eq. (4) is evaluated in the same fashion as a standard 3D RDF except that the distances  $R_{ij}$  are evaluated only in the directions transverse to the shock propagation direction (i.e., using only the  $y$  and  $z$  Cartesian position coordinates for the shock orientation studied here),

$$g(R) = \frac{1}{nN} \left\langle \sum_i \sum_j \delta[R - R_{ij}] \right\rangle, \quad (4)$$

where  $N$  is the total number of molecules,  $n$  is the number density, and  $R_{ij}$  is the distance between centers of mass of molecules  $i$  and  $j$  in a given layer normal to  $[100]$ .

As shown by the results discussed above in connection with Fig. 4, shocks due to impact velocities of  $U_p=0.5$  and  $1.0$  km s $^{-1}$  do not cause melting. The RDFs computed (not shown) for those cases for both initial temperatures support that conclusion: Both pre- and postshock they consist of a collection of sharp peaks characteristic of the crystal structure—the same as for the preshock RDFs for the stronger shock cases discussed below and shown in Fig. 5. In Fig. 5, RDFs for  $U_p=2.0$  and  $3.0$  km s $^{-1}$  impacts are shown pre-shock and for a sequence of postshock times. The  $T_0=50$  K initial temperature results are chosen for illustration, since this corresponds to an initially slightly sharper distribution due to reduced thermal motion compared to  $T_0=200$  K; no significant differences in the time evolution of the RDFs were observed with respect to the two initial tem-

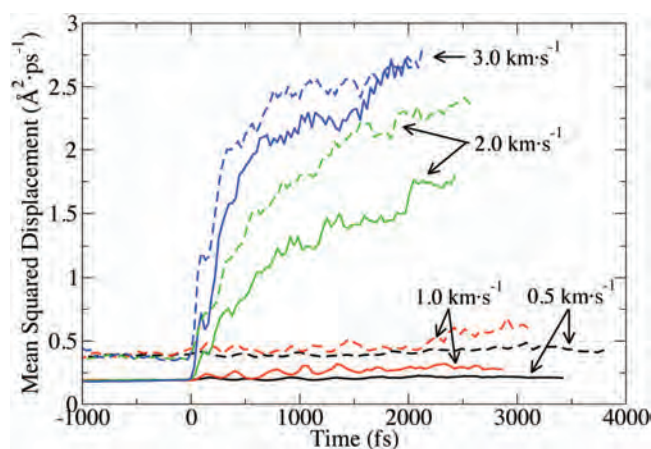


FIG. 6. 2D MSD [see Eq. (5)] of molecular centers of mass vs time for various impact velocities and initial temperatures. Solid lines:  $T_0=50$  K; dashed lines:  $T_0=200$  K. Black:  $U_p=0.5$  km s $^{-1}$ ; red:  $U_p=1.0$  km s $^{-1}$ ; green:  $U_p=2.0$  km s $^{-1}$ ; blue:  $U_p=3.0$  km s $^{-1}$ . Negative values of time correspond to unshocked material.

peratures. As shown in Fig. 5, there is clear evidence of shock-induced translational disordering for both the  $U_p=2.0$  and  $3.0$  km s $^{-1}$  impact velocities. For the  $U_p=2.0$  km s $^{-1}$  impact [see Fig. 5(a)] after 76 fs, at which time the shock front has advanced through two layers of the crystal, there is already a noticeable broadening and reduction of peak intensities. The RDFs for subsequent times (shown at 304, 607, and 2011 fs) evolve such that after 2 ps (when the shock front has advanced through 53 layers of the crystal) the RDF has converged and is characteristic of a liquid. The melting behavior of the system shocked by a  $3.0$  km s $^{-1}$  impact velocity is much faster. The RDF has nearly converged to a final liquidlike state after only 445 fs, at which time the shock front has advanced through only 14 layers.

### D. 2D MSD

2D MSDs of the molecular centers of mass  $\{\mathbf{R}\}$  were computed layer-by-layer following shock front passage by monitoring center-of-mass motion transverse to the direction of shock propagation. The shock direction was excluded in order to avoid complications from the large inertial motion and abrupt stagnation associated with shock compression. The moving reference frame described in Sec. II C was used to average over a large number of molecules by setting  $t=0$  for each layer as the shock front passed through it. Thus, in Eq. (5) we define MSD in the standard way except that  $\mathbf{R}_i$  is the 3D displacement vector projected into the  $(100)$  plane, and the average is accumulated over molecules in many distinct layers with time origins defined in terms of the moving reference frame,

$$\text{MSD}(t) = \langle |\mathbf{R}(t) - \mathbf{R}(0)|^2 \rangle. \quad (5)$$

The relationship of the 2D MSD to the self-diffusion coefficient  $D$  is

$$\text{MSD}(t) = 4Dt. \quad (6)$$

The results of the 2D MSD analysis are shown in Fig. 6. Prior to shock passage the value of MSD for crystals at each temperature is small and essentially constant with time as



expected for a solid. Following the passage of the two weaker shocks ( $U_p=0.5$  and  $1.0 \text{ km s}^{-1}$ ) the MSD rises somewhat and settles at a new steady-fluctuating value consistent with the shock-heated material. For these cases the material does not melt. The recursions observed in the shocked material may be due to interactions among transverse waves in the shocked material since, undoubtedly, the uniaxial compression resulting from the shock sets up shear stresses in the material which will relax eventually to values that render the state in the compressed material as close to hydrostatic as can be achieved given the highly anisotropic nature of the shock compression.

The two stronger shocks,  $U_p=2.0$  and  $3.0 \text{ km s}^{-1}$  (four upper traces in Fig. 6), indicate significant translational mobility. The MSD plots for  $U_p=3.0 \text{ km s}^{-1}$  (two upper traces in Fig. 6) exhibit two distinct stages postshock, namely, a steep rise in MSD immediately following the shock, followed by a less steep and roughly linear rise in MSD for longer times. We interpret the first stage as arising from system readjustment during the rapid shock-induced compression, and the second as indicative of self-diffusion characteristic of a liquid phase. For the  $U_p=3.0 \text{ km s}^{-1}$  impact velocity, the data reach the linear-growth stage at  $\sim 450 \text{ fs}$  for  $T_0=50 \text{ K}$  and  $\sim 300 \text{ fs}$  for  $T_0=200 \text{ K}$ . Fitting Eq. (6) to the corresponding regions leads to predictions  $D=0.12 \text{ \AA}^2 \text{ ps}^{-1}$  for  $T_0=50 \text{ K}$  and  $D=0.09 \text{ \AA}^2 \text{ ps}^{-1}$  for  $T_0=200 \text{ K}$ .

For the  $U_p=2.0 \text{ km s}^{-1}$  impact velocity the transition between initial and final regions is less well defined; however, the simulation data for both initial temperatures are nominally linear after  $t \sim 550 \text{ fs}$  (third and fourth traces from the top in Fig. 6), and therefore indicative of a liquid rather than a vitrified state. The resulting self-diffusion coefficients obtained from fits to Eq. (6) are  $D=0.09 \text{ \AA}^2 \text{ ps}^{-1}$  for  $T_0=50 \text{ K}$  and  $D=0.11 \text{ \AA}^2 \text{ ps}^{-1}$  for  $T_0=200 \text{ K}$ . Thus, it appears that although the stronger shocks caused by  $U_p=3.0 \text{ km s}^{-1}$  impacts will deposit considerably more kinetic energy into the crystal and will therefore result in increased self-diffusion (all other factors being equal), by coincidence the increased compression associated with the  $U_p=3.0 \text{ km s}^{-1}$  shock, which will suppress self-diffusion, approximately balances the thermal effect such that the self-diffusion coefficients for the two cases are similar.

Experimental data have been reported for the equilibrium melting curve<sup>61</sup> of nitromethane as a function of pressure and for the atmospheric pressure self-diffusion coefficient as a function of temperature.<sup>24</sup> The experimental equilibrium melting curve data of Piermarini *et al.* were fitted as a function of pressure (gigapascals) with the result  $T_m(P)=100 \ln P+389.2$ . Due to rapid decomposition at high temperatures and pressures, the data only extend to  $P=1.54 \text{ GPa}$  and  $T=433 \text{ K}$ . If this relationship is extrapolated to the pressures we investigated (Table II) for the  $200 \text{ K}$  initial temperature, then melting points of  $T_m=584$  and  $671 \text{ K}$  are predicted for the calculated pressures of  $7.0$  and  $16.9 \text{ GPa}$  ( $U_p=1.0$  and  $2.0 \text{ km s}^{-1}$ , respectively). Our simulation results indicate that melting occurs for  $U_p=2.0 \text{ km s}^{-1}$ , but not for  $U_p=1.0 \text{ km s}^{-1}$ . The corresponding temperatures, calculated  $2 \text{ ps}$  after shock passage, are  $524$  and  $302 \text{ K}$ . The

calculated value of  $524 \text{ K}$  for  $U_p=2.0 \text{ km s}^{-1}$  is below the extrapolated melting point of  $671 \text{ K}$ . However, even if the experimental relationship holds for pressures as high as  $17 \text{ GPa}$ , note that the calculated temperature of  $524 \text{ K}$  is an average over all degrees of freedom. In a subsequent publication<sup>62</sup> we will show that in these nonequilibrium simulations, the energy is very unevenly partitioned at short times, with the phonon modes exhibiting substantial superheating. Price *et al.*<sup>24</sup> reported values of the 3D self-diffusion coefficient between  $0.128$  and  $0.335 \text{ \AA}^2 \text{ ps}^{-1}$  for temperatures between  $251.1$  and  $314.1 \text{ K}$ . Also, Thompson and co-workers<sup>36,37</sup> have reported equilibrium atmospheric-pressure self-diffusion coefficient values ranging from  $0.065$  to  $0.384 \text{ \AA}^2 \text{ ps}^{-1}$  for temperatures between  $255$  and  $374 \text{ K}$  computed using MD simulations with the SRT force field. Our range of computed values of the 2D self-diffusion coefficient,  $0.09 \text{ \AA}^2 \text{ ps}^{-1} \leq D \leq 0.12 \text{ \AA}^2 \text{ ps}^{-1}$  is qualitatively consistent with both the experimental and published theoretical values.

#### IV. SUMMARY AND CONCLUSIONS

Characterizing dynamic molecular-scale properties of material under extreme states in terms of structural or geometric descriptors defined for some static, reference molecule is complicated due to the large intramolecular vibrational distortions and rotational and translational displacements that can occur. The Eckart–Sayvetz condition provides a rigorous approach by which such arbitrarily distorted and displaced molecules can be mapped onto the geometry of a reference molecule. We have applied the Eckart–Sayvetz alignment condition to the analysis of MD simulation results for shock loaded nitromethane crystal. By tracking the gradient of the kinetic energy along the shock direction as a function of time, the position of the shock front could be determined with high accuracy. Further, by using a spatiotemporal reference frame centered on the shock front for the data analysis, it was possible to significantly increase the statistical precision of the results.

Starting from two different initial temperatures below the normal melting point, we simulated supported shock waves propagating in crystalline nitromethane along the  $[100]$  direction for four shock strengths that span the HEL for that crystal orientation. The focus of the study was on the time evolution of two structural order parameters plus one transport coefficient that characterize the onset of melting, which is the mechanism by which the system and orientation studied relaxes above the HEL. Specifically, we studied an orientational order parameter defined as one-third of the trace of the rotation matrix that satisfies the Eckart–Sayvetz condition [see Eqs. (1) and (2)], the 2D RDF calculated for planes perpendicular to  $[100]$ , and the 2D self-diffusion coefficient for individual nitromethane molecules.

Shocks resulting from impact speeds of  $U_p=0.5$  and  $1.0 \text{ km s}^{-1}$  led to elastic deformation only, at least for the  $\sim 4 \text{ ps}$  time scale of the simulations. For shocks initiated in crystal with an initial temperature of  $T_0=200 \text{ K}$ , the result was an increase in structural order in the material. By contrast, at an initial temperature of  $T_0=50 \text{ K}$  for which thermal

fluctuations are already quite small a  $0.5 \text{ km s}^{-1}$  shock led to a barely discernable increase in order, whereas the  $1.0 \text{ km s}^{-1}$  shock led to a small amount of disordering in the material. These results can be understood in terms of the interplay between increased disordering associated with shock heating of the material and damping of fluctuations due to sample compression.

Shocks resulting from flyer impact speeds of  $U_p=2.0$  and  $3.0 \text{ km s}^{-1}$  led to shock-induced melting on a picosecond (or less) time scale. In these cases the effects of initial crystal temperature were marginal, but could be discerned in each of the three measures of structure and transport considered. Nominal time scales for melting are shortest for the orientational order parameter; those based on loss of structure in the 2D RDF and the onset of 2D molecular self-diffusion are slower, with induction times for achieving linear growth of 2D MSD measured relative to shock passage time trailing slightly those for loss of local structural order. This is consistent with a general picture of melting in which loss of orientational order on lattice sites precedes more widespread disruption of spatial structure, with onset of molecular self-diffusion requiring even more time to develop in the material.

While the component of the analysis employed here that required the Eckart–Sayvetz condition was restricted to properties of entire molecules (specifically, molecular orientation), the Eckart–Sayvetz frame can also be exploited to facilitate precise analysis of detailed intramolecular dynamics, for instance, intramolecular vibrational energy redistribution within molecules. In fact, it is in these latter kinds of situations that the Eckart–Sayvetz frame should be particularly useful (and for which it has been most widely applied in the gas-phase chemical physics literature), as reliable predictions of those phenomena require accurate methods for superimposing instantaneous Cartesian descriptions of arbitrarily distorted and displaced molecules onto a laboratory-fixed reference frame that can be used in turn to define a rigorous basis for defining modal energy partitioning. This will be the subject of a forthcoming publication.

The stronger shocks considered here were predicted to result in pressures and temperatures in excess of  $P=30 \text{ GPa}$  and  $T=1000 \text{ K}$ , respectively (see Table II); for such states neglect of chemistry is clearly an approximation, although it is unclear based on experimental data how much chemistry would occur on the short time scale of the simulations. Thus, while the goal of the present study is to characterize within a purely mechanical representation the fundamental events associated with relaxation of the initial shock state in (100)-oriented nitromethane, it would also be of considerable interest to compare the results obtained here to those that would result from corresponding simulations using the REAXFF (Ref. 6) force field. Such a comparison would of course be complicated and indirect since, presumably, the two force field models would not yield identical predictions for even the fundamental equilibrium thermophysical and mechanical properties for mild thermodynamic conditions. Nevertheless, the results of such a comparison would likely be highly illuminating.

## ACKNOWLEDGMENTS

This work was supported by a DOD MURI grant managed by the Army Research Office under Grant No. W911NF-05-1-0265.

- <sup>1</sup>Y. B. Zel'dovich and Y. P. Raizer, *Physics of Shock Waves and High-Temperature Hydrodynamic Phenomena* (Dover, Mineola, NY, 2002).
- <sup>2</sup>K. Kadau, T. C. Germann, P. S. Lomdahl, R. C. Albers, J. S. Wark, A. Higginbotham, and B. L. Holian, *Phys. Rev. Lett.* **98**, 135701 (2007).
- <sup>3</sup>E. M. Bringa, A. Caro, Y. Wang, J. M. Victoria, B. McNaney, A. Remington, R. F. Smith, B. R. Torralva, and H. Van Swyngenhoven, *Science* **309**, 1838 (2005).
- <sup>4</sup>A. J. Heim, N. Gronbech-Jensen, E. M. Kober, and T. C. Germann, *Phys. Rev. E* **78**, 046710 (2008).
- <sup>5</sup>E. J. Reed, M. R. Manaa, L. E. Fried, K. R. Glaesemann, and J. D. Joannopoulos, *Nat. Phys.* **4**, 72 (2008).
- <sup>6</sup>A. Strachan, A. C. T. van Duin, D. Chakraborty, S. Dasgupta, and W. A. Goddard III, *Phys. Rev. Lett.* **91**, 098301 (2003).
- <sup>7</sup>Z. Wang, D. G. Cahill, J. A. Carter, Y. K. Koh, A. Lagutchev, N.-H. Seong, and D. D. Dlott, *Chem. Phys.* **350**, 31 (2008).
- <sup>8</sup>C. A. Bolme, S. D. McGrane, D. S. Moore, and D. J. Funk, *J. Appl. Phys.* **102**, 033513 (2007).
- <sup>9</sup>J. E. Patterson, Z. A. Dreger, M. Miao, and Y. M. Gupta, *J. Phys. Chem. A* **112**, 7374 (2008).
- <sup>10</sup>B. L. Holian, *Shock Waves* **5**, 149 (1995).
- <sup>11</sup>M. J. Cawkwell, T. D. Sewell, L. Zheng, and D. L. Thompson, *Phys. Rev. B* **78**, 014107 (2008).
- <sup>12</sup>T. C. Germann and K. Kadau, *Int. J. Mod. Phys. C* **19**, 1315 (2008).
- <sup>13</sup>A. Tokmakoff, M. D. Fayer, and D. D. Dlott, *J. Phys. Chem.* **97**, 1901 (1993).
- <sup>14</sup>S. Ye and M. Koshi, *J. Phys. Chem. B* **110**, 18515 (2006).
- <sup>15</sup>C. M. Tarver, *J. Phys. Chem. A* **101**, 4845 (1997).
- <sup>16</sup>L. E. Fried and A. J. Ruggiero, *J. Phys. Chem.* **98**, 9786 (1994).
- <sup>17</sup>V. Bouyer, I. Darbord, P. Hervé, G. Baudin, C. Le Gallic, F. Clément, and G. Chavent, *Combust. Flame* **144**, 139 (2006).
- <sup>18</sup>P. C. Lysne and D. R. Hardesty, *J. Chem. Phys.* **59**, 6512 (1973).
- <sup>19</sup>J. M. Winey, G. E. Duvall, M. D. Knudson, and Y. M. Gupta, *J. Chem. Phys.* **113**, 7492 (2000).
- <sup>20</sup>J. C. Deák, L. K. Iwaki, and D. D. Dlott, *J. Phys. Chem. A* **103**, 971 (1999).
- <sup>21</sup>S. Shigeto, Y. Pang, Y. Fang, and D. D. Dlott, *J. Phys. Chem. A* **112**, 232 (2008).
- <sup>22</sup>M. Citroni, F. Datchi, R. Bini, M. Di Vaira, P. Pruzan, B. Canny, and V. Schettino, *J. Phys. Chem. B* **112**, 1095 (2008).
- <sup>23</sup>R. Ouillon, J.-P. Pinan-Lucarré, B. Canny, P. Pruzan, and P. Ranson, *J. Raman. Spectrosc.* **39**, 354 (2008).
- <sup>24</sup>W. S. Price, H. Ide, and Y. Arata, *J. Chem. Phys.* **113**, 3686 (2000).
- <sup>25</sup>S. A. Sheffield, D. M. Dattelbaum, R. Engelke, R. R. Alcon, B. Crouzet, D. L. Robbins, D. B. Stahl, and R. L. Gustavsen, in Proceedings of the 13th International Detonation Symposium, Norfolk, VA, 23–28 July 2006 (unpublished) p. 401.
- <sup>26</sup>D. Margitis, E. Kaxiras, M. Elstner, Th. Fraunheim, and M. R. Manaa, *J. Chem. Phys.* **117**, 788 (2002).
- <sup>27</sup>H. Liu, J. Zhao, D. Wei, and Z. Gong, *J. Chem. Phys.* **124**, 124501 (2006).
- <sup>28</sup>F. J. Zerilli, J. P. Hooper, and M. M. Kulkja, *J. Chem. Phys.* **126**, 114701 (2007).
- <sup>29</sup>M. W. Conroy, I. I. Oleynik, S. V. Zybin, and C. T. White, *J. Phys. Chem. A* **113**, 3610 (2009).
- <sup>30</sup>E. J. Reed, J. D. Joannopoulos, and L. E. Fried, *Phys. Rev. B* **62**, 16500 (2000).
- <sup>31</sup>S. A. Decker, T. K. Woo, D. Wei, and F. Zhang, Proceedings of the 12th International Detonation Symposium, San Diego, CA, 11–16 August 2002 (unpublished) p. 724.
- <sup>32</sup>M. R. Manaa, E. J. Reed, L. E. Fried, G. Galli, and F. Gygi, *J. Chem. Phys.* **120**, 10146 (2004).
- <sup>33</sup>H. E. Alper, F. Abu-Awwad, and P. Politzer, *J. Phys. Chem. B* **103**, 9738 (1999).
- <sup>34</sup>D. C. Sorescu, B. M. Rice, and D. L. Thompson, *J. Phys. Chem. B* **104**, 8406 (2000). There were two typographical errors in that paper (referred to hereafter as SRT). Equation 6 for the harmonic three-center covalent bending angle should not contain the factor of 1/2 that appears there. Also, the energy coefficient  $V_\phi$  for the  $\text{N}_2\text{--O}_4\text{--O}_3\text{--C}_1$  improper dihedral

- angle interaction in Table 1 is exactly twice as large as it should be. Both of these were corrected in Ref. 35; the use of the parameter values in Table 1 of Ref. 35 in Eq. (3) of that paper leads to the normal-mode frequencies and eigenvector projections listed in columns M1 and P1 of Table 2 of the original SRT article. Another feature of the SRT force field for nitromethane that should be appreciated is that it does not possess permutation symmetry with respect to hydrogen atom exchange, with the consequence that it is necessary to number the atoms in accord with the convention shown in Fig. 1 of the SRT paper [and Fig. 1a of Ref. 35].
- <sup>35</sup> P. M. Agrawal, B. M. Rice, and D. L. Thompson, *J. Chem. Phys.* **119**, 9617 (2003).
  - <sup>36</sup> D. C. Sorescu, B. M. Rice, and D. L. Thompson, *J. Phys. Chem. A* **105**, 9336 (2001).
  - <sup>37</sup> A. Siavosh-Haghighi and D. L. Thompson, *J. Chem. Phys.* **125**, 184711 (2006).
  - <sup>38</sup> L. Zheng, S.-N. Luo, and D. L. Thompson, *J. Chem. Phys.* **124**, 154504 (2006).
  - <sup>39</sup> A. Siavosh-Haghighi and D. L. Thompson, *J. Phys. Chem. C* **111**, 7980 (2007).
  - <sup>40</sup> V. N. Kabadi and B. M. Rice, *J. Phys. Chem. A* **108**, 532 (2004).
  - <sup>41</sup> H. Liu, J. Zhao, G. Ji, Z. Gong, and D. Wei, *Physica B* **382**, 334 (2006).
  - <sup>42</sup> N. Desbiens, E. Bourasseau, and J.-B. Maillet, *Mol. Simul.* **33**, 1061 (2007).
  - <sup>43</sup> A. Hervouët, N. Desbiens, E. Bourasseau, and J.-B. Maillet, *J. Phys. Chem. B* **112**, 5070 (2008).
  - <sup>44</sup> N. Desbiens, E. Bourasseau, J.-B. Maillet, and L. Souldard, *J. Hazard. Mater.* **166**, 1120 (2009).
  - <sup>45</sup> T. Megyes, S. Bálint, T. Grósz, T. Radnai, I. Bakó, and L. Almásy, *J. Chem. Phys.* **126**, 164507 (2007).
  - <sup>46</sup> S. Hayaki, H. Sato, and S. Sakaki, *J. Mol. Liq.* **147**, 9 (2009).
  - <sup>47</sup> W. Smith, *Mol. Simul.* **32**, 933 (2006).
  - <sup>48</sup> S. F. Trevino, E. Prince, and C. R. Hubbard, *J. Chem. Phys.* **73**, 3001 (1980).
  - <sup>49</sup> D. T. Cromer, R. R. Ryan, and D. Schiferl, *J. Phys. Chem.* **89**, 2315 (1985).
  - <sup>50</sup> M. P. Allen and D. J. Tildesley, *Computer Simulation of Liquids* (Oxford University Press, Oxford, 1987).
  - <sup>51</sup> W. M. Jones and W. F. Giauque, *J. Am. Chem. Soc.* **69**, 983 (1947).
  - <sup>52</sup> S. Root, R. J. Hardy, and D. R. Swanson, *J. Chem. Phys.* **118**, 3161 (2003).
  - <sup>53</sup> V. Yu. Klimenko and A. N. Dremin, *Sov. Phys. Dokl.* **24**, 984 (1979); **25**, 288 (1980), (both are English-language translations of earlier papers in Russian).
  - <sup>54</sup> V. V. Zhakhovskii, S. V. Zybin, K. Nishihara, and S. I. Anisimov, *Phys. Rev. Lett.* **83**, 1175 (1999).
  - <sup>55</sup> *LASL Shock Hugoniot Data*, edited by S. P. Marsh (University of California, Berkeley, 1980), p. 599.
  - <sup>56</sup> C. Eckart, *Phys. Rev.* **47**, 552 (1935).
  - <sup>57</sup> A. Sayvetz, *J. Chem. Phys.* **7**, 383 (1939).
  - <sup>58</sup> See, for example, J. Vanicek and W. H. Miller, *J. Chem. Phys.* **127**, 114309 (2007).
  - <sup>59</sup> K. N. Kudin and A. Y. Dymarsky, *J. Chem. Phys.* **122**, 224105 (2005).
  - <sup>60</sup> D. J. Heisterberg, <http://www.ccl.net/cca/software/SOURCES/FORTTRAN/fites/>.
  - <sup>61</sup> G. J. Piermarini, S. Block, and P. J. Miller, *J. Phys. Chem.* **93**, 457 (1989).
  - <sup>62</sup> R. Dawes, A. Siavosh-Haghighi, T. D. Sewell, and D. L. Thompson (unpublished).

# Shock-induced melting of (100)-oriented nitromethane: Energy partitioning and vibrational mode heating

Richard Dawes,<sup>a)</sup> Ali Siavosh-Haghighi, Thomas D. Sewell, and Donald L. Thompson<sup>b)</sup>  
*Department of Chemistry, University of Missouri-Columbia, Columbia, Missouri 65211-7600, USA*

(Received 10 August 2009; accepted 13 November 2009; published online 10 December 2009)

A study of the structural relaxation of nitromethane subsequent to shock loading normal to the (100) crystal plane performed using molecular dynamics and a nonreactive potential was reported recently [J. Chem. Phys. **131**, 064503 (2009)]. Starting from initial temperatures of  $T_0=50$  and 200 K, shocks were simulated using impact velocities  $U_p$  ranging from 0.5 to 3.0 km s<sup>-1</sup>; clear evidence of melting was obtained for shocks initiated with impacts of 2.0 km s<sup>-1</sup> and higher. Here, we report the results of analyses of those simulation data using a method based on the Eckart frame normal-mode analysis that allows partitioning of the kinetic energy among the molecular degrees of freedom. A description of the energy transfer is obtained in terms of average translational and rotational kinetic energies in addition to the rates of individual vibrational mode heating. Generally, at early times postshock a large superheating of the translational and rotational degrees of freedom (corresponding to phonon modes of the crystal) is observed. The lowest frequency vibrations (gateway modes) are rapidly excited and also exhibit superheating. Excitation of the remaining vibrational modes occurs more slowly. A rapid, early excitation of the symmetric C–H stretch mode was observed for the shock conditions  $T_0=50$  K and  $U_p=2.0$  km s<sup>-1</sup> due to a combination of favorable alignment of molecular orientation with the shock direction and frequency matching between the vibration and shock velocity. © 2009 American Institute of Physics. [doi:10.1063/1.3271349]

## I. INTRODUCTION

A shock wave propagating through a material leads to discontinuities in density, stress state, temperature, and entropy. The requirements of conservation of mass, momentum, and energy across the shock front give rise to the well-known Rankine–Hugoniot jump relations that specify postshock states in the material in terms of the initial state for a given set of shock parameters, under the assumptions that the shock is steady (i.e., spatially invariant with respect to time in a reference frame centered on the shock front) and uniform (i.e., spatially homogeneous transverse to the direction of shock wave propagation).<sup>1</sup> Shock waves in molecular materials lead to nonthermal partitioning of energy among the inter- and intramolecular degrees of freedom,<sup>2–4</sup> the phonon and vibron modes, respectively. Characterizing this energy partitioning and the time scales for its equilibration is the focus of the present paper.

It is generally accepted that the initial excitation and subsequent approach to thermal equilibrium in a shocked molecular crystal occurs by a mechanism known as *up-pumping* in which the shock initially excites preferentially the long wavelength lattice phonons, leading to significant excitation of those modes. These, in turn, couple most strongly to those lowest frequency molecular vibrations (gateway modes) that overlap with or are in near resonance with the optical phonon frequencies, and which have densely spaced energy levels and thus are essentially classical. The

dominant pathway for energy transfer to the high-frequency vibrons is via intramolecular vibrational redistribution (IVR). This occurs on time scales that are long compared to that for shock passage over a molecule in the crystal. Thus, thermal equilibration occurs in a hierarchical fashion: lattice excitation → low frequency vibronic excitation of gateway modes → IVR among the rest of the intramolecular modes.

Theoretical models have been proposed for the basic mechanisms of energy up-pumping in shocked materials.<sup>5–8</sup> Coupled with recent experimental advances,<sup>9–11</sup> these have provided useful information concerning energy transfer rates and pathways. However, complete specification of those theoretical models and assessment of their fundamental foundations require additional information concerning the detailed dynamics of initial shock excitation and subsequent relaxation in shocked molecular materials. Molecular dynamics (MD) simulations can be used to study such phenomena and to provide some of the necessary details. Moreover, MD is well suited for studying shock excitation due to the short time scales and spatially localized nature of the shock front. It is easy to compute the total energy deposited in a molecular material due to shock loading but information about the time-dependent modal partitioning of that energy is critical in order to advance our understanding beyond the qualitative level associated with the use of simple analytic models.<sup>5–8</sup> The main concerns in MD simulations are the accuracy of the force field and the validity of the classical approximation. We have chosen to use a force field that has been shown to accurately describe the solid and liquid states and the transitions between them, but which has, as do all analytic force fields, some imperfections; however, it is sufficiently accu-

<sup>a)</sup>Present address: Combustion Research Facility, Sandia National Laboratories, P.O. Box 969, Livermore, CA 94551.

<sup>b)</sup>Electronic mail: thompsondon@missouri.edu.



rate for the purpose of the present study. Classical mechanics is widely used because unlike quantum dynamics, it can be used for systems containing many atoms; not because it is expected to account accurately for all phenomena. The usual *caveat* applies to the results we report here—the reader needs to keep in mind the neglect of quantum effects.

Energy transfer in liquid nitromethane has been the subject of several experimental<sup>12–20</sup> and theoretical<sup>21–41</sup> studies. Much less is known about the solid phase for which fundamental properties such as directional sound speeds in the crystal have not yet been measured. Previously, we discussed the structural relaxations that occur on short time scales ( $\sim 4$  ps or less) subsequent to shock wave passage in crystalline nitromethane.<sup>42</sup> The results were based on MD simulations of shock wave propagation along the  $[100]$  crystal direction. In these three-dimensionally periodic constant volume-energy (*NVE*) simulations, a high aspect-ratio crystal slab of fully flexible molecules thermalized to an initial temperature  $T_0$  of 50 or 200 K (which is below the normal melting point of  $\sim 245$  K for this force field<sup>30,32–34</sup>) was impacted with velocity  $U_p$  (0.5, 1.0, 2.0, or 3.0 km s<sup>-1</sup>) into a stationary piston comprised of stationary, rigid molecules. This led to a shock wave that propagated through the flexible slab with a shock velocity  $U_s$  measured relative to the stationary piston. A gap  $\sim 500$  Å thick was introduced at one end of the simulation cell to eliminate interactions between periodic images parallel to the shock direction. The conditions studied in the previous paper<sup>42</sup> span the Hugoniot elastic limit (HEL) for the (100)-oriented crystal; for both initial temperatures we observed elastic compression for shocks with impact velocities of  $U_p=0.5$  and 1.0 km s<sup>-1</sup>, and shock-induced melting for shocks with impact velocities  $U_p \geq 2.0$  km s<sup>-1</sup>. We note that since the difference in shock pressures for the 1.0 and 2.0 km s<sup>-1</sup> impacts is approximately 10 GPa, we cannot rule out the possibility of some additional inelastic phenomenon at intermediate impact velocities. Here, we report the results of further analysis of the simulations described in Ref. 42, in which the focus was on geometric features that characterize shock-induced melting; namely, analyses of a molecular orientational order parameter, the pair distribution function, and mean-squared displacement. In the present study the goal was to investigate the time scales for excitation of individual intermolecular and intramolecular vibrational normal modes in the shocked crystal as functions of initial temperature and shock strength.

A key feature of the analysis performed in our previous<sup>42</sup> and the present study is the use of the Eckart–Sayvetz conditions<sup>43,44</sup> for defining alignment between the Eckart frame for an arbitrarily distorted and displaced molecule and that of a reference molecule that is fixed in the laboratory frame. The Eckart frame is widely used in studies of the chemical dynamics of gas-phase molecules. Such a procedure is important in the present context since, in general, shock excitation of a molecular crystal introduces significant intramolecular distortions as well as molecular rotations and translations, particularly so in situations that involve an order-disorder transition, such as melting. The Eckart frame can be used to define a rigorous separation of orientation from the internal degrees of freedom, which we exploit to

calculate translational and vibrational normal-mode kinetic energies and thus partition the kinetic energies. Another element of the analysis designed to improve the statistical precision of the results was the use of a reference frame centered on the shock front, which moves through the material at a constant speed in the case of supported shocks. By defining spatiotemporal origins relative to the instant of shock passage through a given plane in the crystal, it is possible to average the results at particular times over tens of thousands of individual molecules.

The rest of the paper is arranged as follows. In Sec. II details of the normal-mode projections will be described. Section III contains results for four different shock velocities and two initial temperatures. Section IV is the summary and conclusion.

## II. METHOD OF ANALYSIS

### A. Moving reference frame

Details of the simulations, force field, and moving reference frame have been given previously.<sup>42</sup> The moving reference frame was implemented slightly differently in the present study. Specifically, derived dynamical quantities were evaluated with 4 fs time resolution, which corresponds to the actual data capture frequency for positions and velocities from the simulations; whereas in the preceding study, these densely spaced individual observations were coarse grained according to molecular layer measured relative to shock front position.<sup>45</sup> That is, for the range of initial conditions and shock parameters considered, as the shock front propagated through the crystal in the earlier study, it was assigned to a given molecular layer normal to (100) for between 8 and 15 consecutive 4 fs snapshots, corresponding to the time required for the shock front to transit that layer for a given impact velocity  $U_p$  [cf. Fig. 1(b) of Ref. 42]. The focus of the present study is on rapid modal excitations. Therefore, in order to maintain 4 fs resolution the time histories for each neighboring layer were offset by the closest multiple of 4 fs, and added. For example, with an impact velocity  $U_p = 3.0$  km s<sup>-1</sup> and initial temperature  $T_0 = 50$  K, the shock front required an average of 31.8 fs to transit each layer, thus the time history for the closest neighboring layer was offset by eight 4 fs time steps (32.0 fs), and then added. A consequence of maintaining 4 fs resolution rather than collecting data by layer is that less data contribute to the averages at a given observation time. For  $t=0$  (i.e., at the shock front) the total amount of data is composed of 150(layers)  $\times$  24(molecules/layer) = 3600 molecules; whereas in the preceding study the number of molecules considered was between 8 and 15 times larger depending on the initial temperature and shock strength.

### B. Normal-mode projections

Normal-mode projection is commonly used in analyses of MD simulations. For details of force field analyses for single molecules in the gas phase, the reader is referred to one of the standard texts.<sup>46</sup> Here we describe the details of the procedure necessary for applying normal-mode projections to molecules in a strongly perturbed bulk material.



The first consideration is the reference structure. Normal-mode projection methods require the normal-mode eigenvectors of a representative reference molecule. Whereas for a single molecule the gas-phase minimum-energy structure is used, a molecule in a crystal (or in solution) can have a significantly different minimum-energy structure. Our strategy was to compare both but use the more realistic *in situ* crystal structure for the analyses. After obtaining a minimum-energy structure for an isolated gas-phase molecule (using a conjugate gradient minimization algorithm and only the intramolecular part of the force field), we computed normal-mode frequencies and eigenvectors; a mass-weighted Hessian was computed numerically at the minimum-energy structure using four- and five-point fourth-order-accurate finite difference formulas with a step size of 0.0001 bohr. Since for an isolated molecule the internal force field is invariant to translation and rotation, the corresponding “frequencies” formally should be zero but in practice, they will be nonzero due to numerical tolerances. Since the geometry optimization was performed to a very tight tolerance ( $1 \times 10^{-12}$  a.u.) and the Hessian computed with very high accuracy, the frequencies of the translation and rotation modes were less than  $0.02 \text{ cm}^{-1}$ . Next, to examine the effect of the crystal environment, a small, roughly cubic block of nitromethane composed of  $3 \times 4 \times 5$  unit cells (240 molecules) was equilibrated at 1 K and atmospheric pressure. Using the final configuration from this simulation, a larger block was constructed by forming a  $5 \times 5 \times 5$  supercell of the smaller blocks, thus containing a total of 30 000 molecules. A single molecule close to the center was chosen for the Hessian analysis. A conjugate gradient algorithm was used to produce a minimum-energy structure for the central molecule in the field of the other 29 999 molecules (whose positions were held fixed) using the complete inter- and intramolecular force fields. Unlike an isolated gas-phase molecule, a molecule in a crystal has nonzero forces related to translation (*T*) and/or rotation (*R*) of that molecule within the rest of the crystal; thus, the six lowest eigenvalues of the mass-weighted Hessian will not be zero. It also results in *T* and *R* contamination of the intramolecular vibrational mode vectors (note the distinction between initial system temperature,  $T_0$ , and the use of the symbol *T* for the translational components of kinetic energy). The magnitudes of the six lowest frequencies and the degree of mixing with the other vibrational modes depend on the system conditions and the force field. At low pressure where the intramolecular terms dominate and the vibron mode frequencies are only slightly perturbed relative to the gas phase, the mixing will be small. In our results the contamination was minimal ( $<1\%$ – $2\%$ ) and confined to the lowest frequency modes, but we chose to project out *T* and *R* and thus obtain  $3N-6=15$  pure vibrational modes for a single nitromethane molecule in the crystal field. A set of translational and rotational eigenvectors was constructed, thus completing the set of 21 orthonormal mass-weighted eigenvectors. Although mode-projection results for the shock simulations were very similar for both choices of reference molecule (gas phase and crystal), the reference molecule from the crystal was used in all the results.

TABLE I. Qualitative assignments and frequencies ( $\text{cm}^{-1}$ ) for the SRT force field used in this study.

Mode	Description	Gas phase	Crystal
1	Torsion	116.9	121.7
2	Out-of-plane NO <sub>2</sub> rock	460.6	464.9
3	NO <sub>2</sub> wag	605.0	604.5
4	NO <sub>2</sub> bend/CN stretch	811.2	807.4
5	NO <sub>2</sub> symmetric stretch	821.4	816.3
6	In-plane CH <sub>3</sub> rock <sup>a</sup>	1053.1	1053.3
7	Out-of-plane CH <sub>3</sub> rock <sup>a</sup>	1149.8	1148.5
8	CH <sub>3</sub> umbrella	1368.2	1371.1
9	CH <sub>3</sub> symmetric bend	1434.2	1428.9
10	CH <sub>3</sub> asymmetric bend	1436.0	1431.2
11	CH <sub>3</sub> umbrella/CN stretch	1507.7	1519.9
12	NO <sub>2</sub> asymmetric stretch	1618.2	1600.2
13	CH <sub>3</sub> symmetric stretch	2961.2	2960.7
14	Out-of-plane CH <sub>3</sub> asymmetric stretch <sup>b</sup>	3093.7	3087.4
15	In-plane CH <sub>3</sub> asymmetric stretch <sup>c</sup>	3095.0	3093.8

<sup>a</sup>In-plane and out-of-plane methyl group rocking modes are dominated by hydrogen motions that are approximately parallel and perpendicular, respectively, to the plane containing the NO<sub>2</sub> group.

<sup>b</sup>The in-plane asymmetric CH<sub>3</sub> stretch mode is dominated by displacements of the two H atoms whose equilibrium positions are approximately symmetric with respect to the plane defined by the NO<sub>2</sub> group.

<sup>c</sup>The out-of-plane asymmetric CH<sub>3</sub> stretch mode is dominated by displacements of two H atoms, one of which has an equilibrium position nominally perpendicular to the plane defined by the NO<sub>2</sub> group.

The frequencies and qualitative assignments obtained from the gas-phase and crystal-phase Hessian analyses are listed in Table I. The frequencies corresponding to the crystal structure are only slightly different from those obtained for an isolated gas-phase molecule, and the minimum-energy structure in the crystal is only slightly distorted relative to the gas-phase geometry (*C*<sub>1</sub> point group in the crystal and *C*<sub>s</sub> in the gas phase). The intramolecular contributions to the Sorescu–Rice–Thompson<sup>29</sup> (SRT) force field used here were parametrized to reproduce gas-phase (scaled) fundamental frequencies calculated using the B3LYP/6-31G\* level of density functional theory and basis set combination. The scaled frequencies, in turn, are in reasonably good agreement with experimental values for the liquid and crystal.<sup>29</sup> Thus, combined with the sizable set of additional measured equilibrium thermophysical properties for nitromethane that have been accurately reproduced by others,<sup>30–34</sup> as well as the favorable comparison between simulated<sup>35</sup> and measured<sup>16</sup> lifetimes and pathways following mode-specific methyl stretching excitation in the liquid, it indicates that the SRT force field is accurate, at least for reasonably small distortions about the equilibrium crystal structure.

The reference molecule for the Hessian analyses described above was initially oriented so that the principal axes of the molecule coincided with the *x*-, *y*-, and *z*-axes of the laboratory frame. The largest moment of inertia (roughly aligned with the C–N bond) was aligned with the *x*-axis, the next largest moment of inertia with the *y*-axis, and the smallest with the *z*-axis. This choice of alignment is arbitrary and does not affect the internal vibrational mode projections but does mean that the [100] shock direction and crystal frame would not coincide with the molecular frame defined by the

principal axes. In order to facilitate a more intuitive interpretation of the translational kinetic energy results with respect to the shock direction, the translational vectors were redefined, namely, they were aligned with the lattice vectors (and the laboratory frame). Thus, the  $x$ -direction corresponds precisely to the shock direction in the translational mode projection results discussed below.

With the reference molecule oriented and the mode vectors defined, a projection analysis was performed for each molecule in the shock simulations. The necessary alignment procedure was described in Ref. 42, but is such an essential part of the analysis that we present it again here. Since, in general, shock excitation of a molecule introduces significant intramolecular distortion as well as whole-body rotations and translations, the Eckart axis condition<sup>43</sup>

$$\sum_{i=1}^N m_i \mathbf{r}'_i \times (\mathbf{U} \mathbf{r}_i) = 0, \quad (1)$$

is particularly useful since it defines a rigorous separation of orientation from the internal degrees of freedom. In Eq. (1),  $m$  is the mass,  $\mathbf{r}$  and  $\mathbf{r}'$  are instantaneous and reference structures, respectively, with coincident centers of mass and  $\mathbf{U} \in SO(3)$  is the required rotation matrix. It can be shown that this is equivalent to minimizing the mass-weighted mean square displacement,

$$\min_{U \in SO(3)} \sum_{i=1}^N m_i |\mathbf{r}'_i - (\mathbf{U} \mathbf{r}_i)|^2. \quad (2)$$

We used a quaternion-based algorithm to solve for the rotation matrix  $\mathbf{U}$ .<sup>47</sup> Application of the  $3 \times 3$  rotation matrix  $\mathbf{U}$  to the coordinates of a particular analysis molecule aligns its Eckart frame with that of the reference molecule; the Cartesian velocities transform in the same way as the positions. Once so oriented, the positions and velocities were projected onto the normal-mode vectors of the reference molecule, thus transforming the MD simulation data from the Cartesian frame into the molecular normal coordinates. Since the 21 molecular normal coordinates include all 15 internal normal-mode vibrations as well as the three molecular translations and three rotations (thus forming a complete set), the total kinetic energy is exactly the same in either representation. We have neglected the coupling between vibration and rotation.

The possibility of methyl rotation, leading to symmetry-equivalent rotamers, introduced additional complexity since the Hessian was obtained at a single minimum-energy reference point corresponding to a particular (but arbitrary) rotamer. If the structure of an energy-equivalent rotamer is simply projected onto a reference molecule defined in terms of a different rotamer minimum then since the mode vectors comprise a complete set of coordinates, the projection will still be successful. However, a linear combination of (likely large) displacements will result due to describing one rotamer in terms of displacements from another. Clearly such a projection is undesirable since the harmonic approximation to the potential energy expressed in terms of those normal coordinate displacements would be highly inaccurate. Thus, to ensure that the correct projection was achieved in a

straightforward and automated fashion, separate projections were performed for all permutations of identical nuclei, and the result corresponding to the structure with the lowest harmonic potential energy was retained. Note that excepting this step in the analysis, normal-mode potential energies are not used since even once the most accurate geometric permutation is obtained, the normal coordinate displacements would, in general, be sufficiently large to render the harmonic approximation to the modal potential energy inaccurate.

### C. Energy partitioning

Using the moving frame and projection techniques described above, raw data from the shock simulations were transformed into a molecular modal description of kinetic energies with 4 fs temporal resolution, averaging over thousands of molecules at each observation. The 15 individual vibrational kinetic energies at a given time relative to shock passage were summed to give the average vibrational kinetic energy. Similarly, the individual directional components of translation and rotation were combined to obtain average kinetic energies for those kinds of motions. Since the analysis was performed in the frame of a stationary piston impacted by a slab of crystal material, the rapid change in translational kinetic energy in the  $x$ -shock direction is convenient for automatically identifying the location of the shock front. However, in order to compute meaningful translational energies that are consistent throughout the material (corresponding for example to the  $T_0=50$  or 200 K temperatures in the unshocked material), the center-of-mass motion of each molecular layer was subtracted out at each analysis snapshot. Thus the computed translational, rotational, and vibrational kinetic energies properly correspond to relative motion within a local frame in the material.

## III. RESULTS

### A. Translation

The Cartesian components of translational kinetic energy are plotted in Fig. 1 ( $T_0=200$  K) and Fig. 2 ( $T_0=50$  K) as a function of time, where  $t=0$  is the arrival time of the shock front. More precisely,  $t=0$  is the time at which the  $x$ -component of the gradient of kinetic energy passes through its maximum as the shock front passes over a given molecular layer in the crystal; cf. Figs. 1 and 2 of Ref. 42. Note that in these figures the ordinate scales differ from panel to panel. As discussed in Sec. II C, the center-of-mass motion of each layer was projected out so that relative motion could be extracted despite the overall abrupt stagnation associated with shock compression. Thus while the  $x$ -component (shock direction) of the overall translational kinetic energy, which was used to locate the shock front, undergoes a large change upon the arrival of the shock front, the *relative*  $x$ -axis motion within each layer is not necessarily the dominant contribution to changes in the kinetic energy.

As shown in Fig. 1, at  $T_0=200$  K the behavior of the translational normal-mode kinetic energies is qualitatively similar for each of the four shock strengths. Specifically, there is an impact-velocity-dependent superheating of the  $x$ -component (shock direction) of kinetic energy. This

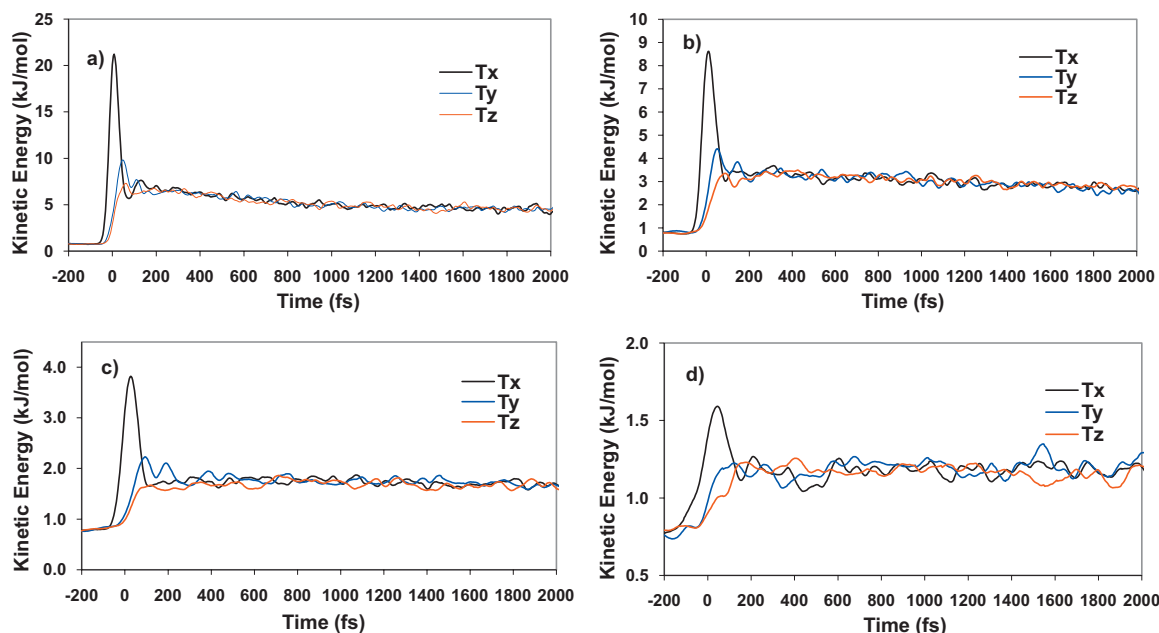


FIG. 1. Time histories of the components of translational kinetic energy are shown for various impact velocities. [Panel (a)]  $U_p=3.0$  km s $^{-1}$ ; [panel (b)]  $U_p=2.0$  km s $^{-1}$ ; [panel (c)]  $U_p=1.0$  km s $^{-1}$ ; [panel (d)]  $U_p=0.5$  km s $^{-1}$ . The initial temperature is  $T_0=200$  K. Note that the ordinate scales differ.

$x$ -component equilibrates rapidly with the other translational modes, prior to the slower process of equilibration with rotational and vibrational degrees of freedom, which is discussed below. For  $U_p \geq 1.0$  km s $^{-1}$ , the  $y$ -component of kinetic energy also overshoots the long-time average value although much less so than for the  $x$ -component; whereas the  $z$ -component is always the slowest to gain energy and for none of the impact velocities considered does it exhibit significant superheating for this initial temperature. Note that for this initial temperature all three components have approximately equal kinetic energies within 300 fs of shock front passage.

For the initial temperature  $T_0=50$  K (see Fig. 2) the shock propagates through a more ordered crystal than in the case of  $T_0=200$  K (see Fig. 1), thus the results are qualitatively different. For  $T_0=50$  K, the net magnitude of superheating of the translational modes is less at a given shock strength than for the corresponding ones at the higher initial temperature. Moreover, although the  $x$ -component is always the one excited initially, the  $y$ -component superheats by a similar amount and on nearly the same time scale. In the case of a  $U_p=3.0$  km s $^{-1}$  impact, the  $y$ -component actually achieves a higher kinetic energy than the  $x$ -component. Finally, the  $z$ -component of translation is considerably more

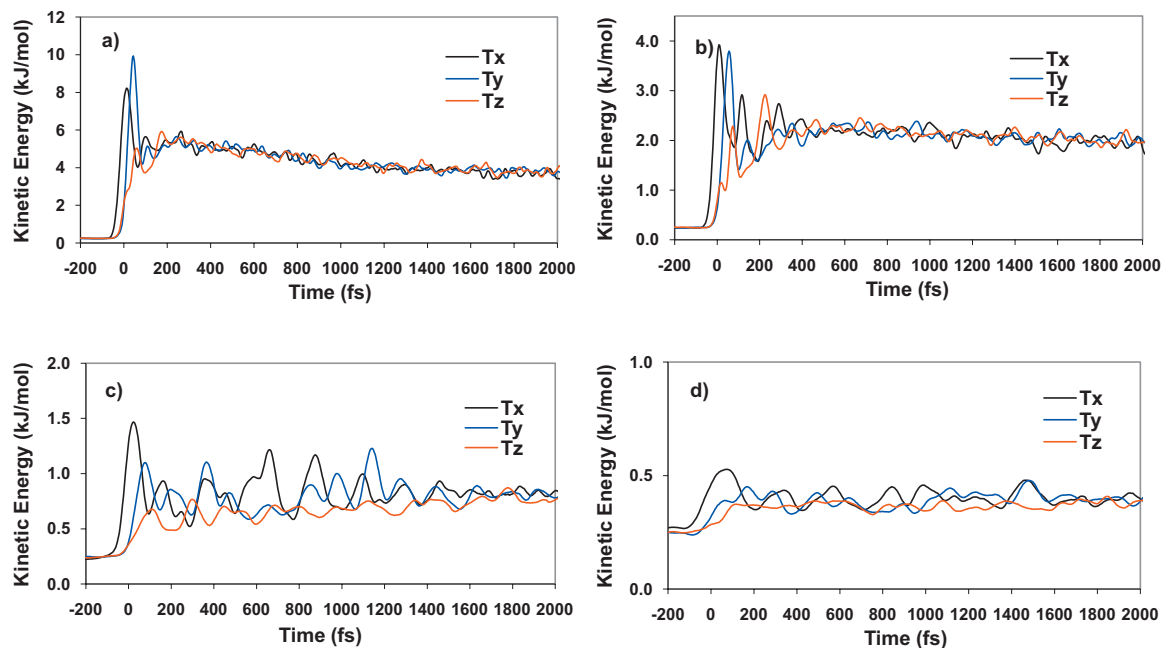


FIG. 2. As in Fig. 1 but for initial temperature  $T_0=50$  K. Note that the ordinate scales differ.

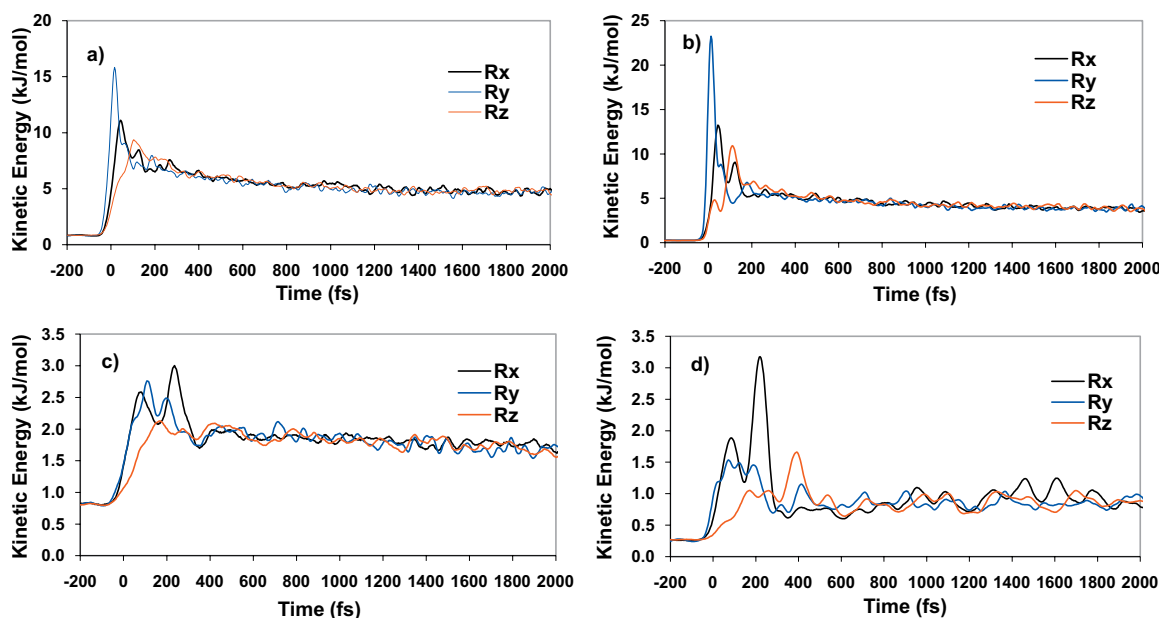


FIG. 3. Time histories of the components of rotational energy are shown for various impact velocities and initial temperatures. [Panel (a)]  $U_p=3.0$  km s $^{-1}$  and  $T_0=200$  K; [panel (b)]  $U_p=3.0$  km s $^{-1}$  and  $T_0=50$  K; [panel (c)]  $U_p=1.0$  km s $^{-1}$  and  $T_0=200$  K; [panel (d)]  $U_p=1.0$  km s $^{-1}$  and  $T_0=50$  K. Note that the ordinate scales differ.

involved in this case, and there is considerable “beating” among the components for times considerably longer than was the case for  $T_0=200$  K.

## B. Rotation

The rotational kinetic energies about the Cartesian axes are shown in Fig. 3 for  $U_p=3.0$  km s $^{-1}$  and  $U_p=1.0$  km s $^{-1}$  for  $T_0=200$  and 50 K, respectively. For the stronger shock strengths, [panels (a) and (b)], for which shock-induced melting occurs, there is significant superheating of the y-component of the rotational energy. As shown in Fig. 1 of Ref. 42, the nitromethane molecules in the crystal are oriented with the C–N bond at an angle with respect to the [100] axis; the [100] shock direction is roughly orthogonal to the molecular frame y-axis but projects onto a combination of the molecular x- and z-axes. Thus, impacts along the [100] direction will tend to produce forces (effectively, torques) about the molecular y-axis, leading to initial excitation of that component of rotational motion. As seen in Fig. 3, the superheating is much more pronounced at  $T_0=50$  K, for which the initial crystal order is less disturbed by thermal motion [panel (b)] than for  $T_0=200$  K [panel (a)]. For both initial temperatures at  $U_p=3.0$  km s $^{-1}$  all three rotational modes superheat (x and z to a lesser extent than y). The weaker shocks,  $U_p=1.0$  km s $^{-1}$  [see panels (c) and (d) of Fig. 3], which as shown in Ref. 42 do not cause significant loss of rotational order or melting, do not result in superheating of the y-component of rotation.

## C. Vibration

The molecules in each layer of the equilibrium crystal are arranged in dimer pairs with C–N bonds approximately parallel to the x-z plane<sup>42</sup> such that for shocks propagating normal to (100) half the molecules are shocked nominally

from the methyl end and the other half from the nitro end. Since for classical dynamics the flux of kinetic energy for each mode can be computed from the projection of time-dependent forces onto that mode,<sup>48,49</sup> we have performed a separate analysis of the modal kinetic energies for both initial orientations. Figure 4 shows the vibrational mode-resolved kinetic energies as a function of time (with  $t=0$  defined at the time of maximum shock direction gradient in the kinetic energy, discussed above), for the strong shock case  $U_p=3.0$  km s $^{-1}$  for initial temperature  $T_0=50$  K. For reference, note that the equilibrium modal kinetic energy of  $\frac{1}{2}$  kT is equal to 0.21 and 0.83 kJ mol $^{-1}$  for  $T_0=50$  and 200 K, respectively. Panels (a)–(c) and (d)–(f) in Fig. 4 contain results for molecules for which the shock impinges nominally upon the methyl end and nitro end, respectively, of the molecules. Panels (a)–(c) each contain results for five successively higher-frequency vibrational normal modes and similarly for panels (d)–(f); modes 1–5, 6–10, and 11–15, respectively (see Table I). The ordinate scales vary throughout the six panels in Fig. 4. Assuming equipartition, the near-asymptotic value of the modal kinetic energy for this case was determined to be 3.39 kJ mol $^{-1}$ ; this value was obtained from the time average of the “total” average kinetic energy trace in Fig. 7(b) (discussed below) over the postshock interval  $1800 \text{ fs} \leq t \leq 2000 \text{ fs}$ . Generally, for a given impact velocity (only one of which, 3.0 km s $^{-1}$ , is shown in Fig. 4) the rates of modal excitation depend primarily on the frequency of the mode, with the lower-frequency modes gaining energy more rapidly. This is consistent with the concept of low-frequency vibrations acting as gateway modes that provide a pathway for energy to excite higher-frequency vibrational modes of the molecules, with subsequent redistribution and overall equilibration by way of slower vibrational energy redistribution processes.



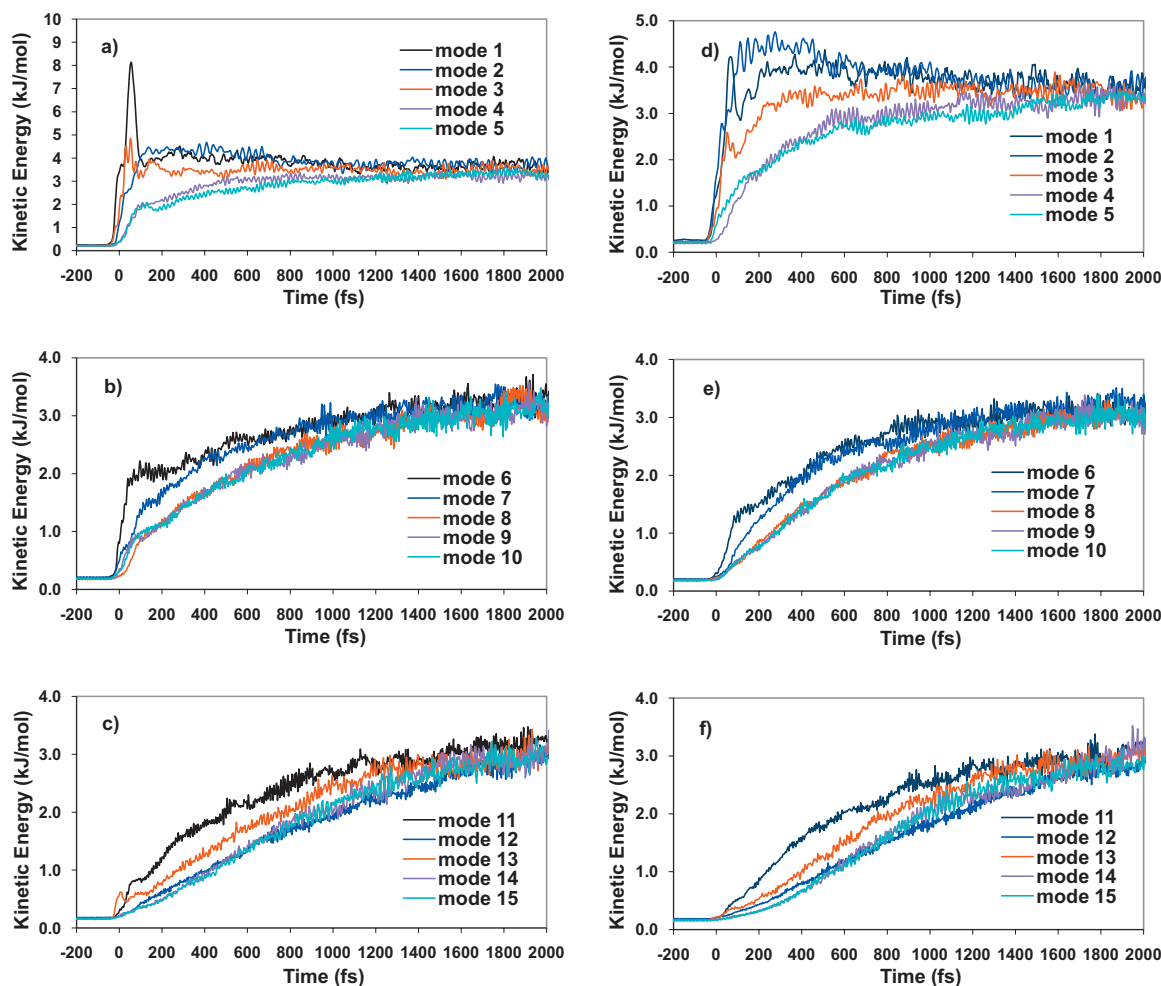


FIG. 4. Time histories of modal vibrational kinetic energies are shown for impact velocity  $U_p=3.0$  km s $^{-1}$  and initial temperature  $T_0=50$  K. In panels (a)–(c) results are shown for molecules in which the shock wave first impinges on the “methyl end” of the molecule, whereas those in panels (d)–(f) correspond to the molecules first impinged on the “nitro end” of the molecule. In each trio of panels results for the 15 vibrational modes are depicted in groups of five successively higher frequencies (low-, mid-, and high-frequency modes, respectively). The mode identities are given in Table I.

Within this general picture, however, there is significant richness in the detailed rates of excitation that depend on factors such as impact velocity, initial temperature, and initial orientation of the molecules relative to the shock front. For example, comparing the results for the low-frequency modes (up to 816.3 cm $^{-1}$ ) shock impact on the methyl end and nitro end of the molecules, respectively, panels (a) and (d) in Fig. 4, shows that the torsional mode (mode 1, 121.7 cm $^{-1}$ ) exhibits significantly greater superheating when the molecules are hit on the methyl end than on the nitro end. The results in panels (c) and (f) for the high-frequency modes (11–15) including NO $_2$  asymmetric stretch and C–H stretches show that there is a slight early excitation of mode 13 (C–H symmetric stretch, 2960.7 cm $^{-1}$ ) for the methyl end shock [panel (c)]. This is due to a favorable projection of the shock forces onto this specific mode. This effect is also dependent on the shock velocity and is much more significant in the  $U_p=2.0$  km s $^{-1}$  results (Fig. 6, discussed below). For the  $U_p=3.0$  km s $^{-1}$  impact all of the modes are fairly well equilibrated after 2 ps although the lower-frequency modes [see Figs. 4(a) and 4(d)] are still hotter than the high-frequency modes [see Figs. 4(c) and 4(f)]. The results for

$U_p=3.0$  km s $^{-1}$  at  $T_0=200$  K (not shown) are qualitatively similar to those shown for  $T_0=50$  K in Fig. 4. The differences for  $T_0=200$  K are mainly that due to increased thermal motion, the effect of early excitations through favorable mode projections is reduced.

Figure 5 shows the results for  $U_p=1.0$  km s $^{-1}$  at  $T_0=50$  K for those molecules oriented such that the shock impinges on the methyl end. Assuming equipartition, the near-asymptotic value of the modal kinetic energy for this case was determined to be 0.45 kJ mol $^{-1}$ ; this value was obtained from the time average of the total average kinetic energy trace in Fig. 7(e) (discussed below) over the post-shock interval 1800 fs  $\leq t \leq$  2000 fs. In this case, which is below the threshold for shock-induced melting, the torsion is rapidly superheated and the lower-frequency modes increase in energy more rapidly than the higher-frequency ones, but the rates of equilibration are much slower than for the  $U_p=3.0$  km s $^{-1}$  case shown in Fig. 4. Even after 2 ps, most of the higher-frequency modes exhibit very little excitation. Indeed, with one exception, the transfer of energy into the higher-frequency modes is so inefficient that one cannot easily identify the arrival of the shock front based on plots of



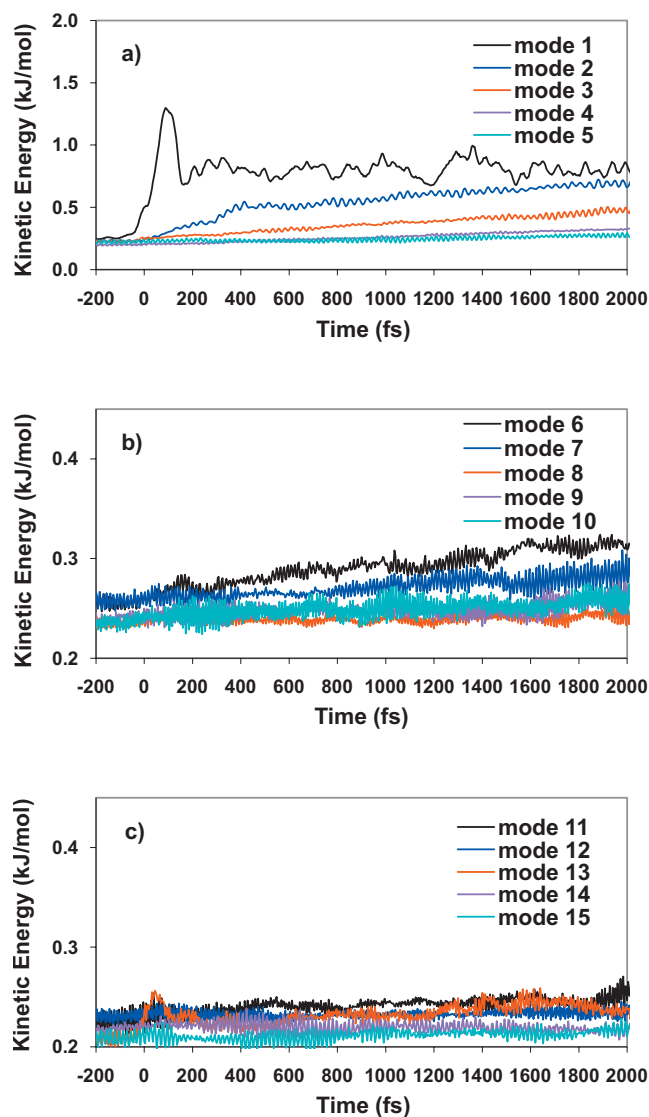


FIG. 5. Time histories of modal vibrational kinetic energies are shown for an impact velocity of  $U_p = 1.0 \text{ km s}^{-1}$  and initial temperature of 50 K for those molecules for which the shock wave first impinges on the methyl end. [Panel (a)] Low-frequency modes; [panel (b)] mid-frequency modes; [panel (c)] high-frequency modes. The mode identities are given in Table I. Note that the ordinate scale in panel (a) differs from those in panels (b) and (c).

modal kinetic energies. The exception again originates due to favorable alignment of the C–H symmetric stretching mode (mode 13) with the shock forces. In this case a statistically meaningful—although still very small (with a magnitude of just several hundredths of a kJ/mol)—impulsive heating of that mode is observed during arrival of the shock.

In Fig. 6 the anomalous excitation of the symmetric C–H stretch (mode 13) is shown for an impact velocity of  $U_p = 2.0 \text{ km s}^{-1}$  for three different cases. Panel (a) shows the maximal effect observed in the simulations, which occurs for  $T_0 = 50 \text{ K}$  and  $U_p = 2.0 \text{ km s}^{-1}$ , for molecules for which initial impact occurs on the methyl groups. Panel (b) shows the significantly reduced effect that occurs for the same initial temperature and impact velocity when the shock impinges on the nitro end of the molecules. Finally, panel (c) shows the reduced effect observed for  $T_0 = 200 \text{ K}$  (methyl end) due to increased thermal motion.

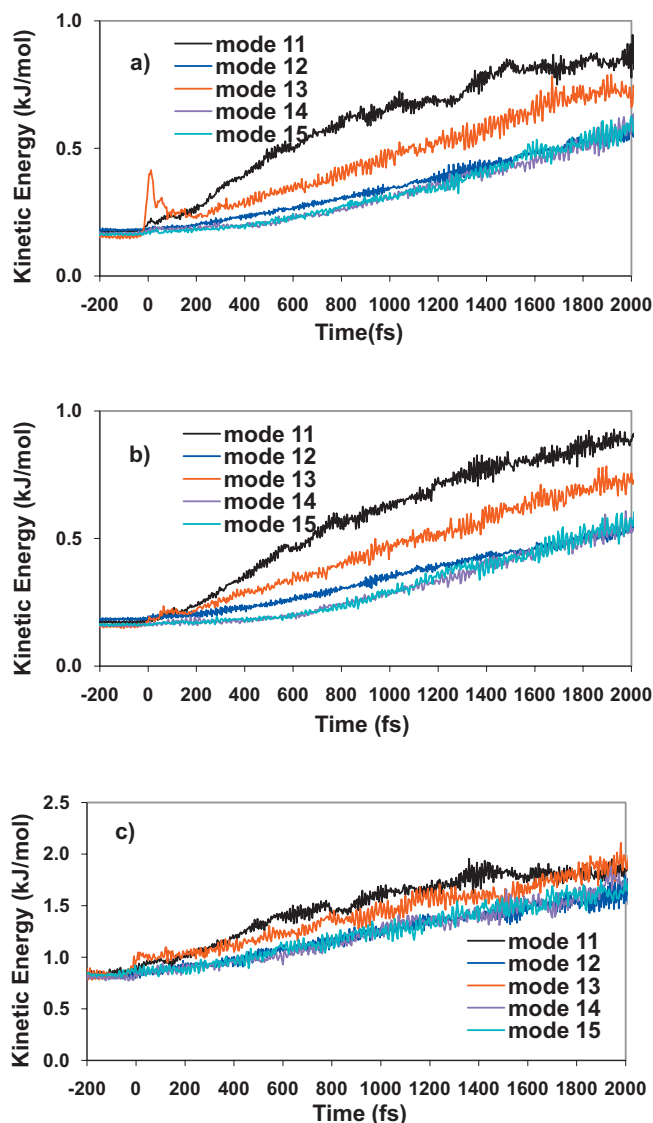


FIG. 6. Time histories of high-frequency modal vibrational kinetic energies are shown for an impact velocity of  $U_p = 2.0 \text{ km s}^{-1}$ . [Panel (a)]  $T_0 = 50 \text{ K}$ , impact on methyl end molecules; [panel (b)]  $T_0 = 50 \text{ K}$ , impact on nitro end molecules; [panel (c)]  $T_0 = 200 \text{ K}$ , impact on methyl end molecules. The mode identities are given in Table I. Note that the ordinate scale in panel (c) differs from those in panels (a) and (b).

## D. Temperatures

The kinetic energy in the shocked material is not Boltzmann distributed in general and therefore a measure of temperature based on elementary concepts from equilibrium thermodynamics does not rigorously apply.<sup>50,51</sup> Nevertheless, to provide an intuitive feel for the initial partitioning and long-time shock heating introduced by shocks of various strengths it is of interest to relate the average kinetic energies in the various kinds of degrees of freedom with “temperatures”—while remaining cognizant of the fact that for some time interval subsequent to shock excitation, the distributions of kinetic energies are not Boltzmann. Thus, temperatures defined simply as the average translational, rotational, vibrational, and total kinetic energies are shown in Fig. 7 as functions of time. Note that the ordinate ranges differ from panel to panel. In all cases the total temperature rises quickly toward a steady-fluctuating value that corre-

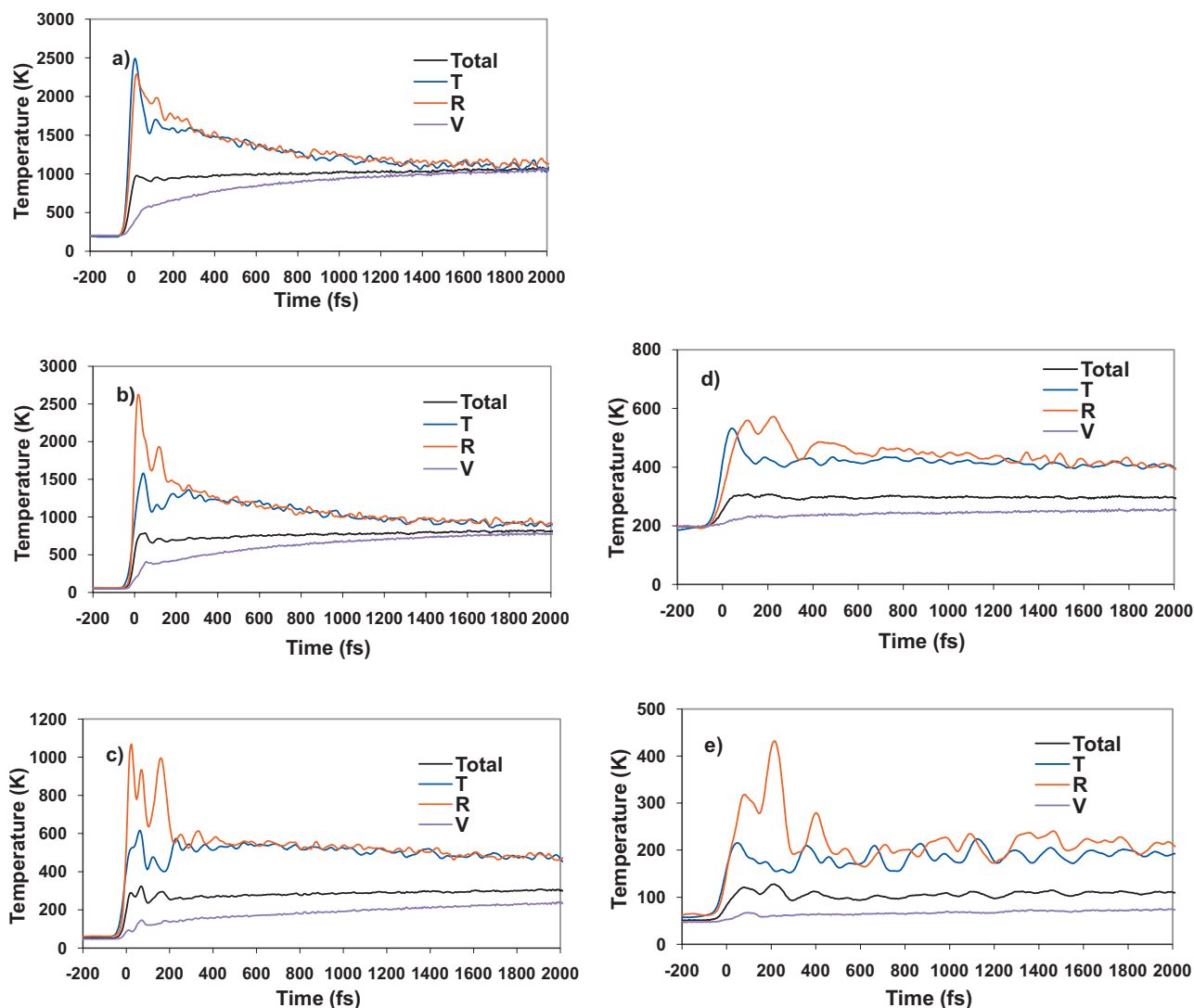


FIG. 7. Time histories of average kinetic energies (reported as temperatures; see discussion) are shown for various impact velocities and initial temperatures. [Panel (a)]  $U_p=3.0$  km s $^{-1}$  and  $T_0=200$  K; [panel (b)]  $U_p=3.0$  km s $^{-1}$  and  $T_0=50$  K; [panel (c)]  $U_p=2.0$  km s $^{-1}$  and  $T_0=50$  K; [panel (d)]  $U_p=1.0$  km s $^{-1}$  and  $T_0=200$  K; [panel (e)]  $U_p=1.0$  km s $^{-1}$  and  $T_0=50$  K.

sponds to overall shock-induced heating. The partitioning of the energy indicates that at early times, postshock, the aggregated degrees of freedom of a given type (i.e., translation, rotation, and vibration), are far from equilibrated with the others and therefore the simple average of the total kinetic energy is a poor measure by which to predict chemical reaction rates. In general, the translational and rotational degrees of freedom rapidly superheat, while the vibrational energy increases much more slowly. The rates of equilibration among the various degrees of freedom depend strongly on the shock strength. For  $U_p=3.0$  km s $^{-1}$  impacts [panels (a) and (b) for  $T_0=200$  and 50 K, respectively], the partitioned temperatures have largely equilibrated with each other after 2 ps; in this case higher initial temperature leads to less distinction between translational and rotational energies at short times. For the weaker shock strengths [panels (c)–(e)] it is clear that the rates of equilibration are much slower. For example, for the  $U_p=1.0$  km s $^{-1}$  impacts [panels (d) and (e)], even after 2 ps the vibrational energies have increased only slightly while the translational and rotational ones are essentially in equilibrium with one another after only 500 fs.

An exception to these general trends is observed for  $U_p=2.0$  km s $^{-1}$  impact at  $T_0=50$  K [panel (c)]. As discussed in Sec. III C dealing with vibrational modal excitation, the favorable alignment and frequency matching between the shock forces and the symmetric C–H stretching mode caused a rapid early heating of that one specific vibrational mode. This is reflected in the associated vibrational kinetic energy.

#### IV. SUMMARY AND CONCLUSIONS

We have presented a MD study of the magnitudes and time scales for excitation of inter- and intramolecular modal degrees of freedom in shock-compressed nitromethane crystal for two initial temperatures and four shock strengths that span the HEL for the (100)-oriented crystals considered; relaxation of the crystal shocked to states above the HEL for this orientation occurs by melting. The Eckart–Sayvetz condition was used to align the Eckart frames<sup>43</sup> of molecules in the crystal with a reference molecule defined in the laboratory frame, for which normal-mode eigenvectors and eigenvalues were determined in the effective field of the crystal at

1 K and atmospheric pressure. The modal kinetic energies were computed as functions of time for translational, rotational, and vibrational normal modes of the molecule. Since the normal modes define an orthonormal frame, the total kinetic energy of a molecule at any time is recovered exactly by this procedure. By restricting the treatment to consider only the modal kinetic energies, we avoid complications associated with anharmonic effects in the potential energy that would severely contaminate (invalidate) predictions of normal-mode total energies for the highly distorted molecular geometries accessed in some of the simulations. Finally, by considering a reference frame centered on the shock front, which propagates through the crystal at constant velocity for a given impact velocity and initial temperature, we were able to perform averages over thousands of molecules to obtain precise predictions of the molecular vibrational modal kinetic energies and the partitioning of total kinetic energy among the translational, rotational, and vibrational degrees of freedom as functions of time (or equivalently, distance) behind the shock front.

The results indicate that for impact velocities of  $U_p = 3.0 \text{ km s}^{-1}$ , near-complete equilibration among the translational, rotational, and vibrational degrees of freedom occurs within the 2 ps time scale of the simulations; initial temperature has relatively little effect, excluding details at short times. At lower shock strengths, however, equilibration among the various degrees of freedom is not complete on that time scale. This is particularly interesting for the case  $U_p = 2.0 \text{ km s}^{-1}$ ,  $T_0 = 50 \text{ K}$  for which we determined previously that shock-induced melting occurs.<sup>42</sup> That is, even though within 2 ps following shock excitation the molecules for this particular set of shock parameters are orientationally and translationally disordered relative to the crystal structure in ways that are characteristic of a liquid, the average vibrational, rotational, and translational temperatures are not in thermal equilibrium. The rates of equilibration observed once melting has occurred are surely influenced by liquefaction but this effect is not resolved in our data, likely due to the dominant shock velocity dependence on uniaxial compression and temperature rise (cf. Table II of Ref. 42).

Rates and overall magnitudes of excitation of the vibrational normal modes are sensitive to initial temperature, impact velocity, and orientation of the molecules relative to the direction of shock propagation. In the (100)-oriented crystal studied here, half of the molecules in a given crystal layer containing a (100) plane are shocked nominally from the methyl end while the other half are shocked nominally from the nitro end. We find for  $U_p = 3.0 \text{ km s}^{-1}$  impacts, for which melting occurs, that the relative rates of initial excitation of individual molecular vibrations depend sensitively on which end of the molecule is impinged upon by the shock front, particularly in the case of low-frequency vibrations and also for one of the C–H stretch modes, for which a favorable alignment between the normal-mode eigenvector and the shock forces on the molecule leads to an anomalous excitation of that mode for certain impact velocities. In general, higher initial temperature suppresses these mode-specific excitations, presumably due to increased thermal fluctuations

that tend to decrease the level of specificity with which the shock forces project onto particular normal-mode eigenvectors.

The results presented here are in general agreement with a picture of vibrational up-pumping in shocked molecular materials, wherein the low-frequency lattice phonon modes (or quasiphonons in the case of liquid) are the ones initially excited by the passage of a shock wave, followed by relaxation into low-frequency “gateway” vibrations that overlap with, or are close in frequency to, the lattice modes, and subsequent relaxation on longer time scales into the higher-frequency vibrational modes of the crystal. What these results add to this picture, however, is that specific pathways and rates of excitation will also depend on the orientation of the shock wave relative to the crystal structure. This raises the question of whether, by optimizing parameters such as crystal orientation, shock strength, and initial thermodynamic state, it might be possible to control the initial deposition of energy in a shocked crystal in a way that might be spectroscopically observable or perhaps even practically useful.

The neglect of quantum effects in a classical simulation could result in some aphysical behavior of the energy transfer as well as impacting the condensed phase dynamics more generally. Quantum dynamics treatments of many-degrees-of-freedom systems under shock conditions have yet to be carried out. Mowrey *et al.*<sup>52</sup> reported a two-dimensional quantum wave packet study of individual diatomic molecules impacting a hard wall. Those authors found that the quantum rates of direct, single-collision vibrational excitation varied greatly with the exact form of the model potential, but were always less efficient than classical predictions; they speculated that energy transfer might be more efficient in more complex systems undergoing multiple collisions. The nitromethane molecule has 15 internal degrees of freedom including a dense set of low-frequency gateway modes. Thus while quantum effects could significantly affect the resonant C–H stretch excitation observed in our classical simulations (cf. discussion of Fig. 6 in Sec. III C), the general up-pumping mechanism for exciting the high-frequency modes through IVR is still likely to hold. Quantum effects in the dynamics of liquids such as translational diffusion and orientational relaxation could also be important considerations. Habershon *et al.*<sup>53</sup> recently reported a study of liquid water in which they found that quantum effects may tend to cancel, resulting in only a net 15% increase in diffusion and relaxation rates. They found that while intermolecular zero point energy (ZPE) and tunneling disrupted the hydrogen-bonding network thereby increasing translational diffusion and orientational relaxation, intramolecular ZPE tended to increase molecular dipoles, thus strengthening intermolecular interactions and lowering the rates of those processes. Since dipole-dipole interactions are also important for the structure and dynamics of condensed phase nitromethane, it is possible that the accuracy of classical simulations for it similarly benefits from a cancellation of quantum effects.

## ACKNOWLEDGMENTS

This work was supported by the U.S. Army Research Office under the MURI Project No. W911NF-05-1-0265.

- <sup>1</sup>R. Courant and K. O. Friedrichs, *Supersonic Flow and Shock Waves* (Springer-Verlag, New York, 1977).
- <sup>2</sup>A. J. Heim, N. Gronbech-Jensen, E. M. Kober, and T. C. Germann, *Phys. Rev. E* **78**, 046710 (2008).
- <sup>3</sup>E. J. Reed, M. R. Manaa, L. E. Fried, K. R. Glaesemann, and J. D. Joannopoulos, *Nat. Phys.* **4**, 72 (2008).
- <sup>4</sup>A. Strachan, A. C. T. van Duin, D. Chakraborty, S. Dasgupta, and W. A. Goddard III, *Phys. Rev. Lett.* **91**, 098301 (2003).
- <sup>5</sup>A. Tokmakoff, M. D. Fayer, and D. D. Dlott, *J. Phys. Chem.* **97**, 1901 (1993).
- <sup>6</sup>S. Ye and M. Koshi, *J. Phys. Chem. B* **110**, 18515 (2006).
- <sup>7</sup>C. M. Tarver, *J. Phys. Chem. A* **101**, 4845 (1997).
- <sup>8</sup>L. E. Fried and A. J. Ruggiero, *J. Phys. Chem.* **98**, 9786 (1994).
- <sup>9</sup>Z. Wang, D. G. Cahill, J. A. Carter, Y. K. Koh, A. Lagutchev, N.-H. Seong, and D. D. Dlott, *Chem. Phys.* **350**, 31 (2008).
- <sup>10</sup>C. A. Bolme, S. D. McGrane, D. S. Moore, and D. J. Funk, *J. Appl. Phys.* **102**, 033513 (2007).
- <sup>11</sup>J. E. Patterson, Z. A. Dreger, M. Miao, and Y. M. Gupta, *J. Phys. Chem. A* **112**, 7374 (2008).
- <sup>12</sup>V. Bouyer, I. Darbord, P. Hervé, G. Baudin, C. Le Gallic, F. Clément, and G. Chavent, *Combust. Flame* **144**, 139 (2006).
- <sup>13</sup>P. C. Lysne and D. R. Hardesty, *J. Chem. Phys.* **59**, 6512 (1973).
- <sup>14</sup>J. M. Winey, G. E. Duvall, M. D. Knudson, and Y. M. Gupta, *J. Chem. Phys.* **113**, 7492 (2000).
- <sup>15</sup>J. C. Deák, L. K. Iwaki, and D. D. Dlott, *J. Phys. Chem. A* **103**, 971 (1999).
- <sup>16</sup>L. C. Dias, M. A. B. Ferreira, and C. F. Tormena, *J. Phys. Chem. A* **112**, 232 (2008).
- <sup>17</sup>M. Citroni, F. Datchi, R. Bini, M. Di Vaira, P. Pruzan, B. Canny, and V. Schettino, *J. Phys. Chem. B* **112**, 1095 (2008).
- <sup>18</sup>R. Ouillon, J.-P. Pinan-Lucarré, B. Canny, P. Pruzan, and P. Ranson, *J. Raman Spectrosc.* **39**, 354 (2008).
- <sup>19</sup>W. S. Price, H. Ide, and Y. Arata, *J. Chem. Phys.* **113**, 3686 (2000).
- <sup>20</sup>S. A. Sheffield, D. M. Dattelbaum, R. Engelke, R. R. Alcon, B. Crouzet, D. L. Robbins, D. B. Stahl, and R. L. Gustavsen, Proceedings of the 13th International Detonation Symposium, Norfolk, VA, 23–28 July 2006 (unpublished), p. 401; ONR Report No. ONR 351-07-01, 2006.
- <sup>21</sup>D. Margetis, E. Kaxiras, M. Elstner, Th. Fraunheim, and M. R. Manaa, *J. Chem. Phys.* **117**, 788 (2002).
- <sup>22</sup>H. Liu, J. Zhao, D. Wei, and Z. Gong, *J. Chem. Phys.* **124**, 124501 (2006).
- <sup>23</sup>F. J. Zerilli, J. P. Hooper, and M. M. Kukulja, *J. Chem. Phys.* **126**, 114701 (2007).
- <sup>24</sup>M. W. Conroy, I. I. Oleynik, S. V. Zybin, and C. T. White, *J. Phys. Chem. A* **113**, 3610 (2009).
- <sup>25</sup>E. J. Reed, J. D. Joannopoulos, and L. E. Fried, *Phys. Rev. B* **62**, 16500 (2000).
- <sup>26</sup>S. A. Decker, T. K. Woo, D. Wei, and F. Zhang, Proceedings of the 12th International Detonation Symposium, San Diego, CA, 11–16 August 2002 (unpublished), p. 724; U. S. Office of Naval Research Report No. ONR 333-05-2, 2005.
- <sup>27</sup>M. R. Manaa, E. J. Reed, L. E. Fried, G. Galli, and F. Gygi, *J. Chem. Phys.* **120**, 10146 (2004).
- <sup>28</sup>H. E. Alper, F. Abu-Awwad, and P. Politzer, *J. Phys. Chem. B* **103**, 9738 (1999).
- <sup>29</sup>D. C. Sorescu, B. M. Rice, and D. L. Thompson, *J. Phys. Chem. B* **104**, 8406 (2000); there were two typographical errors in the original presentation of this force field (referred to hereafter as SRT). Equation 6 in SRT for the harmonic three-center covalent bending angle should not contain the factor of  $\frac{1}{2}$  that appears there. Also, the energy coefficient  $V_\phi$  for the  $N_2-O_4-O_3-C_1$  improper dihedral angle interaction in Table 1 of SRT is exactly twice as large as it should be. Both of these typographical errors were fixed in Table 1 of Ref. 30 (referred to here as ART); thus, the use of all parameters appearing in Table 1 of ART in conjunction with the intramolecular potential energy functions in Eq. 3 of that paper leads to the normal-mode frequencies and eigenvector projections listed in columns M1 and P1 of Table 2 of the original SRT article. Another feature of the SRT force field model for nitromethane that should be appreciated is that it does not possess permutation symmetry with respect to hydrogen atom exchange, with the consequence that it is important for a correct implementation of the potential to number the atoms in accord with the convention shown in Fig. 1 of SRT (or Fig. 1a of ART).
- <sup>30</sup>P. M. Agrawal, B. M. Rice, and D. L. Thompson, *J. Chem. Phys.* **119**, 9617 (2003).
- <sup>31</sup>D. C. Sorescu, B. M. Rice, and D. L. Thompson, *J. Phys. Chem. A* **105**, 9336 (2001).
- <sup>32</sup>A. Siavosh-Haghighi and D. L. Thompson, *J. Chem. Phys.* **125**, 184711 (2006).
- <sup>33</sup>L. Zheng, S.-N. Luo, and D. L. Thompson, *J. Chem. Phys.* **124**, 154504 (2006).
- <sup>34</sup>A. Siavosh-Haghighi and D. L. Thompson, *J. Phys. Chem. C* **111**, 7980 (2007).
- <sup>35</sup>V. N. Kabadi and B. M. Rice, *J. Phys. Chem. A* **108**, 532 (2004).
- <sup>36</sup>H. Liu, J. Zhao, G. Ji, Z. Gong, and D. Wei, *Physica B* **382**, 334 (2006).
- <sup>37</sup>N. Desbiens, E. Bourasseau, and J.-B. Maillet, *Mol. Simul.* **33**, 1061 (2007).
- <sup>38</sup>A. Hervouët, N. Desbiens, E. Bourasseau, and J.-B. Maillet, *J. Phys. Chem. B* **112**, 5070 (2008).
- <sup>39</sup>N. Desbiens, E. Bourasseau, J.-B. Maillet, and L. Souillard, *J. Hazard. Mater.* **166**, 1120 (2009).
- <sup>40</sup>T. Megyes, S. Bálint, T. Grósz, T. Radnai, I. Bakó, and L. Almásy, *J. Chem. Phys.* **126**, 164507 (2007).
- <sup>41</sup>S. Hayaki, H. Sato, and S. Sakaki, *J. Mol. Liq.* **147**, 9 (2009).
- <sup>42</sup>A. Siavosh-Haghighi, R. Dawes, T. D. Sewell, and D. L. Thompson, *J. Chem. Phys.* **131**, 064503 (2009).
- <sup>43</sup>C. Eckart, *Phys. Rev.* **47**, 552 (1935).
- <sup>44</sup>A. Sayvetz, *J. Chem. Phys.* **7**, 383 (1939).
- <sup>45</sup>The crystal structure of nitromethane is such that the molecules form layers of dimer pairs in planes perpendicular to the [100] crystal direction [cf. Fig. 1(b) of Ref. 42].
- <sup>46</sup>For instance, E. B. Wilson, Jr., J. C. Decius, and P. C. Cross, *Molecular Vibrations: The Theory of Infrared and Raman Vibrational Spectra* (Dover, New York, 1980).
- <sup>47</sup>D. J. Heisterberg, see: <http://www.ccl.net/cca/software/SOURCES/FORTTRAN/fitest/>.
- <sup>48</sup>V. S. Vikhrenko, C. Heidelberg, D. Schwarzer, V. B. Nemtsov, and J. Schroeder, *J. Chem. Phys.* **110**, 5273 (1999).
- <sup>49</sup>C. Heidelberg, V. S. Vikhrenko, D. Schwarzer, and J. Schroeder, *J. Chem. Phys.* **110**, 5286 (1999).
- <sup>50</sup>V. Yu Klimenko and A. N. Dremin, *Sov. Phys. Dokl.* **24**, 984 (1979).
- <sup>51</sup>V. Yu Klimenko and A. N. Dremin, *Sov. Phys. Dokl.* **25**, 288 (1980).
- <sup>52</sup>R. C. Mowrey, M. L. Elert, and C. T. White, *AIP Conf. Proc.* **845**, 409 (2006).
- <sup>53</sup>S. Habershon, T. E. Markland, and D. E. Manolopoulos, *J. Chem. Phys.* **131**, 024501 (2009).



# Shock-induced transformations in crystalline RDX: A uniaxial constant-stress Hugoniotat molecular dynamics simulation study

Dmitry Bedrov,<sup>1,a)</sup> Justin B. Hooper,<sup>1</sup> Grant D. Smith,<sup>1</sup> and Thomas D. Sewell<sup>2</sup>

<sup>1</sup>*Department of Materials Science and Engineering, University of Utah, Salt Lake City, Utah 84112, USA*

<sup>2</sup>*Department of Chemistry, University of Missouri-Columbia, Columbia, Missouri 65211-7600, USA*

(Received 27 April 2009; accepted 19 June 2009; published online 21 July 2009)

Molecular dynamics (MD) simulations of uniaxial shock compression along the [100] and [001] directions in the  $\alpha$  polymorph of hexahydro-1,3,5-trinitro-1,3,5-triazine ( $\alpha$ -RDX) have been conducted over a wide range of shock pressures using the uniaxial constant stress Hugoniotat method [Ravelo *et al.*, Phys. Rev. B **70**, 014103 (2004)]. We demonstrate that the Hugoniotat method is suitable for studying shock compression in atomic-scale models of energetic materials without the necessity to consider the extremely large simulation cells required for an explicit shock wave simulation. Specifically, direct comparison of results obtained using the Hugoniotat approach to those reported by Thompson and co-workers [Phys. Rev. B **78**, 014107 (2008)] based on large-scale MD simulations of shocks using the shock front absorbing boundary condition (SFABC) approach indicates that Hugoniotat simulations of systems containing several thousand molecules reproduced the salient features observed in the SFABC simulations involving roughly a quarter-million molecules, namely, nucleation and growth of nanoscale shear bands for shocks propagating along the [100] direction and the polymorphic  $\alpha$ - $\gamma$  phase transition for shocks directed along the [001] direction. The Hugoniotat simulations yielded predictions of the Hugoniot elastic limit for the [100] shock direction consistent with SFABC simulation results. © 2009 American Institute of Physics. [DOI: 10.1063/1.3177350]

## I. INTRODUCTION

Practical explosive formulations—for instance, gun and rocket propellants or military high explosives (HEs)—are often morphologically complex filled-polymer composites comprised of HE crystallites with multimodal size distributions and complicated damage states (chemical purity, voids, cracks, etc.) bound together by binder phases that often include numerous components such as plasticizers and stabilizers. In contrast to most filled-polymer composites, in HE composites the filler is the dominant constituent, ranging from ~50% by weight in some propellants to ~95% in certain high performance military plastic-bonded explosives. Among the more commonly used HE compounds are TNT, RDX, HMX, PETN, and TATB.<sup>1</sup> Generically, crystals of these medium-sized polyatomic molecules have rather high compressibilities (initial bulk modulus of ~10 GPa) yet also are quite brittle, exist in multiple low-symmetry polymorphs, and in some cases exhibit large mechanical anisotropies. It is interesting to note that HE crystals share these qualitative features with many pharmaceutical substances, leading in both cases to practical challenges in synthesis, characterization, handling, and end-use processing and stability.

Understanding and predicting explosive initiation and the critical parameters for transition to detonation in HE materials, whether under an intended or unintended thermomechanical stimulus, is an important and challenging problem. At its heart is the need to understand the complex and typically multiscale processes by which localization of en-

ergy can lead to regions in the material with temperature and stress sufficiently high (known colloquially as hot spots) to promote rapid molecular decomposition that in turn can lead to ignition and detonation. Such an understanding, and certainly a predictive capability, requires a detailed knowledge of the fundamental properties of the constituent materials and interactions among them such as thermophysical and elastic mechanical parameters, mechanisms and energetics of inelastic deformation, chemical reaction rates and mechanisms, and physico-chemical interactions at material interfaces. In general this information is needed as functions of temperature, stress, and, in some cases, mechanical strain rate. Although progress has been made recently toward obtaining this information experimentally,<sup>2–8</sup> doing so has proven to be challenging due to the intrinsic material and chemical characteristics of energetic materials as well as the wide range of thermodynamic variables over which data are needed.

Due in part to the paucity of reliable and consistent experimental data for the equilibrium thermophysical and mechanical properties of energetic molecular crystals for states away from room temperature or atmospheric pressure, atomic-scale simulation methods [e.g., molecular dynamics (MD) or Monte Carlo] have received increasing acceptance in recent years as a means of obtaining information concerning some of the fundamental properties and processes indicated above; see, for example, Refs. 9–14. The results obtained so far indicate that, given an accurate force field and careful consideration of the suitability of the approximation of classical statistical mechanics for predicting some quantity

<sup>a)</sup>Electronic mail: d.bedrov@utah.edu.



of interest (specific heat being an example of one that should be approached with caution), atomistic simulations can yield accurate temperature- and pressure-dependent predictions of PVT and elastic mechanical properties of energetic materials.

While there exists a sizeable body of literature containing predictions of equilibrium energetic material properties from atomistic MD simulations, progress toward understanding nonequilibrium processes including chemistry has been slower.<sup>15,16</sup> The prototypical nonequilibrium phenomena relevant to energetic materials research are mechanical or thermal shock loading. There are a number of ways to simulate mechanical shock waves using microcanonical MD simulations; the common feature among them is that they involve collisions between two pieces of material with relative velocity sufficiently large that the resulting wave propagation is supersonic and features a near-discontinuous pressure gradient as opposed to an acoustic disturbance that moves at the sound speed and evolves smoothly according to the linear wave equation.<sup>17–19</sup> The most common approach is to simulate a rigid slab of material (a piston or flyer plate) that impacts with whole-body velocity  $U_p$  onto (or, equivalently, is impacted by) a finite-length sample of material in which the resulting dynamics will be studied; this leads to a supported shock wave in the sample for which the shock velocity  $U_s$  is constant in time. Periodic boundary conditions with fixed simulation cell dimensions are applied in the directions transverse to shock propagation so that the resulting volumetric compression is uniaxial. When the shock wave reaches the free surface of the sample a reflected wave is generated that propagates rapidly back into the shocked sample, thereby limiting severely the time for which a given volume element in the material remains in the thermodynamic state resulting from the initial shock. (The locus of thermodynamic states accessible by shock loading from a given initial thermodynamic condition is known as the Hugoniot.<sup>20</sup>) Thus, due to the speed at which a shock wave passes through a sample, one typically needs to consider simulation cells that are quite long in the direction parallel to shock wave propagation; for example, the transit time for a shock propagating with a velocity of 5 km/s through a sample of length 100 nm is only 20 ps. This issue is particularly challenging in case of molecular organic crystals where formation of defects, transitions to a new phase, or complex chemistry typically involve activated processes whose induction time will often exceed considerably the shock wave transit time across any simulation cell that could be studied with existing computers.

A modification to standard microcanonical shock simulation methods designed to mitigate the need for extremely large simulation cells has been proposed recently by Thompson and co-workers.<sup>21,22</sup> The approach, known as the shock front absorbing boundary condition (SFABC), entails the carefully timed introduction/application of a second confining piston in the simulation cell that serves to capture the shocked sample at the moment of maximum compression in a way such that the initial volume/energy state generated by the shock is sustained. Implementation of the SFABC algorithm ensures that no reflected waves propagate back through the sample; therefore, observation times in the shock-

compressed material can be extended indefinitely. Another useful feature of the SFABC is that, since it is implemented entirely in the microcanonical (*NVE*) ensemble,<sup>23</sup> the detailed dynamics are “exact” throughout the simulation. Nevertheless, this method does have drawbacks as discussed in Ref. 22, the most severe of which is that it does not guarantee that the initially shocked material will remain on the Hugoniot locus should physical or chemical relaxations occur. This is critical if such processes are accompanied by large density or energy changes.

Other approaches exist for atomic-scale simulations of matter on the Hugoniot locus. Among these are the Hugoniotstat<sup>24,25</sup> method, the multiscale MD/continuum approach,<sup>26,27</sup> and a very recent approach for sampling, via a nonlinear stochastic process, microscopic configurations of a system on the Hugoniot, properly distributed according to a canonical (Boltzmann–Gibbs) measure.<sup>28</sup> Although these methods differ in significant ways, the feature common among them is that they enable simulations of shocked states without the need to treat extremely large simulation cells. In particular, the purpose of the Hugoniotstat approach, which is described in more details in Sec. II, is to reproduce the final state of the shock-compressed material while bypassing the need to resolve the shock wave explicitly; instead the system is uniaxially and homogeneously compressed at a finite strain rate while dynamic, integral feedback ensures that the final shocked state satisfies the Rankine–Hugoniot relations for mass, momentum, and energy. This method has been applied extensively to study plastic deformations in a number of atomic crystals including metals and metal oxides,<sup>29,30</sup> but has yet to be applied to the study of polyatomic energetic materials.

In the present study we apply the Hugoniotstat method to  $\alpha$ -hexahydro-1,3,5-trinitro-1,3,5-triazine crystal (RDX). Our choice of RDX for this work is motivated by several factors. First, while RDX is a comparatively well characterized HE material that is used in a number of important HE formulations, the details of structural transformations in this material under shock loading are not completely understood. Second, at room temperature and pressure, RDX crystallizes into an orthorhombic unit cell that contains eight molecules in the *Pbca* space group; while obviously far more complicated than a simple metal, the orthorhombic symmetry class of  $\alpha$ -RDX crystal simplifies considerably the implementation of the Hugoniotstat method. Finally, large-scale MD simulations of RDX shock loading along the [100] direction have been reported based on the SFABC approach,<sup>22</sup> therefore allowing a head-to-head comparison of the results obtained using the Hugoniotstat method to those resulting from microcanonical MD methods. This latter point is particularly important for two reasons: First, the Hugoniotstat simulations are performed using equations of motion that are derived from an extended Lagrangian, whereas “standard” MD simulations of shocks, including the SFABC approach, are performed using Newton’s equations in unmodified form in the microcanonical (*NVE*) ensemble; second, given the comparatively large size and complexity of the RDX molecule, including its non-spherical shape and the presence of 57 intramolecular degrees of freedom per isolated molecule, along with its com-

paratively low crystal symmetry (compared to bcc metals for instance), it is important to benchmark the Hugoniot predictions against those obtained from large-scale MD to ensure that the fundamental processes predicted by the former coincide with those of the latter and that, for example, the small system sizes used in Hugoniot simulations do not suppress mechanical instabilities that might occur on larger length scales.

## II. SIMULATION DETAILS

### A. Force field

To our knowledge the only RDX-specific flexible-molecule force field that has been published is the one due to Boyd *et al.*<sup>31</sup> However, Cawkwell *et al.*<sup>22</sup> determined that the force field developed by Smith and co-workers<sup>32,33</sup> for simulation of HMX—another cyclic nitramine compound with a similar molecular structure ( $C_4H_8N_8O_8$ ; HMX is simply the eight-member ring analog of RDX)—yielded accurate predictions for the room temperature and room pressure unit cell lattice parameters and elastic tensor, atmospheric pressure coefficient of thermal expansion, and room temperature isothermal compression curve for RDX.<sup>22,34</sup> Moreover they also found that under hydrostatic compression simulations using this force field predict a transition between the  $\alpha$  and  $\gamma$  polymorphs. Therefore, to enable a direct comparison between the results obtained here using the Hugoniot approach and those obtained previously by Cawkwell *et al.*<sup>22</sup> using the SFABC approach, we used the same force field as Cawkwell *et al.*

### B. Hugoniot method

Conceptually the Hugoniot method is similar to the conventional isobaric-isothermal simulation protocols proposed by Nosé<sup>35</sup> and Hoover<sup>36</sup> in that it couples, via a set of extra degrees of freedom  $\eta$  and  $\zeta$  in the equations of motion, a system of particles to an external bath in a way that drives the system toward the thermodynamic state and statistical mechanical ensemble of interest. Here the thermodynamic state is specified using the Rankine–Hugoniot relations<sup>37</sup> that enforce mass, momentum, and energy conservation in the pre- and post-shock states of the material. The extra degree of freedom  $\eta_i$  corresponds to dimensionless strain rate and plays the role of a *piston* or a *barostat* that ensures that the component of stress in the direction of wave propagation  $i$  stays at the desired value  $P_{ii}$ . The remaining degree of freedom  $\zeta$  is the dimensionless heat-flow variable (the *ergostat*), which ensures that the internal energy of the system satisfies the Hugoniot relation for energy,

$$E_H = E_0 + 0.5(P_{ii} + P_0)(V_0 - V), \quad (1)$$

where the subscripts “0” and  $H$  refer to properties in the unshocked material and on the Hugoniot locus, respectively;  $E$ ,  $V$ , and  $P$  are internal energy, specific volume, and pressure, respectively. During a Hugoniot simulation an integral feedback scheme analogous to that in isobaric-isothermal ( $NPT$ ) MD simulations is used to sustain  $P_{ii}$  and  $E_H$  at the desired values. The final equations of motion for the Hugoniot are<sup>25</sup>

$$\begin{aligned} \dot{r}_i &= u_i + \nu_P \eta r_i, \\ \dot{u}_i &= a_i - (\nu_P \eta + \nu_H \zeta) u_i, \\ \dot{L}_i &= \nu_P \eta L_i, \\ \dot{\zeta} &= \frac{\nu_H}{W_E} (E - E_H) - \beta_H \zeta, \\ \dot{\eta} &= \frac{\nu_P}{B_0} (P_{ii} - \sigma_{ii}) - \beta_P \eta. \end{aligned} \quad (2)$$

In these equations  $i$  denotes the direction of shock compression and  $L_i$  denotes the length of the simulation cell along that direction; for the orthogonal directions  $\eta$ ,  $\dot{\eta}$ , and  $\dot{L}$  each have zero magnitude (in general  $L$  is a vector whose components are unequal, but here only the component  $L_i$  varies with time since by construction the compression is uniaxial). The quantities  $\nu_H$  and  $\nu_P$  are coupling rate parameters (or frequencies) for the heat-flow (ergostat) and strain-rate (barostat) variables, respectively, and  $\beta_H$  and  $\beta_P$  are the corresponding damping coefficients. The material bulk modulus at the initial pressure is  $B_0$ . The unsubscripted variables  $E$ ,  $V$ , and  $\sigma_{ii}$  are instantaneous values of the internal energy, specific volume, and stress tensor component parallel to the shock direction. The instantaneous value of  $E_H$  is determined using Eq. (1) with  $P_{ii}$  replaced by  $\sigma_{ii}$ . Finally, the parameter  $W_E$  is the ergostat mass, which controls the rate of the heat flux to/from the system when deviation of the instantaneous internal energy from the target Hugoniot energy [Eq. (1)] is detected.

When applied to atomic crystals earlier versions of the Hugoniot method,<sup>24</sup> as well as other approaches where uniaxial compression was imposed instantaneously (i.e., infinite strain rate),<sup>25</sup> resulted in disordering of the material that was not observed in MD simulations with an explicit shock wave. By contrast, simulations of atomic crystals using the Hugoniot method described above, in which both the barostat and ergostat have dynamical feedback with the system, yielded good agreement with simulation results for uniaxial compression using an explicit shock wave.<sup>25</sup> Specifically, in addition to predicting accurately the pressure-volume-temperature dependence of the crystal below and above the Hugoniot elastic limit (HEL), simulations using the barostat-ergostat Hugoniot method also predicted structural deformations and defect densities similar to those observed in the explicit shock studies. While the success of the Hugoniot approach has been demonstrated in several preceding works it is necessary to remember that, as with any Nosé–Hoover-like constraint method, the Hugoniot only guarantees that the average of the constrained property is equal to the desired value. Thermodynamic fluctuations observed in this kind of simulation can depend on coupling parameters controlling the extended degrees of freedom (e.g., barostat and ergostat frequencies and damping constants). The detailed influence of those parameters on thermodynamic fluctuations and final results in Hugoniot simulations has not to our knowledge been systematically investi-

gated, although a more sophisticated constrained simulation method has been proposed recently that reduces some of this uncertainty in parameter selection.<sup>28</sup>

### C. Selection of simulation parameters

As discussed extensively in the original papers on the Hugoniosat method,<sup>24,25</sup> the selection of parameters associated with the extended degrees of freedom should be performed with care in order to minimize uncertainties and potential artifacts in prediction of the HEL. Here, the choice of physically reasonable values for coupling and damping parameters was based on recommendations of Ravelo and co-workers.<sup>25,38</sup> The ergostat parameter  $\nu_H$  was chosen to be close to the mean natural lattice frequency of RDX molecules in the crystal at 295 K, obtained from the Fourier transform of the RDX molecular center-of-mass velocity autocorrelation function calculated from equilibrium MD simulations in the *NVT* ensemble. Based on this exercise a value of  $\nu_H = 1.5 \text{ ps}^{-1}$  was used in all our simulations. The parameter  $\beta_H$  was set to  $2\nu_H = 3.0 \text{ ps}^{-1}$  to ensure critical damping of the heat flow.<sup>25</sup>

The barostat frequency  $\nu_P$  was chosen such that the maximum strain rate imposed by the piston in the Hugoniosat simulation is close to but not higher than the strain rate observed in the shock wave during explicit shock MD simulations. The latter was estimated as  $u_p/\lambda$ , where  $u_p$  is the piston velocity and  $\lambda$  is the observed shock wave thickness as obtained from SFABC simulations of shock compression of RDX.<sup>22</sup> Analysis of temperature and density profiles from SFABC simulations of shock propagation along the [100] direction with  $u_p = 1 \text{ km/s}$  (corresponding to a Hugoniot shock pressure of 7.9 GPa) yielded a shock wave thickness  $\lambda$  on the order of 2 and 3 nm. This provides us with an estimate of  $0.3\text{--}0.5 \text{ ps}^{-1}$  for the maximum strain rate. Thus, to achieve a comparable strain rate, as well as its critical damping, values  $\nu_P = 5 \text{ ps}^{-1}$  and  $\beta_P = 30 \text{ ps}^{-1}$  were employed. To verify that the final results of Hugoniosat simulations were insensitive to the choice of the barostat parameters, for compression along the [100] direction we conducted simulations for  $P_{xx} = 9.5 \text{ GPa}$  with  $\nu_P = 10.0$  and  $2.5 \text{ ps}^{-1}$  while keeping all other parameters the same. In these simulations the maximum strain rate was a factor of two different (larger/smaller) than in simulations using  $\nu_P = 5 \text{ ps}^{-1}$ . While the evolution of extent of compression and temperature in these runs was different during the initial stages, they both converged to the same final state as the simulation using our nominal frequency  $\nu_P = 5 \text{ ps}^{-1}$ . The final compression states for all three runs were very similar, while all final temperatures were within a degree of one another. Interestingly, simulations using the larger strain rate initially showed overheating of the system by about 20 K (compared to the final temperature). However, as those simulations continued the system cooled down to essentially the same temperature as observed in the other two systems. This indicates that so long as the selected barostat parameters are within a broad, physically reasonable range, the final state of the Hugoniosat simulation should be independent of the choice of those parameters.

Finally, the mass parameter  $W_E$  was chosen such that the

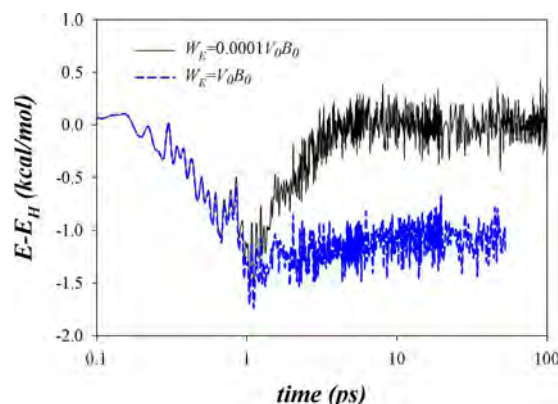


FIG. 1. Time evolution of the Hugoniot energy difference per molecule  $E - E_H$  obtained from Hugoniosat simulations of shock compression along [100] using two different  $W_E$  parameters for the case  $P_{xx} = 8.0 \text{ GPa}$ . [See Eq. (2).]

ergostat effectively controls the heat flux to/from the system with a response/relaxation time that is fast compared to the few-to-several hundred picosecond overall time scales of our simulations. As can be seen from Eq. (2), if  $W_E$  is too large compared to the  $E - E_H$  difference then the ergostat variable  $\zeta$  will vary slowly, therefore requiring long simulation trajectory times to ensure complete sampling at a given Hugoniot state. If on the other hand  $W_E$  is too small then the energy flux to/from the system will be unphysically fast, which can lead to an inappropriate energy distribution for intramolecular degrees of freedom. In previous Hugoniosat simulations of atomic crystals different choices for the value of  $W_E$  were used. In some simulations  $W_E = B_0 V_0$  was used,<sup>25</sup> whereas in another study  $W_E = E_{\text{coh}}$  was used, where  $E_{\text{coh}}$  is the cohesive energy of the system.<sup>38</sup> We determined empirically that for our simulations of RDX crystal use of  $W_E = 0.0001 B_0 V_0$  ensures that, subsequent to the initial transient during equilibration, there are no significant deviations of the internal energy  $E$  from the Hugoniot energy condition  $E_H$  (Eq. (1)). By contrast, simulations with  $W_E = B_0 V_0$  led to sluggish response of the ergostat which would require a very long simulation trajectory to achieve the Hugoniot energy condition. This is clearly illustrated in Fig. 1 where we show the evolution of  $E - E_H$  per RDX molecule as a function of time for Hugoniosat simulations using these two different values for  $W_E$ .

### D. Simulation protocol

Hugoniosat simulations using Eq. (2) were conducted using the finite difference integration scheme given by Holian and Ravelo.<sup>38</sup> Three-dimensionally periodic primary simulation cells with dimensions of  $81.3 \times 68.7 \times 63.9 \text{ \AA}^3$  and  $122.2 \times 102.8 \times 95.8 \text{ \AA}^3$ , corresponding to 1728 and 5832 RDX molecules, respectively, were studied for an initial temperature of 300 K and atmospheric pressure. These initial conditions correspond to molecular volume of  $V_0 = 206.5 \text{ \AA}^3$  and total energy per molecule (including intramolecular contributions) of  $E_0 = 335.8 \text{ kcal/mol}$ . A time step of 0.2 fs was used in all cases to allow accurate treatment of the rapidly varying intramolecular degrees of freedom (bonds and bends). A cutoff radius of 10.0  $\text{\AA}$  was used for nonbonded interactions and for the real part of electro-



static interactions. The particle mesh Ewald approach was used to calculate the reciprocal part of electrostatic interactions;<sup>39</sup> an  $\alpha$  parameter  $\alpha=0.3$  was used in conjunction with 70 and 110 grid points for systems containing 1728 and 5832 molecules, respectively. For each system size five independent initial configurations were created by extracting snapshots at 10 ps intervals from a conventional isochoric-isothermal (*NVT*) simulation in the uncompressed state at a temperature  $T_0=300$  K. As pointed out above, the center-of-mass velocity autocorrelation function in RDX crystal at 300 K decays on the order of a few hundred femtoseconds; therefore a 10 ps interval between successive snapshots is sufficiently long to yield uncorrelated phase space points for subsequent studies. Production run lengths using the Hugoniotat methodology were at least 300 ps for conditions below the HEL and up to 1.0 ns for systems at or above the HEL.

### III. RESULTS AND DISCUSSION

#### A. Compression along the [100] direction

We begin our discussion with analysis of the uniaxial compression along the [100] crystal direction, which corresponds to the  $x$ -axis in our chosen laboratory frame. Taking into account the reported indentation data for RDX at room temperature and atmospheric pressure,<sup>40,41</sup> no known slip system should be activated for shocks propagating along this direction. Cawkwell *et al.*<sup>22</sup> in their SFABC study considered shocks propagating along the [100] direction for shock pressures of 5.0 and 7.9 GPa;<sup>42</sup> the results for 5.0 GPa shocks indicate elastic response whereas those at 7.9 GPa lead to inelastic deformation characterized by formation of nanoscopic *shear bands* in the material. Therefore, the HEL for RDX shocked in the [100] direction is somewhere between these two pressures.

Analysis of plate impact experiments for oriented RDX single crystals shocked in the [100] direction with maximum stress of about 2.25 GPa revealed several unexpected and peculiar features in the measured velocity profiles, including large shot-to-shot variation in the observed profiles;<sup>43</sup> it was noted in that same study, however, that crystals prepared for shocks in the [100] direction were highly subject to cracking, which may have some role in the observed results. A time-resolved Raman spectroscopy study of RDX single crystals under hydrostatic and shock loading showed that independent of loading type (hydrostatic compression versus planar shock wave) and crystal orientation (shocks along the [111], [210], and [100] were investigated), the  $\alpha$ - to  $\gamma$ -RDX phase transition occurred for pressures above 3.9 GPa.<sup>44</sup> Interestingly, an induction time of at least 100 ns after reaching the maximum stress elapsed prior to observation of the transformed phase. Practical limits on computing resources preclude us from performing such long simulations; therefore, we would not expect *a priori* to observe the  $\alpha$ - $\gamma$  transition in the present study.

#### 1. Time evolution

In Figs. 2(a)–2(d) we show, respectively, the time evolution of the stress component  $\sigma_{xx}$  parallel to [100] in the crys-

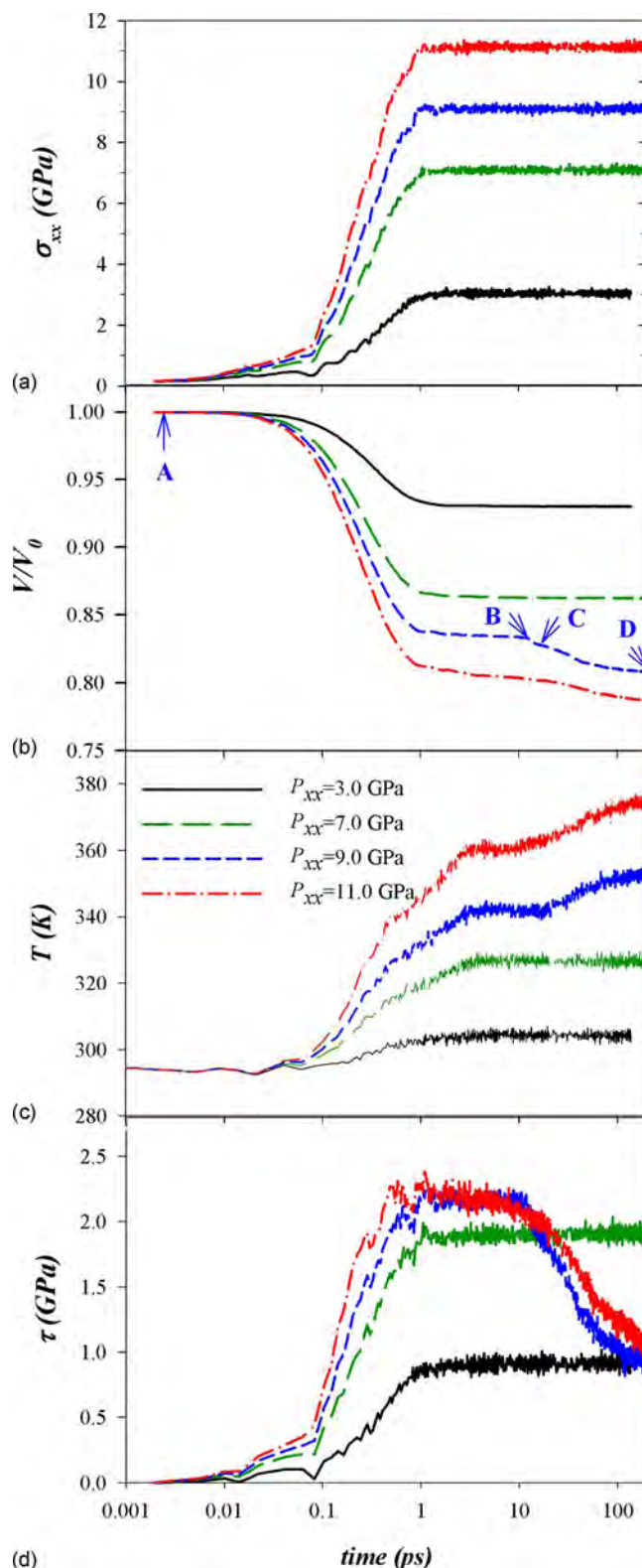


FIG. 2. Time evolution of (a) stress along compression direction, (b) volumetric compression ratio, (c) temperature, and (d) shear stress in RDX crystal obtained from Hugoniotat simulations of shock compression along [100] for various shock strengths below and above the HEL.

tal, the volume compression ratio  $V/V_0$ , the temperature  $T$ , and the shear stress  $\tau=0.5(\sigma_{xx}-0.5(\sigma_{yy}+\sigma_{zz}))$  obtained from Hugoniotat simulations for shock pressures of  $P_{xx}=3.0, 7.0, 9.0$ , and 11.0 GPa. Figure 2(a) indicates that for all systems the desired stress along the shock direction is reached within

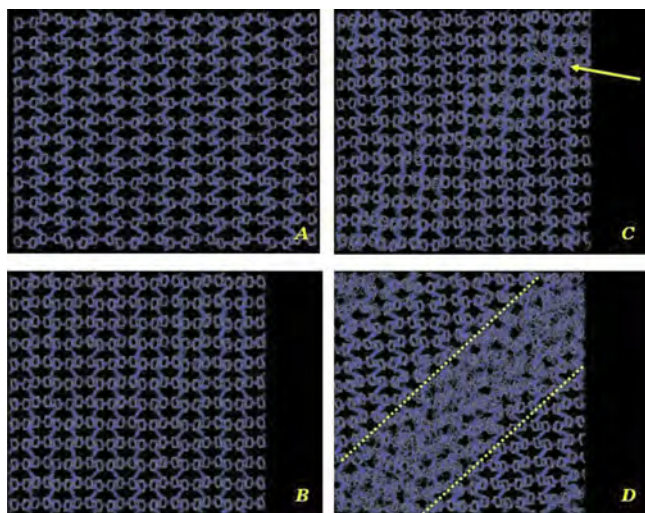


FIG. 3. Snapshots obtained from Hugoniotat simulations of RDX crystal (1728 molecules) shocked along [100] with  $P_{xx}=9.0$  GPa: (a)  $t=0$  ps, (b)  $t=10$  ps, (c)  $t=15$  ps, and (d)  $t=200$  ps. For picture clarity only carbon and nitrogen atoms are shown.

1 ps of simulation after which the instantaneous value fluctuates around the target value  $P_{xx}$ . Note the absence of overshoot in  $\sigma_{xx}$  at early time and also that at no point in the simulation is  $\sigma_{xx}$  significantly larger than the imposed shock pressure  $P_{xx}$ ; these features indicate that the value of the damping parameter  $\beta_p$  is appropriate with the consequence that the probability of spurious structural deformations in the material arising due to artificial, large-amplitude overshoot or subsequent excursions of the stress is minimized.

In Fig. 2(b) the evolution of the volumetric compression ratio  $V/V_0$  (which in this study is equal to the uniaxial compression ratio  $x/x_0$ ) is shown for the same set of shock pressures as in Fig. 2(a). For the cases  $P_{xx}=3.0$  and  $7.0$  GPa the strain increases smoothly to a final value within 1 ps. By contrast, for  $P_{xx}=9.0$  GPa the system compresses to  $V/V_0 \sim 0.83$  during the first picosecond, remains at this compression for about 9 ps longer, and then undergoes a subsequent compression to  $V/V_0 \sim 0.807$  indicating some kind of physical relaxation in the material. The analysis of system snapshots extracted from different points along this trajectory and shown in Fig. 3 allows better understanding of the structural changes that occur for this shock pressure. As can be seen by comparing snapshots A ( $t=0$  ps) and B ( $t=10$  ps), despite a noticeable compression along the [100] direction the essential crystal symmetry is preserved suggesting that the material has undergone elastic deformation. However, snapshot C ( $t=15$  ps) exhibits local regions with significant translational, orientational, and conformational disorder compared to the adjacent elastically compressed crystal; these eventually grow and lead to a region of amorphized material oriented at  $45^\circ$  relative to [100] and zonal to [010]—a nanoscale shear band (snapshot D,  $t=200$  ps). Similar behavior is observed for  $P_{xx}=11.0$  GPa, although at this higher pressure the induction time between initial compression and first appearance of obvious defects in crystal structure is decreased, leading to a nearly continuous strain increase as a function of time. The results shown in Figs. 2(a), 2(b), and 3 clearly

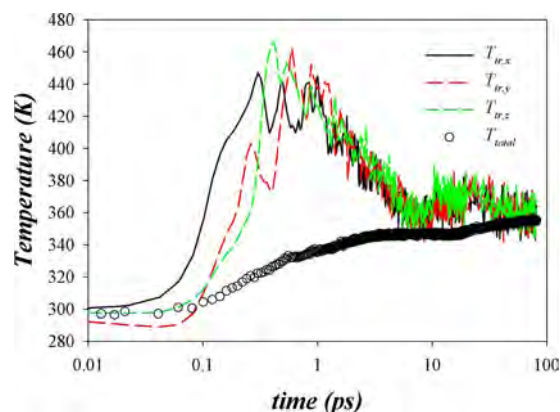


FIG. 4. Time evolution of total temperature and temperature corresponding to molecular translational quasitemperatures obtained from Hugoniotat simulations of shock compression along [100] at  $P_{xx}=9.0$  GPa.

indicate that the HEL for shock compression along the [100] direction in  $\alpha$ -RDX crystal is exceeded for shock pressures larger than about 7.0 GPa, and that the mode of relaxation associated with this mechanical instability is the formation of nanoscale shear bands in the material.

Figure 2(c) shows the time dependence of total temperature (based on the total kinetic energy) in the system for the same set of pressures discussed in the two preceding paragraphs. For pressures below the HEL the temperature increases during the first 3–5 ps of the simulation and then exhibits fluctuations about a constant value. However, for  $P_{xx}=9.0$  and 11.0 GPa a two-step temperature increase is observed. The first, as for the lower pressures, is associated with elastic compression, whereas the second coincides with the nucleation and growth of the shear band; this can be seen clearly by comparing the time evolution of system temperature and extent of compression shown in Figs. 2(b) and 2(c).

It is instructive to compare the time evolution of the quasitemperature defined by molecular translational degrees of freedom to the total temperature. Figure 4 contains time histories for the total temperature and for contributions from molecular (center-of-mass) translational degrees of freedom for shock pressure  $P_{xx}=9.0$  GPa. The latter was defined as  $T_{tr,i} = \sum m_{\text{mol}} v_{\text{com},i}^2 / (3N_{\text{mol}} k_B)$ , where  $m_{\text{mol}}$  is the molecular mass,  $v_{\text{com},i}$  is the velocity of molecular center of mass in the direction  $i$  ( $i=x,y,z$ ),  $N_{\text{mol}}$  is the total number of molecules, and the sum is over all molecules in the system. Note that since a single RDX molecule contains 21 atoms the total number of degrees of freedom per molecule is  $3N=63$ , and therefore together the three translational degrees of freedom account for about 5% of the total. The large difference observed in Fig. 4 between the total temperature, which is dominated by intramolecular vibrations, and quasitemperatures due to translational degrees of freedom clearly illustrates that during Hugoniotat simulations the initial excitation rates and asymptotic time scales for thermalization (redistribution of kinetic energy toward equipartition) differ among the various kinds of degrees of freedom in the system. Specifically, degrees of freedom associated with low frequencies—phonons and low-frequency vibrons—initially absorb significant amounts of kinetic energy, whereas high frequency vibrons, such as covalent bond-stretching or



angle-bending vibrations, are not noticeably excited during the initial compression; several picoseconds are required for the system to approach thermal equilibrium in the new state on the Hugoniot locus.

In Fig. 2(d), the time evolution of the shear stress  $\tau$  is shown for four different pressures. For  $P_{xx}=3.0$  and 7.0 GPa the shear stress reaches a steady value on the time scale for which  $\sigma_{xx}$  reaches the target value  $P_{xx}$ . As expected, the asymptotic value of  $\tau$  is strongly dependent on shock pressure  $P_{xx}$ . However, for both  $P_{xx}=9.0$  and 11.0 GPa initially (i.e., in the region of quasielastic compression prior to shear band formation)  $\tau$  reaches the same plateau value  $\tau \sim 2.3$  GPa; as the shear bands grow into the material the shear stresses reduce considerably. From these results we conclude that  $\tau \sim 2.3$  GPa is approximately the maximum shear stress that RDX crystal can support under uniaxial compression along [100]. Uniaxial compressions that would drive the system toward higher shear stress result in a mechanical instability; in this case amorphization and shear band formation.

The reduction in the shear stress observed in the simulations at longer times accompanying shear band formation is puzzling. We think that this behavior is an artifact of the small system size coupled with the use of periodic boundary conditions in the simulations. Specifically, the shear band that forms transits completely the primary simulation cell and therefore is of infinite length due to periodic boundary conditions [cf. Fig. 3(d)]. In realistic, macroscopic size crystals shear bands are of finite extent (for instance, they do not typically cross one another even in isotropic media) and therefore a crystal crisscrossed with finite shear bands can still support a shear stress, albeit one that is weaker than in the elastic regime. (See also Fig. 5 in Ref. 22.)

## 2. Pressure-volume-temperature dependence

Thermodynamic properties on the Hugoniot locus for  $\alpha$ -RDX crystal shock loaded along [100] as obtained from Hugoniotat simulations are shown in Fig. 5. In Fig. 5(a) the final volume compression ratio  $V/V_0$  of the system, obtained from averaging over the last 50 ps of the trajectory, is shown as a function of applied shock pressure  $P_{xx}$ . Error bars are comparable to the symbol size. A clear steplike change in the  $P$ - $V/V_0$  dependence that corresponds to the HEL can be seen at  $P_{xx} \sim 8.0$  GPa. Also shown in Fig. 5(a) are the results from Ref. 22 that were obtained using the SFABC explicit shock wave simulation method. It can be seen that whereas below the HEL shock pressure the SFABC yields a slightly larger compression compared to the Hugoniotat method, above the HEL the opposite effect is observed.

As was discussed in Ref. 22 and in Sec. I of this article, while the isoergic-isochoric state captured by application of the SFABC does, by construction, correspond to the volume and energy of the shocked sample at the moment the SFABC is applied, subsequent physical or chemical relaxations in the material may cause the SFABC stress/volume/energy state to depart from the Hugoniot conditions [Eq. (1)] at subsequent times. The Hugoniotat method, on the other hand, imposes a constant stress condition along the compression direction and therefore, by construction, ensures that the asymptotic state

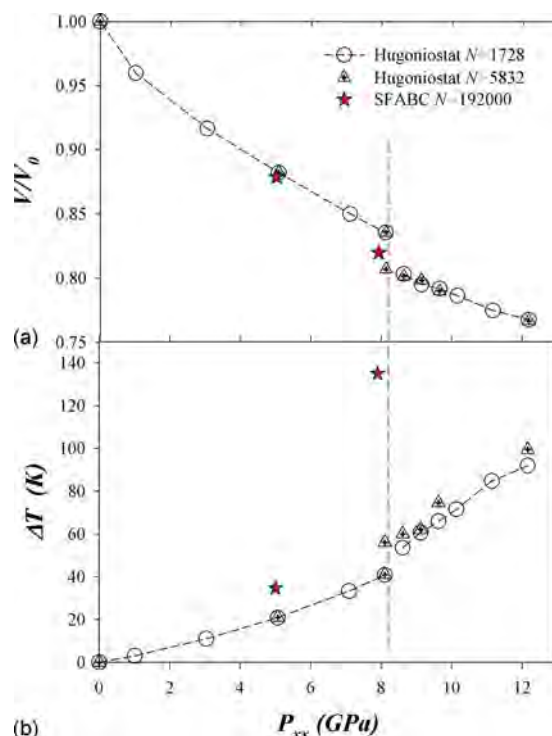


FIG. 5. (a) Final strain and (b) temperature of RDX shocked along [100] as a function of shock pressure  $P_{xx}$  obtained from Hugoniotat simulations (present study) and SFABC simulations (Ref. 22).

of the shocked material will remain on the Hugoniot locus defined by the Rankine–Hugoniot jump conditions. However, the detailed dynamics of the system on the way to this asymptotic state and thermodynamic fluctuations can potentially deviate from those that would be obtained in the natural system due to the presence of the extended degrees of freedom in the equations of motion associated with the Hugoniot constraint. The results in Fig. 2 demonstrate that for conditions above but close to the HEL in  $\alpha$ -RDX shocked along [100], the development of shear bands with concomitant changes in system strain and other quantities occurs over hundreds of picoseconds. Since in the SFABC simulations the system is captured in an isochoric state after only about 40 ps, by which time the shear bands are not fully developed, it is not surprising that the final system strain obtained from this simulation is smaller than the one obtained from Hugoniotat simulations. Moreover, as shear bands continue to form in the SFABC simulation after transition to isochoic-isoergic conditions, the stress in the shock direction will reduce and hence the final state of SFABC simulation would not coincide with the shock state established initially at the instant of application of the second piston in the SFABC.

In Fig. 5(b) the temperature rise  $\Delta T = (T_{\text{final}} - T_0)$  is shown as a function of shock pressure. As the shock pressure increases the temperature of the shocked material increases. The increase is smooth until the shock pressure exceeds the HEL, at which point a jump in the temperature rise is observed. Figure 5(b) also shows that below the HEL the temperature rise predicted from the SFABC simulations of Cawkwell *et al.*<sup>22</sup> is comparable to those obtained from Hugoniotat simulations. The greater temperature rise in the case of SFABC simulations compared to Hugoniotat simu-

lations for states below the HEL can be understood by taking into account that whereas C–H bond lengths were constrained in the SFABC simulations, in the Hugoniotat simulations no geometric constraints were applied. Consequently the specific heat in the SFABC simulations was somewhat lower than in the Hugoniotat simulations. Because of this difference, the temperature in the SFABC simulations in Ref. 22 at a given shock strength would be expected to be somewhat larger than those in our Hugoniotat studies (see also the discussion in the following paragraph). By contrast, above the HEL the SFABC method predicts a temperature rise significantly larger than those of the Hugoniotat simulations. It is difficult to determine with certainty the exact source(s) of this discrepancy. We think, however, that the explanation originates at least partially from the fact that SFABC simulations above the HEL underestimate the final compression and stress in the shock direction, which can result in a release of larger amount of stored elastic energy and hence increased heating. Another potential source for significantly higher temperature increase during SFABC simulations is viscous heating in shear bands between sliding crystal domains. Examination of Fig. 4 in Ref. 22 indicates that the shear bands formed in those simulations are also infinite (due to periodic boundary conditions) in the directions lateral to shock wave propagation. Because parts of simulated sample have nonzero momentum ( $U_p$  in the direction of the shock wave), this can cause excessive (artificial) sliding of crystal domains along the shear bands leading to substantial viscous heating. In a real macroscopic system shear bands are not infinite and therefore substantial sliding of crystal domains is less likely due to the presence of percolating continuous crystal domains [cf. Fig. 5 in Ref. 22 which was obtained from a (quasi-2D) simulation]. Unfortunately, Ref. 22 does not report the extent of heating for the quasi-2D simulation, but we speculate that the heating there would be smaller. Finally, in our Hugoniotat simulations, as pointed above, the formed shear bands are also infinite due to periodic boundary conditions; however, by construction in the Hugoniotat approach, the system compression is implemented through rescaling of simulation cell dimension during which the position of *all* atoms is rescaled. In this case there is no net momentum creation for any part of simulated material and hence there are no driving forces to create extensive sliding of crystal domains along the nascent shear bands. Hence, no excessive viscous heating is observed in the Hugoniotat simulations. We are currently conducting further investigations of these effects and will report on them in future publications.

It is also important to note that the Debye temperatures for high frequency vibronic modes are far higher than room temperature; therefore, in the true quantum system, most of those modes would be almost exclusively in the respective vibrational ground states for the conditions studied here. However, since in the present simulations all degrees of freedom are treated classically, equipartition results in  $k_B T/2$  of kinetic energy per degree of freedom, resulting in a higher heat capacity and lower shock Grüneisen parameter compared to experiments. Our calculations show that for simulations of  $\alpha$ -RDX crystal at 300 K and atmospheric pressure

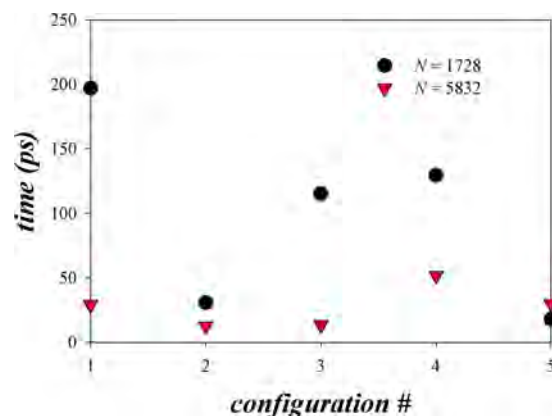


FIG. 6. Time of the onset of shear band instability observed in Hugoniotat simulations of shock compression along [100] for five different initial configurations each for two different size systems. The shock pressure is  $P_{xx} = 8.5$  GPa.

with no bond constraints, the heat capacity is about 2.2 times higher and the Grüneisen parameter is about 1.9 times lower than the values ( $C_v = 1077.0$  J kg K and  $\Gamma = 1.103$ ) estimated using experimental room-temperature values for isobaric heat capacity, the coefficient of volumetric thermal expansion, density, and isentropic bulk modulus.<sup>22</sup> This well-known deficiency associated with the use of classical mechanics to simulate molecular systems results in significant underestimation of shock heating in the Hugoniotat simulations compared to what would be expected in laboratory experiments. A more detailed discussion of the potential influence of this issue for shocks in  $\alpha$ -RDX propagating along [100] can be found in Ref. 22.

### 3. Influence of initial conditions and system size

As described above in Sec. II, five independent initial conditions were generated for each system studied. For  $P_{xx}$  below the HEL the final compression and temperature rise were basically indistinguishable for all initial configurations and both system sizes. However, above the HEL some variation between properties obtained from different systems was observed. For example, for  $P_{xx} = 8.0$  GPa one of the five systems considered for  $N=5832$  eventually deformed inelastically, while the other four systems, as well as all five systems with  $N=1728$ , did not do so over the entire simulation. The onset time for inelastic deformation to occur near the HEL can vary significantly as illustrated in Fig. 6, where we show for  $P_{xx} = 8.5$  GPa the time corresponding to onset of shear band nucleation characterized by the beginning of the second step relaxation in the time evolution of  $V/V_0$  (e.g., point C in Fig. 2(b)). For the smaller system ( $N=1728$ ) the spread of this onset time spans almost an order of magnitude. By contrast, the larger system ( $N=5832$ ) led to a significantly smaller range of values for the onset time of shear band formation. Thus, while each of the simulations eventually reaches the same compression, the larger size systems reach that value considerably faster than smaller ones for shock strengths above but close to the HEL. For higher pressures (not shown) the spread in onset time observed for different instances of the same system practically disappears,

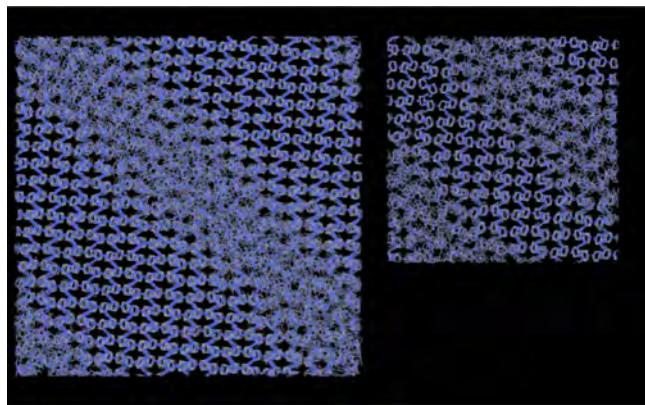


FIG. 7. Final snapshots from Hugoniot simulations of RDX crystal compressed along [100] at  $P_{xx}=9.5$  GPa using two different size systems ( $N=1728$  and  $N=5832$ ). For picture clarity only carbon and nitrogen atoms are shown.

although larger systems always exhibit a somewhat faster onset of inelastic deformation than do the smaller systems at a given pressure.

The comparison in the preceding paragraph illustrates that the larger system is more robust for identifying the HEL. Presumably this is because nucleation of the shear band instability is thermally activated, such that the probability to nucleate the first shear band in the system in some fixed time interval is simply proportional to system size. However, taking into account the increased computational expense for the larger system it turns out to be almost equivalent computationally to run smaller systems for longer times. Also away from the HEL threshold the smaller systems seem to capture all of the essential features of the physics while requiring considerably less computational effort. On the other hand, taking into account that shear bands involve at least a few molecular layers, at a minimum one should take care not to use simulation cell dimensions comparable to the width of the shear band since doing so would surely lead to an artificial suppression of instabilities. In Fig. 7 we compare snapshots of shear bands formed at  $P_{xx}=9.5$  GPa for the two system sizes studied here. The results in Fig. 7 indicate that the width of the shear bands is essentially independent of the system size for the two cases considered. However, from examination of Fig. 5 it appears that despite essentially equal extents of compression for the two different sized systems, the temperature rise for shock states above the HEL is systematically a few degrees higher for the larger ones, indicating some influence of the system size. Finally, we want to point out that the shear bands observed in Ref. 22 from SFABC simulations were noticeably wider, and the temperature rise significantly larger, than the corresponding results obtained in the current work. While above we provided several potential sources for the noted discrepancies, based on the simulation data that are currently available we cannot definitively conclude that the finite-size effect does not make some contribution to the observed differences. It is possible that while the current Hugoniot simulations capture the dominant features of the shock deformation, the small system sizes may potentially impose some artifacts on the final state of the material, one of which is a decreased extent of

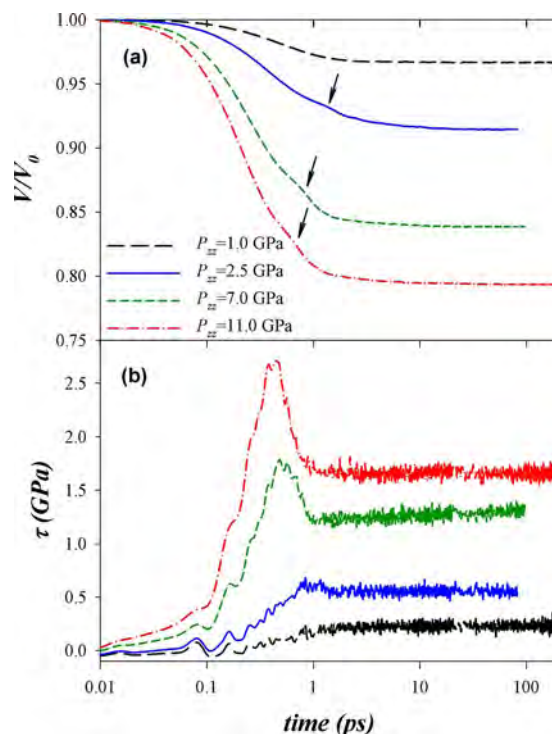


FIG. 8. Time evolution of (a) volume compression ratio and (b) shear stress of RDX crystal obtained from Hugoniot simulations of shock compression along [001] direction at various shock loadings.

amorphization and viscous flow (note that the “shear band” for the smaller system shown in Fig. 7 still retains some evidence for translational and possibly orientational order) with a corresponding smaller amount of heating behind the shock. This issue will be further investigated in future studies.

## B. Compression along the [001] direction

We also investigated the shock compression of  $\alpha$ -RDX crystal along the [001] direction, corresponding to the  $z$  direction in our simulations. While we are unaware of any experimental data for shock loading along this direction, previous simulations<sup>45</sup> of uniaxial compression along this direction exhibited the  $\alpha$ - to  $\gamma$ -RDX phase transition for pressures above 2.0 GPa. Moreover, Gupta and co-workers<sup>44</sup> reported a lack of crystal orientation dependence for the  $\alpha$ - $\gamma$  phase transformation in their studies of shock loading on (111), (210), and (100) planes.

Hugoniot simulations for compression along the [001] direction were conducted for a wide interval of pressures following a simulation protocol similar to that described above for compression along [100]. In Fig. 8(a) we present the time evolution of the compression ratio for a sampling of the pressures studied. For  $P_{zz} < 2.0$  GPa a featureless, monotonic approach to a steady-state value is observed. For higher pressures, however, a shoulder can be observed prior to reaching the plateau value, possibly indicating the onset of some conformational or structural transition in the material. The analysis of the crystal at these compressions confirmed that this shoulder is a signature of the  $\alpha$ - to  $\gamma$ -RDX phase transition. Figure 9 illustrates the difference between confor-



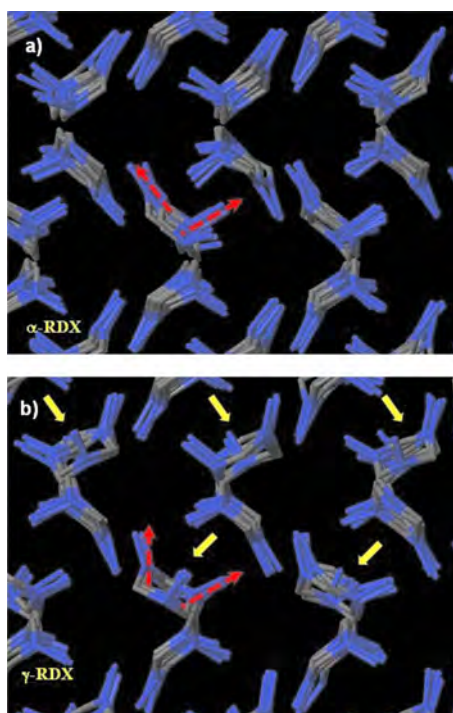


FIG. 9. Snapshots of molecular conformations in RDX crystal (a) in the unshocked state ( $\alpha$ -RDX) and (b) shocked along [001] direction with  $P_{zz} = 2.5$  GPa ( $\gamma$ -RDX). Only carbon and nitrogen atoms are shown. Solid arrows indicate molecules which have undergone conformational transition, dashed arrows illustrate changes in orientation of nitro groups for one of those molecules which has undergone conformational transition.

mations in the initial state (uncompressed  $\alpha$ -RDX crystal, panel a) and the final state obtained for  $P_{zz} = 2.5$  GPa ( $\gamma$ -RDX crystal, panel b). The latter corresponds to the  $Pca2_1$  space group seen previously in the simulations of Cawkwell and Sewell<sup>45</sup> and for which Davidson *et al.*<sup>46</sup> reported the complete experimental structure determination recently.

Figure 8(a) also shows that even for relatively high uniaxial compressions along the [001] direction there is no indication of the amorphization that was observed for compressions along [100]; that is, there is no evidence for a subsequent significant change in volume following the initial compression. This is further supported by Fig. 8(b) where the time evolution of the shear stress is shown for the same set of shock pressures considered in Fig. 8(a). For  $P_{zz} > 2.0$  GPa the shear stress increases, reaches a maximum, and then relaxes to a steady value that depends on the applied  $P_{zz}$ . The time required to reach the peak shear stress coincides closely with the structural deformations associated with  $\alpha$ - to  $\gamma$ -RDX phase transition. Figure 8(b) further indicates that this transition results in significant lowering of the shear stress in spite of the absence of amorphization in the material. Due to the phase transition, the shear stress obtained for a given shock compression along the [001] direction is noticeably lower than the value obtained for the same shock pressure in the [100] direction. Even at  $P_{zz} = 11.0$  GPa the shear stress is only about 1.7 GPa, indicating a relatively low shear modulus. We speculate that this is one reason why no nanoscale shear banding was observed for compression along [001] even for these relatively high shock pressures.

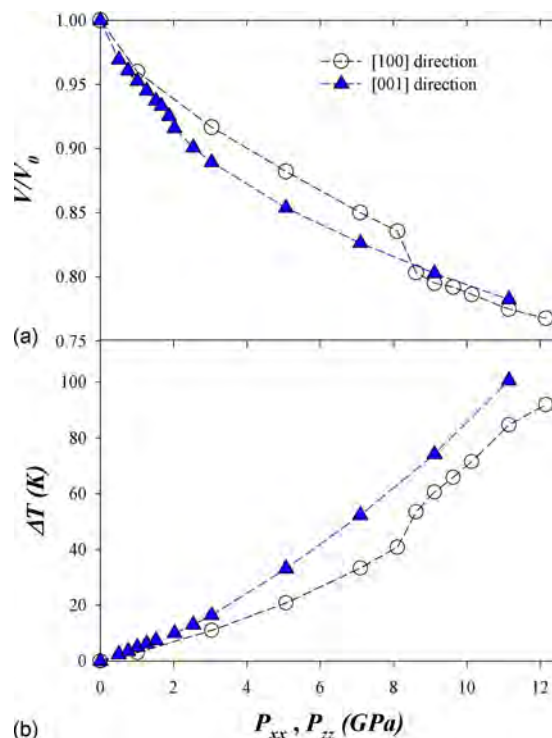


FIG. 10. (a) Final volume compression ratio and (b) temperature of RDX crystal shocked along [100] or [001] as a function of shock pressure ( $P_{xx}$  or  $P_{zz}$ , respectively) using Hugoniot simulations.

Finally, in Fig. 10 we compare the pressure-volume-temperature dependencies of RDX crystal shock compressed along the [100] and [001] directions. Because the  $\alpha$  to  $\gamma$  transition that occurs during shock compression along [001] is accompanied by  $\sim 3\%$  volume decrease,<sup>46</sup> RDX crystal is more compressible along [001] than along [100]. This increased compressibility results in more shock heating for a given shock pressure applied to (001) compared to the corresponding result for loading on (100).

#### IV. DISCUSSION AND CONCLUSION

MD simulation methods have the potential to provide unprecedented details regarding the physics and chemistry in the extreme environments resulting from shock wave excitation. The major obstacles to the practical and reliable application of such methods are (1) the need for accurate descriptions of interatomic forces for far-from-equilibrium configurations including chemical reactions and electronic excited states, (2) the more fundamental challenge of assessing the (in)sufficiency of the approximation of classical mechanics for simulating the atomic-scale behavior of matter, and (3) the need to simulate high-aspect-ratio pieces of material that are extremely long in the direction parallel to shock propagation in order to be able to study slow relaxation phenomena in the shocked material, while needing at the same time to simulate large cross sections of material to ensure that important physics are not suppressed due to finite-size effects in directions transverse to shock wave propagation.

The present study is focused on the third of the challenges summarized above. Specifically, we have applied the



uniaxial constant-stress Hugoniot method as described by Ravelo *et al.*<sup>25</sup> to the study of shock-induced inelastic deformation phenomena in oriented crystals of  $\alpha$ -RDX. The Hugoniot method is fundamentally similar to widely applied methods for simulating familiar thermodynamic ensembles such as isochoric-isothermal (*NVT*) or isobaric-isothermal (*NPT*) based on numerical integration of a set of equations of motion derived from Lagrangians that include coupling to external “bath” degrees of freedom. In this case, however, the external degrees of freedom are developed so as to sample the thermodynamic state resulting from shock wave excitation of the material based on the Rankine–Hugoniot jump conditions. The principal advantage to the Hugoniot method is that it allows sampling of the long-time thermodynamic state of a material resulting from shock wave excitation (that is, sampling of a state on the Hugoniot locus) without the need to accommodate the very large (from an atomistic simulation MD perspective) pieces of material that are required to simulate directly the passage of a shock wave through a sample while providing access to postshock times in the material sufficiently long for the dominant physical relaxations to occur before the simulation is rendered useless due to severe interference effects resulting from reflected waves at the end of the simulation cell.

In this paper we demonstrated that simulations using the Hugoniot approach can be used effectively to study shock-induced phase transition and inelastic deformation in polyatomic organic molecular crystals. Specifically we investigated the uniaxial compression of crystals of the energetic material  $\alpha$ -RDX along the [100] and [001] directions. The computational framework provided by the Hugoniot approach allowed us to perform many simulations that spanned a wide interval of applied pressures. The results were compared to those obtained from large-scale MD simulations using the SFABC method developed by Thompson and co-workers<sup>21,22</sup> in which shock waves propagate explicitly through the system. We demonstrated that Hugoniot simulations involving only a few-thousand RDX molecules exhibit qualitatively the same structural transformations observed in the computationally more demanding SFABC simulations, which employed roughly a quarter-million molecules.

For compressions along [100] and pressures below 8.0 GPa, purely elastic deformations were observed, while pressures greater than 8.0 GPa led to formation of nanoscale shear bands similar to those seen in the SFABC simulations. While the nucleation threshold pressure and nominal structure of shear bands predicted using the two methods are consistent, the extent of compression as well as predicted temperature rise are noticeably different for states above the HEL. The differences in final compression for states above the HEL can be explained readily since the SFABC approach is designed to capture a system in which the shock wave is simulated explicitly in the volume-energy state corresponding to the moment when the shock wave reaches the end of the simulation cell. By contrast, the Hugoniot approach maintains the system in a state of constant uniaxial stress, a state consistent with the Rankine–Hugoniot jump conditions. For shock compression along the [001] direction we ob-

served a transformation from  $\alpha$ -RDX to  $\gamma$ -RDX for shock pressures greater than 2.0 GPa. Compression to higher pressures (up to 12.0 GPa) did not indicate any subsequent inelastic deformation processes.

We point out that in our simulations all degrees of freedom have been treated classically. As discussed above this leads to noticeable overestimation of the heat capacity and underestimation of the Grüneisen parameter compared to a corresponding quantum mechanical treatment of RDX crystal at room temperature. As a result the temperature rise due to elastic and inelastic deformations obtained from our simulations is significantly less than would be expected for a quantized system. More accurate (compared to experimental values) predictions of heat capacity and Grüneisen parameter would result from simulations in which high-frequency degrees of freedom (e.g., covalent bonds) were constrained. This would lead to a greater extent of heating and, presumably, a modest lowering of the threshold shock strengths for mechanical instabilities to occur. The effects of such constraints on the detailed dynamics of the system are unknown, however.

Finally, we note that the validity of the Rankine–Hugoniot jump relations between pre- and post-shock states in the material depends on two criteria that, strictly speaking, often will not be satisfied. These are (1) that the wave profile of the shocked system is steady (i.e., constant in time in a frame centered on the shock front) and (2) that the state of the shocked material is uniform with respect to spatial variations. Strictly speaking, the first criterion can only be true in material that is shocked to states below the HEL (no inelastic deformation) or to overdriven states for which all inelastic deformation occurs immediately at the shock front. Shock excitation to states between these two limits corresponds to an unsteady region in which the system will exhibit two waves characterized by different velocities, which therefore will separate in time. (The lead shock is known as the elastic precursor while the secondary wave, which propagates at most sonically in the compressed material, is often referred to as the “plastic wave.”) The second criterion, uniformity, presumably would be satisfied below the HEL but not in the two-wave region nor, necessarily, in the overdriven region; the case of shear bands studied here and by Cawkwell *et al.*<sup>22</sup> provides a clear example where this condition would not be met in general since, for example, the temperature (shear stress) in the shear bands prior to thermal (stress) equilibration will be higher (lower) than in the adjacent material. Thus, while both the Hugoniot method and the SFABC approach can provide useful insights and detailed information concerning the physics of shocked molecular materials, the strengths and weaknesses of each need to be evaluated carefully in terms of the criteria discussed in this paragraph (as well as the other potential caveats identified earlier in this article) prior to use in any particular application.

## ACKNOWLEDGMENTS

This work was supported by the University of Utah Center for the Simulation of Accidental Fires and Explosions (C-SAFE), funded by the Department of Energy, Lawrence Livermore National Laboratory, under Subcontract No.

B341493. T.D.S. is supported by the U.S. Army Research Office under Grant No. W911NF-05-1-0265. The authors thank Marc Cawkwell for sharing the results of his simulations and M. Sam Shaw and Ralph Menikoff for useful discussions. Additionally, T.D.S. thanks M. Sam Shaw for a critical reading of the manuscript.

- <sup>1</sup>2,4,6-trinitrotoulene (TNT), hexahydro-1,3,5-trinitro-1,3,5-triazine (RDX), octahydro-1,3,5,7-tetranitro-1,3,5,7-tetrazocine (HMX), pentaerythritol tetranitrate (PETN), and 1,3,5-triamino-2,4,6-trinitrobenzene (TATB).
- <sup>2</sup>Z. A. Dreger, in *Static Compression of Energetic Materials*, edited by S. M. Peiris and G. J. Piermarini (Springer, New York, 2008), p. 219.
- <sup>3</sup>C. A. Bolme, S. D. McGrane, D. S. Moore, V. H. Whitley, and D. J. Funk, *Appl. Phys. Lett.* **93**, 191903 (2008).
- <sup>4</sup>C. A. Bolme, S. D. McGrane, D. S. Moore, and D. J. Funk, *J. Appl. Phys.* **102**, 033513 (2007).
- <sup>5</sup>J. E. Patterson, Z. A. Dreger, M. Miao, and Y. M. Gupta, *J. Phys. Chem. A* **112**, 7374 (2008).
- <sup>6</sup>Z. Wang, D. G. Cahill, J. A. Carter, Y. K. Koh, A. Lagutchev, N.-H. Seong, and D. D. Dlott, *Chem. Phys.* **350**, 31 (2008).
- <sup>7</sup>E. Surber, A. Lozano, A. Lagutchev, H. Kim, and D. D. Dlott, *J. Phys. Chem. C* **111**, 2235 (2007).
- <sup>8</sup>L. L. Stevens, N. Velisavljevic, D. E. Hooks, and D. M. Dattelbaum, *Propellants, Explos., Pyrotech.* **33**, 286 (2008).
- <sup>9</sup>B. M. Rice and T. D. Sewell, in *Static Compression of Energetic Materials*, edited by S. M. Peiris and G. J. Piermarini (Springer, New York, 2008), p. 255.
- <sup>10</sup>T. D. Sewell, R. Menikoff, D. Bedrov, and G. D. Smith, *J. Chem. Phys.* **119**, 7417 (2003).
- <sup>11</sup>D. C. Sorescu, B. M. Rice, and D. L. Thompson, *J. Phys. Chem. B* **103**, 6783 (1999).
- <sup>12</sup>D. C. Sorescu, B. M. Rice, and D. L. Thompson, *J. Phys. Chem. A* **103**, 989 (1999).
- <sup>13</sup>D. C. Sorescu, J. A. Boatz, and D. L. Thompson, *J. Phys. Chem. A* **105**, 5010 (2001).
- <sup>14</sup>O. Borodin, G. D. Smith, D. Bedrov, and T. D. Sewell, *J. Phys. Chem. B* **112**, 734 (2008).
- <sup>15</sup>A. Strachan, A. van Duin, D. Chakraborty, S. Dasgupta, and W. A. Goddard, *Phys. Rev. Lett.* **91**, 098301 (2003).
- <sup>16</sup>K. Nomura, R. K. Kalia, A. Nakano, and P. Vashishta, *Appl. Phys. Lett.* **91**, 183109 (2007).
- <sup>17</sup>B. L. Holian, *Shock Waves* **13**, 489 (2004).
- <sup>18</sup>S. Zhao, T. C. Germann, and A. Strachan, *J. Chem. Phys.* **125**, 165707 (2006).
- <sup>19</sup>E. Jaramillo, T. D. Sewell, and A. Strachan, *Phys. Rev. B* **76**, 064112 (2007).
- <sup>20</sup>R. Courant and K. O. Friedrichs, *Supersonic Flow and Shock Waves* (Springer, New York, 1999).
- <sup>21</sup>A. V. Bolesta, L. Zheng, D. L. Thompson, and T. D. Sewell, *Phys. Rev. B* **76**, 224108 (2007).
- <sup>22</sup>M. J. Cawkwell, T. D. Sewell, L. Zheng, and D. L. Thompson, *Phys. Rev. B* **78**, 014107 (2008).
- <sup>23</sup>The method introduces at most a single step discontinuity in the total system energy and no discontinuity in the forces of the atoms other than those that comprise the second piston.
- <sup>24</sup>J.-B. Maillet, M. Mareschal, L. Souillard, R. Ravelo, P. S. Lomdahl, T. C. Germann, and B. L. Holian, *Phys. Rev. E* **63**, 016121 (2000).
- <sup>25</sup>R. Ravelo, B. L. Holian, T. C. Germann, and P. S. Lomdahl, *Phys. Rev. B* **70**, 014103 (2004).
- <sup>26</sup>E. J. Reed, L. E. Fried, and J. D. Joannopoulos, *Phys. Rev. Lett.* **90**, 235503 (2003).
- <sup>27</sup>E. J. Reed, L. E. Fried, M. R. Manaa, and J. D. Joannopoulos, in *Chemistry at Extreme Conditions*, edited by M. R. Manaa (Elsevier, New York, 2005), Chap. 10, p. 297.
- <sup>28</sup>J.-B. Maillet and G. Stoltz, "Sampling Constraints in Average: The Example of Hugoniot Curves," *Appl. Math. Res. Express* (in press).
- <sup>29</sup>S. Bernard and J.-B. Maillet, *Phys. Rev. B* **66**, 012103 (2002).
- <sup>30</sup>K. Kadau, T. C. Germann, P. S. Lomdahl, and B. L. Holian, *Phys. Rev. B* **72**, 064120 (2005).
- <sup>31</sup>S. Boyd, M. Gravelle, and P. Politzer, *J. Chem. Phys.* **124**, 104508 (2006).
- <sup>32</sup>G. D. Smith and R. Bharadwaj, *J. Phys. Chem. B* **103**, 3570 (1999).
- <sup>33</sup>D. Bedrov, G. D. Smith, and T. D. Sewell, *AIP Conf. Proc.* **620**, 399 (2001).
- <sup>34</sup>M. J. Cawkwell and T. D. Sewell (unpublished).
- <sup>35</sup>S. Nosé, *J. Chem. Phys.* **81**, 511 (1984).
- <sup>36</sup>W. G. Hoover, *Phys. Rev. A* **31**, 1695 (1985).
- <sup>37</sup>M. L. Wilkins, *Computer Simulation of Dynamic Phenomena* (Springer, New York, 1999).
- <sup>38</sup>B. L. Holian and R. Ravelo, "A Practical Guide to Molecular-Dynamics Simulations of Shock Waves," *Shock Waves* (in press).
- <sup>39</sup>U. Essmann, L. Perera, M. L. Berkowitz, T. Darden, H. Lee, and L. G. Pedersen, *J. Chem. Phys.* **103**, 8577 (1995).
- <sup>40</sup>H. G. Gallagher, P. J. Halfpenny, J. C. Miller, and J. N. Sherwood, *Philos. Trans. R. Soc. London, Ser. A* **339**, 293 (1992).
- <sup>41</sup>K. J. Ramos, D. E. Hooks, and D. F. Bahr, "Direct observation of plasticity and quantitative hardness measurements in single crystal cyclotrimethylene trinitramine by nanoindentation," *Philos. Mag.* (in press).
- <sup>42</sup>In the original publication of Ref. 22 authors reported shock pressures of 5.7 and 9.7 GPa. However, later they discovered a mistake in their calculations of shock velocity and shock pressure. In the subsequently published erratum correct shock pressure of 5.0 GPa for  $U_p=0.63$  km/s and 7.9 GPa for  $U_p=1.0$  km/s has been reported.
- <sup>43</sup>D. E. Hooks, K. J. Ramos, and R. Martinez, *J. Appl. Phys.* **100**, 024908 (2006).
- <sup>44</sup>J. E. Patterson, Z. A. Dreger, and Y. M. Gupta, *J. Phys. Chem.* **111**, 10897 (2007).
- <sup>45</sup>M. J. Cawkwell and T. D. Sewell, private communication (September 2008).
- <sup>46</sup>A. J. Davidson, I. D. H. Oswald, D. J. Francis, A. R. Lennie, W. G. Marshall, D. I. A. Millar, C. R. Pulham, J. E. Warren, and A. S. Cumming, *Cryst. Eng. Comm.* **10**, 162 (2008).

# Optimal sampling efficiency in Monte Carlo simulation with an approximate potential

Joshua D. Coe,<sup>1,a)</sup> Thomas D. Sewell,<sup>2</sup> and M. Sam Shaw<sup>1</sup>

<sup>1</sup>Theoretical Division, Los Alamos National Laboratory, Los Alamos, New Mexico 87545, USA

<sup>2</sup>Department of Chemistry, University of Missouri-Columbia, Missouri 65211-7600, USA

(Received 6 February 2009; accepted 19 March 2009; published online 22 April 2009)

Building on the work of Iftimie *et al.* [J. Chem. Phys. **113**, 4852 (2000)] and Gelb [J. Chem. Phys. **118**, 7747 (2003)], Boltzmann sampling of an approximate potential (the “reference” system) is used to build a Markov chain in the isothermal-isobaric ensemble. At the end points of the chain, the energy is evaluated at a more accurate level (the “full” system) and a composite move encompassing all of the intervening steps is accepted on the basis of a modified Metropolis criterion. For reference system chains of sufficient length, consecutive full energies are statistically decorrelated and thus far fewer are required to build ensemble averages with a given variance. Without modifying the original algorithm, however, the maximum reference chain length is too short to decorrelate full configurations without dramatically lowering the acceptance probability of the composite move. This difficulty stems from the fact that the reference and full potentials sample different statistical distributions. By manipulating the thermodynamic variables characterizing the reference system (pressure and temperature, in this case), we maximize the average acceptance probability of composite moves, lengthening significantly the random walk between consecutive full energy evaluations. In this manner, the number of full energy evaluations needed to precisely characterize equilibrium properties is dramatically reduced. The method is applied to a model fluid, but implications for sampling high-dimensional systems with *ab initio* or density functional theory potentials are discussed. © 2009 American Institute of Physics. [DOI: 10.1063/1.3116788]

## I. INTRODUCTION

Characterization of thermodynamic equilibrium using Markov chain Monte Carlo (MC)<sup>2</sup> methods is now well-established practice.<sup>1–4</sup> Instead of building time averages for an ensemble of trajectories, as in molecular dynamics (MD),<sup>1,2,5</sup> configurational integrals are sampled directly at points dictated by a random walk. New points are added to the Markov chain on the basis of an acceptance criterion, most often that of Metropolis,<sup>6</sup> and the simulation is complete when variance in (thermodynamic) ensemble averages has dropped to an acceptable level. This level varies inevitably with application, but the number of steps required to achieve a target variance generally rises with the dimensionality of configuration space. For this reason, precision sampling of high-dimensional systems remains a serious challenge.

Methodological improvements in solving the electronic Schrödinger equation, coupled with steady advances in computing power, have made single-point calculation of *ab initio*<sup>7</sup> (AI) or density functional theory<sup>8</sup> (DFT) energies routine even for very large systems.<sup>7</sup> Paired with algorithms for extracting forces from wave functions (or densities) analytically,<sup>9</sup> these improvements lead directly to steady growth in the application of AIMD.<sup>10</sup> The potential energy surface (PES) in AIMD is built “on the fly” using quantum

chemistry in place of *ad hoc* functional forms, permitting more robust and accurate sampling of phase space. Expanded use of AIMD has not been matched, however, by commensurate growth of AI (MC)<sup>2</sup>, although the use of AI potentials in (MC)<sup>2</sup> simulation has been the subject of very recent attention.<sup>11,12</sup> While MD steps are collective and deterministic, standard (MC)<sup>2</sup> steps are individual and stochastic; the computational exchange made in substituting MD for (MC)<sup>2</sup> is that of force calculation at every time step in return for steps encompassing all particles in the system. The single-particle character of standard (MC)<sup>2</sup> steps can be exploited to lower their cost from  $O(N^2)$  to  $O(N)$  in a system of  $N$  particles described by a pair potential, but no analogous reduction is afforded self-consistent potentials including interaction levels much higher than the pair. It remains true, however, that (MC)<sup>2</sup> possesses inherent flexibility unavailable to MD,<sup>13</sup> such as constant temperature or pressure sampling without need of a stochastic bath, or chemical equilibrium sampling without need of a reactive potential surface.<sup>14</sup> For these reasons, it is worthwhile to explore (MC)<sup>2</sup> algorithms harnessing the accuracy of AI quantum chemistry without requiring full system energy evaluation following every single-particle displacement.

One alternative is to build trial moves from collective displacement of several or even all particles. The acceptance probability of a collective move will be much lower than that of its constituents taken independently, however, because

<sup>a)</sup>Electronic mail: jcoe@lanl.gov.

single-particle steps are chosen randomly and thus lack information regarding intermolecular forces (except for variants such as force bias<sup>15</sup> and “smart”<sup>16</sup> MC). This fact is illustrated clearly in a hard-sphere fluid, where the likelihood that two particles will overlap increases monotonically with the number of particles displaced; if a collective step yields even a single overlap, its acceptance probability will vanish entirely. This will result in many wasted trial steps, a weighty consideration if each acceptance test requires significant computing time. The radius of trial moves could be dramatically reduced in order to salvage the acceptance probability, but only at the expense of slow configuration space exploration; as before, precise equilibrium averages will require many energy evaluations. In this sense MD steps can be viewed as “directed” forms of multiparticle (MC)<sup>2</sup> moves, in that time-reversible integration of the equations of motion guarantees energy conservation and thus unit acceptance probability of the “trial move.” No such guarantee exists when trial moves are chosen stochastically.

An alternative means of building (MC)<sup>2</sup> steps was introduced recently by Ifitimie *et al.*,<sup>17</sup> followed by an independent treatment from Gelb.<sup>18</sup> Although several monikers have been applied,<sup>19</sup> we will refer to this procedure as nested Markov chain MC (N(MC)<sup>2</sup>). The method is conceptually related to (MC)<sup>2</sup> with stochastic potential switching,<sup>20</sup> multiple “time steps,”<sup>21</sup> multilevel summation,<sup>22</sup> resolution exchange,<sup>23</sup> and hybrid replica exchange.<sup>24</sup> In N(MC)<sup>2</sup> a series of elementary moves (in the *NPT* ensemble, single particle or volume adjustments), each accepted with Boltzmann weight, is made in a “reference” system defined by an inexpensive (but less accurate) potential. At the end points of this sequence, the energy is evaluated again with a more accurate potential defining the “full” system. Through appropriate modification of the acceptance criterion, the reference system Markov chain is transformed into a composite trial step accepted with Boltzmann weight in the full system. As long as the reference potential captures adequately the physics of the full potential, these composite trial moves retain a reasonable probability of acceptance; the more reference steps comprising a composite move (or the less capably the reference potential captures the interactions present in the full potential), the lower its acceptance probability. The difficulty is that the reference and full potentials sample different statistical distributions, and so the number of reference steps combinable into a composite step is strongly limited by the practical need of a reasonable acceptance probability for the latter. In spite of this difficulty, N(MC)<sup>2</sup> permits (MC)<sup>2</sup> sampling of an accurate potential without having to evaluate it following every single-particle displacement, and in this sense represents an important step toward realistic implementation of (MC)<sup>2</sup> with an AI potential. Although its application already has

been fairly extensive,<sup>12,25</sup> the present work attempts to improve upon the original N(MC)<sup>2</sup> algorithm by addressing its principal weakness; namely, the potentially poor overlap of reference and full distributions.

In order to minimize the number of full energy evaluations required to achieve target variance in ensemble averages, configurations at which the full energy is evaluated should be as decorrelated (*vide infra*) as possible. Decorrelation requires separation by a large number of reference steps, a number constrained also by the acceptance probability for the composite step. By manipulating the thermodynamic variables of the reference system, we show how to maximize the overlap of reference and full distributions. This procedure maximizes also the acceptance probability for composite steps built from a fixed number of reference steps, minimizes the correlation of energies sampled in the full system, and thereby lowers considerably the number of full energy evaluations needed to sample with high precision.

Section II describes the potentials used to generate the results that follow. The next sections provide a brief overview of conventional MC sampling (III) and basic N(MC)<sup>2</sup> (IV). Section V contains our primary contribution, wherein we outline a means of optimizing N(MC)<sup>2</sup> sampling efficiency. Section VI summarizes and offers some suggestions for further development.

## II. POTENTIAL MODEL

The N(MC)<sup>2</sup> procedure evaluates the energy of a configuration using two different potentials: an approximate potential for single-particle steps and a more accurate one for composite steps. We assume that quantities for comparison with experiment are computed in the full system. In the present work, the purpose of which is to test and optimize the procedure, we will utilize combinations of pair potentials equal in computational expense but differing in their parametrization. In the future, a model potential will be used as reference for a full system characterized with DFT.<sup>26</sup>

The model potentials used below describe diatomic molecules of fixed bond length and with interaction sites at their atomic centers. Pairwise interaction of atomic sites *a* and *b* are modeled with the Buckingham exponential-6 potential,

$$\varphi(r_{ab}) = \frac{\varepsilon}{\alpha - 6} \left( 6e^{\alpha(1-r_{ab})} - \frac{\alpha}{r_{ab}^6} \right), \quad (1)$$

where

$$r_{ab}^2 = \frac{0.25r_{ij}^2(l_i^2 + l_j^2) + (-1)^a(\mathbf{r}_{ij} \cdot \mathbf{l}_i) + (-1)^b(\mathbf{r}_{ij} \cdot \mathbf{l}_j) + (-1)^{a+b}0.5(\mathbf{l}_i \cdot \mathbf{l}_j)}{r_0^2}. \quad (2)$$



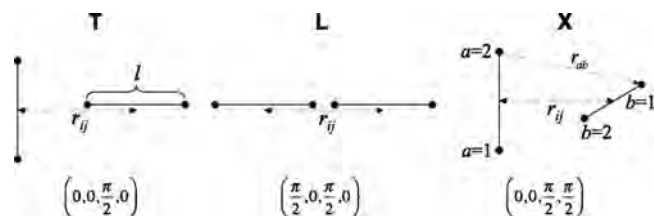


FIG. 1. Diatomic pair configurations used to illustrate the anisotropy of the potential defined by Eqs. (1)–(4) and its variation with intramolecular bond length  $l$  in Fig. 2. Bond lengths are fixed at 1.10 Å in the full system, but varied from 0.90 to 1.05 Å in the reference systems. Configuration types **T**, **L**, and **X** are characterized by the four angles  $(\theta_1, \chi_1, \theta_2, \chi_2)$ , where  $\theta$  and  $\chi$  represent rotation of molecules 1 and 2 within and out of the plane of the page, respectively. Diatomic bond vectors in the **T** and **L** configurations therefore are coplanar, whereas those in the **X** configuration are perpendicular. Clockwise rotations are positive, and all angle values are zeroed to those in the parallel configuration (not shown).

The site-site separation distance  $r_{ab}$  has been expressed in terms of the center-of-mass (COM) separation vector ( $\mathbf{r}_{ij}$ ) for interacting molecules  $i$  and  $j$ , and the individual bond vectors  $\mathbf{l}_i$  and  $\mathbf{l}_j$  (of lengths  $l_i$  and  $l_j$ ). The full interaction of two diatomics is then

$$\varphi_{ij} = \sum_{a=1}^2 \sum_{b=1}^2 \varphi(r_{ab}). \quad (3)$$

The potential parameters  $\alpha$ ,  $\varepsilon$ , and  $r_0$  were chosen to roughly approximate compressed nitrogen fluid on its shock Hugoniot locus.<sup>27</sup> Details of the fitting procedure used to determine these parameters will be described in an upcoming publication.<sup>26</sup> The final values are

$$\begin{aligned} \varepsilon &= 34.156 \text{ K}, \\ r_0 &= 4.037 \text{ Å}, \\ \alpha &= 12.29. \end{aligned} \quad (4)$$

We enforced a minimum allowable  $r_{ab}$  slightly greater than the  $\text{N}_2$  bond length ( $r_{ab}^{\min} = 1.20$  Å) as a guarantee of smooth behavior throughout the simulations. In testing the  $\text{N}(\text{MC})^2$  procedure,  $l_i$  and  $l_j$  were fixed at 1.10 Å in the full system but shortened in 0.05 Å increments to generate a series of reference systems. The reference potential approaches a purely spherical COM interaction as  $l_j \rightarrow 0$ , thus providing a poorer approximation to the full potential. Because bond lengths in the full system are fixed, and  $l_i = l_j$  in all reference systems, we will refer only to  $l$  (and always in the context of the reference system) in what follows.

Although each site-site interaction described by Eq. (1) is spherical, the sum of these interactions (3) for a pair of molecules is highly anisotropic. Figure 1 schematically illustrates some of the quantities appearing in Eqs. (1) and (2) for a pair of molecules. The pair is drawn in three fiducial configurations<sup>28</sup> labeled **T**, **L**, and **X**, defined by the quartet of angles  $(\theta_1, \chi_1, \theta_2, \chi_2)$ .  $\theta(\chi)$  is the angle in (out of) the plane of the paper, and angles are zeroed to the configuration in which the molecules are parallel to one another (not shown). The subscripts label the molecules. Figure 2 displays the variation in potential for each of these configurations as a function of COM separation and bond length  $l$ . The full

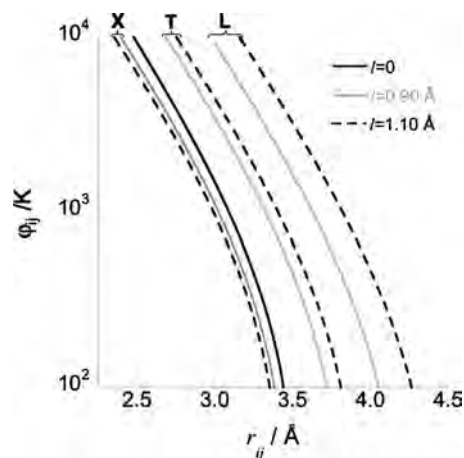


FIG. 2. Illustration of the pair potential defined by Eqs. (1)–(4) as a function of the COM separation  $r_{ij}$ . The full potential ( $l=1.10$  Å) is compared to a spherical potential ( $l=0$ , where all configurations are equivalent), as well as to the reference potential with the shortest bond length ( $l=0.90$  Å). Variations in potential  $\varphi_{ij}$  are plotted on a log scale, revealing its highly anisotropic character. See Fig. 1 for an explanation of the **X**, **T**, and **L** configurations.

potential ( $l=1.10$  Å) is compared with a purely spherical potential ( $l=0$ ) and one of the reference potentials ( $l=0.90$  Å) used below. The ordinate is drawn on a log scale, and it is clear that the reference potential may differ substantially both from the full potential and from that of a purely isotropic interaction.

### III. STANDARD MC SAMPLING

In keeping with an earlier presentation of the  $\text{N}(\text{MC})^2$  method,<sup>18</sup> we have adopted the structure and notation of Ref. 29 to describe MC sampling. Matrices are indicated by bold lettering, and their individual elements by a subscripted, italicized form of the same symbol. The system is described by a state vector  $\boldsymbol{\pi}$ , each element of which defines the probability that the system is in state  $\pi_i$ . These probabilities vary as steps are added to the Markov chain, a process performed by repeated application of the transition matrix  $\mathbf{p}$  to the state vector  $\boldsymbol{\pi}$ ,

$$\boldsymbol{\pi}^T(n)\mathbf{p} = \boldsymbol{\pi}^T(n+1). \quad (5)$$

Here we have written the states as transposed column vectors and indicated the step number by  $n$ . Following Metropolis,<sup>6</sup> we demand that the  $\pi_i$  be asymptotically distributed according to their Boltzmann weights,

$$\pi_i^* \propto e^{W_i}, \quad (6)$$

where

$$\boldsymbol{\pi}^* = \lim_{n \rightarrow \infty} \boldsymbol{\pi}(1)\mathbf{p}^n. \quad (7)$$

In the isothermal-isobaric ensemble,<sup>30</sup> for which the corresponding potential is the Gibbs free energy,<sup>31</sup>

$$W_i = -\beta(U_i + PV_i) + N \ln V_i, \quad (8)$$

$U_i$  and  $V_i$  are the internal energy and volume (respectively) of state  $i$ ,  $N$  is the total number of atoms in the system, and  $\beta$  has its usual meaning as the inverse product of temperature with the Boltzmann constant  $(k_B T)^{-1}$ . A simple step toward realization of Eq. (6) is construction of the transition matrix  $\mathbf{p}$  such that

$$\boldsymbol{\pi}^* \mathbf{p} = \boldsymbol{\pi}^*, \quad (9)$$

meaning that once reached, the limiting distribution is permanently maintained. This is known as the *balance condition*. The elements of  $\mathbf{p}$  define the probability of transition between various states, meaning that

$$p_{ij} \geq 0 \quad \forall i, j. \quad (10)$$

Conservation of probability mandates that

$$\sum_j p_{ij} = 1 \quad \forall i \quad (11)$$

as well. Equation (11) identifies  $\mathbf{p}$  as a *stochastic* matrix. The Markov chain is irreducible (or ergodic) if there exists some  $n$  such that

$$[p^n]_{ij} > 0, \quad \forall i, j, \quad (12)$$

establishing that any final state can be reached from any initial state simply by repeated application of  $\mathbf{p}$  to an (arbitrary) initial state vector  $\boldsymbol{\pi}(1)$ . If  $\mathbf{p}$  is stochastic, irreducible, and aperiodic, the Perron–Frobenius theorem<sup>4</sup> ensures that it possesses a single left eigenvector having unit eigenvalue, and that this eigenvector represents the limiting distribution. This guarantee does not, however, ensure that the limiting distribution is the Boltzmann distribution. For this, an explicit form of  $p_{ij}$  compatible with Eq. (6) must be specified.

A helpful constraint in this regard is *microscopic reversibility*,

$$\pi_i p_{ij} = \pi_j p_{ji}. \quad (13)$$

Although Eq. (13) is unnecessarily strong,<sup>1,32</sup> its combination with Eq. (11) guarantees satisfaction of Eq. (9). We now restrict  $p_{ij}$  to the product form

$$p_{ij} = q_{ij} \alpha_{ij}, \quad (14)$$

where  $q_{ij}$  is the (marginal) probability of making a trial step from state  $i$  to state  $j$  and  $\alpha_{ij}$  is the (conditional) probability of accepting such a move. The average number of systems attempting this transition will be  $\pi_i q_{ij}$ , and the average number attempting the reverse transition will be  $\pi_j q_{ji}$ . Metropolis *et al.*<sup>6</sup> were the first to show that Eq. (6) will be satisfied when

$$\alpha_{ij} = \min\left(\frac{q_{ji}\pi_j}{q_{ij}\pi_i}, 1\right), \quad (15)$$

if the  $\pi_i$  are defined as  $e^{W_i}$ . In the (very common) event that the marginal distribution is uniform and thus  $q_{ij} = q_{ji}$  by construction, this reduces to

$$\alpha_{ij} = \min(e^{W_j - W_i}, 1). \quad (16)$$

The choice of  $\alpha_{ij}$  given in Eqs. (15) and (16) satisfies microscopic reversibility as well, so long as there is a nonzero probability of remaining in the same state,

$$p_{ii} = 1 - \sum_{j \neq i} p_{ij} \neq 0. \quad (17)$$

The matrix elements  $q_{ij}$  represent the probability of making a trial move, such as a displacement or a volume change. For single-particle displacements limited to a sphere of cutoff radius  $r_c$ ,  $q_{ij}$  is the uniform probability of choosing a trial state  $j$  in which a single particle has been moved to a different point within the sphere; this uniformity is what permits reduction of Eq. (15) to Eq. (16). For more sophisticated move types such as the composite moves introduced below, the distribution of trial moves may *not* be uniform, in which event  $\mathbf{q}$  will assume a more complicated form. In that case, the simple decomposition of  $p_{ij}$  assumed in Eq. (14) can be leveraged to yield the new matrix  $\alpha$  in relatively straightforward fashion. This procedure is illustrated in Sec. IV.

#### IV. NESTED MARKOV CHAIN MC

The N(MC)<sup>2</sup> procedure distinguishes the full system of interest from a reference system defined by an alternate potential. In what follows, reference system quantities will be indicated with superscripted zeros. Reference and full system volumes are identical, so no attempt will be made to distinguish the two.

Consider a sequence of  $M$  elementary reference steps connecting configurations  $i$  and  $j$ . Each of these steps is accepted on the basis of the standard Metropolis criterion (15) using reference system energies. We wish to transform this sequence of steps accepted in the reference system into a *trial* step made in the *full* system. The full system  $q_{ij}$  are no longer drawn from a uniform distribution; rather, they are built from a sequence of  $M$  points accepted with Boltzmann weight in the reference system. What is the appropriate form of the new  $\alpha_{ij}$ , the acceptance probability in the full system? The full system  $q_{ij}$  are

$$\begin{aligned} q_{ij} &= \prod_{k=1}^M p_{k-1,k}^{(0)} = \prod_{k=1}^M q_{k-1,k}^{(0)} \alpha_{k-1,k}^{(0)} \\ &= \prod_{k=1}^M q_{k-1,k}^{(0)} \min\left(\frac{\pi_k^{(0)} q_{k,k-1}^{(0)}}{\pi_{k-1}^{(0)} q_{k-1,k}^{(0)}}, 1\right), \end{aligned} \quad (18)$$

meaning that

$$\frac{q_{ij}}{q_{ji}} = \frac{q_{0,1}^{(0)} \min\left(\frac{\pi_1^{(0)} q_{1,0}^{(0)}}{\pi_0^{(0)} q_{0,1}^{(0)}}, 1\right) \times q_{1,2}^{(0)} \min\left(\frac{\pi_2^{(0)} q_{2,1}^{(0)}}{\pi_1^{(0)} q_{1,2}^{(0)}}, 1\right) \times \cdots \times q_{M-1,M}^{(0)} \min\left(\frac{\pi_M^{(0)} q_{M,M-1}^{(0)}}{\pi_{M-1}^{(0)} q_{M-1,M}^{(0)}}, 1\right)}{q_{M,M-1}^{(0)} \min\left(\frac{\pi_{M-1}^{(0)} q_{M-1,M}^{(0)}}{\pi_M^{(0)} q_{M,M-1}^{(0)}}, 1\right) \times \cdots \times q_{2,1}^{(0)} \min\left(\frac{\pi_1^{(0)} q_{1,2}^{(0)}}{\pi_2^{(0)} q_{2,1}^{(0)}}, 1\right) \times q_{0,1}^{(0)} \min\left(\frac{\pi_0^{(0)} q_{0,1}^{(0)}}{\pi_1^{(0)} q_{1,0}^{(0)}}, 1\right)}. \quad (19)$$

Following Gelb,<sup>18</sup> note that

$$\frac{q_{k-1,k}^{(0)} \min\left(\frac{\pi_k^{(0)} q_{k,k-1}^{(0)}}{\pi_{k-1}^{(0)} q_{k-1,k}^{(0)}}, 1\right)}{q_{k,k-1}^{(0)} \min\left(\frac{\pi_{k-1}^{(0)} q_{k-1,k}^{(0)}}{\pi_k^{(0)} q_{k,k-1}^{(0)}}, 1\right)} = \frac{\pi_k^{(0)}}{\pi_{k-1}^{(0)}}, \quad (20)$$

which, in combination with reordering of factors in Eq. (19), implies that

$$\frac{q_{ij}}{q_{ji}} = \frac{\pi_1^{(0)}}{\pi_i^{(0)}} \times \frac{\pi_2^{(0)}}{\pi_1^{(0)}} \times \frac{\pi_3^{(0)}}{\pi_2^{(0)}} \times \cdots \times \frac{\pi_j^{(0)}}{\pi_{M-1}^{(0)}} = \frac{\pi_j^{(0)}}{\pi_i^{(0)}}. \quad (21)$$

Substituting Eq. (21) into Eq. (15) gives

$$\alpha_{ij} = \min\left(\frac{\pi_j \pi_i^{(0)}}{\pi_i \pi_j^{(0)}}, 1\right), \quad (22)$$

the acceptance probability of composite moves required for Metropolis sampling of the full potential. In comparing  $\alpha_{ij}$  with  $\alpha_{ij}^{(0)}$ , the standard ratio of Boltzmann factors for initial and final states of the full system has been augmented by the inverse of the standard ratio in the reference system (to which Gelb refers as a “correction factor”). The  $\pi_k^{(0)}$  in Eq. (22) are evaluated using the reference system temperature ( $T^{(0)}$ ) and pressure ( $P^{(0)}$ ), but this in no way precludes use of a different pressure ( $P$ ) and temperature ( $T$ ) in building  $\pi_k$  for the full system. Abbreviating the difference between full and reference potentials for state  $k$  as  $W_k - W_k^{(0)} \equiv \delta W_k$  and  $\delta W_j - \delta W_i \equiv \Delta W$ , Eq. (22) can be re-expressed as

$$\alpha_{ij} = \begin{cases} 1, & \Delta W \geq 0 \\ e^{\Delta W}, & \Delta W < 0, \end{cases} \quad (23)$$

If the reference energy always was related to the full energy by a simple constant shift

$$U_n^{(0)} + c = U_n, \quad (24)$$

the product in Eq. (22) would never deviate from unity, and thus *all* composite moves would be accepted, regardless of the magnitude of  $M$ . A distribution of  $\delta W$  implies a distribution of  $\Delta W$ , the mean of which is determined by the extent to which the reference potential deviates from the full (or by the number of reference steps between full energy evaluations). Because a Dirac  $\delta(0)$  distribution of  $\Delta W$  would yield unit acceptance probability, reducing the absolute value of the first two moments of the  $\Delta W$  distribution raises the mean value of  $\alpha_{ij}$  in Eq. (23). These moments are dictated partly by the thermodynamic state of the reference system, a fact upon which we build the optimization procedure described in Sec. V.

Unless otherwise indicated all full system results are for a 3-D periodic system of 100 diatomic molecules at temperature  $T=728$  K and pressure  $P=4.84$  GPa, although our methodology is in no way restricted to such extreme environments. After an equilibration period of  $O(10^4)$  reference steps,<sup>33</sup> results were collected from an additional  $O(10^7)$  reference steps and averaged over 5–10 Markov chains started from randomly chosen initial conditions.

The rate of convergence for ensemble averages depends on the statistical independence of the sampling points in a sense now defined. The left panel of Fig. 3 presents the distribution of reference energy per particle  $u^{(0)}$  as given by Eqs. (1)–(4) and for  $l=1.00$  Å, calculated at a fixed number of steps  $O$  from a reference configuration  $j$ . At an offset  $O=10$  steps, the energies  $u^{(0)}(j)$  and  $u^{(0)}(j+O)$  are highly correlated and thus the distribution is narrowly peaked about  $u^{(0)}(j)$ . As the offset grows larger, the distribution widens gradually up to  $O=3000$ , at which point the distribution ceases to broaden. The right panel provides a quantitative measure of this effect through the standard deviation  $\sigma$  of the Gaussian distribution. The width of the distribution at  $O$

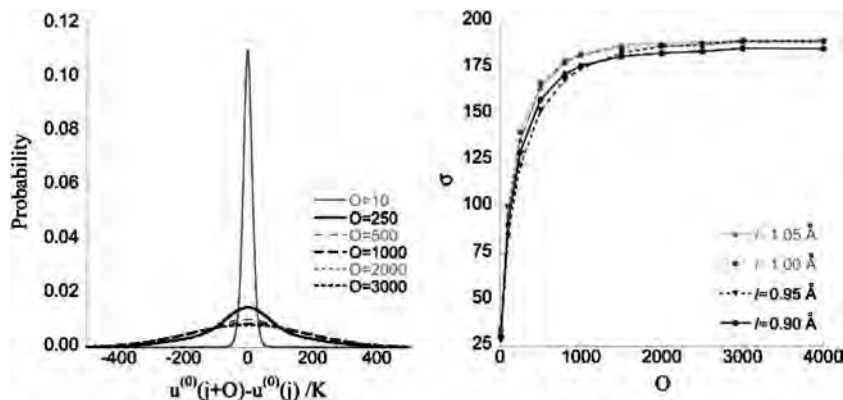


FIG. 3. Correlation of reference energy per particle  $u^{(0)}$  at configurations  $j$  with those separated by a fixed number of steps  $O$  for  $l=1.00$  Å. The left panel shows the uniform broadening of the Gaussian distribution as the offset rises. The right panel illustrates convergence of the distribution width, as characterized by standard deviation  $\sigma$  for several different values of  $l$ . At offset  $O_{\text{corr}}=3000$  steps, the energies are approximately decorrelated and the Gaussian width constant.



=4000 is indistinguishable from that at  $O=3000$ . In fact, energies are correlated only slightly at  $O=500$ , but a conservative estimate of  $O_{\text{corr}}$  is made in order to clarify the benchmarks provided below. We define the correlation length  $O_{\text{corr}}$ , then, to be equal roughly to 3000 for this set of reference potentials.

Gelb's presentation of the  $N(\text{MC})^2$  method<sup>18</sup> suggested a metric for evaluating its computational efficiency (maximum speedup), but did not attempt to quantify its sampling efficiency. Because the reference and full potentials used here do not differ in computational expense, we reverse the emphasis and defer discussion of the total efficiency (some combination of sampling and computational efficiencies) for a later work.<sup>26</sup> The sampling efficiency of the method provides a measure of the rate at which it will explore the relevant space. This quantity is not determined by the acceptance probability alone, but in balancing the need to separate full energy evaluations by as many reference steps as possible (up to  $O_{\text{corr}}$ ) with maintenance of a reasonable acceptance probability for each composite move. In light of these considerations, we define the sampling efficiency  $E_s$  for a given reference potential (characterized here by  $O_{\text{corr}}$ ) and offset  $O$  as

$$E_s(O, O_{\text{corr}}) \equiv \frac{\bar{\alpha} \min(O, O_{\text{corr}})}{O_{\text{corr}}}, \quad (25)$$

where  $\bar{\alpha}$  is the average acceptance probability of a composite move from state  $i$  to state  $j$  when the states are separated by  $O$  reference steps, and the min function reflects the efficiency loss in increasing  $O$  beyond  $O_{\text{corr}}$ . The min function really should be replaced by one passing smoothly to  $O_{\text{corr}}$ , but Eq. (25) is sufficient for our purposes here. The possible range of  $E_s$  as defined by Eq. (25) is  $[0,1]$ , and the goal of the procedure introduced below will be to maximize this quantity through variation of  $\bar{\alpha}$ . If  $O$  is large but  $\bar{\alpha}$  is small, then accepted composite steps will explore configuration space rapidly but much computational effort will be wasted on rejected steps; for small  $O$  and large  $\bar{\alpha}$ , composite steps will be accepted with high probability but little ground will be covered in the process.

We now examine the performance of  $N(\text{MC})^2$  for  $l$  values in the range of 0.90–1.05 Å. Figure 4 illustrates the acceptance probability and Fig. 5 the sampling efficiency as defined by Eq. (25) for  $O=1$ –3000. As the reference potential deviates more strongly from the full potential (i.e., as  $l$  decreases), the performance of the method deteriorates rapidly, as evidenced by the downward shift in both the acceptance probability and efficiency curves. As is to be expected, the acceptance probability also falls as the magnitude of the offset rises. The inset in Fig. 4 demonstrates the ability to obtain a good acceptance probability even with a poor reference potential, albeit at the cost of lowering  $O$  (meaning that a greater number of total sampling points will be required). In this context it is important to emphasize that using  $O$  values close to  $O_{\text{corr}}$  is ideal, but not at all necessary for sampling the full potential much more efficiently than with conventional  $(\text{MC})^2$ . On this point, note that the efficiency using any reference potential is minimal at  $O=1$ , which corresponds roughly to conventional  $(\text{MC})^2$ . Efficiency no

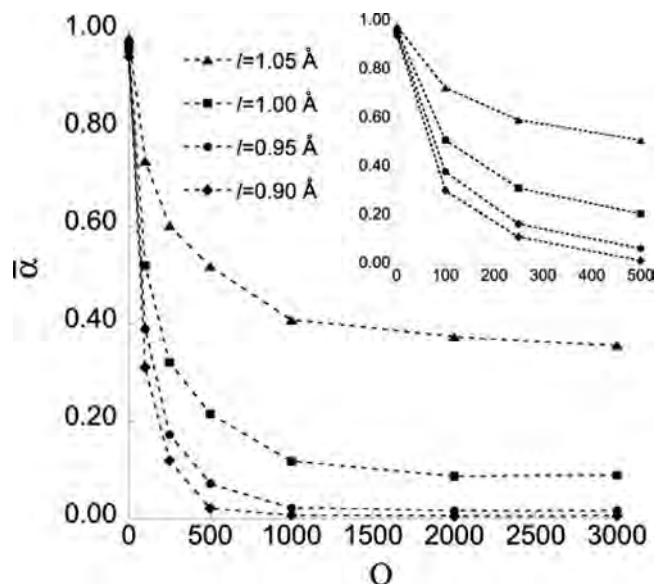


FIG. 4. Acceptance probabilities obtained using the  $N(\text{MC})^2$  procedure with the potential defined by Eqs. (1)–(4). Bondlength  $l$  is held fixed at 1.10 Å in the full system, but varied from 1.05 to 0.90 Å in the reference systems. Acceptance probabilities diminish rapidly as the offset  $O$  between full energy evaluations increases or as the similarity of the reference and full potentials lessens. For all points, statistical errors in  $\bar{\alpha}$  are smaller than the symbol size. The inset enlarges the behavior at small  $O$ , showing that better acceptance probabilities can be obtained even with the poorest reference potential by shortening the reference system Markov chain.

longer increases monotonically with the offset as the reference potential deviates more strongly from the full potential; results for  $l=0.95$  Å and  $l=0.90$  Å exhibit maxima around  $O=250$  steps. These results will be scrutinized quantitatively below, after introducing an optimized variant of  $N(\text{MC})^2$ .

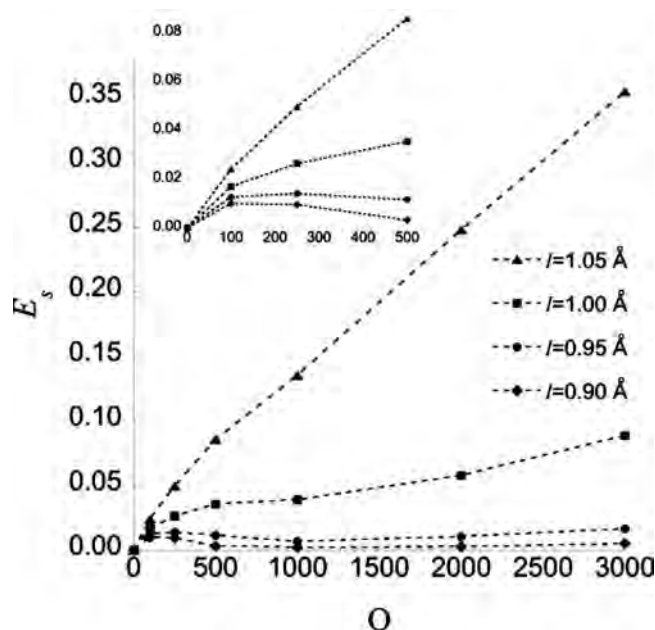


FIG. 5. Sampling efficiencies  $E_s$  corresponding to the acceptance probabilities shown in Fig. 4 and as defined by Eq. (25) in the text. Local maxima occur at small  $O$  as the quality of the reference potential deteriorates, but note efficiencies are minimal at  $O=1$ , corresponding roughly to that of standard MC. The inset enlarges the behavior at small  $O$ .



## V. OPTIMIZED N(MC)<sup>2</sup> PROCEDURE

The average acceptance probability  $\bar{A}$  for composite steps connecting configurations  $i$  and  $j$  can be expressed exactly in the limit that  $i$  and  $j$  are fully decorrelated,

$$\bar{A} \equiv \lim_{O \rightarrow O_{\text{corr}}} \bar{\alpha}. \quad (26)$$

The initial states  $i$  will, by construction, possess relative weights  $e^{W_i}$  drawn from the full distribution. The final states  $j$  will, in the  $O_{\text{corr}}$  limit, be drawn randomly from the reference distribution and thus carry weights  $e^{W_j^{(0)}}$ . The acceptance probability of a composite trial step from state  $i$  to state  $j$  is  $\alpha_{ij}$ , and this quantity is averaged over the configuration and volume spaces of all decorrelated  $(i, j)$  pairs to obtain  $\bar{A}$ ,

$$\begin{aligned} \bar{A} &= \frac{\int \int \int \int \alpha_{ij} e^{W_i + W_j^{(0)}} d\tau_i dV_i d\tau_j dV_j}{\int \int \int \int e^{W_i + W_j^{(0)}} d\tau_i dV_i d\tau_j dV_j} \\ &= \frac{\int \int \int \int \alpha_{ij} e^{\delta W_i} (e^{W_i^{(0)} + W_j^{(0)}}) d\tau_i dV_i d\tau_j dV_j}{\int \int \int \int e^{\delta W_i} (e^{W_i^{(0)} + W_j^{(0)}}) d\tau_i dV_i d\tau_j dV_j}. \end{aligned} \quad (27)$$

Because composite steps are built from a sequence of elementary moves accepted with Boltzmann weight in the reference system, the terms appearing in parenthesis in Eq. (27) are implicitly taken into account when (MC)<sup>2</sup> sampling on the basis of the reference potential. Indicating a double average over initial and final states by nested brackets, Eq. (27) can be condensed as follows:

$$\bar{A} = \frac{\langle \langle \alpha_{ij} e^{\delta W_i} \rangle \rangle_0}{\langle \langle e^{\delta W_i} \rangle \rangle_0}, \quad (28)$$

where the subscripted “0” indicates that the averaging is performed entirely in the reference ensemble.  $\bar{A}$  can be built from Eq. (28) by sampling  $\delta W$  at a collection of decorrelated configurations (each separated by  $O \geq O_{\text{corr}}$  reference steps), meaning that the sampled points will be drawn purely from the reference distribution and thus without application of Eq. (22). We refer to this reference distribution sampling as the “reweighting” calculation,<sup>34,35</sup> and  $\bar{A}$  evaluated on this basis will be denoted  $\bar{A}_{rw}$ .  $\bar{A}_{rw}$  constitutes an *a priori* estimate of  $\bar{A}$ , in the sense that it provides an acceptance probability for N(MC)<sup>2</sup> composite steps (but only in the  $O_{\text{corr}}$  limit) without recourse to an actual N(MC)<sup>2</sup> simulation.

We now step through the procedure for performing an optimized N(MC)<sup>2</sup> simulation at a prescribed set of thermodynamic conditions ( $P=P', T=T'$ ). The reference (full) system weights  $W_k^{(0)}$  ( $W_k$ ) appearing in Eq. (27) depend on the reference (full) system temperature and pressure through Eq. (8), meaning that  $\bar{A} \equiv f(P^{(0)}, T^{(0)}, P, T)$ . Hereafter, the variable dependencies of  $\bar{A}$  will be listed in this order. From a single set of reference configurations collected in the reweighting calculation at  $(P^{(0)}, T^{(0)})$ , a family of  $\bar{A}_{rw}$  differing only in the values assigned to  $(P, T)$  can be constructed from Eq. (28). Because it is the thermodynamic state of the full system *only* that we wish to match with experiment,  $(P^{(0)}, T^{(0)})$  can be treated separately from  $(P, T)$  and the latter varied as free parameters in order to maximize  $\bar{A}_{rw}$  for a

given set of configurations. Previously<sup>34</sup> we applied a similar idea to the thermodynamics of fluid N<sub>2</sub> as described by DFT, but strictly in the context of reweighting configurations already sampled using traditional (MC)<sup>2</sup>. The reference system parameters can be varied to yield maximal  $\bar{A}_{rw} = \bar{A}_{\text{max}}^{(0)}$  at optimal  $(P^{(0)} = P_{\text{opt}}^{(0)}, T^{(0)} = T_{\text{opt}}^{(0)})$ ,

$$\begin{aligned} \bar{A}_{\text{max}}^{(0)}(P_{\text{opt}}^{(0)}, T_{\text{opt}}^{(0)}, P', T') &= \max\{\bar{A}_{rw}(x, y, P, T) : P_1^{(0)} \leq x \\ &\leq P_2^{(0)}, T_1^{(0)} \leq y \leq T_2^{(0)} : P = P', T = T'\}, \end{aligned} \quad (29)$$

where the reference system  $(x, y) = (P^{(0)}, T^{(0)})$  has been scanned over a given domain. This approach is permissible, but requires iteratively resampling  $\delta W$  (which includes evaluation of the full potential). Alternatively one can satisfy

$$\begin{aligned} \bar{A}_{\text{max}}(P', T', P_{\text{opt}}, T_{\text{opt}}) &= \max\{\bar{A}_{rw}(P^{(0)}, T^{(0)}, x, y) : P^{(0)} = P', T^{(0)} \\ &= T' : P_1 \leq x \leq P_2, T_1 \leq y \leq T_2\}, \end{aligned} \quad (30)$$

using the same set of reference configurations for each  $(x, y)$  pair. In general,  $\bar{A}_{\text{max}}^{(0)}$  is a function of  $(P, T)$  and  $\bar{A}_{\text{max}}$  is a function of  $(P^{(0)}, T^{(0)})$ ; in Eqs. (29) and (30), we have specified an actual *value* for these functions at designated values of  $(P^{(0)}, T^{(0)}, P, T)$ . Upon solution of Eq. (30) there are at least two different ways of returning the full system to the thermodynamic state of interest at  $(P=P', T=T')$ . The first is to collect reweighting samples at multiple  $(P^{(0)}, T^{(0)})$ , solve Eq. (30) at each thermodynamic state to yield a set of corresponding  $(P_{\text{opt}}, T_{\text{opt}})$  pairs, calculate ensemble averages at each new pair using the optimized N(MC)<sup>2</sup> procedure, then interpolate between those averages to obtain approximate values at the  $(P=P', T=T')$  combinations desired. We will take this approach in a future publication<sup>26</sup> where N(MC)<sup>2</sup> will be used to characterize the shock Hugoniot locus of N<sub>2</sub> over a wide range of thermodynamic conditions. Here we assume a simpler approach, more suitable for use of N(MC)<sup>2</sup> at an isolated thermodynamic state. After solving Eq. (30) for  $(P_{\text{opt}}, T_{\text{opt}})$ , we linearly extrapolate back to the original, de-

TABLE I. Summary of optimized N(MC)<sup>2</sup> parameters for four different reference potentials ( $l=0.90-1.05$  Å). Acceptance probabilities  $\bar{A}_{rw}$  are defined *a priori* by evaluation of Eq. (28) with reweighting samples;  $\bar{A}_{\text{MC}}$  are calculated *a posteriori* from N(MC)<sup>2</sup> simulation at the specified conditions.  $\bar{A}_{\text{max}}$  represents  $\bar{A}_{rw}$  following solution of Eq. (30). All acceptance probabilities are listed in the form  $\bar{A} \equiv f(P^{(0)}, T^{(0)}, P, T)$ . Uncertainties in the final digit of the acceptance probabilities are indicated in parenthesis.

$l$ (Å)	1.05	1.00	0.95	0.90
$T'$ (K)	728	728	728	728
$P'$ (GPa)	4.84	4.84	4.84	4.84
$T_{\text{opt}}$ (K)	756	796	846	867
$P_{\text{opt}}$ (GPa)	5.08	5.35	5.74	6.08
$T_{\text{opt}}^{(0)}$ (K)	700	660	610	589
$P_{\text{opt}}^{(0)}$ (GPa)	4.60	4.33	3.94	3.60
$\bar{A}_{rw}(P', T', P', T')$	0.367(5)	0.069(3)	0.010(1)	0.001(0)
$\bar{A}_{\text{MC}}(P', T', P', T')$	0.355(6)	0.084(3)	0.018(3)	0.006(1)
$\bar{A}_{\text{max}}(P', T', P_{\text{opt}}, T_{\text{opt}})$	0.512(5)	0.195(5)	0.061(3)	0.024(2)
$\bar{A}_{\text{MC}}(P', T', P_{\text{opt}}, T_{\text{opt}})$	0.553(7)	0.279(9)	0.077(9)	0.030(5)
$\bar{A}_{\text{MC}}(P_{\text{opt}}^{(0)}, T_{\text{opt}}^{(0)}, P', T')$	0.548(6)	0.252(7)	0.078(6)	0.021(5)

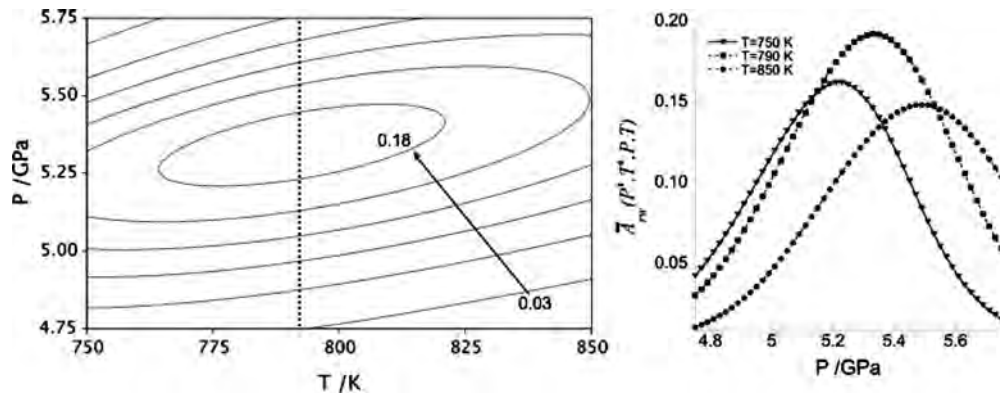


FIG. 6. Maximization of the acceptance probability  $\bar{A}_{rw}(P', T', P, T)$  by variation in full system pressure and temperature in Eq. (30). The contours in the left panel show acceptance probabilities for pressures of 4.75–5.75 GPa and temperatures of 750–850 K. The arrow points in the direction of uniformly increasing contour values; the dotted line indicates the isotherm containing the maximum acceptance probability. Three such isotherms are plotted in the right panel, including the one containing the  $\bar{A}_{rw}$  maximum at  $T=790$  K.

sired  $(P', T')$  and apply the same transformation to the reference variables, yielding approximate  $(P_{\text{opt}}^{(0)}, T_{\text{opt}}^{(0)})$ ,

$$P_{\text{opt}}^{(0)} \approx P^{(0)} + (P' - P_{\text{opt}}), \quad T_{\text{opt}}^{(0)} \approx T^{(0)} + (T' - T_{\text{opt}}). \quad (31)$$

Optimized N(MC)<sup>2</sup> is then performed at  $(P_{\text{opt}}^{(0)}, T_{\text{opt}}^{(0)}, P', T')$ . Concrete examples of this procedure are shown in Table I. Beginning at  $T=T^{(0)}=T'=728$  K and  $P=P^{(0)}=P'=4.84$  GPa, unoptimized N(MC)<sup>2</sup> simulations were carried out with all four reference system bond lengths  $l$  and the resultant  $\bar{A}_{\text{MC}}(P', T', P', T')$  recorded.  $\bar{A}_{\text{MC}}$  values represent an *a posteriori* estimate of  $\bar{A}$ , calculated simply as the number of accepted composite steps divided by the total number of composite trial steps in a N(MC)<sup>2</sup> simulation. The reference distribution of  $\delta W$  was then sampled at  $O(10^4)$  points, from which  $\bar{A}_{rw}(P', T', P', T')$  was built using Eq. (28).  $P$  and  $T$  were varied with Eq. (30) to yield  $\bar{A}_{\text{max}}$  and  $(P_{\text{opt}}, T_{\text{opt}})$ , then Eq. (31) was used to generate  $(P_{\text{opt}}^{(0)}, T_{\text{opt}}^{(0)})$ . Finally, N(MC)<sup>2</sup> simulations using the two optimized sets  $(P', T', P_{\text{opt}}, T_{\text{opt}})$  and  $(P_{\text{opt}}^{(0)}, T_{\text{opt}}^{(0)}, P', T')$  were performed to yield the corresponding  $\bar{A}_{\text{MC}}$ . Note that optimized reference

system variables were obtained by solution of Eq. (31), not Eq. (29); thus, no *a priori* estimate of  $\bar{A}_{\text{MC}}(P_{\text{opt}}^{(0)}, T_{\text{opt}}^{(0)}, P', T')$  is available. Numbers in parenthesis indicate statistical uncertainty in the final digit recorded. Discrepancies of greater than one  $\sigma$  between theoretical and computed values most likely reflect use of incompletely decorrelated samples.

We found the surface describing  $\bar{A}_{rw}$  as a function of  $P$  and  $T$  (or  $P^{(0)}$  and  $T^{(0)}$ ) to be generally smooth, and the scanned range of pressure and temperature values can be squeezed iteratively in combination with finer meshes until a maximum is located; this approach proceeds with little difficulty. The left panel in Fig. 6 presents a contour plot of predicted acceptance probabilities scanned over range of 750–850 K and 4.75–5.75 GPa for the reference potential  $l=1.00$  Å. Contour values were obtained in the process of solving Eq. (30), so the temperature and pressure being varied are that of the full system. The arrow points in the direction of uniformly increasing contour values, and the vertical dotted line marks the temperature at which  $\bar{A}_{rw}$  is maximal. A trio of acceptance probability “isotherms” drawn from the contour plot is depicted in the right panel; these curves scan

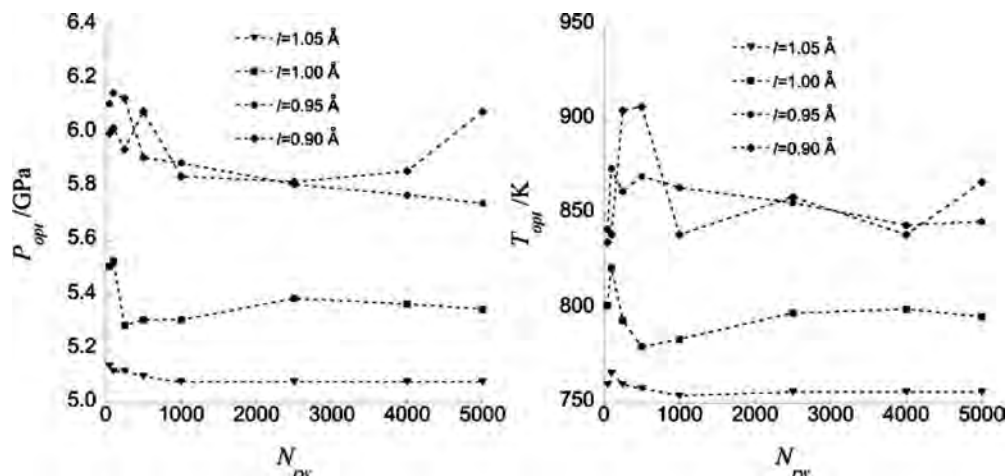


FIG. 7. Convergence of optimized  $(P=P_{\text{opt}}, T=T_{\text{opt}})$  as a function of the number of reweighting points  $N_{rw}$ . For each value of  $N_{rw}$ ,  $(P_{\text{opt}}, T_{\text{opt}})$  are found by solution of Eq. (30) using  $\bar{A}_{rw}$  built from Eq. (28). As the quality of the reference potential increases ( $l \rightarrow 1.10$  Å), so does the speed of convergence.

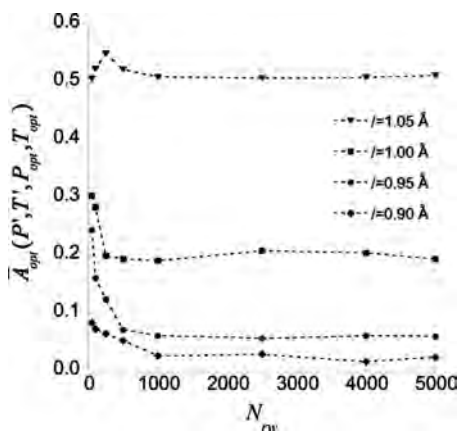


FIG. 8. Convergence of the optimal acceptance probability  $\bar{A}_{\text{opt}}(P', T', P_{\text{opt}}, T_{\text{opt}})$  as a function of reweighted sampling points  $N_{rw}$ .  $\bar{A}_{rw}$  is built from Eq. (28) and optimized using Eq. (30). All four potentials roughly converge within 1000 steps, although convergence becomes slightly oscillatory as the potential deviates further from the full potential. For  $N_{rw} \geq 1000$ , the statistical errors are roughly the size of the symbols.

$\bar{A}_{rw}$  over a range of pressures at fixed temperature. The overall maximum is clearly identifiable at  $T=790$  K and  $P=5.35$  GPa.

Solution of Eq. (29) or Eq. (30) requires sampling at enough points to provide a reliable estimate of  $\bar{A}_{rw}$  from Eq. (28). If such estimates require a large number of sampling points, then the sampling efficiency gained by optimizing N(MC)<sup>2</sup> will be lost in the overhead of performing the optimization itself. It is reasonable, then, to ask how many sampling points  $N_{rw}$  are required to predict stable values of  $(P_{\text{opt}}, T_{\text{opt}})$  or  $(P_{\text{opt}}^{(0)}, T_{\text{opt}}^{(0)})$ . The convergence of  $(P_{\text{opt}}, T_{\text{opt}})$  with respect to  $N_{rw}$  is illustrated in Fig. 7, where it appears to be faster for reference potentials closer to the full potential; while  $(P_{\text{opt}}, T_{\text{opt}})$  for  $l=1.05$  Å are converged at  $N_{rw}=1000$ ,  $(P_{\text{opt}}, T_{\text{opt}})$  for  $l=0.90$  Å are clearly unconverged even for  $N_{rw}=5000$ . We hasten to note, however, that convergence of the acceptance probability is much more important than convergence of the thermodynamic parameters. If  $\bar{A}_{\text{opt}}$  exhibits a broad, flat peak when expressed as a function of  $P$  and  $T$ , then strict convergence of the latter two is not necessary to ensure a dramatically improved acceptance probability. Figure 8 confirms that this is indeed the case: the  $\bar{A}_{\text{opt}}$  for all four reference potentials stabilize at roughly 1000 steps to the  $(P_{\text{opt}}, T_{\text{opt}})$  shown in Table I.

Having obtained solutions to Eq. (30) and extrapolated back to  $(P_{\text{opt}}^{(0)}, T_{\text{opt}}^{(0)})$  with Eq. (31), we now examine the performance of optimized N(MC)<sup>2</sup> using the new set of thermodynamic reference variables. Optimal acceptance probabilities and efficiencies are shown in Figs. 9 and 10 and should be compared directly to those of Figs. 4 and 5, respectively (note that the ordinate scales in Figs. 5 and 10 differ). Improvements in acceptance probability as a percentage of the unoptimized values for  $O=100-3000$  are shown in Table II. Improvement is significant for all potentials at all values of  $O$ , but the marginal gain increases as  $O$  grows larger and (in general) as the reference potential deviates more strongly from the full potential. The greatest performance improvements are for  $l=0.95$  Å, possibly indicating that already at

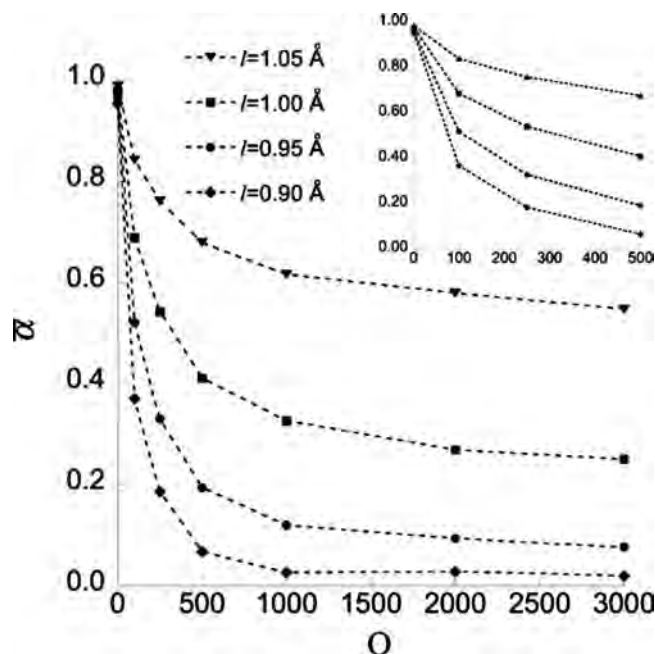


FIG. 9. Average acceptance probabilities  $\bar{\alpha}$  for the optimized N(MC)<sup>2</sup> procedure as a function of the number of reference steps  $O$  taken between full energy evaluations. Results should be compared with the those of the unoptimized procedure, shown in Fig. 4.

$l=0.90$  Å the physics embodied by the reference potential starts to deviate too strongly from that of the full potential for the optimization procedure to be fully effective.

The distribution  $\delta U \equiv U - U^{(0)}$  of potential energy differences sampled by trial states in N(MC)<sup>2</sup> interpolates between the distribution found by Metropolis sampling on the basis of the reference or full potential alone: for small  $O$ , the distribution of trial  $\delta U$  is roughly that encountered in sampling on

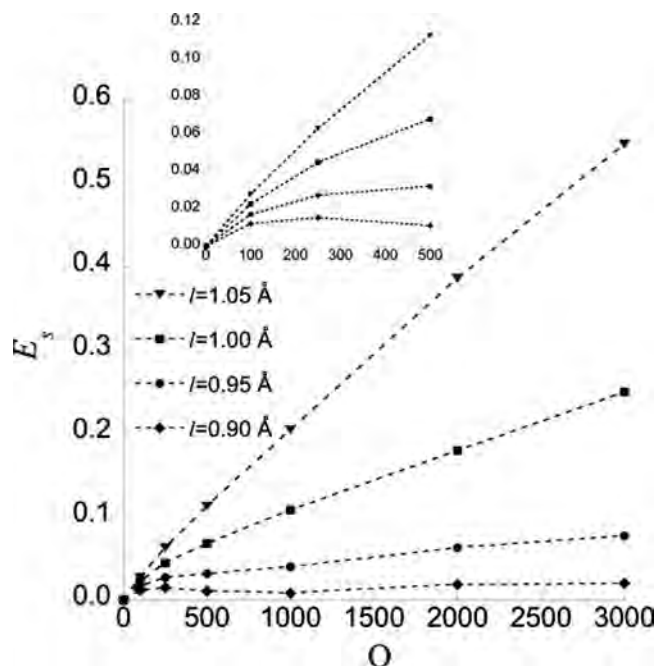


FIG. 10. Sampling efficiency  $E_s$  for the optimized N(MC)<sup>2</sup> procedure as a function of the number of reference steps  $O$  taken between full energy evaluations. Results should be compared to those of the unoptimized procedure, shown in Fig. 5.



TABLE II. Improvements in efficiency for optimized relative to unoptimized N(MC)<sup>2</sup>, as a percentage of efficiency for the latter and as a function of the reference system Markov chain length  $O$ .

$O$	$l=1.05$ Å	$l=1.00$ Å	$l=0.95$ Å	$l=0.90$ Å
100	17	35	31	20
250	26	67	100	60
500	31	89	167	175
1000	51	179	471	350
2000	56	210	473	533
3000	54	182	359	250

the basis of  $U$  only; in the  $O_{\text{corr}}$  limit, the  $\delta U$  distribution corresponds exactly to that found in sampling strictly on the basis of  $U^{(0)}$  (in this case, the trial state loses its “memory” of the initial state). Because trial states are assigned Boltzmann weight in the full system, the acceptance probability of N(MC)<sup>2</sup> steps is reflected indirectly in the overlap of the  $\delta U$  distributions for trial and accepted states (both distributions are a function of volume). Figure 11 illustrates  $\delta u$  [where  $u \equiv (U - U^{(0)})/N$ ] versus  $v$  ( $v \equiv V/N$ ) for  $l=1.05$  Å and  $O=1000$ . Unoptimized N(MC)<sup>2</sup> results are shown in the left panel and optimized results in the right. The overlap of the trial (black points) and accepted [gray (red) points] distributions increases significantly upon optimization, where we have indicated the values of  $(P_0, T_0, P, T)$  used in the underlying simulations. Figure 12 illustrates the same data, but for  $l=0.90$  Å and  $O=1000$ . Again, optimization increases the overlap considerably. The density of accepted points is much lower than in Fig. 11, in keeping with the acceptance probabilities listed in Table II. The system exhibits also a strong tendency to become “trapped” at certain volumes, indicated by the broken, vertical collections of trial points. As stated in Sec. IV, the acceptance probability for N(MC)<sup>2</sup> steps remains good even with a poor reference potential if one is willing to employ a smaller  $O$ . Figure 13 shows the same distributions as in Fig. 12, but for  $O=250$  instead of  $O=1000$ . Not only are the overlaps between trial and accepted distributions greater before and after optimization, but the volume trapping noted in connection with Fig. 12 is absent almost entirely. There is considerably more skew in the trial distribu-

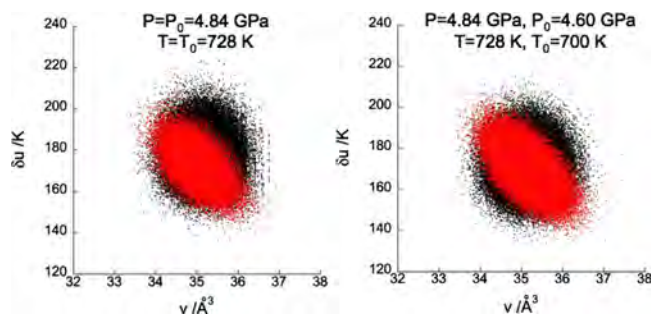


FIG. 11. (Color online) Distribution of energy difference per particle ( $\delta u \equiv (U - U^{(0)})/N$ ) vs volume per particle ( $v \equiv V/N$ ) for the unoptimized (left) and optimized (right) N(MC)<sup>2</sup> procedure at  $l=1.05$  Å and offset  $O=1000$ . The black data represent trial composite steps; the gray (red) data are accepted composite steps. The  $\Delta W$  appearing in Eq. (23) are found from the difference in trial and accepted points. Note the increase in these distributions upon optimization, and thus the decrease in  $\langle\langle\Delta W\rangle\rangle$ .

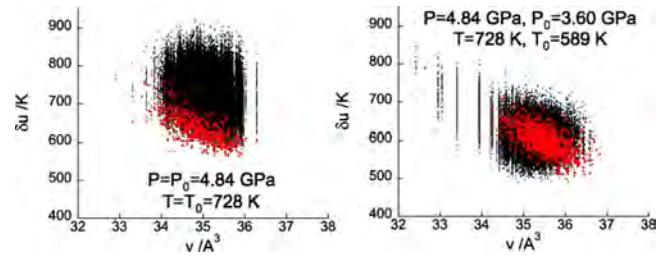


FIG. 12. (Color online) Distribution of energy difference per particle ( $\delta u \equiv (U - U^{(0)})/N$ ) vs volume per particle ( $v \equiv V/N$ ) for the unoptimized (left) and optimized (right) N(MC)<sup>2</sup> procedure at  $l=0.90$  Å and offset  $O=1000$ . The black data represent trial composite steps; the gray (red) data are accepted composite steps; accepted points have been enlarged slightly relative to trial points in order to enhance contrast. The  $\Delta W$  appearing in Eq. (23) are found from the difference in trial and accepted points. Note the change in overlap of the distributions upon optimization.

tion for smaller offsets; this reflects correlation between initial and final points in the composite trial step. Although this combination of reference potential and  $O$  yields high overlap and thus a good acceptance probability, many more sampling points will be required to minimize the variance in ensemble averages.

From the sets of trial and accepted points shown in Figs. 11 and 12, one can build the  $\Delta W$  distributions appearing in Eq. (23), thus establishing a direct link between trial distributions and acceptance probabilities. Figure 14 depicts the  $\Delta W$  distributions built from Figs. 11 (left panel) and Fig. 12 (right panel). As expected, the distributions for the better reference potential ( $l=1.05$  Å) are narrower and their means lie closer to zero. Optimization substantially lowers the absolute value of  $\langle\langle\Delta W\rangle\rangle$  and  $\sigma(\Delta W)$  for both values of  $l$  (we have indicated the double averaging over initial and final points by nested brackets), and both of these factors contribute to a higher average acceptance probability for composite moves. This exercise provides an alternate means of evaluating the performance of the optimization procedure, in that the first two moments of the  $\Delta W$  distribution are closely related to the acceptance probability. Table III provides an overview of these moments (before and after optimization) for all of the potentials surveyed.

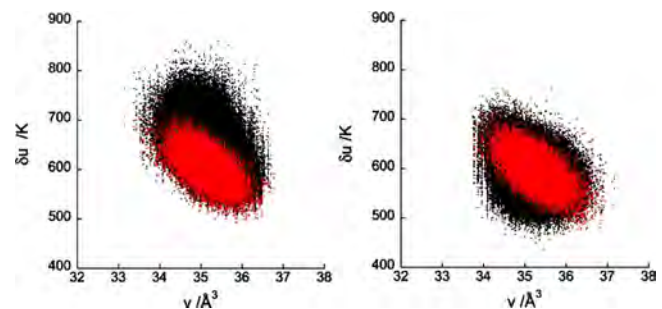


FIG. 13. (Color online) Distribution of energy difference per particle ( $\delta u$ ) vs volume per particle ( $v \equiv V/N$ ) for the unoptimized (left) and optimized (right) N(MC)<sup>2</sup> procedures at  $l=0.90$  Å and offset  $O=250$ . The black data represent trial composite steps; the gray (red) data are accepted composite steps. The  $\Delta W$  appearing in Eq. (23) are found from the difference in trial and accepted points. Even for a poor reference potential, significant acceptance probabilities can be achieved by lowering  $O$  (cf. Fig. 12). Note that for lower values of  $O$ , the correlation of  $\delta u$  and  $v$  remains even in the trial distribution.



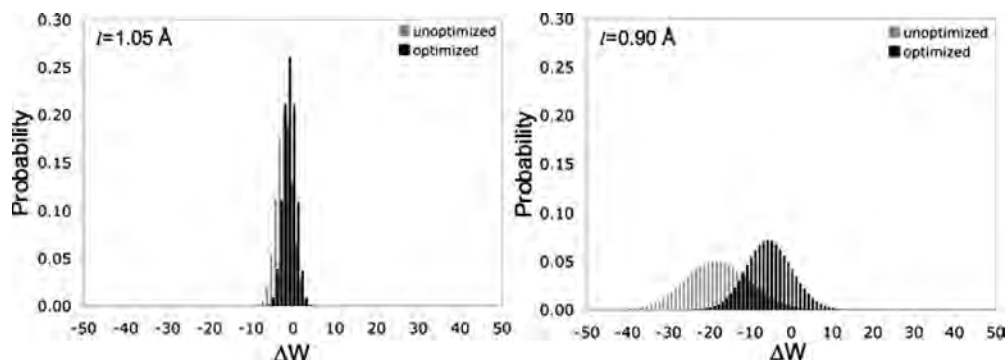


FIG. 14. Direct visualization of the  $\Delta W$  appearing in Eq. (23), taken as the difference in  $\delta W$  for the trial and accepted distributions shown in Fig. 11 (left panel) and Fig. 12 (right panel). Upon optimization, the mean value of  $\Delta W$  shifts closer to zero and the width of the distribution shrinks in both cases. Both of these factors contribute to a higher acceptance probability for composite moves.

## VI. SUMMARY

Nested Markov chain MC (N(MC)<sup>2</sup>) allows (MC)<sup>2</sup> sampling with a potential of given accuracy (the full potential) without needing to evaluate it following every elementary step. By stringing together a sequence of single-particle moves accepted on the basis of a more approximate potential

TABLE III. First two moments in the distribution of  $\Delta W$  appearing in Eq. (23), as a function of the reference system Markov chain length  $O$  and for all of the reference potentials surveyed. The double brackets indicate averaging over initial and final points [ $i$  and  $j$  in Eq. (27)], and values are listed before and after (opt) optimization.

	$\langle\langle\Delta W\rangle\rangle$	$\langle\langle\Delta W\rangle\rangle_{\text{opt}}$	$\sigma(\Delta W)$	$\sigma_{\text{opt}}(\Delta W)$
$l=1.05 \text{ \AA}$				
$O=100$	-0.27	-0.08	1.88	1.32
$O=250$	-0.59	-0.19	1.95	1.34
$O=500$	-0.86	-0.35	2.08	1.37
$O=1000$	-1.38	-0.51	2.34	1.43
$O=2000$	-1.59	-0.63	2.46	1.47
$O=3000$	-1.68	-0.71	2.53	1.77
$l=1.00 \text{ \AA}$				
$O=100$	-1.08	-0.31	3.84	2.72
$O=250$	-2.27	-0.73	4.46	2.80
$O=500$	-3.27	-1.33	4.98	3.01
$O=1000$	-5.10	-1.89	6.32	3.23
$O=2000$	-5.89	-2.40	6.96	3.61
$O=3000$	-5.99	-2.60	6.99	3.67
$l=0.95 \text{ \AA}$				
$O=100$	-1.92	-0.67	5.70	4.47
$O=250$	-4.46	-1.55	7.34	4.83
$O=500$	-7.09	-2.85	9.18	5.41
$O=1000$	-10.72	-4.02	12.02	6.26
$O=2000$	-11.58	-4.98	12.68	6.88
$O=3000$	-11.36	-5.11	12.42	6.89
$l=0.90 \text{ \AA}$				
$O=100$	-2.70	-0.82	7.69	6.13
$O=250$	-6.17	-1.80	9.40	7.19
$O=500$	-12.46	-3.95	14.80	9.44
$O=1000$	-17.25	-5.11	18.96	11.02
$O=2000$	-16.66	-5.53	17.83	10.82
$O=3000$	-18.05	-7.39	19.33	11.68

(the reference system), trial steps in the full system are made to encompass multiple particles. The acceptance probability of this composite step can be maximized in at least two different ways. The first, described above, involves manipulation of the thermodynamic conditions characterizing the reference system such that the variance of the  $\delta U$  versus  $V$  distribution<sup>36</sup> is minimal. A second means of optimization, not explored here, is direct, iterative modification of the reference potential to conform with “targets” (such as average energies or volumes) computed with the full potential. Changes could be made adaptively to the reference potential functional form or its parametrization or (in the case of an AI reference potential) the basis set or level of convergence. An iterative strategy similar to that used in optimal pulse shaping<sup>37</sup> or empirical structure refinement<sup>38</sup> could be employed in combination with the thermodynamic optimization described above to yield an even more efficient route to accurate equilibrium sampling.

Clearly there are limits to the range of reference potentials suitable to any given full potential. Qualitative differences in the nature of intermolecular forces, such as the complete absence of attractions, cannot be salvaged using the optimized N(MC)<sup>2</sup> procedure; hard spheres will never be a good reference for AI water. Once a pair of potentials is different enough that the overlap of their  $\delta U$  versus  $V$  distributions is nearly zero, collecting statistics to evaluate Eq. (27) does become quite difficult. These difficulties were apparent even in the  $l=0.90 \text{ \AA}$  case above, in spite of the fact that our reference and full potentials have the same functional form. Bennett’s methods<sup>39</sup> for estimating  $\Delta W$  surely are useful in this context, but it is unlikely that even optimal performance will be acceptable if such techniques are required simply to estimate  $\bar{A}$  (i.e., thermodynamic optimization can only move the distribution so far). In cases of irretrievably small overlap, one should probably opt for a different set of potentials.

## ACKNOWLEDGMENTS

J.D.C. thanks the Office of the Director at Los Alamos National Laboratory (LANL) for support in the form of a Director’s Postdoctoral Fellowship. M.S.S. is supported by the LANL High Explosives Project of the National Nuclear Security Administration (NNSA) Advanced Strategic Com-

puting Program (HE-ASC). T.D.S. is supported by the LANL Laboratory Directed Research and Development (LDRD) Program and by the Army Research Office under Grant No. W911NF-05-1-0265. LANL is operated by Los Alamos National Security L.L.C. under the auspices of the NNSA and the U.S. Department of Energy, under Contract No. DE-AC52-06NA25396.

- <sup>1</sup>M. P. Allen and D. J. Tildesley, *Computer Simulation of Liquids* (Oxford University Press, Oxford, 1987).
- <sup>2</sup>D. Frenkel and B. Smit, *Understanding Molecular Simulation: From Algorithms to Applications* (Academic, New York, 2002).
- <sup>3</sup>D. P. Landau and K. Binder, *A Guide to Monte Carlo Simulations in Statistical Physics* (Cambridge University Press, Cambridge, 2000).
- <sup>4</sup>W. Feller, *An Introduction to Probability Theory and its Applications*, 2nd ed. (Wiley, New York, 1957).
- <sup>5</sup>B. J. Alder and T. E. Wainwright, *J. Chem. Phys.* **31**, 459 (1959).
- <sup>6</sup>N. Metropolis, A. W. Rosenbluth, M. N. Rosenbluth, A. H. Teller, and E. Teller, *J. Chem. Phys.* **21**, 1087 (1953).
- <sup>7</sup>S. Goedecker, *Rev. Mod. Phys.* **71**, 1085 (1999).
- <sup>8</sup>W. Koch and M. C. Holthausen, *A Chemist's Guide to Density Functional Theory*, 2nd ed. (Wiley-VCH, New York, 2001); R. G. Parr and W. Yang, *Density-Functional Theory of Atoms and Molecules* (Oxford University Press, New York, 1989).
- <sup>9</sup>Y. Yamaguchi, J. D. Goddard, Y. Osamura, and H. F. Schaefer, *A New Dimension to Quantum Chemistry: Analytic Derivative Methods in Ab Initio Molecular Electronic Structure Theory* (Oxford University Press, New York, 1994).
- <sup>10</sup>R. Car and M. Parrinello, *Phys. Rev. Lett.* **55**, 2471 (1985); M. E. Tuckerman, *J. Phys.: Condens. Matter* **14**, R1297 (2002).
- <sup>11</sup>L. D. Crosby and T. L. Windus, *J. Phys. Chem. A* **113**, 607 (2009).
- <sup>12</sup>A. Nakayama, N. Seki, and T. Taketsugu, *J. Chem. Phys.* **130**, 024107 (2009).
- <sup>13</sup>Of course the converse is also true, the most obvious manifestation of which is MC's limitation to equilibrium contexts.
- <sup>14</sup>M. S. Shaw, *J. Chem. Phys.* **94**, 7550 (1991); J. K. Johnson, A. Z. Panagiotopoulos, and K. E. Gubbins, *Mol. Phys.* **81**, 717 (1994); J. K. Johnson, *Adv. Chem. Phys.* **105**, 461 (1998); C. Heath Turner, J. K. Brennan, M. Lissal, W. R. Smith, J. K. Johnson, and K. E. Gubbins, *Mol. Simul.* **34**, 119 (2008).
- <sup>15</sup>C. Pangali, M. Rao, and B. J. Berne, *Chem. Phys. Lett.* **55**, 413 (1978); M. Rao, C. Pangali, and B. J. Berne, *Mol. Phys.* **37**, 1773 (1979).
- <sup>16</sup>P. Rossky, J. D. Doll, and H. L. Friedman, *J. Chem. Phys.* **69**, 4628 (1978).
- <sup>17</sup>R. Iftimie, D. Salahub, D. Wei, and J. Schofield, *J. Chem. Phys.* **113**, 4852 (2000).
- <sup>18</sup>L. D. Gelb, *J. Chem. Phys.* **118**, 7747 (2003).
- <sup>19</sup>These include two-surface MC and the molecular mechanics based importance function method. We eschew the first because it is too evocative of electronically excited states, and the second because it inaccurately characterizes the method's generality.
- <sup>20</sup>C. H. Mak, *J. Chem. Phys.* **122**, 214110 (2005).
- <sup>21</sup>K. Bernacki, B. Hetenyi, and B. J. Berne, *J. Chem. Phys.* **121**, 44 (2004); B. Hetenyi, K. Bernacki, and B. J. Berne, *ibid.* **117**, 8203 (2002).
- <sup>22</sup>A. Brandt, V. Ilyin, N. Makedonska, and I. Suwan, *J. Mol. Liq.* **127**, 37 (2006).
- <sup>23</sup>E. Lyman, F. M. Ytreberg, and D. M. Zuckerman, *Phys. Rev. Lett.* **96**, 028105 (2006); E. Lyman and D. M. Zuckerman, *J. Chem. Theory Comput.* **2**, 656 (2006).
- <sup>24</sup>H. Li and W. Yang, *J. Chem. Phys.* **126**, 114104 (2007).
- <sup>25</sup>P. Bandyopadhyay, *J. Chem. Phys.* **122**, 091102 (2005); P. Bandyopadhyay, *ibid.* **128**, 134103 (2008); P. Bandyopadhyay, *Theor. Chem. Acc.* **120**, 307 (2008); L. D. Gelb and T. N. Carnahan, *Chem. Phys. Lett.* **417**, 283 (2006); R. Iftimie, D. Salahub, and J. Schofield, *J. Chem. Phys.* **119**, 11285 (2003); R. Iftimie and J. Schofield, *ibid.* **114**, 6763 (2001); R. Iftimie and J. Schofield, *Int. J. Quantum Chem.* **91**, 404 (2003); I.-F. W. Kuo, C. J. Mundy, M. J. McGrath, J. I. Siepmann, J. VandeVondele, M. Sprik, J. Hutter, B. Chen, M. L. Klein, F. Mohamed, M. Krack, and M. Parrinello, *J. Phys. Chem. B* **108**, 12990 (2004); D. R. Matusek, S. Osborne, and A. St-Amant, *J. Chem. Phys.* **128**, 154110 (2008); M. J. McGrath, J. I. Siepmann, I.-F. W. Kuo, and C. J. Mundy, *Mol. Phys.* **104**, 3619 (2006); M. J. McGrath, J. I. Siepmann, I.-F. W. Kuo, C. J. Mundy, J. VandeVondele, J. Hutter, F. Mohamed, and M. Krack, *ChemPhysChem* **6**, 1894 (2004); M. J. McGrath, J. I. Siepmann, I.-F. W. Kuo, C. J. Mundy, J. VandeVondele, M. Sprik, J. Hutter, F. Mohamed, M. Krack, and M. Parrinello, *Comput. Phys. Commun.* **169**, 289 (2005); J. Michel, R. D. Taylor, and J. W. Essex, *J. Chem. Theory Comput.* **2**, 732 (2006); J. Michel, M. L. Verdonik, and J. W. Essex, *J. Med. Chem.* **49**, 7427 (2006).
- <sup>26</sup>J. D. Coe, T. D. Sewell, and M. S. Shaw, "Equilibrium thermodynamics of dense fluid nitrogen as described by nested Markov chain Monte Carlo sampling of a density functional theory potential," *J. Chem. Phys.* (submitted).
- <sup>27</sup>Y. B. Zel'dovich and Y. P. Raizer, *Physics of Shock Waves and High-Temperature Hydrodynamic Phenomena* (Dover, Mineola, 2002).
- <sup>28</sup>P. J. Hay, R. T. Pack, and R. L. Martin, *J. Chem. Phys.* **81**, 1360 (1984); J. D. Johnson, M. S. Shaw, and B. L. Holian, *ibid.* **80**, 1279 (1984).
- <sup>29</sup>W. K. Hastings, *Biometrika* **57**, 97 (1970).
- <sup>30</sup>W. W. Wood, *J. Chem. Phys.* **52**, 729 (1970).
- <sup>31</sup>The  $N \ln V_i$  term arises from the use of scaled coordinates.
- <sup>32</sup>V. I. Manousiouthakis and M. W. Deem, *J. Chem. Phys.* **110**, 2753 (1999).
- <sup>33</sup>Due to the absence of strongly attractive forces, as well as the high temperature and pressure of the system, the equilibration periods required were much shorter than for, say, water at STP.
- <sup>34</sup>M. S. Shaw and C. Tymczak, in *Shock Compression of Condensed Matter*, edited by M. D. Furnish (American Institute of Physics, New York, 2005), Vol. 845, p. 179.
- <sup>35</sup>I. R. McDonald and K. Singer, *J. Chem. Phys.* **47**, 4766 (1967).
- <sup>36</sup>This is the case only for the isothermal-isobaric ensemble. In the canonical ensemble, for instance, it would be the  $\delta U$ - $P$  distribution.
- <sup>37</sup>E. C. Carroll, J. L. White, A. C. Florean, P. H. Bucksbaum, and R. J. Sension, *J. Phys. Chem. A* **112**, 6811 (2008); H. Rabitz, *Science* **299**, 525 (2003).
- <sup>38</sup>A. K. Soper, *Chem. Phys.* **202**, 295 (1996); A. K. Soper, *Mol. Phys.* **99**, 1503 (2001).
- <sup>39</sup>C. H. Bennett, *J. Comput. Phys.* **22**, 245 (1976).

# Nested Markov chain Monte Carlo sampling of a density functional theory potential: Equilibrium thermodynamics of dense fluid nitrogen

Joshua D. Coe,<sup>1,a)</sup> Thomas D. Sewell,<sup>2</sup> and M. Sam Shaw<sup>1</sup>

<sup>1</sup>Theoretical Division, Los Alamos National Laboratory, Los Alamos, New Mexico 87545, USA

<sup>2</sup>Department of Chemistry, University of Missouri-Columbia, Columbia, Missouri 65211-7600, USA

(Received 17 April 2009; accepted 20 July 2009; published online 17 August 2009)

An optimized variant of the nested Markov chain Monte Carlo [n(MC)<sup>2</sup>] method [J. Chem. Phys. **130**, 164104 (2009)] is applied to fluid N<sub>2</sub>. In this implementation of n(MC)<sup>2</sup>, isothermal-isobaric (NPT) ensemble sampling on the basis of a pair potential (the “reference” system) is used to enhance the efficiency of sampling based on Perdew–Burke–Ernzerhof density functional theory with a 6-31G\* basis set (PBE/6-31G\*, the “full” system). A long sequence of Monte Carlo steps taken in the reference system is converted into a trial step taken in the full system; for a good choice of reference potential, these trial steps have a high probability of acceptance. Using decorrelated samples drawn from the reference distribution, the pressure and temperature of the full system are varied such that its distribution overlaps maximally with that of the reference system. Optimized pressures and temperatures then serve as input parameters for n(MC)<sup>2</sup> sampling of dense fluid N<sub>2</sub> over a wide range of thermodynamic conditions. The simulation results are combined to construct the Hugoniot of nitrogen fluid, yielding predictions in excellent agreement with experiment. © 2009 American Institute of Physics. [DOI: 10.1063/1.3200904]

## I. INTRODUCTION

The behavior of matter subjected to extreme conditions is a topic of abiding interest, having direct application to shock physics<sup>1</sup> as well as the planetary<sup>2</sup> and geosciences.<sup>3</sup> Its relevance to the latter has assumed new importance in the wake of global climate change, as sequestration of CO<sub>2</sub> in underground reservoirs may constitute a vital component in emission-free processing of fossil fuels.<sup>4</sup> The focus here will be on equilibrium characterization of warm, dense fluids such as those produced by detonation of high explosive (HE) compounds. Specifically, Monte Carlo (MC) simulation<sup>5,6</sup> will be used to characterize the locus of accessible shock states (known as the Hugoniot locus<sup>7</sup>) for molecular nitrogen fluid, an almost ubiquitous component of HE detonation product mixtures.

Recently<sup>8</sup> (hereafter, we will refer to Ref. 8 as Paper 1) we reported a thermodynamic optimization procedure designed to improve the sampling efficiency of the nested Markov chain Monte Carlo [n(MC)<sup>2</sup>] method.<sup>9,10</sup> The n(MC)<sup>2</sup> procedure partitions a standard MC simulation into a reference system defined by an approximate potential and a full system defined by an alternative, more accurate one. A sequence of elementary moves (in the NPT ensemble, these correspond to single-particle displacements or volume adjustments), each accepted with Boltzmann weight in the reference system, is used to build a many-particle composite trial step taken in the full system. A slight modification of the acceptance criterion for these extended trial steps recovers Metropolis sampling of the full potential without having to evaluate it at each configuration. The approach developed in Paper 1 improved the efficiency of the n(MC)<sup>2</sup> technique by

allowing the thermodynamic states of the reference and full systems to vary independently such that their respective distributions attained maximal overlap, thereby raising the mean acceptance probability for trial composite steps. Because the purpose of Paper 1 was merely to illustrate the procedure, the reference and full systems were defined by model potentials not differing in computational expense. The present work serves both to extend the application of optimized (*o*-) n(MC)<sup>2</sup> to a full system characterized by density functional theory (DFT) (Ref. 11) and to construct the shock Hugoniot locus of fluid N<sub>2</sub> at this level of theory.

The following section describes in detail the potentials used, an analytical pair potential for the reference system and DFT for the full system. Section III reviews the principal expressions making up the *o*-n(MC)<sup>2</sup> procedure, referring the reader to previous works for their full justification. Section IV outlines the continuum theory of shock waves as expressed in the Rankine–Hugoniot relations as well as the implementation of these relations in the context of atomistic simulation; this linkage is then illustrated by construction of the N<sub>2</sub> Hugoniot locus from the *o*-n(MC)<sup>2</sup> simulation results discussed in Sec. III. The final section summarizes and offers some thoughts on future implementation of the procedure.

## II. POTENTIAL ENERGY EVALUATION

### A. Specification of the full potential

DFT replaces the antisymmetric *N*-electron wavefunction, expressed in spin-spatial coordinates **x**,

$$\Psi \equiv \Psi(\mathbf{x}_1, \mathbf{x}_2, \dots, \mathbf{x}_N), \quad (1)$$

with the spatial density of a single electron,

<sup>a)</sup>Electronic mail: jcoe@lanl.gov.



$$\rho(\mathbf{r}) = N \int \cdots \int |\Psi(\mathbf{x}_1, \mathbf{x}_2, \dots, \mathbf{x}_N)|^2 ds_1 d\mathbf{x}_2 \cdots d\mathbf{x}_N. \quad (2)$$

Although this procedure appears to entail considerable information loss, the first Hohenberg–Kohn theorem<sup>12</sup> guarantees a unique map from the density to the ground state energy,  $E_g$ ,

$$\rho \Rightarrow \hat{H} \Rightarrow \Psi \Rightarrow E_g. \quad (3)$$

$E_g$  can then be expressed as a functional of the density,  $E_g[\rho]$ , and its constituent parts decomposed<sup>13</sup> in the following manner:

$$E_g[\rho] = T_S[\rho] + J[\rho] + E_{Ne}[\rho] + E_{XC}[\rho]. \quad (4)$$

The various contributions to the total electronic energy are, respectively, the kinetic energy for a gas of noninteracting electrons, the (mean-field) Coulombic repulsion, the Coulombic electron-nuclear attraction, and the exchange-correlation functional. The first three terms are analytically soluble whereas the fourth subsumes all quantum effects (including real-time, dynamic electron correlation, the Pauli principle, the self-interaction correction,<sup>14</sup> and correlated electron contributions to the kinetic energy) and has so far proven strongly resistant to universal description. Although exchange-correlation functionals constructed entirely from first principles have been reported,<sup>15</sup> most  $E_{XC}[\rho]$  are built from fits to a set of experimental and/or *ab initio* data. Different functionals, then, are distinguished primarily by their exchange-correlation component,  $E_{XC}[\rho]$ . The second Hohenberg–Kohn theorem<sup>12</sup> establishes a variational principle for the density in the same manner as for the wavefunction, and the Kohn–Sham equations<sup>13</sup> permit iterative solution for a set of one-electron orbitals in the same manner as the Roothaan equations<sup>16</sup> in Hartree–Fock.

All of the quantum chemical calculations reported below were carried out using GAUSSIAN03.<sup>17</sup> In test calculations on a periodic cubic cell containing 100 N<sub>2</sub> at density  $\rho = 1.46 \text{ g/cm}^3$ , we evaluated the performance of four different  $E_{XC}[\rho]$ : BLYP,<sup>18,19</sup> PBE,<sup>20</sup> PW91,<sup>21</sup> and BVWN.<sup>18,22</sup> All periodic calculations of the liquid-state energy were performed at the  $\Gamma$ -point.<sup>23</sup> In addition to the relative computational speed at the point of basis set convergence, we compared the computed bond length and frequency of the isolated molecule to their experimental values.

The basis sets examined cover the range from minimal [STO-3G (Ref. 24)] to triple zeta with polarization (*d* and *f*) functions, the latter containing 70 basis functions for each molecule. There is no evidence of ionization at the densities of interest here, so diffuse functions were neither necessary nor desirable; energies computed using the 6-311G(3*df*,3*pd*) basis<sup>25</sup> were thus treated as the complete basis set limit (CBSL) for each functional. Table I records the percent deviation in the total energy (relative to that of 100 isolated N<sub>2</sub> molecules) for a periodic box of 100 N<sub>2</sub> molecules in a typical liquid-state configuration drawn from the reference distribution, calculated as a function of  $E_{XC}[\rho]$  and basis set, from that calculated with the same functional at the CBSL. All energies were corrected for basis set superposition error (BSSE),<sup>26</sup> the spurious stabilization conferred upon an atomic center by basis functions “borrowed” from

TABLE I. Percent deviation of the BSSE-corrected energy of 100 N<sub>2</sub> molecules at density of  $\rho = 1.46 \text{ g/cm}^3$ , as a function of basis set and  $E_{XC}[\rho]$ , from that calculated using the same functional at the CBSL [defined as 6-311G(3*df*,3*pd*) (Ref. 25)]. Three of the four functionals tested are converged to roughly 1% using the 6-31G\* basis. Based on these results, the 6-31G\* basis set was used in all subsequent calculations reported in this study.

Basis set	BLYP <sup>a</sup>	PW91 <sup>a</sup>	PBE <sup>a</sup>	BVWN <sup>a</sup>
STO-3G <sup>a</sup>	-40.2	-42.9	-33.8	-34.1
6-31G <sup>b</sup>	2.5	4.6	5.3	0.8
6-31G* <sup>a</sup>	-1.1	-3.1	-1.4	-1.4
6-311G** <sup>c</sup>	-1.0	-2.0	-1.1	-0.7

<sup>a</sup>See text for reference.

<sup>b</sup>Reference 52.

<sup>c</sup>References 27 and 53

another atom. Our target accuracy for the nitrogen Hugoniot was  $\sim 1\%$ , and although this value does not translate directly to an accuracy constraint on the DFT energy, it does serve as a useful guide. All four functionals tested were converged to roughly 1% at the 6-31G\* (Refs. 27 and 28) level, although the performance of PW91 is noticeably worse than that of the other three. Because full system energies computed using any of the four functionals paired with 6-31G\* yielded good accuracy in reasonable time, this basis set was singled out for further tests on the isolated molecule.

Ground state properties recorded in Table II reflect little variation among the various flavors of DFT, although it is interesting that all four outperformed MP2 (Ref. 29) in predicting *l*, the equilibrium bond length (correcting for anharmonicity makes the MP2 value even worse relative to those of DFT). The rightmost column of Table II compares relative timings for each functional paired with the 6-31G\* basis set, and speedup factors were defined as the ratio of time  $\tau$  needed to compute the energy of the full box of 100 N<sub>2</sub> to a reference value  $\tau_{\text{ref}}$ ,

$$\text{speedup} = \frac{\tau}{\tau_{\text{ref}}}. \quad (5)$$

The reference time was defined to be that required by the slowest functional, giving it a speedup factor of unity. PW91

TABLE II. Performance of several exchange-correlation functionals in comparison to those of MP2 and experiment. Points of comparison include ground state bond length *l* and (harmonic-approximation) frequency  $\omega$  of the isolated N<sub>2</sub> molecule, as well as the relative time required for a three-dimensional periodic single-point calculation on the fluid sample of 100 N<sub>2</sub> molecules. All calculations used the 6-31G\* basis set. Speedup factors are defined in the text, the largest value corresponding to the fastest time and the slowest assigned a factor of unity. Based on the results of this simulation, the PBE functional was chosen for use in all subsequent calculations reported.

EXC	<i>l</i> (Å)	$\omega$ (cm <sup>-1</sup> )	Speedup
BLYP	1.118	2337	1.00
PBE	1.117	2360	1.13
PW91	1.116	2364	1.14
BVWN	1.116	2346	1.09
MP2	1.131	2175	...
Expt <sup>a</sup>	1.094	2359	...

<sup>a</sup>Reference 39.



was fastest, although the difference with PBE was practically negligible. On the basis of its being well converged at the 6-31G\* level, predicting satisfactory ground state properties, and (almost) recording the fastest calculation time, the PBE functional was chosen for all subsequent calculations.

We conclude this section with a note regarding omission of local density approximation (LDA) functionals. Although not shown, we also tested SLYP<sup>19,30</sup> and SVWN<sup>22,30</sup> in addition to the generalized gradient approximation functionals examined above. Calculated energies dropped steadily on approach to the CBSL, actually dipping well below zero in the case of SLYP. A negative energy would imply that it is thermodynamically preferable for a sample of nitrogen gas to compress spontaneously to a density of 1.46 g/cm<sup>3</sup>, clearly indicating catastrophic failure of LDA in describing the dense N<sub>2</sub> fluid sample.

## B. Parametrization of the reference potential

Vital to our scheme for building equilibrium averages with DFT energies was a rapidly computable potential function capturing enough of the essential physics to serve as an

adequate reference for the DFT. After having converged an accurate combination of exchange-correlation functional and basis set, we parametrized the reference potential on the basis of this model chemistry.

The exponential-6 (Buckingham) potential was used to describe pairwise interaction,  $\varphi_{ab}$ , of atomic sites  $a$  and  $b$ . The sites reside on diatomic molecules  $i$  and  $j$ , so the complete interaction for a pair of reference system molecules is summarized in

$$\varphi(r_{ab}) = \frac{\varepsilon}{\alpha - 6} \left( 6e^{\alpha(1-r_{ab})} - \frac{\alpha}{r_{ab}^6} \right) \quad (6)$$

and

$$\varphi_{ij} = \sum_{a=1}^2 \sum_{b=1}^2 \varphi(r_{ab}). \quad (7)$$

The site-site radii can be re-expressed in terms of the center-of-mass (c.m.) separation vector  $\mathbf{r}_{ij}$  and bond vectors  $\mathbf{l}_i$  and  $\mathbf{l}_j$  (of lengths  $l_i$  and  $l_j$ ),

$$r_{ab}^2 = \frac{0.25r_{ij}^2(l_i^2 + l_j^2) + (-1)^a(\mathbf{r}_{ij} \cdot \mathbf{l}_i) + (-1)^b(\mathbf{r}_{ij} \cdot \mathbf{l}_j) + (-1)^{a+b}0.5(\mathbf{l}_i \cdot \mathbf{l}_j)}{r_0^2}. \quad (8)$$

Bond lengths were fixed at  $l=1.117$  Å, the value predicted by PBE/6-31G\* for the isolated N<sub>2</sub> molecule. Parameters  $\varepsilon$ ,  $\alpha$ , and  $r_0$  represent the depth of the well, the steepness of the repulsive wall, and the position of the minimum, respectively; their fitted values and the process used to obtain them are provided below. Although Eq. (6) realistically captures the exponential character of hard-core repulsion and the  $r^{-6}$

dependence of dispersion at long range,<sup>31</sup> it also diverges to  $-\infty$  at very short range. Using the parameter set described below, the potential function defined by Eqs. (6)–(8) reaches a maximum value of  $9 \times 10^4$  K at  $r_{ab} \approx 1.15$  Å, so enforcing a minimum allowable separation  $r_{\min} = 1.20$  Å safely avoided the (unphysical) strongly attractive forces present at small values of  $r_{ab}$ .

In order to ensure suitable parameter values, Eq. (6) was fitted to a set of PBE/6-31G\* energies for the N<sub>2</sub> dimer relative to those for a pair of isolated N<sub>2</sub> molecules. The distribution of pair configurations sampled in a fluid was approximated using the four fiducial configuration types depicted in Fig. 1, denoted as  $P$ ,  $L$ ,  $T$ , and  $X$ . Center-of-mass distances were scanned over ranges of 1.59–4.23 Å ( $X$ ), 1.85–4.50 Å ( $P$ ), 1.59–5.29 Å ( $T$ ) and 2.38–6.62 Å ( $L$ ) in roughly 0.25 Å intervals and the difference between Eq. (6) and the PBE result was recorded. The weighted sum of these differences, squared, was then minimized over the domain of the parameter set,

$$\min_{\alpha, \varepsilon, r_0} \text{Err} = \min_{\alpha, \varepsilon, r_0} \left\{ \sum_{l=1}^4 \sum_{k=1}^{N_l} w_{k,l} (\varphi_{ij}^{\text{DFT}}(k, l) - \varphi_{ij}^{\text{exp-6}}(k, l))^2 \right\}, \quad (9)$$

FIG. 1. Diatomic pair configurations used to parametrize the reference potential whose behavior is illustrated in Fig. 2. Bond lengths were held fixed at  $l=1.117$  Å, while c.m. separations  $r_{ij}$  were swept over a range of roughly 1.6–6.6 Å, depending on the configuration type (see text). Configuration types are characterized by four angles,  $(\theta_1, \chi_1, \theta_2, \chi_2)$ , where  $\theta$  and  $\chi$  represent rotation of molecules 1 and 2 within and out of the plane of the page. Clockwise rotations are positive, and all angle values are zeroed to those of the  $P$  configuration.

where  $l$  runs over the set of pair configuration types  $\{P, L, T, X\}$  and  $k$  indexes the  $N_l$  discrete values of  $r_{ij}$ . The weights,

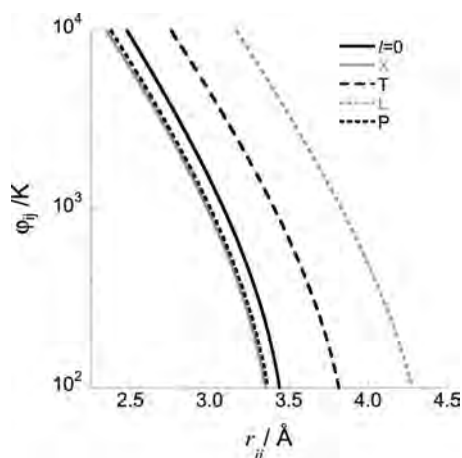


FIG. 2. The pair potential defined by Eqs. (6)–(8) and (12) as a function of c.m. separation  $r_{ij}$  for the diatomic pair configurations illustrated in Fig. 1 (X, T, L, and P) and a fixed bond length  $l=1.117$  Å. Comparison of these curves with the purely spherical potential ( $l=0$  Å) reveals the anisotropic character of  $\phi_{ij}$ . Note that the ordinate is plotted on a log scale.

$$w_{k,l} = \frac{1}{(\max\{\phi_{ij}^{\text{DFT}}(k,l), \phi_{\text{sw}}\})^2}, \quad (10)$$

were chosen to forestall disproportionate contributions from large c.m. separations (unlikely to be of much importance in the dense fluid regime sampled below) by setting  $\phi_{\text{sw}}=1000$  K, and the weighted root mean square error (wRMSE) was evaluated as

$$\text{wRMSE} = \sqrt{\frac{\text{Err}}{\sum_{l=1}^4 N_l}}. \quad (11)$$

This procedure yielded the following best-fit parameter values

$$\varepsilon = 34.156 \text{ K},$$

$$r_0 = 4.037 \text{ Å}, \quad (12)$$

$$\alpha = 12.29,$$

with a wRMSE of 0.189. At fixed parameter values  $\phi_{ab}$  is determined entirely by the site-site separation ( $r_{ab}$ ), but it is important to note that the full interaction of two diatomics ( $\phi_{ij}$ ) is highly anisotropic. The character of the reference potential defined by Eqs. (6)–(8) and (12) is illustrated in Fig. 2, where we have plotted  $\phi_{ij}$  over a range of  $r_{ij}$  for the four fiducial configuration types shown in Fig. 1. These should be compared not only with one another but also with a purely spherical potential ( $l=0$ ) for which the four configuration types collapse into one.

In order to estimate the magnitude of many-body effects, we compared the standard pair energy,

$$U_{AB}^{(2)} = U_{AB} - U_A - U_B, \quad (13)$$

with an “effective” pair energy for molecules in the liquid,

$$U_{AB}^* = U_{\text{box}} + U_{\text{box-AB}} - U_{\text{box-A}} - U_{\text{box-B}}, \quad (14)$$

where  $U_A$  ( $U_B$ ) is the total energy of isolated molecule A(B),  $U_{AB}$  is that of two molecules taken together,  $U_{\text{box}}$  is the en-

ergy of a box containing 100 molecules in the liquid state, and  $U_{\text{box-X}}$  is that of the same box with the designated molecule or pair removed. Under the assumption that many-body effects terminate at three-body interactions, it can be shown (see Appendix A) that the sum over all A and B of  $U_{AB}^* - U_{AB}^{(2)}$  gives the many-body energy of the sample to within a constant factor. For a pair of molecules<sup>32</sup> taken from a liquid-state configuration at  $T=3267$  K and  $P=16.8$  GPa,  $U_{AB}^{(2)}/k_B = 4519$  K and  $U_{AB}^*/k_B = 3030$  K [it is important to note that in evaluating Eqs. (13) and (14), all atoms removed were replaced with a ghost basis set just as in standard counterpoise calculations], giving a many-body stabilization per pair of approximately 1500 K, or one-third of the isolated pair energy. Although a rough estimate only, this provides strong *prima facie* evidence of an appreciable many-body contribution to the energy, and thus motivation for moving beyond straightforward use of pair potentials when high accuracy is required.

### III. NESTED MARKOV CHAIN MONTE CARLO SAMPLING

The following provides only a brief overview of *o-n*(MC)<sup>2</sup>; for a more complete treatment, see Paper 1. In standard MC sampling with the Metropolis algorithm, a trial step drawn from a uniform distribution (also known as the marginal distribution) is accepted with probability<sup>33</sup>

$$\alpha_{ij} = \min\left(\frac{\pi_j}{\pi_i}, 1\right), \quad (15)$$

where  $\pi_k$  represents the relative weight assigned to configuration space point  $k$ .  $\pi_k \propto e^{W_k}$  in classical statistics and  $W_k$  is a thermodynamic function appropriate to the ensemble being sampled. In the isothermal–isobaric (*NPT*) ensemble used below,  $W$  is defined as

$$W_k \equiv -\beta(U_k + PV_k) + N \ln V_k, \quad (16)$$

the final term of which results from the use of scaled coordinates.<sup>5,34</sup>  $U$ ,  $V$ , and  $\beta$  represent internal energy, volume, and inverse temperature  $(kT)^{-1}$ , respectively. Trial moves consist of single-particle displacements and volume adjustments, and the relative probabilities of attempted move types are chosen *a priori* according to the needs of the simulation. Ensemble averages of some property  $X$  can be approximated by discrete quadrature according to

$$\langle X \rangle_{NPT} = \frac{\int \pi(\tau, V) X d\tau dV}{\int \pi(\tau, V) d\tau dV} \approx \frac{1}{N_s} \sum_{i=1}^{N_s} X_i, \quad (17)$$

where  $\tau$  represents the full array of system coordinates and the sum runs over the  $N_s$  configurations sampled by the MC simulation. The variance in such averages will decrease as  $N_s$  rises and, in the limit of fully decorrelated samples, the scaling relation assumes the well-known form  $\sigma_X \sim N_s^{-1/2}$ . Configurations sampled consecutively using standard MC are related by elementary moves; that is, they are *highly* correlated. If the system energy is expressible in a simple analytical form, then the use of highly correlated samples can be compensated for by accumulating sufficiently large values of  $N_s$ . The difficulty arises when one requires both

high accuracy, such as that offered by an *ab initio* or DFT potential, and high precision, which requires many decorrelated sampling points. If each acceptance test (energy evaluation) is costly in terms of computing time, then being forced to collect strongly correlated samples may preclude precision sampling on purely practical grounds.

A method for sampling an accurate and expensive potential without requiring the strongly correlated samples of conventional MC was introduced by Iftimie *et al.*,<sup>9</sup> reformulated by Gelb,<sup>10</sup> and refined by the current authors.<sup>8</sup> The n(MC)<sup>2</sup> method concatenates a sequence of elementary moves, each accepted with Boltzmann weight on the basis on an approximate reference potential. At the endpoints of this sequence a modified Metropolis test is used to recover a Boltzmann distribution of states based on a different (and hopefully, more accurate) potential. We will refer to the elementary steps taken independently as *reference* steps (taken in the reference system), and the entire sequence of reference steps bookended by evaluations of the second potential as a *full* step (taken in the full system, characterized by the full potential.) Consecutive full system energies are partially decorrelated by the intervening sequence of reference steps. If the full potential is more expensive than the reference potential, then n(MC)<sup>2</sup> lowers the total cost of the calculation by limiting the  $N_s$  required for a target  $\sigma_X$  on averages taken in the full system. Indicating reference system quantities with superscripted “0,” the form of the acceptance probability required for Metropolis sampling of the partially decorrelated (full) potential is<sup>8–10</sup>

$$\alpha_{ij} = \min\left(1, \frac{\pi_i \pi_j^{(0)}}{\pi_j \pi_i^{(0)}}\right). \quad (18)$$

To summarize, a sequence of trial steps taken in the reference system and accepted according to (15) is used to build a trial step taken in the full system that is accepted according to (18). Note that the standard ratio of Boltzmann factors for the initial and final states in the full system has been “corrected” by the inverse of this ratio for the reference system. Following our previous treatment, we express the difference in full and reference system weights for state  $k$  as  $\delta W_k \equiv W_k - W_k^{(0)}$  and the difference in  $\delta W$  for consecutive full system configurations as  $\Delta W \equiv \delta W_i - \delta W_j$ . Equation (18) can then be recast as

$$\alpha_{ij} = \begin{cases} 1, & \Delta W \geq 0 \\ e^{\Delta W}, & \Delta W < 0. \end{cases} \quad (19)$$

The total speedup factor  $S$  gained by sampling the full potential with n(MC)<sup>2</sup> rather than with traditional MC can be given in terms of the computing time needed to reach a target variance requiring  $N_d$  decorrelated evaluations of the full potential. The cost of collecting these directly through standard Metropolis sampling is

$$\Lambda = N_d O_{\text{corr}} \lambda, \quad (20)$$

where  $\lambda$  is the computational expense of making an elementary move with the full potential.  $O_{\text{corr}}$  is an effective correlation length (assumed to be roughly equal for reference and full potentials) statistically equivalent to a single random

sample drawn from the distribution. It is only an effective length in the sense that it incorporates the inefficiency of rejected steps as well as net motion through configuration space, and therefore it will vary with the maximum trial step radius. For the purposes of this discussion, we assume this radius to be set such that the mean acceptance probability of elementary trial steps made using either potential is the same. The total cost of collecting  $N_d$  decorrelated samples using the n(MC)<sup>2</sup> procedure is then

$$\Lambda' = \frac{N_d O_{\text{corr}} \lambda^{(0)} + \frac{N_d O_{\text{corr}} \lambda}{O}}{\bar{\alpha}}, \quad (21)$$

where  $\lambda^{(0)}$  is the cost of an elementary move made with the reference potential,  $\bar{\alpha}$  is the mean acceptance probability of trial composite steps, and  $O$  is the number of reference steps comprising a single composite step. The speedup factor is the ratio of  $\Lambda$  and  $\Lambda'$ ,

$$S = \frac{\Lambda}{\Lambda'} = \frac{\bar{\alpha} \lambda}{\lambda^{(0)} + \frac{\lambda}{O}}. \quad (22)$$

In his presentation of n(MC)<sup>2</sup>, Gelb<sup>10</sup> made the additional simplification that  $\lambda/\lambda^{(0)} = O(N)$  when a pair potential is used as reference for an  $N$ -body potential such as DFT. Because the prefactor in such scaling relations can be highly significant, we include it explicitly and simplify Eq. (22) further such that

$$S = \frac{\bar{\alpha}}{\frac{1}{\kappa N} + \frac{1}{O}}, \quad (23)$$

where  $\lambda/\lambda^{(0)} = \kappa N$ . Although we have not attempted to quantify  $\kappa$  carefully, a conservative estimate of its value in our simulations is  $O(10^7)$ , whereas a large value for  $O$  would be  $O(10^3)$ . Therefore we ignore the first term in the denominator and obtain as an approximate speedup factor

$$S \approx \bar{\alpha} O. \quad (24)$$

This is an intuitively satisfying result, indicating that when the cost of evaluating the reference potential is negligible compared to that of evaluating the full potential, the speedup from using n(MC)<sup>2</sup> over MC is roughly equal to the effective length (actual length tempered by average probability of acceptance) of composite steps taken in the full system.

The presence of  $\bar{\alpha}$  in the denominator of Eq. (21) suggests a simple prescription for raising the value of  $S$ : Increase the mean acceptance probability of trial composite steps. Although composite steps built from a sequence of elementary steps taken on the reference potential lower the correlation between consecutive evaluations of the full potential, differences between the reference and full system distributions impose practical limits on the length of these sequences. That is, because the distributions generally will peak in different regions of configuration space, the greater the number of elementary steps taken on the reference potential between acceptance tests taken on the full potential,

the more the reference system Markov chain will “drift” back to the center of its own distribution (see especially Figs. 11–14 in Paper 1) and thereby lower the mean acceptance probability of trial composite steps. Conversely, the greater the difference in distribution of reference and full potentials, the lower the mean acceptance probability of trial composite steps built from a fixed number of elementary steps taken on the reference potential. It would seem, then, that raising the mean acceptance probability of trial composite steps requires shifting one or both of the reference and full distributions such that their overlap is enhanced.

As detailed in Paper 1, the average acceptance probability for  $n(\text{MC})^2$  steps can be expressed exactly in the limit that a pair of configurations  $i$  and  $j$  are decorrelated. We express the mean acceptance probability in this limit as

$$\bar{A} \equiv \lim_{O \rightarrow O_{\text{corr}}} \bar{\alpha}. \quad (25)$$

An initial state  $i$  will, by construction, possess relative weight  $e^{W_i}$  if the goal is to sample the full distribution. The final state  $j$  will, in the  $O_{\text{corr}}$  limit, be drawn randomly from the reference distribution and thus carry weight  $e^{W_j^{(0)}}$ . Note that the acceptance probability  $\alpha_{ij}$  given in Eq. (18) also can be expressed in terms of  $\delta W$  and  $W^{(0)}$  for states  $i$  and  $j$  so that  $\alpha_{ij}$  averaged over the configuration and volume spaces of all decorrelated  $(i, j)$  pairs gives

$$\begin{aligned} \bar{A} &= \frac{\iiint \alpha_{ij} e^{W_i + W_j^{(0)}} d\tau_i dV_i d\tau_j dV_j}{\iiint e^{W_i + W_j^{(0)}} d\tau_i dV_i d\tau_j dV_j} \\ &= \frac{\iiint \alpha_{ij} e^{\delta W_i} (e^{W_i^{(0)} + W_j^{(0)}}) d\tau_i dV_i d\tau_j dV_j}{\iiint e^{\delta W_i} (e^{W_i^{(0)} + W_j^{(0)}}) d\tau_i dV_i d\tau_j dV_j}. \end{aligned} \quad (26)$$

The integrals in Eq. (26) can be estimated by sampling  $\delta W$  at  $N_{\text{rw}}$  configurations drawn from the reference distribution; for the combination of potentials used here,  $N_{\text{rw}} = O(100)$ . We refer to this process as the reweighting<sup>35</sup> calculation, and estimates of  $\bar{A}$  built in this manner will be denoted  $\bar{A}_{\text{rw}}$ . Note that the terms appearing in parenthesis in Eq. (26) are present implicitly when  $i$  and  $j$  are sampled from the reference distribution so that Eq. (26) can be written more succinctly as

$$\bar{A} = \frac{\langle \langle \alpha_{ij} e^{\delta W} \rangle \rangle_0}{\langle \langle e^{\delta W} \rangle \rangle_0}, \quad (27)$$

where the subscripted zeros indicate that the distribution being sampled is that of the reference potential. Because the  $\delta W$  appearing in Eq. (26) depend on the full system pressure and temperature through Eq. (16), a single set of  $N_{\text{rw}}$  points sampled from the reference distribution at a given  $P^{(0)}$  and  $T^{(0)}$  can be used to build a family of  $\bar{A}_{\text{rw}}$  varying parametrically as functions of  $P$  and  $T$ . It is appropriate to express  $\bar{A}_{\text{rw}}$  as a function of all four thermodynamic variables,  $\bar{A}_{\text{rw}} \equiv f(P^{(0)}, T^{(0)}, P, T)$ , and all subsequent references to  $\bar{A}_{\text{rw}}$  will list them in this order. Note that  $\bar{A}_{\text{rw}}$  is an *a priori* estimate of acceptance probability for composite steps taken with the  $n(\text{MC})^2$  procedure in that it predicts acceptance probabilities without reliance upon an actual  $n(\text{MC})^2$  simulation. If one desires full system thermodynamic data at  $(P=P', T=T')$ , a

reweighting calculation performed at those conditions can be followed by variation in  $P$  and  $T$  so as to maximize  $\bar{A}_{\text{rw}}$ . We express this optimization procedure as follows:

$$\begin{aligned} \bar{A}_{\text{rw}}^{(\text{max})} &\equiv \bar{A}_{\text{rw}}(P', T', P_{\text{opt}}, T_{\text{opt}}) \\ &= \max\{\bar{A}_{\text{rw}}(P^{(0)}, T^{(0)}, x, y) : P^{(0)} = P', T^{(0)} = T' : P_1 \\ &\leq x \leq P_2, T_1 \leq y \leq T_2\}. \end{aligned} \quad (28)$$

The initial domain covered by the full system variables can be chosen generously, then squeezed incrementally in conjunction with finer meshes; we have found the  $\bar{A}_{\text{rw}}$  surface to vary smoothly with  $(x, y) = (P, T)$ , as illustrated in Fig. 6 of Paper 1. There we obtained  $(P=P_{\text{opt}}, T=T_{\text{opt}})$  for full system variables, then extrapolated linearly back to the original  $(P=P', T=T')$ , and applied the same transformation to the reference system variables to yield  $(P^{(0)} \approx P_{\text{opt}}, T^{(0)} \approx T_{\text{opt}})$ . In this way, optimized  $n(\text{MC})^2$  simulations could be carried out at the full system conditions desired but with reference system conditions designed to maximize the *a priori* acceptance probability of composite steps taken in the full system. The approach taken here is slightly different in that we performed  $n(\text{MC})^2$  sampling with the optimal set  $(P^{(0)}=P', T^{(0)}=T', P=P_{\text{opt}}, T=T_{\text{opt}})$  resulting from Eq. (28). This generated full system thermodynamic conditions different from the original  $(P', T')$ , and an expansion procedure described in the next section was used to recover results at  $(P, T)$  on the Hugoniot.

Data illustrating the reweighting, optimization, and optimized  $n(\text{MC})^2$  simulation results are shown in Table III. The  $\delta W$  distribution was sampled at  $N_{\text{rw}}$  configurations drawn from the reference distribution at the  $(P^{(0)}=P', T^{(0)}=T')$  pairs shown in the two leftmost columns.  $\bar{A}_{\text{rw}}^{(0)} \equiv \bar{A}_{\text{rw}}(P', T', P', T')$  was built using Eq. (27), then maximized according to Eq. (28) to yield  $\bar{A}_{\text{rw}}^{(\text{max})}$  at  $(P=P_{\text{opt}}, T=T_{\text{opt}})$ ; the resulting  $P_{\text{opt}}$  and  $T_{\text{opt}}$  are shown in the third and fourth columns of Table III. One measure of the procedure's effectiveness is the ratio of the optimized to original *a priori* acceptance probabilities,  $\bar{A}_{\text{rw}}^{(\text{max})}/\bar{A}_{\text{rw}}^{(0)}$ ; as shown in the right side of the table, the predicted acceptance probabilities rose by factors of roughly 1.5–25. Note that minor absolute variations in  $\bar{A}_{\text{rw}}^{(0)}$  (a small number) can make large differences in the ratio. After maximizing  $\bar{A}_{\text{rw}}$  through variation in  $P$  and  $T$  as in Eq. (28), optimized  $n(\text{MC})^2$  simulations were performed using the  $(P', T', P_{\text{opt}}, T_{\text{opt}})$  combinations that resulted. The number of elementary steps taken in the reference system used to build a composite step made in the full system was  $O=150$ , whereas  $O_{\text{corr}} \approx 1000$  for the reference and full potentials chosen in Sec. II (cf. Fig. 3 in Paper 1). The average speedup factor  $S$  achieved in sampling the full potential with  $o\text{-}n(\text{MC})^2$  rather than traditional MC was just over 50.

No attempt was made in the present work to maximize  $O$ , the number of elementary steps in the reference system used to build a trial composite step in the full system. This potential loss of efficiency is compensated for partly by a higher mean acceptance probability at lower  $O$  values, but the ideal situation would be one in which optimization were performed directly on  $S$  rather than on  $\bar{A}_{\text{rw}}$ . This, in turn,



TABLE III. Summary of the reweighting and optimization procedures described in the text. The  $\delta W$  distribution was sampled at  $N_{\text{rw}}$  configurations defined by the thermodynamic conditions ( $P^{(0)}=P'$ ,  $T^{(0)}=T'$ ). The *a priori* acceptance probability  $\bar{A}_{\text{rw}}^{(0)} \equiv \bar{A}_{\text{rw}}(P', T', P', T')$  was then calculated from Eq. (27), followed by optimization according to Eq. (28) to yield  $\bar{A}_{\text{rw}}^{(\text{max})} \equiv \bar{A}_{\text{rw}}(P', T', P_{\text{opt}}, T_{\text{opt}})$ . The effectiveness of the optimization is reflected in the ratio  $\bar{A}_{\text{rw}}^{(\text{max})}/\bar{A}_{\text{rw}}^{(0)}$ . The speedup factor  $S \approx \alpha O$  is given for optimized n(MC)<sup>2</sup> simulations in which  $O=150$  and  $O_{\text{corr}} \approx 1000$ .

$P^{(0)}=P'$	$T^{(0)}=T'$	$P_{\text{opt}}$	$T_{\text{opt}}$	$N_{\text{rw}}$	$\bar{A}_{\text{rw}}^{(0)}$ (%)	$\bar{A}_{\text{rw}}^{(\text{max})}$ (%)	$\bar{A}_{\text{rw}}^{(\text{max})}/\bar{A}_{\text{rw}}^{(0)}$	$S$
6.30	728	4.84	615	563	0.49	4.14	8.45	41.6
9.70	1424	7.48	1200	394	0.49	8.84	18.04	55.3
11.90	1893	9.22	1606	478	0.82	3.73	4.55	60.4
14.90	2540	11.94	2206	430	0.59	6.78	11.49	55.3
15.80	2730	12.52	2355	484	0.34	7.96	23.41	52.9
19.20	3490	16.79	3267	532	2.94	9.59	3.26	64.7
20.50	3795	16.60	3270	444	0.63	13.01	20.65	53.3
20.60	3812	16.93	3417	386	2.25	8.62	3.83	56.7
23.00	4375	19.98	4079	380	1.74	7.32	4.21	27.7
23.20	4410	19.63	3886	444	2.49	5.89	2.37	76.0
23.30	4434	17.58	3361	443	1.84	3.09	1.68	34.5
23.50	4475	21.27	4308	441	3.72	5.97	1.60	55.2
24.70	4765	19.58	3854	525	0.42	1.50	3.57	60.5
25.20	4877	20.75	4362	439	2.30	3.65	1.59	56.5
27.40	5421	22.01	4769	426	0.76	3.91	5.14	60.7
28.90	5785	21.29	4765	420	1.17	3.20	2.74	40.7
30.00	6062	23.06	5156	492	0.67	2.91	4.34	41.2
40.50	8847	34.90	8308	429	5.48	7.86	1.43	40.0

would require an analytical expression for the acceptance probability in Eq. (27) in terms of  $O$ , as well as more extensive reweighting calculations over variable  $O$ . Empirical examination of the variation in  $\bar{\alpha}$  with  $O$  can be found in Paper 1.

In order to limit the computational overhead of the reweighting and optimization procedures, it is desirable that  $\bar{A}_{\text{rw}}^{(\text{max})}$  converge for  $N_{\text{rw}}$  as small as possible; otherwise, efficiency gained in using the optimized form of n(MC)<sup>2</sup> will be lost in performing the optimization procedure itself. As discussed in Paper 1 (and particularly in connection with Figs. 7 and 8 there),  $\bar{A}_{\text{rw}}^{(\text{max})}$  tends to converge faster than  $(P_{\text{opt}}, T_{\text{opt}})$  due to its exhibiting a broad flat peak as a function of  $P$  and  $T$ . Figure 3 illustrates the convergence behavior of  $\bar{A}_{\text{rw}}^{(\text{max})}$  for five pairs of  $(P=P', T=T')$  spanning the full range of conditions included in Table IV. All five states exhibited an initial decline in  $\bar{A}_{\text{rw}}^{(\text{max})}$  as reweighting samples were added but stabilized roughly in the neighborhood of  $N_{\text{rw}}=100-500$ . While convergence was incomplete in most cases (particularly for the more extreme thermodynamic states), it still was adequate to ensure large efficiency increases relative to standard n(MC)<sup>2</sup> or conventional MC sampling on the basis of the full potential.

#### IV. THE NITROGEN HUGONIOT

The Hugoniot locus is comprised of thermodynamic states accessible by shock loading of an initial state. In this section we describe application of the *o*-n(MC)<sup>2</sup> method to construction of the Hugoniot locus for N<sub>2</sub> fluid and compare our predictions to experimental data. Prior to doing so, how-

ever, we briefly summarize the continuum theory of shock waves as well as the statistical approximations underlying atomistic treatment.

Consider a sample of material having specific volume  $V_0$  (volume per unit mass =  $1/\rho_0$ ) and specific internal energy  $E_0$ , struck by a piston moving at speed  $u_p$ . If  $c_0$  is the sound speed in the material at zero pressure and  $u_p \ll c_0$ , the impact will create an acoustic wave moving through the sample at speed  $c_0$ ; pistons having speeds of  $u_p \sim 0.01c_0$  or greater will generate shock waves characterized by discontinuous density gradients at the wave front. Mass, momentum, and energy conservation in samples initially at rest at zero pressure

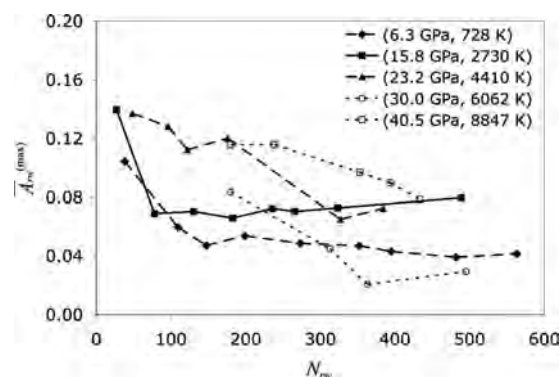


FIG. 3. Convergence behavior of  $\bar{A}_{\text{rw}}$  with respect to the number of reweighted sampling points  $N_{\text{rw}}$ , for five combinations of initial  $(P=P', T=T')$ . All combinations show an initial decrease in acceptance probability, but level out at roughly  $N_{\text{rw}}=500$ .  $\bar{A}_{\text{rw}}$  is an *a priori* estimate of  $\bar{\alpha}$  in the decorrelated limit ( $O=1000$ ), and therefore much lower than the  $\bar{\alpha}$  computed *a posteriori* from n(MC)<sup>2</sup> simulation at  $O=150$ .

TABLE IV. Summary of simulation data used in Figs. 4–8.

$P$ (GPa)	$T$ (K)	$V$ (cm <sup>3</sup> /g)	$\sigma(V)$ (cm <sup>3</sup> /g)	$U$ (kJ/g)	$\sigma(U)$ (kJ/g)	$E$ (kJ/g)	$\Delta E_c$ (kJ/g)	$\Delta T$ (K)	$\Delta E$ (kJ/g)	$\Delta V$ (cm <sup>3</sup> /g)
4.84	615	0.7126	0.0090	0.714	0.029	1.174	0.070	-31	-0.045	-0.0102
7.48	1 200	0.6678	0.0059	1.107	0.060	2.062	0.121	-75	-0.115	-0.0015
8.00	1 172	0.6590	0.0074	1.178	0.052	2.107	-0.012	9	0.010	0.0006
9.22	1 606	0.6535	0.0068	1.431	0.052	2.762	0.276	-224	-0.236	-0.0085
10.00	1 557	0.6299	0.0080	1.590	0.061	2.875	0.050	-39	-0.041	-0.0017
11.94	2 206	0.6195	0.0054	1.819	0.056	3.733	0.273	-210	-0.236	-0.0061
12.00	1 957	0.6112	0.0070	1.873	0.071	3.543	0.015	-13	-0.014	-0.0003
12.52	2 355	0.6228	0.0088	1.843	0.059	3.904	0.291	-207	-0.220	-0.0114
15.00	2 585	0.5863	0.0068	2.337	0.091	4.628	0.001	-1	-0.001	0.0000
16.60	3 270	0.5874	0.0092	2.594	0.094	5.575	0.451	-350	-0.348	-0.0123
16.79	3 267	0.5872	0.0074	2.530	0.079	5.508	0.322	-253	-0.285	-0.0044
16.93	3 417	0.5760	0.0060	2.737	0.097	5.867	0.543	-464	-0.536	-0.0008
17.58	3 361	0.5686	0.0054	2.823	0.148	5.896	0.297	-200	-0.296	-0.0001
19.58	3 854	0.5682	0.0079	3.096	0.153	6.671	0.417	-310	-0.357	-0.0061
19.63	3 886	0.5594	0.0066	3.074	0.074	6.681	0.325	-250	-0.282	-0.0044
19.98	4 079	0.5508	0.0103	3.053	0.088	6.858	0.299	-158	-0.218	-0.0081
20.00	3 704	0.5514	0.0070	3.137	0.097	6.559	0.001	0	-0.001	0.0000
20.75	4 362	0.5544	0.0063	3.307	0.106	7.401	0.623	-425	-0.544	-0.0076
21.27	4 308	0.5583	0.0070	3.172	0.105	7.211	0.302	-229	-0.266	-0.0033
21.29	4 765	0.5599	0.0064	3.449	0.104	7.957	1.058	-769	-0.940	-0.0111
22.01	4 769	0.5482	0.0102	3.439	0.121	7.951	0.686	-549	-0.532	-0.0139
23.06	5 156	0.5404	0.0087	3.722	0.178	8.631	0.924	-728	-0.852	-0.0062
25.00	4 915	0.5286	0.0093	3.935	0.245	8.597	0.083	-61	-0.079	-0.0003
30.00	6 218	0.5123	0.0044	4.426	0.108	10.429	-0.056	49	0.054	0.0002
34.90	8 308	0.5054	0.0054	5.319	0.183	13.483	1.144	-951	-1.089	-0.0031
35.00	7 612	0.4999	0.0079	5.194	0.156	12.638	0.166	-141	-0.144	-0.0013
40.00	9 096	0.4775	0.0079	6.179	0.533	15.158	0.441	-290	-0.466	0.0012
45.00	10 675	0.4752	0.0032	6.387	0.132	17.002	0.377	-324	-0.356	-0.0009

( $P_0 \approx 0$ ) yield for specific volume ( $V_H$ ), density ( $\rho_H = 1/V_H$ ), pressure ( $P_H$ ), and specific internal energy ( $E_H$ ) behind the shock front<sup>36</sup>

$$P_H = \rho_0 u_s u_p, \quad (29)$$

$$\rho_H = \rho_0 \left( \frac{u_s}{u_s - u_p} \right), \quad (30)$$

$$E_H = E_0 + \frac{1}{2} P_H (V_0 - V_H) = E_0 + \frac{1}{2} P_H \left( \frac{\rho_H - \rho_0}{\rho_H \rho_0} \right), \quad (31)$$

where  $u_s$  is the shock front velocity,  $u_p$  is the particle velocity (equal to the piston velocity), and final values have been designated by a subscripted  $H$  for Hugoniot. These expressions are known collectively as the Rankine–Hugoniot relations or jump conditions. Equations (29)–(31) identify the locus of states thermodynamically accessible to the sample upon shock compression of a given initial state, and in this they embed considerable information regarding the material equation of state (EOS).

Two important variables in Eq. (31) are  $E$ , the specific internal energy or energy per unit mass, and  $V$ , specific volume or volume per unit mass. Thermodynamic contributions and simulation averages are discussed most naturally in terms of total energy and volume of an  $N$ -particle system or even energy and volume per particle; in order to maximize transparency, we will employ the same variable notation in

all these cases. That is,  $E$  will designate specific internal energy as well as energy per particle and energy of an  $N$ -particle system. Likewise,  $V$  will designate related volume variables. It is straightforward to distinguish among usages by context or units. Note that the conversion factor  $M/N_A$  is g/particle where  $M$  is the molecular weight ( $M = 28.0134$  g/mol for  $N_2$ ) and  $N_A$  is Avogadro's number ( $6.0221\,367 \times 10^{23}$  particles/mol). Multiplying both sides of Eq. (31) by  $M/N_A$  changes the  $E$  and  $V$  variables from energy/g and volume/g to energy/particle and volume/particle, leaving the equation unchanged except for the meaning of  $E$  and  $V$ .

$E$  readily separates into three distinct components for a  $N$ -particle system,

$$E = E_{id} + E_v + E_{ex}, \quad (32)$$

the first two of which can be evaluated using standard forms<sup>37</sup>

$$E_{id} = \frac{5}{2} N k_B T \quad (33)$$

is the ideal translational and rotational contribution of a linear rigid rotor, and

$$E_v = \frac{N k_B \Theta_v}{e^{\Theta_v/T} - 1} \quad (34)$$

is the energy of a quantum harmonic oscillator. The temperature range sampled was too low for electronic excitation to

play a significant role,<sup>38</sup> and the vibrational temperature  $\Theta_v = \hbar\omega/k_B$  was evaluated using the experimentally determined nitrogen frequency at zero pressure.<sup>39</sup> Vibrational zero point energy was included separately in the reference heat of formation and specific internal energy  $E_0$ , which were determined from measured thermodynamic properties of liquid  $N_2$ . The zero of energy is that for isolated  $N_2$  molecules at  $T=0$  K. The excess contribution  $E_{\text{ex}}$  is defined by

$$E_{\text{ex}} = \langle U \rangle, \quad (35)$$

where  $\langle U \rangle$  is the average configurational energy calculated from  $o\text{-n}(\text{MC})^2$  simulation.

According to Eq. (31),  $E_H$  corresponds to values of  $E$  which are zeros of the function

$$f(E) = E - E_0 - \frac{1}{2}P(V_0 - V_H), \quad (36)$$

where  $V_H$  is chosen as an independent variable,  $P(V_H, E)$  is determined by the EOS, and  $E_H(V_H)$  is the dependent variable expressed as a function of  $V_H$ . Solutions to Eq. (36) define a locus of pressure and temperature combinations ( $P = P_H$ ,  $T = T_H$ ) comprising the Hugoniot. Maximization of  $\bar{A}_{\text{rw}}$  with Eq. (28) generated a set of ( $P = P_{\text{opt}}$ ,  $T = T_{\text{opt}}$ ) at which  $o\text{-n}(\text{MC})^2$  simulations were performed; this set differed from the original, desired ( $P = P'$ ,  $T = T'$ ). The original combinations were chosen on the basis of previously reported reweighting calculations,<sup>40,41</sup> as states near the Hugoniot locus. In order to extract thermodynamic information at Hugoniot states from  $o\text{-n}(\text{MC})^2$  results collected at ( $P, T$ ) pairs not on the Hugoniot, a mapping between the two sets of conditions must be provided. For ( $P, T$ ) sufficiently close to ( $P_H, T_H$ ), volume and energy can be expanded to first order about their simulation values,

$$\begin{aligned} V_H - V &\equiv \Delta V \approx \left. \frac{\partial V}{\partial T} \right|_P (T_H - T) + \left. \frac{\partial V}{\partial P} \right|_T (P_H - P) \\ &= \left. \frac{\partial V}{\partial T} \right|_P \cdot \Delta T + \left. \frac{\partial V}{\partial P} \right|_T \cdot \Delta P, \end{aligned} \quad (37)$$

$$\begin{aligned} E_H - E &\equiv \Delta E \approx \left. \frac{\partial E}{\partial T} \right|_P (T_H - T) + \left. \frac{\partial E}{\partial P} \right|_T (P_H - P) \\ &= \left. \frac{\partial E}{\partial T} \right|_P \cdot \Delta T + \left. \frac{\partial E}{\partial P} \right|_T \cdot \Delta P. \end{aligned} \quad (38)$$

Here,  $P$  and  $T$  are fixed parameters in the  $NPT$  ensemble, while  $U$  and  $V$  represent the average energy and volume ( $U = \langle U \rangle_{P,T}$ ,  $V = \langle V \rangle_{P,T}$ ) calculated from  $o\text{-n}(\text{MC})^2$  simulation at a prescribed pressure and temperature;  $E$  is related to  $\langle U \rangle$  by Eqs. (32)–(35). If  $P = P_H$  by construction, the second of the two terms in each of the above expansions vanishes; the goal then is to recover the Hugoniot temperature  $T_H$  corresponding to a given  $P_H$ . Toward this end, Eq. (31) can be restated in terms of differences between simulation results and Hugoniot values,

$$E + \Delta E = E_0 + \frac{1}{2}P_H(V_0 - V - \Delta V), \quad (39)$$

into which substitution of Eqs. (37) and (38) produces

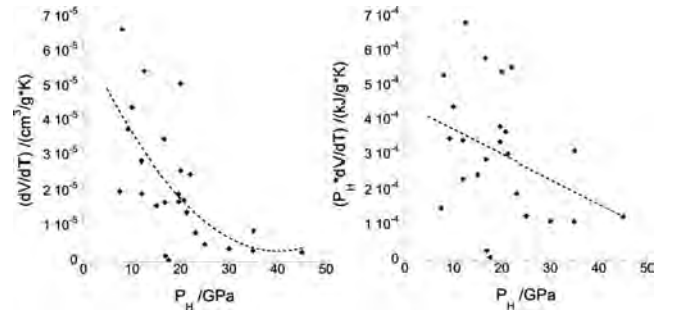


FIG. 4. Partial derivatives of volume with respect to temperature at fixed pressure (left panel), as calculated from results of  $o\text{-n}(\text{MC})^2$  simulation performed at the ( $P = P_{\text{opt}}$ ,  $T = T_{\text{opt}}$ ) combinations shown in Table IV. The right panel shows the same data, but following multiplication by pressure; as described in the text, these pressures are taken to correspond to Hugoniot values ( $P = P_H$ ) by construction. The partial derivative is evaluated using Eq. (44), and the dashed lines represent quadratic (left) and linear (right) fits to the data. Note the difference in ordinate scales.

$$E + \left. \frac{\partial E}{\partial T} \right|_P \cdot \Delta T = E_0 + \frac{1}{2}P_H \left( V_0 - V - \left. \frac{\partial V}{\partial T} \right|_P \cdot \Delta T \right). \quad (40)$$

Using Eq. (31) to define the difference between the computed energy  $E$  and  $E_H$ , then substituting in Eq. (40) gives

$$\begin{aligned} \Delta E_c &\equiv E - E_0 - \frac{1}{2}P_H(V_0 - V) \\ &= - \left( \frac{1}{2}P_H \left. \frac{\partial V}{\partial T} \right|_P + \left. \frac{\partial E}{\partial T} \right|_P \right) \Delta T, \end{aligned} \quad (41)$$

which yields upon slight rearrangement

$$\Delta T = \frac{-\Delta E_c}{\left( \left. \frac{\partial E}{\partial T} \right|_P + \frac{1}{2}P_H \left. \frac{\partial V}{\partial T} \right|_P \right)}, \quad (42)$$

the desired relation. The ideal and quantum harmonic oscillator contributions to  $\partial E / \partial T$  are trivial to evaluate using Eqs. (33) and (34), and the rest of the denominator in Eq. (42) can easily be recast (see Appendix B) in terms of simulation parameters and results

$$\left. \frac{\partial \langle U \rangle}{\partial T} \right|_P = \frac{\beta}{T} [P(\langle UV \rangle - \langle U \rangle \langle V \rangle) + \langle U^2 \rangle - \langle U \rangle^2], \quad (43)$$

$$\left. \frac{\partial \langle V \rangle}{\partial T} \right|_P = \frac{\beta}{T} [P(\langle UV \rangle - \langle U \rangle \langle V \rangle) + \langle V^2 \rangle - \langle V \rangle^2], \quad (44)$$

where ensemble averages once again have been indicated explicitly.  $P_H$  and  $T_H$  can now be substituted into Eqs. (37) and (38) to produce  $E_H$  and  $V_H$ . Upon combination of Eqs. (29) and (30) to generate  $u_s$  and  $u_p$ , the Hugoniot locus is completely specified.

Figures 4 and 5 illustrate in more detail the manner in which Eq. (42) was used to recover temperature values on the Hugoniot.  $\Delta E_c$  was evaluated using Eqs. (33)–(35), with  $\langle U \rangle$  given by the average DFT energy predicted from

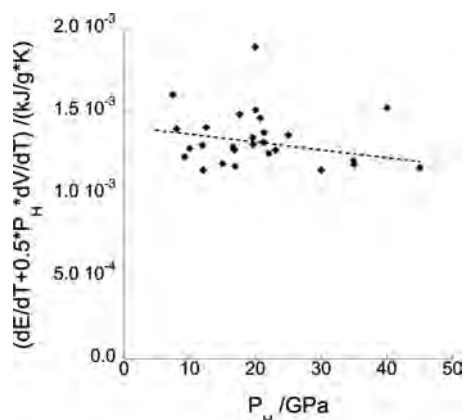


FIG. 5. Evaluation of the denominator appearing in Eq. (42) as calculated from results of  $o$ - $n(\text{MC})^2$  simulation performed at the  $(P=P_{\text{opt}}, T=T_{\text{opt}})$  combinations shown in Table IV. As described in the text, these pressures are taken to correspond to Hugoniot values ( $P=P_H$ ) by construction and the corresponding Hugoniot values for temperature are recovered by use of Eq. (42). The dashed line is a linear fit to the data.

$o$ - $n(\text{MC})^2$  simulation at the pressure and temperature combinations shown in Table III. The pressures at which simulations were performed were also taken to fall on the Hugoniot (*vide supra*), and the derivatives appearing in the denominator of Eq. (42) were evaluated using Eqs. (43) and (44) and the equilibrium averages computed from simulation. The derivative of volume with respect to temperature at each  $(P=P_{\text{opt}} \equiv P_H, T=T_{\text{opt}})$  combination is shown in Fig. 4 (left panel), as well these derivatives multiplied by their corresponding pressures (right panel). The data in the left and right panels are fit to linear and quadratic functions (dashed lines), respectively. Figure 5 illustrates the entire denominator of Eq. (42) built from the component pieces appearing in Fig. 4.

Recovery of  $T_H$  permitted determination of  $V_H$  through application of Eq. (37), enabling construction of the  $\text{N}_2$  Hugoniot locus in Fig. 6 ( $P$ - $V$  plane) and Fig. 7 ( $u_s$ - $u_p$  plane). The nitrogen Hugoniot has been measured<sup>42–44</sup> or calculated<sup>38,40,41</sup> on a number of occasions previously, but only in a few instances have calculations using a self-consistent potential such as DFT<sup>40,45,46</sup> been reported. Open circles in Fig. 6 represent  $o$ - $n(\text{MC})^2$  results calculated at  $(P_{\text{opt}}, T_{\text{opt}})$  and then shifted to the Hugoniot locus  $(P_H, T_H)$  in the manner described above. The solid line is a fit of those results to an exponential function. Although components of the shifts (illustrated in Figs. 4 and 5) possess relatively large uncertainties, the net uncertainties are comparable to or smaller than the statistical uncertainties in the simulated states themselves; error estimates are given in Table IV but omitted from the figures for clarity. The 28 MC data points shown explicitly in Fig. 6 have been replaced with a quadratic fit in Fig. 7 for ease of viewing, but otherwise symbols and shading have been preserved across the two figures for each data set depicted. Agreement with experimental data in the molecular regime—which we take to be 40–45 GPa or less—taken from Refs. 42 (squares), 43 (filled circles), and 44 (triangles) is excellent. [See the following paragraph for discussion of the higher pressure region for which the

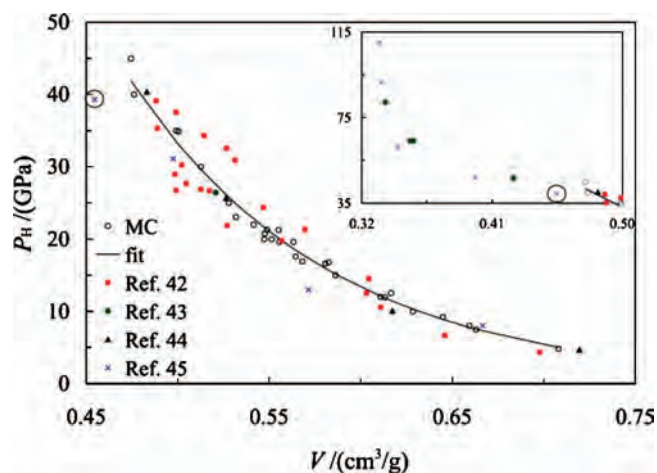


FIG. 6.  $\text{N}_2$  Hugoniot in the  $P$ - $V$  plane. Experimental results (filled symbols) are taken from Refs. 42–44; theoretical points were calculated using  $o$ - $N(\text{MC})^2$  (open circles, present work) and AIMD (cross, Ref. 45). MC simulations were restricted to the molecular regime (up to  $P=40$ –45 GPa), and have been shifted according to Eq. (42). The inset displays the high-pressure region that includes ionization; an AIMD result in the transition region has been circled in both the inset and main figure in order to facilitate visual passage between the two. The solid line is an exponential fit through the 28  $o$ - $N(\text{MC})^2$  data points.

$o$ - $n(\text{MC})^2$  methodology was not applied.] In addition to the experimental results we have included those of a previous calculation<sup>45</sup> made using *ab initio* molecular dynamics (AIMD) in the  $NVT$  ensemble with a PW91 exchange-correlation functional and Vanderbilt ultrasoft pseudopotentials<sup>47</sup> (crosses). This particular implementation was designed specifically to capture electronic and dissociation effects in the high temperature and pressure region; however, the small system size (32 atoms=16 molecules) and the use of pseudopotentials introduce uncertainties that are difficult to quantify. Only four of the calculated points fell in the molecular regime, but these were in qualitative agreement with experiment. The shock and particle veloci-

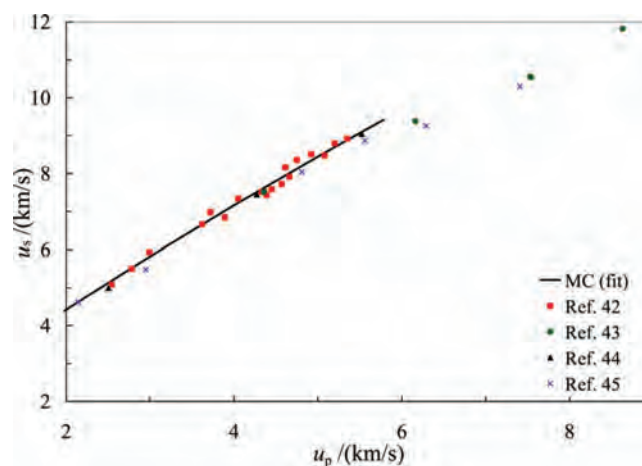


FIG. 7.  $\text{N}_2$  Hugoniot in the  $u_s$ - $u_p$  plane. Experimental results (filled symbols) are taken from Refs. 42–44; theoretical results were calculated using  $o$ - $N(\text{MC})^2$  (solid line, present work) and AIMD (cross Ref. 45). MC simulations were restricted to the molecular regime (up to  $P=40$ –45 GPa), and have been shifted according to Eq. (42). Here, for ease of viewing, the 28 individual  $o$ - $N(\text{MC})^2$  points results shown explicitly in Fig. 6 were replaced by a quadratic fit after transformation between the  $P$ - $V$  and  $u_s$ - $u_p$  planes.



ties,  $u_s$  and  $u_p$ , in Fig. 7 are based on the same fundamental information as are  $P$  and  $V$  in Fig. 6 ( $P_H$  and  $V_H$  are derived from  $u_s$ ,  $u_p$ , and the Hugoniot jump conditions, Eqs. (29)–(31), although the relationship in the  $u_s$ – $u_p$  plane is nearly linear. Again, however, the trend is that the present calculations are in excellent agreement with the experimental data below  $u_p \approx 6$  km/s.

Thus far we have focused exclusively on pressures of 45 GPa and below, but Figs. 6 and 7 also include higher pressure regions where dissociation, ionization, and electronically excited states become important. Trends in the experimental data of Nellis *et al.*<sup>43</sup> and AIMD simulation results of Kress *et al.*<sup>45</sup> are in good agreement generally, and both clearly reflect an abrupt change between  $P=40$  and 47 GPa; here we focus specifically on the transition region in which dissociation emerges as an important factor. At  $P=31$  GPa, the specific volume predicted by *ab initio* molecular dynamics AIMD (with  $7 \pm 3\%$  dissociation) is near the average of the measured data scatter (Fig. 6); at 39 GPa ( $16 \pm 9\%$  dissociation by interpolation of Table I in Ref. 45) it is significantly less than that predicted by experiment. These facts suggest that the calculated dissociation is overestimated in the transition region. By way of contrast, the present results fall well within the experimental scatter for pressures up to 40 GPa. If dissociation were important in this region, we would expect the  $o$ -N(MC)<sup>2</sup> results to begin to deviate from experiment at pressures lower than those for which they actually do. Taken collectively, the measured and calculated data suggest that dissociation is not significant to the Hugoniot below the transition region found at  $P \sim 40$ –45 GPa. This transition region *could* reflect to a two-wave structure, in which case shock velocity  $u_s$  is established by a leading wave whereas the particle velocity  $u_p$  is determined on the basis of either thermodynamics or kinetics that leads to a secondary wave propagating in the material. Examples where this could occur include a first order phase transition with a large volume change or relaxation from the highest metastable state that can be maintained before the kinetics allow a return to equilibrium on a time scale that is short compared to the time resolution of the shock experiment. If a single wave is assumed in such an instance, then the predicted  $P$  and  $V$  will be incorrect. The hallmark of two-wave structure is constant  $u_s$  across some interval of  $u_p$ ; but, unfortunately, there is only one data point in the transition region shown. For this reason, it is unclear whether the data reflect a *bona fide* two-wave structure or merely a region of rapid transition.

Note that the present calculations assume the validity of the rigid rotor and quantum harmonic oscillator approximations. Raman line shifts in liquid nitrogen singly shocked to  $P=10$ –20 GPa and doubly shocked to  $P=15$ –40 GPa have been measured<sup>48</sup> and calculated using a first-principles approach.<sup>49</sup> Both fundamental ( $0 \rightarrow 1$ ) and hot band ( $1 \rightarrow 2$ ,  $2 \rightarrow 3$ , and  $3 \rightarrow 4$ ) transitions indicated that vibrational energies increased  $\sim 1\%$  in the singly shocked state and  $\sim 2\%$  in the doubly shocked state. There was no indication of vibrational potential softening even at the highest pressure measured; the data imply rather that vibrations are very weakly coupled to other modes, in conformity with the assumptions

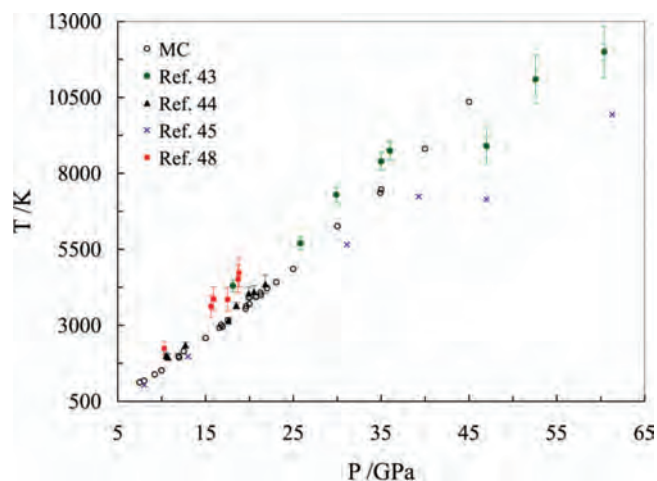


FIG. 8. Temperatures measured (filled symbols, Refs. 43, 44, and 48) or calculated (Ref. 45 and present work) on the  $N_2$  Hugoniot.

made here. We have treated shocked nitrogen in the molecular phase as undergoing negligible electronic excitation as well, given that the lowest electronic excited state in  $N_2$  has a relative energy of roughly 6 eV. This energy, and the ground state dissociation energy of approximately 10 eV, are to be compared with a temperature equivalent of 1 eV or less on the principal Hugoniot up to  $P \sim 45$  GPa.

Several techniques for temperature measurement on the Hugoniot have been reported previously, each of which potentially introduces systematic errors of unknown magnitude due to assumptions made in the analysis. Figure 8 shows measured data compared with the present calculations and those of Kress *et al.*<sup>45</sup> The temperature data of Nellis *et al.*<sup>43</sup> increase along a trend line that coincides well with the MC results up to  $P=36$  GPa, as would be expected under conditions of negligible dissociation. The next highest temperature measurement, obtained at  $P=47$  GPa is significantly cooler than this trend predicts, as would be expected should onset of significant dissociation occur for conditions between the two measured data points. A new trend is established at higher pressure, corresponding to a partially dissociated phase in which some fraction of kinetic energy has been expended to break the nitrogen triple bond, resulting in lower temperatures than would be found for molecular nitrogen. The interpretation of the temperature data is the same as that of the  $P$ - $V$  and  $u_s$ – $u_p$  results: There is negligible dissociation at pressures below 40–45 GPa, but a significant amount at pressures higher than this.

## V. SUMMARY AND CONCLUSIONS

We have used the  $o$ -n(MC)<sup>2</sup> algorithm with a DFT potential to generate the Hugoniot locus of  $N_2$  fluid for pressures and temperatures relevant to HE detonation. After collecting several hundred configurations at which to evaluate  $\delta W$  for a number of  $(P, T)$  combinations, the *a priori* acceptance probability defined by Eq. (27) was maximized as a function of  $P$  and  $T$  to yield optimal thermodynamic conditions at which to perform n(MC)<sup>2</sup> sampling. The  $o$ -n(MC)<sup>2</sup> simulations were then carried out at temperature and pressure combinations not necessarily on the Hugoniot locus, but

from which Hugoniot states could be recovered by use of the expansion procedure defined in Eqs. (37) and (38) and culminating in Eqs. (42)–(44). The method yields both high accuracy and high precision. It is worth noting that in contrast to previous calculations<sup>45</sup> the current approach includes all electrons (no pseudopotential approximation) and readily accommodates a system more than six times larger than the earlier study, thereby reducing the likelihood of finite-size effects in the results.

An analytical reference potential was used in this work, but  $o$ -n(MC)<sup>2</sup> should work equally well with two different *ab initio*, DFT, or semiempirical potentials. The reference potential could rely on a more approximate algorithm or a smaller basis set, so long as (1) its correspondence to the full potential still permits a reasonable offset  $O$  between full energy evaluations and (2) it can still be evaluated rapidly. The full potential would then consist of a fully converged calculation at a higher level of theory.

The  $o$ -n(MC)<sup>2</sup> method provides a versatile framework in which to carry out precision MC sampling of accurate potentials, and it would be worthwhile to make detailed comparison of its performance to that of AIMD.<sup>50</sup> Straightforward formulation of efficiency metrics such as Eq. (24) is impossible without determination of a quantitative relation between the average single-particle displacement in accepted MC steps and in AIMD time steps. This is a nontrivial task, and perhaps it would be simpler to calculate the number of AIMD steps required to yield decorrelated configurations, then compare this with the number of composite  $o$ -n(MC)<sup>2</sup> steps needed for the same purpose; even given these two quantities, still it is not at all clear that their ratio would not vary strongly from one system to the next. Aside from efficiency considerations, MC methods accommodate generalized ensemble sampling much more naturally than does MD, some of the advantages of which (e.g., the ability to calculate transport properties) disappear when standard thermostats and barostats are invoked due to their inherently stochastic foundation.<sup>51</sup>

## ACKNOWLEDGMENTS

J.D.C. thanks the Office of the Director at Los Alamos National Laboratory (LANL) for the support in the form of a

Director's Postdoctoral Fellowship. M.S.S. is supported by the LANL High Explosives Project of the National Nuclear Security Administration (NNSA) Advanced Strategic Computing Program (HE-ASC). T.D.S. is supported by the LANL Laboratory Directed Research and Development (LDRD) Program and by the (U.S.) Army Research Office under Grant No. W911NF-05-1-0265. LANL is operated by Los Alamos National Security L.L.C. under the auspices of the NNSA and the United States Department of Energy under Contract No. DE-AC52-06NA25396.

## APPENDIX A: AVERAGE MANY-BODY CONTRIBUTION PER PAIR

Here we prove the claim that  $U_{AB}^* - U_{AB}^{(2)}$  as defined by Eqs. (13) and (14) in the text gives an average many-body contribution per pair that, when summed over all  $A$  and  $B$ , returns the total configurational energy of the system under the assumption that many-body effects terminate at third order. The total energy as a sum of two- and three-body interactions is given by

$$U_{\text{box}} = \frac{1}{2} \sum_{i=1}^N \sum_{j=1}^N \varphi_{ij} + \frac{1}{6} \sum_{i=1}^N \sum_{j=1}^N \sum_{k=1}^N \lambda_{ijk} = U_N^{(2)} + U_N^{(3)}, \quad (\text{A1})$$

where  $U_x^{(y)}$  represents the  $y$ -body contribution to the total energy of a  $x$ -particle system. Let  $U_{\text{box}-A}$  equal the box energy with molecule  $A$  removed,

$$\begin{aligned} U_{\text{box}-A} &= \frac{1}{2} \sum_{i=1}^N \sum_{j=1}^N \varphi_{ij} + \frac{1}{6} \sum_{i=1}^N \sum_{j=1}^N \sum_{k=1}^N \lambda_{ijk} = U_{\text{box}} - \frac{1}{2} \sum_{j=1}^N \varphi_{Aj} \\ &\quad - \frac{1}{2} \sum_{i=1}^N \varphi_{iA} - \frac{1}{6} \sum_{j=1}^N \sum_{k=1}^N \lambda_{Ajk} - \frac{1}{6} \sum_{i=1}^N \sum_{k=1}^N \lambda_{iAk} \\ &\quad - \frac{1}{6} \sum_{i=1}^N \sum_{j=1}^N \lambda_{ijA} = U_{\text{box}} - \sum_{j=1}^N \varphi_{Aj} - \frac{1}{2} \sum_{i=1}^N \sum_{j=1}^N \lambda_{ijA}, \end{aligned} \quad (\text{A2})$$

and assume an analogous relation for  $U_{\text{box}-B}$ . When both  $A$  and  $B$  are removed together,

$$\begin{aligned} U_{\text{box}-AB} &= \frac{1}{2} \sum_{i=1}^N \sum_{j=1}^N \varphi_{ij} + \frac{1}{6} \sum_{i=1}^N \sum_{j=1}^N \sum_{k=1}^N \lambda_{ijk} = U_{\text{box}} - \frac{1}{2} \sum_{j=1}^N \varphi_{Aj} - \frac{1}{2} \sum_{i=1}^N \varphi_{iA} \\ &\quad - \frac{1}{6} \sum_{j=1}^N \sum_{k=1}^N \lambda_{Ajk} - \frac{1}{6} \sum_{i=1}^N \sum_{k=1}^N \lambda_{iAk} - \frac{1}{6} \sum_{i=1}^N \sum_{j=1}^N \lambda_{ijA} \\ &= U_{\text{box}} - \sum_{j=1}^N \varphi_{Aj} - \frac{1}{2} \sum_{i=1}^N \sum_{j=1}^N \lambda_{ijA} - \frac{1}{2} \sum_{i=1}^N \sum_{k=1}^N \lambda_{ijB} + \frac{1}{2} (\varphi_{AB} + \varphi_{BA}) + \frac{1}{6} \sum_{k=1}^N (\lambda_{ABk} + \lambda_{AkB} + \lambda_{kAB} + \lambda_{BAk} + \lambda_{BkA} + \lambda_{kBA}) \\ &= E + (E_{\text{box}-A} - E_{\text{box}}) + (E_{\text{box}-B} - E_{\text{box}}) + \varphi_{AB} + \sum_{\substack{k=1 \\ k \neq A, B}}^N \lambda_{ABk}. \end{aligned} \quad (\text{A3})$$

From Eq. (A3) one can define an effective pair energy including an average many-body correction as

$$U_{AB}^* \equiv \varphi_{AB} + \sum_{\substack{k=1 \\ k \neq A, B}}^N \lambda_{ABk} \\ = U_{\text{box}} + U_{\text{box-AB}} - U_{\text{box-A}} - U_{\text{box-B}}, \quad (\text{A4})$$

equivalent to Eq. (14) in the text. Note that

$$\frac{1}{2} \sum_{i=1}^N \sum_{\substack{j=1 \\ i \neq j}}^N U_{ij}^* = \frac{1}{2} \sum_{i=1}^N \sum_{\substack{j=1 \\ i \neq j}}^N \varphi_{ij} + \frac{1}{2} \sum_{i=1}^N \sum_{\substack{j=1 \\ i \neq j}}^N \sum_{\substack{k=1 \\ i \neq j \neq k}}^N \lambda_{ijk} = U_N^{(2)} + 3U_N^{(3)} \quad (\text{A5})$$

by comparison with Eq. (A1). If the difference between effective pair and standard pair energies is defined as  $\delta U_{ij} \equiv U_{ij}^* - U_{ij}^{(2)}$ , then the average value of these three quantities in a  $N$ -body system is given by

$$\bar{U}^* = \frac{1}{N(N-1)} \sum_{i=1}^N \sum_{\substack{j=1 \\ i \neq j}}^N U_{ij}^*, \quad (\text{A6})$$

$$\bar{U}^{(2)} = \frac{1}{N(N-1)} \sum_{i=1}^N \sum_{\substack{j=1 \\ i \neq j}}^N U_{ij}^{(2)}, \quad (\text{A7})$$

$$\bar{\delta U} = \frac{1}{N(N-1)} \sum_{i=1}^N \sum_{\substack{j=1 \\ i \neq j}}^N \delta U_{ij}, \quad (\text{A8})$$

and the total values by

$$U_N^* = \frac{N(N-1)}{2} \bar{U}^*, \quad (\text{A9})$$

$$U_N^{(2)} = \frac{N(N-1)}{2} \bar{U}^{(2)}, \quad (\text{A10})$$

$$\delta U_N = \frac{N(N-1)}{2} \bar{\delta U}. \quad (\text{A11})$$

The box energy expressed in terms of Eqs. (A10) and (A11) is then

$$U_{\text{box}} = U_N^{(2)} + \delta U_N. \quad (\text{A12})$$

By equating the box energy of Eq. (A5) with that of Eq. (A12) one finds that

$$3U_N^{(3)} = \frac{1}{2} \sum_{i=1}^N \sum_{\substack{j=1 \\ i \neq j}}^N \delta U_{ij}, \quad (\text{A13})$$

the relation to be proved.

## APPENDIX B: DERIVATION OF EQUATIONS (43) and (44)

Treating  $\langle U \rangle$  as a function of  $\beta = (kT)^{-1}$  and applying the chain rule,

$$\left. \frac{\partial \langle U \rangle}{\partial T} \right|_P = \frac{\partial \beta}{\partial T} \left. \frac{\partial \langle U \rangle}{\partial \beta} \right|_P. \quad (\text{B1})$$

The first factor is trivial,

$$\frac{\partial \beta}{\partial T} = -\frac{\beta}{T}. \quad (\text{B2})$$

Recall that an ensemble-averaged quantity  $X$  is defined as

$$\langle X \rangle = \frac{\int \int X e^W d\tau dV}{\int \int e^W d\tau dV}, \quad (\text{B3})$$

where  $W$  represents the thermodynamic weight appropriate to the ensemble being sampled; for the isothermal-isobaric ensemble,  $W$  is given in Eq. (16) of the text. For the sake of brevity we drop the explicit indication of constant  $P$  in the derivatives of Eq. (B1) and the  $N \ln V$  factor appearing in the exponential of Eq. (16), then write out explicitly the integrals appearing in the right-hand side of Eq. (B1),

$$\frac{\partial \langle U \rangle}{\partial \beta} = - \frac{(\int \int (U + PV) U e^{-\beta(U+PV)} d\tau dV) (\int \int e^{-\beta(U+PV)} d\tau dV)}{(\int \int e^{-\beta(U+PV)} d\tau dV)^2} + \frac{(\int \int U e^{-\beta(U+PV)} d\tau dV) (\int \int (U + PV) e^{-\beta(U+PV)} d\tau dV)}{(\int \int e^{-\beta(U+PV)} d\tau dV)^2}. \quad (\text{B4})$$

Using Eq. (B3), Eq. (B4) becomes

$$\frac{\partial \langle U \rangle}{\partial \beta} = - \langle U(U + PV) \rangle + \langle U \rangle \langle U + PV \rangle \\ = P(\langle U \rangle \langle V \rangle - \langle UV \rangle) + \langle U \rangle^2 - \langle U^2 \rangle. \quad (\text{B5})$$

Combining Eqs. (B2) and (B5) gives

$$\left. \frac{\partial \langle U \rangle}{\partial T} \right|_P = \frac{\beta}{T} [P(\langle U \rangle \langle V \rangle - \langle UV \rangle) + \langle U \rangle^2 - \langle U^2 \rangle], \quad (\text{B6})$$

identical to Eq. (43) in the text. The derivation of Eq. (44) proceeds in a fashion perfectly analogous to that detailed here for Eq. (40).

- <sup>1</sup>See the Shock Compression of Condensed Matter series in the AIP Conference Proceedings, available at <http://proceedings.aip.org/proceedings/top.jsp>.
- <sup>2</sup>M. J. Gillain, D. Alfe, J. Brodholt, L. Vocadlo, and G. D. Price, *Rep. Prog. Phys.* **69**, 2365 (2006).
- <sup>3</sup>D. J. Depaolo and F. M. Orr, *Phys. Today* **61**(8), 46 (2008).
- <sup>4</sup>*IPCC Special Report on Carbon Dioxide Capture and Storage*, edited by B. Metz (Cambridge University Press, Cambridge, 2004).
- <sup>5</sup>M. P. Allen and D. J. Tildesley, *Computer Simulation of Liquids* (Oxford University Press, Oxford, 1987).
- <sup>6</sup>D. Frenkel and B. Smit, *Understanding Molecular Simulation: From Algorithms to Applications* (Academic, New York, 2002).
- <sup>7</sup>Y. B. Zel'dovich and Y. P. Raizer, *Physics of Shock Waves and High-Temperature Hydrodynamic Phenomena* (Dover, Mineola, NY, 2002).
- <sup>8</sup>J. D. Coe, T. D. Sewell, and M. S. Shaw, *J. Chem. Phys.* **130**, 164104 (2009).
- <sup>9</sup>R. Iftimie, D. Salahub, D. Wei, and J. Schofield, *J. Chem. Phys.* **113**, 4852 (2000).
- <sup>10</sup>L. D. Gelb, *J. Chem. Phys.* **118**, 7747 (2003).
- <sup>11</sup>W. Koch and M. C. Holthausen, *A Chemist's Guide to Density Functional Theory*, 2nd ed. (Wiley-VCH, Weinheim, FRG, 2001); R. G. Parr and W. Yang, *Density-Functional Theory of Atoms and Molecules* (Oxford University Press, New York, 1989).
- <sup>12</sup>P. Hohenberg and W. Kohn, *Phys. Rev.* **136**, B864 (1964).
- <sup>13</sup>W. Kohn and L. J. Sham, *Phys. Rev.* **140**, A1133 (1965).
- <sup>14</sup>J. P. Perdew and A. Zunger, *Phys. Rev. B* **23**, 5048 (1981).
- <sup>15</sup>K. Burke, J. P. Perdew, and Y. Wang, in *Electronic Density Functional Theory: Recent Progress and New Directions*, edited by J. F. Dobson, G. Vignale, and M. P. Das (Plenum, New York, 1998).
- <sup>16</sup>C. C. J. Roothaan, *Rev. Mod. Phys.* **23**, 69 (1951).
- <sup>17</sup>M. J. Frisch, G. W. Trucks, H. B. Schlegel *et al.*, GAUSSIAN 03, Revision C.02, Gaussian, Inc., Wallingford CT, 2004.
- <sup>18</sup>A. D. Becke, *Phys. Rev. A* **38**, 3098 (1988).
- <sup>19</sup>C. Lee, W. Yang, and R. G. Parr, *Phys. Rev. B* **37**, 785 (1988).
- <sup>20</sup>J. P. Perdew, K. Burke, and M. Ernzerhof, *Phys. Rev. Lett.* **77**, 3865 (1996).
- <sup>21</sup>J. P. Perdew, in *Electronic Structure of Solids*, edited by P. Ziesche and H. Eschrig (Akademie Verlag, Berlin, 1991).
- <sup>22</sup>S. H. Vosko, L. Wilk, and M. Nusair, *Can. J. Phys.* **58**, 1200 (1980).
- <sup>23</sup>C. Pisani, *Quantum-Mechanical Ab-Initio Calculation of the Properties of Crystalline Materials* (Springer-Verlag, Berlin, 1996).
- <sup>24</sup>J. B. Collins, P. R. Schleyer, J. S. Binkley, and J. A. Pople, *J. Chem. Phys.* **64**, 5142 (1976); W. J. Hehre, R. F. Stewart, and J. A. Pople, *ibid.* **51**, 2657 (1969).
- <sup>25</sup>A. D. McLean and G. S. Chandler, *J. Chem. Phys.* **72**, 5639 (1980).
- <sup>26</sup>S. F. Boys and F. Bernardi, *Mol. Phys.* **19**, 553 (1970).
- <sup>27</sup>M. J. Frisch, J. A. Pople, and J. S. Binkley, *J. Chem. Phys.* **80**, 3265 (1984).
- <sup>28</sup>W. J. Hehre, R. Ditchfield, and J. A. Pople, *J. Chem. Phys.* **56**, 2257 (1972).
- <sup>29</sup>C. Moller and M. S. Plesset, *Phys. Rev.* **46**, 618 (1934).
- <sup>30</sup>J. C. Slater, *Phys. Rev.* **81**, 385 (1951).
- <sup>31</sup>A. J. Stone, *The Theory of Intermolecular Forces* (Oxford University Press, Oxford, 1996).
- <sup>32</sup>The pair was chosen on the basis of its placement at roughly the center of the simulation cell and its constituents being "nearest neighbors" and thus sharing a substantial repulsive interaction.
- <sup>33</sup>N. Metropolis, A. W. Rosenbluth, M. N. Rosenbluth, A. H. Teller, and E. Teller, *J. Chem. Phys.* **21**, 1087 (1953).
- <sup>34</sup>W. W. Wood, in *Physics of Simple Liquids*, edited by J. S. Rowlinson and G. S. Rushbrooke (Wiley, New York, 1968), p. 115.
- <sup>35</sup>I. R. McDonald and K. Singer, *J. Chem. Phys.* **47**, 4766 (1967).
- <sup>36</sup>R. Courant and K. O. Friedrichs, *Supersonic Flow and Shock Waves* (Springer, New York, 1999).
- <sup>37</sup>See, for instance, D. A. McQuarrie, *Statistical Mechanics* (University Science Books, Sausalito, CA, 2000).
- <sup>38</sup>J. D. Johnson, M. S. Shaw, and B. L. Holian, *J. Chem. Phys.* **80**, 1279 (1983).
- <sup>39</sup>G. Herzberg, *Spectra of Diatomic Molecules* (Van Nostrand Reinhold, New York, 1950).
- <sup>40</sup>M. S. Shaw and C. Tymczak, in *Shock Compression of Condensed Matter*, edited by M. D. Furnish (American Institute of Physics, Melville, NY, 2005), Vol. 845, p. 179.
- <sup>41</sup>M. S. Shaw and C. Tymczak, in *Proceedings of the 13th International Detonation Symposium* edited by J. Kennedy (Office of Naval Research, Norfolk, VA, 2006), Paper No. ONR 351-07-01, p. 1181.
- <sup>42</sup>R. D. Dick, *J. Chem. Phys.* **52**, 6021 (1970).
- <sup>43</sup>W. J. Nellis, N. C. Holmes, A. C. Mitchell, and M. van Thiel, *Phys. Rev. Lett.* **53**, 1661 (1984); W. J. Nellis and A. C. Mitchell, *J. Chem. Phys.* **73**, 6137 (1980); W. J. Nellis, H. B. Radousky, D. C. Hamilton, A. C. Mitchell, N. C. Holmes, K. B. Christianson, and M. van Thiel, *ibid.* **94**, 2244 (1991).
- <sup>44</sup>V. N. Zubarev and G. S. Telegin, *Sov. Phys. Dokl.* **7**, 34 (1962).
- <sup>45</sup>J. D. Kress, S. Mazevet, L. A. Collins, and W. W. Wood, *Phys. Rev. B* **63**, 024203 (2000).
- <sup>46</sup>S. Mazevet, J. D. Johnson, J. D. Kress, L. A. Collins, and P. Blottiau, *Phys. Rev. B* **65**, 014204 (2001).
- <sup>47</sup>D. Vanderbilt, *Phys. Rev. B* **41**, 7892 (1990).
- <sup>48</sup>D. S. Moore, S. C. Schmidt, M. S. Shaw, and J. D. Johnson, *J. Chem. Phys.* **90**, 1368 (1989).
- <sup>49</sup>J. D. Coe, T. D. Sewell, M. S. Shaw, and E. M. Kober, *Chem. Phys. Lett.* **464**, 265 (2008).
- <sup>50</sup>R. Car and M. Parrinello, *Phys. Rev. Lett.* **55**, 2471 (1985); M. E. Tuckerman, *J. Phys.: Condens. Matter* **14**, R1297 (2002).
- <sup>51</sup>P. H. Hunenberger, *Adv. Polym. Sci.* **173**, 105 (2005).
- <sup>52</sup>R. Ditchfield, W. J. Hehre, and J. A. Pople, *J. Chem. Phys.* **54**, 724 (1971).
- <sup>53</sup>R. Krishnan, J. S. Binkley, R. Seeger, and J. A. Pople, *J. Chem. Phys.* **72**, 650 (1980).



# Molecular dynamics study of the crystallization of nitromethane from the melt

Ali Siavosh-Haghighi, Thomas D. Sewell,<sup>a)</sup> and Donald L. Thompson<sup>b)</sup>

Department of Chemistry, University of Missouri-Columbia, Columbia, Missouri 65211-7600, USA

(Received 29 June 2010; accepted 1 October 2010; published online 16 November 2010)

The crystallization of nitromethane,  $\text{CH}_3\text{NO}_2$ , from the melt on the (100), (010), (001), and (110) crystal surfaces at 170, 180, 190, 200, 210, and 220 K has been investigated using constant-volume and -temperature (*NVT*) molecular dynamics simulations with a realistic, fully flexible force field [D. C. Sorescu, B. M. Rice, and D. L. Thompson, *J. Phys. Chem. B* **104**, 8406 (2000)]. The crystallization process and the nature of the solid-liquid interface have been investigated by computing the molecular orientations, density, and radial distribution functions as functions of time and location in the simulation cell. During crystallization the translational motion of the molecules ceases first, after which molecular rotation ceases as the molecules assume proper orientations in the crystal lattice. The methyl groups are hindered rotors in the liquid; hindrance to rotation is reduced upon crystallization. The width of the solid-liquid interface varies between 6 and 13 Å (about two to five molecular layers) depending on which crystal surface is exposed to the melt and which order parameter is used to define the interface. The maximum rate of crystallization varies from 0.08 molecules  $\text{ns}^{-1} \text{Å}^{-2}$  for the (010) surface at 190 K to 0.41 molecules  $\text{ns}^{-1} \text{Å}^{-2}$  for the (001) surface at 220 K. © 2010 American Institute of Physics. [doi:10.1063/1.3504610]

## I. INTRODUCTION

We have been using molecular dynamics (MD) to investigate the fundamental properties of phase changes in molecular solids and liquids. Although we have studied various molecular and ionic materials, we have focused on nitromethane as a prototypical organic solid because of its size, dipole moment, and the availability of experimental data. We report here a MD study of the crystallization of nitromethane from the melt. We have developed a fully flexible force field that accurately reproduces most of the mechanical, thermodynamic, and spectroscopic properties of the gas-phase molecule, crystal, and liquid; that is, the Sorescu, Rice, and Thompson (SRT) (Ref. 1) force field. The SRT force field<sup>1</sup> was originally developed based on experimental data and quantum chemistry results. It accurately reproduces most of the properties of the solid and liquid phases. The nitromethane crystal is orthorhombic, belongs to space group  $P2_12_12_1$ , and contains four molecules per unit cell.<sup>2,3</sup> The SRT force field has been shown to predict liquid properties that are in good agreement with experimental data.<sup>4</sup> It predicts vibrational frequencies in good agreement with *ab initio* and experimental values, for both atmospheric and elevated pressures.<sup>1,5</sup> Several studies<sup>6–9</sup> of nitromethane based on the SRT force field demonstrate its accuracy for predicting the melting point. Recently, Brennan *et al.*<sup>10</sup> used a reaction ensemble Monte Carlo (RxMC) method<sup>11</sup> to study a pressure-induced structural transition in solid nitromethane (discussed below) using the fully flexible SRT force field as well as a reduced-dimensionality simplification.

Nitromethane is a good prototype for studying phase

changes in organic condensed phases. It has a relatively large dipole moment (3.46 D) resulting in a crystal structure in which the molecules are arranged as dimers with two dimers per unit cell; the molecules are stacked in columns along the *c* axis, as noted by Dick.<sup>12</sup> Figure 1 shows two unit cells of the crystal looking down onto the (001), (100), and (010) faces. There is some evidence for transient pairing of molecules in the liquid.<sup>13–18</sup> The methyl group in nitromethane is essentially a free rotor in the gas phase with a barrier to rotation of only  $\sim 6$  cal/mol.<sup>19</sup> Trevino and Rymes<sup>3</sup> determined the barrier to methyl rotation in the crystal to be 234 cal/mol. Raman spectra studies of single crystals carried out by Cromer *et al.*<sup>20</sup> have shown, for temperatures close to room temperature, that the methyl groups are essentially free rotors for pressure less than 0.6 GPa; whereas at pressures higher than 3.5 GPa the methyl rotation is frozen.<sup>20</sup> The SRT force field<sup>1</sup> accurately describes these features of methyl motion in the crystal.

Most atomic-scale simulation studies of crystallization have been done for Lennard-Jones systems<sup>21–23</sup> and metals.<sup>24–28</sup> Davidchack and Laird<sup>29</sup> have reported a precise calculation of the interfacial free energy change in the Lennard-Jones system. Amini and Laird<sup>30</sup> have shown correlations between the interfacial free energies and rates of growth on different crystallographic faces of the Lennard-Jones crystal. Simulations of crystallization from a liquid in contact with a supporting substrate is of interest since it reveals molecular details of how the molecular structure of the crystal bed imposes a molecular quasicrystalline order in the liquid that in turn affects the rate and the phase of the grown crystal.<sup>31–33</sup> Molecular dynamics simulations of homogeneous nucleation and growth of polyatomic molecular crystals from the melt require times on the order of

<sup>a)</sup>Electronic mail: sewellt@missouri.edu.

<sup>b)</sup>Electronic mail: thompsondon@missouri.edu.

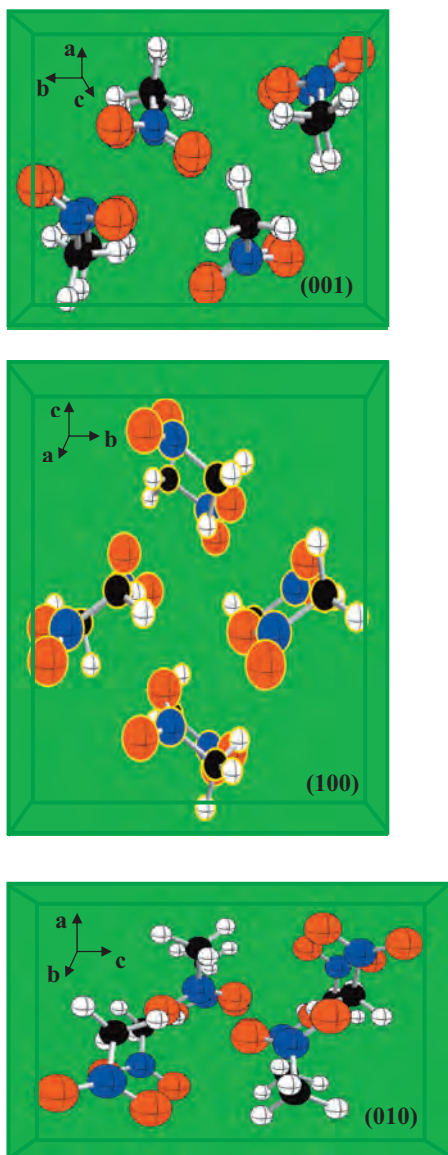


FIG. 1. Three projections of the nitromethane crystal. The crystal face shown in each panel corresponds to the plane of the page; for example, in the case of the (001) the plane of the page contains a (001) crystal plane. The structure is taken from Trevino *et al.* (Ref. 2) There are four molecules per unit cell. The molecules have antiparallel orientations due to strong dipolar interactions.

nanoseconds.<sup>34–36</sup> Molecular dynamics studies have been reported for the crystallization of polymers<sup>37–42</sup> and molecular crystals such as water.<sup>35,36,43–45</sup> Water has attracted the most attention because of its atmospheric<sup>35,36,44</sup> and biological<sup>45</sup> significance. Besides water, hydrocarbons, particularly small alkanes, have been used to study crystallization of small organic molecules.<sup>46–48</sup> Esselink *et al.*<sup>48</sup> reported the results of MD simulations of the nucleation and crystal growth of *n*-alkanes ( $C_nH_{2n+2}$ ;  $n=4–12$ ) from an amorphous state. Nucleation and crystal growth of  $N_2$  (Ref. 49) and  $CO_2$  (Ref. 50) have been studied by Monte Carlo (MC) techniques. Piana *et al.*<sup>51,52</sup> studied the crystallization of urea from solution using MC simulations.

The rate of the growth of a crystal is known to be a function of the crystallographic orientation of the interface<sup>23,30,53</sup> as well as the temperature.<sup>34</sup> The dependence

of the rate of crystal growth on the crystallographic face of the solid exposed to the liquid is related to the change in free energy for the associated liquid-crystal transition. Wilson and Frenkel<sup>34</sup> described the temperature dependence of the rate of crystal growth from the melt. Broughton, Gilmer, and Jackson<sup>53</sup> modified the Wilson–Frenkel theory. It predicts that the rate of crystal growth increases with temperature, passing through a maximum value before dropping to zero at the melting point. To our knowledge this model has not been used to describe crystallization in molecular systems, and it is unclear to us how well the assumptions underlying it would be satisfied for the case of complicated, nonspherical, conformationally complex polyatomic molecules.

In order to study the mechanism of crystallization at the molecular level it is necessary to define the solid-liquid interface. Perhaps the most widely used definition is based on density.<sup>53,65,68</sup> Structural parameters based on center-of-mass coordinates of particles,<sup>64,69</sup> radial distribution functions,<sup>49,50</sup> orientational order,<sup>37,38,48</sup> diffusion coefficient,<sup>53,65,67</sup> potential energy,<sup>65,69</sup> and properties due to the special nature of a system, for example, the charge profile,<sup>54</sup> have also been used to define interfaces. Esselink *et al.*<sup>48</sup> used intermolecular distances and the relative orientational ordering of neighboring molecules to define the interface in their studies of crystallization of *n*-alkanes. The widths calculated using these various properties vary considerably depending on which is used.<sup>64,69</sup>

We report here the results of a full-dimensional MD study of the crystallization of nitromethane liquid exposed to (100), (010), (001), and (110) crystallographic faces. To our knowledge there are no experimental data concerning the nitromethane crystal habit to guide our choices of crystal orientations for study, thus we chose faces that are considerably different with the idea that they could provide more insight into crystallization mechanisms. Some of these faces may not exist on a crystal grown from the melt in the laboratory.

We characterized the spatial aspects of crystallization by using radial distribution functions, the molecular number density, and an orientational order parameter to characterize the width of the interface between the melt and crystal phases. Intermolecular and intramolecular relaxation times were studied using autocorrelation functions of molecular centers of mass, orientational order parameters, methyl group rotation, and calculations of 3D diffusion coefficients. The dependence of the rates on crystallographic orientation at the solid-liquid interface and temperature was also studied. Although there are no experimental data available for comparison, the previous studies<sup>1,4,6–9</sup> that validate the SRT nitromethane force field for related properties and processes give us confidence that the current simulation results should be reliable.

## II. METHODS

Constant-volume constant-temperature (*NVT*) simulations were performed using DL-POLY (v. 2.15) (Ref. 55) with the SRT (Ref. 1) flexible-molecule nitromethane force field. The intermolecular forces are described by the Buckingham

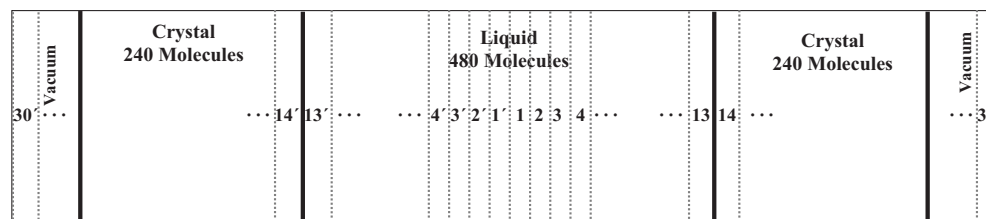


FIG. 2. Schematic 2D depiction of the 3D periodic simulation cell, and spatial partitioning thereof, used for the analysis of the crystallization. The liquid is bounded on both sides by crystalline slabs. The outer face of each crystal slab is exposed to vacuum to accommodate changes in volume as crystallization proceeds. The width of each subvolume  $n$  along the horizontal axis is 2.56 Å; these are labeled 30', 29', ..., 2', 1', 1, ..., 29, 30. Because of the symmetry of the simulation cell the properties of the molecules in subvolumes  $n$  and  $n'$  were averaged and referred to simply as subvolume  $n$ .

(exp-6) potential plus Coulombic interactions with fixed partial charges on the nuclei. The intramolecular interactions are represented by a sum of Morse potentials for the bond stretches, harmonic oscillators for bond angles, and cosine series for the HCNO dihedral angles and the improper dihedral describing the C–NO<sub>2</sub> out-of-plane deformation.

Although the dynamics of a process can be affected by a thermostat, which involves modification of the equations of motion,<sup>56</sup> this should not be a problem in the case of crystal growth, which is usually considered to occur stochastically.<sup>57,58</sup> Thus, we have used *NVT* simulations to compute the rate of crystallization as a function of temperature for neat liquid in contact with the (100), (010), (001), or (110) crystal faces. Projections of the measured nitromethane crystal structure are illustrated in Fig. 1, looking down onto the (001), (100), and (010) crystallographic faces. The 3D periodic primary simulation cell used in this study is illustrated schematically in Fig. 2. A liquid region containing 480 molecules in all cases, obtained from a separate *NVT* simulation at  $T=256$  K which is just above the SRT melting point ( $251 \pm 5$  K),<sup>7–9</sup> is bracketed on either side by seed crystals containing 240 molecules apiece with the selected crystal face initially in contact with the liquid. The size of the seed crystal was  $5a \times 4b \times 3c$  in all cases. Using the crystal unit cell lattice parameters  $a=5.244$  Å,  $b=6.320$  Å, and  $c=8.730$  Å reported by Trevino *et al.*<sup>2</sup> based on single crystal x-ray diffraction measurements at  $T=224$  K, this yields a nearly cubic seed crystal. We neglected the small (<0.9%) variations of the unit cell parameters that would exist due to thermal expansion over the 50 K range studied. Simple rotations of the seed crystals were performed to orient them with the selected face in contact with the liquid region for a given simulation.<sup>59</sup> A gap, comprising approximately one-sixth of the overall simulation cell length in the long dimension, that is, the direction normal to the solid-liquid interface, was added at the outer edge of each crystal slab to avoid interactions between the free crystal surfaces and to accommodate volume changes due to crystallization. (Simulations performed without the empty spaces did not exhibit any crystallization even after 1500 ps of simulation time; this is accord with the results for metals).<sup>60</sup>

The initial configuration of the simulation cell used to study crystal growth for liquid in contact with the (100) face at  $T=190$  K is shown in Fig. 3 (top). The initial dimensions of the simulation cell were  $X=157.32$  Å,  $Y=25.28$  Å, and  $Z=26.19$  Å, where Cartesian directions  $X$ ,  $Y$ , and  $Z$  are parallel to crystal directions  $a$ ,  $b$ , and  $c$ , respectively, and the

length for  $X$  includes 13 Å gaps that have been added to the outer face of each crystal slab as discussed above. The *NVT* simulations were performed with a fixed time step of 0.75 fs at 10 K intervals over the range  $T=170$ – $220$  K for total times of 1200 ps ( $1.6 \times 10^6$  time steps), of which the first 200 ps ( $2.67 \times 10^5$  time steps) were regarded as equilibration and not used in the data analyses discussed below. The temperatures studied are well below the computed melting point ( $251 \pm 5$  K) for the SRT force field.<sup>7–9</sup> Data for analysis were stored every 375 fs. The middle and bottom panels of Fig. 3 are snapshots of the simulation cell at the end of equilibration ( $t=200$  ps) and the end of the simulation ( $t=1200$  ps), respectively. By 1000 ps between two and three layers of new crystal have been formed at each (100) crystal-liquid interface.

Our goal was to simulate crystallization under steady-state conditions. During the 200 ps equilibration interval, the atomic velocities were rescaled every five time steps to yield the target temperature. The flux of thermal energy from the system<sup>67,69</sup> during the production phase of the simulations ( $200 \text{ ps} \leq t \leq 1200 \text{ ps}$ ) was maintained by the Nosé–Hoover thermostat; the selected relaxation time constant, 2.00 ps, is significantly faster than the rate of crystal growth. To ensure that the fixed transverse lattice dimensions did not strongly affect the results, we calculated the time-averaged stress tensor for each system during the 1.0 ns production phase. The

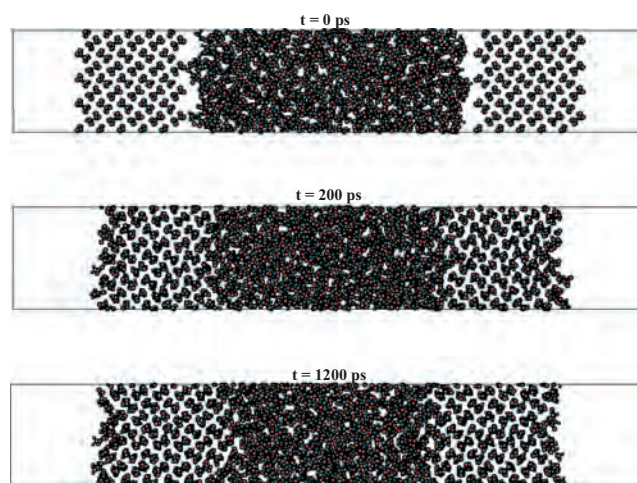


FIG. 3. Instantaneous configurations of the simulation cell for crystal growth on the (100) face at  $T=190$  K:  $t=0$ , beginning of the simulation;  $t=200$  ps, end of the equilibration period; and  $t=1200$  ps, end of the simulation.



maximum average diagonal components obtained from any simulation were  $|\sigma_{xx}| < 219$  atm,  $|\sigma_{yy}| < 924$  atm, and  $|\sigma_{zz}| < 1220$  atm; the maximum average value for any off-diagonal component  $|\sigma_{i \neq j}|$  was less than 22 atm. These mean values are smaller than the corresponding fluctuations and are sufficiently close to zero for the purposes of the present study.

It has been shown that a nearby second interface (closer than 25 Å in the case of Lennard-Jones systems) can affect the rate of crystallization.<sup>64,69</sup> With one exception the combinations of cell lengths and simulation times considered in our study are such that the two crystallization interfaces remain sufficiently far apart that the rates of crystallization are unaffected. (In that exceptional case, discussed in Sec. III D, our analysis was restricted to time intervals for which the distance between the growing interfaces was 30 Å or more.)

The radial distribution function (RDF), molecular number density, and orientational order parameter, as defined previously,<sup>9</sup> were monitored as functions of time within rectangular fixed-size subvolumes (dashed lines in Fig. 2) 2.56 Å in width that subdivide the simulation cell along its longest dimension, as described previously.<sup>8,9</sup> (The distance 2.56 Å is one-half the  $a$  unit cell lattice parameter, or roughly one molecular diameter.) Thus, the simulation cell was divided into  $2n$  ( $n=30$ ) fixed-volume slabs tagged as 30', 29', ..., 2', 1', 1, 2, ..., 29, 30 from left to right as illustrated in Fig. 2. Because of the symmetry of the simulation cell the properties of the molecules in subvolumes  $n$  and  $n'$  were averaged; thus when we refer to results for *subvolume*  $n$  we are actually describing the arithmetic average of those obtained for subvolumes  $n$  and  $n'$ .

Out of concern that a thermostat might affect the detailed dynamics of crystallization, we performed a short (15.0 ps) constant-energy constant-volume (NVE) simulation for the case of liquid in contact with the (001) crystal face. The initial condition for this microcanonical trajectory was the phase space point at  $t=500$  ps from the corresponding NVT simulation at  $T=210$  K. The step size for the microcanonical trajectory was 0.75 fs; data were stored every 37.5 fs. Autocorrelation functions were computed for center-of-mass translation, molecular orientation in the laboratory frame, and methyl group rotation

$$C_{uu}(\tau) = \langle u(t) \cdot u(t + \tau) \rangle, \quad (1)$$

where  $u(t + \tau)$  is the instantaneous center-of-mass position vector, C–N bond vector, or methyl group orientation for a given molecule at a time delay  $\tau$  relative to the corresponding values  $u(t)$  at time  $t$ . The autocorrelation functions for molecules in the crystal, liquid, and interfacial regions were obtained as ensemble averages over ten arbitrarily selected molecules taken from each region, with the usual averaging over equivalent time origins. Molecules in the interfacial region were examined individually to ensure that they remained in an interfacial subvolume over the entire 15.0 ps time interval used to generate the autocorrelation functions.

### III. RESULTS AND DISCUSSION

#### A. Radial distribution function, molecular number density, and orientational order parameter

The progress of crystallization was monitored by computing for each subvolume as a function of time the three-dimensional center-of-mass radial distribution function (3D RDF), the molecular number density, and the orientational order parameter  $\langle \cos \theta \rangle$ , where  $\theta$  is the instantaneous angle between the C–N bond vector in a molecule and the  $c$  crystal axis. As described in Sec. II, the simulation cell has two equivalent crystal-liquid interfaces, which we treated as equivalent for averaging purposes. Initially the liquid and crystalline subvolumes defining the interface are  $n=13$  and 14, respectively. The RDF, molecular number density, and orientational order parameters for subvolumes 9–14, which initially are liquid except for subvolume 14, are shown in Fig. 4 for the NVT simulation of crystal growth on the (100) surface at  $T=190$  K. The RDF curves were obtained by averaging over 18.75 ps time windows at the beginning and end of the production simulation ( $t=200$  ps and  $t=1200$  ps, respectively). The RDFs (left column, Fig. 4) for subvolumes 9–14 obtained during the initial time window are shown by the red points while those for the final time window are shown in blue. Subvolume 9 remains liquid throughout the simulation, while subvolumes 11–13 crystallize; the result for subvolume 10 is equivocal. Subvolume 13, which is liquid initially, is in contact with the crystal bed and therefore exhibits some characteristics of the crystal at the beginning of the simulation. The RDF results in Fig. 4 show that between three and four molecular layers have crystallized, and that at the end of the simulation subvolumes 11, 12, and 13 have a RDF structure corresponding essentially to the crystal. By contrast, subvolume 10 is interfacial, with a peak in the RDF at  $\sim 6.5$  Å during the last 18.75 ps of the simulation. Addition of three molecular layers to the crystal (corresponding to longitudinal growth by 1.5 unit cells or about 7.7 Å) yields a crystallization rate of  $\sim 0.11$  molecule  $\text{ns}^{-1} \text{Å}^{-2}$  or an interface growth rate of  $\sim 6.4$  ( $\pm \sim 2.6$ ) Å  $\text{ns}^{-1}$ . The large error bar is a consequence of the uncertainty:  $\pm \sim 1$  layer out of 3 depending on whether layer 10 is counted among the number of crystal layers grown in the simulation.

The number densities in subvolumes 9–14 are plotted as functions of time in the middle column of Fig. 4 for crystal growth on the (100) surface at  $T=190$  K. Values for bulk liquid and crystal were obtained from separate simulations at  $T=190$  K and are shown as red and blue horizontal lines, respectively. Overall, the behavior of the molecular number density is consistent with the results obtained for the variation of the RDF. Specifically, by the end of the simulation the RDFs for subvolumes 13, 12, 11, and to some extent subvolume 10 exhibit crystal-like features; the molecular number densities for those same subvolumes by the end of the simulation have clearly shifted toward the value for the crystal (blue line), indicative of crystallization. By contrast, the molecular number density of subvolume 9 corresponds initially



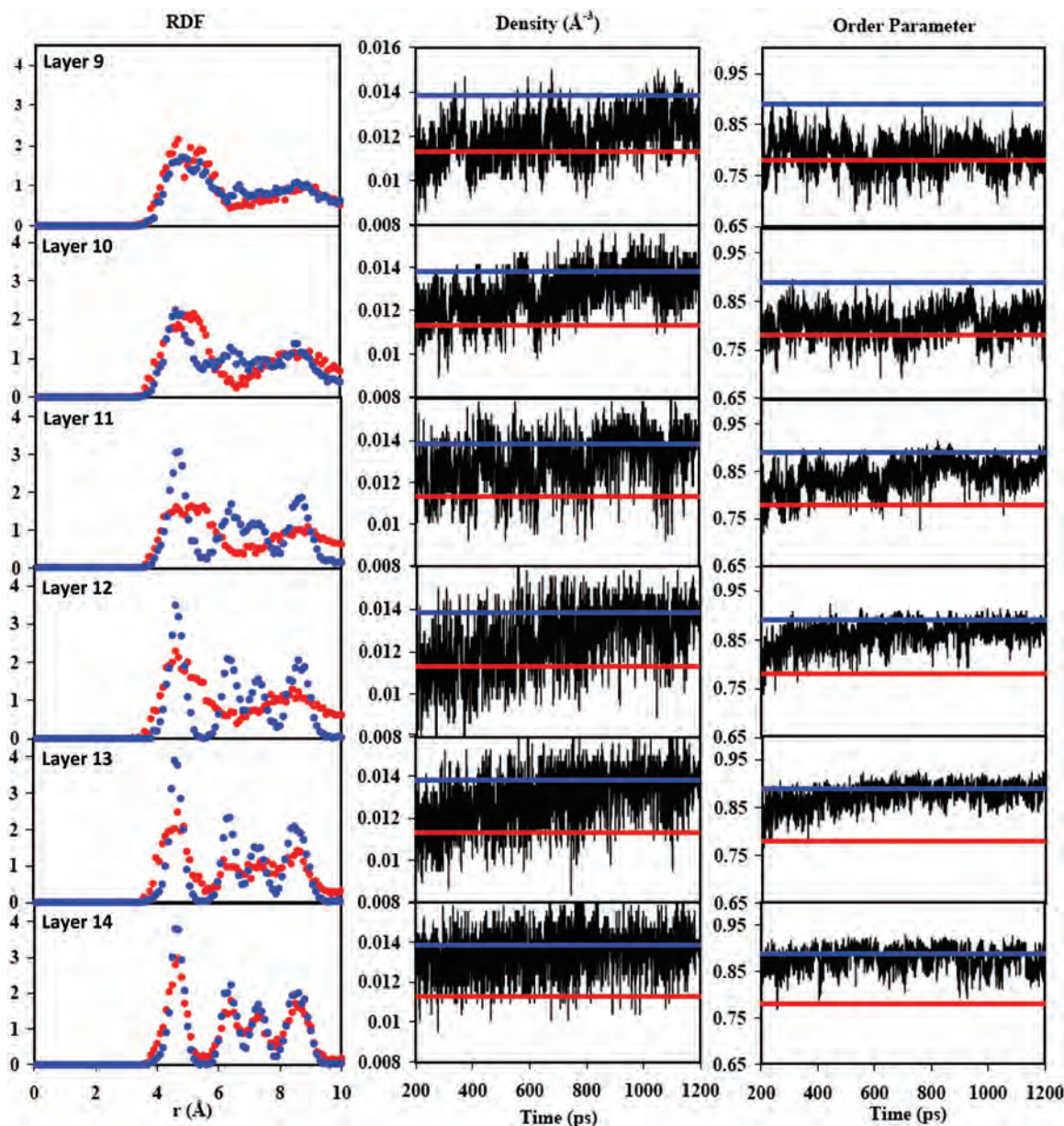


FIG. 4. Structural properties for subvolumes 9–14 for simulation of crystallization on the (100) crystal face of nitromethane at  $T=190$  K. Left-hand column: RDF. Center column: molecular center-of-mass number density ( $\text{\AA}^{-3}$ ). Right-hand column: orientational order parameter. In the case of the RDF results, time averages over the initial 18.75 ps (red symbols) and final 18.75 ps (blue symbols) are shown. For the molecular number density and orientational order parameters time histories are shown for the entire 1000 ps production simulation; red and blue horizontal lines correspond to the corresponding values of those properties for the bulk liquid and crystal, respectively.

to that of the liquid (compare to the red line); and, while it does increase over the course of the simulation, it never reaches the density of the crystal (blue line). The growth rates obtained from the molecular number density are the same as those obtained from the RDF results to within the limited precision of the simulations.

The orientational order parameters for subvolumes 9–14 are plotted as functions of time in the last column of Fig. 4 for crystal growth on the (100) surface at temperature  $T=190$  K. The results indicate loss of orientational disorder of the molecules as they crystallize. Only subvolume 13 gains full orientational order by the end of the simulation, although layer 12 appears to be close. Thus, orientational relaxation in the crystal lattice lags behind translational registration. Inter-

estingly, the orientational order parameter for layer 13 exhibits smaller fluctuations about the value for the bulk crystal (blue line) than does that for layer 14, which is always part of the crystal (separated from the liquid by one layer at the beginning of the simulation).

Since the order parameter is an average over all molecules within a given subvolume at a given instant in time it represents an average of a single-molecule function over about 20–24 molecules/layer irrespective of material phase and therefore has relatively small fluctuations. By contrast, the density is simply the instantaneous number of molecules within a given subvolume; since the number of molecules within a given subvolume can vary by one or two over any brief time interval there can be a concomitant variation of

$\sim 5\%$ – $10\%$  in the density. However, it is the general trends in Fig. 4 that are significant for the present purpose and not the details of the fluctuations.

Solid-liquid interfaces are difficult to study experimentally,<sup>61–63</sup> thus MD or Monte Carlo simulations have provided much of what we know about their properties.<sup>21,64–67</sup> As mentioned in the Introduction, calculations have shown that the width of the crystal-liquid interface in Lennard-Jones systems depends on which crystal face is exposed to the melt.<sup>6,68,69</sup> Lennard-Jones crystal-liquid interfaces involving (100) and (001) crystal faces were found to be wider than those involving (111) faces.<sup>66–69</sup> Galejs *et al.*<sup>68</sup> and Gulam Razul *et al.*<sup>64</sup> have reported results for the dependence of the interfacial widths for various faces of the Lennard-Jones system in contact with the liquid. They determined the width of the (001) interface to be 0.3 to 0.4 Lennard-Jones radii wider than those for the (011) and (111) faces, for which interface widths of  $\sim 5.0$  radii were obtained. Also, the density of the liquid in the immediate neighborhood of the interface has been predicted to increase by up to 10% relative to the bulk value depending on which crystal face is exposed to the melt;<sup>53</sup> for example, the Lennard-Jones liquid density profile at the (001) interface shows no increase in density relative to the bulk liquid value while there is a significant increase (about 10%) for the liquid in contact with the (111) and (011) faces.<sup>53</sup>

Although the precision of the simulations is rather low, the RDF, molecular number density, and orientational order parameter results indicate that the width of the solid-liquid interface depends somewhat on the property used to define it. The most conservative definition of the interface between two pure phases in a two-phase system is the one that maximizes the spatial interval over which distinctions between the bulk phases can be discerned within a given statistical precision. Estimates of the interface width for crystallization on the (100) face at  $T=190$  K based on the RDF results (see Fig. 4, left-hand column) yield values of  $\sim 10$ – $13$  Å; 10 Å, four molecular layers if subvolume 10 is not included as part of the interface at the end of the simulation. The width estimated from the density is  $\sim 10$  Å, in accord with the lower value based on the RDF. Overall (results are not shown for all cases), based on the RDF results we obtain estimates for the widths of the crystal-liquid interface of about four or five molecular diameters ( $\sim 10$ – $13$  Å) for the (100) and (001) interfaces and about three or four molecular diameters ( $\sim 7.5$  Å to  $\sim 10$  Å) for the (010) and (110) interfaces. The estimates based on the RDF predict the widest spatial variation and thus should be used as the defining criterion since it is the most conservative definition of interfacial width. Thus, while nitromethane and Lennard-Jonesium are too different to warrant specific comparisons, the range of orientation-dependent interfacial widths obtained from our simulations is generally consistent with those obtained for simple Lennard-Jones models.

## B. Autocorrelation functions

The details of the dynamics of crystal growth for liquid in contact with the (001) crystal face at  $T=210$  K were in-

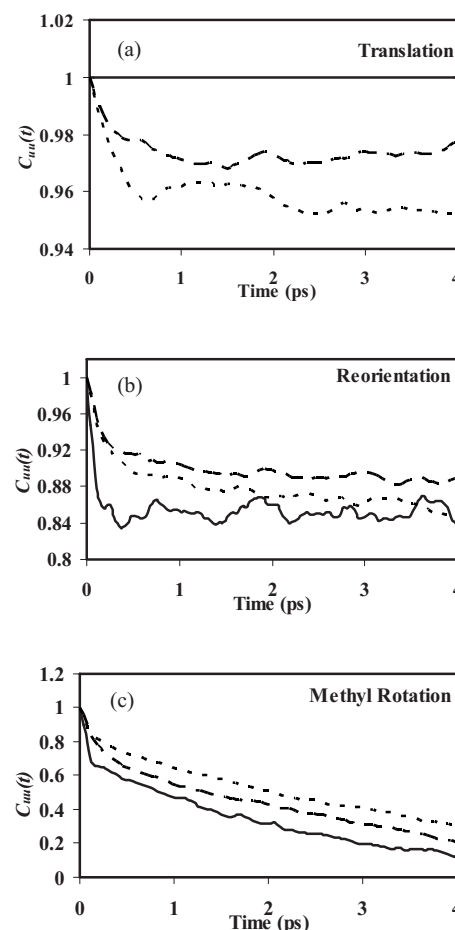


FIG. 5. Autocorrelation functions for center-of-mass molecular translation (a), orientational relaxation (b), and rotation of the methyl group (c) obtained from a NVE simulation initiated from a phase space point taken approximately half-way through the NVT simulation of crystallization on the (001) face at  $T=210$  K. Solid, dashed, and dotted curves correspond to results obtained for the bulk crystal, molecules in the interfacial region, and the bulk liquid, respectively.

vestigated by calculating autocorrelation functions  $C_{uu}(t)$  for molecular translation, molecular reorientation, and rotation of the methyl group in the crystal, liquid, and interfacial region. As noted at the end of Sec. II, in order to eliminate any effects due to a thermostat, these simulations were performed in the NVE ensemble starting from a phase space point taken from the corresponding NVT simulation. The autocorrelation functions for molecular translation, molecular reorientation, and methyl rotation are shown in Figs. 5(a)–5(c), respectively. In each panel the results for the crystal are represented by solid lines, those for the interfacial region by dashed lines, and those for the liquid by dotted lines. The molecules used to calculate  $C_{uu}(t)$  for the crystal and liquid phases were taken from regions in the simulation cell far from any interface; those for the interfacial region were taken from subvolumes 9–13 as indicated by the RDF analysis.

Figure 5(a) shows  $C_{uu}(t)$  for molecular translation. As expected the autocorrelation function for the crystal does not decay significantly (solid curve). On the 4 ps time scale considered here  $C_{uu}(t)$  for molecular translations in the liquid (dotted curve) decays to a lower value than that for the in-

surface (dashed curve), indicative of restricted translational motion in the neighborhood of the interface. [Note however that the values of all three autocorrelation functions are still  $>0.95$  at 4.0 ps. For reference, relaxation of  $C_{uu}(t)$  to zero for the liquid at  $T=190$  K was estimated to require more than 90 ps.] Interestingly, the autocorrelation functions for the liquid and interface both decrease from unity [i.e.,  $\tau=0$  in  $C_{uu}(\tau)$ ] at about the same rate suggesting qualitatively similar center-of-mass translational dynamics of interfacial and liquid phase molecules on a subpicosecond time scale. This general behavior will also be seen for autocorrelation functions of the other properties discussed below, although the time intervals over which these initially overlapping decays persist vary from  $\sim 0.1$  to  $\sim 0.3$  ps depending on which property is studied.

The autocorrelation function for molecular rotation is shown in Fig. 5(b). At short time delays ( $\tau \leq 0.3$  ps), the rotational diffusion properties of molecules in the liquid (dotted curve) and interfacial (dashed curve) regions are similar to one another but quite distinct from what is obtained for molecules in the crystal (solid curve);  $C_{uu}(t)$  for the crystal decays more rapidly than those for the interface and liquid. At longer times ( $0.3 \text{ ps} < \tau < \sim 10$  ps, only shown out to  $\tau=4.0$  ps in Fig. 5) orientations for molecules near the interface are more strongly self-correlated in time than those for molecules in either the liquid or crystal. This is indicative of the transition of molecules in the interfacial region from a liquidlike to a crystal-like environment. At longer times ( $\tau > \sim 20$  ps, not shown) the rotational autocorrelation function of the liquid decays to the long-time value expected for a liquid.

The autocorrelation function for methyl group rotation is shown in Fig. 5(c). In this case the  $C_{uu}(t)$  for the liquid (dotted curve) lies above that for the interface (dashed curve), which in turn is higher than the one for the crystal (solid curve). This result suggests that on average hindrance to methyl rotation is greatest in the disordered liquid state, lowest in the crystal (nearly a free rotor), and intermediate in the neighborhood of the interface where molecules are becoming registered in the lattice. This is consistent with the predictions of published quantum molecular dynamics simulations.<sup>70</sup> The rotational kinetic energy of the methyl groups,  $E_r = I\omega^2/2$ , where  $I$  and  $\omega$  are the instantaneous moment of inertia and angular velocity for methyl rotation about the C–N bond axis, respectively, was averaged over the molecules in each subvolume during the 15.0 ps NVE simulation. The results are plotted in Fig. 6 and show clearly that the average rotational kinetic energy of the methyl group increases upon passing from the liquid, through the interface, and into the crystal. This is consistent with the interpretation of the methyl rotational dynamics discussed in the preceding paragraph.

### C. Rates of crystallization

We obtained rates of crystallization using two methods: (1) the time dependence of the system potential energy and (2) the time-dependent numbers of individual molecules in each phase as determined by molecular self-diffusion coeffi-

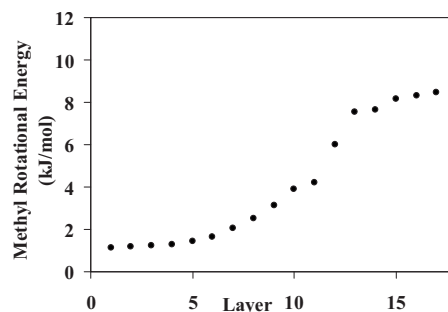


FIG. 6. Average methyl group rotational kinetic energy vs subvolume index (see Fig. 2) for crystal growth on the (100) face at  $T=190$  K.

icients. As crystallization proceeds toward completion the molar potential energy of the system decreases toward the value corresponding to that of the crystal at the given temperature. Along the way the rate at which the potential energy decreases is proportional to the rate at which molecules initially in the melt join the crystal. Figure 7 shows the time history of the total potential energy of the simulation cell for crystal growth on the (100) surface at  $T=190$  K. The distance between the two crystal-liquid interfaces was never less than 44 Å and therefore they could be confidently treated as independent. The potential energy difference per molecule between the pure crystal and pure liquid at  $T=190$  K is  $29.67 \text{ kJ mol}^{-1} \text{ molecule}^{-1}$  based on separate simulations for each pure phase. The decrease in potential energy during the simulation was  $(1078 \pm \sim 250) \text{ kJ mol}^{-1}$ , which corresponds to the crystallization of about 18 molecules (about 0.75 molecular layers). This is in accord with the estimate based on the orientational order parameter results shown in the right-hand column of Fig. 4.

Table I lists the rates of change of the potential energy, divided by the cross-sectional area of the simulation cell, for each temperature and melt-crystal interface studied. The results indicate that for all temperatures considered the rate of crystal growth on the (001) crystal face is considerably larger than on the other faces. In fact, at  $T=210$  K the entire liquid phase crystallized on the (001) face before the end of the simulation. The results also show that the rate of crystallization increases steadily with increasing temperature for growth on the (001) and (100) surfaces whereas for growth on the (010) and (110) faces the rate reaches a maximum at  $T=190$  K and then decreases with further increase in temperature. These results indicate that the free energy change

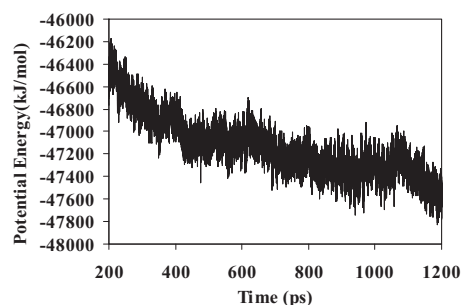


FIG. 7. Time history of the system potential energy during crystal growth on the (100) face at  $T=190$  K.



TABLE I. Rate of change of system potential energy ( $\text{kJ mol}^{-1}\text{\AA}^{-2}\text{ns}^{-1}$ ) for crystallization from the melt on various crystal faces at various temperatures. (Restricted to times for which the two crystal-liquid interfaces in the simulation cell were separated by at least  $30\text{ \AA}$ .)

Surface	$T$ (K)					
	170	180	190	200	210	220
(100)	29.76	40.88	52.29	64.92	69.54	87.45
(010)	38.73	53.18	62.68	62.64	47.57	44.76
(001)	69.00	153.88	167.81	224.73	305.01	333.29
(110)	42.04	55.11	89.36	30.01	7.36	— <sup>a</sup>

<sup>a</sup>No crystallization occurred during 1200 ps total simulation time.

for nitromethane crystallization depends considerably on which crystal face is in contact with the melt, in accord with the findings of Amini and Laird<sup>30</sup> for Lennard-Jones systems. Our calculated temperature-dependent crystal growth rates are not described well by the modified Wilson–Frenkel theory.<sup>34,53</sup> Although we have not attempted a detailed analysis of why this is true, we tentatively attribute it to the complexity of nitromethane crystal compared to the simple atomic system upon which the theoretical model is based. Nitromethane forms a noncubic crystal of nonspherical particles on lattice sites, has intramolecular vibrational degrees of freedom, and thus differs significantly from a simple atomic solid.

We monitored crystal growth at the (100) surface at  $T=190\text{ K}$  by counting the numbers of molecules in the crystal and liquid phases as a function of time. To determine the number of molecules that belong to each phase we calculated the self-diffusion coefficient of the molecules for successive nonoverlapping 66 ps time windows. A molecule was regarded as belonging to the crystal during a given time window if its self-diffusion coefficient was less than or equal to  $0.026\text{ \AA}^2/\text{ps}$  (that is, the self-diffusion coefficient, essentially zero, obtained in a separate simulation of the solid at  $T=190\text{ K}$ ). The results are shown in Fig. 8(a); they correspond directly to those shown in Fig. 7. During the initial 200–300 ps interval there is a rapid increase of the number of molecules in the crystal phase (mostly during the 200 ps equilibration phase). There is a corresponding rapid drop in the potential energy during this same time interval as shown by the results in Fig. 7. From  $t\sim 300\text{ ps}$  to almost  $t\sim 1000\text{ ps}$  there is a gradual, but not exclusively monotonic, change in the number of molecules in each phase; the variation of the potential energy in Fig. 7 is consistent with this observation: the rate of decrease of potential energy becomes nearly constant, but with small nonmonotonic variations. Starting at  $t\sim 1000\text{ ps}$  however and continuing to the end of the simulation there is another sharp increase in the number of molecules in the solid phase.

The stages of crystal growth seen in the results in Fig. 8(a) raise once again the question of whether crystallization is a concerted process in which the molecules crystallize in pairs or even larger groups. The results in Figs. 7 and 8(a) correspond to the net crystallization of only 36 molecules per interface, which is insufficient to allow strong conclusions concerning the mechanism by which molecules join the crystal. Thus, we performed a simulation for liquid in contact

with the (001) face at the same temperature ( $T=190\text{ K}$ ), for which we computed self-diffusion coefficients based on consecutive nonoverlapping 20 ps time windows; the results are shown in Fig. 8(b). The almost continuous variation in the number of the molecules suggests that, at least for this particular case, crystallization does not occur in a concerted manner but rather is dominated by the stochastic dynamics of individual molecules. [Note: the “bump” at  $t\sim 750\text{ ps}$  in Fig. 8(b) is an artifact of starting a new simulation using a new velocity distribution and the last configuration from the previous simulation.]

The simulation at  $T=210\text{ K}$  for liquid in contact with the (001) face resulted in complete crystallization of the sample [see Fig. 8(c)]. The crystallization rate for this simulation is about  $0.378\text{ molecules ns}^{-1}\text{ \AA}^{-2}$  or  $\sim 20.5\text{ \AA ns}^{-1}$ . We observe in Fig. 8(c) that, following equilibration, the rate

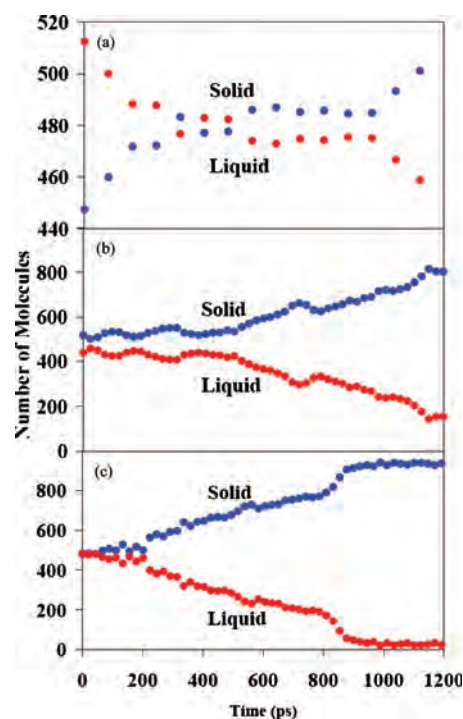


FIG. 8. (a) Time histories of the numbers of nitromethane molecules determined to be in the crystal (blue symbols) and liquid (red symbols) during crystal growth based on 3D self-diffusion coefficients calculated separately for each molecule in the system. The cases shown are for crystal growth on: (a) the (100) face at  $T=190\text{ K}$ , (b) the (001) face at  $T=190\text{ K}$ , and (c) the (001) face at  $T=210\text{ K}$ . In case (c) the system fully crystallized by  $t\sim 900\text{ ps}$ .



of crystallization is almost constant until  $t \sim 750$  ps. At this point, which corresponds to the time at which the distance between the two solid-liquid interfaces in our simulation decreases to about 30 Å, the rate of crystallization increases rapidly and goes to completion within about 150 ps. By contrast, almost 500 ps were required to crystallize the same number of molecules when the interfaces were separated by more than 30 Å. The effects of the presence of a nearby interface have been a matter of concern when creating steady-state interfaces<sup>64,69</sup> and, as shown here, also need to be considered when performing crystallization simulations. It is interesting to note that in spite of the relatively rapid crystallization of the liquid in Fig. 8(c) we did not detect a grain boundary or other major crystal defect in the final crystal. An animation of the entire simulation cell for this case plus two additional ones in which only the subset of molecules that comprises a single molecular layer in the final crystal is shown are available as supplementary material.<sup>71</sup>

#### D. Effects of intramolecular flexibility

It has been shown in previous simulations that the melting point of nitromethane is independent of whether intramolecular degrees of freedom are included.<sup>6</sup> In light of this, we performed simulations using the rigid-molecule version of the SRT nitromethane force field to ascertain the effects of ignoring intramolecular flexibility on crystallization. The specific case studied is liquid in contact with the (001) crystal face at  $T=210$  K for which, as noted just above, the system crystallized completely within less than 1 ns. The results are shown in Fig. 9. Figure 9(a) was obtained from a simulation using the fully flexible SRT force field while Fig. 9(b) was obtained using the rigid-molecule version. In both cases the initial seed crystal was on the right. The results indicate that crystallization of nitromethane is dominated by intermolecular interactions; the main qualitative difference in the crystallization of flexible versus rigid molecules is that in the latter case the methyl group can be trapped in incorrect orientations. In the case of flexible molecules [see Fig. 9(a)] it is impossible to identify at the end of the simulation where the initial liquid-crystal interface was located, whereas in the case of rigid molecules [see Fig. 9(b)] the boundary between the seed crystal and the grown crystal is clearly identifiable due to thermal noise in the latter. (The seed crystal in the latter simulation was completely rigid.) The presence of mis-oriented methyl groups in the rigid-molecule simulations can easily be seen by comparing Fig. 9(a) to Fig. 9(b).

To test whether such defects are readily annealed we performed a flexible-molecule simulation starting from the final configuration from the rigid-molecule simulation. Figure 9(c) contains a plot of the system potential energy as a function of time obtained from the flexible-molecule simulation starting from the rigid-molecule configuration shown in Fig. 9(b). The horizontal line in Fig. 9(c) is the average potential energy obtained from a separate equilibrium simulation of the crystal at  $T=210$  K using the fully flexible force field. As expected, there is a rapid initial drop in potential energy, requiring only about 2 ps, as the system geometry rearranges upon release of the geometric constraints. We find

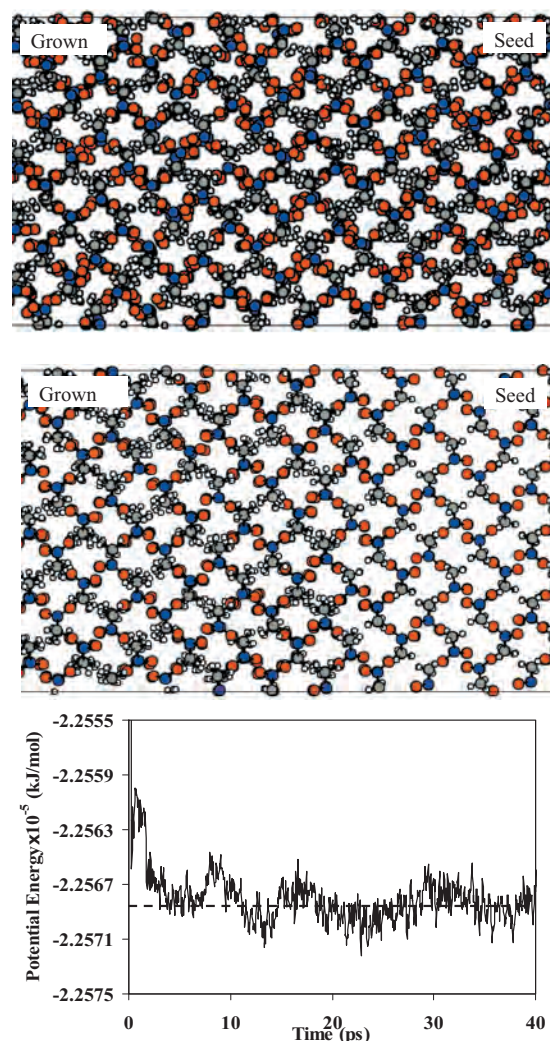


FIG. 9. Top: Snapshot of nitromethane crystal grown using the fully flexible SRT force field starting from liquid in contact with the (001) crystal face at  $T=210$  K; Middle: same as top panel except that a rigid-molecule force field was used in the simulation. Bottom: Time history of the system potential energy obtained using the fully flexible potential starting from the rigid-molecule-based crystal shown in the middle panel. The horizontal line shows the time-averaged potential energy obtained from a separate simulation of the crystal at  $T=210$  K.

that, after the initial relaxation, the structural properties of the flexible molecule obtained in this simulation are identical to those obtained using the flexible model from the outset. However, it is important to note that the rigid-molecule system required 1650 ps of simulation time to crystallize completely whereas the flexible-molecule simulation underwent complete crystallization in only 750 ps.

#### IV. CONCLUSIONS

We have studied the atomic-level mechanism of the crystallization of nitromethane at various crystal-liquid interfaces. We carried out MD simulations at 10 K intervals over the range  $T=170$ – $220$  K for crystal faces (100), (010), (001), and (110) in contact with the pure melt. We studied crystal growth and interfacial properties by monitoring the spatial and temporal evolution of radial distribution functions (RDFs), molecular number density, an orientational order parameter, and molecular self-diffusion coefficients. The results

show that during crystallization molecules first achieve correct translational ordering followed by rotational relaxation that leads to molecules properly oriented in the crystal structure.

The width of the interface varies with the crystallographic orientation of the crystal face in contact with the liquid. Based on the orientational order parameter we calculated widths as wide as  $\sim 13$  Å (about five molecular diameters) for crystal growth on (100) and (001) faces. The interfacial widths calculated for growth on (110) and (010) faces were  $\sim 10$  Å (about four molecular diameters). The width of the crystal-liquid interface depends on the criterion used to define the crystalline state. We find that definitions based on the RDF and density lead to predictions of wider interfaces than those based on the orientational order parameter. For example, for crystal growth on the (100) face a definition of the interface based on the orientational order parameter results in prediction of an interface about 6 Å wide whereas a definition based on the RDF leads to a prediction of an interface width of about 13 Å.

The rate of the crystallization is a function of temperature as well as the crystallographic orientation of interface. The calculated rates of crystallization vary between about  $0.08 \text{ molecule ns}^{-1} \text{ Å}^{-2}$  ( $2.5 \text{ Å ns}^{-1}$ ) for growth on the (010) surface at  $T=190$  K to  $0.41 \text{ molecule ns}^{-1} \text{ Å}^{-2}$  ( $22.4 \text{ Å ns}^{-1}$ ) for growth on the (001) surface at  $T=220$  K. The temperature at which the maximum rate of crystallization of nitromethane occurs is different for different surfaces.

## ACKNOWLEDGMENTS

We are grateful to Dr. Jenel Vatamanu for several fruitful discussions. We thank Professor Jennifer Swift and Ms. Ilana Goldberg for a very informative discussion on crystallization. This work was supported by a DOD MURI grant managed by the Army Research Office and by the Los Alamos National Laboratory LDRD program.

- <sup>1</sup>D. C. Sorescu, B. M. Rice, and D. L. Thompson, *J. Phys. Chem. B* **104**, 8406 (2000).
- <sup>2</sup>S. F. Trevino, E. Prince, and C. R. Hubbard, *J. Chem. Phys.* **73**, 2996 (1980).
- <sup>3</sup>S. F. Trevino and W. H. Rymes, *J. Chem. Phys.* **73**, 3001 (1980).
- <sup>4</sup>D. C. Sorescu, B. M. Rice, and D. L. Thompson, *J. Phys. Chem.* **105**, 9336 (2001).
- <sup>5</sup>A. J. Wells and E. B. Wilson, *J. Chem. Phys.* **9**, 314 (1941); D. C. Smith, C. Pan, and J. R. Nielsen, *ibid.* **18**, 706 (1950); W. J. Jones and N. Sheppard, *Proc. R. Soc. London, Ser. A* **304**, 135 (1968); C. Trinquecoste, M. Rey-Lafon, and M.-T. Forel, *Spectrochim. Acta, Part A* **30**, 813 (1974); D. C. McKean and R. J. Watt, *J. Mol. Spectrosc.* **61**, 184 (1976).
- <sup>6</sup>P. M. Agrawal, B. M. Rice, and D. L. Thompson, *J. Chem. Phys.* **119**, 9617 (2003).
- <sup>7</sup>L. Zheng, S.-N. Luo, and D. L. Thompson, *J. Chem. Phys.* **124**, 154504 (2006).
- <sup>8</sup>A. Siavosh-Haghighi and D. L. Thompson, *J. Phys. Chem. C* **111**, 7980 (2007).
- <sup>9</sup>A. Siavosh-Haghighi and D. L. Thompson, *J. Chem. Phys.* **125**, 184711 (2006).
- <sup>10</sup>J. K. Brennan, B. M. Rice, and M. Lisal, *J. Phys. Chem. C* **111**, 365 (2007).
- <sup>11</sup>J. K. Johnson, A. Z. Panagiotopoulos, and K. E. Gubbins, *Mol. Phys.* **81**, 717 (1994); W. R. Smith and B. Triska, *J. Chem. Phys.* **100**, 3019 (1994).
- <sup>12</sup>J. J. Dick, *J. Phys. Chem.* **97**, 6193 (1993).
- <sup>13</sup>P. A. D. de Maine, M. M. de Maine, A. A. Briggs, and G. E. McAlonie, *J. Mol. Spectrosc.* **4**, 398 (1960).

- <sup>14</sup>R. D. Verderame, J. A. Lannon, L. E. Harris, W. J. Thomas, and E. A. Lucia, *J. Chem. Phys.* **56**, 2638 (1972).
- <sup>15</sup>P. J. Miller, S. Block, and G. J. Piermarini, *J. Phys. Chem.* **93**, 462 (1989).
- <sup>16</sup>T. Megyes, S. Bálint, T. Grósz, T. Radnai, I. Bakó, and L. Almásy, *J. Chem. Phys.* **126**, 164507 (2007).
- <sup>17</sup>R. S. Cataliotti, G. Paliani, L. Mariani, S. Santini, and M. G. Giorgini, *J. Phys. Chem.* **96**, 2961 (1992).
- <sup>18</sup>M. G. Giorgini, P. Foggi, R. S. Cataliotti, M. R. Distefano, A. Morresi, and L. Mariani, *J. Chem. Phys.* **102**, 8763 (1995).
- <sup>19</sup>E. Tannenbaum, R. J. Myers, and W. D. Gwinn, *J. Chem. Phys.* **25**, 42 (1956).
- <sup>20</sup>D. T. Cromer, R. R. Ryan, and D. Schiferl, *J. Phys. Chem.* **89**, 2315 (1985).
- <sup>21</sup>B. B. Laird and A. D. J. Haymet, *Chem. Rev. (Washington, D.C.)* **92**, 1819 (1992).
- <sup>22</sup>E. Burke, J. Q. Broughton, and G. H. Gilmer, *J. Chem. Phys.* **89**, 1030 (1988).
- <sup>23</sup>H. E. A. Huitema, M. J. Vlot, and J. P. van der Eerden, *J. Chem. Phys.* **111**, 4714 (1999).
- <sup>24</sup>H. H. Kart, M. Uludogan, T. Cagin, and M. Tomak, *J. Non-Cryst. Solids* **342**, 6 (2004).
- <sup>25</sup>C. Desgranges and J. Delhommelle, *J. Am. Chem. Soc.* **129**, 7012 (2007).
- <sup>26</sup>H. Herrmann, N. Mattern, S. Roth, and P. Uebele, *Phys. Rev. B* **56**, 13888 (1997).
- <sup>27</sup>S. Valkealahti and M. Manninen, *J. Phys.: Condens. Matter* **9**, 4041 (1997).
- <sup>28</sup>T. Zykova-Timan, R. E. Rozas, J. Horbach, and K. Binder, *J. Phys.: Condens. Matter* **21**, 464102 (2009).
- <sup>29</sup>R. L. Davidchack and B. B. Laird, *J. Chem. Phys.* **118**, 7651 (2003).
- <sup>30</sup>M. Amini and B. B. Laird, *Phys. Rev. Lett.* **97**, 216102 (2006).
- <sup>31</sup>T. Yamamoto, K. Nozaki, A. Yamaguchi, and N. Urakami, *J. Chem. Phys.* **127**, 154704 (2007).
- <sup>32</sup>S. H. Garofalini and S. Zhang, *J. Am. Ceram. Soc.* **93**, 235 (2010).
- <sup>33</sup>N. Matsubara, T. Ogata, T. Mitani, S. Munetoh, and T. Motooka, *Jpn. J. Appl. Phys.* **48**, 03B006 (2009).
- <sup>34</sup>J. P. van der Eerden, in *Crystal Growth, From Fundamentals to Technology*, edited by G. Müller, J. Métrois, and P. Rudolph (Elsevier, Amsterdam, 2004), pp. 187–239.
- <sup>35</sup>M. Matsumoto, S. Saito, and I. Ohmine, *Nature (London)* **416**, 409 (2002).
- <sup>36</sup>H. Nada, J. P. van der Eerden, and Y. Furukawa, *J. Cryst. Growth* **266**, 297 (2004).
- <sup>37</sup>T. Yamamoto and K. Sawada, *J. Chem. Phys.* **123**, 23496 (2005).
- <sup>38</sup>H. Yang, Z. Li, Z. Lu, and C. Sun, *Polymer* **45**, 6753 (2004).
- <sup>39</sup>L. Xu, Z. Fan, H. Zhang, and H. Bu, *J. Chem. Phys.* **117**, 6331 (2002).
- <sup>40</sup>N. A. Mehl and L. Rebenfeld, *J. Polym. Sci., Part B: Polym. Phys.* **33**, 1249 (1995).
- <sup>41</sup>T. Krause, G. Kalinka, C. Auer, and G. Hinrichsen, *J. Appl. Polym. Sci.* **51**, 399 (1994).
- <sup>42</sup>N. Waheed, M. J. Ko, G. C. Rutledge, and C. Gregory, *Progress in Understanding of Polymer Crystallization*, Lecture Notes in Physics (Springer, Berlin, 2007), p. 457.
- <sup>43</sup>M. A. Carignano, P. B. Shepson, and I. Szleifer, *Mol. Phys.* **103**, 2957 (2005).
- <sup>44</sup>See, for example: Y. Furukawa and W. Shimada, *J. Cryst. Growth* **128**, 234 (1993).
- <sup>45</sup>J. Baardnes, L. H. Kondejewski, R. S. Hodges, H. Chao, C. Kay, and P. L. Davis, *FEBS Lett.* **463**, 87 (1999).
- <sup>46</sup>P. Yi and G. C. Rutledge, *J. Chem. Phys.* **131**, 134902 (2009).
- <sup>47</sup>A. Jabbarzadeh and R. I. Tanner, *J. Non-Newtonian Fluid. Mech.* **160**, 11 (2009).
- <sup>48</sup>K. Esselink, P. J. A. Hirbers, and B. W. H. van Beest, *J. Chem. Phys.* **101**, 9033 (1994).
- <sup>49</sup>J. Leyssale, J. Delhommelle, and C. Millot, *J. Chem. Phys.* **122**, 104510 (2005).
- <sup>50</sup>J. Leyssale, J. Delhommelle, and C. Millot, *J. Chem. Phys.* **122**, 184518 (2005).
- <sup>51</sup>S. Piana and J. D. Gale, *J. Am. Chem. Soc.* **127**, 1975 (2005).
- <sup>52</sup>S. Piana, M. Reyhani, and J. D. Gale, *Nature (London)* **438**, 70 (2005).
- <sup>53</sup>J. Q. Broughton, G. H. Gilmer, and K. A. Jackson, *Phys. Rev. Lett.* **49**, 1496 (1982).
- <sup>54</sup>L. Vrbka and P. Jungwirth, *J. Phys. Chem. B* **110**, 18126 (2006).

- <sup>55</sup>W. F. Smith and T. R. Forester, DL\_POLY, copyright The Council for the Central Laboratory of the Research Councils, Daresbury Laboratory at Daresbury, Nr. Warrington, 1996.
- <sup>56</sup>M. P. Allen and D. J. Tildesley, *Computer Simulation of Liquid* (Oxford, New York, 1987), p. 227.
- <sup>57</sup>K. A. Jackson, in *Crystal Growth, From Fundamentals to Technology*, edited by G. Müller, J. Métis, and P. Rudolph (Elsevier, Amsterdam, 2004), p. 27.
- <sup>58</sup>A. C. Levi and M. Kotrla, *J. Phys.: Condens. Matter* **9**, 299 (1997).
- <sup>59</sup>It was found in one of our previous simulations (Ref. 9) that melting points calculated for individual crystal faces are insensitive to transverse simulation cell sizes for dimensions identical to those considered here. We choose the long axis of our primary simulation cell, that is, the direction normal to the liquid-solid interface, always to be parallel to the  $x$ -axis in a right-handed Cartesian frame. For our chosen reference orientation of the seed crystal the  $a$ ,  $b$ , and  $c$  crystal directions are directed along the  $x$ ,  $y$ , and  $z$  Cartesian axes, respectively, such that by default the (100) plane is exposed to the liquid. Simple rotations of the seed crystal were used to expose other faces to the liquid. For example, rotation by  $\pi/2$  about the  $z$ -axis exposes the (010) face, etc.
- <sup>60</sup>F. D. Ditolla, E. Tosatti, and F. Ercolessi, in *Monte Carlo and Molecular Dynamics of Condensed Matter Systems*, edited by K. Binder and G. Ciccotti (SIF, Bologna, 1996), Vol. 49, p. 366.
- <sup>61</sup>E. Johnson, *Science* **296**, 477 (2002); J. M. Howe, *Interfaces in Materials* (Wiley, New York, 1997).
- <sup>62</sup>*Recent Technological Advances*, edited by K. Tsuji, J. Injuk, and R. van Grieken (Wiley, West Sussex, England, 2004).
- <sup>63</sup>J. M. Howe and H. Saka, *Mater. Res. Bull.* **29**, 920 (2004); J. F. van der Veen and H. Reichert, *ibid.* **29**, 958 (2004).
- <sup>64</sup>M. S. Gulam Razul, E. V. Tam, M. E. Lam, P. Linden, and P. G. Kusalik, *Mol. Phys.* **103**, 1929 (2005).
- <sup>65</sup>J. Q. Broughton and G. H. Gilmer, *J. Chem. Phys.* **84**, 5741 (1986).
- <sup>66</sup>R. L. Davidchack and B. B. Laird, *J. Chem. Phys.* **108**, 9452 (1998).
- <sup>67</sup>D. Y. Sun, M. Asta, and J. J. Hoyt, *Phys. Rev. B* **69**, 174103 (2004).
- <sup>68</sup>R. J. Galejs, H. J. Raveche, and G. Lie, *Phys. Rev. A* **39**, 2574 (1989).
- <sup>69</sup>M. S. Gulam Razul, J. G. Hendry, and P. G. Kusalik, *J. Chem. Phys.* **123**, 204722 (2005).
- <sup>70</sup>M. E. Tuckerman and M. L. Klein, *Chem. Phys. Lett.* **283**, 147 (1998).
- <sup>71</sup>See supplementary material at <http://dx.doi.org/10.1063/1.3504610> for three animations of the simulation at  $T=210$  K for liquid in contact with the (001) face.



# A Molecular Dynamics Study of Classical Vibrational Spectra in Hydrostatically Compressed Crystalline Nitromethane

Ali Siavosh-Haghighi, Richard Dawes,<sup>†</sup> Thomas D. Sewell,\* and Donald L. Thompson

Department of Chemistry, University of Missouri—Columbia, Columbia, Missouri 65211-7600, United States

Received: September 23, 2010; Revised Manuscript Received: November 9, 2010

The effects of pressure on the vibrational spectra of crystalline nitromethane have been studied by computing normal-mode frequencies and eigenvectors and classical power spectra at several hydrostatic pressures between 0 and 27.3 GPa using the full-dimensional Sorescu–Rice–Thompson (*J. Phys. Chem. B* **2000**, *104*, 8406) (SRT) valence force field. The purpose of the study was to determine the limits within which the SRT force field, and classical mechanics more generally, captures the qualitative pressure effects observed experimentally. The current results exhibit good overall agreement between the calculated normal-mode frequencies (and especially their pressure-dependent shifts) and those obtained in published experimental and theoretical studies. Comparisons of the pressure dependencies near room temperature of classical power spectra to experimental pressure-dependent infrared (IR) spectra for particular vibrational modes yield, in the case of the CN stretch, a CH<sub>3</sub> deformation, and the NO<sub>2</sub> asymmetric stretch, intriguingly similar evolution of spectral intensity with respect to pressure, whereas for the case of the NO<sub>2</sub> symmetric stretch mode the classical result bears little similarity to the experimental result.

## I. Introduction

Shock waves in molecular materials lead to complicated, nonthermal partitioning of energy among the inter- and intramolecular degrees of freedom.<sup>1–8</sup> It is generally accepted that the initial excitation and subsequent approach to thermal equilibrium in a shocked molecular crystal occurs by a mechanism known as *up-pumping* in which the shock initially excites the lattice phonons of the crystal, leading to significant excitation of those modes.<sup>1,9–12</sup> These, in turn, couple most strongly to those lowest frequency molecular vibrations (gateway modes) that overlap or are close to resonance with the lattice modes. The dominant pathway for energy transfer to the high-frequency vibrations is intramolecular vibrational energy relaxation (IVR). This occurs on time scales (several picoseconds or more) that are long compared to that for shock passage over a molecule in the crystal (for example, roughly 20–40 fs for nitromethane). A recent paper by Hooper<sup>1</sup> on the theory of energy transfer in shocked energetic crystals summarizes succinctly the current understanding of the mechanisms and time scales for these processes. Coupled with recent experimental advances,<sup>13–15</sup> theoretical models have provided useful information concerning energy transfer rates and pathways in shock loaded molecular materials.

Molecular dynamics (MD) is an effective tool for the study of phenomena in and immediately behind a shock wave due to the relatively short temporal and spatial scales involved in the transient events of primary interest.<sup>2,3,5–8,16–20</sup> However, the validity of the results of a MD simulation depends on the accuracy of the force field and the validity of the classical approximation. An abiding concern, particularly if the goal is to understand the detailed dynamics, is the accuracy of the force field used to propagate the classical equations of motion. Depending on the thermodynamic states of interest, it may be necessary to use a force field that includes the possibility of

chemical reactivity. However, in many cases, nonreactive models are sufficient. Regardless, prior to using a force field to make predictions of fundamental properties or processes for which quantitative accuracy is important, it should be validated as fully as possible against experimental data or reliable electronic-structure information. Since most MD simulations are performed for thermodynamic states close to room temperature and atmospheric pressure, the emphasis in most validation efforts is on sampling the configuration space likely to be explored under such conditions (for a specific exception, see ref 21); therefore, the reliability of such force field parametrizations for applications involving more extreme thermodynamic states is questionable (see, for example, ref 22).<sup>23</sup>

As a prototypical energetic material, nitromethane has been heavily studied for many years. The phase diagram,<sup>24–27</sup> equation of state,<sup>28–31</sup> spectroscopic properties,<sup>32–39</sup> and reaction chemistry<sup>40–44</sup> are relatively well characterized and understood, both experimentally and theoretically. Because nitromethane is a liquid at atmospheric pressure and room temperature, less is known about the crystal phase; for example, the second-order elastic tensor has never been measured, and the first (to our knowledge) theoretical prediction of that property has only very recently been reported.<sup>45</sup> Moreover, even as recently as 1994 there was debate concerning the possible existence of multiple phases at high pressure.<sup>25</sup> It has now been established that there are only two phases, both with the same space group, between zero pressure and 40 GPa near room temperature.<sup>24</sup> Given the large number of published journal articles for nitromethane, not to mention a sizable body of work that appears only in conference proceedings (see, for example, ref 46), in the following paragraphs we briefly summarize only a few theoretical and experimental studies of particular relevance to the present work.

*Ab initio* and density-functional theory (DFT) calculations as well as simulations based on empirical force fields have been used to study the chemical and physical properties of nitromethane as functions of temperature and pressure.<sup>47–56</sup> These include calculations of crystal and liquid structures and transport

<sup>†</sup> Current address: Department of Chemistry, Missouri University of Science and Technology, Rolla, MO 65409.



coefficients,<sup>35,49,56,57,61,63,68</sup> melting,<sup>64–67</sup> crystallization,<sup>58</sup> isothermal compression curves at zero Kelvin (“cold curves”) and other constitutive relationships,<sup>47,48,50,51,53</sup> electronic band gaps,<sup>6,48,53</sup> vibrational spectra,<sup>50</sup> properties in the shocked state,<sup>2,6,21,22,28,55</sup> and chemical reactivity.<sup>6,40,52</sup> Byrd et al.<sup>51</sup> showed convincingly, using plane-wave electronic-structure methods for several different energetic materials including nitromethane, that both standard and hybrid DFT significantly overestimate the unit cell volume as the complete basis set (CBS) limit is approached. More recently, Conroy et al.<sup>47</sup> reported plane-wave DFT calculations of hydrostatic and uniaxial compression of crystalline nitromethane. They compared results obtained with and without empirical corrections designed to mitigate errors arising from lack of dispersion interactions in DFT. The results, which are for a basis set near the CBS limit, do not allow an unequivocal conclusion because, for the case of hydrostatic compression (for which multiple data sets are available for comparisons), the outcome of whether uncorrected or corrected DFT yields better agreement with experiment depends on both the particular structural parameter and pressure interval.

The electronic-structure study that is most germane to the current work is due to Liu et al.<sup>50</sup> They used the ABINIT<sup>59</sup> code to calculate the compression curve for crystalline nitromethane at zero Kelvin subject to preservation of the initial space group. These data were used to fit the zero pressure bulk modulus and its initial pressure derivative using the Murnaghan<sup>60</sup> equation. They calculated density-dependent intramolecular distortions, changes in the electronic band gap, and the normal-mode frequencies of the unit cell as functions of pressure. Their results are generally consistent with the experimental pressure-dependent infrared (IR) and Raman spectra discussed below.

In a separate study, Liu et al.<sup>22</sup> used MD with an empirical force field developed specifically for liquid nitromethane by Alper et al.<sup>61</sup> to study the hydrostatic compression and Hugoniot locus of liquid nitromethane for pressures up to about 24 GPa. Liu et al. obtained isothermal compression curves that are much stiffer than those obtained from both experiment<sup>24–26</sup> and earlier simulations<sup>68</sup> for pressures greater than 2 GPa; states on the Hugoniot locus as determined using the iterative approach due to Kress et al.<sup>62</sup> similarly indicate an unrealistically strong interatomic repulsion that arises from the use of Lennard-Jones potentials for the nonbonded interactions in the force field model of Alper et al.

Tuckerman and Klein<sup>56</sup> performed Car–Parrinello MD simulations of nitromethane as a function of temperature near atmospheric pressure using a three-dimensionally periodic simulation cell containing two unit cells. They computed the vibrational density of states of the entire system as well as for individual atom types. From a Boltzmann inversion of the probability distributions of the dihedral angles obtained from their simulations, they deduced an effective free-energy profile for methyl rotation in the liquid state and concluded that the barrier in the liquid is higher than the experimentally determined value in the crystal. Reed et al.<sup>6</sup> have also carried out quantum MD simulations. They focused on the chemical decomposition of nitromethane behind a strong shock. They determined that shock impact velocities higher than 6 km/s are necessary to initiate chemical decomposition in crystalline nitromethane on the time scale of their simulations but that under those conditions a semimetallic layer forms in the material immediately behind the shock front. Such high velocity impacts correspond to pressures far in excess of the Chapman–Jouguet detonation pressure of nitromethane ( $\sim 12$  GPa<sup>40</sup>) and far above those considered in the present work. For the force field used in the

current work,<sup>63,64</sup> an impact velocity of 3.0 km/s yields a shock pressure of about 30 GPa.<sup>3</sup>

Courtecuisse et al.<sup>25</sup> reported a phase diagram for nitromethane based on Raman spectra for temperatures between 20 and 350 °C and pressures between 0 and 35 GPa. They argued for three previously unknown crystal phases (III, IV, and V) in addition to the well-accepted phases I and II; they determined an existence interval for each phase from changes in the slopes of the variation of NO<sub>2</sub>, CN, and CH<sub>3</sub> spectral peaks with pressure. Subsequently, Citroni et al.<sup>24</sup> reported IR and Raman spectra of crystalline nitromethane for pressures up to 27.3 GPa and Ouillon et al.<sup>32</sup> studied changes in the Raman spectra between about 10 and 12 GPa. Citroni et al.<sup>24</sup> argued that the observed changes in the positions of the NO<sub>2</sub> and CH<sub>3</sub> peaks at about 11 GPa indicate the formation of a CH $\cdots$ O hydrogen-bonding-like network that stabilizes the CH<sub>3</sub> groups in an eclipsed orientation relative to the NO<sub>2</sub> plane for pressures higher than 11 GPa rather than evidence for the structural phase changes proposed by Cortecuisse et al.<sup>25</sup> Ouillon et al.<sup>32</sup> suggested that the changes they observed are due to polarization of the NO<sub>2</sub> groups arising from rearrangement of molecules in the unit cell that results in stronger intermolecular O $\cdots$ H interactions. From the latter two studies, it seems fairly certain that near room temperature nitromethane exhibits only two phases—the low-pressure form below 3.5 GPa and the high-pressure form which differs primarily in a rotation of the methyl groups by  $\sim 45^\circ$  relative to the low-pressure phase. Most relevant to the present study are the plots of IR and Raman spectra for selected modes for several pressures between 0 and 27.3 GPa reported by Citroni et al.<sup>24</sup>

Our interest is in understanding in atomic detail, mainly using force-field-based methods such as MD and Monte Carlo, processes that occur in molecularly complex materials over temperature and pressure intervals of approximately 300–3000 K and 0–40 GPa, respectively. Both stationary (i.e., equilibrium) and nonstationary (i.e., transient) phenomena are of interest. Sorescu, Rice, and Thompson have developed a force field<sup>63,64</sup> for the prototypical energetic material nitromethane that has been calibrated and validated against a comparatively large body of experimental and theoretical data. It accurately describes the crystal and liquid states and the melting transition.<sup>65–68</sup> More recently, it has been used to study effects of shocks on the crystal.<sup>2,3</sup> Although the SRT force field for nitromethane has been validated against experiment and electronic-structure theory for a number of structural and dynamical properties, the pressure dependence of the vibrational spectroscopy has not been investigated. Understanding this dependence is particularly important for interpreting shock wave simulations, since the initially non-Boltzmann distribution of energy created by passage of a shock wave and the subsequent pathways for thermal equilibration will be affected by the characters and coupling strengths among the normal modes for states far from the room temperature, atmospheric pressure potential-energy minimum. Since no experimental data exist for time- and mode-resolved vibrational spectroscopy in shocked nitromethane, the experimental and theoretical studies of vibrational spectra under hydrostatic compression mentioned above provide the best available data sets for assessing the accuracy of the SRT nitromethane force field vibrational structure at elevated pressures relevant to shock excitation.

In the present study, we investigate the pressure dependence of the vibrational modes in crystalline nitromethane using the SRT force field. Hydrostatic compression results were obtained at 1 K using normal-mode analysis<sup>69</sup> and at finite temperature

using classical power spectra.<sup>70</sup> The normal-mode analysis results are directly comparable to those obtained by Liu et al.<sup>50</sup> using electronic-structure theory and to the experimental data of Citroni et al.<sup>24</sup> In contrast to the normal-mode analyses, which yield a set of discrete eigenvalues (vibrational frequencies) at the potential-energy minimum for a given stress state, the power-spectra results (classical vibrational density of states), which are obtained at finite temperatures, can be compared to the experimental spectra for particular vibrational bands at various pressures. Thus, it is possible to compare and contrast the measured and calculated pressure evolutions, which typically involve the shifting of spectral intensity and splitting and emergence of peaks in the spectra as the pressure is increased. In section II, we briefly summarize the SRT force field, the details of the MD simulations, and the approach taken for the normal-mode and power-spectral analysis of the crystal. Results are presented in section III and conclusions in section IV.

## II. Computational Details

**A. Force Field.** The empirical flexible force field developed by Sorescu, Rice, and Thompson<sup>63</sup> (see also Agrawal et al.<sup>64</sup>) was used in the current study. The potential consists of a sum of intramolecular and intermolecular interactions. The intramolecular potential is described by Morse potentials for the six covalent bond distances, harmonic potentials for the nine three-atom bending angles, and trigonometric functions for the seven torsional interactions (including one used to describe the “wag” angle between the C atom and the plane formed by the NO<sub>2</sub> group); intramolecular nonbonded (1–4) interactions are not included. The intermolecular potential is pairwise and consists of exponential repulsions, dispersion terms ( $R^{-6}$ ), and Coulomb interactions ( $R^{-1}$ ) with fixed partial atomic charges on the nuclei. The SRT force field has been shown to accurately predict the crystal structure at 1 atm at room and cryogenic temperatures,<sup>63</sup> linear and volumetric isothermal compressions,<sup>63</sup> linear and volumetric thermal expansion coefficients,<sup>63</sup> melting point at normal and elevated pressures,<sup>64–67</sup> liquid self-diffusion constants,<sup>66</sup> and energy transfer pathways and time scales following excitation of CH stretching modes in the liquid.<sup>35</sup>

**B. Simulation Details.** At temperatures below 244.77 K and atmospheric pressure, nitromethane crystallizes in the orthorhombic space group  $P2_12_12_1$  with four molecules per unit cell (see Figure 1).<sup>27</sup> A three-dimensionally periodic simulation supercell of the crystal containing 1120 molecules was constructed by replicating the experimental unit cell by factors of 8, 7, and 5, respectively, along the  $a$ ,  $b$ , and  $c$  crystal axes, that is, an  $8 \times 7 \times 5$  supercell. Initial lattice dimensions and atomic positions were taken from the neutron diffraction crystal structure determination of Trevino and Rymes.<sup>27</sup> The cutoff distance for nonbonded interactions was set to 11.0 Å. Electrostatic interactions were evaluated using the Ewald summation procedure.<sup>71</sup> All energy minimization and molecular dynamics simulations discussed below were performed using the DL\_POLY (v 3.06) simulation code.<sup>72</sup>

The MD simulation protocol was divided into three stages. First, isothermal–isobaric (NPT) simulations were performed using the Martyna–Tuckerman–Klein<sup>73</sup> constant stress barostat algorithm as implemented in DL\_POLY to sample the desired isothermal hydrostatic stress state at temperatures of 1, 250, and 298 K for pressures of 0.0001, 1.1, 3.2, 7.6, 11.0, 15.0, and 27.3 GPa (hereafter we refer to 0.0001 GPa simply as 0 GPa). The NPT simulations were performed for 45 ps. It was determined that 5 ps was sufficient to achieve a steady-fluctuating pressure/temperature state; thus, the final 40 ps of

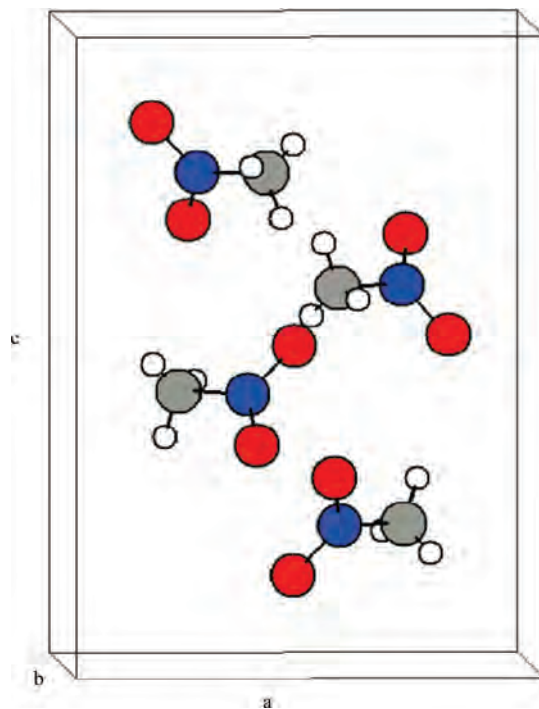


**Figure 1.** Unit cell of nitromethane. The crystal belongs to the  $P2_12_12_1$  space group and contains four molecules per unit cell.

each NPT equilibration trajectory was used to determine the average lattice parameters corresponding to the prescribed stress state and temperature. Initial phase space points for successively higher pressures were taken from simulations at the next lower pressure once a steady-fluctuating state had been obtained. Following NPT equilibration for a given temperature and pressure, isothermal–isochoric (NVT) simulations were performed for 45 ps using the average lattice parameters corresponding to that state. A fixed time step of 0.75 fs was used during both the NPT and NVT equilibration stages. The final vector of positions and velocities from the NVT equilibration was used as the initial condition for a 40 ps constant volume–energy (NVE) production stage, simulated with a fixed step size of 0.1 fs. Cartesian positions and velocities during the production stage of the simulation were stored every 4 fs for subsequent analysis.

**C. Vibrational Analysis.** Normal-mode frequencies and eigenvectors for a single molecule in the explicit field of the crystal were obtained as a function of pressure using a combination of NPT simulations, energy minimization, and numerical determination of the Hessian matrix. Specifically, the NPT, NVT, and NVE simulations described above were used to obtain representative instantaneous configurations for total energies corresponding to  $\sim 1$  K at each pressure studied. Starting from these low-energy configurations for each pressure, a geometry optimization was performed for one molecule in the crystal by minimizing its potential energy in the instantaneous crystal field of the remaining 1119 molecules using a conjugate gradient algorithm. Since the total energy corresponded to a temperature of  $\sim 1$  K, the thermal fluctuations of the 1119 molecules about the equilibrium positions in the crystal were negligibly small. Normal-mode analysis was performed using fourth-order accurate numerical second derivatives of the potential energy for the energy-minimized molecule to obtain normal-mode frequencies and eigenvectors.<sup>69</sup> A similar calculation was also performed for a contiguous energy-minimized unit cell within the 1 K primary cell to ensure that

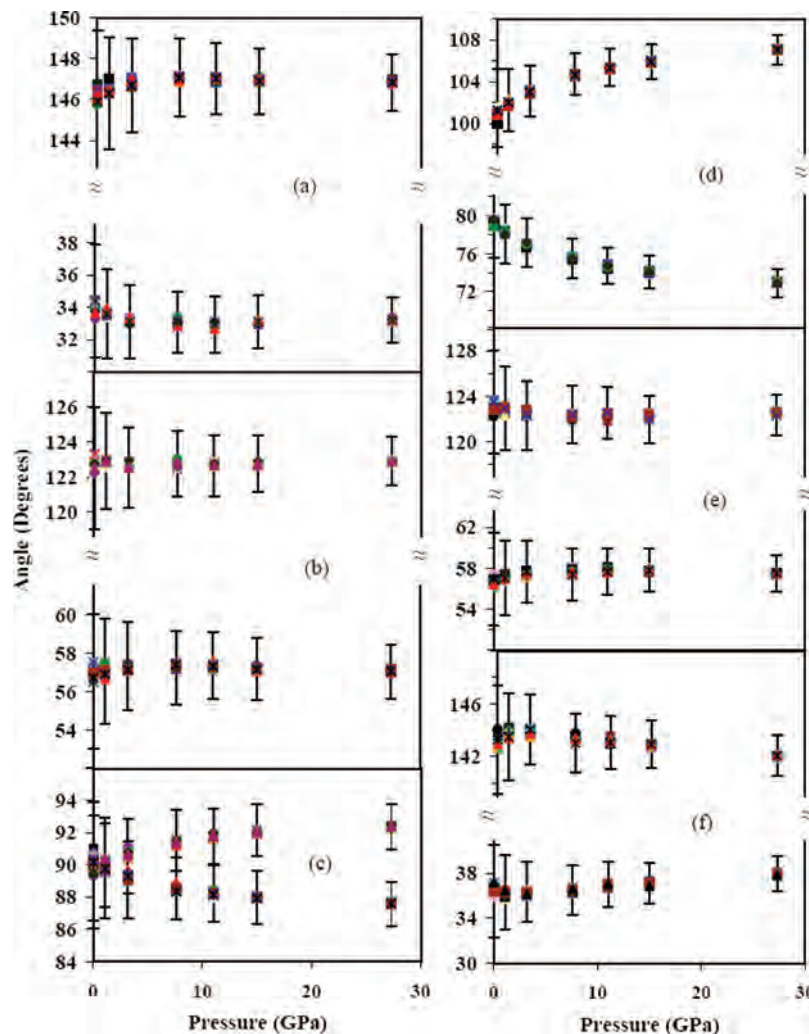


**Figure 2.** Variation with pressure of the angle between the CN bonds in nitromethane and (a) the *a* crystal axis, (b) the *b* crystal axis, and (c) the *c* crystal axis. Panels d–f are the same as panels a–c except that the angles between the NO bond vectors and the crystal axes are shown. The temperature is  $T = 250$  K.

the normal-mode eigenvectors and frequencies were essentially unaffected by the choice to base the analysis on a single molecule in the crystal field. While the molecular vibrations (vibrons) and nonacoustic lattice modes (optical phonons) cannot be separated formally, practically the distinction between such modes is clear upon analysis of the eigenvectors. Finally, for comparison, in addition to the crystal phase normal-mode analyses, vibrational eigenvectors and frequencies were obtained for a gas-phase molecule.

Power spectra, computed as Fourier transforms of the autocorrelation functions for mass-weighted Cartesian velocity time histories obtained from the 40 ps NVE trajectories, were used to evaluate the vibrational dynamics of the system as functions of pressure and nominal temperature. Spectra for selected internal coordinates were also computed. The power spectrum for dynamical variable  $v(t)$ , with mean  $\langle v(t) \rangle_t = 0$ , is given by<sup>70</sup>

$$I_{vv}(\omega) = \frac{1}{2\pi} \int_0^{t_{\max}} d\tau C_{vv}(\tau) \exp(-i\omega\tau) \quad (1)$$

where

$$C_{vv}(\tau) = \frac{\int_0^{t_{\max}} dt v(t) v(t + \tau)}{\int_0^{t_{\max}} dt v(t) v(t)} \quad (2)$$

Here,  $t_{\max}$  is the length of the time history,  $\tau$  is a time offset, and  $\omega$  is the frequency.

### III. Results and Discussion

**A. Structural Features.** We find no evidence for structural phase transitions in crystalline nitromethane at pressures between 0 and 27.3 GPa other than the rotation of the methyl groups that has been observed both experimentally<sup>26</sup> and for the SRT force field.<sup>63</sup> Figure 2 contains plots of the angles formed between the *a*, *b*, and *c* crystal axes and the CN bonds (panels a–c) and NO bonds (panels d–f) as functions of pressure, taken from  $2 \times 2 \times 2$  blocks containing 32 molecules located at the center of the 1120-molecule primary cell. The choice of location of the  $2 \times 2 \times 2$  block is of course arbitrary, since the results correspond to a three-dimensionally periodic system with no voids, surfaces, or other internal interfaces. The temperature is 250 K. The individual symbols correspond to the mean values of those angles for individual molecules; thus, there are 32 points for each pressure in each panel of the figure. The uncertainties shown correspond to one standard deviation of the normal



**TABLE 1: Calculated and Measured Normal-Mode Vibrational Frequencies of Nitromethane**

mode	assignment	$\nu$ (cm <sup>-1</sup> )	mode <sup>a</sup>	assignment <sup>a</sup>	$\nu^a$ (cm <sup>-1</sup> )
1	CH <sub>3</sub> asym. str.	3094	1	CH <sub>3</sub> asym. str.	3117
2	CH <sub>3</sub> asym. str.	3087	2	CH <sub>3</sub> asym. str.	3075
3	CH <sub>3</sub> sym. str.	2961	3	CH <sub>3</sub> sym. str.	2998
4	NO <sub>2</sub> asym. str.	1600	4	NO <sub>2</sub> asym. str.	1575
5	CH <sub>3</sub> sym. def. and CN str.	1520	5	CH <sub>3</sub> sym. def.	1430
6	CH <sub>3</sub> sym. bend	1431	7	NO <sub>2</sub> sym. str.	1415
7	CH <sub>3</sub> asym. bend	1429	6	CH <sub>3</sub> asym. def.	1416
8	CH <sub>3</sub> sym. def.	1371	8	CH <sub>3</sub> sym. def.	1382
9	out-of-plane CH <sub>3</sub> rock	1148	9	NCH sym. def. and NO <sub>2</sub> wag	1122
10	in-plane CH <sub>3</sub> rock	1053	10	NCH antisym. def.	1112
11	CN str., NO <sub>2</sub> bend, and NO <sub>2</sub> sym. str.	816	11	CN str. and NO <sub>2</sub> bend	936
12	NO <sub>2</sub> wag	807	13	NO <sub>2</sub> wag	611
13	CN stretch and NO <sub>2</sub> bend	604	12	CN stretch and NO <sub>2</sub> bend	671
14	NO <sub>2</sub> rock	465	14	NO <sub>2</sub> rock	495
15	torsion	122	<i>b</i>	<i>b</i>	<i>b</i>

<sup>a</sup> Experimental results from Ouillon et al.<sup>32,37</sup> <sup>b</sup> Not reported.

distribution (not the standard deviation of the mean) from the overall set of observations obtained during the 40 ps interval during which simulation data were accumulated at a given pressure. There are two branches for each case due to the symmetry elements of the crystal structure. In general, as expected, the spread of the mean values and widths of the sampled distributions decrease with increasing pressure, reflecting the reduced regions of configuration space sampled by the system as the pressure increases at fixed temperature. While these order parameters indicate gradual pressure-dependent changes of the heavy-atom orientations in the lattice, the changes are small in magnitude and occur smoothly, suggesting the absence of any phase transitions in the crystal structure. This is consistent with experiment,<sup>24</sup> although the measured data do indicate the formation of a hydrogen-bonding-like network in the crystal at high pressures that would not be captured with the fixed partial atomic charge electrostatic model used in the SRT force field.

**B. Pressure-Dependent Normal-Mode Frequencies.** The vibrational frequencies and assignments in the crystal determined from the normal-mode analysis described in section II.C are presented in Table 1; experimental results from Ouillon et al.<sup>32,37</sup> are included for comparison. There is rather good mode-by-mode agreement with the experimental frequencies. Our calculated frequencies on the 1 K isotherm are plotted as a function of pressure in Figure 3. Linear coefficients of pressure-induced vibrational frequency shifts from the present work (2 GPa <  $P$  < 14 GPa), the theoretical study by Liu et al.,<sup>50</sup> and the experimental study of Citroni et al.<sup>24</sup> are shown in Table 2. The Liu et al. results were taken directly from Table 6 of ref 50 (0 GPa ≤  $P$  ≤ 12 GPa on the 0 K isotherm); the results from Citroni et al. were estimated from Figures 5 and 7 of ref 24 (Raman results collected at 250 K and IR results collected at 298 K, respectively) for pressures between 2 and 12 GPa. In general, the vibrational frequencies blue shift monotonically with increasing pressure (see Figure 3 and Table 2). As with the experimental data<sup>24,32</sup> and the theoretical results reported by Liu et al.<sup>50</sup> based on three-dimensionally periodic DFT, the magnitude of the overall shifting varies mode to mode. However, in contrast to experimental observations of the infrared and Raman spectra for which several new peaks emerge in the spectra under increasing pressure (cf. Figures 4–7 of ref 24 and Figures 2 and 3 of ref 32), there is no evidence for abrupt changes in the calculated pressure-dependent normal-mode frequencies obtained in the present study or in the electronic-structure predictions.<sup>50</sup> The peak splittings observed experi-

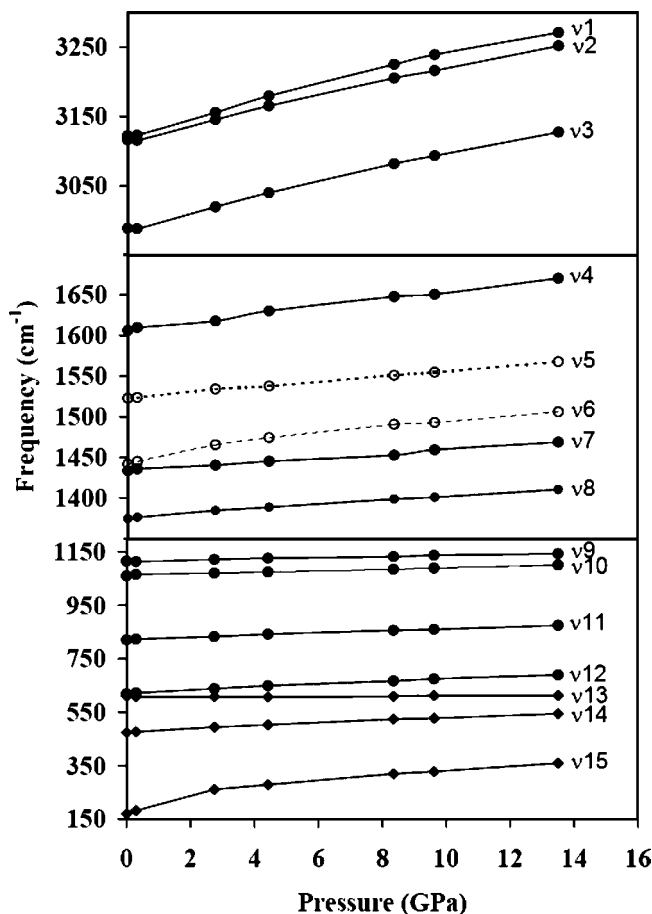


**Figure 3.** Pressure-dependent vibrational frequencies of nitromethane obtained from normal-mode analysis on the 1 K isotherm. The results should be compared to those presented in Figures 5 (Raman,  $T = 250$  K) and Figure 7 (IR,  $T = 298$  K) of Citroni et al.<sup>24</sup> and Figure 7 (electronic structure, 0 K) of Liu et al.<sup>50</sup>

mentally would not be observed in the current normal-mode analysis, which corresponds to a single molecule in a static crystal field. While some of the fundamental normal-mode frequencies at zero pressure differ significantly from one study to the next, the mode-by-mode pressure-induced blue shifts are remarkably similar among them.

**C. Normal-Mode Eigenvector Projections.** An interesting question is the extent to which the character of a given vibrational normal mode changes as the pressure is increased. To assess this for nitromethane, we have calculated projections

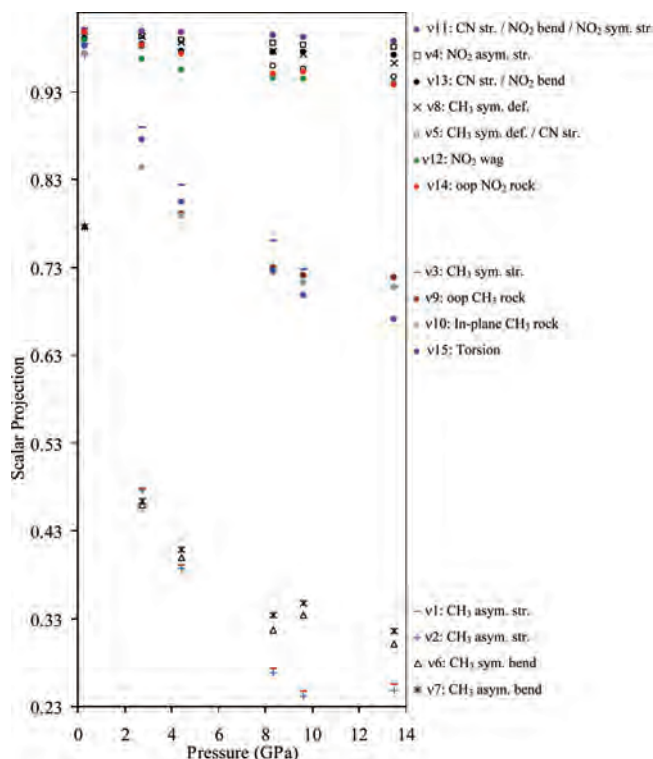


**TABLE 2: Calculated and Measured Pressure-Induced Linear Frequency Shifts in Nitromethane Crystal (Units Are  $\text{cm}^{-1}\cdot\text{GPa}^{-1}$ ; Mode Numbers Are the Same as for Table 1)**

mode	this work <sup>a</sup>	Liu et al. <sup>b</sup>	Citroni et al. <sup>c</sup>
1	10.7	8.2	6.2
2	9.9	6.5	6.2
3	10.0	2.7	8.7
4	4.9	3.0	4.0
5	3.1	1.1	<i>d</i>
6	3.8	1.0	3.9
7	2.6	1.0	2.5
8	2.4	0.6	0.7
9	2.0	1.7	3.5
10	2.8	2.0	1.4
11	3.9	4.6	3.7
12	4.8	4.6	2.7
13	0.5	0.6	3.2
14	4.7	3.7	4.5
15	9.1	<i>d</i>	<i>d</i>

<sup>a</sup> SRT force field, normal-mode analysis,  $2 \text{ GPa} \leq P \leq 14 \text{ GPa}$ .<sup>b</sup> DFT, normal-mode analysis,  $0 \text{ GPa} \leq P \leq 12 \text{ GPa}$ . Taken from Table 6 of ref 50. <sup>c</sup> Experiment, estimated from ref 24 using main peak data (where present) for  $2 \text{ GPa} \leq P \leq 14 \text{ GPa}$ . Results for all modes are based on Figure 5 (Raman spectroscopy at  $T = 250 \text{ K}$ ) except for mode 8, which is based on Figure 7 (IR spectroscopy at  $T = 298 \text{ K}$ ). <sup>d</sup> No data reported.

(Duschinsky rotation matrices)<sup>74,75</sup> between the eigenvectors for molecular normal modes in the crystal at various pressures  $P$  and those at atmospheric pressure. In general, a rigid displacement is necessary to account for changes (molecular distortion and rotation) in the energy-minimized geometry with increasing pressure. Therefore, the Eckart frames<sup>76,77</sup> of the structures were aligned before performing the mode projections. Since the normal-mode eigenvectors comprise an orthonormal set, the scalar projection between a given eigenvector and itself at a given pressure is unity, whereas the scalar projection between two different eigenvectors at a given pressure is zero. Thus, the closer the scalar projection between the eigenvector for a given mode at pressure  $P = 0$  and the eigenvector for that same mode at some other pressure is to unity, the less the effect of pressure on that mode. The results of these calculations are shown in Figure 4, where the scalar projections  $\hat{\mathbf{e}}_k(P \geq 0) \cdot \hat{\mathbf{e}}_k(P = 0)$  for each mode (diagonal elements of the Duschinsky rotation matrix) are shown as a function of pressure for  $P < 14 \text{ GPa}$ . It is of interest to note that the results for individual modes separate qualitatively into three groups: one in which the modes are nearly independent of pressure [ $\hat{\mathbf{e}}_k(14 \text{ GPa}) \cdot \hat{\mathbf{e}}_k(0 \text{ GPa}) \geq \sim 0.93$ ], one in which they are moderately pressure dependent [ $\sim 0.65 \leq \hat{\mathbf{e}}_k(14 \text{ GPa}) \cdot \hat{\mathbf{e}}_k(0 \text{ GPa}) \leq \sim 0.73$ ], and a third group in which the scalar projection is considerably smaller [ $\sim 0.23 \leq \hat{\mathbf{e}}_k(14 \text{ GPa}) \cdot \hat{\mathbf{e}}_k(0 \text{ GPa}) \leq \sim 0.33$ ]. The scalar projection for a given mode decreases essentially monotonically. It is possible that the detailed behaviors observed on close inspection of Figure 4 reflect a subtle interplay between the coupled intra- and intermolecular contributions to the potential energy and the molecular packing at a given hydrostatic pressure, but we have not pursued that here. Comparing the results in Figure 4 and the vibrational frequencies listed in Table 1 (and shown in Figure 3), there does not appear to be a strong correlation between frequency and extent of decrease of the projection. Rather, we find that the eigenvectors dominated by heavy-atom displacements are the least affected by pressure, while those with large contributions of H-atom displacements are more strongly affected. Among the latter, the tendency is for the modes of lower symmetry to be the most strongly affected by pressure.

**Figure 4.** Scalar projections between the eigenvectors for vibrational modes for a single nitromethane molecule in the crystal at elevated pressure with corresponding zero-pressure eigenvectors. The results correspond to the 1 K isotherm.

This is consistent with the rotation of the methyl group that occurs between atmospheric pressure and 3.5 GPa both experimentally<sup>26,78</sup> and for the SRT force field.<sup>63</sup>

**D. Power Spectra for  $P = 0 \text{ GPa}$ .** Figure 5 contains plots of the power spectra for mass-weighted Cartesian velocities at zero pressure and temperatures of  $T = 1 \text{ K}$  and  $T = 250 \text{ K}$  (panel a) and for selected internal coordinates for zero pressure and  $T = 250 \text{ K}$  (panel b). The qualitative features in Figure 5a, which corresponds to the vibrational density of states of the system, are in accord with expectations. Vibrational normal modes are associated with sharp peaks in the power spectrum for the comparatively low energies considered here. Some peaks, for example, those corresponding to the in-plane and out-of-plane asymmetric CH stretches at approximately  $3095 \text{ cm}^{-1}$ , are not readily distinguishable due to near degeneracy for the SRT force field model. Although they remain separated as the temperature is increased from 1 to 250 K, several of the peaks in the vibronic region of the 250 K spectrum are broadened and red-shifted relative to the 1 K spectrum due to anharmonicity in the potential. The relatively well-defined lattice modes ( $\nu \leq 250 \text{ cm}^{-1}$ ) observed at 1 K broaden into essentially a continuum of states at 250 K. Only one molecular vibration, the torsion located at approximately  $122 \text{ cm}^{-1}$ , overlaps with the lattice phonon region. This suggests that the torsion might be an important gateway mode for up-pumping<sup>1</sup> of energy initially localized in the lattice modes by shock wave excitation into the intramolecular modes of the molecule. However, recent simulation results for shock waves in nitromethane indicate a more complicated situation wherein there exists a significant dependence of the sequence of modal excitations on the relative orientation of the molecules in the crystal and the direction of shock wave propagation.<sup>2,3</sup>

The results in Figure 5b underscore the fact that the vibrational normal modes involve complicated combinations of

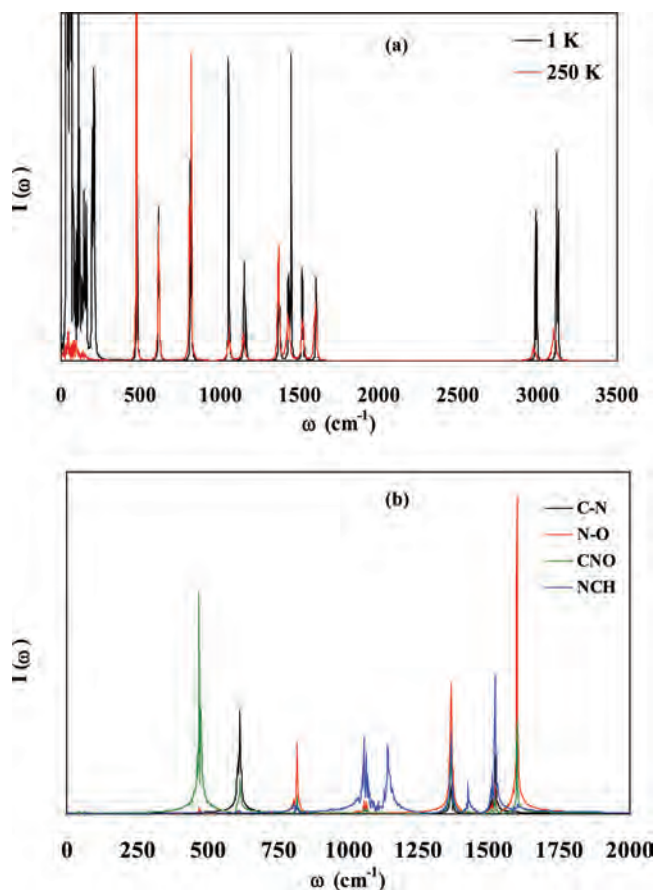


**Figure 5.** Power spectra of nitromethane crystal calculated using the SRT force field: (a) spectra obtained from the mass-weighted velocity–velocity autocorrelation function for  $P = 0$  GPa and  $T = 1$  K (black) and  $T = 250$  K (red); (b) spectra obtained at  $P = 0$  GPa and  $T = 250$  K for selected internal coordinates: CN bond (black), NO bond (red), CNO angle (green), and NCH angle (blue).

the displacements of those internal coordinates used to approximate the potential-energy function. In particular, we plot as separate traces in Figure 5b spectra for the CN bonds (black), NO bonds (red), CNO angles (green), and NCH angles (blue). While not all internal coordinates contribute significantly to the amplitude for all peaks in the spectrum (indeed, some peaks are strongly dominated by just one or two internal coordinate types), most internal coordinates contribute amplitude to several of the peaks in the system. Exceptions to this are the CH bonds and the torsional mode, none of which is shown, which contribute significantly to the power-spectral amplitude only for the highest and lowest frequencies, respectively. A simple mapping of the spectrum based on Cartesian velocities (Figure 5a) onto the internal coordinate spectra in Figure 5b is not practical, since the latter correspond to nonlinear combinations of the Cartesian displacements, complicated even further by the mass weighting of the velocities in the former.

**E. Power Spectra at Elevated Pressure.** Power spectra based on the vibrational density of states (mass-weighted velocities) were computed at  $T = 298$  K for several hydrostatic pressures between  $P = 0$  and 15 GPa. The purpose of these calculations was to assess the pressure-induced shifts and qualitative changes in the spectra, and to make qualitative comparisons to pressure dependencies in the experimental infrared and Raman data. The results are shown in Figure 6; panels a, b, and c correspond to the CN stretching mode, a  $\text{CH}_3$  deformation mode, and the  $\text{NO}_2$  asymmetric stretching mode, respectively, as determined from the normal-mode eigenvectors

of a single molecule in the explicit crystal field (calculated as described in section II.C). These are also the modes considered by Citroni et al. (see Figure 6 in ref 24). In order to facilitate comparisons to the experimental data, the widths of the intervals in the frequency domain (i.e., abscissa intervals in Figure 6) are approximately the same as in Figure 6 of ref 24. The specific interval limits differ, however, because the nominal experimental peak positions are somewhat different than the simulated ones.

**CN Stretch.** Comparisons of the results for the CN bond stretch mode shown in Figure 6a and those of Figure 6a of ref 24,  $\nu_{11}$  in both cases (see Table 1), are intriguing. In particular, with increasing pressure, we observe in the simulation results a split peak that exhibits a progressive blue shift in frequencies; the higher-frequency peak shifts more rapidly with increasing pressure. Also, the amplitude of the higher-frequency component decreases while that for the lower-frequency component increases, leading to two broad, strongly mixed peaks with roughly equal amplitudes at the highest pressures. The experimental data show a qualitatively similar result: as the pressure is increased, a single peak splits into two (or, according to Citroni et al.,<sup>24</sup> a new one emerges) and the original peak gradually decreases in amplitude. Note that the onset of changes in the simulated spectra occurs at lower pressure than in the experiments and also that experimentally the recorded IR intensity of the original peak essentially disappears at the highest pressure, whereas in our power spectrum calculations it is present over the entire pressure interval studied.

**$\text{CH}_3$  Deformation.** The comparison between experiment and simulation for the  $\text{CH}_3$  deformation mode shown here in Figure 6b and in Figure 6b of ref 24,  $\nu_8$  in both cases, is similarly intriguing. Focusing on the left-hand band centered at around  $1375\text{ cm}^{-1}$  in Figure 6b of ref 24, which corresponds to  $\nu_8$  at low pressures, Citroni et al. identified two peaks: a single one at low pressure and a second one that emerges starting at 10.8 GPa. As before, the peaks blue shift somewhat as the pressure is increased. In the simulated spectra (Figure 6b) at low pressure, we observe one broad or possibly two closely separated peaks. With increasing pressure, the band clearly separates into two distinct peaks with comparable intensity. At the highest pressure, the lower-frequency peak has greater amplitude than the higher-frequency one, in qualitative agreement with the experimental result. Note that in Figure 6b of ref 24 Citroni et al. also observed what they identified as the  $\text{NO}_2$  symmetric stretch mode and a  $\text{CH}_3$  deformation mode,  $\nu_7$  and  $\nu_6$ , respectively, centered around  $1415\text{ cm}^{-1}$  at low pressure. While the SRT force field predicts a pair of normal modes close to this frequency interval, also denoted  $\nu_7$  and  $\nu_6$  and centered around  $1430\text{ cm}^{-1}$  at low pressure, we assign both of these modes as  $\text{CH}_3$  bending motions. Moreover, in contrast to the experimental result (see Figure 6b of ref 24 where there are two well-defined regions of intensity), the amplitude of these modes in the calculated power spectra is completely overwhelmed by intensity from  $\nu_8$ . Therefore, we do not attempt to make further comparisons between  $\nu_7$  and  $\nu_6$  for the experimental and simulated cases.

**$\text{NO}_2$  Asymmetric Stretch.** Finally, in Figure 6c, results are shown for the  $\text{NO}_2$  asymmetric stretch region ( $\nu_4$ , the right-hand peak of the two that appear in Figure 6c); these results should be compared to Figure 6c of ref 24. The simulated spectrum for this case bears some similarities but also some differences compared to the experimental result. The blue shift in the simulation spectrum is noticeably larger than the measured one. Also, the simulations fail to predict the pair of peaks that emerge at lower frequencies in the experimental spectrum as

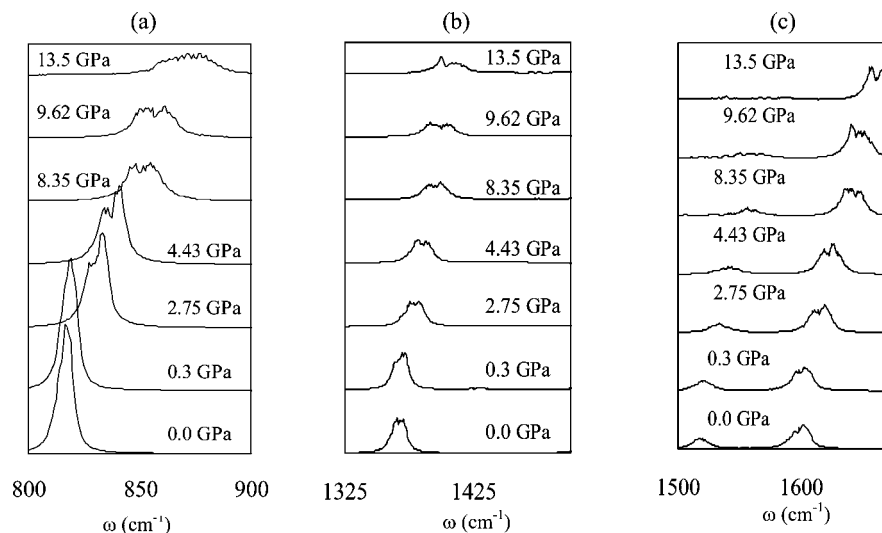


**Figure 6.** Pressure-dependent power spectra obtained at  $T = 298$  K for particular vibrational modes studied in the experimental work by Citroni et al.<sup>24</sup> Left to right: (a) CN stretch ( $\nu_{11}$ ); (b)  $\text{CH}_3$  umbrella region ( $\nu_8$ ); (c)  $\text{NO}_2$  asymmetric stretch ( $\nu_4$ ). The results in panels a, b, and c should be compared to Figure 6a, b, and c, respectively, of Citroni et al.

the pressure increases. However, the regions of highest amplitude in both the simulated and experimental spectra become considerably more structured as the pressure increases; the theoretical and experimental results at the highest pressures are arguably similar to one another.

We reiterate that, while there are numerous similarities between the simulated and measured spectra (peaks splitting and emergence of new ones), the onset of significant changes in the simulated spectra occurs at lower pressures than in the measured ones. This point is distinct from the overall magnitudes of blue shifts of the central peaks, which can be easily computed from the results in Figure 3 of the present work and from Figures 5 and 7 of Citroni et al.<sup>24</sup> The point is, in the classical simulations, the simulated spectra first begin to broaden or split at pressures considerably lower than in the experiments, even if the spectral envelopes and overall blue shifts are rather similar at the highest pressures; see the results in section III.B. Also, perhaps unsurprisingly, the relative amplitudes of the modes can be quite different in the classical spectra compared to the measured ones. Indeed, the relative intensities of IR and Raman spectra can differ significantly for the same material due to the different mechanisms providing intensity to those spectroscopies.

## F. Discussion

The results shown above raise several important and interesting issues about the use of classical force fields to simulate materials at elevated pressures. It is important to note that the intramolecular force field used here to simulate nitromethane was parametrized to yield agreement with the normal-mode frequencies and eigenvectors obtained from good quality density-functional theory electronic-structure calculations.<sup>63</sup> Likewise, the pairwise Buckingham-plus-fixed-partial-charges intermolecular potential is arguably the most widely used form in molecular simulations at present, and as noted earlier, the SRT potential has been shown by others to yield reasonably accurate predictions of the linear and volumetric hydrostatic compression and isobaric thermal expansion. Thus, it is useful to probe the limitations of such a force field model for predicting high-pressure properties at a level of detail (e.g., mode-by-mode spectral analysis) that extends beyond what is typically considered in equation of state studies for molecular materials. This is particularly relevant in light of the increasing use of MD to

simulate the response of complicated molecular materials to shock wave loading.

The detailed relationships among mechanical resonance conditions, specific modal couplings, and energy transfer in large polyatomic molecules are not generally well understood. In condensed-phase systems, the presence of nearly degenerate high-frequency vibrons and large numbers of bath modes may further complicate matters. On the basis of the results for pressure-induced frequency shifts shown in Figure 3 and Table 2, which indicate essentially monotonic and in most cases increasing vibrational frequencies with increasing hydrostatic pressure, one might predict the pathways for IVR (or vibrational relaxation more generally) not to depend strongly on pressure. However, the results shown for the pressure-induced changes in characters of the individual vibrational normal modes in Figure 4, which indicate large variations from one mode to the next, suggest that this may not be the case. Thus, it is of considerable interest from a fundamental viewpoint to understand whether, or to what extent, IVR pathways at low pressure differ from those that exist at high hydrostatic pressure or nonhydrostatic stress. To our knowledge, this has not been explored previously.

Direct comparisons between measured vibrational spectra and classical power spectra must be interpreted with caution. In particular, even though nitromethane is an example of a molecular system for which all 15 vibronic modes are both infrared and Raman active,<sup>39</sup> there is no reason to expect that the relative intensities of the peaks in classical power spectra, which we interpret in the traditional way as the mechanical frequency density of some dynamical variable  $q(t)$  in the Fourier decomposition of the motion of the dynamical system that contains it, will necessarily agree with those measured using either IR or Raman spectroscopy. In particular, while this interpretation of power spectra is equally valid for quantum and classical mechanics (assuming suitable averaging over vibrational phases in the latter), the absence of quantized selection rules and quantum mechanical oscillator strengths in classical mechanics calls into question even the kinds of qualitative comparisons between experimentally measured and classically simulated spectra as were made above, let alone attempts at quantitative comparisons.



While the use of electronic-structure theory as a means of obtaining atomic forces within an otherwise classical mechanical treatment of the dynamics of a system (often called quantum MD) would mitigate some of the possibly serious issues identified above, namely, the probable need to treat polarization or charge transfer under high pressure, or chemical reactivity under even more extreme conditions, it would not completely resolve the issues surrounding prediction of spectroscopy and dynamic behavior, since the underlying methods for simulating the time-dependent behavior of the system are still classical in nature. Thus, even if one were to compute the Fourier transform of the time-dependent dipole moment vector or polarizability tensor obtained from a quantum MD simulation, the resulting spectra would likely still differ from the measured IR or Raman spectra due to the different distributions in phase space sampled by the classical (MD) and quantum mechanical (experimental) systems.

#### IV. Conclusions

We have performed calculations designed to assess the accuracy of the Sorescu–Rice–Thompson<sup>63</sup> (SRT) empirical form atomic force field for nitromethane with respect to pressure-dependent shifts and other changes in the vibrational spectrum under isothermal hydrostatic compression. This information is useful in that it allows a comparatively detailed assessment of the reliability of the forces that arise in the SRT force field for equilibrium thermodynamic states far from normal conditions; this new information is complementary to the large number of preceding studies that show that the force field accurately reproduces equilibrium structural and dynamic properties at moderately elevated temperatures and pressures. Normal-mode analysis was used to determine the eigenvectors and eigenvalues (frequencies) for a single molecule in the explicit field of the crystal on the 1 K isotherm for hydrostatic compressions between  $P = 0$  and 15 GPa. The results indicate good agreement with experimental results reported by Citroni et al.<sup>24</sup> for  $T = 298$  K and also with an electronic-structure calculation for  $T = 0$  K due to Liu et al.<sup>50</sup> Power spectra were used to obtain the classical vibrational density of states at  $T = 298$  K for seven pressures between atmospheric pressure and 15 GPa. Using a combination of empirical theoretical normal-mode assignments for the SRT force field and corresponding experimental assignments of modes, the pressure-induced changes in three different regions in the vibrational spectrum were compared. The simulated results for the CN stretching mode, a CH<sub>3</sub> deformation mode, and the NO<sub>2</sub> asymmetric stretching mode yielded results in reasonably good agreement with experiment in that the blue shifts of the vibrational fundamentals with increasing pressure were largely similar. In fact, this was true for most of the 14 vibrational modes observed experimentally. Moreover, the overall evolution of the intensity for those three spectral regions is intriguingly similar in terms of pressure-induced peak splitting or emergence of new peaks within the spectral regions studied. While largely qualitative in nature, overall, the results reported here further validate the accuracy of the SRT force field parametrization for nitromethane, suggesting that, within the limits of the classical approximation and the SRT-specific restriction to unreactive processes in nitromethane, simulations using this force field can be expected to provide reliable information concerning detailed dynamics for thermodynamic states far from normal conditions of temperature and pressure.

**Acknowledgment.** This work was supported by the U.S. Army Research Office under MURI project W911NF-05-1-0265

and by the Laboratory Directed Research and Development Program at Los Alamos National Laboratory under contract number 73763-001-09.

#### References and Notes

- (1) Hooper, J. J. *Chem. Phys.* **2010**, *132*, 014507.
- (2) R. Dawes, R.; Siavosh-Haghighi, A.; Sewell, T. D.; Thompson, D. L. *J. Chem. Phys.* **2009**, *131*, 224513.
- (3) Siavosh-Haghighi, A.; Dawes, R.; Sewell, T. D.; Thompson, D. L. *J. Chem. Phys.* **2009**, *131*, 064503.
- (4) Cawkwell, M. J.; Sewell, T. D.; Zheng, L.; Thompson, D. L. *Phys. Rev. B* **2008**, *78*, 014107.
- (5) Jaramillo, E.; Strachan, A.; Sewell, T. D. *Phys. Rev. B* **2007**, *76*, 064112.
- (6) Reed, E. J.; Manaa, M. R.; Fried, L. E.; Glaesemann, K. R.; Joannopoulos, J. D. *Nat. Phys.* **2008**, *4*, 72.
- (7) Heim, A. J.; Gronbeck-Jensen, N.; Kober, E. M.; Germann, T. C. *Phys. Rev. E* **2008**, *78*, 046710.
- (8) Strachan, A.; van Duin, A. C. T.; Chakraborty, D.; Dasgupta, S.; Goddard, W. A., III. *Phys. Rev. Lett.* **2003**, *91*, 098301.
- (9) Tokmakoff, A.; Fayer, M. D.; Dlott, D. D. *J. Phys. Chem.* **1993**, *97*, 1901.
- (10) Tarver, C. M. *J. Phys. Chem. A* **1997**, *101*, 4845.
- (11) Fried, L. E.; Ruggiero, A. J. *J. Phys. Chem.* **1994**, *98*, 9786.
- (12) Ye, S.; Koshi, M. *J. Phys. Chem. B* **2006**, *110*, 18515.
- (13) Wang, Z.; Cahill, D. G.; Carter, J. A.; Koh, Y. K.; Lagutchev, A.; Seong, N.-H.; Dlott, D. D. *Chem. Phys.* **2008**, *350*, 31.
- (14) Patterson, J. E.; Dreger, Z. A.; Miao, M.; Gupta, Y. M. *J. Phys. Chem. A* **2008**, *112*, 7374.
- (15) Bolme, C. A.; McGrane, S. D.; Moore, D. S.; Funk, D. J. *J. Appl. Phys.* **2007**, *102*, 033513.
- (16) Cawkwell, M. J.; Ramos, K. J.; Hooks, D. E.; Sewell, T. D. *J. Appl. Phys.* **2010**, *107*, 063512.
- (17) Hoover, W. G.; Hoover, C. G. *Phys. Rev. E* **2009**, *80*, 011128.
- (18) Holian, B. L.; Lomdahl, P. S. *Science* **1998**, *280*, 2085.
- (19) Klimenko, V. Yu.; Dremin, A. N. *Sov. Phys. Dokl.* **1980**, *25*, 288.
- (20) Klimenko, V. Yu.; Dremin, A. N. *Sov. Phys. Dokl.* **1979**, *24*, 984.
- (21) Desbiens, N.; Bourasseau, E.; Maillet, J.-B. *Mol. Simul.* **2007**, *33*, 1061.
- (22) Liu, H.; Zhao, J.; Ji, G.; Gong, Z.; Wei, D. *Physica B* **2006**, *382*, 334.
- (23) Rice, B. M.; Sewell, T. D. Equilibrium Molecular Dynamics. In *Shock Wave and High Pressure Phenomena: Static Compression of Energetic Materials*; Peiris, S. M., Piermarini, G. J. Eds.; Springer-Verlag: Berlin, 2008; pp 255–290.
- (24) Citroni, M.; Datchi, F.; Bini, R.; Di Vaira, M.; Pruzan, P.; Canny, B.; Schettino, V. *J. Phys. Chem. B* **2008**, *112*, 1095.
- (25) Courtecuisse, S.; Cancell, F.; Fabre, D.; Petitot, J.-P. *J. Chem. Phys.* **1995**, *102*, 968.
- (26) Cromer, D. T.; Ryan, R. R.; Schiferl, D. *J. Phys. Chem.* **1985**, *89*, 2315.
- (27) Trevino, S. F.; Rymes, W. H. *J. Chem. Phys.* **1980**, *73*, 3001.
- (28) Desbiens, N.; Bourasseau, E.; Maillet, J.-B.; Souillard, L. *J. Hazard. Mater.* **2009**, *166*, 1120.
- (29) Winey, J. M.; Duvall, G. E.; Knudson, M. D.; Gupta, Y. M. *J. Chem. Phys.* **2000**, *113*, 7492.
- (30) Lysne, P. C.; Hardesty, D. R. *J. Chem. Phys.* **1973**, *59*, 6512.
- (31) Menikoff, R. Hot Spot Formation from Shock Reflections. *Shock Waves*, submitted for publication.
- (32) Ouillon, R.; Pinan-Lucarré, J.-P.; Canny, B.; Pruzan, P.; Ranson, P. *J. Raman Spectrosc.* **2008**, *39*, 354.
- (33) Shigeto, S.; Pang, Y.; Fang, Y.; Dlott, D. D. *J. Phys. Chem. A* **2008**, *112*, 232.
- (34) Deak, J. C.; Iwaki, L. K.; Dlott, D. D. *J. Phys. Chem. A* **1999**, *103*, 971.
- (35) Kabadi, V. N.; Rice, B. M. *J. Phys. Chem. A* **2004**, *108*, 532.
- (36) Pinan-Lucarré, J.-P.; Ouillon, R.; Canny, B.; Pruzan, P.; Ranson, P. *J. Raman Spectrosc.* **2003**, *34*, 819.
- (37) Ouillon, R.; Pinan-Lucarré, J.-P.; Ranson, P.; Baranovic, G. *J. Chem. Phys.* **2002**, *116*, 4611. 2002.
- (38) Courtecuisse, S.; Cansell, F.; Fabre, D.; Petitot, P. P. *J. Chem. Phys.* **1998**, *108*, 7350.
- (39) Wells, A. J.; Wilson, E. B., Jr. *J. Chem. Phys.* **1941**, *9*, 314.
- (40) Hervouët, A.; Desbiens, N.; Bourasseau, E.; Maillet, J.-B. *J. Phys. Chem. B* **2008**, *112*, 5070.
- (41) Bouyer, V.; Darbord, I.; Hervé, P.; Baudin, G.; Le Gallic, C.; Clément, F.; Chavent, G. *Combust. Flame* **2006**, *144*, 139.
- (42) Sheffield, S. A.; Dattelbaum, D. M.; Engelke, R.; Alcon, R. R.; Crouzet, B.; Robbins, D. L.; Stahl, D. B.; Gustavsen, R. L. In *Proceedings of the Thirteenth International Detonation Symposium* (23–28 July 2006; Norfolk, VA; ONR Report Number ONR 351-07-01); p 401.



- (43) Piermarini, G. J.; Block, S.; Miller, P. J. *J. Phys. Chem.* **1989**, *93*, 457.
- (44) Brasch, J. W. *J. Phys. Chem.* **1980**, *84*, 2085.
- (45) Slough, W.; Perger, W. F. *Chem. Phys. Lett.* **2010**, *498*, 97.
- (46) For example: Dattelbaum, D. M.; Sheffield, S. A.; Stahl, D. B.; Dattelbaum, A. M.; Trott, W.; Engelke, R. Influence of Hot Spot Features on the Initiation Characteristics of Heterogeneous Nitromethane. To appear in: *Fourteenth Symposium (International) on Detonation*, 11–16 April 2010, Cour d'Alene, ID.
- (47) Conroy, M. W.; Oleynik, I. I.; Zybin, S. V.; White, C. T. *J. Phys. Chem. A* **2009**, *113*, 3610.
- (48) Zerilli, F. J.; Hooper, J. P.; Kuklja, M. M. *J. Chem. Phys.* **2007**, *126*, 114701.
- (49) Megyes, T.; Bálint, S.; Grósz, T.; Radnai, T.; Bakó, I.; Almásy, L. *J. Chem. Phys.* **2007**, *126*, 164507.
- (50) Liu, H.; Zhao, J.; Wei, D.; Gong, Z. *J. Chem. Phys.* **2006**, *124*, 124501.
- (51) Byrd, E. F. C.; Scuseria, G. E.; Chabalowski, C. F. *J. Phys. Chem. B* **2004**, *108*, 13100.
- (52) Manaa, M. R.; Reed, E. J.; Fried, L. E.; Galli, G.; Gygi, F. *J. Chem. Phys.* **2004**, *120*, 10146.
- (53) Margetis, D.; Kaxiras, E.; Elstner, M.; Fraunheim, Th.; Manaa, M. R. *J. Chem. Phys.* **2002**, *117*, 788.
- (54) Decker, S. A.; Woo, T. K.; Wei, D.; Zhang, F. In *Proceedings of the Twelfth International Detonation Symposium* (11–16 August 2002; San Diego, CA; U.S. Office of Naval Research Report ONR 333-05-2); p 724.
- (55) Reed, E. J.; Joannopoulos, J. D.; Fried, L. E. *Phys. Rev. B* **2000**, *62*, 16500.
- (56) Tuckerman, M. E.; Klein, M. L. *Chem. Phys. Lett.* **1998**, *283*, 147.
- (57) Hayaki, S.; Sato, H.; Sakaki, S. *J. Mol. Liq.* **2009**, *147*, 9.
- (58) Siavosh-Haghighi, A.; Sewell, T. D.; Thompson, D. L. *J. Chem. Phys.* **2010**, *133*, 194501.
- (59) Gonze, X.; Amadon, B.; Anglade, P.-M.; Beuken, J.-M.; Bottin, F.; Boulanger, P.; Bruneval, F.; Caliste, D.; Caracas, R.; Cote, M.; Deutsch, T.; Genovese, L.; Ghosez, Ph.; Giantomassi, M.; Goedecker, S.; Hamann, D. R.; Hermet, P.; Jollet, F.; Jomard, G.; Leroux, S.; Mancini, M.; Mazevet, S.; Oliveira, M. J. T.; Onida, G.; Pouillon, Y.; Rangel, T.; Rignanese, G.-M.; Sangalli, D.; Shaltaf, R.; Torrent, M.; Verstraete, M. J.; Zerah, G.; Zwanziger, J. W. *Comput. Phys. Commun.* **2009**, *180*, 2582. <http://www.abinit.org>.
- (60) Murnaghan, F. D. *Finite Deformation of an Elastic Solid*; Dover: New York, 1951; p 73.
- (61) Alper, H. E.; Abu-Awwad, F.; Politzer, P. *J. Phys. Chem. B* **1999**, *103*, 9738.
- (62) Kress, J. D.; Collins, L. A.; Wood, W. W. *Phys. Rev. B* **2000**, *63*, 024203.
- (63) Sorescu, D. C.; Rice, B. M.; Thompson, D. L. *J. Phys. Chem. B* **2000**, *104*, 8406 There were two typographical errors in the original presentation of this force field. A detailed explanation was given by Dawes et al.; see ref 2.
- (64) Agrawal, P. M.; Rice, B. M.; Thompson, D. L. *J. Chem. Phys.* **2003**, *119*, 9617.
- (65) Siavosh-Haghighi, A.; Thompson, D. L. *J. Phys. Chem. C* **2007**, *111*, 7980.
- (66) Zheng, L.; Luo, S.-N.; Thompson, D. L. *J. Chem. Phys.* **2006**, *124*, 154504.
- (67) Siavosh-Haghighi, A.; Thompson, D. L. *J. Chem. Phys.* **2006**, *125*, 184711.
- (68) Sorescu, D. C.; Rice, B. M.; Thompson, D. L. *J. Phys. Chem. A* **2001**, *105*, 9336.
- (69) Wilson, E. B., Jr.; Decius, J. C.; Cross, P. C. *Molecular Vibrations: the Theory of Infrared and Raman Vibrational Spectra*; Dover: New York, 1980.
- (70) Berens, P. H.; Mackay, D. H. J.; White, G. M.; Wilson, K. R. *J. Chem. Phys.* **1983**, *79*, 2375.
- (71) Allen, M. P.; Tildesley, D. J. *Computer Simulation of Liquids*; Oxford: New York, 1987.
- (72) Smith, W. *Mol. Simul.* **2006**, *32*, 933.
- (73) Martyna, G. M.; Tuckerman, M. E.; Klein, M. L. *J. Chem. Phys.* **1994**, *101*, 4177.
- (74) Duschinsky, F. *Acta Physicochim.* **1937**, *URSS* 7, 551.
- (75) Peng, Q.; Yi, Y.; Shuai, Z.; Shao, J. *J. Chem. Phys.* **2007**, *126*, 114302.
- (76) Eckart, C. *Phys. Rev.* **1935**, *47*, 552.
- (77) Sayvetz, A. *J. Chem. Phys.* **1939**, *7*, 383.
- (78) Yarger, F. L.; Olinger, B. *J. Chem. Phys.* **1986**, *85*, 1534.

JP109106K

# Anomalous hardening under shock compression in (021)-oriented cyclotrimethylene trinitramine single crystals

K. J. Ramos,<sup>1,a)</sup> D. E. Hooks,<sup>1</sup> Thomas D. Sewell,<sup>2</sup> and M. J. Cawkwell<sup>3,b)</sup>

<sup>1</sup>*Dynamic and Energetic Materials Division, Los Alamos National Laboratory, Los Alamos, New Mexico 87545, USA*

<sup>2</sup>*Department of Chemistry, University of Missouri–Columbia, Columbia, Missouri 65211, USA*

<sup>3</sup>*Theoretical Division, Los Alamos National Laboratory, Los Alamos, New Mexico 87545, USA*

(Received 26 April 2010; accepted 3 August 2010; published online 30 September 2010)

We recently proposed that the change observed in the elastic-plastic response of (111)-oriented cyclotrimethylene trinitramine (RDX) crystals under shock compression is caused by an anomalous hardening that is mediated by the homogeneous nucleation of partial dislocation loops with Burgers vector  $0.16[010]$  on (001) [Cawkwell *et al.*, [J. Appl. Phys. **107**, 063512 (2010)]]. The orientation dependencies of the (001)[010] slip system suggested that (021)-oriented RDX crystals should also display an anomalous hardening. Molecular dynamics simulations of (021)-oriented RDX crystals confirm that this slip system is activated at a shock pressure  $1.34 < P \leq 1.54$  GPa. Plate impact experiments on (021)-oriented RDX single crystals show a two-wave elastic-plastic response at 1.0 GPa and an almost overdriven response at 2.25 GPa that is entirely consistent with the theoretical prediction. © 2010 American Institute of Physics. [doi:10.1063/1.3485807]

The elastic-plastic response of the energetic molecular crystal pentaerythritol tetranitrate (PETN) to shock compression was linked to its initiation sensitivity in a seminal series of articles by Dick.<sup>1–4</sup> During these studies it was noted that dependence of the initiation sensitivity on the crystallographic orientation of the shock propagation direction correlated strongly with the activity of dislocation slip systems. A low Hugoniot elastic limit and low impact sensitivity were measured when PETN single crystals were oriented such that a shear stress was resolved on the known slip systems. Similarly, the Hugoniot elastic limit and impact sensitivity were found to be high when PETN single crystals were oriented such that none of the known slip systems were subject to a resolved shear stress. The mechanisms for plastic flow were linked to the relative sizes of the Hugoniot elastic limits whereby low and high values were attributed to the onset of dislocation-mediated plasticity and sterically hindered shear, respectively.

A series of shock compression experiments was performed on oriented single crystals of the orthorhombic energetic molecular crystal cyclotrimethylene trinitramine (RDX) (Ref. 5) owing to the observed correlation in PETN between impact sensitivity and the Hugoniot elastic limits.<sup>6</sup> However, the relative levels at which the Hugoniot elastic limits occurred during plate impact experiments on (100), (210), and (111)-oriented pristine RDX single crystals at a shock pressure of 2.25 GPa did not correlate with the shear stresses resolved on the dislocation slip systems that were known in RDX at that time.<sup>6,7</sup>

Time-resolved interface velocity measurements from the shock compression to 2.25 GPa of (100) and (210)-oriented RDX single crystals showed two-wave, elastic-plastic responses.<sup>6</sup> However, an anomalous response was noted for

(111)-oriented crystals since the interface velocities measured at 2.25 GPa repeatedly appeared to be almost overdriven with a separation between the elastic and plastic waves that was weakly dependent on the propagation distance.<sup>6,8</sup> However, two plate impact experiments where (111)-oriented RDX single crystals were loaded to about 1.0 GPa produced a well defined elastic-plastic response.<sup>8</sup> The change in the elastic-plastic response of (111)-oriented RDX single crystals between 1.0 and 2.25 GPa suggested that an orientation- and pressure-dependent change in the mechanism of plastic flow occurs within this pressure interval.

The mechanisms of plastic flow active in (111)-oriented RDX crystals under shock compression were studied with atomic resolution using molecular dynamics (MD) simulations.<sup>8</sup> Those simulations employed the nonreactive, flexible molecular potential for nitramines that was developed by Smith and Bharadwaj.<sup>9</sup> The simulations revealed that at a threshold shock pressure,  $P^*$ , in the interval  $1.30 < P^* \leq 1.67$  GPa, partial dislocation loops with Burgers vector  $\mathbf{b} \approx 0.16[010]$  nucleate homogeneously on (001). The partial dislocation loops expand rapidly to fill the shock compressed material with a high density of stacking faults. In Ref. 8, we argued that these stacking faults serve as obstacles to the heterogeneous nucleation, glide, and multiplication of perfect dislocations on other slip systems since (001) intersects the slip planes of the perfect dislocations identified or inferred experimentally.<sup>7,10</sup> Thus, the homogeneous nucleation of partial dislocation loops on (001) can be expected to give rise to an anomalous plastic hardening, that is, hardening that is not related to dislocation storage. The observation from MD simulations of the change in the mechanism of plastic flow in (111)-oriented RDX crystals in the interval  $1.30 < P^* \leq 1.67$  GPa agreed quantitatively with the changes seen experimentally in the interface velocity histories measured at 1.24 and 2.25 GPa.

<sup>a)</sup>Electronic mail: kramos@lanl.gov.

<sup>b)</sup>Electronic mail: cawkwell@lanl.gov.

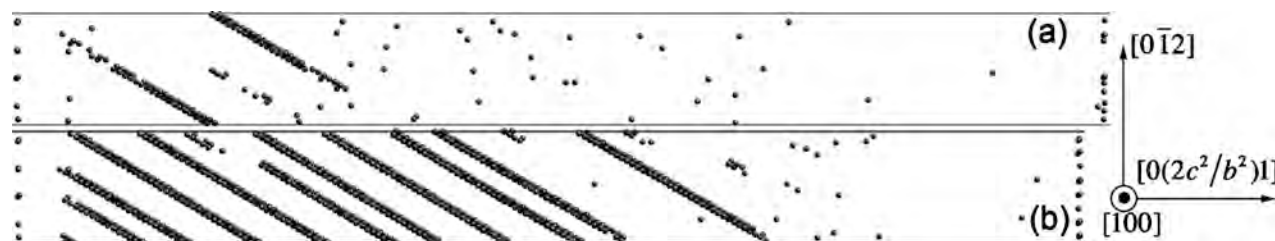


FIG. 1. Snapshots from MD simulations of shock loading at the instant of maximum compression. Only the centers of mass of those molecules with the AEE conformation are depicted. (a)  $P=1.54$  GPa and (b)  $P=2.15$  GPa.

The activity of the (001)[010] slip system in RDX is dependent on both the strength and the crystallographic orientation of the shock. Our earlier work showed that the dependence on orientation of the slip system is determined by the shear stress resolved on the slip plane parallel to the Burgers vector and by the magnitude of the compressive stress acting normal to the slip plane.<sup>8</sup> Calculations of the  $\gamma$ -surface<sup>11</sup> showed that the stacking fault on (001) is rendered metastable by a stress-induced change in the conformation of the three nitro groups in the RDX molecule with respect to the mean plane of the triazine ring from two nitro groups oriented axially and one equatorially (AAE) to one oriented axially and two equatorially (AEE).<sup>8</sup>

Based on our understanding of the stresses required to activate the (001)[010] slip system, we predicted that impacts above a critical pressure on (021)-oriented crystals would result in an anomalous hardening response that is identical to that seen for impacts on (111)-oriented crystals. As a preliminary test of our prediction we performed a series of MD simulations of the propagation of shock waves normal to (021) using exactly the same methods as described in Ref. 8. These simulations employed a simulation cell containing 926 688 atoms that measured 93.8027 Å, 96.6718 Å, and 1000 Å parallel to the mutually perpendicular [100], [012], and  $[0(2c^2/b^2)1]$  directions, respectively, where the latter direction is perpendicular to (021), and  $b$  and  $c$  are the lattice parameters of RDX parallel to [010] and [001], respectively. Simulations were performed with impact velocities,  $U_p$ , equal to 200, 225, 250, 300, and 500 m s<sup>-1</sup> which led to shock pressures,  $P$ , equal to 1.34, 1.54, 1.74, 2.15, and 3.90 GPa, respectively. The MD trajectories computed in each simulation were analyzed to determine locations of stacking faults on (001) by computing for every molecule the conformation of the nitro groups with respect to the mean plane of the ring as in Refs. 8 and 12. These analyses showed that partial dislocation loops did not nucleate homogeneously at 1.34 GPa over the 24 ps duration of the simulation. However, shocks with  $P \geq 1.54$  GPa led to the homogeneous nucleation and expansion of partial dislocation loops on (001) in accord with our simulations of (111)-oriented RDX crystals.<sup>8</sup> The location of molecules that have changed conformation from AAE to AEE during simulations at 1.54 and 2.15 GPa are presented in Figs. 1(a) and 1(b), respectively.

The predicted threshold shock pressure for the homogeneous nucleation of partial dislocation loops in (021)-oriented RDX crystals lies in the interval  $1.34 < P^* \leq 1.54$  GPa. Thus, based on earlier experimental work and the model developed in Ref. 8, we expect to see an anomalous

hardening response in (021)-oriented crystals shock loaded to pressures in excess of this threshold. We have completed a series of flyer-plate-driven shock compression experiments on (021)-oriented RDX single crystals at shock pressures of 1.0 and 2.25 GPa in order to assess the predictions of the anomalous hardening model.

The flyer-plate impact experiments employed solution-grown RDX single crystals that were sectioned and polished to give broad, flat (021) surfaces. The processes used to prepare suitable crystals have been described in detail elsewhere.<sup>6,10</sup> The RDX crystals were mounted in a target assembly that enabled velocity interferometry system for any reflector (VISAR) measurements of the velocity of a RDX/window interface during the passage of a shock. The target assemblies for the 1.0 and 2.25 GPa shots used x-cut quartz and Kel-F-81 anvils, respectively, to transmit a sharp shock from the flyer-plate into the RDX crystal and poly(methylmethacrylate) VISAR windows. We have employed the same window material in the shots at 1.0 and 2.25 GPa to minimize the possibility that the features in the VISAR traces that we ascribe to anomalous hardening are in reality an artifact of the choice of the window material. The targets were loaded in a single-stage light-gas gun and coupled to a VISAR apparatus whose characteristics were described in Ref. 6.

Two shots were performed at a shock pressure of about 1.0 GPa using crystals of thickness 0.99 and 1.93 mm. The corresponding VISAR traces are presented in Fig. 2(a). These traces are indicative of a “normal” two-wave elastic-plastic response where the velocity of the elastic precursor is significantly greater than that of the plastic wave. Two shots were performed at a shock pressure of about 2.25 GPa using

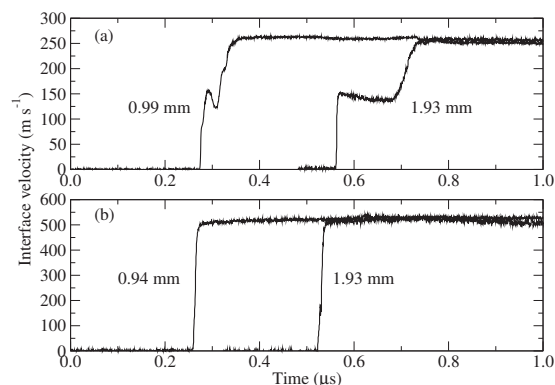


FIG. 2. VISAR interface velocity histories measured for shocks with: (a)  $P \approx 1.0$  GPa and (b)  $P \approx 2.25$  GPa. The thickness of each crystal is marked on the figure.

crystals of thickness 0.94 and 1.93 mm. The corresponding VISAR traces are presented in Fig. 2(b). These VISAR traces are qualitatively distinct from those measured at 1.0 GPa since the velocities of elastic and plastic waves appear to be almost identical. The VISAR apparatus resolves a single rise in the interface velocity from the 0.94 mm thick crystal and a small deviation in the rise of interface velocity at about  $150 \text{ m s}^{-1}$  in the 1.93 mm thick crystal.

The interface velocity histories measured during the shock compression of (021)-oriented RDX crystals of two different thicknesses at 1.0 and 2.25 GPa are entirely consistent with the predictions of the anomalous hardening model. The shots at 1.0 GPa correspond to a stress state that is below the threshold required for the activation of the (001)[010] slip system. While the crystals are oriented such that there is a significant shear stress resolved on the slip plane parallel to [010], the pressure normal to the slip plane is evidently not sufficient to drive the change in molecular conformation that renders the stacking fault metastable. Hence, at 1.0 GPa perfect dislocations that nucleate heterogeneously are responsible for the relatively slow plastic wave. On the other hand, the pressure resolved normal to (001) during shocks with  $P \approx 2.25 \text{ GPa}$  is sufficient to drive the change in molecular conformation that renders the stacking fault metastable. Once this criterion is satisfied, partial dislocation loops nucleate homogeneously and expand rapidly to produce an anomalous hardening. Our earlier work showed that the partial dislocation loops nucleate in bursts at a distance behind the elastic shock front that depends on its peak pressure.<sup>8</sup> Hence, our model also accounts for the observation that a single wave structure was measured for the 0.94 mm thick crystal while a deviation in the initial rise of the interface velocity was measured in the 1.93 mm thick crystal. Over an additional propagation distance of 0.99 mm the peak stress of the elastic precursor decays to the level for which the mean distance between the precursor and the location of the homogeneous nucleation events becomes sufficiently large to be resolved by our VISAR apparatus. Moreover, the threshold shock pressures for the activation of the (001)[010] slip system predicted by our MD simulations and measured experimentally are in concurrence.

A mechanism other than dislocation-mediated anomalous hardening could, in principle, give rise to the abrupt changes in elastic-plastic response of (111) and (021)-oriented crystals between 1.0 and 2.25 GPa. Anomalous hardening requires that a compressive deviatoric stress acts parallel to [001]. However, this stress state could also drive a phase transformation from the  $\alpha$  to the  $\gamma$  polymorph of RDX

(Refs. 13 and 14) whose effects on the elastic-plastic response could be indistinguishable from those we ascribe to anomalous hardening. It is well established that the  $\alpha$  to  $\gamma$  phase transformation occurs under hydrostatic pressure at about 3.9 GPa but since the transformation results in a collapse of the lattice parallel to the [001] direction of the parent phase,<sup>13,15</sup> it is not unreasonable to assume that it can be promoted under shock compression by a deviatoric stress acting normal to (001). However, Patterson *et al.*<sup>16</sup> using oriented RDX single crystals and *in situ* Raman spectroscopy have shown that the shock pressure required for the  $\alpha$  to  $\gamma$  phase transformation is fairly isotropic and is between 3.5 and 4.5 GPa even in (111)-oriented crystals. Hence, based on this evidence it is unlikely that the behavior we have measured for (111) and (021)-oriented crystals can be attributed to a phase transformation rather than dislocation-mediated anomalous hardening.

This work was supported by LANL Laboratory Directed Research and Development funds. The explosive crystal laboratory is supported by the National Nuclear Security Administration, Science Campaign 2. T.D.S. acknowledges support from the U.S. Army Research Office under Grant No. W911NF-05-1-265.

<sup>1</sup>J. J. Dick, *Appl. Phys. Lett.* **44**, 859 (1984).

<sup>2</sup>J. J. Dick, R. N. Mulford, W. J. Spenser, D. R. Pettit, E. Garcia, and D. C. Shaw, *J. Appl. Phys.* **70**, 3572 (1991).

<sup>3</sup>J. J. Dick and J. P. Ritchie, *J. Appl. Phys.* **76**, 2726 (1994).

<sup>4</sup>J. J. Dick, *J. Appl. Phys.* **81**, 601 (1997).

<sup>5</sup>C. S. Choi and E. Prince, *Acta Crystallogr., Sect. B: Struct. Crystallogr. Cryst. Chem.* **28**, 2857 (1972).

<sup>6</sup>D. E. Hooks, K. J. Ramos, and A. R. Martinez, *J. Appl. Phys.* **100**, 024908 (2006).

<sup>7</sup>H. G. Gallagher, P. J. Halfpenny, J. C. Miller, and J. N. Sherwood, *Philos. Trans. R. Soc. London, Ser. A* **339**, 293 (1992).

<sup>8</sup>M. J. Cawkwell, K. J. Ramos, D. E. Hooks, and T. D. Sewell, *J. Appl. Phys.* **107**, 063512 (2010).

<sup>9</sup>G. D. Smith and R. K. Bharadwaj, *J. Phys. Chem. B* **103**, 3570 (1999).

<sup>10</sup>K. J. Ramos, D. E. Hooks, and D. F. Bahr, *Philos. Mag.* **89**, 2381 (2009).

<sup>11</sup>V. Vitek, *Philos. Mag.* **18**, 773 (1968).

<sup>12</sup>M. J. Cawkwell, T. D. Sewell, L. Q. Zheng, and D. L. Thompson, *Phys. Rev. B* **78**, 014107 (2008).

<sup>13</sup>B. Olinger, B. Roof, and H. Cady, *Comportement des Milieux Denses sous Hautes Pressions Dynamiques* (Commissariat à l'Energie Atomique, Paris, 1978), p. 3.

<sup>14</sup>J. A. Ciezak, T. A. Jenkins, Z. Liu, and R. J. Hemley, *J. Phys. Chem. A* **111**, 59 (2007).

<sup>15</sup>A. J. Davidson, I. D. H. Oswald, D. J. Francis, A. R. Lennie, W. G. Marshall, D. I. A. Millar, C. R. Pulham, J. E. Warren, and A. S. Cumming, *Cryst. Eng. Comm.* **10**, 162 (2008).

<sup>16</sup>J. E. Patterson, Z. A. Dreger, and Y. M. Gupta, *J. Phys. Chem. B* **111**, 10897 (2007).



# Molecular dynamics simulations of shock waves in oriented nitromethane single crystals

Lan He, Thomas D. Sewell,<sup>a)</sup> and Donald L. Thompson<sup>b)</sup>*Department of Chemistry, University of Missouri-Columbia, Columbia, Missouri 65211-7600, USA*

(Received 8 December 2010; accepted 11 February 2011; published online 25 March 2011)

The structural relaxation of crystalline nitromethane initially at  $T = 200$  K subjected to moderate ( $\sim 15$  GPa) supported shocks on the (100), (010), and (001) crystal planes has been studied using microcanonical molecular dynamics with the nonreactive Sorescu–Rice–Thompson force field [D. C. Sorescu, B. M. Rice, and D. L. Thompson, *J. Phys. Chem. B* **104**, 8406 (2000)]. The responses to the shocks were determined by monitoring the mass density, the intermolecular, intramolecular, and total temperatures (average kinetic energies), the partitioning of total kinetic energy among Cartesian directions, the radial distribution functions for directions perpendicular to those of shock propagation, the mean-square displacements in directions perpendicular to those of shock propagation, and the time dependence of molecular rotational relaxation as a function of time. The results show that the mechanical response of crystalline nitromethane strongly depends on the orientation of the shock wave. Shocks propagating along [100] and [001] result in translational disordering in some crystal planes but not in others, a phenomenon that we refer to as *plane-specific disordering*; whereas for [010] the shock-induced stresses are relieved by a complicated structural rearrangement that leads to a paracrystalline structure. The plane-specific translational disordering is more complete by the end of the simulations ( $\sim 6$  ps) for shock propagation along [001] than along [100]. Transient excitation of the intermolecular degrees of freedom occurs in the immediate vicinity of the shock front for all three orientations; the effect is most pronounced for the [010] shock. In all three cases excitation of molecular vibrations occurs more slowly than the intermolecular excitation. The intermolecular and intramolecular temperatures are nearly equal by the end of the simulations, with 400–500 K of net shock heating. Results for two-dimensional mean-square molecular center-of-mass displacements, calculated as a function of time since shock wave passage in planes perpendicular to the direction of shock propagation, show that the molecular translational mobility in the picoseconds following shock wave passage is greatest for [001] and least for the [010] case. In all cases the root-mean-square center-of-mass displacement is small compared to the molecular diameter of nitromethane on the time scale of the simulations. The calculated time scales for the approach to thermal equilibrium are generally consistent with the predictions of a recent theoretical analysis due to Hooper [*J. Chem. Phys.* **132**, 014507 (2010)]. © 2011 American Institute of Physics. [doi:10.1063/1.3561397]

## I. INTRODUCTION

Organic solids subjected to shock compression undergo a variety of physical and chemical changes.<sup>1–12</sup> Shocks in energetic organic solids can induce complicated molecular and crystal transformations<sup>1–3</sup> or chemical reactions,<sup>4–7</sup> which can lead to deflagration or detonation.<sup>8–12</sup> Various experimental, computational, and theoretical approaches are being used to increase the level of understanding of the physical and chemical processes that occur in shocked materials.<sup>13–19</sup> Detecting these processes at the molecular level in experiments is highly challenging due to the complicated nature of the materials, the short time and space scales involved in shock-induced processes, and the large optical density of shocked organic materials in the spectral windows of interest.

Experimental studies of the shock response of oriented pentaerythritol tetranitrate (PETN) single crystals by Dick and co-workers<sup>20–24</sup> have shown that shock compression along different crystallographic directions leads to large differences in the initiation sensitivity. Dick *et al.*<sup>20</sup> proposed a *steric hindrance model* for shock initiation sensitivity of energetic materials to explain this. In this model, shock orientations for which there are resolved shear stresses on active crystal slip systems lead to relatively weak hindered plastic deformation and consequently high initiation thresholds (low initiation sensitivity); whereas orientations for which there is no resolved shear stress on any active crystal slip system lead to a material in which shear stresses cannot be relaxed by dislocations, therefore leading to low initiation thresholds (high initiation sensitivity). Predictions of the steric hindrance model for PETN crystal are consistent with the experiment: Shock compression along the most sensitive direction ([110]) results in hindered shear on an active slip plane, whereas no such hindrance occurs for shocks along the least sensitive direction [100].

<sup>a)</sup>Electronic mail: sewellt@missouri.edu.<sup>b)</sup>Electronic mail: thompsondon@missouri.edu.

Patterson *et al.*<sup>25</sup> used Raman spectroscopy to determine whether the orientation-dependent shock response observed for PETN also exists for single crystals of hexahydro-1,3,5-trinitro-*s*-triazine (RDX). Their results<sup>25</sup> showed that shock compression on the (111), (210), and (100) planes in single-crystal RDX led to the  $\alpha - \gamma$  solid-solid phase transition, with no apparent orientation dependence in behavior for shock pressures up to 5.5 GPa. Computational studies of the shock response of the single-crystal RDX have shown nucleation and growth of nanoscale shear bands for shocks propagating along [100],<sup>26,27</sup> homogeneous nucleation and growth of metastable stacking faults for shock loading on the (111) (Ref. 28) and (021) (Ref. 29) planes, and possibly, the polymorphic  $\alpha - \gamma$  phase transition for shocks directed along [001].<sup>27</sup>

These experimental and computational results illustrate the importance of understanding the fundamental effects of shocks on organic crystals. We think that much can be learned from in-depth studies of crystals of simpler molecules such as nitromethane, which is a prototypical explosive and is useful for experimental and theoretical studies designed to understand fundamental behaviors in energetic materials. There have been numerous experimental, computational, and theoretical studies of nitromethane. Dick<sup>30</sup> predicted an anisotropic shock initiation threshold in crystalline nitromethane on the basis of the steric hindrance model. This possibility has not been investigated experimentally because nitromethane is a liquid at room temperature and atmospheric pressure. Indeed, we are unaware of any experimental determinations of the shock Hugoniot locus for solid nitromethane. Siavosh-Haghighi *et al.*<sup>31</sup> and Dawes *et al.*<sup>32</sup> used molecular dynamics (MD) simulations with the vibrationally accurate, nonreactive Sorescu-Rice-Thompson (SRT) force field<sup>33,34</sup> to investigate structural relaxation and energy partitioning among molecular degrees of freedom for crystalline nitromethane shocked along [100] at two initial temperatures (50 and 200 K) and shock pressures of about 3, 7, 17, and 31 GPa, with small differences depending on the initial temperature. Their results predict that melting occurs on short time scales (4 ps or less) when a moderately strong shock ( $P \geq 16.9$  GPa) is applied.

The focus of the present study is to characterize the differences in mechanical and thermal responses to supported shock waves in oriented nitromethane single crystals by performing MD simulations with same nonreactive force field used by Siavosh-Haghighi *et al.*<sup>31</sup> and Dawes *et al.*<sup>32</sup> for shock wave propagations along the [100], [010], and [001] crystal directions. The initial temperature was 200 K. The impact speed was  $2.0 \text{ km s}^{-1}$ , which corresponds to a shock pressure of approximately 15 GPa. We monitored spatially and temporally resolved single- and multiparticle properties prior to and following shock wave excitation by using a moving observation frame centered on the shock front that resolves the thermo-physical and geometric changes induced by the shocks.

The computational and analysis methods are described in Sec. II, the results are presented and discussed in Sec. III, and a summary and conclusions are given in Sec. IV.

## II. METHODS

### A. Force field

The flexible-molecule SRT force field<sup>33,34</sup> was used to describe the intra- and intermolecular interactions in nitromethane. Several studies have shown that this force field accurately reproduces the static and dynamic properties of both liquid and crystalline nitromethane.<sup>35–40</sup> In the SRT force field interactions between covalently bonded atoms are described by Morse potentials, three-center bending interactions by quadratic functions, and four-center out-of-plane and dihedral interactions by cosine functions. Nonbonded interactions, which apply only to atoms in different molecules because 1–4 nonbonded interactions (i.e., intramolecular H $\cdots$ O in nitromethane) are not included in SRT, are described using a Buckingham-plus-charge model with fixed partial charges centered on the nuclei. We have made one minor modification to the SRT force field. Specifically, whereas in the original SRT model each hydrogen and oxygen atom was assigned a slightly different charge based on a gas-phase quantum chemistry calculation of partial atomic charges using the geometry of a nitromethane molecule in the crystal, here we have used a single value (the arithmetic average) of the charge on each type of atom. We refer to this modified SRT model as SRT-(q).

### B. Computational details

The crystal structure of nitromethane at atmospheric pressure is known from x-ray single crystal ( $T = 228 \text{ K}$ ) and neutron powder ( $T = 4.2$  and  $78 \text{ K}$ ) diffraction data.<sup>41,42</sup> It belongs to the orthorhombic space group  $P2_12_12_1$  with four molecules per unit cell. The simulations were performed for a preshock temperature  $T = 200 \text{ K}$ . The lattice parameters for this thermodynamic state were calculated for the SRT-(q) model using isothermal-isobaric (*NPT*) MD with the Nosé-Hoover thermostat-barostat algorithm<sup>43,44</sup> as implemented in the LAMMPS (Ref. 45) code. As shown in Table I, those lattice parameters agree well with previous simulation results<sup>33</sup> using the original SRT force field, yielding a nominal preshock density  $\rho = 1222 \text{ kg m}^{-3}$ . We have used these calculated lattice parameters in all the simulations reported here.

Figure 1 illustrates a simulation in progress. A thermalized crystal of flexible nitromethane molecules (blue and green regions in Fig. 1) was impacted with speed  $u_p$  onto a stationary, rigid piston (tan region in Fig. 1) of crystalline nitromethane with the same crystallographic orientation as

TABLE I. Lattice parameters of nitromethane at  $T = 200 \text{ K}$  and  $P = 1 \text{ atm}$ .

$a$ (Å)	$b$ (Å)	$c$ (Å)	Source
5.2438	6.4970	8.8984	Present work <sup>a</sup>
5.2452	6.5167	8.8808	Sorescu <i>et al.</i> <sup>b</sup>

<sup>a</sup>Calculated from *NPT*-MD simulations using the SRT-(q) force field.

<sup>b</sup>Taken from Sorescu *et al.*, Ref. 37; calculated from *NPT*-MD simulations using the SRT force field as described in Ref. 33.

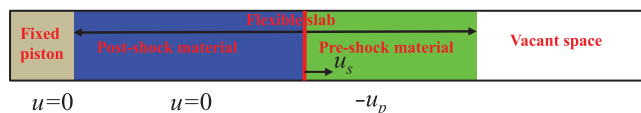


FIG. 1. Schematic diagram of the approach used to generate shock waves. The leftmost (tan) region is the stationary piston comprised of rigid molecules. A slab containing flexible molecules (blue and green regions) equilibrated to 200 K impacts with speed  $u_p$  from the right onto the stationary piston. The interface between the postshock material (blue region) and the preshock material (green region) is the shock front position (solid red line) that advances at shock velocity  $u_s$  from left to right.

the flexible slab to generate a supported shock wave in the flexible slab. There is a vacant space (white region in Fig. 1) to minimize electrostatic interactions between the two interfaces. Three-dimensional (3D) periodic simulation cells were constructed by replicating the unit cell geometry by repeat factors of  $80a \times 8b \times 6c$ ,  $20a \times 65b \times 12c$ , and  $10a \times 8b \times 48c$  (15 360, 62 400, and 15 360 molecules, respectively) for simulating shocks propagating along [100], [010], and [001], respectively; these include the pistons, which are, respectively, of dimensions  $5a \times 8b \times 6c$ ,  $20a \times 4b \times 12c$ , and  $10a \times 8b \times 3c$ . The larger cell size used for the [010] case was employed to avoid finite-size effects. The length of the vacant region was chosen such that the total cell length parallel to the shock propagation direction was 1000 Å in all cases. The crystal structure of nitromethane is such that one can define molecular layers perpendicular to the three shock directions considered here; see Fig. 2. There are 96, 480, and 80 molecules per layer perpendicular to [100], [010], and [001], respectively, and 160, 131, and 192 layers in the respective initial simulation cells (including the piston regions).

Prior to shock loading, isothermal–isochoric (*NVT*) equilibrations were carried out at  $T = 200$  K for 80 000 time steps using velocity Verlet<sup>46</sup> integration with a time step of

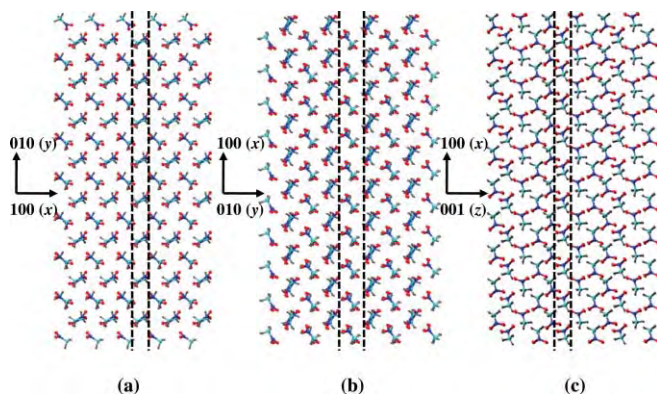


FIG. 2. Nitromethane crystal structure and the definition of molecular layers used in the analysis of the MD results. (a) Initial configuration of the piston for the [100] shock simulation; the 96 molecules between the two dashed lines comprise one molecular layer. (b) Initial configuration of the piston for the [010] shock simulation; only one-half of the vertical size of the  $20a \times 65b \times 12c$  system studied is shown; the 240 molecules between the two dashed lines comprise one molecular layer (480 molecules in the full-size sample). (c) Initial configuration of the piston for the [001] shock simulation; the 80 molecules between the two dashed lines comprise one molecular layer.

0.75 fs. The piston region was included in the equilibration. In order to eliminate breathing motions along the shock direction that result from sudden introduction of free surfaces when the vacant space is added at the end of the crystal (see Fig. 1), new velocities sampled from a Maxwell distribution were assigned to the atoms every 4000th step during the first 40 000 time steps of equilibration, with velocity rescaling every ten time steps to yield an instantaneous average kinetic energy corresponding to 200 K. The final 40 000 time steps of the *NVT* equilibration were performed using the Nosé–Hoover thermostat<sup>47,48</sup> with a relaxation constant of 150 fs. The resulting amplitudes of the breathing motion of the crystal and calculated components of the stress tensor are small; the breathing amplitude is less than 0.5% and the average values for the largest diagonal and off-diagonal stress components are approximately 20 and 5 bars, respectively, indicating that the systems are well equilibrated prior to the shock excitation.

Starting from the final phase space points of the equilibration runs, simulations of supported planar shock waves propagating along [100], [010], and [001] were performed in the microcanonical (*NVE*) ensemble. This was accomplished by setting to zero, and holding at zero, all velocity components of the atoms comprising the piston and adding impact speed  $u_p = 2.0 \text{ km s}^{-1}$  parallel to the direction of shock propagation to the atoms in the flexible slab. This value of the impact speed was chosen to allow direct comparisons to the results of our earlier study of shock-induced melting for shock propagation along [100].<sup>31</sup> The velocity Verlet algorithm was used with a step size of 0.1 fs for the *NVE* simulations. Cartesian positions and velocities were saved every 4 fs for subsequent analysis.

The particle–particle particle–mesh (PPPM) (Ref. 49) method available in LAMMPS was used to evaluate the Coulomb and dispersion interactions. Nonbonded repulsive interactions and the real-space part of the Coulomb and dispersion terms were shifted smoothly to zero at a cutoff distance of 11.0 Å.

### C. Analysis of simulation results

Molecular layers perpendicular to the [100], [010], and [001] crystal directions, which correspond to the  $x$ ,  $y$ , and  $z$  axes, respectively, in the chosen laboratory frame (see Fig. 2) were used to track the position of the shock front during shock propagation by monitoring the time dependencies of (1) the center-of-mass position (CMP) for each layer along the shock direction and (2) the layer with the maximum gradient of kinetic energy. Figure 3 shows, for shocking along [010], the relationship between layer center-of-mass positions (CMP <sub>$y$</sub> , where the subscript denotes the shock direction) and time for 12 evenly spaced molecular layers [see Fig. 3(a)] and the corresponding result based on the maximum gradient of kinetic energy [( $K'_y$ )<sub>max</sub>] criterion [see Fig. 3(b)]. The locus of points where the slopes of the individual CMP layer trajectories change defines the trajectory of the shock front (dashed line). Material within ten molecular layers of either end of



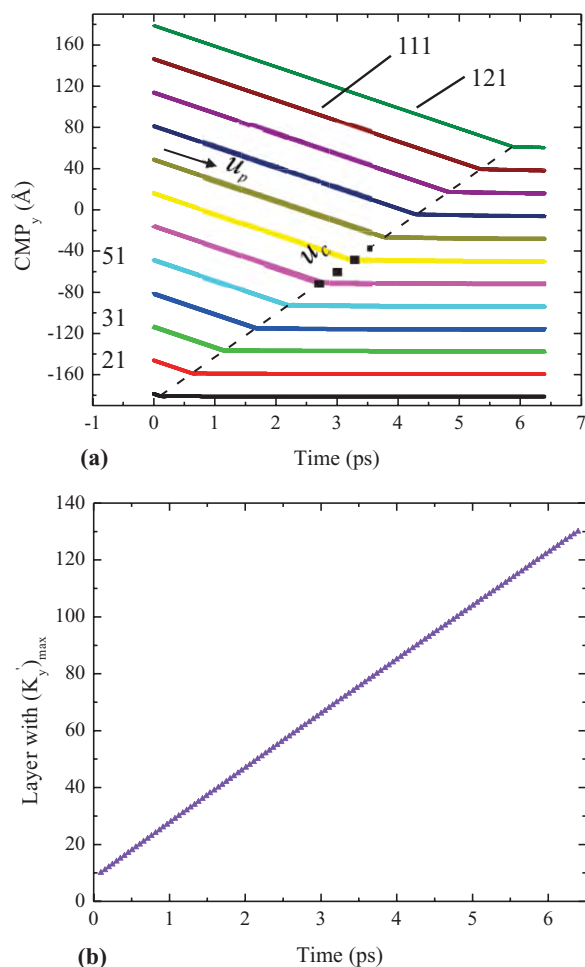


FIG. 3. (a) Center-of-mass position for each layer along the shock direction [010] ( $\text{CMP}_y$ ) as a function of the time during shock propagation (solid lines). The dashed line connecting shock front positions as time evolves tracks the shock trajectory in the  $y$ - $t$  plane; the  $\text{CMP}_y$  velocity is  $u_c$ . The numbers 21, 31, 51, 111, and 121 denote specific layer numbers. (b) Layers with the maximum gradient of kinetic energy [ $(K'_y)_{\max}$ ] plotted as a function of time. The calculation of the maximum gradient of the kinetic energy for each layer is the same as described in Ref. 31.

the flexible slab was excluded from this analysis to minimize possible artifacts due to the rigid piston on one end and the free surface on the other. The velocity of the shock front using the center-of-mass position criterion is the sum of the CMP velocity  $u_c$  and impact speed  $|u_p|$ . The two approaches yield essentially identical results; for example,  $u_s = 6.193 \pm 0.003 \text{ km s}^{-1}$  for the [010] case determined from the CMP layer trajectories and  $u_s = 6.192 \pm 0.002 \text{ km s}^{-1}$  for the same case using the maximum gradient of kinetic energy criterion.

As shown in Fig. 3 the shock velocity is essentially constant, and therefore, the instantaneous position of the shock front defines a convenient time and space origin for analysis of properties as the shock wave moves through the simulation cell. Transforming the raw data from the laboratory frame into the translating reference frame centered on the shock front allows averaging over the resulting equivalent spatial (and temporal) origins in the transformed frame; this yields significantly improved precision in the analysis. To accomplish

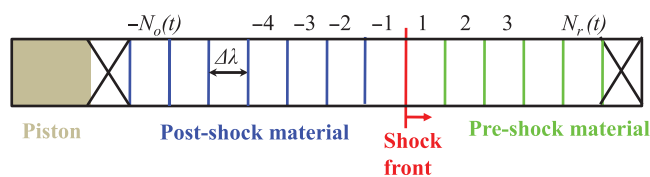


FIG. 4. Schematic diagram of the approach used to define fixed-volume bins for trajectory analysis. In the laboratory frame the spatial origin for the bins translates linearly to the right with time, so as to remain stationary in the reference frame centered on the shock front. The width of the bins  $\Delta\lambda$  is constant. Bins for postshock and preshock materials are labeled by negative and positive integers, respectively; the bin that contains the shock front at any given instant in time is denoted *bin 1*. The number of postshock [ $N_o(t)$ ] and preshock [ $N_r(t)$ ] bins increases and decreases, respectively, with time  $t$ . The total number of bins  $N_b(t) = N_o(t) + N_r(t)$  decreases linearly in time due to compression of the flexible slab as the shock wave advances through the material. Bins, or partial bins, at least  $14 \text{ \AA}$  from either end of the flexible slab (denoted by crosses in the left-most and right-most bins in the figure) are excluded from the analysis of properties.

this transformation we used fixed-width rectilinear bins (and therefore fixed-volume rectilinear bins because the transverse simulation cell lengths are fixed) centered on and moving with the shock front. Specifically, at any given instant in time the material in the flexible slab is divided into  $N_b(t) = N_o(t) + N_r(t)$  bins of width  $\Delta\lambda$  along the shock direction, where  $N_o(t)$  and  $N_r(t)$  are the numbers of postshock and preshock bins, respectively, at time  $t$ , and the product  $N_b(t)\Delta\lambda$  is approximately equal to but less than the length of the flexible slab along the shock direction. Material within at least  $14 \text{ \AA}$  of either end of the flexible slab was excluded from the analysis of properties (except the shock velocity which was discussed above) to minimize possible artifacts due to the rigid piston on one end and free surface on the other. The labeling scheme used for the bins is illustrated in Fig. 4. Positive and negative integers denote preshock and postshock bins, respectively: the bin containing the shock front position at any instant in time is always denoted *bin 1*; there is no *bin 0*. The value of  $N_b(t)$  required to span the flexible slab decreases with time due to shock compression; the numbers of postshock [ $N_o(t)$ ] and preshock [ $N_r(t)$ ] bins increase and decrease, respectively, as the shock front advances through the material. Because the bins are of fixed volume and defined relative to the shock front position, material flows into and out of the bins as the simulation proceeds. The shock front spent an average of 44, 56, and 36 fs in any given bin for shock propagation along [100], [010], and [001], respectively. Thus, given the 4 fs sampling interval, simulation results in a given bin were averaged over 11, 14, and 9 4-fs time intervals for the [100], [010], and [001] shocks, respectively.

Note that the same spatial origin obtained when the shock front first reached a given molecular layer in the crystal (based on the analysis discussed in connection with Fig. 3) was used to define the fixed-volume bins for the entire time when the shock front was in that layer (44, 56, and 36 fs on average for the [100], [010], and [001] shocks, respectively). When the shock front was determined to have advanced from one molecular layer into the next, the fixed-volume bins were remapped. For this reason the preshock and short-time



TABLE II. Shock velocity, pressure, and temperature for shocks along [100], [010], and [001].<sup>a</sup>

	[100]	[010]	[001]
Shock velocity $u_s$ (km s <sup>-1</sup> )	6.253 ± 0.006	6.193 ± 0.003	6.299 ± 0.009
Shock pressure $P_s$ (GPa)	15.27	15.12	15.39
$T_{\text{inter}}/T_{\text{intra}}/T_{\text{total}}$ (K) (at 50 ± 1 Å behind the shock front)	782 ± 2	865 ± 1	794 ± 2
	493 ± 1	556 ± 1	485 ± 1
	534 ± 1	600 ± 1	529 ± 1
$T_{\text{inter}}/T_{\text{intra}}/T_{\text{total}}$ (K) (at 100 ± 1 Å behind the shock front)	695 ± 2	756 ± 1	735 ± 2
	545 ± 1	603 ± 1	551 ± 2
	566 ± 1	625 ± 1	577 ± 2
$T_{\text{inter}}/T_{\text{intra}}/T_{\text{total}}$ (K) (at 200 ± 1 Å behind the shock front)	659 ± 3	679 ± 2	680 ± 3
	610 ± 2	640 ± 1	637 ± 2
	617 ± 2	646 ± 1	643 ± 2

<sup>a</sup>Initial temperature 200 K and impact speed 2.0 km s<sup>-1</sup>.

postshock mass densities exhibit considerable size dependence for bin widths less than the unit cell lattice parameter parallel to a given direction of shock propagation; other properties discussed below were unaffected.

### III. RESULTS

#### A. Shock velocity and shock pressure

The shock velocities  $u_s$  obtained for 2.0 km s<sup>-1</sup> impacts at an initial temperature of 200 K for shock waves propagating parallel to [100], [010], and [001] are given in Table II. The values of the shock velocities in the table were obtained using the CMP layer trajectory analysis discussed in Sec. II C. Error bars in Table II and elsewhere correspond to one standard deviation of the mean. The value of  $u_s$  for the [001] shock is higher than that for the other two directions. However, the fastest shock velocity is only 1.76% larger than the slowest one. For the conditions and orientations considered, the shock velocity in nitromethane is not very sensitive to the crystal orientation. Shock pressures  $P_s$  for the three orientations, calculated from the Rankine–Hugoniot jump relation  $P_s = \rho_0 u_s u_p$ ,<sup>50</sup> are given in Table II. The values range from 15.12 to 15.39 GPa.

The calculated shock velocity  $u_s = 6.253$  km s<sup>-1</sup> for the [100] shock differs by 5.41% from the value  $u_s = 6.61$  km s<sup>-1</sup> reported by Siavosh-Haghighi *et al.*<sup>31</sup> There are three differences between the present study and those of Siavosh-Haghighi *et al.* that could account for the discrepancy. In the present study we used the SRT-(q) force field with dispersion interactions evaluated using the PPPM algorithm, which evaluates  $R^{-6}$  terms directly rather than using a cutoff; however, we do not think that these two differences would affect the shock velocity enough to account for the difference. The third difference is that Siavosh-Haghighi *et al.* used initial density  $\rho_0 = 1280$  kg m<sup>-3</sup> (based on measured lattice parameters at 228 K) rather than 1222 kg m<sup>-3</sup>, which is the value predicted by the SRT-(q) force field at 200 K and 1 atm. Indeed, a shock simulation using the SRT force field at the same initial density as in the Siavosh-Haghighi *et al.* simulations yields a shock velocity  $u_s = 6.623$  km s<sup>-1</sup>, which agrees with their value to within the

$\sim \pm 0.006$  km s<sup>-1</sup> estimated precision for the shock velocity in our calculations.

#### B. Qualitative features of the shocked states

Figure 5 contains projection views of molecular centers of mass along the [010], [001], and [100] directions at the instants of maximum compression (that is, when the shock front reached the right-hand end of the flexible slab) for, respectively, shock propagation along [100], [010], and [001] [panels (a), (c), and (e), respectively]. It is evident that the postshock structures for the [100] and [001] shocks [Figs. 5(a) and 5(e), respectively] are quite distinct from those obtained for the [010] shock [Figs. 5(c) and 5(d)]. The postshock material viewed along different directions [as shown in panels (c) and (d) of Fig. 5] for the [010] case retains some medium-range order that is similar to that of a paracrystal,<sup>51</sup> whereas for the [100] and [001] cases [see Figs. 5(a) and 5(e), respectively], the shocked material appears to lose nearly all crystal order for distances sufficiently far behind the shock front. Thus, in contrast to the observation for shock velocity and shock pressure, the effects of shock orientation are significant. Note that the onset of translational disordering occurs more quickly (i.e., at shorter distances behind the shock front) for the [100] shock than for the [001] one [as shown in panels (a) and (e) of Fig. 5, respectively]. However, in neither case is there complete disordering on the  $\sim 6$  ps time scale of the simulations. This is clear from the results shown in Figs. 5(b) and 5(f). Figure 5(b) is a view of the [100] shock where the molecular centers of mass are projected along [001]. It is obvious that considerable translational order still exists in the plane of the page even for material that has been in the shocked state for the longest time. Figure 5(f) is similar to Fig. 5(b), except that the [001] shock is shown following a counterclockwise rotation of 50° about the [001] axis relative to the projection shown in Fig. 5(e). Although for this case there appears to be less translational order for the material that has been in the shocked state for the longest time, it is apparent that the material has not disordered completely. Note that this is distinct from the behavior of plastic crystals. We refer to this as *plane-specific translational disordering*. It is reasonable to expect that similar plane-specific behaviors

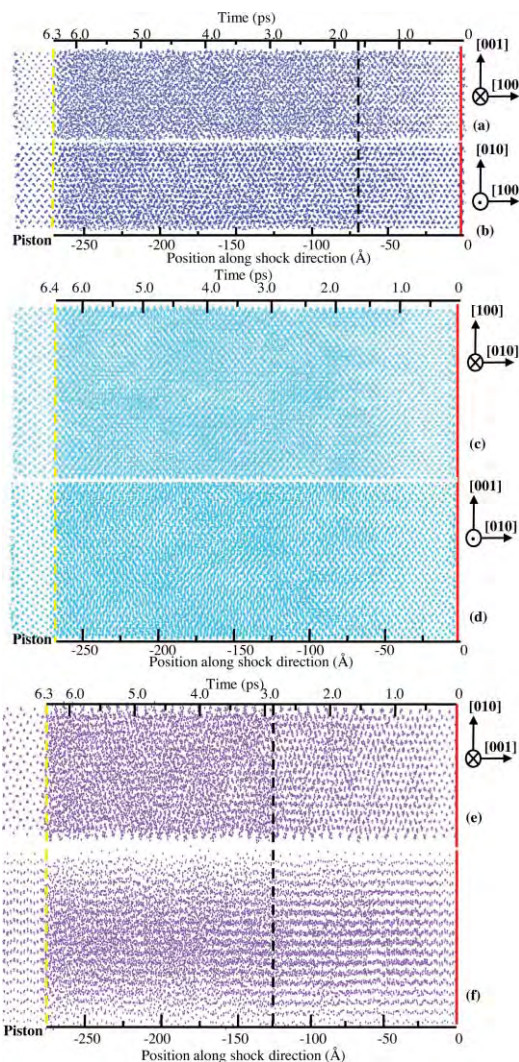


FIG. 5. Projections of snapshots of molecular centers of mass for the three shock simulations studied at the respective instants of maximum compression. Projections along (a) [010] for the [100] shock; (b) [001] for the [100] shock; (c) [001] for the [010] shock; (d) [100] for the [010] shock; (e) [100] for the [001] shock; and (f) [100] followed by a counterclockwise rotation of  $50^\circ$  around the direction [001] for the [001] shock. The bottom abscissa is the distance from the shock front and the top abscissa is the time since the passage of the shock front. The regions to the left of the yellow lines are the fixed pistons; the red solid lines denote the instantaneous shock front positions at the ends of the simulations. The black dashed lines mark the approximate postshock times at which the 2D RDFs shown in Fig. 9 converge to essentially stable values for the [100] and [001] shocks.

might also exist for orientational or intramolecular relaxation and should be investigated for this and other crystals because of their possible relevance to the physical and chemical processes that occur under high shock loading.

### C. Density

The mass density was computed as a function of distance from the shock front using the moving fixed-volume binning approach discussed in Sec. II C and illustrated in Fig. 4. Averaging over equivalent time origins was performed to improve the precision. Plots of the mass density as a func-

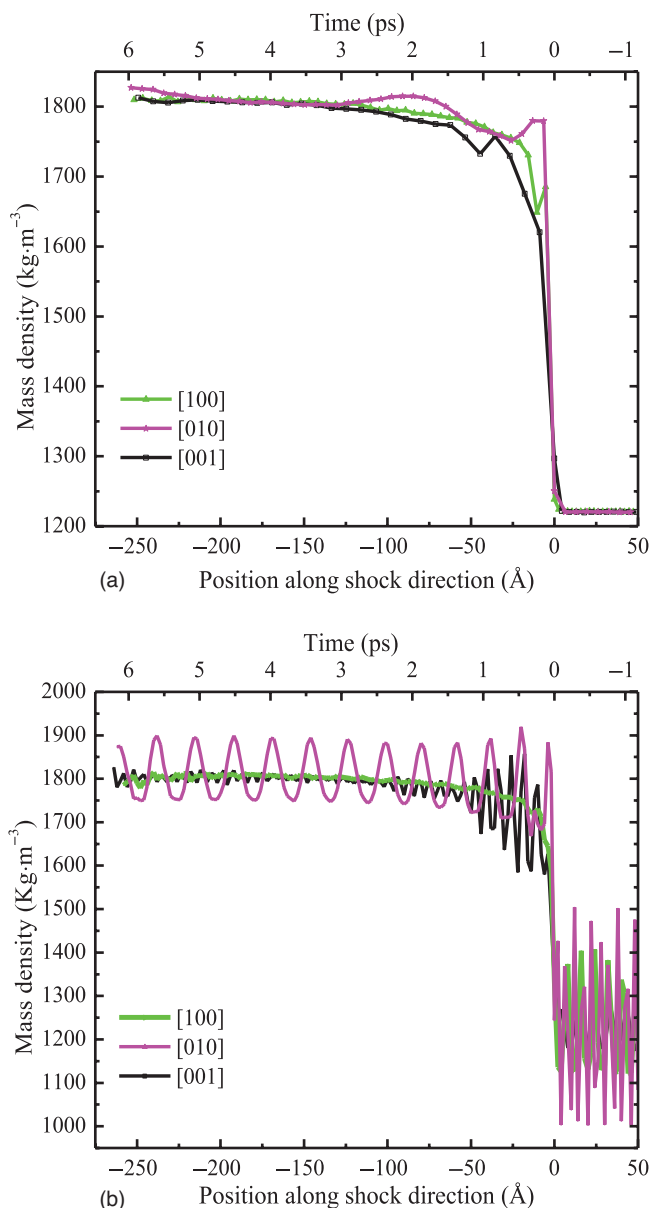


FIG. 6. The mass density as a function of distance from the shock front (bottom abscissa) and time since shock passage (top abscissa). (a) Results for bin widths  $\Delta\lambda$  set equal to the unit cell parameters ( $a$ ,  $b$ , and  $c$  for the [100], [010] and [001] shock directions, respectively); and (b) as in (a) except that  $\Delta\lambda = 2.0$  Å for all three cases. Shocked material is associated with negative values for the position and positive values for time; the time is calculated based on the shock velocity in the [100] case, which is only slightly different from those for the [010] and [001] cases since the shock velocities for all three cases are very similar (see Table II).

tion of distance from the shock front are shown in Fig. 6 for two different values of the bin width  $\Delta\lambda$  for the [100], [010], and [001] shock simulations (shown as green, magenta, and black curves, respectively). The time since the passage of the shock front is shown on the top abscissa. The time in all three cases was calculated by assuming the shock velocity of the [100] case, which is only slightly different than those for the [010] and [001] cases, as shown by the results in Table II.

The results shown in Fig. 6(a) were obtained by setting the bin widths  $\Delta\lambda$  equal to the corresponding  $T = 200$  K unit cell lattice parameters  $a$ ,  $b$ , and  $c$  (see Table I) along the respective shock propagation directions and those in Fig. 6(b) by setting  $\Delta\lambda = 2.0$  Å, the value used for all other property calculations. With the exception of the mass density the calculated properties are relatively insensitive to the value of  $\Delta\lambda$ ;  $\Delta\lambda = 2.0$  Å was found to yield an acceptable compromise between spatial resolution and precision. The instantaneous location of the shock front defines time and space origins for the postshock analysis and therefore allows assignment of individual atoms to particular bins at a given time (see Sec. II C). Furthermore, because the instantaneous location of the shock front when it first reaches a given layer in the crystal is used as the spatial origin for defining the fixed-volume bins for the entire time when the shock front is in that layer, the results for the density (but not for the other properties investigated) exhibit finite-width effects in the preshock regions of the material.

In Fig. 6(a) the preshock densities for the three cases are identical ( $1222 \text{ kg m}^{-3}$ ). The postshock mass densities within the first 100 Å behind the shock front are characterized by three stages: An abrupt increase in density of about  $500 \text{ kg m}^{-3}$ , followed by a small decrease in density, followed by a gradual increase to a relatively stable value. The apparent onset time for relaxation based on density is distinct for the three shock directions; it occurs at about 11 Å (256 fs) behind the shock front for the [100] shock, 26 Å (620 fs) for the [010] shock, and 45 Å (1044 fs) for the [001] shock. The new arrangement of molecules, whether locally crystalline in the case of the [010] shock or relatively disordered as for the [100] and [001] shocks (cf. Fig. 5), persists as the relaxation continues such that the postshock mass density remains essentially constant. The densities at distances far from the shock front position ( $\geq 100$  Å) become nearly identical for shocks propagating along [100] and [001]; the average mass density in this region is  $1808 \text{ kg m}^{-3}$ . The density of the postshock material within the interval from 50 to 130 Å behind the shock front for the [010] case is higher than that for the other two shock orientations, which is evident in Fig. 6(a). The distinct behavior of the density for the [010] shock, in particular its nonmonotonic spatial profile for distances greater than 50 Å behind the shock front, implies multiple stages of relaxation for that shock orientation.

The higher-resolution averaging using  $\Delta\lambda = 2.0$  Å in Fig. 6(b) yields oscillations in both the preshock and postshock materials. The oscillations in the postshock material for a given shock orientation provide a useful qualitative indicator of the times required for relaxation toward a translationally steady or slowly varying postshock condition in the material. Thus, for the [100] shock (green curve) the smoothness of the curve suggests a fairly rapid emergence of some disordering, whereas for the [001] shock (black curve), the considerable oscillations that persist over the first  $\sim 50$  Å (1.16 ps) in the postshock state show that loss of translational order in this case occurs more slowly. Finally, for the [010] shock (magenta curve) in which a crystal/paracrystal transition occurs, the oscillations in the postshock material persist over the entire duration of the simulation, consistent with

the system evolving into a new ordered state. The  $\sim 50$  Å (1.19 ps) interval between initial shock front arrival and the system achieving nearly constant amplitude gives an indication of the scale over which this transition occurs.

## D. Temperature

Spatially resolved intermolecular (lattice) temperature  $T_{\text{inter}}$ , intramolecular (vibrational–rotational) temperature  $T_{\text{intra}}$ , and the total temperature  $T_{\text{total}}$  were computed as functions of position (bottom abscissa) and time (top abscissa) relative to the shock front using the fixed-volume bins as defined in Fig. 4 with  $\Delta\lambda = 2.0$  Å. The values of  $T_{\text{inter}}$ ,  $T_{\text{intra}}$ , and  $T_{\text{total}}$  for each bin were computed using

$$T_{\text{inter}} = \frac{\sum_{i=1}^{N_m} M_i (\mathbf{U}_i - \langle \mathbf{U} \rangle_{c.m.b})^2}{3N_m k_B}, \quad (1)$$

$$T_{\text{intra}} = \frac{\sum_{i=1}^{N_m} \sum_{j=1}^{N_{am} \leq 7} m_j (\mathbf{u}_j - \mathbf{U}_i)^2}{3(N_{am} - 1)k_B N_m}, \quad (2)$$

$$T_{\text{total}} = \frac{\sum_{j=1}^{N_a} m_j (\mathbf{u}_j - \langle \mathbf{U} \rangle_{c.m.b})^2}{3N_a k_B}, \quad (3)$$

where  $M_i$  is the mass of molecule  $i$ .  $\mathbf{U}_i$  is the center-of-mass velocity of molecule  $i$ ,  $\langle \mathbf{U} \rangle_{c.m.b}$  is the center-of-mass velocity of the material in the fixed-volume bin containing the center of mass of molecule  $i$ ,  $N_m$  is the total number of molecules in the bin,  $\mathbf{u}_j$  is the velocity and  $m_j$  is the mass of atom  $j$  in molecule  $i$ ,  $N_{am}$  is the total number of atoms belonging to molecule  $i$  located in the bin ( $N_{am} \leq 7$ ),  $N_a$  is the total number of atoms in the bin, and  $k_B$  is the Boltzmann constant. In many cases where we use the term temperature in this study the system is not at thermal equilibrium. However, temperature as defined by Eqs. (1)–(3) is a convenient, commonly used quantity corresponding to the average kinetic energy. Whether temperature is used in the thermodynamic sense or simply as a means for characterizing spatial and temporal variations of average kinetic energy in the system is clear from the context in which it is used.

Values of the intermolecular, intramolecular, and total temperatures calculated at distances  $50 \pm 1$ ,  $100 \pm 1$ , and  $200 \pm 1$  Å behind the shock front are given in Table II. Plots of the intermolecular, intramolecular, and total temperatures (shown as black, green, and magenta curves, respectively) are shown in Fig. 7 as functions of the distance and time (which is given on the top abscissa) from the shock front. The results for shocks propagating along [100] and [001] are shown as dashed and solid curves, respectively, in panel (a) of Fig. 7 while those for the [010] shock are shown in panel (b) of Fig. 7. Note that the ordinate scales in panels (a) and (b) of Fig. 7 differ. In each case the intermolecular temperature initially rises rapidly and then smoothly approaches a long-time value from above. The amplitude of the transient intermolecular temperature rise is greatest for the [010] shock



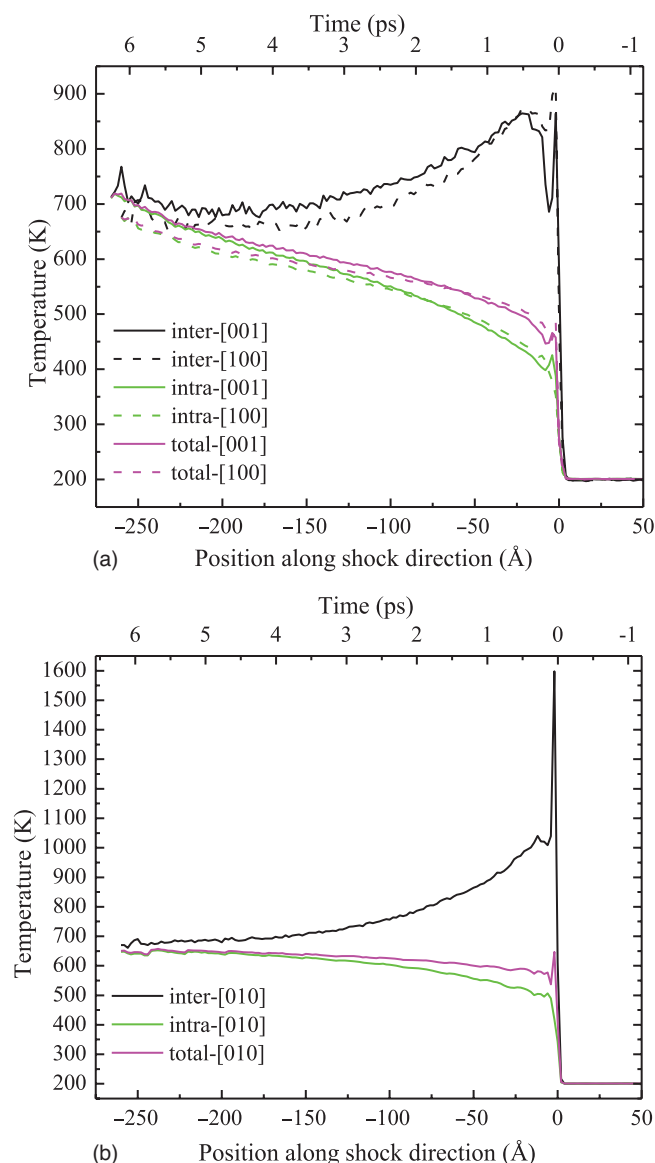


FIG. 7. The intermolecular (lattice), intramolecular (vibrational-rotational), and total temperatures as functions of distance (bottom abscissa) and time (top abscissa) from the shock front. (a) Dashed curves: [100] shock; solid curves: [001] shock. The postshock time in (a) is determined as described in the caption for Fig. 6. (b) [010] shock; the postshock time is determined using the [010] shock velocity.

[panel (b) of Fig. 7] and least for the [001] shock [panel (a) of Fig. 7, solid curve], which appears to be inversely correlated with the calculated Rankine-Hugoniot shock pressure (see Table II). The higher intermolecular temperature obtained for the [010] shock compared to the other two shock directions persists over a region of approximately 100 Å ( $\sim 2.4$  ps) behind the shock front. It is important to note that the amplitude of the apparent intermolecular temperature excursion in the immediate vicinity of the shock front is, in part, due to the large differences in the translational velocity components parallel to the shock propagation direction between molecules in adjacent molecular layers, which in turn arises due to the rapid acceleration (stagnation) of molecular centers of mass along that direction from approximately  $-u_p$  to approximately zero velocity as they collide, in essentially or-

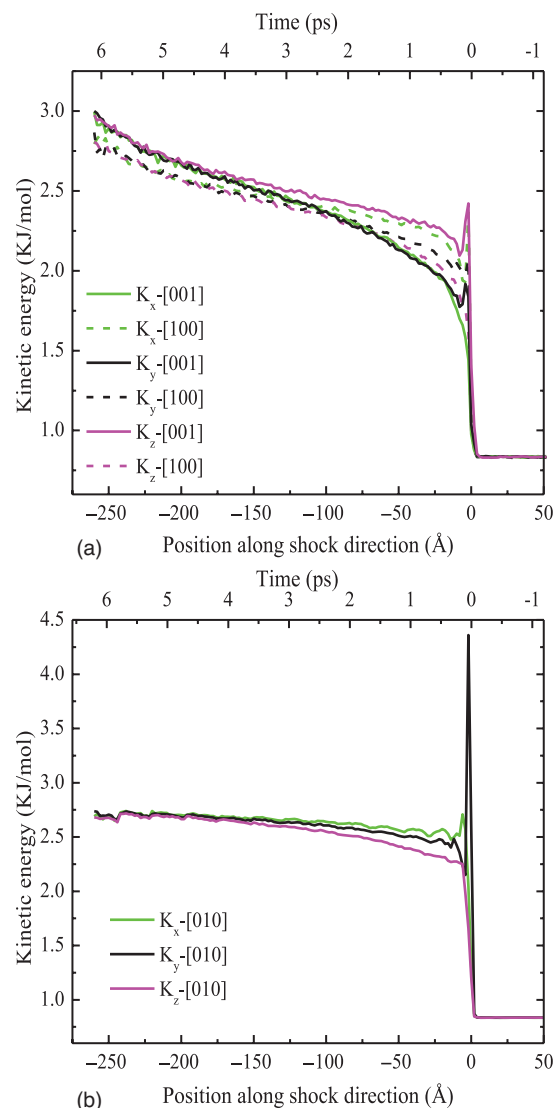


FIG. 8. As in Fig. 7 except the Cartesian components of total kinetic energy are shown.

derly military fashion, with the previously shocked material. Although this contributes to the abrupt, large increases seen in Fig. 7 (and in the longitudinal Cartesian components of kinetic energy discussed below in connection with Fig. 8), this behavior is clearly indicative of a real dynamic effect, which is manifested as “intermolecular temperature.”

In contrast to the results for  $T_{\text{inter}}$ , for all three cases  $T_{\text{intra}}$  increases more slowly and with little transient overexcitation, increasing essentially monotonically to long-time values. These results are consistent with the mechanism in which the initial shock excitation energy is localized in low-frequency lattice modes with subsequent vibrational relaxation into the molecular modes at longer times. For the case of shock propagation along [010] [panel (b)], by distances (times) greater than 175 Å (4.18 ps) behind the shock front, the quantities  $T_{\text{intra}}$  and  $T_{\text{total}}$  approach the same nearly constant value toward which  $T_{\text{inter}}$  also converges on longer times; whereas for the cases of shock propagation along [100] and [001] [panel (a)], by distances (times) greater than 175 Å (greater than 4.16 and 4.06 ps for [100] and [001] directions,



respectively) behind the shock front, the three different temperatures are close to one another, but exhibit a slow increase with time not seen for the [010] case. Overall, these results show that the rate of equilibration is dependent on the shock direction.

The intramolecular temperature  $50 \pm 1$  Å (1.16 ps) behind the shock front is about 485 K for the [001] shock (see Table II), which is slightly lower than the value 493 K obtained for the [100] case (1.18 ps). However, the intramolecular temperature for the [001] shock at the distance  $100 \pm 1$  Å (2.32 ps) behind the shock front becomes higher than that for the [100] case (2.36 ps). The intramolecular temperature for the [001] shock at the distance  $200 \pm 1$  Å behind the shock is 637 K. This is approximately equal to the value calculated for the [010] shock (640 K) and 27 K greater than that calculated for the [100] shock (610 K). The same trends are observed for the total temperatures.

Partitioning total kinetic energy among crystallographic directions [100] ( $x$ ), [010] ( $y$ ), and [001] ( $z$ ) is another way to monitor energy transfer during shock propagation. The calculation of components of total kinetic energy as functions of distance from the shock front position is the same as discussed just above, except that Eq. (4) was used to compute components of total kinetic energy  $K_\beta$  for a given fixed-volume bin.

$$K_\beta = \frac{\sum_{j=1}^{N_a} m_j (\mathbf{u}_j^\beta - \langle \mathbf{U} \rangle_{c.m.b}^\beta)^2}{2N_a}, \quad \beta = x, y, z. \quad (4)$$

Here,  $\mathbf{u}_j^\beta$  denotes Cartesian component  $\beta$  of the velocity of atom  $j$ ,  $\langle \mathbf{U} \rangle_{c.m.b}^\beta$  is the component  $\beta$  of the center-of-mass velocity of the material in a given bin containing atom  $j$ , and  $m_j$  and  $N_a$  have the same meanings as in Eqs. (2) and (3).

Plots of the Cartesian components  $K_x$ ,  $K_y$ , and  $K_z$  (green, black, and magenta curves, respectively) of the total kinetic energy as functions of the postshock distance and time (given on top abscissa) from shock front passage are shown in Fig. 8. The results for the shocks propagating along [100] and [001] are shown in panel (a) of Fig. 8 (dashed curves for [100] and solid curves for [001]) and those for [010] are shown in panel (b) of Fig. 8; note that the ordinate scales in panels (a) and (b) of Fig. 8 differ. The shock first excites the longitudinal kinetic energy component:  $K_x$ ,  $K_y$ , and  $K_z$  for [100], [010], and [001] shocks, respectively. The amplitude of the initial excitation of the longitudinal component of kinetic energy is much larger for [010] than for either [100] or [001]. The  $y$ -component of total kinetic energy for the [010] case goes smoothly to a steady value immediately after shock passage and equilibrates with the other two components by 175 Å ( $>4.18$  ps) behind the shock front. The  $x$ - and  $z$ -components of kinetic energy for the [100] and [001] shock directions increase gradually with time during and immediately after the shock rise and equilibrate with the corresponding other two components within 200 Å ( $\sim 4.7$  ps for [100] and  $\sim 4.64$  ps for [001]) behind the shock front. Note that the gradual increases with time for all the components of the total kinetic energy in the [100] and [001] shock simulations at long postshock times are not observed for the [010] case, which is consis-

tent with the temperature results shown in Fig. 7 and supports the conclusion that the material transformation that occurs for the [010] shock is distinct from those for the [100] and [001] shocks. Note that the shock-direction component of the total kinetic energy in the [001] case ( $z$ ) is always higher than that for the [100] case ( $x$ ), while the two components perpendicular to the shock direction for the [001] shock are somewhat lower than those for the [100] case during the first 125 Å behind the shock front ( $<2.96$  ps for [100] and  $<2.9$  ps for [001]) but become noticeably higher at distances greater than 175 Å ( $>4.12$  ps for [100] and  $>4.06$  ps for [001]).

## E. 2D molecular translational disordering

The snapshots of the simulation cells in Fig. 5 show that the structures of the shocked material far behind the shock front are distinct from those near the shock front. To investigate this we calculated two-dimensional radial distribution functions (2D RDFs) for molecular centers of mass at several different postshock times using the moving-bin averaging scheme illustrated in Fig. 4. The 2D RDF is defined as

$$g(R) = \frac{\sum_i \sum_j \delta(R - r_{ij})}{N_m \rho \pi R^2 \Delta\lambda}, \quad (5)$$

where the center-of-mass to center-of-mass distance  $r_{ij}$  between molecules in a given bin is evaluated only in the directions transverse to the shock propagation (for example, the  $x$  and  $y$  Cartesian position coordinates for the [001] shock);  $R$  is the radius of a cylindrical volume centered on a given molecule, with cylinder axis parallel to the direction of shock propagation and cylinder ends defined by the planes separating fixed-volume bins at a given instant in time;  $N_m$  is the total number of molecules in a given bin at a given instant in time, as defined in Eq. (1);  $\rho$  is the instantaneous number density of a given bin; and  $\Delta\lambda$  is the bin width (2.0 Å in all cases).

The 2D RDFs of the preshock and postshock materials for [100], [010], and [001] shocks are shown in frames (a), (b), and (c), respectively, in Fig. 9. The postshock 2D RDFs for the [100] and [001] cases exhibit qualitatively similar features but distinct from those for the [010] case. Specifically, the 2D RDFs for the [100] and [001] cases exhibit considerable broadening and lower peak intensities starting almost immediately after shock passage (black curves). By 1552 and 2836 fs (these times, and corresponding distances, are represented by black dashed vertical lines in Fig. 5), respectively, for the [100] and [001] cases, the 2D RDF results have nearly converged to final values (green, blue, and cyan curves) although some minor changes can still be seen in the first peak for the [100] shock.

The results for the [100] and [001] cases are indicative of significant shock-induced *plane-specific translational disordering*. As in the case of the density (discussed in Sec. III C), translational disordering in the postshock material occurs earlier for the [100] case than for the [001] case. At times sufficiently long that the results have become essentially stable, the second peak for the [100] case is narrower as well as more sharply peaked than that for the [001] case and the ratio of height of the second peak to that of the first peak

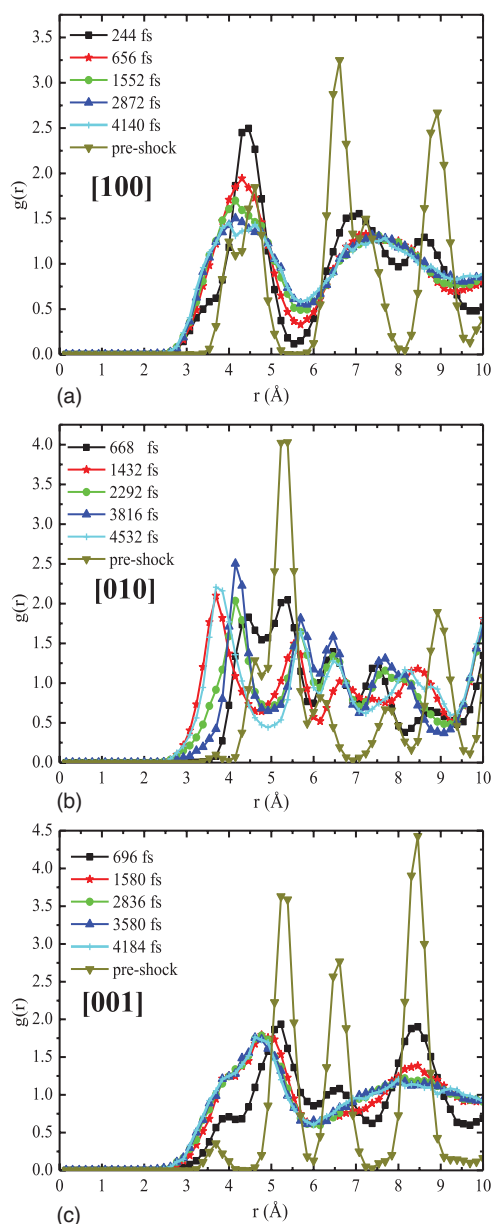


FIG. 9. 2D center-of-mass RDFs for shocks along (a) [100], (b) [010], and (c) [001].

for the [100] shock (0.89) is greater than that for the [001] case (0.68), suggesting greater disordering in the case of the [001] shock. However, in neither case is disordering complete within  $\sim 4$  ps. The RDFs for shock propagation along [010] [Fig. 9(b)] show that the shocked material remains essentially crystalline though the intensity of the peaks at long distances ( $r > 8$  Å) are decreased considerably compared to the corresponding ones in the preshock RDF (consistent with a paracrystalline structure). The fact that the peaks at postshock time  $t = 3816$  fs are higher than corresponding ones at postshock time  $t = 2292$  fs suggests that there may be a gradual annealing of the shocked material that continues for times longer than those studied here. This, in turn, is consistent with the second rise in the density observed in Fig. 6(a) about 5.4 ps (about 225 Å) behind the shock front.

## F. 2D molecular mass transport

The time-dependent two-dimensional mean-square displacement (2D MSD) was calculated as a function of post-shock time using

$$\text{MSD}(t)_i = \langle |\mathbf{R}_i(t) - \mathbf{R}_i(0)|^2 \rangle. \quad (6)$$

The instant at which the shock front reaches the layer containing a given molecule is taken as the time origin for that molecule; the center-of-mass location of that molecule at that instant is denoted  $\mathbf{R}_i(0)$  and those for subsequent times as  $\mathbf{R}_i(t)$ . The 2D MSD is defined in the usual way except that (as discussed for the RDFs in Sec. III E)  $\mathbf{R}_i$  is the projection of the 3D displacement vector into the plane of the shock front. The 2D MSD was constructed separately for each molecule and then averaged over the total number of molecules that have been in the shocked state for time  $t$ . Note that here, in contrast to the usual case for an equilibrium system, there is no averaging over time origins since shock front arrival defines a unique time origin for the subsequent transient dynamics of a given molecule.

The time-dependent 2D MSDs are shown in Fig. 10 for shocks propagating along [100] (green curve), [010] (magenta curve), and [001] (black curve). The result for [010] (magenta curve) exhibits four distinct regions: a monotonic rise at very short times ( $< 0.25$  ps), followed by a region with small slope (0.25–1 ps), followed by a region with larger, nearly constant slope (1–3 ps), followed by a region with essentially zero slope ( $t > 3$  ps). This is consistent with the (para)crystalline structure shown in Figs. 5, 6, and 9. By contrast, the 2D MSD results for the [100] and [001] shocks (green and black curves, respectively) in Fig. 10 exhibit nearly monotonic increases with time for the entire length of the simulations. They overlap with that for the [010] case for postshock times up to 0.25 ps and with each other for postshock times up to 1 ps; after which they diverge. Because the shock pressure (see Table II) and corresponding density (see Fig. 6) for these two cases are similar, we tentatively attribute the more rapid increase of the [001] 2D MSD for times greater than 1 ps to the higher kinetic energy generated in the [001] shock compared to that in the [100] case [see Fig. 7(a) and Table II]. Interestingly, for the [001] case the slope of the 2D MSD over

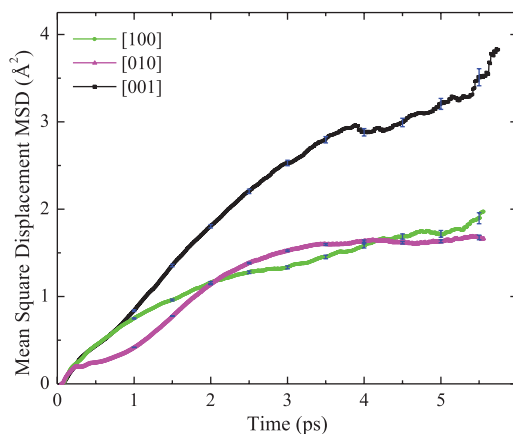


FIG. 10. 2D MSDs of molecular centers of mass vs time.

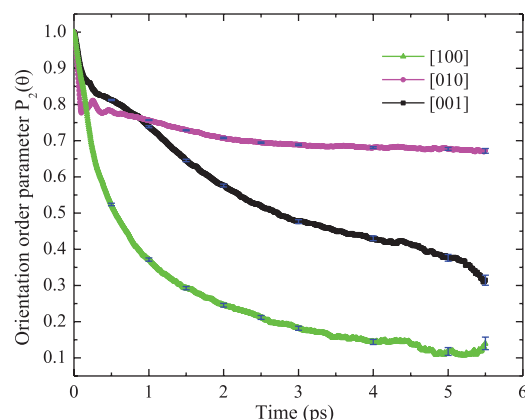


FIG. 11. Orientational order parameter  $P_2(\theta)$  for C–N bond vectors as functions of time.

the time interval 4–5 ps is a little lower than that over the 1–4 ps interval; this feature is real based on the calculated error bars.

It is important to note that the root-mean-square (rms) center-of-mass displacements after 5 ps in the shocked state are all between about 1.3 Å [100] and 1.7 Å [001]. Because these rms displacements are considerably smaller than

any reasonable estimate for the molecular diameter of nitromethane, the results do not allow us to distinguish between ballistic versus normal (albeit very slow) diffusion for the [100] and [001] shock orientations. Nevertheless, the 2D MSD results clearly exhibit a short-time relationship between translational mobility and shock wave orientation. Another possibility consistent with the observed behavior is that plane-specific translational disordering, which can be considered a form of plastic deformation, may lead to different average local molecular displacement vectors for the different shock orientations, giving rise to the observed 2D MSD behaviors.

### G. Molecular rotational relaxation

Rotational disorder in the shocked states was studied by calculating the second Legendre polynomial

$$P_2(\theta) = \left\langle \frac{1}{2}(3 \cos^2 \theta - 1) \right\rangle, \quad (7)$$

where  $\theta$  is the angle formed by the C–N bond vector in a given molecule at time  $t = 0$  and that same bond vector at some later time. The average is over all the molecules in the system, with  $t = 0$  for each molecule defined as the time when

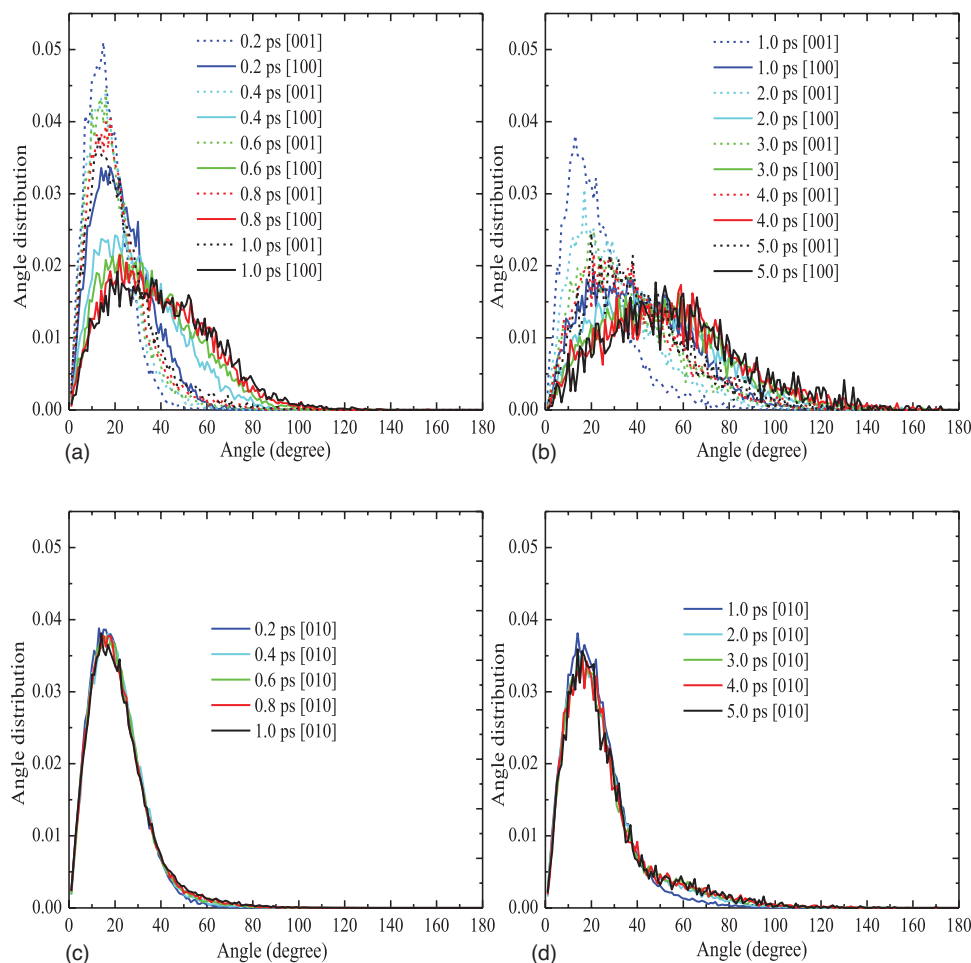


FIG. 12. Molecular rotational distribution functions. (a) Angle distribution functions for five evenly spaced times between 0.2 and 1.0 ps behind the shock front. The results for the [001] shock are shown by the dashed curves and those for [100] by the solid curves. (b) Angle distribution function for five evenly spaced times between 1.0 and 5.0 ps behind the shock front. The results for the [001] shock are shown by the dashed curves and those for [100] by the solid curves. [(c) and (d)]: Same as (a) and (b) except the results are for the [010] shock.

the shock front reaches the layer initially containing it. As for the 2D mean-square displacement, shock front arrival defines a unique time origin for a given molecule such that averaging over time origins is not appropriate. Figure 11 contains plots of  $P_2(\theta)$  versus time for each shock orientation. Green, magenta, and black curves are the results for the [100], [010], and [001] shocks, respectively. The results for the [100] and [001] shocks, in which *plane-specific translational disordering* occurs, differ considerably from each other and qualitatively from those obtained for [010]. For the [100] shock (green curve) the decay of  $P_2(\theta)$  is monotonic; at 5.5 ps after shock passage, the value of  $P_2(\theta)$  is approximately 0.15. For the [001] shock (black curve) the decay of  $P_2(\theta)$  is monotonic with inflection points during the decay at  $t \sim 0.25$  and  $t \sim 1.0$  ps. Neither of these  $P_2(\theta)$  curves is well described by a single exponential. The result for the [010] shock (magenta curve), for which a solid–solid structural rearrangement occurs, exhibits a rapid decrease of  $P_2(\theta)$  during approximately the first 0.5 ps to  $P_2(\theta) \sim 0.77$ , followed by a further slow decay between approximately 0.5 and 2.5 ps. At longer times  $P_2(\theta)$  for this case is nearly constant with a value of  $\sim 0.67$  at 5.5 ps after shock passage.

Another way to characterize the shock-induced loss of orientational order is to plot distributions of  $\theta$  for various postshock times. By definition, the distribution at the instant of shock arrival is a delta function at  $\theta = 0$ , whereas for a liquid, the distribution at times long compared to the rotational decorrelation time is a sine curve. Figure 12 contains normalized distributions of  $\theta$  for all three orientations at several postshock times, averaged over the subset of molecules from the system that have been in the shocked state for those specified amounts of time. Panels (a) and (b) of Fig. 12 contain results for both the [100] and [001] shocks and panels (c) and (d) of Fig. 12 contain results only for the [010] shock. Panels (a) and (c) show results for five instants during the first picosecond after shock arrival, while panels (b) and (d) show results for five instants between 1 and 5 ps after shock arrival. The results for the [100] shock [solid curves in panel (a)] exhibit a much broader distribution of  $\theta$  within the first picosecond after shock arrival compared to those for the [001] shock [dashed curves in panel (a)] or for the [010] shock [panel (c)]. Between 1.0 and 5.0 ps the distributions for the [100] shock [panel (b)] broaden further, particularly between 1.0 and 2.0 ps. At postshock time 1.0 ps the maximum in the distribution of  $\theta$  for [100] occurs at  $\sim 30^\circ$ , while at 5.0 ps the maximum occurs at  $\sim 50^\circ$ . The distribution at 5.0 ps reveals considerable amplitude even for angles larger than  $120^\circ$ . In the case of the [010] shock [panel (c)] the distribution changes relatively little between 0.2 and 1.0 ps; at all five instants the distribution has a maximum probability at  $\theta \sim 17^\circ$ . The main feature to note is the emergence of increasing amplitude with increasing time at relatively large angles ( $40^\circ \leq \theta \leq 80^\circ$ ). The results in panel (d) for the [010] shock for postshock times up to 5 ps are qualitatively similar: the maximum probability remains close to  $\theta = 17^\circ$ ; all five curves fall essentially on top of one another for  $\theta < 40^\circ$ , while for  $\theta > 40^\circ$  there is a noticeable increase in amplitude between 1 and 2 ps after shock arrival, after which the distributions become essentially stationary with increasing time. These results show that the orientational relaxation

in the shocked states is faster for the [100] shock than for the other cases.

#### IV. SUMMARY AND CONCLUSIONS

The anisotropic response of crystalline nitromethane initially at  $T = 200$  K subjected to shock loading to Rankine–Hugoniot shock pressures  $P_s \sim 15$  GPa has been studied using MD simulations with a nonreactive force field. Simulations were performed for shock propagation along the [100], [010], and [001] crystallographic directions. The calculated shock velocities (and therefore Rankine–Hugoniot shock pressures) for these three shock orientations are similar; there is approximately a 2% difference between the maximum and minimum values for both quantities. However, the postshock partitioning and redistribution of the energy imparted by the shock wave is strongly dependent on the shock orientation and leads to orientation-dependent structural relaxation.

Analyses of 2D radial distribution functions and 2D mean-square displacements for the [100] and [001] shocks provide evidence for shock-induced *plane-specific translational disordering* within  $\sim 6$  ps after shock passage; that is, loss of translational order in some planes but not others. A solid–solid structural reordering is observed for shock propagation along [010]. The details of disordering behavior differ for the shocks along [100] and [001]. Specifically, the onset of the loss of translational order as determined from the 2D RDF analysis occurs earlier for the [100]-oriented shock ( $< 656$  fs postshock) than that for the [001] shock ( $< 1580$  fs postshock). However, the overall disordering for the [100] shock is less complete than that for the [001] shock within the postshock time of  $\sim 6$  ps studied here. Mass transport as determined from analysis of 2D mean-square displacements in planes perpendicular to shock propagation is lower for the [100] shock than that for the [001] one. The higher molecular mobility for the [001] shock is tentatively attributed to the higher temperature accessed for that case compared to [100] because the density in the shocked states is nearly equal for the two cases. (In all cases, however, the root mean-square displacement is less than  $1.7$  Å for the  $\sim 6$  ps duration of the simulations and therefore cannot be confidently associated with the normal liquid diffusion behavior even at the high pressures of these simulations.) By contrast, the time evolution of the  $P_2(\theta)$  orientational order parameter and molecular rotation distribution functions show that the [100] case loses molecular orientational order more rapidly than the [001] case.

The results of the 2D RDF, 2-D MSD, orientational order parameter, and molecular rotation distribution function suggest that the postshock material in the [100] case relieves the shock-induced shear stresses via rapid loss of local orientational order and more gradual long-range translational disordering; whereas in the [001] case, the postshock material tends to take the opposite pathway toward the plane-specific translationally disordered state. Although the plane-specific translationally disordered shock states for the [100] and [001] cases are considerably different, neither of them has reached thermal equilibrium on the time scale of the present simulations ( $\sim 6$  ps). Plots of kinetic energies, expressed in



temperature units, among intermolecular (lattice), intramolecular (vibrational–rotational), and overall motions as a function of distance (or, equivalently, time) behind the shocks reveal that the intermolecular modes are the ones initially excited by shock passage. The intermolecular temperatures exhibit large transient excitations, by hundreds of Kelvin for subpicosecond times, for all three orientations. Excitation of the intramolecular modes occurs on a longer (multi-picosecond) time scale and occurs essentially monotonically with little or no transient excess heating of the vibrational degrees of freedom. Plots of Cartesian components of the total kinetic energy show that the motions of molecules initially are excited predominantly parallel to the shock propagation direction. While the time scales for postshock relaxation are generally consistent with previous<sup>31,32</sup> simulations for shocked nitromethane and with the predictions of energy transfer pathways and time scales as discussed recently by Hooper,<sup>15</sup> the simulation results reported here suggest a rich complexity in the mechanical relaxation—in particular the orientation-dependent plane-specific relaxations—that have only partially been explored.

## ACKNOWLEDGMENTS

We are grateful to Dr. Ali Siavosh-Haghighi for many fruitful discussions and assistance with some of the technical aspects of the calculations. This work was supported by a DOD MURI grant managed by the Army Research Office under Grant Number W911NF-05-1-0265 and by the Los Alamos National Security, LLC Laboratory Directed Research and Development program.

- <sup>1</sup>D. E. Hooks, K. J. Ramos, and A. R. Martinez, *J. Appl. Phys.* **100**, 024908 (2006).
- <sup>2</sup>J. J. Dick, D. E. Hooks, R. Menikoff, and A. R. Martinez, *J. Appl. Phys.* **96**, 374 (2004).
- <sup>3</sup>C. S. Coffey and J. Sharma, *Phys. Rev. B* **60**, 9365 (1999).
- <sup>4</sup>I. V. Schweigert and B. I. Dunlap, *J. Chem. Phys.* **130**, 244110 (2009).
- <sup>5</sup>A. Strachan, A. C. T. van Duin, D. Chakraborty, S. Dasgupta, and W. A. Goddard III, *Phys. Rev. Lett.* **91**, 098301 (2003).
- <sup>6</sup>J. Sakata and C. A. Wight, *J. Phys. Chem.* **99**, 6584 (1995).
- <sup>7</sup>V. Bouyer, I. Darbord, P. Hervé, G. Baudin, C. Le Gallic, F. Clément, and G. Chavent, *Combust. Flame*, **144**, 139 (2006).
- <sup>8</sup>R. E. Winter, S. S. Sorber, D. A. Salisbury, P. Taylor, R. Gustavsen, S. Sheffield, and R. Alcon, *Shock Waves* **15**, 89 (2006).
- <sup>9</sup>Y.-X. Zhang and S. H. Bauer, *J. Phys. Chem. B* **101**, 8717 (1997).
- <sup>10</sup>Z. A. Dreger, Y. A. Gruzdkov, and Y. M. Gupta, *J. Phys. Chem. B* **106**, 247 (2002).
- <sup>11</sup>M. Miao, Z. A. Dreger, J. E. Patterson, and Y. M. Gupta, *J. Phys. Chem. A* **112**, 7383 (2008).
- <sup>12</sup>J. E. Patterson, Z. A. Dreger, M. Miao, and Y. M. Gupta, *J. Phys. Chem. A* **112**, 7374 (2008).
- <sup>13</sup>J. Budzien, A. P. Thompson, and S. V. Zybin, *J. Phys. Chem. B* **113**, 13142 (2009).
- <sup>14</sup>W. G. Hoover and C. G. Hoover, *Phys. Rev. E* **80**, 011128 (2009).
- <sup>15</sup>J. Hooper, *J. Chem. Phys.* **132**, 014507 (2010).
- <sup>16</sup>S. Courtecuisse, *J. Chem. Phys.* **102**, 968 (1995).
- <sup>17</sup>J. M. Winey and Y. M. Gupta, *J. Phys. Chem. A* **101**, 9333 (1997).
- <sup>18</sup>D. D. Dlott, *Annu. Rev. Phys. Chem.* **50**, 251 (1999).
- <sup>19</sup>E. Jaramillo, T. D. Sewell, and A. Strachan, *Phys. Rev. B* **76**, 064112 (2007).
- <sup>20</sup>J. J. Dick, R. N. Mulford, W. J. Spencer, D. F. L. Pettit, E. Garcia, and D. C. Shaw, *J. Appl. Phys.* **70**, 3572 (1991).
- <sup>21</sup>J. J. Dick, *J. Appl. Phys.* **81**, 601 (1997).
- <sup>22</sup>C. S. Yoo, N. C. Holmes, P. C. Souers, C. J. Wu, F. H. Ree, and J. J. Dick, *J. Appl. Phys.* **88**, 70 (2000).
- <sup>23</sup>J. J. Dick, *J. Appl. Phys.* **53**, 6261 (1982).
- <sup>24</sup>J. J. Dick, *Appl. Phys. Lett.* **44**, 859 (1984).
- <sup>25</sup>J. E. Patterson, Z. A. Dreger, and Y. M. Gupta, *J. Phys. Chem. B* **111**, 10897 (2007).
- <sup>26</sup>M. J. Cawkwell and T. D. Sewell, *Phys. Rev. B* **78**, 014107 (2008).
- <sup>27</sup>D. Bedrov, J. B. Hooper, G. D. Smith, and T. D. Sewell, *J. Chem. Phys.* **131**, 034712 (2009).
- <sup>28</sup>M. J. Cawkwell, K. J. Ramos, D. E. Hooks, and T. D. Sewell, *J. Appl. Phys.* **107**, 063512 (2010).
- <sup>29</sup>K. J. Ramos, D. E. Hooks, T. D. Sewell, and M. J. Cawkwell, *J. Appl. Phys.* **108**, 066105 (2010).
- <sup>30</sup>J. J. Dick, *J. Phys. Chem.* **97**, 6193 (1993).
- <sup>31</sup>A. Siavosh-Haghighi, R. Dawes, T. D. Sewell, and D. L. Thompson, *J. Chem. Phys.* **131**, 064503 (2009).
- <sup>32</sup>R. Dawes, A. Siavosh-Haghighi, T. D. Sewell, and D. L. Thompson, *J. Chem. Phys.* **131**, 224513 (2009).
- <sup>33</sup>D. C. Sorescu, B. M. Rice, and D. L. Thompson, *J. Phys. Chem. B* **104**, 8406 (2000). There were two typographical errors in the original presentation of this force field. These are corrected in Ref. 31.
- <sup>34</sup>P. M. Agrawal, B. M. Rice, and D. L. Thompson, *J. Chem. Phys.* **119**, 9617 (2003).
- <sup>35</sup>A. Siavosh-Haghighi and D. L. Thompson, *J. Chem. Phys.* **125**, 184711 (2006).
- <sup>36</sup>A. Siavosh-Haghighi and D. L. Thompson, *J. Phys. Chem. C* **111**, 7980 (2007).
- <sup>37</sup>D. C. Sorescu, B. M. Rice, and D. L. Thompson, *J. Phys. Chem. A* **105**, 9336 (2001).
- <sup>38</sup>L. Zheng, S.-N. Luo, and D. L. Thompson, *J. Chem. Phys.* **124**, 154504 (2006).
- <sup>39</sup>A. Siavosh-Haghighi, T. D. Sewell and D. L. Thompson, *J. Chem. Phys.* **133**, 194501 (2010).
- <sup>40</sup>A. Siavosh-Haghighi, R. Dawes, T. D. Sewell, and D. L. Thompson, *J. Phys. Chem. B* **115**, 693 (2011).
- <sup>41</sup>D. T. Cromer, R. R. Ryan, and D. Schiferl, *J. Phys. Chem.* **89**, 2315 (1985).
- <sup>42</sup>S. F. Trevino, E. Prince, and C. R. Hubbard, *J. Chem. Phys.* **73**, 2996 (1980).
- <sup>43</sup>S. Nosé, *J. Chem. Phys.* **81**, 511 (1984).
- <sup>44</sup>W. G. Hoover, *Phys. Rev. A* **34**(3), 2499 (1986).
- <sup>45</sup>S. J. Plimpton, *J. Comput. Phys.* **117**, 1 (1995).
- <sup>46</sup>M. P. Allen and D. J. Tildesley, *Computer Simulation of Liquids* (Oxford University Press, Oxford, 1987).
- <sup>47</sup>S. Nosé, *Mol. Phys.* **52**, 255 (1984).
- <sup>48</sup>W. G. Hoover, *Phys. Rev. A* **31**(3), 1695 (1985).
- <sup>49</sup>S. J. Plimpton, R. Pollack, and M. Stevens, *Proceedings of the Eighth SIAM Conference on Parallel Processing for Scientific Computing*, 14–17 March 1997, Minneapolis, MN.
- <sup>50</sup>Y. B. Zel'dovich and Y. P. Raizer, *Physics of Shock Waves and High-Temperature Hydrodynamic Phenomena* (Dover, Mineola, NY, 2002).
- <sup>51</sup>R. Hosemann, G. Willmann, and B. Roessler, *Phys. Rev. A* **6**, 2243 (1972).

# Simulations of Deformation Processes in Energetic Materials

R.H.B. Bouma<sup>1</sup>, A.E.D.M. van der Heijden<sup>1</sup>,  
T.D. Sewell<sup>2</sup> and D.L. Thompson<sup>2</sup>

<sup>1</sup>*TNO Technical Sciences*

<sup>2</sup>*University of Missouri*

<sup>1</sup>*The Netherlands*

<sup>2</sup>*USA*

## 1. Introduction

The sensitivity of energetic materials has been studied extensively for more than half a century, both experimentally and numerically, due to its importance for reliable functioning of a munition and avoidance or mitigation of accidents (Bowden & Yoffe, 1952). While the shock initiation of an explosive under nominal conditions is relatively well understood from an engineering perspective, our understanding of initiation due to unintended stimuli (weak shock or fragment impact, fire, damaged explosive charge) is far less complete. As an example, one cannot exclude the ignition of an explosive due to mechanical deformation, potentially leading to low- or even high-order explosion/detonation as a consequence of mechanical stimuli with strain rates and pressures well below the shock sensitivity threshold. During the last two decades there has been an increased interest in the scientific community in understanding initiation sensitivity of energetic materials to weak insults.

A relationship between energy dissipation and rate of plastic deformation has been developed for crystalline energetic materials (Coffey & Sharma, 1999). Chemical reactions are initiated in crystalline solids when a crystal-specific threshold energy is exceeded. In this sense, initiation is linked to the rate of plastic deformation. However, practical energetic materials are usually heterogeneous composites comprised of one or more kinds of energetic crystals (the filler, for which the mass fraction can exceed 90%) bound together with a binder matrix that often consists of several different polymer, plasticizer, and stabilizer materials. Clearly, the mechanical behavior of these polymer-bonded (plastic-bonded) explosives (PBXs) is far more complicated than for neat crystals of high explosive. It is necessary in realistic constitutive modeling of energetic compositions to incorporate features reflecting the complex, multiphase, multiscale structural, dynamical, and chemical properties; see, for example, Bennett et al., 1998, and Conley & Benson, 1999. The goal in constitutive modeling is to bridge the particulate nature at the mesoscale to the mechanical properties at the macroscale.

The macroscale deformations applied to PBX composites in experiments are generally not the same as the local deformation fields in a component crystal within the composite. This has been demonstrated using grain-resolved mesoscale simulations wherein the individual grains and binder phases in a PBX are resolved within a continuum simulation framework.

Baer & Trott (2002) studied the spatial inhomogeneities in temperature and pressure that result when a shock wave passes through a sample of material. The statistical properties of the shocked state were characterized using temporal and spatial probability distribution functions of temperature, pressure, material velocity and density. The results showed that reactive waves in composite materials are distinctly different from predictions of idealized, traditional models based on singular jump state analysis.

Energy and stress localization phenomena culminating in rapid, exothermic chemistry are complex processes, particularly for shocks near the initiation threshold, for which subvolumes of material corresponding to the tails of the distribution functions of temperature and pressure are where initiation will begin. Therefore, a detailed understanding of composite energetic materials initiation requires knowledge of how thermal and mechanical energies are transferred through the various constituents and interfaces of a PBX; how the distributed energy causes structural changes associated with plasticity or phase transformations; and, when these processes (among others) lead to sufficiently high localization of energy, how and at what rate chemical reactions occur as functions of the local stress, temperature, and thermodynamic phase in the material. Each of these can in principle be studied by using molecular dynamics (MD) simulations. Distributions of field variables available from mesoscale simulations can be sampled to provide input to MD simulations; alternatively, results obtained from MD simulations can be used to guide the formulation of, and determine parameters for, improved mesoscale descriptions of the constituent materials in the PBX, for structurally perfect materials as well as ones containing various kinds of crystal lattice defects, voids, crystal surface features, and material interfaces (Kuklja & Rashkeev 2009; Sewell, 2008; Strachan et al., 2005; Shi & Brenner, 2008).

This chapter gives an overview of simulations of deformation processes in energetic materials at the macro-, meso-, and molecular scales. Both non-reactive and reactive processes are considered. Macroscale simulations are usually developed to mimic real life situations (for example, munitions performance under intended conditions or response under accident scenarios) or are used in the development of small-scale experiments designed to elucidate fundamental properties and behaviors. Because macroscale simulations lack detailed information concerning microscopic physics and chemistry, their use for predicting energetic materials initiation is generally limited to engineering applications of the types mentioned above. For many applications, however, the macroscopic treatment is sufficient to characterize and explain the deformation behavior of PBXs. At the other extreme of space and time scales, MD can be used to simulate the fine-scale details of deformation, including detailed mechanisms of phase changes, chemistry, and processes that occur at material interfaces or other spatial heterogeneities. Mesoscale simulation and theory is required to bridge the gap between these limiting cases.

The outline of the remainder of the chapter is as follows: First, the macroscopic deformation of a PBX, treated as a homogeneous material, is discussed. Specific examples are provided in which experimental data and simulation results are compared. Next, a sampling of the various approaches that can be applied for mesoscale modeling is presented. Representative simulations based on grain-resolved simulations are discussed. Finally, an overview of applications of molecular scale modeling to problems of thermal-mechanical-chemical properties prediction and understanding deformation processes on submicron scales is given, with specific references to the literature to highlight current capabilities in these areas.

## 2. Simulation of deformation at the macroscale: Plastic-bonded explosives treated as homogeneous material

The low-velocity impact vulnerability of energetic materials is typically studied by using simulations of deformations at the macroscale. For example, the engineering safety margin for acceptable crush-up limits of an encased energetic material is the most widely-used parameter in modern barrier design to prevent sympathetic detonation in ammunition storage sites. The accidental detonation of a storage module will lead to blast, ground shock, and propulsion of the barriers placed around that storage module. These accelerated barriers can impact adjacent storage modules and crush the munitions contained therein. The development of munition-specific acceptance criteria (Tancreto et al., 1994), and the comparison of double flyer-plate impact and crush-test results with simulation results (Malvar, 1994) helped advance the successful design of the so-called High Performance Magazine (Hager et al., 2000). Munitions are nowadays categorized into sensitivity groups based on robustness and sensitivity. The initiation threshold of a sensitivity group is expressed as the required kinetic energy and impulse per unit area from an impacting barrier to cause a reaction in munitions of that sensitivity group.

The concept of sensitivity groups allows for the design of other storage configurations through engineering models. One example is the simulation of barrier propulsion by the detonation of a single storage module containing 5 ton TNT equivalent of explosives, for which simulated results have been verified experimentally (Bouma et al., 2003; van Wees et al., 2004); see Fig. 1. However, design parameters related to the barrier do not describe the processes that may lead to ignition, and certainly do not help in formulating insensitive explosive compositions.

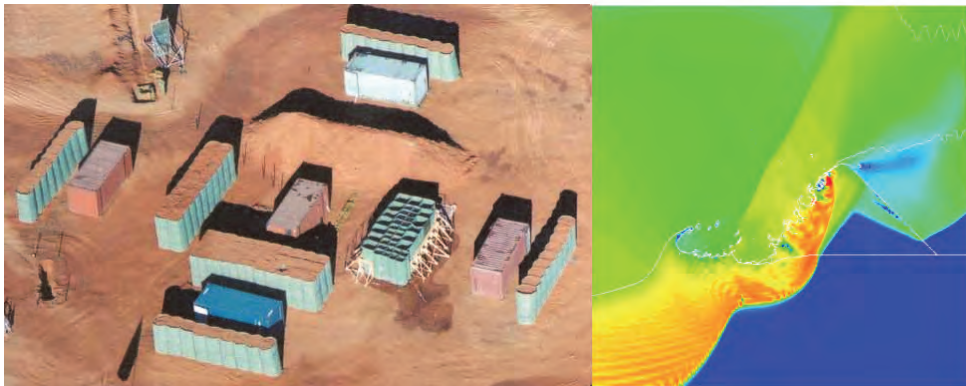


Fig. 1. Left: Experiment prior to detonation of 5 ton TNT equivalent of explosives in the central 24 ft container, which is surrounded by four different barrier designs and four munition storage modules. Right: The simulated results illustrate the pressure contours 5 ms after the detonation of 5 ton TNT equivalent of explosives, and the disintegration and movement of the trapezoid-shaped barrier in the photograph towards an adjacent storage module.

Many experimental tests, including the Susan impact test and friability test (UN, 2008), Steven impact test (Chidester et al., 1998), set-back generator (Sandusky et al., 1998), spigot intrusion (Wallace, 1994), drop-weight and projectile impact, and split Hopkinson pressure



bar (Siviour et al., 2004), study the response of a PBX under mechanical loading conditions that are specific to particular accident scenarios. Collectively, these tests span a wide range of geometric complexity and data richness. For some of them the results are expressed in relatively qualitative terms; for example, the Steven test where the severity of the mechanical insult to a stationary target with high explosive is based on the impact velocity of a projectile, and reaction violence is based on criteria such as amount of PBX recovered, damage to the target containment, and blast pressure at some distance from the location of projectile/target impact. In other tests more sophisticated experimental methods and highly instrumented diagnostics allow the detailed mechanical behavior to be inferred from the data; for example, the split Hopkinson pressure bar. In many cases simulations are required to aid in the interpretation of the data; specific examples for the split Hopkinson pressure bar, Steven impact, and LANL impact tests can be found in (Bailly et al., 2011; Gruau et al., 2009; Scammon et al., 1998).

The ballistic impact chamber is a specific drop-weight impact test designed to impose a shear deformation in a cylindrical sample of explosive (Coffey, 1995). (The name drop-weight impact test originates with the fact that the impact velocity depends on the height from which the weight is dropped onto the sample.) If a relationship between energy dissipation and rate of plastic deformation is known, the deformation rate can be used to define a mechanical initiation threshold (Coffey & Sharma, 1999). A drop-impact load impinges on the striker, which loads a cylindrical sample between the striker and an anvil (see Fig. 2) The cylinder is compressed along the cylinder axis and expands radially. The shear rate in the ballistic impact chamber is described by

$$\frac{d\gamma}{dt} \approx \frac{r_{t=0}}{h^2} \sqrt{\frac{h_{t=0}}{h}} \frac{dh}{dt} \quad (1)$$

with  $r$  and  $h$  the radius and the height of the sample, respectively,  $\gamma$  the shear, and  $t$  the time. The shear rate is largest near the perimeter of the cylinder. Initiation is detected by photodiodes. Knowing the striker velocity  $dh/dt$  and the time of initiation, the required shear rate for initiation  $d\gamma/dt$  can be calculated. Measured shear rate thresholds are given by Namkung & Coffey (2001).

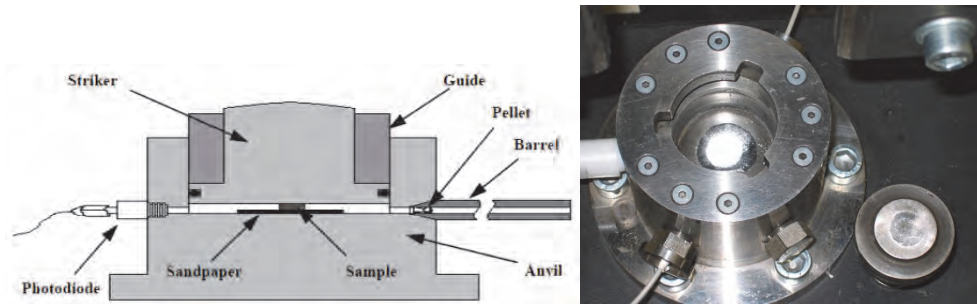


Fig. 2. Left: Schematic cross section of the ballistic impact chamber. Right: Top view of the chamber. The sample can be seen in the center of the chamber. Attached to the side are two fiber optic cables and a pressure transducer. The striker is located to the right of the chamber assembly.

The deformation of energetic materials in the ballistic impact chamber according to equation 1 has been verified by simulations of a cylindrical sample of PBXN-109 (64 wt% cyclotrimethylene trinitramine, 20 wt% aluminium and 16 wt% polybutadiene-based binder), 6.35 mm in diameter and 1.75 mm in height (Meuken et al., 2006). In this example, the drop weight had an impact velocity of 3 m·s<sup>-1</sup>, and the striker achieved an initial velocity of  $\approx 6$  m·s<sup>-1</sup> due to elastic collision. The simulation was carried out using the ANSYS Autodyn software suite, a versatile explicit analysis tool for modeling the nonlinear dynamics of solids, fluids, gases and interactions among them. (Autodyn provides, for example, finite element solvers for computational structural dynamics and mesh-free particle solvers for high velocities, large deformation and fragmentation (Autodyn, Birnbaum et al., 1987).) The resulting shear rate in PBXN-109 as a function of time is shown in the right-hand panel of Fig. 3. The maximum shear rate of approximately  $8 \times 10^5$  s<sup>-1</sup> is reached shortly before the end of the negative acceleration of the striker, at a radial distance about 70% of the sample radius (Bouma et al., 2007). The shear rate values from equation 1 and the Autodyn simulation are comparable, except the rise in shear rate in the simulation occurs at a longer time since impact. The deformation is complex – there are small oscillations visible in Fig. 3 due to the shock and reflection waves that travel through the striker and anvil. Evaluation of the shear sensitivity according to equation 1 is non-trivial, and simulations are key to interpreting this “simple” cylindrical compression experiment. The analysis requires that the sample not resist compression by the striker prior to initiation and that an accurate value of the striker velocity is known. In the example discussed here the first requirement is satisfied so long as the time to reaction is less than 90% of the original sample height divided by twice the drop weight velocity at the moment of impact. The experimentally determined shear initiation threshold in the ballistic impact chamber of PBXN-109 is  $1.7 \times 10^5$ – $2.0 \times 10^5$  s<sup>-1</sup>. A simulation that approximates the experimental conditions and which includes chemical reaction yields an ignition time of 180  $\mu$ s. The chemical reaction model used in the simulation is limited to an Arrhenius-type ignition term; a more sophisticated treatment of chemistry that includes, for instance, the Lee-Tarver (Lee & Tarver, 1980) growth term has not been performed (Zerilli et al., 2002).

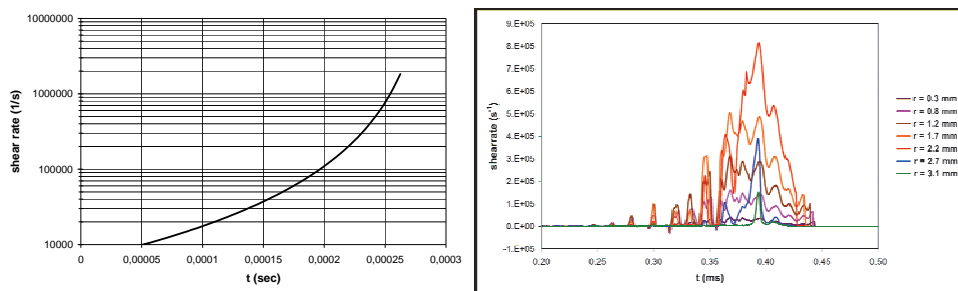


Fig. 3. Left: Shear rate vs. time, calculated using equation 1. The deformation starts at  $t = 0$  and is monitored until the height of the sample is equal to 10% of the initial height. Right: Same as the left-hand panel except the result is obtained from an Autodyn simulation. Results in the right-hand panel are shown for points near the sample-anvil interface and originally located at radial distances  $r = 0.3, 0.8, 1.2, 1.7, 2.2, 2.7$ , and  $3.1$  mm from the center of the sample; deformation of the sample starts at  $t = 0.07$  ms.

The shear-rate threshold just discussed should also apply to other experimental configurations. For example, PBXN-109 has been subjected to an explosion-driven deformation (Meuken et al., 2006). Steel cylinders were filled with PBXN-109 and a layer of 3.0, 4.0, or 5.0 mm plastic explosive, covering one-third of the circumference of the steel cylinder, was detonated; the results are shown in Fig. 4. In the 3-mm layer case the PBXN-109 was slightly extruded from the deformed steel cylinder without any sign of reaction. In the 4-mm layer case there was a mild reaction, as shown by the slightly expanded steel cylinder. In the 5-mm layer case a violent reaction of the PBXN-109 was observed, resulting in fragmentation of the steel cylinder.

Figure 5 shows the 2-D simulation set-up of the deformation experiment (left panel); as well as the shear rate (right panel) in the PBXN-109, calculated close to the inner surface of the steel cylinder as a function of the angle (where angle  $\theta=0^\circ$  corresponds to the center of the deformation layer). The maximum shock pressure is  $\approx 0.5$  GPa, which is well below the 2.2–5.2 GPa initiation pressure of PBXN-109 in the large scale gap test (Doherty & Watt, 2008). The maximum shear rates in Fig. 5 are  $0.72 \times 10^5$ ,  $1.19 \times 10^5$ , and  $1.51 \times 10^5$  s<sup>-1</sup>, respectively, for the 3-, 4-, and 5-mm layer experiments. The initiation threshold in this deformation test resembles the threshold in the ballistic impact chamber.

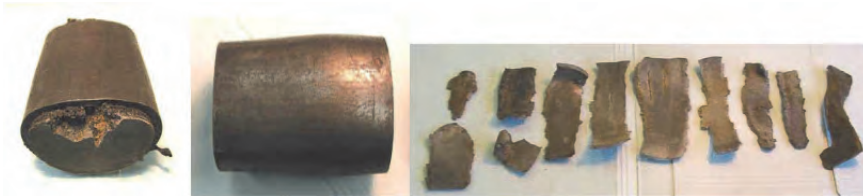


Fig. 4. Explosion-driven deformation of steel-cased PBXN-109 charges. The deformation results from the detonation of a layer of plastic explosive that partially surrounds the PBXN-109 charges (see Fig. 5). Results are shown for plastic explosive layer thicknesses of 3 mm (left), 4 mm (middle) and 5 mm (right).

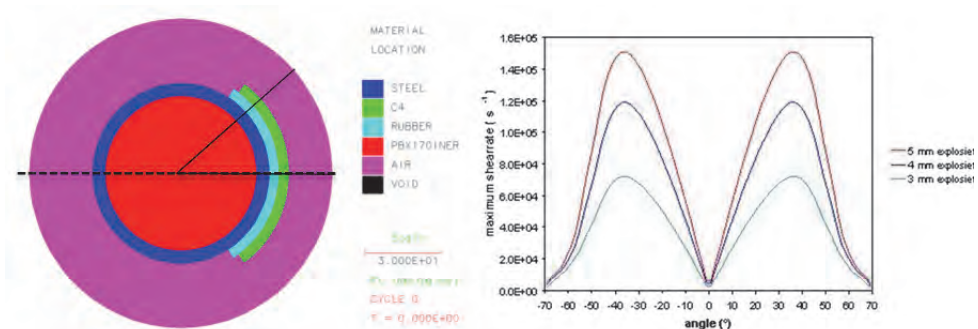


Fig. 5. Left: Schematic configuration for 2-D Autodyn simulation of an explosive deformation test. Right: Maximum shear rates in PBXN-109 as functions of the angle  $\theta$  when deformed by explosive layers of thickness 3 mm (green), 4 mm (blue), and 5 mm (red).

The maximum shear rate depends on the test configuration. The friability test (UN, 2008) and the LANL impact test (Bennett et al., 1998) have been simulated for the explosive PBXN-109, and the Steven impact test (Vandersall et al., 2006) for explosive composition C4, to correlate the severity of mechanical deformation to initiation of the explosive, see table 1 (Bouma & Meuken, 2004). Permanent deformation and extensive fracturing of the PBX in the friability test, in which a flat-ended cylindrical projectile is fired into a rigid steel target, are evident in Fig. 6 (left-hand panel, from Bouma, 1999) as well as the simulated evolution of shear rate (right-hand panel). The largest calculated shear rate,  $\sim 0.45 \times 10^5 \text{ s}^{-1}$ , occurs near the edges of the  $\varnothing 18 \text{ mm}$  sample. The experimental result in the left-hand panel of Fig. 6 shows that this rate is too low to cause initiation; this is qualitatively consistent with the threshold maximum shear rates discussed in connection with Figs. 3-5. The extensive fracture of the material, which is deliberately induced in this test, has not been modeled.



Fig. 6. Left: Permanent deformation and fracture of a PBX containing 80% HMX at 91, 110, 121, and 154  $\text{m}\cdot\text{s}^{-1}$  impact velocity in a friability test. Right: The evolution of shear rate at various radial distances from the sample in the friability test and near the explosive/steel interface for PBXN-109 at 150  $\text{m}\cdot\text{s}^{-1}$  impact velocity. The maximum shear rate develops near the outer radius.

The Steven impact test has been simulated near the experimental initiation thresholds for explosives PBX 9404 and PBX 9501, respectively 31-34  $\text{m}\cdot\text{s}^{-1}$  and 39-54  $\text{m}\cdot\text{s}^{-1}$  (Chidester et al., 1998). Again, the calculated shear rates of  $\approx 10^5 \text{ s}^{-1}$  confirm experimental initiation thresholds. Note that the experimental threshold for C4 is an impact velocity of more than 195  $\text{m}\cdot\text{s}^{-1}$  (Vandersall et al., 2006), resulting in a shear rate of at least  $1.8 \times 10^5 \text{ s}^{-1}$ . In the LANL impact test a pusher impacts a thin rectangular slab of explosive of the same thickness (Bennett et al., 1998). The violence of reaction depends on the diameter and shape of the pusher (result not shown). The calculated peak shear rate of  $16 \times 10^5 \text{ s}^{-1}$  is large but is very localized, within 1 mm of the edge of the  $\varnothing 10 \text{ mm}$  pusher, and has duration  $< 1 \mu\text{s}$ .

An analytical model has been developed that links mechanical properties and particle sizes with the thermal ignition of an explosive. This micro-structural model (Browning, 1995) is based on 1) Hertz contact stress between two particles of the same diameter in relation to the applied normal pressure, 2) mechanical work due to sliding motion under a normal pressure, and 3) thermo-chemical decomposition due to an applied and local heat flux (the latter originating from the mechanical work in the Hertzian contact points). The ignition criterion in the model requires the evaluation of the pressure and the shear rate at the macroscale (Browning, 1995; Gruau et al., 2009; Scammon et al., 1998). Scammon et al. (1998) evaluate the parameter

$$p^{2/3} \left( \frac{dy}{dt} \right)_{\max}^{1.27} t_{\text{ign}}^{1/4} \quad (2)$$



Configuration, explosive	Test specifics	Shear rate / $s^{-1}$	Experimental observation
Explosion driven deformation, PBXN-109	3 mm deformation layer 4 mm deformation layer 5 mm deformation layer	Max. $0.72 \times 10^5$ Max. $1.19 \times 10^5$ Max. $1.51 \times 10^5$	No reaction Burn Violent reaction
Ballistic Impact Chamber, PBXN-109		$1.7 \times 10^5$ - $2.0 \times 10^5$ at initiation	Initiation
Friability test, PBXN-109	18 mm $\varnothing$ , 9 gram, 150 $m \cdot s^{-1}$ impact velocity	Max. $0.4 \times 10^5$ - $0.5 \times 10^5$	No reaction
LANL impact test, PBXN-109	10 mm blunt steel pusher at 196 $m \cdot s^{-1}$ into 25 mm $\times$ 20 mm sample	Max. $16 \times 10^5$	Not available
Steven impact test, C4	50 $m \cdot s^{-1}$ impact velocity 100 $m \cdot s^{-1}$ impact velocity 157-195 $m \cdot s^{-1}$ impact velocity	Max. $0.5 \times 10^5$ Max. $1.8 \times 10^5$	No reaction

Table 1. Comparison of shear rates calculated in simulation of various test configurations of PBXN-109 and explosive composition C4 to experimental results.

with time to ignition  $t_{ign}$ , assuming that pressure  $p$  and shear rate  $d\gamma/dt$  are constant. Ignition is associated with the parameter exceeding an explosive-specific value. The underlying thermo-chemical model has been analyzed in detail for HMX only. However, equation 2 (or the corresponding expression for variable pressure and shear strain rate loading histories (Browning & Scammon, 2001; Gruau et al., 2009)), may not be directly applicable to non-HMX PBXs. The thermo-chemical decomposition in the above model requires a thermo-chemical simulation of the ignition time as a function of thermal energy fluence through a crystal-crystal contact surface area, and involves explosive-specific decomposition chemistry that can be measured, for example, in a one-dimensional time-to-explosion (ODTX) test (Hsu et al., 2010). This may lead to different exponents in eq. 2 for non-HMX PBXs.

As shown in this section, a macroscopic treatment is generally sufficient to characterize and explain the deformation behavior of PBXs. However, since macroscopic models treat the PBX as a homogeneous material, their use for predicting energetic materials initiation is rather limited. As a first step to a more detailed description of the deformation and initiation behavior of energetic materials, mesoscale simulations can be performed that include the influence of the particulate nature of PBX formulations.

### 3. Simulation of deformation at the mesoscale: The influence of particulate nature of plastic-bonded explosives

The influence of the particulate nature at the mesoscale can be accounted for in different ways. One can 1) fit a continuum model with particle-specific features to experimental data; 2) simulate the mechanical behavior of a representative volume element with the mechanical

properties of its constituents and determine the collective mechanical behavior; or, 3) when sufficient computer resources are available, simulate the mechanical behavior with spatially resolved explosive grains and binder.

An example of the first approach is based on the statistical crack mechanics model (Dienes, 1985) in combination with a five-component Maxwell visco-elasticity model, fitting the parameters to experimental Young's moduli spanning eight orders of magnitude of relaxation times (Bennett et al., 1998). Constitutive equations are obtained for implementation into the DYNA3D nonlinear, explicit finite element code for solid and structural mechanics (DYNA3D). An example of the second approach is the construction of a continuum constitutive model based on homogenization procedures applied to realistic 2-D or 3-D representative volume element microstructures obtained, for instance, from digital images of cross sections (De & Macri, 2006) or X-ray microtomography (Bardenhagen et al., 2006) of a PBX. An example of the third approach is the direct simulation at the mesoscale of the propagation of a shock wave through randomly packed crystal ensembles (Baer & Trott, 2002). Probabilistic distribution functions of wave field variables such as pressure, density, particle velocity, chemical composition, and temperature are studied to gain insight into the initiation and growth of reactions in heterogeneous materials. For additional studies of grain-resolved systems see Baer (2002), Reaugh (2002), and Handley (2011); the latter is a recent Ph.D. dissertation that includes a thorough review of mesoscale simulations and theory applied to PBXs.

During mechanical deformation of a PBX interfacial de-bonding can occur and crystals may even crack. Figure 7 contains a scanning electron micrograph of HMX crystals in a hydroxy-terminated-polybutadiene binder. A cylindrical sample of this explosive, 9 grams in weight and 18 mm in diameter, has been impacted at  $92 \text{ m}\cdot\text{s}^{-1}$  against a steel plate. The micrograph corresponds to a section near the impact site in the friability test and demonstrates interfacial de-bonding as well as crystal cracking (Scholtes et al., 2002). These phenomena can also be simulated. Figure 8 gives the principal stress in uniaxial compression of PBX 9501 at 2% overall strain. The computational model is  $0.465 \text{ mm} \times 0.495 \text{ mm}$  and contains 25 particles. De-bonding occurs when the work applied perpendicular or tangential to an interface exceeds the normal or shear cohesive energy, respectively. The cohesive energies used to generate the left- and right-hand panels of Fig. 8 are, respectively, below and above the experimentally derived values. The extent of interfacial de-bonding decreases with increasing cohesive energy between the particle and binder phases. The increase in cohesive energy results in a large stress localization within crystals, which increases the probability for cracks to develop within the crystal (Yan-Qing & Feng-Lei, 2009). Note that the peak shear rates in the impact experiment of Fig. 7 are of the order of  $10^3 \text{ s}^{-1}$ , whereas the simulation results shown in Fig. 8 are for a strain rate of  $1.2 \times 10^{-3} \text{ s}^{-1}$ .

The particulate nature of most energetic materials and the imperfection of the component crystals (for example, grain boundaries, seeding crystals, voids, cracks, lattice defects, solvent inclusions) not only influence the deformation behaviour of the PBX but also the sensitivity to shock (Doherty & Watt, 2008; van der Heijden & Bouma, 2004a, 2004b, 2010). Examples of imperfections are shown in Figs. 9 and 10. On the left is an optical micrograph of a cross section of an RDX crystal. The crystal outer surface is irregular, grains have grown into each other, and there are multiple defects with sizes of the order of  $10 \text{ }\mu\text{m}$ . On the right a scanning electron micrograph of the cross section of an RDX crystal from the same lot (RDX type II obtained from Dyno) is shown. At this magnification, one can see voids with

sizes on the order of hundreds of nm, as well as a string of voids extending vertically across the image; note that this latter structure is not a grain boundary. Fig. 10 shows two confocal scanning laser micrographs with a Dyno Type II RDX crystal at the left and a BAe Royal Ordnance RDX crystal at the right. By using a confocal scanning laser microscope in reflection mode it is possible to make optical slices from a transparent object down to a thickness of about 0.5  $\mu\text{m}$ . In this way, local differences in the refractive index inside a crystal will be revealed as bright spots on a dark background. The images are recorded with a Leica TCS SL confocal system using a DM6000 B microscope equipped with a 40X objective, zoom factor setting of 2. The spots indicate locations with a different refractive index from the surrounding area and correspond most likely to small inclusions present in the crystal. Also of interest are the “diffuse” areas within the crystals in the left-hand panel of Fig. 10. The differences in spot density for the two RDX lots obtained from different producers are assumed to be correlated with the difference in mechanical sensitivity (Thompson et al., 2010) and shock sensitivity (Doherty & Watt, 2008).

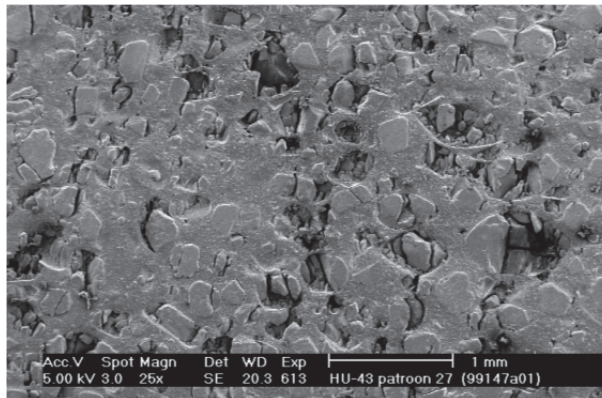


Fig. 7. Interfacial debonding and crystal cracking in a friability test (Scholtes et al., 2002).

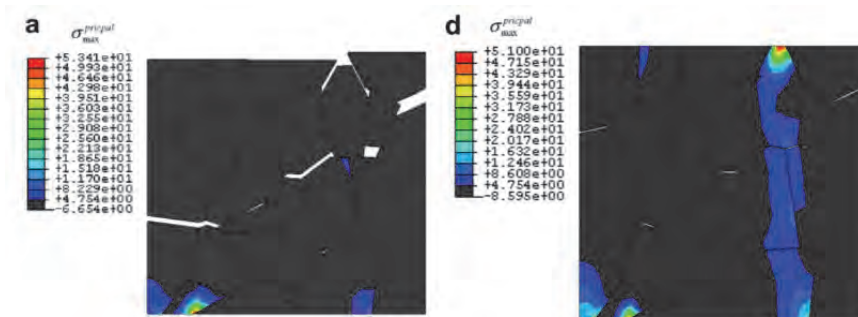


Fig. 8. Maximum principal stress in uniaxial compression of PBX 9501 (Reprinted from Yan-Qing & Feng-Lei, 2009, © 2008, with permission from Elsevier). The two simulations are identical except that the particle/binder cohesive energy used to generate the right-hand panel is four times that used to generate the left-hand panel.

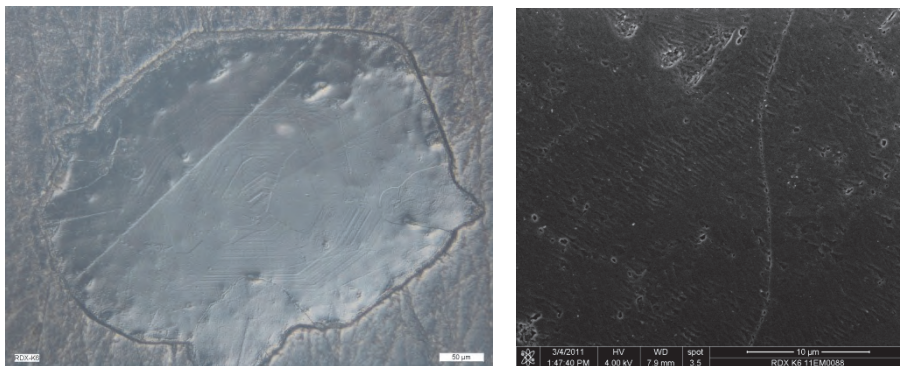


Fig. 9. Optical micrograph (left) and scanning electron micrograph (right) of a cross-section of a crystal of Dyno type II RDX (Thompson et al., 2010).

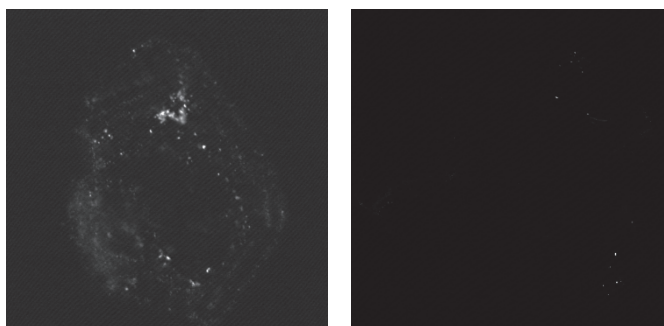


Fig. 10. Confocal scanning laser micrographs for two different qualities of RDX crystals, produced at a focal plane below the surface. Left:  $93.5\ \mu\text{m} \times 93.5\ \mu\text{m}$  image of Dyno type II RDX. Right: a  $375\ \mu\text{m} \times 375\ \mu\text{m}$  image of BAe Royal Ordnance RDX (Thompson et al., 2010).

Ideally, a simulation at the meso- or molecular-scale should incorporate microstructural features such as grain boundaries, packing of particles, defects, and voids. A new method to create a computational set-up with a random pack of arbitrary shapes of particles has been applied to “typical” HMX crystals by Stafford & Jackson (2010). Armstrong (2009) has reviewed dislocation mechanics modeling of energetic materials. The review covers experimental mechanics studied through indentation-hardness properties, impact properties in various test geometries, and granular compaction. The thermal dissipation of energy is associated with individual dislocation motions, which may induce a strong adiabatic heating through dislocation pile-up avalanches. Lei and Koslowski (2010) have published a phase field dislocation dynamics model for low-symmetry organic crystals. Using only information about the crystallography and elastic constants they were able to predict the onset of plastic deformation in sucrose and paracetamol. (Although these are not energetic materials, the fundamental physics and materials science developed by Lei and Koslowski would apply equally well to energetic crystals.) Lei and Koslowski identified several properties that could be provided from atomic-scale simulations. The use of MD simulations as a means of providing input to, or guiding the formulation of, mesoscale models will be discussed in the next section.



#### 4. Simulation of deformation at the molecular scale: Structural changes and chemical reactions near lattice defects, voids, and interfaces

Atomic-level simulation methods – MD and Monte Carlo (MC) – in which individual atoms or chemical functional groups are treated explicitly can be used to understand and predict the equilibrium and dynamic properties of energetic crystals, binders, and interfaces between them. In MD a set of classical (e.g., Newton's) equations of motion are solved in terms of the interatomic forces, possibly with additional terms corresponding to coupling of the system to an external thermostat (Hoover, 1985; Nosé, 1984), barostat (Martyna et al., 1996; Parrinello et al., 1981), or other constraint such as to sample a Hugoniot state of a material (Maillet & Stoltz, 2008; Ravelo et al., 2004; Reed et al., 2003) to confine the simulation to a particular ensemble, leading to a trajectory (time history) of particle positions and momenta from which physical properties can be calculated in terms of appropriate statistical averages or time correlation functions (Tuckerman, 2010). The interatomic forces required for MD can be obtained from a parameterized empirical force field or from electronic structure calculations wherein the forces are obtained directly from the instantaneous electronic wave function of the system.

Monte Carlo sampling of configuration space is usually performed using a random walk based on a Markov chain constructed to satisfy microscopic reversibility and detail balance in an appropriate statistical ensemble. (See, for example: Frenkel & Smit, 2002; Wood, 1968.) Because the sequence of states in a Markov chain does not comprise a dynamical trajectory, only properties that can be expressed as averages of some microscopic function of configuration in phase space that does not explicitly involve the time can be computed. Metropolis MC (Metropolis et al., 1953), the version of MC most frequently used in molecular simulations, does not require evaluation of forces but rather only differences in potential energy between adjacent states (configurations) sampled by the Markov chain. Although in many cases MC and MD can be used equally effectively, in practice Monte Carlo is not used as widely as MD in simulations of energetic materials; therefore here we focus on MD.

Electronic structure calculations are sometimes used to study the structures, energies, charge distributions and higher multipole moments, spectroscopy, and reaction pathways. These properties can be calculated for isolated molecules, clusters, or periodic structures, usually at zero Kelvin; however, the effects of finite temperature can be incorporated, for example, by using the quasi-harmonic approximation (for example, Zerilli & Kukla, 2007), explicitly from MD trajectories, (Manaa et al., 2009; Tuckerman & Klein, 1998) or using an appropriate MC sampling scheme (Coe et al., 2009a, 2009b). Most practical electronic structure calculations for energetic materials are performed using methods based on the Kohn-Sham density functional theory (DFT) (Koch & Holthausen, 2001), although *ab initio* methods are used in some cases (Molt et al., 2011).

The advantage of atomic-level simulation methods is the detailed information they can provide. For instance, a MD simulation provides the time histories of the phase space coordinates along a trajectory, from which any classical property of the system, including detailed reaction chemistry can, in principle, be computed. The main obstacle to the use of atomic methods in practical multi-scale simulation frameworks is the small spatiotemporal scales that can be studied – approximately tens of millions of atoms for time scales of nanoseconds or less – and the requirement, at least for accurate studies rather than ones designed to examine basic qualitative features of the material response, to have a reliable description of the inter-atomic forces within the given thermodynamic regime of interest.

(While the development of parallel, linear scaling algorithms for electronic structure studies of condensed phase systems has considerably increased the numbers of atoms that can be studied (see, for example, Bock et al., 2011; Kresse et al., 2011), system sizes and simulation times tractable based on electronic structure theory calculations are far smaller than those using analytical force fields.) A more fundamental question in the case of MD or MC simulations is that of the applicability of classical statistical mechanics or dynamics for the study of molecular phenomena.

In the following we discuss ways by which atomic-scale information can be incorporated within a multiscale simulation framework, providing specific examples relevant to energetic materials. The focus of most MD simulations of energetic materials has been on predicting physical properties in the absence of chemistry. A major (and ongoing) hurdle to reliably treating complex chemistry in MD simulations is the difficulty of describing the forces for the variety of electronic structures that would be explored at the high temperatures and pressures corresponding to the von Neumann spike or Chapman-Jouguet state of a detonating explosive. Currently, the methods to do this are plane-wave DFT or parameterized analytic representations such as the ReaxFF (van Duin et al., 2001; Strachan et al., 2005) or AIREBO (Stuart et al., 2000; Liu & Stuart, 2007) force fields. Han et al. (2011) have recently published simulations of the thermal decomposition of condensed phase nitromethane studied using ReaxFF.

In general, there are two approaches to the multiscale problem. The arguably simpler approach is a sequential (or “handshaking”) one in which specific physical properties required in mesoscale or macroscopic simulations – for example, thermal, transport, or mechanical properties – are calculated as functions of temperature and pressure and used directly in the larger-scale simulations. Assuming the validity of classical mechanics, the major challenge to obtaining reliable predictions for such quantities is the need to realistically account for defect structures that can be of sizes that exceed the limited MD spatiotemporal scales. Reliable predictions of properties or structures of rate-dependent materials or ones with extended interfaces are also difficult to model due to the large time and space scales associated with them; for example, binders in energetic materials are usually based on polymers (often with other additives such as plasticizers or stabilizers) that exhibit both viscoelastic behavior and in some cases complex microphase-segregated morphologies and non-negligible concentration gradients in the neighborhood of interfaces. Such simulations are quite challenging within a MD framework; see, for example, Jaidann et al. (2009). Nevertheless, in some instances it is possible to regard MD predictions as comprising bounding cases (for example, limit of perfect crystals). Moreover, for many properties of interest experimental data either do not exist for conditions away from room temperature/atmospheric pressure or have large apparent uncertainties based on disparate results obtained for a given property using different experimental techniques. In such instances the results of atomic simulations can be used to extend the intervals over which needed parameter values can be estimated or to discriminate among inconsistent data sets.

Examples are included in Table 2, which includes the results of various measurements or calculations of the second-order elastic tensors for PETN,  $\alpha$ -RDX, and  $\beta$ -HMX; and Table 3 which contains the pressure and temperature dependence of the bulk and shear moduli of crystalline TATB for the Reuss (uniform stress) and Voigt (uniform strain) bounds. Note the wide variation in some of the experimentally determined values, particularly for RDX and HMX. In each case, the MD results – based on force fields that were not parameterized using elasticity data – yield predictions in good agreement with the most recent, and presumably most accurate, experimental data based on impulsive stimulated thermal scattering.

A difficulty with direct application of sequential approaches is that, even if a given property appears in a mesoscopic theory and can be calculated directly and accurately using atomic methods, possibly including temperature and pressure dependencies, use of those accurate property values which are treated as adjustable parameters in mesoscale simulations may lead initially to decreased predictive capability compared to experimental results; that is, an improved subgrid model or more accurate physically-based parameter specification may disrupt the overall calibration of the mesoscale model.

The other general approach to multiscale simulation of energetic materials is the concurrent method in which two different levels of material description are included simultaneously within a single simulation domain. One example where such an approach would be useful is grain-resolved mesoscale simulations wherein regions of atomically resolved material are contained within a larger volume of material treated using continuum mechanics. Such an approach would be particularly useful for mesoscopic studies of the effects of intra-crystal defects (dislocations, grain boundaries, voids) or intermaterial interfaces (crystal-binder, High Explosive (HE)-metal) where localization of temperature, stress, or microscopic strain rate might be large leading to large gradients in the material (often called *hot spots*) wherein chemical reactions are likely to occur. In addition to theoretical difficulties with formulating a single simulation method in which particles and continuum regions are treated seamlessly, concurrent methods are difficult to implement due to the high degree of time sub-cycling required given the large difference between the time step in a MD simulation ( $\sim 0.01$ -1 fs) compared to the time step in even a high resolution mesoscale simulation ( $\sim 0.1$  ns). Other possibilities for progress based on concurrent approaches include using different levels of description (and, tacitly assumed, different accuracies of forces) within a single MD computational domain; for example, use within a limited region such as the neighborhood of an interface of a force description based on electronic structure or empirically-calibrated force fields that include chemical reaction surrounded by a (typically much larger) region of material represented by a less accurate but computationally cheaper model (for instance one with fixed intramolecular connectivity that does not treat chemical reaction). Applications of the *computational materials design facility* (for example, Jaramillo-Botero et al., 2011 and references therein) illustrate the potential of such methods.

Another approach to extending the space and time scales accessible to molecularly-detailed methods that has been used with increasing frequency is particle-based coarse-graining in which chemical functional groups or entire molecules or collections of molecules are treated as effective particles, with corresponding effective potentials. As an example, Desbiens et al. (2007, 2009) have developed a model for nitromethane in which the four atoms of the methyl group are treated as a single particle. This simplified model has been parameterized using a MC optimization approach, and shown to yield good agreement with several measured quantities, including second shock temperatures. Gee and co-workers (Gee et al., 2006; Lin et al., 2007) have developed a coarse-grained description for PETN in which individual PETN molecules are represented by a five-bead model (nominally the tetramethyl carbon and the four nitrate pendent groups) (Gee et al., 2006), and have used this model to study surface diffusion of PETN molecules on different PETN crystal faces (Lin et al., 2007). Izvekov et al. (2010) have developed a formalism for systematic coarse-graining of molecular materials and applied it to nitromethane; both a one-site model, in which the molecules are treated as single particles, and a two-site model, in which the methyl group and nitro groups are treated as distinct particles, were developed. The approach, which is based on a systematic calibration of effective coarse-grained particle-particle interactions using potential-of-mean-force calculations for fully atomic systems, was shown in the case of a density-dependent potential

formulation to reproduce the nitromethane liquid structure and shock Hugoniot locus. Lynch et al. (2008) have developed a simplified model for  $\alpha$ -HMX in which individual molecules are treated as single particles; a novel aspect of this reduced dimensionality “mesodynamics” (Strachan & Holian, 2005) potential function is that it includes the effects of intramolecular vibrational degrees of freedom through incorporation of implicit degrees of freedom. The model, which is only intended to provide a schematic representation of HMX, has been used to study spall behavior in the shocked crystals. With all coarse-graining or multiscale methods, a key requirement is to capture the dominant features of the physics at the finer scale when passing from one scale to the next larger one, and to minimize the amount of non-essential information that is carried along. The specific requirements will vary depending on the material type, the thermodynamic and mechanical loading regime of interest, and the fidelity of the higher-scale model in which the finer-scale results are to be used.

	C <sub>11</sub>		C <sub>33</sub>	C <sub>44</sub>		C <sub>66</sub>	C <sub>12</sub>	C <sub>13</sub>					
<b>PETN</b>													
Ultrasonics <sup>a</sup>	17.22		12.17	5.04		3.95	5.44	7.99					
ISTS <sup>b</sup>	17.12		12.18	5.03		3.81	6.06	7.98					
MD/MC <sup>c</sup>	17.6		10.5	4.66		4.92	4.7	6.65					
	C <sub>11</sub>	C <sub>22</sub>	C <sub>33</sub>	C <sub>44</sub>	C <sub>55</sub>	C <sub>66</sub>	C <sub>12</sub>	C <sub>13</sub>	C <sub>23</sub>				
<b>RDX</b>													
MC <sup>d</sup>	26.9	24.1	17.7	8.4	5.3	7.6	6.27	5.68	6.32				
Ultrasonics <sup>e</sup>	25.02	19.6	17.93	5.17	4.07	6.91	8.2	5.8	5.9				
Brillouin <sup>f</sup>	36.67	25.67	21.64	11.99	2.72	7.68	1.38	1.67	9.17				
RUS <sup>g</sup>	25.6	21.3	19.0	5.38	4.27	7.27	8.67	5.72	6.4				
ISTS <sup>b</sup>	25.15	20.08	18.21	5.26	4.06	7.10	8.23	5.94	5.94				
Energy Minimized <sup>h</sup>	25.0	23.8	23.4	3.1	7.7	5.2	10.6	7.6	8.8				
	C <sub>11</sub>	C <sub>22</sub>	C <sub>33</sub>	C <sub>44</sub>	C <sub>55</sub>	C <sub>66</sub>	C <sub>12</sub>	C <sub>13</sub>	C <sub>23</sub>	C <sub>15</sub>	C <sub>25</sub>	C <sub>35</sub>	C <sub>46</sub>
<b><math>\beta</math>-HMX</b>													
ISLS <sup>i</sup>	20.8	---	18.5	---	6.1	---	---	12.5	---	-0.5	---	1.9	---
Brillouin <sup>j</sup>	18.41	14.41	12.44	4.77	4.77	4.46	6.37	10.50	6.42	-1.10	0.83	1.08	2.75
ISTS <sup>k</sup>	20.58	19.69	18.24	9.92	7.69	10.67	9.65	9.75	12.93	-0.61	4.89	1.57	4.42
MD/MC <sup>l</sup>	22.2	23.9	23.4	9.2	11.1	10.1	9.6	13.2	13.0	-0.1	4.7	1.6	2.5

a. Winey & Gupta, 2001.

b. Sun et al., 2008. ISTS: Impulsive stimulated thermal scattering.

c. Borodin et al., 2008. Composite MD/MC simulations using flexible molecules.

d. Sewell and Bennett, 2000. MC simulations using rigid molecules.

e. Haussuhl, 2001. The crystal axes used in the original publication have been transformed to coincide with that used here.

f. Haycraft et al., 2006.

g. Schwarz et al., 2006. RUS: Resonant ultrasound spectroscopy.

h. Munday et al., 2011. Molecular mechanics using flexible molecules.

i. Zaug, 1998. Partial determination. ISLS: Impulsive stimulated light scattering.

j. Stevens & Eckhardt, 2005.

k. Sun et al., 2009.

l. Sewell et al., 2003.

Table 2. Second-order elastic coefficients of PETN, RDX, and  $\beta$ -HMX determined using various methods. Units are GPa.



Pressure (GPa)	$K_{\text{Reuss}}$	$K_{\text{Voigt}}$	$G_{\text{Reuss}}$	$G_{\text{Voigt}}$
0.0	13.2	20.3	1.8	11.5
4.0	46.1	62.7	5.2	27.9
8.0	73.3	97	6.5	37.9

Table 3. Calculated pressure-dependent Reuss average and Voigt average bulk and shear moduli for TATB crystal. Units are GPa. The temperature is  $T = 300$  K. (Adapted from Bedrov et al., (2009).)

Menikoff & Sewell (2002) have reviewed the physical properties and processes needed for mesoscale simulations of HMX. Among the properties required that can be reliably computed for pure materials using atomic-level modeling methods are the thermodynamic phase boundaries between the polymorphic forms of the crystal and the melting point as a function of pressure; the coefficients of thermal expansion and isothermal compression; the heat capacity as a function of temperature and, in general, pressure; the modal and volumetric Gruneisen coefficient; the elastic tensor and derived isotropic moduli as functions of temperature and pressure; the elastic-plastic yield surface, which in general is temperature and stress dependent, and may also exhibit a strain-rate dependence; and thermal conductivity and shear viscosity as functions of pressure and temperature. A number of these properties have been computed for HMX and used in continuum simulations: the elastic tensor (Sewell et al., 2003; Barton et al., 2009; Zamiri & De, 2010), the temperature-dependent shear viscosity of the liquid (Bedrov et al., 2000; Dienes et al., 2006), the temperature-dependent specific heat (Goddard et al., 1998; Sewell & Menikoff, 2004). Other properties discussed by Menikoff and Sewell that must be considered in a realistic simulation are the “damage” state of the material, for instance size and distributions of cracks; the nature and density of defects within the crystals; and the effects of material interfaces on the composite behavior. Bedrov et al. (2003) have discussed how some of these properties can be obtained from MD simulations. More recently, Rice and Sewell (2008) reviewed atomic-scale simulations of physical properties in energetic materials, with a focus on predictions of properties for systems in thermal equilibrium.

Single-crystal plasticity of RDX has been studied using atomic-level simulation methods and, in some cases, compared to experimental results. Cawkwell and co-workers (Cawkwell et al., 2010; Ramos et al. 2010) have used MD simulations of the shock response of initially defect-free (111)- and (021)-oriented RDX single crystals to interpret the “anomalous” elastic-plastic response observed in flyer plate experiments for that orientation, wherein the evolution with increasing impact strength of VISAR velocity profiles for the (111) orientation transforms from a clear two-wave elastic-plastic structure to a nearly-overdriven structure over an interval of shock pressures that is narrow compared to the results obtained for other crystal orientations. The MD results show that, above a well-defined threshold shock strength, stacking faults nucleate homogeneously in the material then rapidly propagate, leading to mechanical hardening consistent with the abrupt transition from a two-wave structure to a nearly overdriven one (Cawkwell et al., 2010). Based on the results for the (111)-oriented crystal, Ramos et al. (2010) predicted that similar behavior should arise for shocks in (021)-oriented RDX, a result that was confirmed both from MD simulations and flyer plate experiments. Chen et al. (2008) performed large-scale MD simulations of nanoindentation of (100)-oriented RDX crystal by a diamond indenter using a version of the ReaxFF reactive force field (van Duin et al., 2001; Strachan et al., 2005). They observed localized damage in the region of the indenter, and calculated a material hardness that is

consistent with experimental data. They concluded that dominant slip occurs in the (210) plane along the  $[\bar{1}20]$  direction. Ramos et al. (2009) have reported atomic-force microscopy/nanoindentation experiments for oriented RDX crystals. Because Ramos et al. did not study indentation for the (100) surface, a direct comparison between their data and the MD results of Chen et al. is not possible.

Energetic material crystals (and organic crystals generally) often crystallize into low-symmetry space groups, exhibit polymorphism (*c.f.*, the multiple crystal phases of HMX (see Refs. 2-5 in Sewell et al., 2003) and RDX (Millar et al. (2010), and references therein; and Munday et al. (2011))), and are often highly anisotropic in terms of thermal, mechanical, and surface properties (the graphitic-like stacking of layers in TATB crystal provides an extreme case (Kolb & Rizzo, 1979; Bedrov et al., 2009)). This can lead to anisotropic elastic-plastic shock response (Hooks et al., 2006; Menikoff et al., 2005; Winey & Gupta, 2010) and even anisotropic shock initiation thresholds, as has been shown by (Dick, 1984; Dick et al., 1991, 1997) for the case of PETN crystal.

A number of MD studies have been performed to assess shock-induced phase transitions, anisotropic shock response, and effects of crystal surface properties on polymer adhesion properties. Thompson and co-workers have studied melting in RDX, and noted a structural transition that occurs for temperatures just below the melting point (Agrawal et al, 2006). Thompson and co-workers have also studied the melting (Agrawal et al., 2003; Zheng et al., 2006; Siavosh-Haghighi, 2006) and crystallization (Siavosh-Haghighi et al., 2010) of nitromethane using a non-reactive force field (Sorescu et al., 2000; Agrawal et al., 2003), including a prediction of the pressure dependence of the melting point,  $T_m = T_m(P)$  (Siavosh-Haghighi & Thompson, 2011; see Fig. 11). Using that same force field Thompson and coworkers have studied the shock strength dependence for (100)-oriented crystals (Siavosh-Haghighi et al., 2009; Dawes et al. 2009). They found that considerable disordering occurs for shock strengths of 2.0 km·s<sup>-1</sup> and greater. By projecting the instantaneous kinetic energy of individual molecules in the system onto the normal mode eigenvectors for a single molecule in the explicit crystal field they characterized the detailed energy transfer between the shock and molecular translational, rotational, and vibrational modes of the molecule. The results showed that, among the vibrational modes, shock excitation first excites the low-frequency modes; subsequent excitation of higher frequency vibrations occurs on longer time scales, with an approximately monotonic dependence between the frequency of a given mode and the time required for it to reach a steady-fluctuating energy in the shocked state. Further, the detailed energy transfer pathways differ for molecules that are impacted “methyl end first” versus “nitro end first” in the (100) shock orientation. (This latter point is interesting in light of the observation by Nomura et al. (2007a) for the case of reactive ReaxFF (van Duin et al., 2001; Strachan et al., 2005) shocks propagating along [100] in RDX that molecules belonging to the two distinct orientations in the crystal respond differently to the shock; one group of molecules undergoes chemical reaction while the other exhibits flattening and rotation without chemistry.)

He et al. (2011) studied shocks in oriented nitromethane crystals impacted at 2.0 km·s<sup>-1</sup> using MD with the same force field as Dawes et al. (2009). They observed significant differences in the responses to shocking along the [100], [010], and [001] directions. Jaramillo et al. (2007) studied the shock response of (100)-oriented  $\alpha$ -HMX using a non-reactive force field model (Smith & Bharadwaj, 1999; Bedrov et al., 2002) for impact strengths between 0.5 and 2.0 km·s<sup>-1</sup>. They observed a clear transition between elastic, elastic-plastic, and overdriven behavior in the crystals. Their results show that at lower pressures plasticity is mediated by

the nucleation and spread of crystallographic dislocations, whereas at higher pressures there is a transition from dislocations to the formation of nanoscale shear bands in the material. They noted that regions of material associated with these defects had larger local temperatures. Eason and Sewell (2011) have used a non-reactive force field (Borodin et al., 2008) to study the shock response of (100)- and (001)-oriented PETN. These orientations were found to be insensitive and sensitive, respectively, to shock initiation in the experiments by Dick and coworkers (Dick, 1984; Dick et al., 1991, 1997). For  $1.0 \text{ km}\cdot\text{s}^{-1}$  shocks, Eason and Sewell (2011) observed the formation of defects in (110) planes for (100)-oriented shocks, but only elastic compression for (001)-oriented shocks; see Fig. 12.

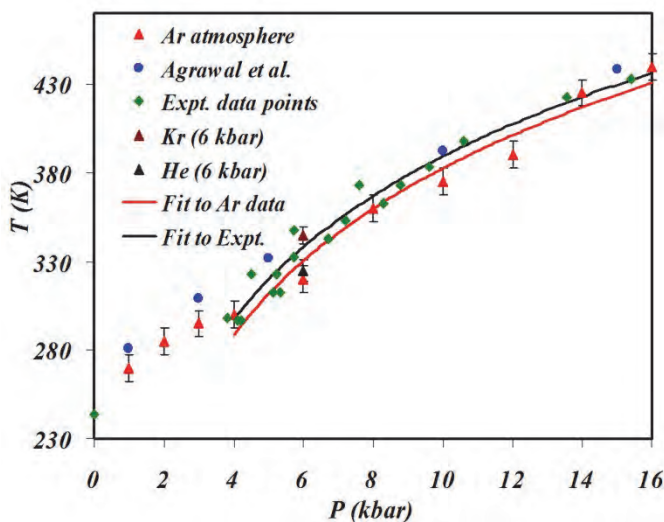


Fig. 11. Computed and experimental melting curves for nitromethane. The MD simulation results were obtained using the SRT force field (Sorescu et al., 2003). See Siavosh-Haghighi & Thompson (2011) and references therein.

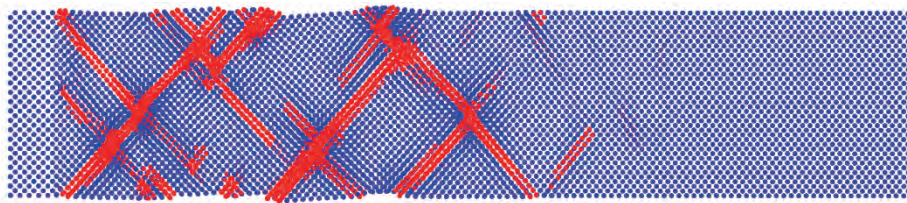


Fig. 12. Snapshot from a MD simulation of a shock wave propagating along [100] in PETN crystal. Only molecular centers of mass are shown. At the left end of the system is a rigid piston; the shock wave propagates from left to right. The snapshot corresponds to the instant of maximum compression (that is, the time when the shock front reaches the right-hand end of the sample). Blue corresponds to the piston, unshocked material, or elastically shock-compressed material. Red corresponds to molecules that have undergone locally inelastic compression.

Zybin and coworkers (Budzien et al. 2009; Zybin et al., 2010) studied the reactive dynamics of PETN using the ReaxFF force field. Budzien et al. studied the onset of chemistry for shocks propagating along [100] with impact velocities of 3 or 4 km·s<sup>-1</sup>. Zybin et al. (2010) studied the anisotropic initiation sensitivity of PETN in conjunction with a compress-and-shear model. By imposing rapid compression followed by rapid shear, with specific combinations of those two deformation types chosen to emulate the possible interactions between oriented shocks and probable slip systems, they were able to correlate the buildup of stresses, local temperatures, and onset of chemistry with the experimentally observed initiation anisotropy.

Atomic-level simulations of shock waves interacting with pre-existing defects or interfaces have been performed. Various models ranging in complexity from highly schematic ( $2AB \rightarrow A_2 + B_2 + \Delta H$ ) to relatively realistic ( $RDX \rightarrow$  small molecule products) have been used. Shi and Brenner (2008), using a reactive force field model for the schematic energetic material nitrogen cubane (overall stoichiometry  $N_8(s) \rightarrow 4N_2(g)$ ), have studied the effects of faceted interfaces on energy localization and detonation initiation. These simulations are of particular interest because of discussions of whether, or to what extent, the relative shock insensitivity of certain RDX formulations can be attributed to smoothed crystal edges obtained by treatment by surfactants or mechanical milling. Shi and Brenner identified shock focusing and local compression of the facets as two mechanisms for hotspot formation; which one dominates in a given situation depends on the shock impedance mismatch between the binder and energetic crystal. Using a version of the ReaxFF reactive force field (van Duin, 2001; Strachan, 2005), Nomura et al. (2007b) studied the collapse of single 8-nm diameter cylindrical voids in RDX crystal for the case of shock propagation along the [100] direction, with piston impact velocities of 1 and 3 km·s<sup>-1</sup> (shock velocities of ~3 and ~9 km·s<sup>-1</sup>, respectively). They observed the formation of nanojets during void collapse, which led to energy focusing when the jet impinged on the downstream wall of the void. For the weaker shock the local heating from jet impact on the downstream wall remained largely localized near the collapsed jet/wall interface stagnation zone, whereas for the stronger shock a conical region of material extending into the downstream wall underwent vibrational heating. For the stronger shock the dominant reaction during void closure was N-N bond cleavage; smaller reaction products ( $N_2$ ,  $H_2O$ , HONO) were rapidly generated once the nanojet reached the downstream wall. Cawkwell and Sewell (2011) have performed preliminary studies of void collapse in various oriented single crystals of RDX. Figure 13 contains a snapshot, taken when the shock wave reached the far end of the simulation cell, of the molecular centers of mass of an RDX crystal subsequent to the passage of a shock wave with piston impact speed 0.5 km·s<sup>-1</sup> over a 20 nm cylindrical void in a (210) shock. Molecules initially on the surface of the cylindrical void are colored blue; all others are colored red. The results indicate considerable structural complexity in the shock response, including regions of intense plastic deformation, stacking faults, and a stress-induced phase transition. Note also the large asymmetry of the void collapse process; for the crystal orientation and impact speed chosen, lateral jets form from the top and bottom of the void and collide near the geometric center of the original void. Using a reactive force field for the model reactive diatomic material  $2AB \rightarrow A_2 + B_2 + \Delta H$ , Herring *et al.* (Herring *et al.*, 2010) performed a detailed study, in 2-D, of the effects of void size and geometrical arrangement on thresholds for initiation. They considered a number of geometric arrangements of circular voids including single voids, voids on square and triangular lattices, and randomly arranged voids. Although the AB system is a highly



idealized model, it captures many features of reactive waves in real materials (Heim, 2007, 2008a, 2008b).

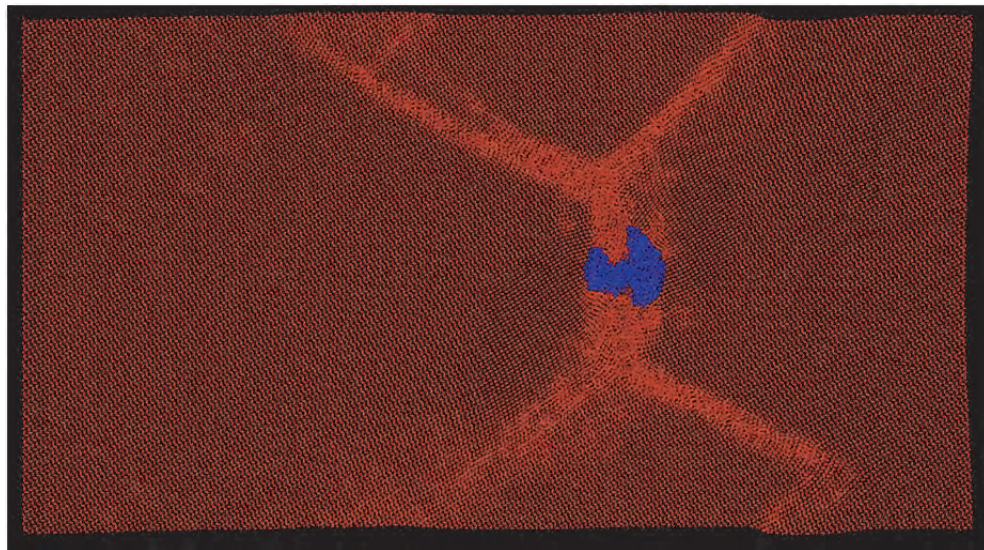


Fig. 13. Snapshot from a MD simulation of void collapse in (210)-oriented RDX. Only molecular centers of mass are shown. (Cawkwell & Sewell, 2011.)

As illustrated by the preceding discussion, MD simulations of energetic materials constituent materials and structures can be used in a variety of ways with objectives that range from near-quantitative predictions of spectroscopic or thermo-mechanical properties needed directly within existing constitutive or reactive burn models but currently unavailable, sparse, or unreliable with present-day experimental methods; to ones designed to reveal or refine existing understanding of fundamental dynamical processes associated with material dynamics (inelastic deformation, stress-induced phase transitions); to more qualitative ones designed to answer basic questions about, for example, material response in the presence of seeded defects and how material response changes with variations in the geometric features of those defects or how the morphology of a heterogeneous system affects the shock-induced localization of energy.

## 5. Conclusions

An important motivation for the simulation of deformation processes in energetic materials is the desire to avoid accidental ignition of explosives under the influence of a mechanical load. This requires the understanding of material behavior at macro-, meso- and molecular scales.

Experimental methods to determine the sensitivity of energetic materials to an external stimulus can be directly interpreted in terms of test severity in order to rank explosives. Simulation at the macroscale facilitates interpretation of experimental results; for example, by exceeding certain threshold values the ignition of a specific explosive composition is anticipated. Presented thresholds are related to 1) shear rate, 2) a pressure-, shear-rate- and

load-duration-dependent parameter, and 3) a parameter incorporating time-varying pressure and shear-rate loading. The latter two approaches are based on a micro-structural model. Unfortunately, results are applied only to PBX9501 or similar HMX-containing explosive compositions. Starting from the same micro-structural model however, one may arrive at a threshold parameter for PBXs containing energetic crystals other than HMX.

Simulations of PBXs including features from the mesoscale can be categorized as follows. First, one can use continuum models with particle-specific features that are fitted to experimental data and use those continuum models as input for simulations at the macroscale. Secondly, one can determine the collective mechanical behavior by simulation of a representative volume element with the mechanical properties of all individual constituents. And thirdly, one can simulate the mechanical behavior in deformation processes directly at the mesoscale, and interpret the results in terms of probabilistic distribution functions of wave field variables.

Atomic-level simulations of energetic materials can be used to predict physical properties such as equations of state, transport coefficients, and spectroscopic features, and to study fundamental processes such as energy transfer, inelastic deformation, phase transitions, and reaction chemistry. These are among the properties needed for the development and parameterization of improved mesoscale models. Depending on the accuracy of the force field used, these predictions can be expected to be semi-quantitative or to reveal general features of materials behavior in complicated polyatomic materials. Studies of the effects of defects, voids, or material interfaces on the physical properties and dynamic response can be studied in detail; although the results must be interpreted with caution if the goal is to link directly to the mesoscale, due to the disparity between defect sizes or number densities that can be simulated using MD and those that occur in real materials.

## 6. Acknowledgments

The authors acknowledge support from the U. S. Defense Threat Reduction Agency. R.H.B.B. and A.E.D.M.H. acknowledge support from The Netherlands Ministry of Defence. T.D.S. acknowledges support from the U. S. Office of Naval Research and the Los Alamos National Laboratory LDRD program. T.D.S and D.L.T. acknowledge support from a DOD MURI grant managed by the U. S. Army Research Office.

## 7. References

- Agrawal, P.M., Rice, B.M., Zheng, L., & Thompson, D.L. (2006). Molecular dynamics simulations of hexahydro-1,3,5-trinitro-1,3,5-s-triazine (RDX) using a combined Sorescu-Rice-Thompson AMBER force field. *Journal of Physical Chemistry B* 110, 26185.
- Agrawal, P.M., Rice, B.M. & Thompson, D.L. (2003). Molecular dynamics studies of the melting of nitromethane. *Journal of Chemical Physics* 119, 9617.
- Armstrong, R. W. (2009). Dislocation mechanics aspects of energetic material composites. In: *Reviews on Advanced Materials Science* 19, Ovid'ko, I.A., (Ed), pp. 14-34.
- Autodyn, <http://www.ansys.com/Products/Simulation+Technology/Explicit+Dynamics/ANSYS+AUTODYN>.

- Baer, M.R. & Trott, W.M. (2002). Theoretical and experimental mesoscale studies of impact-loaded granular explosive and simulant materials. *Proceedings of 12<sup>th</sup> International Detonation Symposium*, San Diego, USA, August 2002.
- Baer, M.R. (2002). Modeling heterogeneous energetic materials at the mesoscale. *Thermochimica Acta* 384, 351.
- Bailly, P., Delvare, F., Vial, J., Hanus, J. L., Biessy, M. & Picart, D. (2011). Dynamic behavior of an aggregate material at simultaneous high pressure and strain rate: SPHB triaxial tests. *International Journal of Impact Engineering*, 38, (2011), pp. 73-84.
- Bardenhagen, S.G., Brydon, A.D., Williams, T.O. & Collet, C. (2006). Coupling grain scale and bulk mechanical response for PBXs using numerical simulations of real microstructures. *AIP Conference Proceedings*, 845 (2006), pp. 479-482.
- Barton, N.R., Winter, N.W. & Reaugh, J. E. (2009). Defect evolution and pore collapse in crystalline energetic materials. *Modelling and Simulation in Materials Science and Engineering*, 17, 035003.
- Bedrov, D., Smith, G.D. & Sewell, T.D. (2000). Temperature-dependent shear viscosity coefficient of octahydro-1,3,5,7-tetranitro-1,3,5,7-tetrazocine (HMX): A molecular dynamics simulation study. *Journal of Chemical Physics* 112, 7203.
- Bedrov, D., Ayyagari, C., Smith, G.D., Sewell, T.D., Menikoff, R. & Zaug, J.M. (2001). Molecular dynamics simulations of hmx crystal polymorphs using a flexible molecule force field, *Journal of Computer-Aided Materials Design* 8, 77.
- Bedrov, D., Smith, G.D. & Sewell, T.D. (2003). Thermodynamic and mechanical properties from atomistic simulations, in *Energetic Materials, Volume 12: Part 1. Decomposition, Crystal, and Molecular Properties (Theoretical and Computational Chemistry)*, Murray, J.S. and Politzer, P. Eds. (Elsevier, Amsterdam).
- Bedrov, D., Borodin, O., Smith, G.D., Sewell, T.D., Dattelbaum, D.M. & Stevens, L.L. (2009). A molecular dynamics simulation study of crystalline 1,3,5-triamino-2,4,6-trinitrobenzene as a function of pressure and temperature. *Journal of Chemical Physics* 131, 224703.
- Bennett, J.G., Haberman, K.S., Johnson, J.N., Asay, B.W. & Henson, B.F. (1998). A constitutive model for the non-shock ignition and mechanical response of high explosives. *J. Mech. Phys. Solids*, 46, (1998), pp. 2302-2322.
- Birnbaum, N.K., Cowler, M.S., Itoh, M., Katayama, M. & Obata, H. (1987). AUTODYN - an interactive nonlinear dynamic analysis program for microcomputers through supercomputers. *Proceedings of 9<sup>th</sup> Int. Conf. on Structural Mechanics in Reactor Technology*, Lausanne, Switzerland, 1987.
- Bock, N., Challacombe, M., Gan, C.-K., Henkelman, G., Nemeth, K., Niklasson, A.M.N., Odell, A., Schwegler, E., Tymczak, C.J. & Weber, V. (2011). FreeON. Los Alamos National Laboratory (LA-CC 01-2, LA-CC-04-086) <http://freeon.org>.
- Borodin, O., Smith, G.D., Sewell, T.D., and Bedrov, D. (2008). Polarizable and nonpolarizable force fields for alkyl nitrates. *Journal of Physical Chemistry B* 112, 734.
- Bouma, R.H.B., Courtois, C., Verbeek, H.J. & Scholtes, J.H.G. (1999). Influence of mechanical damage on the shock sensitivity of plastic bonded explosives. *Proceedings of Insensitive Munitions & Energetic Materials Technology Symposium*, Tampa, USA, November 1999.

- Bouma, R.H.B., Verbeek, H.J. & van Wees, R.M.M. (2003). Design of barriers for the prevention of sympathetic detonation in out-of-area munition storage. *Proceedings of 30<sup>th</sup> International Pyrotechnics Seminar*, Saint Malo, France, June 2003.
- Bouma, R.H.B. & Meuken, B. (2004). Explosive and mechanical deformation of PBXN-109. *Proceedings of workshop on shear stress evaluation and contribution to the ignition of PBX*, Institut für Chemische Technologie, Pfinztal, Germany, June 2004.
- Bouma, R.H.B., Meuken, B. & Verbeek, H.J. (2007). Shear initiation of Al/MoO<sub>3</sub>-based reactive materials. *Propellants, Explosives, Pyrotechnics*, 32, (2007), pp. 447-453.
- Bowden, F.P. & Yoffe, Y.D. (1952). *Initiation and growth of explosion in liquids and solids*, Cambridge University Press, ISBN 0 521 31233 7, Cambridge, United Kingdom.
- Browning, R.V. (1995). Microstructural model of mechanical initiation of energetic materials. *Proceedings of APS Conference on Shock Compression of Condensed Matter*, Seattle, USA.
- Browning, R.V. & Scammon, R.J. (2001). Microstructural modal of ignition for time varying loading conditions, *Proceedings of APS Conference on Shock Compression of Condensed Matter*, CP620, 987-990.
- Browning, R.V. & Scammon, R.J. (2002). Influence of mechanical properties on non-shock ignition. *Proceedings of 12<sup>th</sup> Int. Detonation Symposium*, San Diego, USA, August 2002.
- Budzien, J., Thompson, A.P. & Zybin, S.V. (2009). Reactive molecular dynamics simulations of shock through a single crystal of pentaerythritol tetranitrate. *Journal of Physical Chemistry B* 113, 13142.
- Cawkwell, M.J., Sewell, T.D., Zheng, L. & Thompson, D.L. (2008). Shock-induced shear bands in an energetic molecular crystal: Application of shock-front absorbing boundary conditions to molecular dynamics simulations, *Physical Review B* 78, 014107.
- Cawkwell, M.J., Ramos, K.J., Hooks, D.E. & Sewell, T.D. (2010). Homogeneous dislocation nucleation in cyclotrimethylene trinitramine under shock loading. *Journal of Applied Physics* 107, 063512.
- Cawkwell, M.J. and Sewell, T.D. (2011). Unpublished results.
- Chen, Y.-C., Nomura, K.-i., Kalia, R.K., Nakano, A. & Vashishta, P. (2008). Molecular dynamics nanoindentation simulation of an energetic material. *Applied Physics Letters* 93, 171908.
- Chidester, S.K., Tarver, C.M. & Garza, R. (1998). Low amplitude impact testing and analysis of pristine and aged solid high explosives. *Proceedings of 11<sup>th</sup> Int. Detonation Symposium*, Snowmass, USA.
- Coe, J.D., Sewell, T.D. & Shaw, M.S. (2009). Optimal sampling efficiency in Monte Carlo simulation with an approximate potential. *Journal of Chemical Physics* 130, 164104.
- Coe, J.D., Sewell, T.D. & Shaw, M.S. (2009). Nested Markov chain Monte Carlo sampling of a density functional theory potential: Equilibrium thermodynamics of dense fluid nitrogen. *Journal of Chemical Physics* 131, 074105.
- Coffey, C.S. (1995). Impact testing of explosives and propellants. *Propellants, Explosives, Pyrotechnics*, 20, (1995), pp. 105-115.
- Coffey, C.S. & Sharma, J. (1999). Plastic deformation, energy dissipation, and initiation of crystalline explosives. *Physical Review B – Condensed Matter and Materials Physics*, 60, (1999), pp. 9365-9371.



- Conley, P.A. & Benson, D.J. (1999). An estimate of the linear strain rate dependence of octahydro-1,3,5,7-tetranitro-1,3,5,7-tetrazocine. *Journal of Applied Physics*, 939. (199), pp. 6717-6728.
- Dawes, R., Siavosh-Haghighi, A., Sewell, T.D. & Thompson, D.L. (2009). Shock-induced melting of (100)-oriented Nitromethane: Energy partitioning and vibrational mode heating. *Journal of Chemical Physics* 131, 224513.
- De, S. & Macri, M. (2006). Modeling the bulk mechanical response of heterogeneous explosives based on microstructural information. *Proceedings of 13<sup>th</sup> Int. Detonation Symposium* 373., Norfolk, USA.
- Desbiens, N., Bourasseau, E. & Maillet, J.-B. (2007). Potential optimization for the calculation of shocked liquid nitromethane properties, *Molecular Simulation* 33, 1061.
- Desbiens, N., Bourasseau, E., Maillet, J.-B. & Soulard, L. (2009). Molecular based equation of state for shocked liquid nitromethane. *Journal of Hazardous Materials* 166, 1120.
- Dick, J.J. (1984). Effect of crystal orientation on shock initiation sensitivity of pentaerythritol tetranitrate explosive. *Applied Physics Letters* 44, 859.
- Dick, J.J., Mulford, R.N., Spencer, W.J., Pettit, D.R., Garcia, E. & Shaw, D.C., (1991). Shock response of pentaerythritol tetranitrate single crystals. *Journal of Applied Physics* 70, 3572.
- Dick, J.J. (1997). Anomalous shock initiation of detonation in pentaerythritol tetranitrate crystals. *Journal of Applied Physics* 81 601.
- Dienes, J.K. (1985). A statistical theory of fragmentation processes, *Mechanics of Materials*, Vol 4, 325-335.
- Dienes, J.K., Zuo, Q.H. & Kersher, J.D. (2006). Impact initiation of explosives and propellants via statistical crack mechanics. *Journal of the Mechanics and Physics of Solids* 54, 1237.
- Doherty, R.M. & Watt, D.S. (2008). Relationship between RDX properties and sensitivity. *Propellants, Explosives, Pyrotechnics*, 33, (2008), pp. 4-13.
- DYNA3D (2005). User Manual, Available from [https://www-eng.llnl.gov/pdfs/mdg\\_dyna3d.pdf](https://www-eng.llnl.gov/pdfs/mdg_dyna3d.pdf)
- Eason, R.M. and Sewell, T.D. (2011). Unpublished results.
- Frenkel, D. & Smit. B. (2002) *Understanding Molecular Simulation*, 2<sup>nd</sup> Ed. (Academic Press, San Diego.)
- Gee, R.H., Wu, C. & Maiti, A. (2006). Coarse-grained model for a molecular crystal. *Applied Physics Letters* 89, 021919.
- Goddard, W.A., Meiron, D.I., Ortiz, M., Shepherd, J.E. & Pool, J. (1998). *Technical Report 032, Center for Simulation of Dynamic Response in Materials*, California Institute of Technology. <http://www.cacr.caltech.edu/ASAP/publications/cit-asci-tr/cit-asci-tr032.pdf>.
- Goldman, N., Reed, E.J. & Fried, L.E. (2009). Quantum mechanical corrections to simulated shock Hugoniot temperatures. *Journal of Chemical Physics* 131, 204103.
- Gruau, C., Picart, D., Belmas, R., Bouton, E., Delmaire-Sizes, F., Sabatier, J. & Trumel, H. (2009). Ignition of a confined high explosive under low velocity impact. *International Journal of Impact Engineering*, 36, (2009), pp. 537-550.
- Hager, K., Tancreto, J. & Swisdak, M. (2000). High Performance Magazine non-proagation wall design criteria. *Proceedings of 29<sup>th</sup> DDESB Seminar*, New Orleans, USA, July 2000.

- Han, S.-p., van Duin, A.C.T., Goddard, W.A. III & Strachan, A. (2011) Thermal decomposition of condensed-phase nitromethane from molecular dynamics from ReaxFF reactive dynamics. *Journal of Physical Chemistry B* 115, 6534.
- Handley, C.A. (2011). Numerical modeling of two HMX-based plastic-bonded explosives at the mesoscale. Ph. D. thesis, St. Andrews University. Available from <http://research-repository.st-andrews.ac.uk>
- Haussühl, S. (2001). Elastic and thermoelastic properties of selected organic crystals: acenaphthene, trans-azobenzene, benzophenone, tolane, trans-stilbene, dibenzyl, diphenyl sulfone, 2,20-biphenol, urea, melamine, hexogen, succinimide, pentaerythritol, urotropine, malonic acid, dimethyl malonic acid, maleic acid, hippuric acid, aluminium acetylacetonate, iron acetylacetonate, and tetraphenyl silicon. *Z. Kristallogr.* 216, 339.
- Haycraft, J.J., Stevens, L.L., & Eckhardt, C.J. (2006). The elastic constants and related properties of the energetic material cyclotrimethylene trinitramine (RDX) determined by Brillouin scattering, *Journal of Chemical Physics*, 124, 024712.
- He, L. Sewell, T.D. & Thompson, D.L. (2011). Molecular dynamics simulations of shock waves in oriented nitromethane single crystals. *Journal of Chemical Physics* 134, 124506.
- Heim, A.J., Grønbech-Jensen, N., Germann, T.C., Holian, B.L., Kober, E.M. & Lomdahl, P.S. (2007). Influence of interatomic bonding potentials on detonation properties. *Physical Review E* 76, 026318.
- Heim, A.J., Grønbech-Jensen, N., Kober, E.M., Erpenbeck, J.J. & Germann, T.C. (2008a). Interaction potential for atomic simulations of conventional high explosives. *Physical Review E* 78, 046709.
- Heim, A.J., Grønbech-Jensen, N. Kober, E.M. & Germann, T.C. (2008b). Molecular dynamics simulations of detonation instability. *Physical Review E* 78, 046710.
- Hooks, D.E., Ramos, K.J. & Martinez, A.R. (2006). Elastic-plastic shock wave profiles in oriented single crystals of cyclotrimethylene trinitramine (RDX) at 2.25 GPa. *Journal of Applied Physics* 100, 024908.
- Hoover, W.G. (1985). Canonical dynamics: Equilibrium phase-space distributions. *Physical Review A* 31, 1695.
- Hsu, P.C., Hust, G., Howard, M. & Maienschein, J.L. (2010). The ODTX system for thermal ignition and thermal safety study of energetic materials, *Proceedings of the 14<sup>th</sup> Int. Detonation Symposium*, Coeur D'Alene, USA
- Izvekov, S., Chung, P.W. & Rice, B.M. (2010). The multiscale coarse-graining method: Assessing its accuracy and introducing density dependent coarse-grain potentials. *Journal of Chemical Physics* 133, 064109.
- Jaidann, M., Lussier, L.-S., Bouamoul, A., Abou-Rachid, H. & Brisson, J. (2009). Effects of interface interactions on mechanical properties in RDX-based PBXs HTPB-DOA: Molecular dynamics simulations. In *Lecture Notes in Computer Science* 5545 (Proceedings of the ICCS, 2009, Part II). Allen, G. et al. (Eds.) (Springer-Verlag, Berlin) 131.
- Jaramillo, E., Sewell, T.D. & Strachan, A. (2007). Atomic-level view of inelastic deformation in a shock loaded molecular crystal. *Physical Review B* 76, 064112.
- Jaramillo-Botero, A., Nielsen, R., Abrol, R., Su, J. Pascal, T., Mueller, J. & Goddard, W.A. III (2011). First-principles-based multiscale, multiparadigm molecular mechanics and

- dynamics methods for describing complex chemical processes. *Top. Curr. Chem.* DOI: 10.1007/128\_2010\_114 (Springer-Verlag, Heidelberg).
- Koch, W. & Holthausen, M.C. (2001). *A Chemist's Guide to Density Functional Theory*, 2<sup>nd</sup> Ed. (Wiley-VCH, Weinheim).
- Kolb, J.R. & Rizzo, H.F. (1979). Growth of 1,3,5-triamino-2,4,6-trinitrobenzene (TATB) I. Anisotropic thermal expansion. *Propellants, Explosives, and Pyrotechnics* 4, 10.
- Kresse, G. et al. (2011). Vienna *Ab Initio* Simulation Package (VASP), Department of Computational Physics, Universität Wien, Wien, Austria, <http://cms.mpi.univie.ac.at/vasp/>.
- Kuklja, M. & Rashkeev, S.N. (2009). Interplay of decomposition mechanisms at shear-strain interface. *The Journal of Physical Chemistry C* 113, pp. 17-20.
- Lee, E.L. & Tarver, C.M., Phenomenological model of shock initiation in heterogeneous explosives. *Physics of Fluids*, Vol. 23 (1980), p. 2362.
- Lei, L. & Koslowski, M., (2011). Mesoscale modeling of dislocations in molecular crystals. *Philosophical Magazine* 91, 865.
- Lin, P.-H., Khare, R., Weeks, B.L. & Gee, R.H. (2007). Molecular modeling of diffusion on a crystalline pentaerythritol tetranitrate surface. *Applied Physics Letters* 91, 104107.
- Liu, A. & Stuart, S.J. (2008). Empirical bond-order potential for hydrocarbons: Adaptive treatment of van der Waals interactions. *Journal of Computational Chemistry* 29, 601.
- Lynch, K., Thompson, A. & Strachan, A. (2009) Coarse-grain modeling of spall failure in molecular crystals: Role of intra-molecular degrees of freedom. *Modelling and Simulation in Materials Science and Engineering* 17, 015007.
- Maillet, J.-B. & Stoltz, G. (2008). Sampling constraints in average: The example of Hugoniot curves. *Applied Mathematics Research eXpress* 2008, abn004.
- Malvar, L.J. (1994). Development of HPM nonpropagation walls: test results and Dyna3D predictions of acceptor response. *Proceedings of 26<sup>th</sup> DDESB Seminar*, New Orleans, USA, August 1994.
- Manaa, M.R., Reed, E.J., Fried, L.E. & Goldman, N. (2009). Nitrogen-rich heterocycles as reactivity retardants in shocked insensitive explosives. *Journal of the American Chemical Society* 131, 5483.
- Martyna, G.J., Tuckerman, M.E., Tobias, D.J. & Klein, M.L. (1996). Explicit reversible integration algorithms for extended systems dynamics. *Molecular Physics* 87, 1117.
- Menikoff, R. & Sewell, T.D. (2002). Constituent properties of HMX needed for mesoscale simulations. *Combustion Theory and Modeling* 6, 103.
- Menikoff, R., Dick, J. J. & Hooks, D. E. (2005). Analysis of wave profiles for single-crystal cyclotetramethylene tetranitramine. *Journal of Applied Physics* 97, 023529.
- Menikoff, R. (2008). Comparison of constitutive models for plastic-bonded explosives. *Combustion Theory and Modeling* 12, 73.
- Menikoff, R. (2011). Hot spot formation from shock reflections. *Shock Waves* 21, 141.
- Metropolis, N. Rosenbluth, A.W., Rosenbluth, M.N., Teller, A.H. & Teller, E. (1953). Equation of state calculations by fast computing machines. *Journal of Chemical Physics* 21, 1087.
- Meuken, B., Martinez Pacheco, M., Verbeek, H.J., Bouma, R.H.B. & Katgerman, L. (2006). Shear initiated reactions in energetic and reactive materials. *Mater. Res. Soc. Symp. Proc. Vol. 896*, (2006) 0896-H06-06, pp. 1-6.

- Millar, D.I.A., Oswald, I.D.H., Barry, C., Francis, D.J., Marshall, W.G., Pulham, C.R. & Cumming, A.S. (2010). Pressure-cooking of explosives – the crystal structure of  $\epsilon$ -RDX as determined by X-ray and neutron diffraction. *Chemical Communications* 46, 5662.
- Molt, R.W. Jr., Watson, T. Jr., Lotrich, V.F. & Bartlett, R.J. (2011). RDX geometries, excited states, and revised energy ordering of conformers via MP2 and CCSD(T) methodologies: Insights into decomposition mechanism. *Journal of Physical Chemistry A* 115, 884.
- Munday, L. B., Chung., P. W., Rice, B. M., and Solares, S. D. (2011). Simulations of high-pressure phases in RDX. *Journal of Physical Chemistry B* 115, 4378.
- Namkung, J. & Coffey, C.S. (2001). Plastic deformation rate and initiation of crystalline explosives. *Proceedings of Shock Compression of Condensed Matter*, Furnish, M.D., Thadhani, N.N. & Horie, Y. (Eds), CP620, (2001), pp. 1003-1006.
- Nomura, K.-i., Kalia, R.K., Nakano, A. & Vashishta, P. (2007a). Dynamic transition in the structure of an energetic crystal during chemical reactions at shock front prior to detonation. *Physical Review Letters* 99, 148303.
- Nomura, K.-i., Kalia, R.K., Nakano, A. & Vashishta, P. (2007b). Reactive nanojets: Nanostructure-enhanced chemical reactions in a defected energetic crystal. *Applied Physics Letters*, 91, 183109.
- Nosé, S. (1984). A unified formulation of the constant temperature molecular dynamics methods. *Journal of Chemical Physics* 81, 511.
- Parrinello, M. & Rahman, A. (1981). Polymorphic transitions in single crystals: A new molecular dynamics method. *Journal of Applied Physics* 52, 7182.
- Ramos, K.J., Hooks, D.E. & Bahr, D.F. (2009). Direct observation of plasticity and quantitative hardness measurements in single crystal cyclotrimethylene trinitramine by nanoindentation. *Philosophical Magazine* 89, 2381.
- Ramos, K.J., Hooks, D.E., Sewell, T.D. & Cawkwell, M.J. (2010). Anomalous hardening under shock compression in (021)-oriented cyclotrimethylene trinitramine single crystals. *Journal of Applied Physics* 108, 066105.
- Ravelo, R., Holian, B.L., Germann, T.C. & Lomdahl, P.S. (2004). Constant-stress Hugoniot method for following the dynamical evolution of shocked matter. *Physical Review B* 70, 014103.
- Reaugh, J.E. (2002). Grain-scale dynamics in explosives, Lawrence Livermore National Laboratory Unclassified Report UCRL-ID-150388.
- Reed, E.J., Fried, L.E. & Joannopoulos, J.D. (2003). A method for tractable dynamical studies of single and double shock compression. *Physical Review Letters* 90, 235503.
- Rice, B.M. & Sewell, T.D. (2008). Molecular dynamics simulations of energetic materials at thermodynamic equilibrium, in *Energetic Materials at Static High Pressures*, Piermarini G. and Peiris, S.M., Eds. (Springer-Verlag, Heilderberg).
- Sandusky, H.W., Paul Chamber, G. & Carlson, V.J. (1998). Setback simulation of fielded and candidate explosive fill for 5"/54 guns. *Proceedings of 1998 JANNAF Propulsion Systems Hazards Subcommittee Meeting*, CPIA Publ. 681, Vol. II, p. 137-145.
- Scammon, R.J., Browning, R.V., Middleditch, J., Dienes, J.K., Haberman, K.S. & Bennett, J.G. (1998). Low amplitude insult project: structural analysis and prediction of low order reaction. *Proceedings of 11<sup>th</sup> Int. Detonation Symposium*, Snowmass, USA, August 1998.



- Scholtes, J.H.G., Bouma, R.H.B., Weterings, F.P., & van der Steen, A.C. (2002). Thermal and mechanical damage of PBXs. *Proceedings of 12<sup>th</sup> International Detonation Symposium*, San Diego, USA, August 2002.
- Schwarz, R.B., Hooks, D.E., Dick, J.J., Archuleta, J.I., and Martinez, A.R. (2005). Resonant ultrasound spectroscopy measurement of the elastic constants of cyclotrimethylene trinitramine. *Journal of Applied Physics* 98, 056106.
- Sewell, T. D., and Bennett, C. M. (2000). Monte Carlo calculations of the elastic moduli and pressure-volume-temperature equation of state for hexahydro-1,3,5-trinitro-1,3,5-triazine. *Journal of Applied Physics* 88, 88.
- Sewell, T.D. (2008). Atomistic-based mesoscopic constitutive models for high explosive constituent materials. *Final report for project 49449-EG*, (2008).
- Sewell, T.D., Menikoff, R., Bedrov, D. & Smith, G.D. (2003). A molecular dynamics simulation study of elastic properties of HMX. *Journal of Chemical Physics* 119, 7417.
- Shane Stafford, D. & Jackson, T.L. (2010). Using level sets for creating virtual random packs of non-spherical convex shapes. *Journal of Computational Physics* 229, (2010), 3295-3315.
- Shi, Y. & Brenner, D.W. (2008). Molecular simulation of the influence of interface faceting on the shock sensitivity of a model plastic bonded explosive, *Journal of Physical Chemistry B* 112, 14898.
- Siavosh-Haghighi, A., & Thompson, D.L. (2006). Molecular dynamics simulations of surface-initiated melting of nitromethane. *Journal of Chemical Physics* 125, 184711.
- Siavosh-Haghighi, A., Dawes, R., Sewell, T.D. & Thompson, D.L. (2009). Shock-induced melting of (100)-oriented nitromethane: Structural relaxation. *Journal of Chemical Physics* 131, 064503.
- Siavosh-Haghighi, A., Sewell, T.D., and Thompson, D.L. (2010). Molecular dynamics study of the crystallization of nitromethane from the melt. *Journal of Chemical Physics* 133, 194501.
- Siavosh-Haghighi, A. and Thompson, D.L. (2011). Unpublished results.
- Siviour, C.R., Williamson, D.M., Grantham, S.G., Palmer, S.J.P., Proud, W.G. & Field, J.E. (2004), Split Hopkinson bar measurements of PBXs, In: *Shock Compression of Condensed Matter*, Furnish, M.D., Gupta, Y.M. & Forbes, J.W. (eds.), CP706, American Institute of Physics.
- Smith, G. D. & Bharadwaj, R.K. (1999). Quantum chemistry based force field for simulations of HMX. *Journal of Physical Chemistry B* 103, 3570.
- Sorescu, D.C., Rice, B.M. & Thompson, D.L. (2000). Theoretical studies of solid nitromethane. *Journal of Physical Chemistry B* 104, 8406.
- Stevens, L.L., & Eckhardt, C. J. (2005). The elastic constants and related properties of  $\beta$ -HMX determined by Brillouin scattering, *Journal of Chemical Physics* 122, 174701.
- Strachan, A. & Holian, B.L. (2005). Energy exchange between mesoparticles and their internal degrees of freedom. *Physical Review Letters* 94, 014301.
- Strachan, A., Kober, E.M., van Duin, A.C.T., Oxgaard, J. & Goddard III, W.A. (2005). Thermal decomposition of RDX from reactive molecular dynamics. *The Journal of Chemical Physics*, 122, 054502.
- Stuart, S.J., Tutein, A.B., & Harrison, J.A. (2000). A reactive potential for hydrocarbons with intermolecular interactions. *Journal of Chemical Physics* 112, 6472.

- Sun, B., Winey, J.M., Hemmi, N., Dreger, Z.A., Zimmerman, K.A., Gupta, Y.M., Torchinsky, D.H., & Nelson, K.A. (2008). Second-order elastic constants of pentaerythritol tetranitrate and cyclotrimethylene trinitramine using impulsive stimulated thermal scattering. *Journal of Applied Physics* 104, 073517.
- Sun, B., Winey, J. M., Gupta, Y. M., & Hooks, D. E. (2009). Determination of second-order elastic constants of cyclotetramethylene tetranitramine ( $\beta$ -HMX) using impulsive stimulated thermal scattering. *Journal of Applied Physics* 106, 053505.
- Swantek, A.B. & Austin, J.M. (2010). Collapse of void arrays under stress wave loading. *Journal of Fluid Mechanics* 649, 399.
- Tancreto, J., Swisdak, M. & Malvar, J. (1994). High Performance Magazine acceptor threshold criteria. *Proceedings of 26<sup>th</sup> DDESB Seminar*, Miami, USA, August 1994.
- Thompson, D., Sewell, T., Bouma, R.H.B. & van der Heijden, A.E.D.M. (2010). Investigation of fundamental processes and crystal-level defect structures in metal-loaded high-explosive materials under dynamic thermo-mechanical loads and their relationships to impact survivability of munitions. Project HDTRA1-10-1-0078.
- Tuckerman, M.E. (2010). *Statistical Mechanics: Theory and Molecular Simulation* (Oxford University Press, U.S.A.)
- Tuckerman, M.E. & Klein, M.L. (1998). Ab initio molecular dynamics study of solid nitromethane. *Chemical Physics Letters* 283, 147.
- UN (2008). *Recommendations on the transport of dangerous goods, Manual of tests and criteria*. Available from <https://unp.un.org/Details.aspx?pid=17299>.
- Van Duin, A.C.T., Dasgupta, S., Lorant, F. & Goddard, W. A. III (2001). ReaxFF: A reactive force field for hydrocarbons. *Journal of Physical Chemistry A* 105, 9396.
- Van der Heijden, A.E.D.M. & Bouma, R.H.B. (2004). Crystallization and characterization of RDX, HMX and Cl-20. *Crystal Growth and Design*, 4, (2004), 999-1007.
- Van der Heijden, A.E.D.M., Bouma, R.H.B. & van der Steen, A.C. (2004). Physicochemical parameters of nitramines determining shock sensitivity. *Propellants, Explosives, Pyrotechnics* 29 (2004) 304-313.
- Van der Heijden, A.E.D.M. & Bouma, R.H.B. (2010). Energetic Materials: Crystallization and Characterization, in: *Handbook of Material Science Research*, eds. René, C. & Turcotte, E., 2010, ISBN 978-1-60741-798-9.
- Vandersall, K.S., Switzer, L.L. & Garcia, F. (2006). Threshold studies on TNT, Composition B, C-4 and ANFO explosives using the Steven impact test. *Proceedings of 13<sup>th</sup> Int. Detonation Symposium*, Norfolk, USA, July 2006.
- Van Wees, R.M.M., van Dongen, Ph. & Bouma, R.H.B. (2004). The participation of the Netherlands in the UK/AUS defense trial 840. Study of barricades to prevent sympathetic detonation in field storage. *Proceedings of 31<sup>th</sup> DoD Explosives Safety Seminar*, San Antonio, USA, August 2004.
- Wallace, I.G. (1994). Spigot Intrusion. *Proceedings of 26<sup>th</sup> DoD Explosives Safety Seminar*, Miami, USA.
- Winey, J.M. & Gupta, Y.M. (2001). Second-order elastic constants for pentaerythritol tetranitrate single crystals. *Journal of Applied Physics* 90, 1669.
- Winey, J.M. & Gupta, Y.M. (2010). Anisotropic material model and wave propagation simulations for shocked pentaerythritol tetranitrate single crystals. *Journal of Applied Physics* 107, 103505.

- Wood, W.W. (1968) in *Physics of Simple Fluids*, edited by Temperley, H.N.V., Rowlinson, J.S., and Rushbrooke G.S. (North-Holland, Amsterdam), Ch. 5, p. 115.
- Yan-Qing, W. & Feng-Lei, H. (2009). A micromechanical model for predicting combined damage of particles and interface debonding in PBX explosives. *Mechanics of Materials*, 41, (2009), 27-47.
- Zamiri, A.R. & De, S. (2010). Deformation distribution maps of  $\beta$ -HMX molecular crystals. *Journal of Physics D: Applied Physics* 43, 035404.
- Zaug, J. M. (1998). Elastic constants of  $\beta$ -HMX and tantalum, equations of state of supercritical fluids and mixtures and thermal transport determinations. *Proceedings of the 11th International Detonation Symposium*, Snowmass, CO, Aug 31-Sept 4, 498.
- Zerilli, F.J., Guirguis, R.H. & Coffey, C.S. (2002). A burn model based on heating due to shear flow: proof of principle calculations. *Proceedings of 12<sup>th</sup> Int. Detonation Symposium*, San Diego, USA, August 2002.
- Zerilli, F.J. & Kuklja, M.M. (2007). *Ab initio* equation of state of an organic molecular crystal: 1,1-diamino-2,2-dinitroethylene. *Journal of Physical Chemistry A* 111, 1721.
- Zheng, L., Luo, S.-N., & Thompson, D.L. (2006). Molecular dynamics simulations of melting and the glass transition in nitromethane. *Journal of Chemical Physics* 124, 154504.
- Zybin, S.V., Goddard III, W.A., Xu, P., van Duin, A.C.T. & Thompson, A.P. (2010). Physical mechanism of anisotropic sensitivity in pentaerythritol tetranitrate from compressive-shear reaction dynamics simulations. *Applied Physics Letters* 96, 081918.

Reprinted from

# CMC

## Computers, Materials, & Continua

Editors-In-Chief:

**Surya Kalidindi**

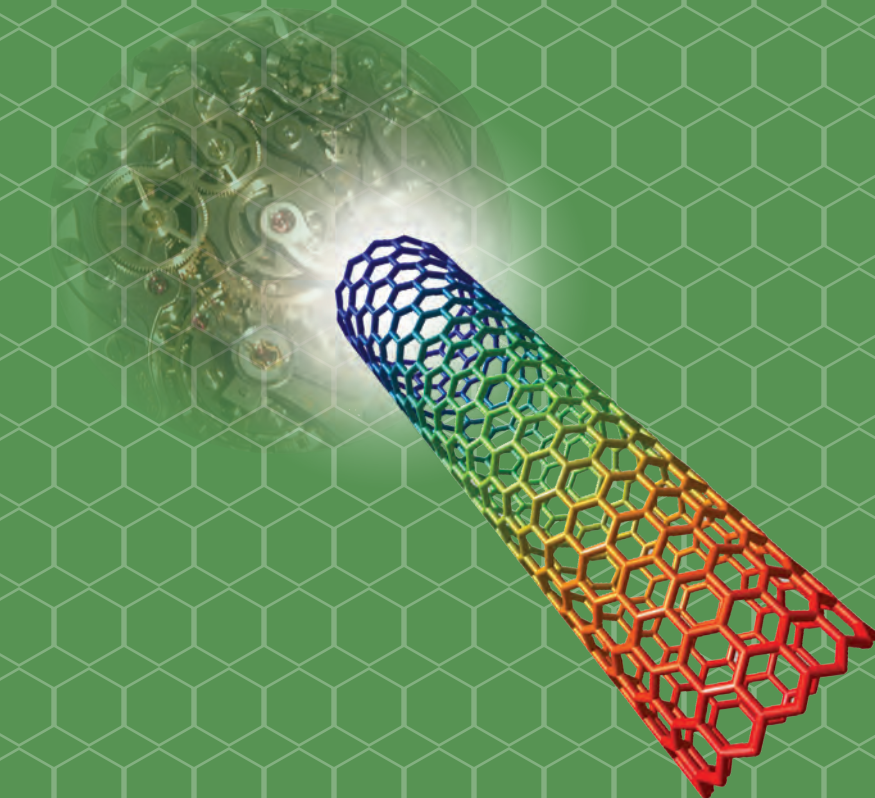
**N. Ramakrishnan**

**Raimund Rolfes**

**Vinod Tewary**

Honorary Editor:

**Satya N. Atluri**



ISSN: 1546-2218 (print)  
ISSN: 1546-2226 (on-line)

**Tech Science Press**



## Multiscale Modeling of Crystalline Energetic Materials.

O. U. Ojeda<sup>1</sup> and T. Çağın<sup>1</sup>

**Abstract:** The large discrepancy in length and time scales at which characteristic processes of energetic materials are of relevance pose a major challenge for current simulation techniques. We present a systematic study of crystalline energetic materials of different sensitivity and analyze their properties at different theoretical levels. Information like equilibrium structures, vibrational frequencies, conformational rearrangement and mechanical properties like stiffness and elastic properties can be calculated within the density functional theory (DFT) using different levels of approximations. Dynamical properties are obtained by computations using molecular dynamics at finite temperatures through the use of classical force fields. Effect of defects on structure is studied using classical molecular dynamics methods. Temperature induced reactions at elevated temperatures have been studied using ab initio molecular dynamics method for moderate size crystals of nitroethane. Furthermore, while presenting the state of the art in the study of modeling energetic materials, the current advances in the area as well as the limitations of each methodology are discussed.

**Keywords:** Multi-Scale, Energetic Materials, DFT, MD.

### 1 Introduction

The need for a multi-scale modeling approach that can probe a material system to provide a description of processes ranging from molecular level to macroscopic behavior is nowhere more obvious than in the study of energetic materials (EM). In order to understand the chemical, physical and mechanical behavior of these materials one needs to employ theories ranging from quantum mechanics/quantum chemistry, molecular dynamics with reactive and non-reactive potentials, statistical thermodynamics, micromechanics, solid mechanics and fluid dynamics allowing for reactions. The energetic materials are stable organic compounds with large negative enthalpies of formation, which are characterized by their ability to undergo chemical transformations starting from the initiation of reactions at the molecular

---

<sup>1</sup> Texas A&M University, College Station, TX, U.S.A.

level to sustaining a supersonic detonation at macroscopic scale. This multi-scale phenomenon is observed if enough external energy, either in the form of a heat pulse or a large pressure wave, is supplied to a secondary EM so that it reacts, a detonation front will form. In this front, a sudden increase in the material density will be accompanied by a release of temperature, detonation products (usually hot gases), and light, in the opposite direction of the detonation front. This sudden release in pressure and temperature, will effect on the un-reacted mass, ahead of the detonation front, increasing the velocity of its propagation. The time scales and characteristic lengths can vary from a few angstroms, as in the case of lengths of bonds and ordering of molecules within a crystal, to a few nanometers; as in the case of the thickness of initiating reactive layer, and up to a large distance as in the case of the of the material experiencing a shock compression of the expanding wave. The study of effect of the steep changes in density and pressure as the shock propagates through the media if defined through a continuum description requires incorporation of high gradients and rapid variation of field variables (Srivathsa and Ramakrishnan 2008). Although the theory of explosions in gas phase is well developed (Zel'dovich and Raizer 2001; Terao 2007), for a condensed detonating secondary energetic material, which is initiated by another more reactive material, like a metal azide or perchlorates (Campbell, Holland, Malin and Cotter 1956; Volker Weiser 2001) a molecular description is far from being complete (Dlott, Peter and Jane 2003).

In the formulation of plastic bonded explosives, crystals of energetic materials are fragmented and compressed with a binder. In order to describe dynamic response of explosive determination of their mechanical properties is essential, since localization of strain energy has long been the suspect of the formation of reaction zones (Sewell, Menikoff, Bedrov and Smith 2003), or “hot-spots”. In addition to this, fracture along a given plane can act as energy barriers and hinder a reaction from completing, hence causing unexpected behavior in some cases.

In the following sections, we aim to present our current effort and relevant results in modeling the complex behavior of energetic materials as well as referring to critical work conducted in this area by other researchers.

We mainly will present a systematic study of crystalline energetic materials and analyze their properties using different levels of theory: at the most fundamental level, we study the ground state properties through the use of the *ab initio* and density functional theory (Kohn and Sham 1965) (DFT) methods. In this study we have used various energetic materials such as cyclotetramethylene tetraaminamine ( $\beta$ tHMX), pentaerythritol tetranitrate (PETN), RDX, Fox-7 and nitromethane (NM). We report on structure, electronic structure, and charge densities as a function of applied mechanical stimuli, under volumetric compression, and anisotropic compres-

sion. The structural, mechanical and dynamical properties at finite temperatures are obtained by molecular dynamics simulations with classical atomistic force fields. From these classical simulations various macroscopic properties are extracted. In order to study the reactions in condensed phase we have used ab initio molecular dynamics methods at elevated temperatures. Furthermore, current advances in the area as well as the limitations and failures of each methodology are discussed.

## 2 Ab Initio Level Modeling of Energetic Materials

Since the earlier studies(Perger, Pandey, Blanco and Zhao 2004); it was clear that a systematic study of the structure and properties of energetic materials was not a simple task that could give meaningful information by the use of a generic basis set. For example, the initial calculated energy barrier for the rearrangement(Dewar and Ritchie 1985) of nitromethane (NM) to methylnitrite (MNT) was 47.0 Kcal/mol. Later, the value of 73.5 Kcal/mol reported by McKee(McKee 1986) indicated dissociation of NM as the most probable pathway. Nonetheless, Hu's group(Hu, He and Chen Liu, Fan-Chen) reported NM breakdown via C-N bond rupture (61.9 kcal/mol) and Nguyen's group(Nguyen, Le, Hajgato, Veszpremi and Lin 2003) have reported direct dissociation to  $\text{CH}_3$  and  $\text{NO}_2$  via radical formation (63 kcal/mol). Twenty years later, investigations with a transfer Hamiltonian indicates that the radical formation is the most probable pathway(McClellan, Hughes and Bartlett 2005).

The adiabatic potential energy surface (PES) of the simplest secondary energetic material, NM, shows a multiple energy minima's, caused by the interaction of the nitro oxygen atoms with the methyl hydrogen (Figure 1). We can expect a more complex potential energy surface (PES) for larger and more complex molecules like pentaerythritoltetranitrate (Gruzdkov, Dreger and Gupta 2004) (PETN) and cyclotrimethylenetrinitramine (RDX).

Due to the size and low symmetry of the relevant systems, earlier studies of EM's focused on simple molecules (Miller 1995; Son, Asay, Bdzil and Kober 1995; Soto 1995; Soulard 1995; Tsai 1995; White, Barrett, Mintmire and Elert 1995) and the development of electrostatic potentials(Pinkerton and Martin 1995). The appearance of periodic boundary condition studies came about much later, with the use of the Hartree-Fock approximation and tools like fixed bonds/angles to reduce the degrees of freedom and thus the size of the calculations(Kunz 1995).

We have focused first on developing knowledge at the electronic level within the DFT approximation on the following systems;  $\beta$ -HMX(Cady, Larson and Cromer 1963; Yoo and Cynn 1999; Stevens and Eckhardt 2005), FOX-7 (Gilardi and George 1984; Bemm and Ostmark 1998; Evers, Klapotke, Mayer, Oehlinger and Welch

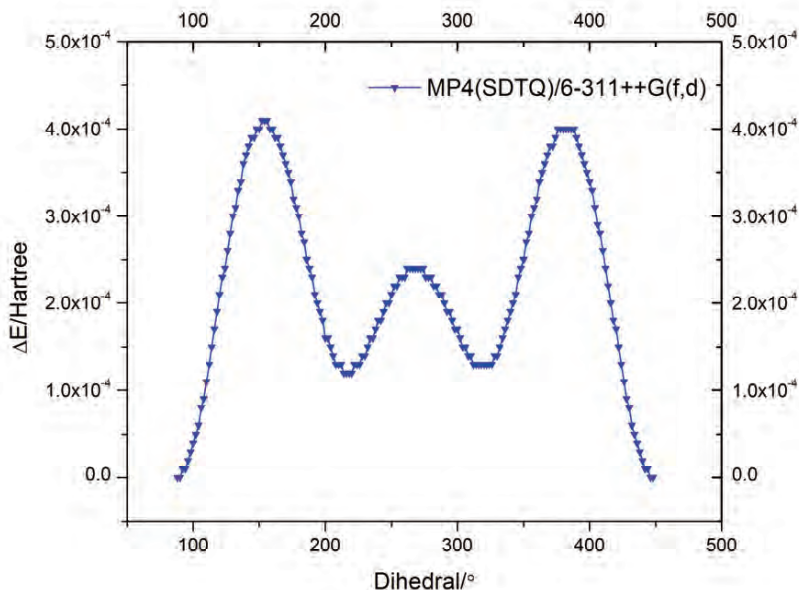


Figure 1: Potential Energy Surface (PES) of NM. The dihedral angle, initially at the optimized position ca.  $90^\circ$  is formed by hydrogen, the central carbon atom and one of the nitro group's oxygen. Increments of  $2^\circ$  used.

2006; Meents, Dittrich, Johnas, Thome and Weckert 2008; Meents, Dittrich, Johnas, Thome and Weckert 2008), TATB(Cady and Larson 1965; John R. Kolb 1979; Bower, Kolb and Pruneda 1980; Lewis L. Stevens 2008), NM(Trevino, Prince and Hubbard 1980; Bagryanskaya and Gatilov 1983; Cromer, Ryan and Schiferl 1985) and PETN-i (Booth and Llewellyn 1947; Olinger, Halleck and Cady 1975; Olinger and Cady 1976; CCSDT 2001).

Energetic materials systems usually have a low symmetry crystal structures. TATB, the system with the lowest symmetry in the unit cell, has a space group P-1, only inversion as the symmetry operation. The higher symmetry system, PETN, is a tetragonal crystal, but its tetrahedral four arm chemical structure, with a  $sp^3$  hybridized central carbon has four resonant nitro groups at the end of these arms, with this stiffer structure, the convergence to small tolerances in both energy (smaller than  $3 \times 10^{-6}$  eV, or  $10^{-7}$  A.U.) of the self-consistent field cycle, and forces ( $5 \times 10^{-4}$  eV/Å) is required, in ab-initio quantum chemistry calculations.



In the case of plane-wave approximation, we have used both ultra-hard and regular projected-augmented wave method potential lists, with the use of the VASP software. At the above tolerances used, we have found convergence to 700 eV for normal potentials, and 1000 eV for ultra-hard potentials. K-point sampling space converged at a Monkhorst-Pack grid size of 2x2x2. Troullier-Martin pseudopotentials (Troullier and Martins 1991), as well as PAW potentials (Kresse and Hafner 1993; Kresse and Hafner 1994; Kresse and Furthmüller 1996; Kresse and Furthmüller 1996; Kresse and Joubert 1999) for the case of plane wave basis have been used. Further calculations on the systems have been performed with the Crystal06 package using an 6-31G\* basis set.

## 2.1 Equilibrium Properties

Under a specified volume or pressure, the corresponding energy for each system can be describe through the use of a proper equation of state (EOS). We have performed calculations on the crystals of cyclotetramethylene tetraaminetrinitrate ( $\beta$ -HMX), pentaerythritol tetranitrate (PETN), RDX, FOX-7 and nitromethane (NM), the results are displayed in Figure 2, in order to determine the EOS and equilibrium properties of each.

Studies on the thermochemical properties of  $\beta$ -HMX and its polymorphic phases. (Choi and Boutin 1970; Brill and Goetz 1979; Main 1985), (Pople, von Rague Schleyer, Kaneti and Spitznagel 1988), (Lyman, Liao and Brand 2002) for schemes based on isodesmic (having the same type of bonds) and isogyric (spin-conserved) in which the effect of different basis sets is explored, indicate that a larger 6-311++G(3df,3pd) basis set on geometries optimized with the 6-31G(d) basis set (Cobos 2005) are required. We have performed calculations with the gradient corrected PBE functional (Perdew, Burke and Ernzerhof 1996) on single crystal models using periodic boundary conditions. Extended basis sets (Gatti, Saunders and Roetti 1994) with primitive coefficients for carbon, hydrogen, nitrogen and oxygen, as implemented in the crystal06 package were employed (Dovesi, Saunders, Roetti, Orlando, Zicovich-Wilson, Pascale, Civalieri, Doll, Harrison, Bush, Ph. and Llunell 2007). Initial structures for these crystals were obtained from the Cambridge crystallographic data base (Database 2007). For the case of molecular crystals, the determination of equations of state is the initial step in understanding how different changes in structure can alter the sensitivity of the material (Zeman, S. 2007).

At each state, relaxation of the atomic positions is achieved through optimization of the ionic degrees of freedom; cell shape is optimized through the corresponding cell parameters. The total energies for each system at a given strained volume were used for fitting through the Birch-Murnaghan (Birch 1947) equation of state (Birch

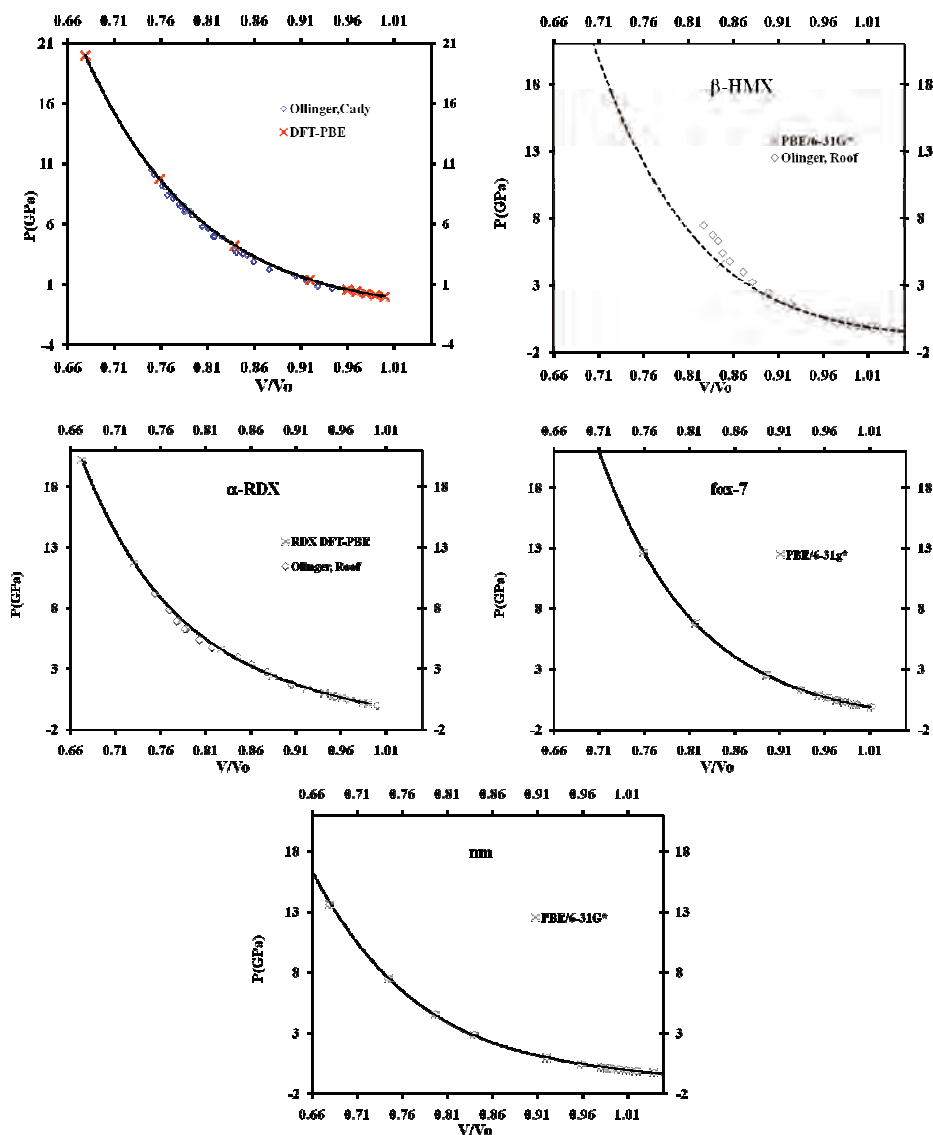


Figure 2: EOS data for PETN, RDX,  $\beta$ -HMX and fox-7; the experimental data (diamond symbols), and the calculated values (squares), using 6-31G\*/PBE functionals (squares). In each case, the Birch - Murnaghan EOS fit also shown (solid black lines).

1978) from which one can infer the equilibrium volume,  $V_o$ , bulk modulus at zero pressure,  $B_o$ , and derivative of bulk modulus,  $B_o'$ , with respect to pressure. For materials in which cohesive forces in the crystal unit cell are mostly covalent, (as opposed to weaker dispersion forces), usually the equation of state is sufficient to predict phase changes and their relative stability.

It is well known that the impact/shock sensitivity of the EM depend strongly on the geometry of the contact relative to the shape of the sample, the material's structure, morphology and its chemical and thermodynamic properties. Finite linear stress models (i.e., second order elastic constants) may give a best initial approximation to the response of the material under hydrostatic pressures. PETN, which has a tetragonal crystal structure, the optimized volume is found to be 3% higher than the experimental one of  $574.638 \text{ \AA}^3$ . Comparison with experimentally observed bulk modulus and equilibrium volumes is summarized in the following table:

Table 1: Equilibrium properties for PETN.

$V_o(\text{\AA}^3)$	$B_o(\text{GPa})$	$B_o'$	Reference
600.3	14.5	6.7	(Sewell, Menikoff et al. 2003)
590.8	9.4	11.3	(Olinger, Halleck et al. 1975)
579.47	14.1	10.4	(Sorescu, Rice and Thompson 1999)
595.46	11.26	10.28	This work

Nitromethane, which is a liquid at ambient conditions, has a crystal unit cell of orthorhombic symmetry (No.19). The equilibrium parameters are summarized in Table 2:

Table 2: Equilibrium Parameters for nitromethane

$V_o(\text{\AA}^3)$	$B_o(\text{GPa})$	$B_o'$	Reference
310.35	6.78	5.88	(Sorescu, Rice and Thompson 2000)
291.87	9.14	6.10	(Sorescu, Rice et al. 2000)
292.7	7.0	5.7	(Cromer and Schiferl 1985)
290.83	8.22	8.47	This work

The use of larger basis sets, better correlation functions, and an improvement in computational hardware, has made DFT the method of choice of most of the ab-initio calculations reported on energetic materials, which now encompass decomposition mechanisms (Maharrey and Behrens 2005) studies, geometry and electronic structure optimization (Xiao, Ju, Xu and Fang 2004; Ju, Xu and Xiao 2005;

Li, Huang and Dong 2005; Zhang, Shu, Zhao, Dong and Wang 2005), heats of formation (Chen and Wu 2001; Korolev, Petukhova, Pivina, Sheremetev, Miroshnichenko and Ivshin 2004; Qiu, Xiao, Ju and Gong 2005; Byrd and Rice 2006) and models for correlation of sensitivity and heats of detonation (Edwards, Eybl and Johnson 2004; Drake, Hawkins, Hall, Boatz and Brand 2005; Moore, Funk and McGrane 2005; Zhao, Zhang and Li 2005; Badders, Wei, Aldeeb, Rogers and Mannan 2006).

## 2.2 *Electronic Band Structures and Charge Densities*

If we let the molecular fragments stand apart at a large distance, while keeping the translational symmetry of the system intact, and perform a SCF calculation, we can obtain the electron density of the non-interacting system. We can determine the difference density map between the electron density of this non-interacting density, and the charge density obtained from the optimized crystal structure of nitromethane. Here, we have used a linear scale, since the difference in the two charge densities is expected to be small. The degree and number of hydrogen bonds can also play a role in the stability and sensitivity of each type of system.

The electronic band-structure, obtained using a 8x8x8 symmetric k-space Monkhorst-Pack integration grid, shown in the following Figure 3 for NM. We have included the Fermi level as a dotted line, to facilitate comparison of the energy levels with the atom projected density of states. To determine the density of states the integration path over the reciprocal space is taken along the high symmetry directions; as displayed in the inset.

The calculated energy band gap at  $\Gamma$  is 1.9E-1 A.U. or 5.24 eV of PETN, Figure 4; which is a characteristic large value for an insulating crystal. There is a larger amount of population coming from oxygen states near the valence band, while the first conduction or excited state band is mostly populated from oxygen and nitrogen states. This indicates the activity the nitrogen and oxygen atoms, which for nitromethane arises only from the nitro groups, in the valence and conduction states.

## 2.3 *Adiabatic Isotropic and Anisotropic Compression of Energetic Materials*

If we consider that the first part of a supersonic detonation or shock is always an adiabatic compression of the solid to the Hugoniot line, the behavior of energetic materials through adiabatic compression is of relevance. The effect of compression in the observed temperature has been studied for shocked states (Zel'dovich and Raizer 2001) assuming a vanishing surface upon detonation as:

$$T = T_0 \exp \left( \int_{p_0}^p \frac{dP}{\frac{\partial E}{\partial V} + p} \right) \quad (1)$$



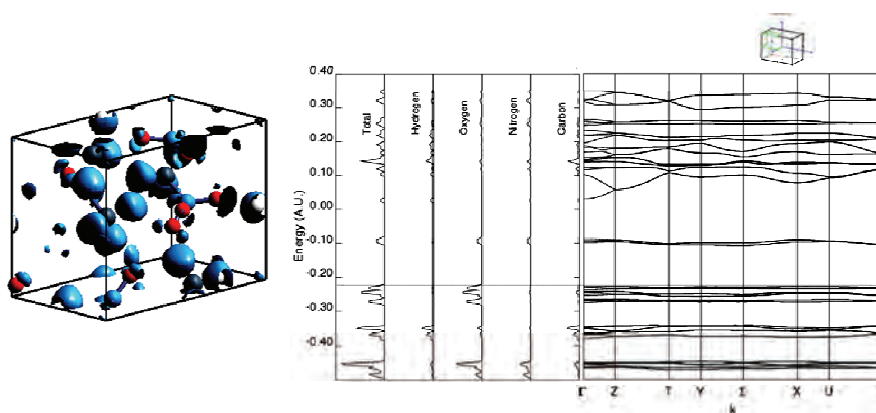


Figure 3: The characteristic large band-gap of these materials can be observed from the electronic band structure (far right), and density of states (center) of Nitromethane. The charge density around each atom is displayed on the left.

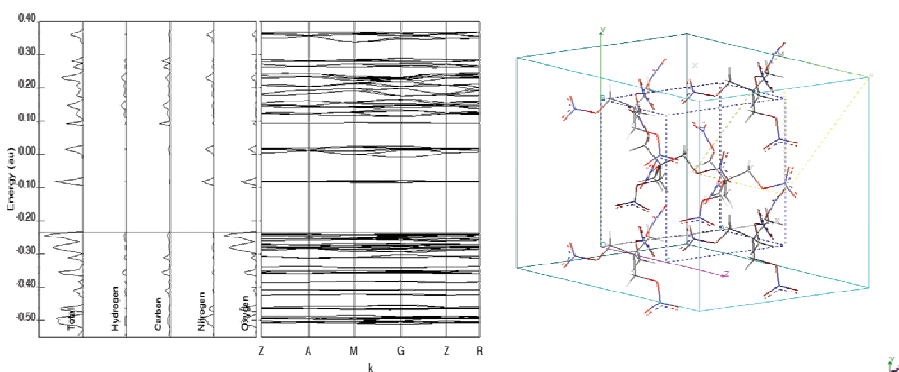


Figure 4: Electronic band structure of PETN. Contribution to the first two available regions above the Fermi energy are due to contributions mostly from oxygen and nitrogen atoms (left). The PETN unit cell (right), the reciprocal space construct is displayed as the outer cube concentric to the primitive cell.

There is an exponential behavior on temperature upon compression. We have studied the uniaxial compression of NM,  $\beta$ -HMX and PETN. Through axial planes and high symmetry family of planes [100], [010], [001], [110], [011], [101] and [111] axes. Prior to each deformation, the system was rotated so the desired plane was oriented along the 'z' axis. We have chosen a somewhat large value of volumetric compression maximum of 30% to understand the behavior that could be encoun-

tered for high-pressure impacts, such as a shock. This value of compression also gave an estimation of each system behavior without compromising the molecular integrity, which constituted each crystal.

Due to symmetry, the compression along [100] and [010] and as well as [101] and [011] directions for PETN are equivalent. This was also observed in the calculated band-structures at different volumetric compression values.

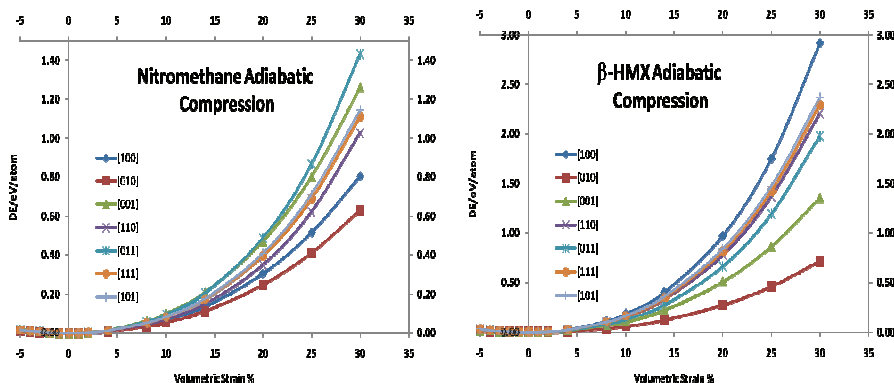


Figure 5: The adiabatic compression behavior of nitromethane (NM) and  $\beta$ -HMX.

From the total change in energy per atom for each system from Figure 5 and Figure 6, we observe that there is a higher energy requirement to attain the compressed state for  $\beta$ -HMX than for the other two systems studied. PETN required a larger energy than NM to be compressed. Uniaxial compression showed the largest change in energy per atom for  $\beta$ -HMX. We can correlate this energy requirement with the trend in sensitivity  $\beta$ tHMX < PETN < NM.

The relationship between an increase in energy that could cause the formation and excited states and anisotropic behavior has been proposed as the cause of anisotropic sensitivity for some systems. We further explore this effect on an adiabatic compression along particular high symmetry planes, for different systems. As the change in energy is correlated with the change in pressure, one would expect there would be substantial change in local temperature along the compression direction with highest energy change.

## 2.4 Effect of Compression on Electronic Properties: variation of band gap.

The variation of band gap as a function of compression is investigated in these energetic material systems. Figure 7 displays the calculated values of band gap for PETN under hydrostatic compression up to 33%. The variation is non linear in

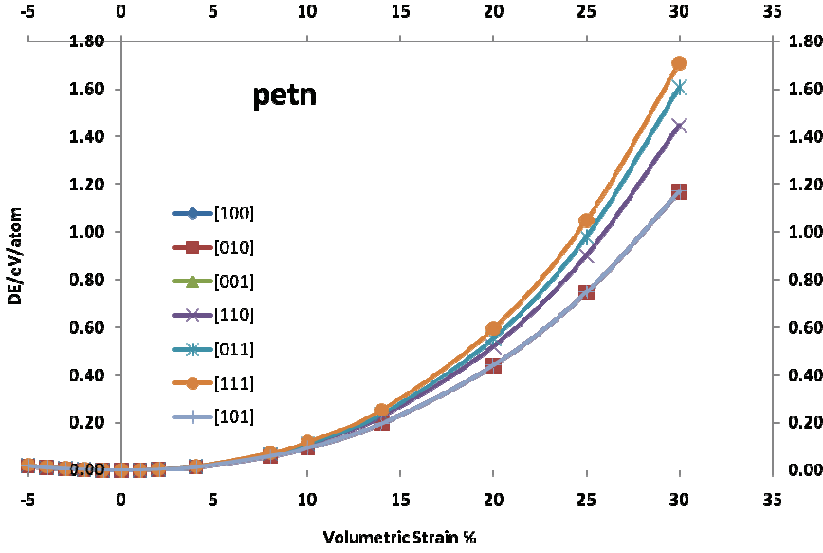


Figure 6: The adiabatic compression of PETN.

volumetric strain. We observe substantial decrease in band gap values, but no band gap closure for the volumetric strain ranges we explored (0% up to 33%).

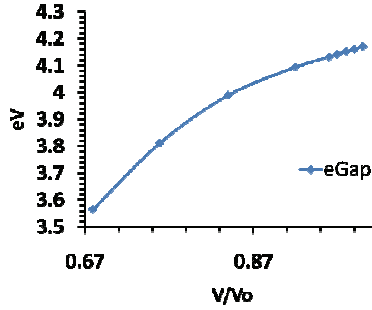


Figure 7: The variation of band gap in PETN under hydrostatic compression.

For PETN and NM, we have calculated the band structure and corresponding band gap along the EOS path. For PETN and NM, we have applied uniaxial compressions along [100], [001], [010], [110], [101], [011] and [111] directions. We observe no band gap closing, even to a value that could be considered to be closed at room temperature (ca. 26 meV) for a hydrostatic compression or for anisotropic

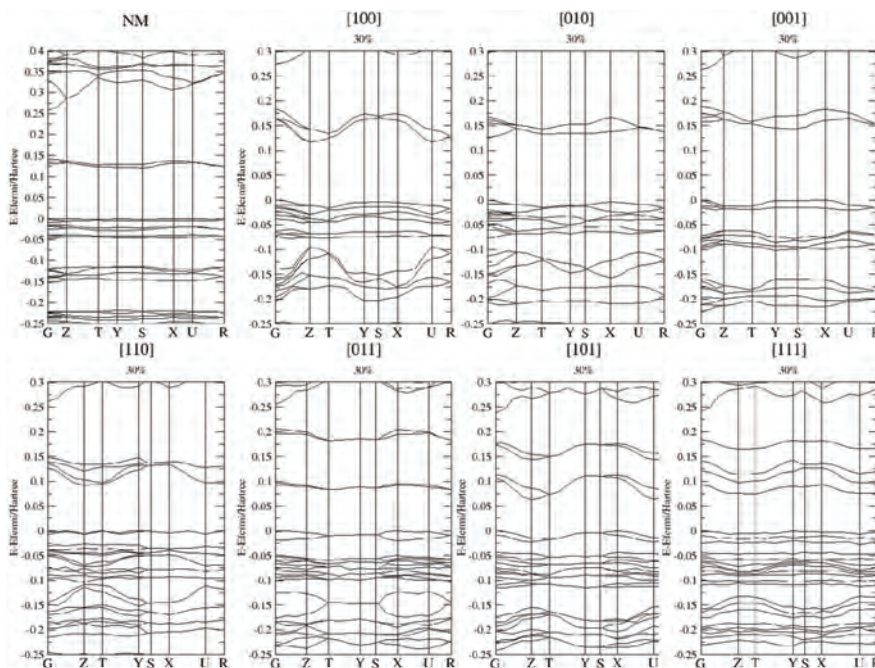


Figure 8: Band structure calculation at the optimized and uniaxially compressed states of NM.

compression. For PETN, we observe almost 2 eV decrease in [111] direction, for NM the decrease is less pronounced even increase is observed in some directions [100], [010] and [001]. The systematic behavior under uniaxial tension is a small but consistent decrease in band gap in all directions tension applied. In order to completely assess the variation of electronic structure as a function of isotropic compression and uniaxial stress one might need to include the effect of defects.

## 2.5 Vibrational Spectra Analysis of Energetic Materials

Coupling of phonons to low frequency or “doorway” modes have been suggested as an initiation path in energetic materials. In the long range limit, ab initio methods allow for the study of changes with respect to a corresponding pressure via vibrational frequency calculations (Tokmakoff, Fayer and Dlott 1993). We have used the optimized geometries for each system to obtain analytical first derivatives with respect to ionic displacements. Each atom is moved in directions along the three axis by a small step; the energy is then calculated self consistently. A total of  $3N+1$  calculations should be performed, but this number is reduced when



the symmetries of crystal are taken into account, as it is commonly implemented in the crystal06 code (Pascale, Zicovich-Wilson, López Gejo, Civalleri, Orlando and Dovesi 2004; Zicovich-Wilson, Pascale, Roetti, Saunders, Orlando and Dovesi 2004). The analytical first derivatives are then used to construct the “Hessian” at  $\Gamma$  point through numerical differentiation. The Hessian is the matrix of second derivatives, or force constants that is diagonalized to calculate the mass-weighted dynamical matrix. The number of eigenvalues obtained follows the  $3N-6$  rule for non-linear molecules, where  $N$  is the number of atoms in the molecule and 6 modes correspond to translations and rotations in three dimensions.

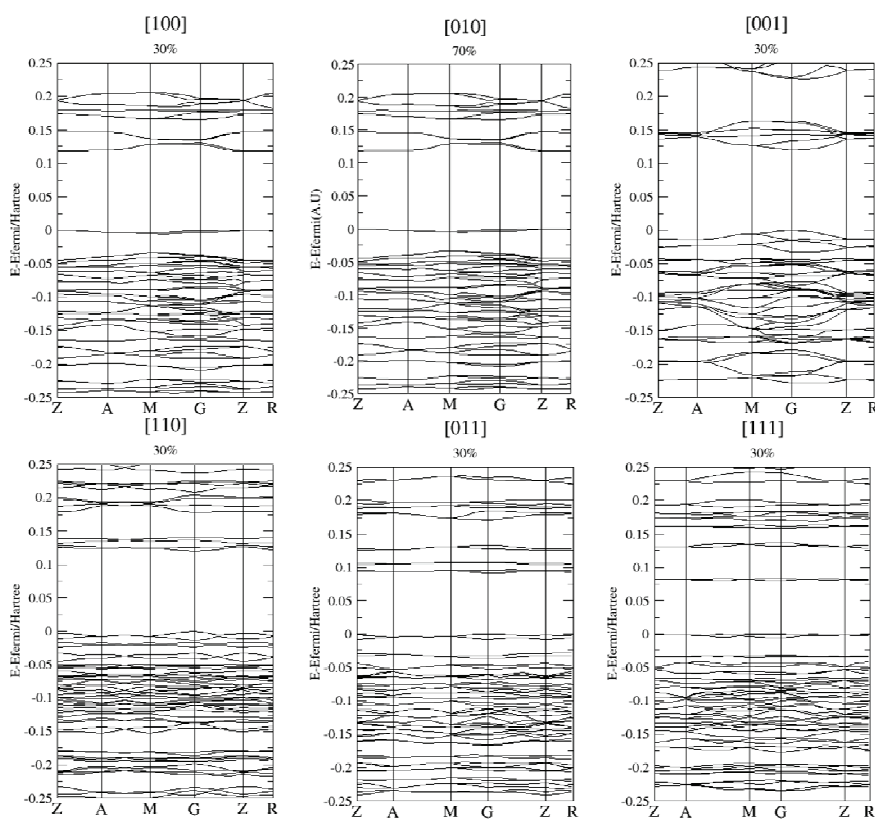


Figure 9: Band structure calculation results at the optimized and under uniaxially compressed states of PETN.

Calculation of the intensities is related to the derivative of the dipole moment with respect to the normal mode coordinate, times its degeneracy. The dipole moment can be obtained from the calculation of the Born effective charges (Zicovich-

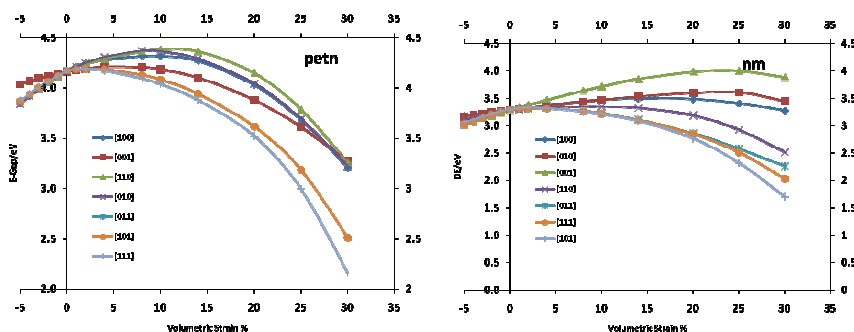


Figure 10: Variation of calculated band gap values of PETN (left) and NM (right) under uniaxial compression conditions.

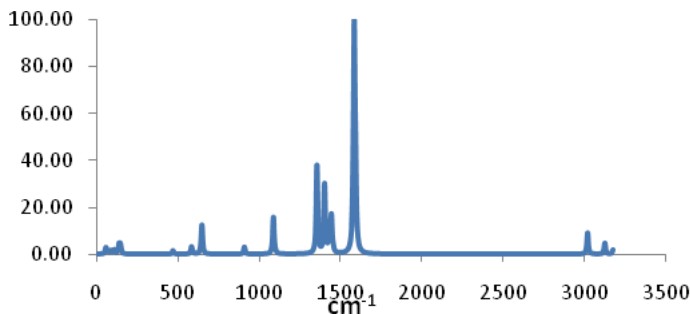


Figure 11: Vibrational spectra of the zero stress structure of NM.

Wilson, Dovesi and Saunders 2001), i.e.; the proportionality constant in the change of polarizability in one direction, with respect to a displacement along another direction.

Large integration grids (XLGRID) and number of K-points (6x6x6 mesh) are required to fulfill the Born charge sum-rule, or the neutrality of the cell. We have further used a tolerance for the differences in the energy for a SCF calculation with a value of 1E-8 A.U. The vibrational spectra, with intensities fitted with the use of Lorentz fits for nitromethane, with a point group  $C_{2v}$  (order 4), is displayed Figure 11.

Assignment of each mode has been performed by direct visualization of the eigenvalues (Ugliengo, Viterbo and Chiari 1993; Ugliengo 2006), and from referenced work (McKean and Watt 1976; Ouillon, Pinan-Lucarre, Ranson and Baranovic

2002). The peak, at  $650\text{ cm}^{-1}$ , is due to the symmetric NO bending that is accompanied by a C-N stretching, B2-mode. The C-N stretching mode has a frequency of  $910\text{ cm}^{-1}$ , versus the reported values (McKean and Watt 1976; Ouillon, Pinan-Lucarre et al. 2002) of  $917\text{ cm}^{-1}$  and  $920\text{ cm}^{-1}$ . Higher in frequency, at 1088, the  $\text{CH}_3$  deformation mode (B1) can be found (Ouillon, Pinan-Lucarre et al. 2002). The next peak corresponds to a  $\text{CH}_3$  bending mode ( $\delta_2$ ), adjacent to the symmetric NO stretching mode. The maximum at  $1441\text{ cm}^{-1}$  corresponds well with the  $\text{CH}_3$  bending mode ( $\nu_{10}$ ). The dominant peak at  $1548\text{ cm}^{-1}$  corresponds the antisymmetric NO stretching mode.

At higher pressures, the relative intensities of low frequency modes (closer to  $50\text{ cm}^{-1}$ ) increase with respect to the modes close to the largest NO-antisymmetric mode. In general we can see that there is no longer a distinction in from the symmetric NO-stretching from the rest of the deformations with the  $\text{CH}_3$  molecule. There are also new peaks appearing in the region from 1432 to 1473. The most predominant peak at pressure of 13.55 GPa is the B1 mode, which is higher in frequency than the other two NO antisymmetric modes (B2, B3), as compared with the 2.89 GPa and 0 GPa states.

At  $1432\text{ cm}^{-1}$ , the NO-symmetric stretch is accompanied by a deformation of the hydrogen bonds of the methyl group. The symmetric stretch is not so pronounced. We also found that the mode at  $1358\text{ cm}^{-1}$  and other modes at lower energies now have non-zero intensities; this would indicate the formation of new bonds or dipole interactions in a regular IR experiment. Also the stretching of the C-N bond, with an oscillation frequency of  $975\text{ cm}^{-1}$ , has reduced its intensity to the normalized value of 1.

Table 3: Vibrational and ZPE corrections from vibrational frequencies. Modes at 0 and higher pressures of Nitromethane, frequency values reported in inverse centimeter ( $\text{cm}^{-1}$ ), pressure values reported in GPa, energy in Hartree/unit cell.

	Frequency			Mode		
Pressure	0	2.89	13.55			
	1584	1589	1609	NO	stretching	Anti symmetric
	1443	1437	1473	CH3	bending	
	1402	1410	1432	NO	stretching	Symmetric
	1355	1348	1438	CH3	bending	
	1087	1095	1397	CH3	bending	
	910	926	975	C-N	stretching	
	650	660	686	NO-CN	deform	
ZPE	0.1996	0.2021	0.2086			

The difficulty of assigning fixed position for the hydrogen atoms, led to the conclusion in earlier reports that at ambient conditions the methyl group was able to rotate freely. We can imagine that now that at these high pressures, most likely the methyl group is fixed, due to electrostatic interactions and hydrogen bonding (as indicated by the large increase in the ice peak closer to  $3000\text{ cm}^{-1}$ ).

Extension along the nitromethane backbone is limited, as indicated by the drastic reduction of the C-N stretch mode. In this way, changes in the structure of the crystal with respect to changes in hydrostatic pressure can be deduced. Changes in conformation and structure can have a direct relationship to properties like elasticity and impact sensitivity.

## **2.6 Mechanical Properties of Energetic Materials by DFT methods.**

It is well known that high energy materials (EM's), for which application ranges from initiators in safety bags, detonation charges, propellants and as secondary explosives, are anisotropically sensitive to heat and mechanical shock (Dick 1984; Dick 1993; Dick 1997). It has been found experimentally, that these materials may undergo detonation by unplanned stimuli. This has raised issues related to transportation cost, safety, logistic and time burdens related to handling of these materials.

For the formulation of plastic bonded explosives, crystals of energetic materials are fragmented and compressed with a binder. Understanding the mechanical properties is required, since localization of strain energy has long been the suspect of the formation of reaction zones (Sewell, Menikoff et al. 2003), or "hot-spots". In addition to this, fractures along a given plane can act as energy barriers and hinder a complete reaction, causing unexpected behavior in some cases. When the applied mechanic shear exceeds the strength of the lattice, plastic deformation arises and multiple dislocations, growth of defects can occur. Therefore the knowledge of the elastic properties is crucial in understanding the material's initial response.

We have performed calculations on the crystals of ( $\beta$ tHMX), NM, RDX, TATB, Fox-7 and PETN using CRYSTAL program. In our earlier work we have studied anisotropic elasticity of various metals, ceramics and oxides using mainly plane wave approaches (Uludogan, Çağın, 2006; Uludogan, Guarin, Gomez, Çağın, Goddard, 2008; Kart, Uludogan, Karaman, Çağın, 2008; Bilge, Kart, Kart, Çağın 2008; Chakrabarty, Çağın, 2008; Kalay, Kart, Kart, Çağın, 2009; Sevik, Çağın, 2009; Pham, Çağın, 2010).

By applying small strains to the crystallographic unit cell, a change from the original, optimized cell energy is obtained. This difference in energy can then be com-



pared in terms of polynomial expansion, to the strain energy;

$$E_0 - E = V_o C_i \eta_j + \frac{V_o}{2} C_{ij} \eta_i \eta_j + \quad (2)$$

Where  $V_o$  is the initial “un-deformed” cell volume, and  $\eta_i$  and  $\eta_j$  are the applied elastic Cauchy or “engineering” type of strains. Since we are interested only on the symmetric part of the strain tensor, we can employ the contracted or “Voigt” notation.  $C_{ij}$  are then the second order elastic constants.

$$C_{ij} = \frac{1}{V_o} \frac{\partial^2 E}{\partial \eta_i \partial \eta_j} \quad (3)$$

If we realize that the initial reference cell is subject to no additional forces, this is, in its “zero stress” state, the first term in the expansions is ignored. Comparison to a second or higher order polynomial fit against a strain-energy curve will enable us to obtain the corresponding second order elastic constants. The resulting second and higher order elastic constants can in turn be related to the anisotropic response of the crystal to mechanical stimuli. Due to the ample experimental data available (Winey and Gupta 2001; Sun, Winey, Hemmi, Dreger, Zimmerman, Gupta, Torchinsky and Nelson 2008), elastic constant values of PETN allow for a direct assessment of the accuracy of the calculation. A summary is found in the following table.

Table 4: Second order elastic constants of PETN. Comparison is made with experimental data, values in GPa. Value of the calculated  $B_o$  from the equation of state.

	6-31G*/PBE	Exp (Sun, Winey et al. 2008)	Exp (Winey and Gupta 2001)
$C_{11}$	17.88	17.12	17.22
$C_{12}$	8.10	6.06	5.44
$C_{33}$	13.44	12.18	12.17
$C_{13}$	10.17	7.98	7.99
$C_{44}$	5.42	5.03	5.04
$C_{66}$	2.95	3.81	3.95
$B_o$	11.79	10.05	9.94
V	592.73	574.64	574.64

For the case of PETN, we have studied the full elastic tensor at different applied pressures. Stability conditions for this tetragonal system are;

$$C_{11} - C_{12} > 0 \quad (4)$$

$$C_{11} + C_{12} + C_{33} > 0 \quad (5)$$

$$(C_{11} + C_{12})C_{33} - 2C_{13}^2 > 0 \quad (6)$$

$$C_{44} > 0 \quad (7)$$

$$C_{66} > 0 \quad (8)$$

The last two conditions are fulfilled clearly for all the applied pressures. This applies for the second condition two, as none of the involved constants takes a negative value. The rest of the conditions at the studied pressure values are summarized in the following table:

Table 5: Mechanical Stability Conditions for PETN.

P	$c_{11}-c_{12}$	$(C_{11}+C_{12})C_{33}-2C_{13}^2$
0.00	9.78	142.35
0.12	10.90	161.44
0.25	12.27	176.68
0.41	13.58	198.24
1.39	21.46	414.79
4.25	41.54	1334.39

For crystal of other symmetries, no instabilities were found.

The value of the elastic constants can provide an insight into the anisotropic strength of the intermolecular interactions. Although there are other various reports that try to relate Cauchy strains with respect to pressure with the value of the elastic constants, we can only take the values as approximate, as the methodology of obtaining them is rather indirect. For example, Brand attempted to obtain the first three elastic constants (Brand 2006) with a STO-3G basis sets and Hartree Fock approximation, but the elastic constants were obtained from stress/strain curves, along each crystal vector (only 3 constants total). For the case of NM, although no available data on the elastic constants was available, the predicted higher sensitivity along the [001] direction, as predicted by the model of steric hindrance, is supported by the lowest value of this constant predicted in our study

Our calculated values for PETN agrees with the calculated by Gupta's group with sound speed experiments (Winey and Gupta 2001). Values of the bulk modulus and its pressure derivative correspond well to the ones found experimentally by Ollinger, Halleck and Cady, (Ollinger, Halleck et al. 1975). The trend  $C_{11} < C_{33}$  for this system is an indication of the increased sensitivity found along the [110] plane. For  $\beta$ -HMX there has been evidence (Palmer and Field 1982) of a cleavage

Table 6: Calculated elastic constants of Energetic Materials. For the systems, NM and b-HMX, this represents the full elasticity tensor. Only the diagonal terms are reported for the remaining systems. The values are in GPa.

	NM	$\beta$ -HMX	Fox-7	RDX	TATB
C <sub>11</sub>	17.38	19.00	37.56	79.66	23.62
C <sub>22</sub>	11.98	17.66	19.79	18.23	76.55
C <sub>33</sub>	11.92	17.88	46.60	17.40	15.00
C <sub>44</sub>	5.02	10.65			
C <sub>55</sub>	3.44	6.01			
C <sub>66</sub>	4.91	8.51			
C <sub>12</sub>	6.42	10.7			
C <sub>13</sub>	9.19	9.93			
C <sub>15</sub>	-	-0.22			
C <sub>23</sub>	7.13	11.81			
C <sub>25</sub>	-	-3.72			
C <sub>35</sub>	-	-2.01			
C <sub>46</sub>	-	-3.83			

plane along the (011) plane, is further supported by the observation of a weaker C<sub>11</sub> constants as compared to C<sub>22</sub> and C<sub>33</sub>. Calculated values for bulk modulus and pressure derivatives are in good agreement with experimental observations (Stevens and Eckhardt 2005).

## 2.7 Empirical Van der Waals correction to DFT energies.

Despite its successful application in many strongly bound systems, current approximations employed within Density Functional Theory (Kohn and Sham 1965) (DFT) methodologies have been unable to correctly predict interactions that are significant to various biological and biochemical molecules (Grimme, Antony, Schwabe and Muck-Lichtenfeld 2007) and neutral molecule crystals like those of rare-gas dimers (Tsuzuki and Luthi 2001; Tao and Perdew 2005), polycyclic and aromatic hydrocarbons (Suzuki, Green, Bumgarner, Dasgupta, Goddard and Blake 1992; Goursot, Mineva, Kevorkyants and Talbi 2007), and energetic materials (Olinger, Halleck et al. 1975; Hemmi, Dreger, Gruzdkov, Winey and Gupta 2006; Byrd and Rice 2007) (EM). Besides being a requirement for developing engineering models and to understand the behavior of the material in the conditions of its envisioned applications, a proper description of the potential energy surface bears further implications when determining thermodynamic properties like bulk modulus, and second and higher order elastic constants.

It has been suggested in literature that the lack of a proper description of the equilibrium volumes in these molecular systems (Blöchl 1994; Kresse and Joubert 1999; Wu, Vargas, Nayak, Lotrich and Scoles 2001; Kurita, Inoue and Sekino 2003; Stefan 2004; Chakarova and Schroder 2005; Thonhauser, Cooper, Shen, Puzder, Hyldgaard and Langreth 2007) can be attributed to the lack of a proper description of the long range induced dipoles by neighboring molecules. To overcome this hurdle, some recent efforts have been directed towards developing methodologies to specific type of systems, like polymers (Kleis and Schroder 2005) or rare-gas dimers. Some attempts to improve current description of intermolecular forces at a higher level of theory include the choosing of a better description of the exchange functional, with some success mostly from parameterized generalized gradient approximations (Tao and Perdew 2005) and other hybrid functionals, i.e.; X3LYP (Xu and Goddard 2004), the use of orbital-dependent functionals (Engel 2003), optimized effective potentials (Qin Wu and Weitao 2003) or the addition of an external correction to the total ground state energy (Gonzalez and Lim 2003; Stefan 2004; Ortmann, Bechstedt and Schmidt 2006). Perturbation methods, like the spin-component-scaled MP2, have been estimated as inadequate for common pi-stacking and hydrogen bonded interactions (Bachorz, Bischoff, Hofener, Klopfer, Ottiger, Leist, Frey and Leutwyler 2008).

We have decided to test the idea of correcting the total energy of the equations of state for NM and PETN, by introducing a damped Buckingham type of potential (Hepburn, Scoles and Penco 1975; LeSar 1984) that accounts for dispersion forces. The implemented empirical term for the dispersion energy was developed by Elstner and Le Sar (LeSar 1984; Marcus, Pavel, Thomas, Sandor and Efthimios 2001):

$$E_{vdW} = \sum_{ij} \frac{c_6^{\alpha\beta}}{R_{ij}^{\alpha\beta 6}} f(R) \quad (9)$$

The damping function used here allows a decay to zero at a value ca. 3 Angstrom, to avoid over counting of energy due to bonding. For ease of comparison, the inner and outer exponents are constantly kept as 7 and 4, to allow for a similar behavior of the decay distance as previously reported results. The parameter “d”, called the decay factor, is related to the value at which the damped function will experience an inflexion (viz.  $1/r^6$ ), a value of 3 is chosen for the present calculations. The form of the functional is important since evaluation of first and higher order derivatives (e.g.; gradients, polarization, etc...) is necessary for calculation of other system properties. In this way, correction of the total energy determined from the Kohn-Sham Hamiltonian is corrected with the addition of an  $E_{vdw}$  term:

$$E_{total} = E_{KS} + E_{vdw} \quad (10)$$

Using polarizability values obtained at the MP2 level, Williams and Malhorta(Williams and Malhotra 2006) have obtained C6 coefficients that can be used in calculations with the 6-21G(\*\*) basis sets used to reproduced the energetic behavior of 24 hydrogen bonding and Van der Waals molecular interaction. These were obtained from scaling DFT energies to values calculated at the MP2/cc-pVQZ level, for dimmers like ethane, formaldehyde, benzene, water, etc.

For PETN, in which 2 type of oxygen atoms, one bridging and a pair sharing a resonant bond in the nitro group are present, two different coefficients for nitrogen have been utilized. For those interactions whose coefficients were not reported, Van der Waals radii and coefficients have been obtained as described previously(Williams and Malhotra 2006), based on hybridization or chemical environment of the atomic species. We have followed the same nomenclature used by Miller, e.g.; a tetrahedral  $sp^3$  carbon is labeled (CTE), a  $sp^3$ -hybridized oxygen is named OTE and so forth. By means of atomic polarizability values ( $p_\alpha$ ), coefficients can then be scaled using also the number of effective electrons, with a methodology proposed by Halgreen. (Halgren 1992),The C6 coefficient is then obtained by means of the Slater-Kirkwood approximation (Slater and Kirkwood 1931):

$$C_6^{\alpha\beta} = \frac{2C_6^\alpha C_6^\beta p_\alpha p_\beta}{C_6^\alpha p_\alpha^2 + C_6^\beta p_\beta^2} \quad (11)$$

Since  $R^{-6}$  interactions should dominate at long enough distances (Alonso and Mañanes 2007), we have considered summation of the  $E_{vdw}$  interactions not in one, but in a super-cell considering 4x4x4 primitive cells. Equilibrium parameters have been additionally been obtained for the systems: m-dinitrobenzene(Trotter and Williston 1966; Wojcik, Mossakowska, Holband and Bartkowiak 2002), 2-4-6-trinitrotoluene (Coleburn and T. P. Liddiard 1966; Coleburn 1970; Golovina, Titkov, Raevskii and Atovmyan 1994; Stevens, Velisavljevic, Hooks and Dattelbaum 2008), ethanol (Brown, Slutsky, Nelson and Cheng 1988), benzene (Cox 1958; Bacon, Curry and Wilson 1964; Jeffrey, Ruble, McMullan and Pople 1987), urea (Fischer and Zarembow 1970; Swaminathan, Craven and McMullan 1984; Haussuhl 2001), cyclohexa-2,5-diene-1,4-dione (Boldyreva 2003) (p-quinone), Benzene-1,3-diol (resorcinol) (Day, Price and Leslie 2001), g-glycine (Boldyreva 2008).

There is a drastic effect on the results obtained from VdW as opposed to neglect of dispersion. Although the difference in the bulk modulus is still bigger than 18%, the small discrepancy (below 5%) between the predicted equilibrium volume and the one used for reference in the initial calculations, indicates that an empirical correction can be further refined to yield values closer to experimental ones, without sacrificing computational time.



Table 7: Effect of VdW correction to DFT energies in the calculation of elastic constants. Values are in GPa. Volume in Å<sup>3</sup>

	C11	C33	C22	V
PETN-NOV	17.67	5.51	-	696.05
PETN-VDW	33.32	11.90	-	609.84
PETN-EXP	23.11	17.35	-	574.64
NM-NOV	58.68	5.25	2.36	254.11
NM-VDW	71.92	9.42	6.06	297.19
Resorcinol-VdW	26.68	57.23	41.96	490.61
Resorcinol-exp	8.60	19.50	28.80	534.70

### 3 Classical Force Field Based Simulations

Models like the Hugoniot equation have been applied to the processing of energetic materials (Firsich 1984; Sun, Garimella, Singh and Naik 2005), and the effect of detonation in pressure shock-waves has been investigated (Novozhilov 2005; Patterson, Lagutchev, Hambir, Huang, Yu and Dlott 2005; Urtiew and Tarver 2005). To this regard, constitutive relationships, like isotherms and isobars, can be obtained for the unreacted crystal by means of molecular dynamics methods. We have performed molecular mechanics and molecular dynamics calculations with the DREIDING force fields (Mayo, Olafson and Goddard 1988) as well as the following force fields; CVFF (Hagler, Huler and Lifson 1974; Hagler and Lifson 1974; Hagler, Dauber and Lifson 1979; Hagler, Lifson and Dauber 1979; Lifson, Hagler and Dauber 1979; Kitson and Hagler 1988; Kitson and Hagler 1988; Pina Dauber-Osguthorpe 1988), Compass (David Rigby 1997; Sun and Rigby 1997; Sun 1998; Sun, Ren and Fried 1998) and Universal (Rappe, Casewit, Colwell, Goddard and Skiff 1992).

Whenever the force field assigned atomic charges were not available (i.e. Universal, DREIDING), a charge equilibration method: the QEq method (Rappe and Goddard 1991) employed for charge assignments. For these simulations, with the Isothermal Isobaric ensemble (NPT) the code LAMMPS (Plimpton 1995), Cerius2 and Materials Studio have been used. Multiple in-house scripts and codes have been developed to analyze and perform data analysis.

We have found that for the pressures closer to ambient conditions, NM will have the largest thermal expansion.

In common applications, compression of EM's with a polymeric binder facilitates casting and machining. This is usually done with a small weight percent of binder included in the formulation. For example, composition LX-16 has 96%w PETN

and the rest as polymer binder (1980). Heterogeneities in the microstructure of polymer-bonded explosives raise difficulties in understanding trends like sensitivity and mechanical properties, as compared to the homogeneous material. Unlike other systems, e.g.; metals, the effect of plasticity in detonation properties of energetic materials remains a nascent topic; processing parameters can have an effect in the sensitivity of the energetic materials. Crystals purified with different solvents, e.g.; cyclohexanone or acetone, will produce different number of cavities and voids (Lionel Borne 1999), and become sources of dislocations. Changing from cyclohexanol/ethanol to  $\gamma$ -butyrolactone/water change the crystallization morphology of RDX from small crystallites to dendrites (Antoine E. D. M. van der Heijden 2008). The effect of the void and vacancy concentration has been suggested to have an effect in the sensitivity of systems like RDX and HMX (Ruth M. Doherty 2008). Crystallization conditions will also have an effect on the specific morphology of the grown crystal habit (Zepeda-Ruiz, Maiti, Gee, Gilmer and Weeks 2006).

Understanding the thermodynamic and elastic effects in sensitivity can help tailor some of the applications of EM's to the civilian realms..(Lozano and Fernandez 2007), and also reduce associated hazard of transporting and handling of the materials. The prepared crystals are usually compressed to achieve high density either with other type of energetic materials, or with a plastic binder. Detonation pressure for a given system will depend (Hartmut Kröber 2008) on the density of the material; therefore, compression to achieve high density in this binder-energetic material matrix is performed. Since there is a small weight percent of plastic binder, stresses localization caused by the close contact of different crystal faces can be expected, specially under conditions of high stress rate (as in direct impacts) or supersonic shock strains.

### ***3.1 Effects of Defects in Energetic Materials.***

It has already been shown that defects have an effect on the sensitivity to impact of the energetic materials. We want to explore the effect of crystal defects on the anisotropic mechanical response of the energetic materials under both hydrostatic and axial compression, and with the application of shock. It has been suggested that grain size and orientation more than void concentration can have an effect on the detonation pressure of some energetic materials (Czerski and Proud 2007; Landeriville, Oleynik and White 2009). By means of molecular dynamics simulations, we show the results of the studies on a commonly used secondary explosive; PETN, which has an anisotropic response to shock detonation. The goal is to understand the role of deformation mechanisms in the initiation of the energetic materials.

The slip plane has been suggested as the (110) plane, with possible Burgers vectors in  $\langle 111 \rangle$  (Gallagher, Halfpenny, Miller, Sherwood and Tabor 1992), other studies

suggest the formation of a slip system in [110](001) (Dick 1984). By means of layer projection, we have created large super cells (up to 868 molecules) of the latter, and studied by means of molecular mechanics and molecular dynamics simulations. Creation of the [110]- and [001]- layers with 3-D periodic boundary condition was performed initially on the single crystal system. This layers were then expanded to a matching length of ca. 35 Å per side. Stacking along the z-axis of the [001] was used for alignment. This created the first set of bi-crystals for simulation. After the results of molecular dynamics simulations were obtained, a larger grain system was set up. In this case the z-direction was doubled in size, with the intention of reducing the finite size effects of the stacking fault in the grain system. The crystal packing of PETN facilitates identification of a discrete number of layers on each side of the grain system.

In order to assess the quality of the force fields, molecular dynamics simulations have been performed in a large (4x4x6) super cell of PETN. The initial applied temperature (50K) was ramped in increments of 50K up to a value of 550K. Averages were obtained for the last 40 ps from the 60 ps run. Equilibrium volumes at 300K (621 Å<sup>3</sup>) are comparable to the experimental reported values (Booth and Llewellyn 1947).

From these runs initial structures of obtained for the succeeding molecular dynamics simulations to obtain the relaxed system's energies, at 50, 250 and 300K. The initial 50K temperature is employed in order increase the temperature gradually of the system to the target value of 300K. There is already a change in the density of the material when prepared along one phase, as compared to the denser packing found in the [110] direction. There is a stacking fault caused by the atom mismatch in the inter-planar spacing of the [110] direction as compared to the [100] direction.

The surface energy is calculated using the following formula:

$$\Delta E = E_1 - nE_0 \quad (12)$$

Here  $E_1$  indicates the grain system energy,  $E_0$  the minimum energy per face ( $E_0/2$ ) and  $n$  is the number of molecules in the system.

From molecular mechanics calculations, which were iterated up to 2000 steps, with a convergence on the energy of  $10^{-3}$  Kcal/mol and a convergence on the forces of 0.5 Kcal/mol/Å, we are able to obtain the energetic of the formation of the system. The first set of results can be observed in the following figure.

Molecular Dynamics Simulations show also a positive energy of formation for the interface. In here, we have been able to construct a thicker bi-crystal. We can see a change in the energy profile close to 9. Closer inspection of the structures shows a change in the crystal orientation, caused by the plane mismatch. We see also a

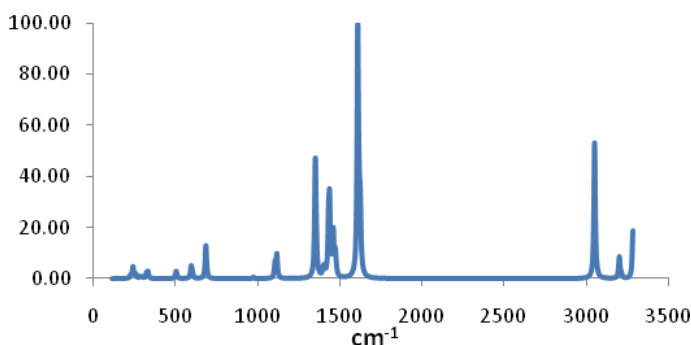


Figure 12: Vibrational spectra of NM, (IR region), corresponding pressure of 13.55 GPa.

reduction in the total energy with respect of temperature.

At the interface, there seems to be a larger number density of nitro groups expanding from the [110] crystal, this could explain the increased reactivity observed for compressions along this direction. Formation of the grain system shows an initial change in the density of material, although the density increases to with the number of layers, it is not expected to reach the value of the defect free system.

After the initial observation of the effect of crystal orientation and sensitivity found in PETN by Dick (Dick 1984), a model of steric hindrance was put forward. In this model, it is assumed that sensitivity will be related to the number of intermolecular close contacts that can be found when straining along a particular direction. Based on surface etchings, Sherwood (Gallagher, Halfpenny et al. 1992) has reported a Burgers vector as  $b < 1, -1, 1 >$  and a length of 1.48 nm. Their study has concluded that for the suggested slip system, steric hindrance would be limited to half as the one observed in our studied system; Although both in the early reports by Dick and Sherwood, acknowledge is made to the high number of intermolecular contacts is made in the (110)(001) grain system, no further discussion is presented. Our simulations indicate that possible smaller Burgers vector can be realized for this type of grain.

#### 4 Ab initio Molecular Dynamics Simulations

The specific properties of high performance and sensitivity have to be considered for stable energetic materials. Higher risk efforts are underway to explore the possibility of meta-stable energetic materials. There has been extensive research to measure the kinetics and elucidate the mechanism of their decomposition for a long

time. The study of thermal decomposition mechanism is essential to engineering design and fundamental to the design and optimization of materials. The kinetics of thermal decomposition is expected to illustrate the mechanisms of initiation and stability. In this section, we will focus on the decomposition pathways in gas-phase and investigate their thermodynamic properties in condense phase, from molecular dynamics simulations within a ‘first principles’ methodology.

C–NO<sub>2</sub> bond rupture is often suggested as an initial step in the thermal decomposition of nitro compounds, because the attachment of nitro groups is relatively weak (Manaa and Fried 1998; Manaa, Reed, Fried and Goldman 2009). The C–N bond dissociates without an apparent transition state structure, and affords two radicals. The calculated reaction enthalpy for gas-phase nitroethane to form radicals is 56.1 kcal/mol at the B3LYP/6-31+G(d) level. To better understand the C–NO<sub>2</sub> bond rupture, a detailed reaction profile was calculated as a function of C–NO<sub>2</sub> bond length.

The converged ( $10^{-7}$  atomic units (au)) wavefunctions from the initial position were used as initial guess for the first Car-Parrinello molecular dynamics run. Since the initial gradients can be very large, an initial kinetic energy of 50K was used. Atoms were allowed to move, and then the kinetic energy was slowly removed. From this “annealing” procedure an equilibrium configuration of the electron density and ionic positions was obtained. The electronic density for each atom was used for the Parrinello-Rahman microcanonical ensemble simulations that followed the damping run.

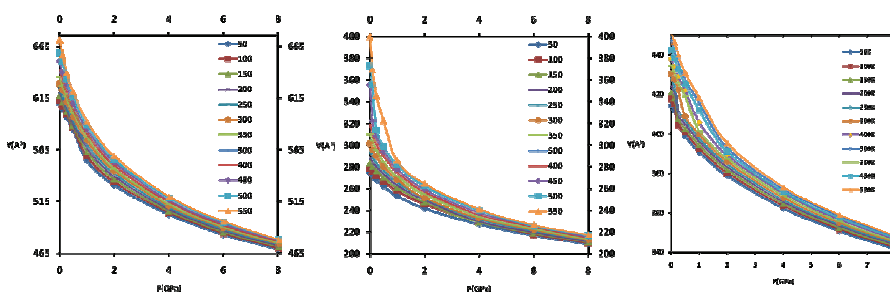


Figure 13: Isotherms for PETN(left), NM(centre), and TATB (right)

An initial equilibration run of 2000 steps, with a step size of 4 au (1 au=0.024188843 femtoseconds). Then a longer run of 2000 steps, with velocity scaling of 200 K was realized, All at 50K and doubled initial temperature. We see from the instantaneous values (Figure 19) that the system is closer to its equilibrium configuration. The



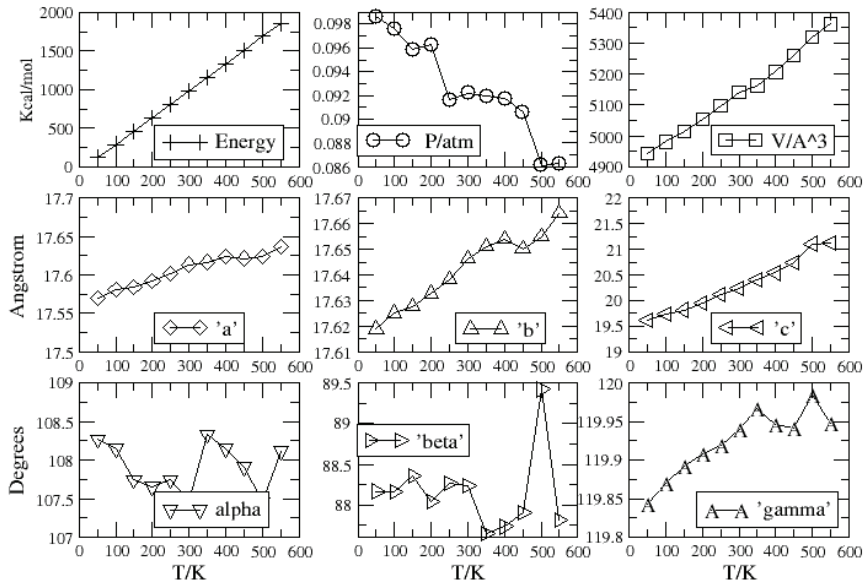


Figure 14: Structure Parameters of TATB at different pressures.

conserved energy (E-con) is in fact stable ca. -225.1261 Hartree. From these simulations we can extract the average value of the electronic (fictitious) kinetic energy, and use as input for constant temperature simulations, with Nose thermostats for the ions and the electrons. This simulation can further be used to obtain equilibrium values and averages at higher temperatures. An upper limit of 300K is proposed, with increments of 50K and averages of 80000 steps.

At the detonation transition, the temperature of NM has been estimated (Bouyer, Darbord, Hervé, Baudin, Le Gallic, Clément and Chavent 2006) as 2500K. Temperatures in excess of  $10^4$  K have been found (Tarasov, Karpenko, Sudovtsov and Tolshmyakov 2007) in compressed air inside detonating PETN.

After the equilibrium volumes were found, a larger Nitroethane cell was constructed, with an approximate density of that of the liquid ( $1\text{g/cm}^3$ ). Here again the challenge was first to obtain an appropriate wavefunction to be used in calculations at higher temperatures. The obtained wavefunction was used as input to perform car-parrinello molecular dynamics at constant volume and energy. This procedure applied to explore determining any or which chemical reactions occurring at a given elevated temperature.

From the different snapshots taken at this initial step, we see even at the lower

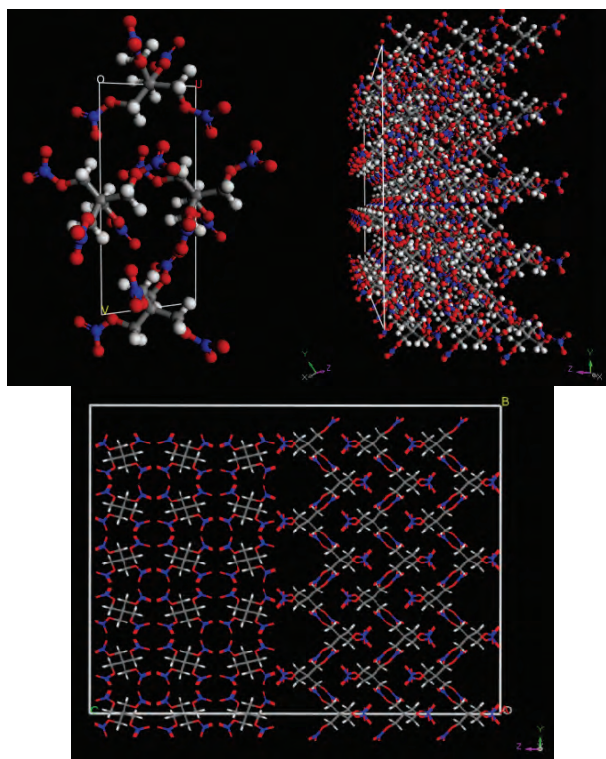


Figure 15: [110] plane (TOP) and [001] layer of PETN. Bottom: [110][001] Grain boundary system of PETN

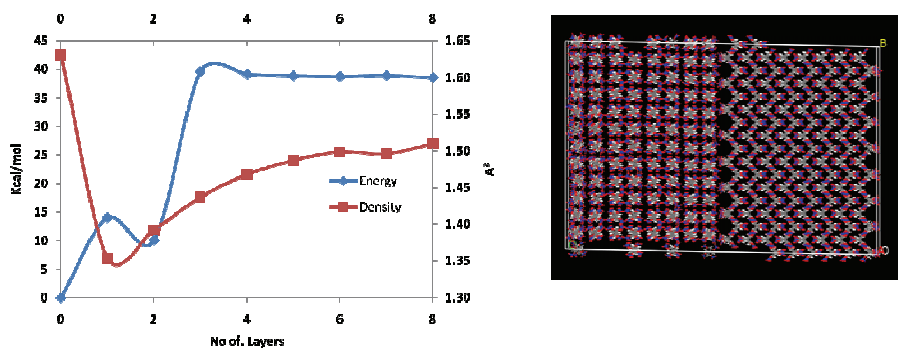


Figure 16: Change in energy and density with respect to number of layers (left), 8 layers system observed from the [001] direction.(right)

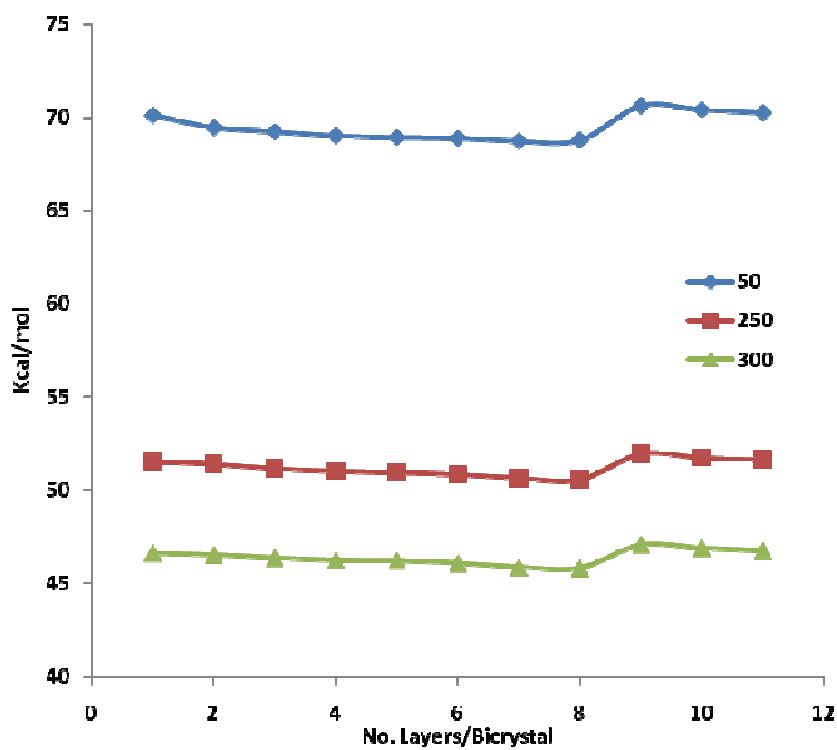


Figure 17: Change in Energy with respect to bi-crystal thickness

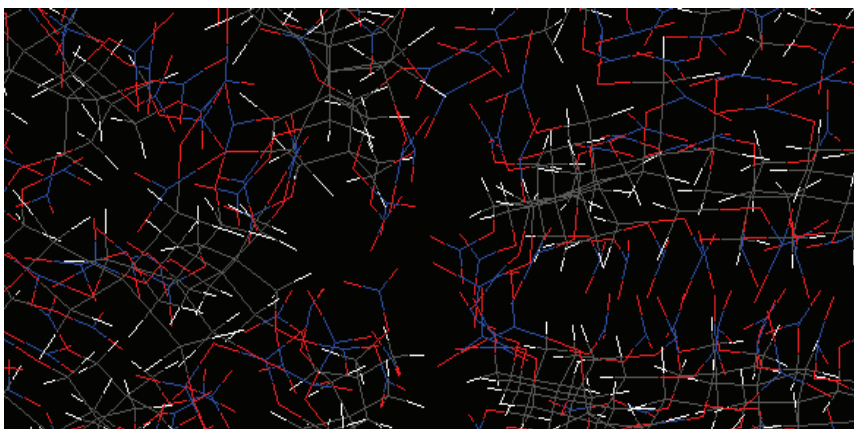


Figure 18: Interface at the [001] direction (LEFT) and the [110] plane (RIGHT), snapshot from the MD simulation at 250K. Oxygen atoms represented in red, nitrogen in blue and carbon as gray (hydrogen is white)

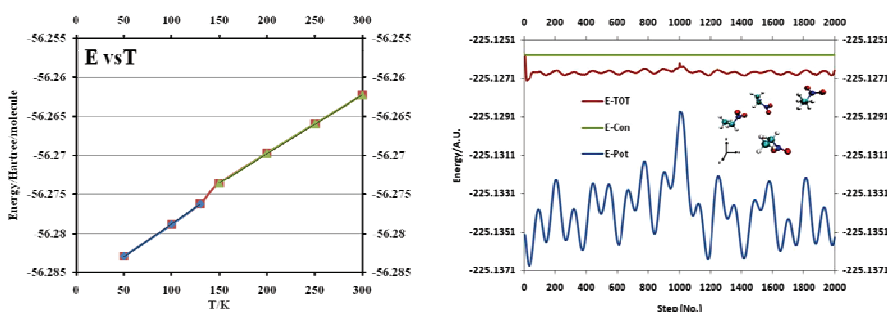


Figure 19: Internal energy of NE as a function of temperature (LEFT); Instantaneous values for the components of energy for 2000 steps of MD simulation of Nitroethane.

temperature of 1000 K, that the initial bond to break is the  $\text{NO}_2$ -ethylene bond. Mulliken population analysis shows a large positive charge on nitrogen (0.65) and a large negative charge on the nearest carbon, -0.67. The Mayer bond order for this atom is less than one (0.68), indicating a looser interaction as in a regular  $\text{sp}^3$  bond. In a recent study, Mathews et al (Mathews and Ball 2009) analyzed the optimized bond lengths and structures of amino substituted nitroethanes, their equilibrium bond distances were never in excess of 1.7 Å. Kwok have suggested a very fast

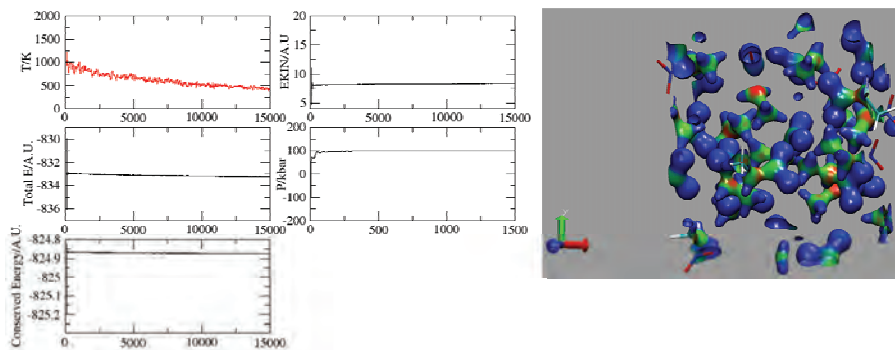


Figure 20: Running average of the larger 15 molecule NVE simulation run (left). Electrostatic potential mapped into the molecular charge density isosurface (0.16 Hartree).

transfer from an excited  $\text{NO}_2$  to the C-N bond as this was suggested as the primary mechanism as studied from Raman spectra (Kwok, Hung and Phillips 1996). Our results indeed find that even in the initial phases of equilibration,  $\text{NO}_2$  bond scission occurs for temperatures of 2000K.

## 5 Concluding Remarks

Based on known compounds, current theoretical calculations are made to design new possible compounds with desirable properties (Kim, Lee, Hyun, Park, Kwack, Kim, Lee and Lee 2004; Zhang, Shu et al. 2005; Zhang, Liu and Lv 2005). Although up until 2004 results using the Hartree-Fock method were usually reported; this has largely evolved to the uses of larger basis sets and exchange correlation functions within the density functional theory (DFT) formalism. Latter use of molecular dynamics and other atomistic level modeling has shown of use when studying the effects of temperature and defects.

Although the value of the  $C_{11}$  constant correlate directly with the experimentally observed sensitivity of the particular systems, (namely  $\text{TATB} > \text{Fox-7} > \text{RDX} > \text{b-HM} > \text{PETN} > \text{NM}$ , TATB, being the most insensitive), prediction of the reactivity and sensitivity of an explosive is complex since it depends on the interaction of mechanical, chemical and thermodynamic conditions. For a perfectly symmetric crystal, compression up to close the initiation pressure showed no signs of mechanical instability. Adiabatic compression showed the largest change in energy for  $\beta$ -HMX. We can correlate this energy requirement with the trend in sensitivity



$\beta$ -HMX<PETN<NM. Through the calculation of the effect of pressure upon band-gap closing, we can conclude that metallization as the initiation step in an adiabatic uniaxial compression of a perfect crystal can be excluded.

In addition to this, fractures along a given plane can act as energy barriers and hinder a complete reaction, causing unexpected behavior in some cases.

We have studied the [110][001] system in PETN.  $\Gamma$  surface calculations showed interaction in the surface of these grains up to molecular layers. Observed changes in density resulting from the stacking of two grains can have an effect on the detonation pressure. Molecular dynamics simulations have shown the effect of temperature. Constant temperature constant pressure dynamics on large systems have shown a higher number of nitro groups oscillating at the interface. Comparison with other types of systems could provide information about the effect of higher nitro number density in the reactivity and sensitivity to detonation. The observation of the increased stability with respect to applied temperature could indicate the formation of this interface at extreme conditions available through compression or heating. Quenching to lower temperatures would nonetheless render the interface unstable.

Explicit modeling of the electronic degrees of freedom at finite temperatures has emerged as a possibility within the Car-Parrinello method. Here, dynamic behavior at different temperatures that govern the behavior of energetic materials can be studied. Processes like hydrogen bonding, structure evolution and preferential conformations can be easily observed. In our particular case study, fission of the C-NO<sub>2</sub> bond is identified as the initial step of nitroethane thermal decomposition. This is confirmed by Mulliken population analysis.

With regard to novel high energy compounds, multiscale modeling could be applied to the study of nitrogen rich compounds (triazolium salts, and their amino and azido substituted relative compounds) and the effects of the structure. The family of nitrogen rich extended ring systems, triazolim, tetrazolium, by-cyclic salts, utropinium, and tetrazine can be compared. These higher volume salts seem to have increased stability to air, light and a low temperature emission. It has been commonly stated that strain in the molecular structure can be related to the detonation pressure and pressure velocity. Elasticity measurements for these compounds will be of special interest for compounds like cubane and azetidinium based compounds, versus aromatic nitrogen salts, like imidazole based compounds.

**Acknowledgement:** The research here supported by ARO-MURI: Insensitive Munitions. O.U.O. acknowledges gratefully CONACYT for its kind support for earlier part of his doctoral work. The authors would like to thank the support of the super-computing centers of Texas A&M College Station and Texas A&M Qatar.

## References

(1980): *LASL Explosive Property Data*. Berkley, CA, University of California Press.

**Alonso, J., Mañanes, A.** (2007): Long-Range van der Waals Interactions in Density Functional Theory. *Theoretical Chemistry Accounts: Theory, Computation, and Modeling (Theoretica Chimica Acta)* 117(4): 467-472.

**Antoine, E. D. M. van, der Heijden, Yves, L. M. C., Emanuela Marino, Richard, H. B. Bouma, Gert, J. H. G. Scholtes, Willem Duvalois, Marc, C. P. M. Roelands** (2008): Energetic Materials: Crystallization, Characterization and Insensitive Plastic Bonded Explosives. *Propellants, Explosives, Pyrotechnics* 33(1): 25-32.

**Bachorz, R. A., Bischoff, F. A., Hofener, S., Kloppe, W., Ottiger, P., Leist, R., Frey, J. A., Leutwyler, S.** (2008): Scope and limitations of the SCS-MP2 method for stacking and hydrogen bonding interactions. *Physical Chemistry Chemical Physics* 10(19): 2758-2766.

**Bacon, G. E., Curry, N. A., Wilson, S. A.** (1964): A Crystallographic Study of Solid Benzene by Neutron Diffraction. *Proceedings of the Royal Society of London. Series A, Mathematical and Physical Sciences* 279(1376): 98-110.

**Badders, N. R., Wei, C., Aldeeb, A. A., Rogers, W. J., Mannan, M. S.** (2006): Predicting the impact sensitivities of polynitro compounds using quantum chemical descriptors. *Journal of Energetic Materials* 24(1): 17-33.

**Bagryanskaya, I. Y., Gatilov, Y. V.** (1983): Crystal structure of nitromethane. *Journal of Structural Chemistry* 24(1): 150-151.

**Bemm, U., Ostmark, H.** (1998): 1,1-Diamino-2,2-dinitroethylene: a Novel Energetic Material with Infinite Layers in Two Dimensions. *Acta Crystallographica Section C* 54(12): 1997-1999.

**Bilge, M., Kart, H.H., Kart, S. O., Çağın, T.** (2009): B3-B1 Phase Transition and Pressure Dependence of the Elastic Properties of ZnS, *Materials Chemistry and Physics* 111, 559-64.

**Birch, F.** (1947): Finite Elastic Strain of Cubic Crystals. *Physical Review* 71(11): 809.

**Birch, F.** (1978): Finite strain isotherm and velocities for single-crystal and Polycrystalline NaCl at high pressures and 300/sup 0/K. *J. Geophys. Res. ; Vol/Issue: 83:B3*: Pages: 1257-1268.

**Blöchl, P. E.** (1994): Projector augmented-wave method. *Physical Review B* 50(24): 17953.

- Boldyreva, E.** (2008): High-pressure diffraction studies of molecular organic solids. A personal view. *Acta Crystallographica Section A* 64(1): 218-231.
- Boldyreva, E. V.** (2003): High-pressure studies of the anisotropy of structural distortion of molecular crystals. *Journal of Molecular Structure* 647(1-3): 159-179.
- Booth, A. D., Llewellyn** (1947): The crystal structure of pentaerythritol tetranitrate. *J. Chem. Soc.*: 837-846.
- Booth, A. D., Llewellyn, F. J.** (1947): The Crystal Structure Of Pentaerythritol Tetranitrate. *Journal of the Chemical Society*(JUN): 837-846.
- Bouyer, V., Darbord, I., Hervé, P., Baudin, G., Le Gallic, C., Clément, F., Chavent, G.** (2006): Shock-to-detonation transition of nitromethane: Time-resolved emission spectroscopy measurements. *Combustion and Flame* 144(1-2): 139-150.
- Bower, J. K., Kolb, J. R., Pruneda, C. O.** (1980): Polymeric Coatings Effect on Surface Activity and Mechanical Behavior of High Explosives. *Industrial & Engineering Chemistry Product Research and Development* 19(3): 326-329.
- Brand, H. V.** (2006): Periodic Hartree-Fock study of the elasticity of pentaerythritol tetranitrate. *Chemical Physics Letters* 418(4-6): 428-432.
- Brill, T. B., Goetz, F.** (1979): Laser Raman Spectra of a-, b-, g-, and d-Octogydro-1, 3,5,7-tetranitro-1,3,5,7-tetrazocine and Their Temperature Dependence. *The Journal of Chemical Physics* 83(3): 340-346.
- Brown, J. M., Slutsky, L. J., Nelson, K. A., Cheng, L.-T.** (1988): Velocity of Sound and Equations of State for Methanol and Ethanol in a Diamond-Anvil Cell. *Science* 241(4861): 65-67.
- Byrd, E. F. C., Rice, B. M.** (2006): Improved prediction of heats of formation of energetic materials using quantum mechanical calculations. *Journal of Physical Chemistry A* 110(3): 1005-1013.
- Byrd, E. F. C., Rice, B. M.** (2007): Ab Initio Study of Compressed 1,3,5,7-Tetranitro-1,3,5,7-tetraazacyclooctane (HMX), Cyclotrimethylenetrinitramine (RDX), 2,4,6,8,10,12-Hexanitrohexaazaisowurzitane (CL-20), 2,4,6-Trinitro -1,3,5- benzenetriamine (TATB), and Pentaerythritol Tetranitrate (PETN). *J. Phys. Chem. C* 111(6): 2787-2796.
- Cady, H. H., Larson, A. C.** (1965): The crystal structure of 1,3,5-triamino-2,4,6-trinitrobenzene. *Acta Crystallographica* 18(3): 485-496.
- Cady, H. H., Larson, A. C., Cromer, D. T.** (1963): The crystal structure of [alpha]-HMX and a refinement of the structure of [beta]-HMX. *Acta Crystallographica* 16(7): 617-623.
- Campbell, A. W., Holland, T. E., Malin, M. E., Cotter, T. P.** (1956): Detonation Phenomena in Homogeneous Explosives. *Nature* 178(4523): 38-39.

**CCSDT** (2001): PERYTN11, Cambridge Crystallographic Database.

**Chakarova, S. D., Schroder, E.** (2005): van der Waals interactions of polycyclic aromatic hydrocarbon dimers. *The Journal of Chemical Physics* 122(5): 054102-054105.

**Chakrabarty, A., Çağın, T.** (2008): Modeling Mechanical and Thermal Properties of Nanotube Based Nanostructures, *CMC: Computers, Materials & Continua* 3, 167-189.

**Chen, C., Wu, J. C.** (2001): Correlations between theoretical and experimental determination of heat of formation of certain aromatic nitro compounds. *Computers & Chemistry* 25(2): 117-124.

**Choi, S. C., Boutin, H. P.** (1970): A study of the crystal structure of b-Cyclotetramethylene tetranitramine by neutron diffraction. *Acta Crystallographica* B26: 1235-1240.

**Cobos, C. J.** (2005): DFT study of the thermochemistry of gas-phase 1,3,5,7-tetranitro-1,3,5,7-tetraazacyclooctane ([beta]-HMX). *Journal of Molecular Structure: THEOCHEM* 714(2-3): 147-152.

**Coleburn, N. L.** (1970): Dynamic Bulk Moduli of Several Solids Impacted by Weak Shockwaves. *The Journal of the Acoustical Society of America* 47(1B): 269-272.

**Coleburn, N. L., T. P. Liddiard, J.** (1966): Hugoniot Equations of State of Several Unreacted Explosives. *The Journal of Chemical Physics* 44(5): 1929-1936.

**Cox, E. G.** (1958): Crystal Structure of Benzene. *Reviews of Modern Physics* 30(1): 159.

**Cromer, D. T., Ryan, R. R., Schiferl, D.** (1985): The structure of nitromethane at pressures of 0.3 to 6.0 GPa. *The Journal of Physical Chemistry* 89(11): 2315-2318.

**Cromer, D. T. R. R. R., Schiferl, D.** (1985): Structure of nitromethane at pressures of 0.3 to 6.0 GPa. *J. Phys. Chem. ; Vol/Issue: 89:11*: Pages: 2315-2318.

**Czerski, H., Proud, W. G.** (2007): Relationship between the morphology of granular cyclotrimethylene-trinitramine and its shock sensitivity. *Journal of Applied Physics* 102(11): 113515-113518.

**Database, C. S.** (2007): CCSD, CCSD.

**David Rigby, H. S., Eichinger, B. E.** (1997): Computer simulations of poly(ethylene oxide): force field, pvt diagram and cyclization behaviour. *Polymer International* 44(3): 311-330.

**Day, G. M., Price, S. L., Leslie, M.** (2001): Elastic Constant Calculations for Molecular Organic Crystals. *Crystal Growth & Design* 1(1): 13-27.

**Dewar, M. J. S., Ritchie, J. P.** (1985): Thermolysis of molecules containing NO<sub>2</sub>

groups. *Journal of Organic Chemistry* (50): 1031-1036.

**Dick, J. J.** (1984): Effect of crystal orientation on shock initiation sensitivity of pentaerythritol tetranitrate explosive. *Applied Physics Letters* 44(9): 859-861.

**Dick, J. J.** (1993): Orientation-dependent explosion sensitivity of solid nitromethane. *J. Phys. Chem.* 97(23): 6193-6196.

**Dick, J. J.** (1997): Anomalous shock initiation of detonation in pentaerythritol tetranitrate crystals. *Journal of Applied Physics* 81(2): 601-612.

**Dllott, D. D., Peter, P., Jane, S. M.** (2003): Chapter 6 Fast molecular processes in energetic materials. *Theoretical and Computational Chemistry*, Elsevier. **Volume 13**: 125-191.

**Dovesi, R., Saunders, V. R., Roetti, C., Orlando, R., Zicovich-Wilson, C. M., Pascale, F., Civalieri, B., Doll, K., Harrison, N. M., Bush, I. J., Ph., D. A., Llunell, M.** (2007): Crystal06, [www.crystal.unito.it](http://www.crystal.unito.it).

**Drake, G. W., Hawkins, T. W., Hall, L. A., Boatz, J. A., Brand, A. J.** (2005): Structural and theoretical investigations of 3,4,5-triamino-1,2,4-triazolium salts. *Propellants Explosives Pyrotechnics* 30(5): 329-337.

**Edwards, J., Eybl, C., Johnson, B.** (2004): Correlation between sensitivity and approximated heats of detonation of several nitroamines using quantum mechanical methods. *International Journal of Quantum Chemistry* 100(5): 713-719.

**Engel, E.** (2003): Orbital-dependent functionals for the exchange-correlation energy: a third generation of density functionals. *A primer in Density Functional Theory*. C. Fiolhais, F. Nogueira and M. Marques. Berlin, Springer.

**Evers, J., Klapotke, T. M., Mayer, P., Oehlinger, G., Welch, J.** (2006):  $\alpha$ - and  $\beta$ -FOX-7, Polymorphs of a High Energy Density Material, Studied by X-ray Single Crystal and Powder Investigations in the Temperature Range from 200 to 423 K. *Inorganic Chemistry* 45(13): 4996-5007.

**Firsich, D. W.** (1984): Energetic Materials Separation and specific polymorph preparations via thermal gradient sublimation. *Journal of Hazardous Materials* 9: 133-137.

**Fischer, G., Zarembow, J.** (1970): Elastic properties of urea monocrystals. *Comptes Rendus Hebdomadaires Des Seances De L'Academie Des Sciences Serie B* 270(13): 852-&.

**Gallagher, H. G., Halfpenny, P. J., Miller, J. C., Sherwood, J. N. and Tabor, D.** (1992): Dislocation Slip Systems in Pentaerythritol Tetranitrate (PETN) and Cyclotrimethylene Trinitramine (RDX) [and Discussion]. *Philosophical Transactions: Physical Sciences and Engineering* 339(1654): 293-303.

**Gatti, C., Saunders, V. R., Roetti, C.** (1994): Crystal field effects on the topolog-



ical properties of the electron density in molecular crystals: The case of urea. *The Journal of Chemical Physics* 101(12): 10686-10696.

**Gibbs, T. R., Popolato, A., Baytos, J. F.** (1980): *LASL explosive property data*. Berkeley CA., University of California Press

**Gilardi, R. D., George, C. F.** (1984): CIWMAW. *Cambridge Structural Database*, The Cambridge Crystallographic Data Centre.

**Golovina, N. I., Titkov, A. N., Raevskii, A. V., Atovmyan, L. O.** (1994): Kinetics and Mechanism of Phase Transitions in the Crystals of 2,4,6-Trinitrotoluene and Benzotrifuroxane. *Journal of Solid State Chemistry* 113(2): 229-238.

**Gonzalez, C., Lim, E. C.** (2003): Evaluation of the Hartree-Fock Dispersion (HFD) Model as a Practical Tool for Probing Intermolecular Potentials of Small Aromatic Clusters: Comparison of the HFD and MP2 Intermolecular Potentials. *J. Phys. Chem. A* 107(47): 10105-10110.

**Goursot, A., Mineva, T., Kevorkyants, R., Talbi, D.** (2007): Interaction between n-Alkane Chains: Applicability of the Empirically Corrected Density Functional Theory for Van der Waals Complexes. *J. Chem. Theory Comput.* 3(3): 755-763.

**Grimme, S., Antony, J., Schwabe, T., Muck-Lichtenfeld, C.** (2007): Density functional theory with dispersion corrections for supramolecular structures, aggregates, and complexes of (bio)organic molecules. *Organic & Biomolecular Chemistry* 5(5): 741-758.

**Gruzdikov, Y. A., Dreger, Z. A., Gupta, Y. M.** (2004): Experimental and Theoretical Study of Pentaerythritol Tetranitrate Conformers. *The Journal of Physical Chemistry A* 108(29): 6216-6221.

**Hagler, A. T., Dauber, P., Lifson, S.** (1979): Consistent force field studies of intermolecular forces in hydrogen-bonded crystals. 3. The C:OH-O hydrogen bond and the analysis of the energetics and packing of carboxylic acids. *Journal of the American Chemical Society* 101(18): 5131-5141.

**Hagler, A. T., Huler, E., Lifson, S.** (1974): Energy functions for peptides and proteins. I. Derivation of a consistent force field including the hydrogen bond from amide crystals. *J. Am. Chem. Soc.* 96(17): 5319-5327.

**Hagler, A. T., Lifson, S.** (1974): Energy functions for peptides and proteins. II. Amide hydrogen bond and calculation of amide crystal properties. *Journal of the American Chemical Society* 96(17): 5327-5335.

**Hagler, A. T., Lifson, S., Dauber, P.** (1979): Consistent force field studies of intermolecular forces in hydrogen-bonded crystals. 2. A benchmark for the objective comparison of alternative force fields. *Journal of the American Chemical Society* 101(18): 5122-5130.

**Halgren, T. A.** (1992): The representation of van der Waals (vdW) interactions in molecular mechanics force fields: potential form, combination rules, and vdW parameters. *J. Am. Chem. Soc.* 114(20): 7827-7843.

**Hartmut Kröber, U. T.** (2008): Crystallization of Insensitive HMX. *Propellants, Explosives, Pyrotechnics* 33(1): 33-36.

**Hausuhl, S.** (2001): Elastic and thermoelastic properties of selected organic crystals: acenaphthene, trans-azobenzene, benzophenone, tolane, trans-stilbene, dibenzyl, diphenyl sulfone, 2,2'-biphenol, urea, melamine, hexogen, succinimide, pentaerythritol, urotropine, malonic acid, dimethyl malonic acid, maleic acid, hippuric acid, aluminium acetylacetonate, iron acetylacetonate, and tetraphenyl silicon. *Zeitschrift Fur Kristallographie* 216(6): 339-353.

**Hemmi, N., Dreger, Z. A., Gruzdkov, Y. A., Winey, J. M., Gupta, Y. M.** (2006): Raman Spectra of Shock Compressed Pentaerythritol Tetranitrate Single Crystals: Anisotropic Response. *J. Phys. Chem. B* 110(42): 20948-20953.

**Hepburn, J., Scoles, G., Penco, R.** (1975): A simple but reliable method for the prediction of intermolecular potentials. *Chemical Physics Letters* 36(4): 451-456.

**Hu, W.-F., He, T.-J., Chen, D.-M.** (Liu, Fan-Chen): Theoreticak study of the  $\text{CH}_3\text{NO}_2$  unimolecular decomposition potential energy surfaces. *Journal of Physical Chemistry A* 106(32): 7294-7303.

**Jeffrey, G. A., Ruble, J. R., McMullan, R. K., Pople, J. A.** (1987): The Crystal Structure of Deuterated Benzene. *Proceedings of the Royal Society of London. Series A, Mathematical and Physical Sciences* 414(1846): 47-57.

**John R. Kolb, H. F. R.** (1979): Growth of 1,3,5-Triamino-2,4,6-trinitrobenzene (TATB) I. Anisotropic thermal expansion. *Propellants, Explosives, Pyrotechnics* 4(1): 10-16.

**Ju, X. H., Xu, X. J., Xiao, H. M.** (2005): Computational study of picric acid and potassium picrate. *Journal of Energetic Materials* 23(2): 121-130.

**Kalay, M., Kart, H. H., Kart, S. O., Çağın, T.** (2009): Structural parameters, elastic constants and transition pressures of ZnO from first-principle calculations, *J. Alloy. Comp.* 484, 431-438

**Kart, S. O., Uludogan, M., Karaman, I., Çağın, T.** (2008): DFT Studies on Structure, Mechanics and Phase Behavior of Magnetic Shape Memory Alloys:  $\text{Ni}_2\text{MnGa}$  *Phys. Stat. Sol. (a)* 205, 1026-35

**Kim, C. K., Lee, K. A., Hyun, K. H., Park, H. J., Kwack, I. Y., Kim, C. K., Lee, H. W., Lee, B. S.** (2004): Prediction of physicochemical properties of organic molecules using van der Waals surface electrostatic potentials. *Journal of Computational Chemistry* 25(16): 2073-2079.

- Kitson, D. H., Hagler, A. T.** (1988): Catalysis of a rotational transition in a peptide by crystal forces. *Biochemistry* 27(19): 7176-7180.
- Kitson, D. H., Hagler, A. T.** (1988): Theoretical studies of the structure and molecular dynamics of a peptide crystal. *Biochemistry* 27(14): 5246-5257.
- Kleis, J., Schroder, E.** (2005): van der Waals interaction of simple, parallel polymers. *The Journal of Chemical Physics* 122(16): 164902-164907.
- Kohn, W., Sham, L. J.** (1965): Self-Consistent Equations Including Exchange and Correlation Effects. *Physical Review* 140(4A): A1133.
- Korolev, V. L., Petukhova, T. V., Pivina, T. S., Sheremetev, A. B., Miroshnichenko, E. A., Ivshin, V. P.** (2004): Studies on the structure and thermochemical properties of nitro- and nitrosopipicazines by the methods of quantum chemistry. *Khimiya Geterotsiklicheskikh Soedinenii*(12): 1817-1839.
- Kresse, G., Furthmüller, J.** (1996): Efficiency of ab-initio total energy calculations for metals and semiconductors using a plane-wave basis set. *Computational Materials Science* 6(1): 15-50.
- Kresse, G., Furthmüller, J.** (1996): Efficient iterative schemes for ab initio total-energy calculations using a plane-wave basis set. *Physical Review B* 54(16): 11169.
- Kresse, G., Hafner, J.** (1993): Ab initio molecular dynamics for liquid metals. *Physical Review B* 47(1): 558.
- Kresse, G., Hafner, J.** (1994): Norm-conserving and ultrasoft pseudopotentials for first-row and transition elements. *Journal of Physics: Condensed Matter*(40): 8245.
- Kresse, G., Joubert, D.** (1999): From ultrasoft pseudopotentials to the projector augmented-wave method. *Physical Review B* 59(3): 1758.
- Kunz, B. A.** (1995): *An Ab Initio Investigation of Crystalline PETN*. Decomposition, Combustion, and Detonation Chemistry of Energetic Materials, Boston, Materials Research Society.
- Kurita, N., Inoue, H., Sekino, H.** (2003): Adjustment of Perdew-Wang exchange functional for describing van der Waals and DNA base-stacking interactions. *Chemical Physics Letters* 370(1-2): 161-169.
- Kwok, W. M., Hung, M. S., Phillips, D. L.** (1996): Femtosecond photodissociation dynamics of nitroethane and 1-nitropropane in the gas and solution phases from resonance Raman intensity analysis. *Molecular Physics*, Taylor & Francis Ltd. 88: 517-531.
- Landerville, A. C., Oleynik, I. I., White, C. T.** (2009): Reactive Molecular Dynamics of Hypervelocity Collisions of PETN Molecules. *The Journal of Physical Chemistry A* 113(44): 12094-12104.

**LeSar, R.** (1984): Electron-gas plus damped-dispersion model for intermolecular forces. The rare-gas and hydrogen-helium, hydrogen-neon, and hydrogen-argon potentials. *J. Phys. Chem.* 88(19): 4272-4278.

**Lewis L. Stevens, N. V., Daniel E. Hooks, Dana M. Dattelbaum,** (2008): Hydrostatic Compression Curve for Triamino-Trinitrobenzene Determined to 13.0 GPa with Powder X-Ray Diffraction. *Propellants, Explosives, Pyrotechnics* 33(4): 286-295.

**Li, J. S., Huang, Y. G., Dong, H. S.** (2005): A theoretical study of polynitropyridines and their N-oxides. *Journal of Energetic Materials* 23(3): 133-149.

**Lifson, S., Hagler, A. T., Dauber, P.** (1979): Consistent force field studies of intermolecular forces in hydrogen-bonded crystals. 1. Carboxylic acids, amides, and the C:O.cntdot..cntdot..cntdot.H- hydrogen bonds. *Journal of the American Chemical Society* 101(18): 5111-5121.

**Lionel Borne, J.-C. P., Christian Spyckerelle,** (1999): Quantitative Characterization of Internal Defects in RDX Crystals. *Propellants, Explosives, Pyrotechnics* 24(4): 255-259.

**Lozano, A., Fernandez, J.** (2007): Surface hardening of railway crossings comprises high frequency generation and sonic impacting prior to explosion on hardened surface. *ES2275366*. P. O. European. Spain, Corral, Bescos M. ES2275366: 7.

**Lyman, J. L., Liao, Y.-C., Brand, H. V.** (2002): Thermochemical functions for gas-phase, 1,3,5,7-tetranitro-1,3,5,7-tetraazacyclooctane (HMX), its condensed phases, and its larger reaction products. *Combustion and Flame* 130(3): 185-203.

**Maharrey, S., Behrens, R.** (2005): Thermal decomposition of energetic materials. 5. Reaction processes of 1,3,5-trinitrohexahydro-s-triazine below its melting point. *Journal of Physical Chemistry A* 109(49): 11236-11249.

**Main, P.** (1985): Structure of the fourth form of 1,3,5,7-tetraazacyclooctane (g-hmx), 2C<sub>4</sub>H<sub>8</sub>N<sub>8</sub>O<sub>8</sub>·0.5H<sub>2</sub>O. *Acta Crystallographica* C41(1351-1354):

**Manaa, M. R., Fried, L. E.** (1998): DFT and ab Initio Study of the Unimolecular Decomposition of the Lowest Singlet and Triplet States of Nitromethane. *The Journal of Physical Chemistry A* 102(48): 9884-9889.

**Manaa, M. R., Reed, E. J., Fried, L. E., Goldman, N.** (2009): Nitrogen-Rich Heterocycles as Reactivity Retardants in Shocked Insensitive Explosives. *Journal of the American Chemical Society* 131(15): 5483-5487.

**Marcus, E., Pavel, H., Thomas, F., Sandor, S., Efthimios, K.** (2001): Hydrogen bonding and stacking interactions of nucleic acid base pairs: A density-functional-theory based treatment. *The Journal of Chemical Physics* 114(12): 5149-5155.

- Mathews, K. Y., Ball, D. W.** (2009): Computational study of the structures and properties of aminonitroethane molecules. *Journal of Molecular Structure: THEOCHEM* 902(1-3): 15-20.
- Mayo, S. L., Olafson, B. D., Goddard, W. A.** (1988): DREDING: A generic force field for molecular simulations *Journal of Physical Chemistry* 94: 8897-8909.
- McClellan, J. J., Hughes, T. F., Bartlett, R. J.** (2005): Application of the transfer Hamiltonian formalism to high-energy model systems. *International Journal of Quantum Chemistry* 105(6): 914-920.
- McKean, D. C., Watt, R. A.** (1976): Vibrational spectra of nitromethanes and the effects of internal rotation. *Journal of Molecular Spectroscopy* 61(2): 184-202.
- McKee, M. L.** (1986): Ab initio study of rearrangements on the nitromethane potential energy surface. *Journal of the American Chemical Society* 108(19): 5784-5792.
- Meents, A., Dittrich, B., Johnas, S. K. J., Thome, V., Weckert, E. F.** (2008): Charge-density studies of energetic materials: CL-20 and FOX-7. *Acta Crystallographica Section B* 64(1): 42-49.
- Meents, A., Dittrich, B., Johnas, S. K. J., Thome, V., Weckert, E. F.** (2008): Charge-density studies of energetic materials: CL-20 and FOX-7. Corrigendum. *Acta Crystallographica Section B* 64(4): 519.
- Miller, M. S.** (1995): *Three-phase combustion modelling: frozen ozone, a prototype system*. Decomposition, Combustion, and Detonation Chemistry of Energetic Materials, Boston, Materials Research Society.
- Moore, D. S., Funk, D. J., McGrane, S. D.** (2005): At the confluence of experiment and simulation: Ultrafast laser spectroscopic studies of shock compressed energetic materials. *Chemistry at Extreme Conditions*: 369-397.
- Nguyen, M. T., Le, H. T., Hajgato, B., Veszpremi, T., Lin, M. C.** (2003): Nitromethanemethyl nitrite rearrangement: a persistent discrepancy between theory and experiment. *Journal of Physical Chemistry A* 107(21): 4286-4291.
- Novozhilov, B. V.** (2005): Combustion of energetic materials in an acoustic field (review). *Combustion Explosion and Shock Waves* 41(6): 709-726.
- Olinger, B., Cady, H. H.** (1976): *The hydrostatic compression of explosives and detonation products to 10 GPa (100 kbars) and their calculated shock compression: results for PETN, TATB, CO<sub>2</sub> and H<sub>2</sub>O*. Sixth symposium on detonation, Coronado, California, Office of naval research.
- Olinger, B., Halleck, P. M., Cady, H. H.** (1975): The isothermal linear and volume compression of pentaerythritol tetranitrate (PETN) to 10 GPa (100 kbar) and the calculated shock compression. *The Journal of Chemical Physics* 62(11): 4480-



4483.

**Ortmann, F., Bechstedt, F., Schmidt, W. G.** (2006): Semiempirical van der Waals correction to the density functional description of solids and molecular structures. *Physical Review B (Condensed Matter and Materials Physics)* 73(20): 205101-205110.

**Ouillon, R., Pinan-Lucarre, J. P., Ranson, P., Baranovic, G.** (2002): Low-temperature Raman spectra of nitromethane single crystals. Lattice dynamics and Davydov splittings. *The Journal of Chemical Physics* 116(11): 4611-4625.

**Palmer, S. J. P., Field, J. E.** (1982): The deformation and fracture of b-HMX. *Proc. R. Soc. London, Ser. A* 383: 399-407.

**Pascale, F., Zicovich-Wilson, C. M., López Gejo, F., Civalleri, B., Orlando, R., Dovesi, R.** (2004): The calculation of the vibrational frequencies of crystalline compounds and its implementation in the CRYSTAL code. *Journal of Computational Chemistry* 25(6): 888-897.

**Patterson, J. E., Lagutchev, A. S., Hambir, S. A., Huang, W., Yu, H. and Dlott, D. D.** (2005): Time- and space-resolved studies of shock compression molecular dynamics. *Shock Waves* 14(5-6): 391-402.

**Perdew, J. P., Burke, K., Ernzerhof, M.** (1996): Generalized Gradient Approximation Made Simple. *Physical Review Letters* 77(18): 3865.

**Perger, W. F., Pandey, R., Blanco, A. M., Zhao, J.** (2004): First-Principles intermolecular binding energies in organic molecular crystals. *Elsevier Science*. Amsterdam, Netherlands: 12.

**Pham, H. H., Çağın, T.** (2010) Lattice Dynamics and second and third order elastic constants of Iron at elevated pressures. *CMC: Computers, Materials & Continua*, this issue.

**Pinkerton, A. A., Martin, A.** (1995): *Charge densities and electrostatic potentials for energetic materials*. Decomposition, Combustion, and Detonation Chemistry of Energetic Materials, Boston, Materials Research Society.

**Plimpton, S.** (1995): Fast Parallel Algorithms for Short-Range Molecular Dynamics. *Journal of Computational Physics* 117: 1-19.

**Pnina Dauber-Osguthorpe, V. A. R., David J. Osguthorpe, Jon Wolff, Monique Genest, Arnold T. Hagler,** (1988): Structure and energetics of ligand binding to proteins: *Escherichia coli* dihydrofolate reductase-trimethoprim, a drug-receptor system. *Proteins: Structure, Function, and Genetics* 4(1): 31-47.

**Pople, J. A., von Rague Schleyer, P., Kaneti, J., Spitznagel, G. W.** (1988): Accurate theoretical estimates of the electron affinities of AH<sub>n</sub> molecules by isogyric comparisons. Proton affinities of AH<sub>n</sub><sup>-</sup> anions. *Chemical Physics Letters* 145(5):

359-364.

**Qin Wu, H. O., Weitao, Y.** (2003): Algebraic Equation And Iterative Optimization For The Optimized Effective Potential In Density Functional Theory. *Journal of Theoretical & Computational Chemistry* 2(4): 627-638.

**Qiu, L., Xiao, H. M., Ju, X. H., Gong, X. D.** (2005): Theoretical study of the structures and properties of cyclic nitramines: Tetranitrotetraazadecalin (TNAD) and its isomers. *International Journal of Quantum Chemistry* 105(1): 48-56.

**Rappe, A. K., Casewit, C. J., Colwell, K. S., Goddard, W. A., Skiff, W. M.** (1992): UFF, a full periodic table force field for molecular mechanics and molecular dynamics simulations. *Journal of the American Chemical Society* 114(25): 10024-10035.

**Rappe, A. K., Goddard, W. A.** (1991): Charge equilibration for molecular dynamics simulations. *The Journal of Physical Chemistry* 95(8): 3358-3363.

**Ruth M. Doherty, Duncan S. W.** (2008): Relationship Between RDX Properties and Sensitivity. *Propellants, Explosives, Pyrotechnics* 33(1): 4-13.

**Sevik, C., Çağın, T.** (2009): Structure and electronic properties of CeO<sub>2</sub>, ThO<sub>2</sub> and their alloys, *Phys. Rev B.* 80, 014108

**Sewell, T. D., Menikoff, R., Bedrov, D., Smith, G. D.** (2003): A molecular dynamics simulation study of elastic properties of HMX. *The Journal of Chemical Physics* 119(14): 7417-7426.

**Slater, J. C., Kirkwood, J. G.** (1931): The Van der Waalls forces in gases. *Physical Review* 37: 682-697.

**Son, S. F., Asay, B. W., Bdzil, J. B., Kober, E. M.** (1995): *Reaction Rate Modeling in the deflagration to detonation transition of granular energetic materials*. Decomposition, Combustion, and Detonation Chemistry of Energetic Materials, Boston, Materials Research Society.

**Sorescu, D. C., Rice, B. M., Thompson, D. L.** (1999): Theoretical Studies of the Hydrostatic Compression of RDX, HMX, HNIW, and PETN Crystals. *The Journal of Physical Chemistry B* 103(32): 6783-6790.

**Sorescu, D. C., Rice, B. M., Thompson, D. L.** (2000): Theoretical Studies of Solid Nitromethane. *J. Phys. Chem. B* 104(35): 8406-8419.

**Soto, M. R.** (1995): *A theoretical study of BF+OH and BO+HF reactions*. Decomposition, Combustion, and Detonation Chemistry of Energetic Materials, Boston, Materials Research Society.

**Soulard, L.** (1995): *Molecular dynamics calculations on the properties of the reaction zone in the liquid explosive*. Decomposition, Combustion, and Detonation Chemistry of Energetic Materials, Boston, Materials Research Society.

**Srivathsa, B., Ramakrishnan, N.** (2008): An analytical model for explosive compaction of powder to cylindrical billets through axial detonation. *Computers, Materials and Continua*, 7(1): 9-23.

**Stevens, L. L., Eckhardt, C. J.** (2005): The elastic constants and related properties of beta-HMX determined by Brillouin scattering. *The Journal of Chemical Physics* 122(17): 174701-174708.

**Stevens, L. L., Velisavljevic, N., Hooks, D. E., Dattelbaum, D. M.** (2008): The high-pressure phase behavior and compressibility of 2,4,6-trinitrotoluene. *Applied Physics Letters* 93(8): 081912-081913.

**Sun, B., Winey, J. M., Hemmi, N., Dreger, Z. A., Zimmerman, K. A., Gupta, Y. M., Torchinsky, D. H., Nelson, K. A.** (2008): Second-order elastic constants of pentaerythritol tetranitrate and cyclotrimethylene trinitramine using impulsive stimulated thermal scattering. *Journal of Applied Physics* 104(7): 073517-073516.

**Sun, D. W., Garimella, S. V., Singh, S., Naik, N.** (2005): Numerical and experimental investigation of the melt casting of explosives. *Propellants Explosives Pyrotechnics* 30(5): 369-380.

**Sun, H.** (1998): COMPASS: An ab Initio Force-Field Optimized for Condensed-Phase Applications Overview with Details on Alkane and Benzene Compounds. *The Journal of Physical Chemistry B* 102(38): 7338-7364.

**Sun, H., Ren, P., Fried, J. R.** (1998): The COMPASS force field: parameterization and validation for phosphazenes. *Computational and Theoretical Polymer Science* 8: 229-246.

**Sun, H., Rigby, D.** (1997): Polysiloxanes: ab initio force field and structural, conformational and thermophysical properties. *Spectrochimica Acta Part A: Molecular and Biomolecular Spectroscopy* 53(8): 1301-1323.

**Suzuki, S., Green, P. G., Bumgarner, R. E., Dasgupta, S., Goddard, W. A., III and Blake, G. A.** (1992): Benzene Forms Hydrogen Bonds with Water. *Science* 257(5072): 942-945.

**Swaminathan, S., Craven, B. M., McMullan, R. K.** (1984): The crystal structure and molecular thermal motion of urea at 12, 60 and 123 K from neutron diffraction. *Acta Crystallographica Section B* 40(3): 300-306.

**Tao, J., Perdew, J. P.** (2005): Test of a nonempirical density functional: Short-range part of the van der Waals interaction in rare-gas dimers. *The Journal of Chemical Physics* 122(11): 114102-114107.

**Tarasov, M., Karpenko, I., Sudovtsov, V., Tolshmyakov, A.** (2007): Measuring the brightness temperature of a detonation front in a porous explosive. *Combustion, Explosion, and Shock Waves* 43(4): 465-467.

- Terao, K.** (2007): *Irreversible phenomena : ignitions, combustion, and detonation waves*. Berlin; New York, Springer.
- Thonhauser, T., Cooper, V. R., Shen, L., Puzder, A., Hyldgaard, P. and Langreth, D. C.** (2007): Van der Waals density functional: Self-consistent potential and the nature of the van der Waals bond. *cond-mat/0703442*.
- Tokmakoff, A., Fayer, M. D., Dlott, D. D.** (1993): Chemical reaction initiation and hot-spot formation in shocked energetic molecular materials. *The Journal of Physical Chemistry* 97(9): 1901-1913.
- Trevino, S. F., Prince, E., Hubbard, C. R.** (1980): Refinement of the structure of solid nitromethane. *The Journal of Chemical Physics* 73(6): 2996-3000.
- Trotter, J., Williston, C. S.** (1966): Bond lengths and thermal vibrations in m-dinitrobenzene. *Acta Crystallographica* 21(2): 285-288.
- Troullier, N., Martins, J. L.** (1991): Efficient pseudopotentials for plane-wave calculations. *Physical Review B* 43(3): 1993.
- Tsai, D. H.** (1995): *Hot spots in a molecular solid under rapid compression: energy sharing among the T-R-V degrees of freedom*. Decomposition, Combustion, and Detonation Chemistry of Energetic Materials, Boston, Materials Research Society.
- Tsuzuki, S., Luthi, H. P.** (2001): Interaction energies of van der Waals and hydrogen bonded systems calculated using density functional theory: Assessing the PW91 model. *The Journal of Chemical Physics* 114(9): 3949-3957.
- Ugliengo, P.** (2006): MOLDRAW: A Program to Display and Manipulate Molecular and Crystal Structures. Torino.
- Ugliengo, P., Viterbo, D., Chiari, G.** (1993): MOLDRAW - Molecular Graphics On A Personal-Computer. *Zeitschrift Fur Kristallographie* 207: 9-23.
- Uludogan, M., Çağın, T., Goddard W.A.** (2006): First Principles Approach to BaTiO<sub>3</sub> Turk. J. Phys. 30, 277-285.
- Uludogan, M., Guarin, D.P., Gomez, Z. E., Çağın, T., Goddard W.A.** (2008): DFT studies on ferroelectric ceramics and their alloys *CMES: Computer Modeling in Engineering and Sciences*, Vol. 24, 215-38
- Urtiew, P. A., Tarver, C. M.** (2005): Shock initiation of energetic materials at different initial temperatures (review): *Combustion Explosion and Shock Waves* 41(6): 766-776.
- Volker Weiser, S. K., Norbert Eisenreich,** (2001): Influence of the Metal Particle Size on the Ignition of Energetic Materials. *Propellants, Explosives, Pyrotechnics* 26(6): 284-289.

- White, C. T., Barrett, J. J. C., Mintmire, J. W., Elert, M. L.** (1995): *Effects of nanoscale voids on the sensitivity of model energetic materials*. Decomposition, Combustion, and Detonation Chemistry of Energetic Materials, Boston, Materials Research Society.
- Williams, R. W., Malhotra, D.** (2006): van der Waals corrections to density functional theory calculations: Methane, ethane, ethylene, benzene, formaldehyde, ammonia, water, PBE, and CPMD. *Chemical Physics* 327(1): 54-62.
- Winey, J. M., Gupta, Y. M.** (2001): Second-order elastic constants for pentaerythritol tetranitrate single crystals. *Journal of Applied Physics* 90(3): 1669-1671.
- Wojcik, G., Mossakowska, I., Holband, J., Bartkowiak, W.** (2002): Atomic thermal motions studied by variable-temperature X-ray diffraction and related to non-linear optical properties of crystalline meta-di-nitrobenzene. *Acta Crystallographica Section B* 58(6): 998-1004.
- Wu, X., Vargas, M. C., Nayak, S., Lotrich, V., Scoles, G.** (2001): Towards extending the applicability of density functional theory to weakly bound systems. *The Journal of Chemical Physics* 115(19): 8748-8757.
- Xiao, H. M., Ju, X. H., Xu, L. N., Fang, G. Y.** (2004): A density-functional theory investigation of 3-nitro-1,2,4-triazole-5-one dimers and crystal. *Journal of Chemical Physics* 121(24): 12523-12531.
- Xu, X., Goddard, W. A., III** (2004): From The Cover: The X3LYP extended density functional for accurate descriptions of nonbond interactions, spin states, and thermochemical properties. *PNAS* 101(9): 2673-2677.
- Yoo, C.-S., Cynn, H.** (1999): Equation of state, phase transition, decomposition of beta-HMX (octahydro-1,3,5,7-tetranitro-1,3,5,7-tetrazocine) at high pressures. *The Journal of Chemical Physics* 111(22): 10229-10235.
- Zel'dovich, Y. B., Raizer, Y. P.** (2001): *Physics of shock waves and high-temperature hydrodynamic phenomena*. Mineola, N.Y., Dover Publications.
- Zeman, S.** (2007): Sensitivities of High Energy Compounds. *High Energy Density Materials*: 195-271.
- Zepeda-Ruiz, L. A., Maiti, A., Gee, R., Gilmer, G. H., Weeks, B. L.** (2006): Size and habit evolution of PETN crystals—a lattice Monte Carlo study. *Journal of Crystal Growth* 291(2): 461-467.
- Zhang, C. Y., Shu, Y. J., Zhao, X. D., Dong, H. S., Wang, X. F.** (2005): Computational investigation on HEDM of azoic and azoxy derivatives of DAF, FOX-7, TATB, ANPZ and LLM-105. *Journal of Molecular Structure-Theochem* 728(1-3): 129-134.
- Zhang, Y. X., Liu, D. B., Lv, C. X.** (2005): Preparation and characterization of



reticular nano-HMX. *Propellants Explosives Pyrotechnics* 30(6): 438-441.

**Zhao, Q. H., Zhang, S. W., Li, Q. S.** (2005): A direct ab initio dynamics study of the initial decomposition steps of gas phase 1,3,3-trinitroazetidine. *Chemical Physics Letters* 412(4-6): 317-321.

**Zicovich-Wilson, C. M., Dovesi, R., Saunders, V. R.** (2001): A general method to obtain well localized Wannier functions for composite energy bands in linear combination of atomic orbital periodic calculations. *The Journal of Chemical Physics* 115(21): 9708-9719.

**Zicovich-Wilson, C. M., Pascale, F., Roetti, C., Saunders, V. R., Orlando, R., Dovesi, R.** (2004): Calculation of the vibration frequencies of crystalline compounds and its implementation in the crystal code. *Journal of Computational Chemistry* 25: 888-897.



## **CMC: Computers, Materials, & Continua**

ISSN: 1546-2218 (Print); 1546-2226(Online)

Journal website:

<http://www.techscience.com/cmc/>

Manuscript submission

<http://submission.techscience.com>

Published by

Tech Science Press

5805 State Bridge Rd, Suite G108

Duluth, GA 30097-8220, USA

Phone (+1) 678-392-3292

Fax (+1) 678-922-2259

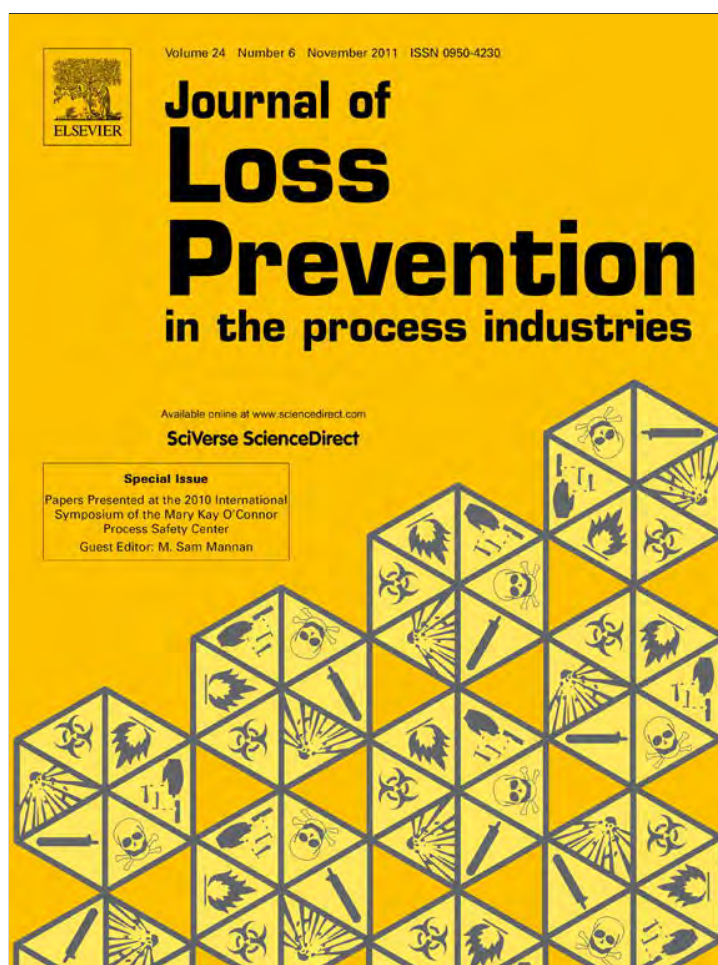
Email: [sale@techscience.com](mailto:sale@techscience.com)

Website: <http://www.techscience.com>

Subscription: <http://order.techscience.com>

### **CMC is Indexed & Abstracted in**

**Applied Mechanics Reviews; Cambridge Scientific Abstracts (Aerospace and High Technology; Materials Sciences & Engineering; and Computer & Information Systems Abstracts Database); Engineering Index (EMBASE, Compendex, Geobase and Scopus, SecienceDirect Navigator); INSPEC Databases; Mechanics; Science Citation Index; Science Navigator; Zentralblatt fur Mathematik.**



This article appeared in a journal published by Elsevier. The attached copy is furnished to the author for internal non-commercial research and education use, including for instruction at the authors institution and sharing with colleagues.

Other uses, including reproduction and distribution, or selling or licensing copies, or posting to personal, institutional or third party websites are prohibited.

In most cases authors are permitted to post their version of the article (e.g. in Word or Tex form) to their personal website or institutional repository. Authors requiring further information regarding Elsevier's archiving and manuscript policies are encouraged to visit:

<http://www.elsevier.com/copyright>



Contents lists available at ScienceDirect

# Journal of Loss Prevention in the Process Industries

journal homepage: [www.elsevier.com/locate/jlpi](http://www.elsevier.com/locate/jlpi)



## Anisotropic behavior of energetic materials at elevated pressure and temperature

O.U. Ojeda Mota\*, Tahir Çağın\*

Laboratory of Computational Engineering of Nanomaterials, Artie McFerrin Department of Chemical Engineering, Texas A&M University College Station, TX 77840, USA

### ARTICLE INFO

#### Article history:

Received 7 June 2011

Accepted 7 June 2011

#### Keywords:

Energetic materials

Molecular modeling

Ab initio

Anisotropy

Nitromethane

Pentaerythritol tetranitrate

### ABSTRACT

First principles and molecular dynamics methods were used to study energetic materials (EM) of varying sensitivity, particularly nitromethane (NM) and pentaerythritol tetranitrate (PETN). Molecular and electronic structure, as well as anisotropic elastic properties, variation of charge distributions, and stress-strain behavior of these three materials were investigated. Information obtained from different levels of theory is useful to reveal and assess the anisotropic sensitivity of the studied systems. For NM, we observe a crystallographic phase transformation and a drastic change in its mechanical behavior. PETN is observed to be mechanically stable within the studied pressure range, with a marked anisotropic behavior when compressed at elevated temperatures.

© 2011 Elsevier Ltd. All rights reserved.

### 1. Introduction

Applications for energetic materials (EM) range from initiators in safety bags to detonation charges, propellants and secondary explosives. It has been found experimentally that these materials may undergo detonation by un-planned stimuli. It is well known that high EM's display anisotropic sensitivity to heat and/or mechanical shock (Dick, 1984, 1993, 1997). Naturally, this has raised serious issues associated with safety, logistics, and time burdens related to handling of these materials, as well as the cost associated with these issues. To understand their behavior, various physical and chemical correlations have been proposed (Shaw, 1973; Zeman, 1995). Properties like the number and positions of the substituents, bond length, and partial charges of the molecular constituents in the gas phase, have been used to correlate the trends in sensitivity of these mostly nitro group containing molecular crystals (Brill & James, 1993).

For processing of plastic bonded explosives, crystals of EM's are fragmented and compressed with a polymer matrix binder. Localization of strain energy has been the suspect of the formation of reaction zones (Sewell, Menikoff, Bedrov, & Smith, 2003), or "hot-spots". Thus, a clear understanding of the relevant mechanical properties is essential. In addition to this, compression along a given plane can act as energy barriers and hinder a complete reaction, causing runaway reactions and unexpected behavior. In

this sense, observed reactivity and sensitivity of an explosive is influenced by an interplay between mechanical, chemical, and thermodynamic conditions. The prerequisite for the prevention of unexpected behavior while processing of EM's is to understand the phenomena at the molecular level, which requires assessment beyond empirical correlations.

Before any bond breaks and reactions occur, an orbital has to get polarized and charge localization increases at certain group atoms or chemical groups. Molecules interacting with each other, as in condensed phase, can give rise to charge localization not observable for the same isolated molecule. Even though there are numerous attempts to correlate the electronic properties as calculated from gas-phase and quantum chemical studies (Li, Huang, & Dong, 2005; Badders, Wei, Aldeeb, Rogers, & Mannan, 2006; Byrd & Rice, 2006; Hu, He, & Chen, 2002; Zhang, Shu, Huang, et al., 2005; Zhang, Shu, Zhao, et al., 2005; Manaa & Fried, 1998; Manelis, 2003), studies that relates charges in molecular crystal at different conditions are scarce (Byrd & Rice, 2007; Sorescu, Rice, & Thompson, 1999; Kuklja & Kunz, 1999). In case if only the gas phase studies used in correlations, the results will be in contradiction with observed experimental trends (Hu et al., 2002).

First principles based computational methods (ab initio quantum chemistry, density functional theory, molecular dynamics with accurate interaction potentials) are shown to be suitable to study different thermodynamic properties (Yuan & Smith, 2009; Woodward & Ketchum, 2001) at multiple length and time scales. This enable researchers to employ 'virtual experiments' to study the energetic behavior and crystallographic phase changes at elevated temperatures and pressures without the risk of exposure to unsafe conditions. For instance one can study the highly reactive

\* Corresponding authors. Tel.: +1 979 862 1449.

E-mail addresses: [ulises@tamu.edu](mailto:ulises@tamu.edu) (O.U.O. Mota), [tcagin@mail.che.tamu.edu](mailto:tcagin@mail.che.tamu.edu) (T. Çağın).



molecular crystals at the ground state through the use of density functional theory (DFT)(Kohn & Sham, 1965). One can include the effect of temperature and pressure through the use of molecular dynamics (MD), employing time averages over the trajectory to determine thermodynamic properties. More specifically, DFT can also be used to determine pressure dependence of second order elastic constants, variation in charge localization under the influence of applied pressure or anisotropic mechanical loads, such as in response to uniaxial compression or applied shear stresses. More specifically MD is valuable to obtain molecular level information under extreme conditions such as shock or hypervelocity impact where fast evolution of thermodynamic states need to be observed and assessed within short time scales (Arman et al., 2011).

Herein, we present a systematic study of the mechanical properties as a function of external pressure for nitromethane (NM) and pentaerythritol tetranitrate (PETN), which have distinct impact and shock sensitivities (Gibbs, Popolato, & Baytos, 1980; Winey & Gupta, 2001). For example, PETN has a reported impact sensitivity which ranges between 12 cm and 27 cm (height for 50% chance of detonation) in drop hammer tests (Gibbs et al., 1980), as compared to a value higher than 320 cm for NM. PETN is known to be moderately sensitive to shock compression, while NM is sensitive to shock detonation. We will attempt to correlate these properties with overall thermodynamic behavior using DFT and MD methods. The main objective is to find information at the different level of theories employed, and compare and contrast system related information on the processes that could lead to unsafe behavior.

## 2. Theory and methods

By means of localized basis sets that are used to represent all-electron systems, we performed first principles calculations on the crystals of PETN and NM. These calculations are conducted within DFT(Kohn & Sham, 1965) level, with gradient corrected Perdew-Burke-Ernzerhof (PBE) functional for exchange and correlation(Perdew, Burke, & Ernzerhof, 1996). For these calculations we use extended basis sets(Gatti, Saunders, & Roetti, 1994) for carbon, hydrogen, nitrogen and oxygen, as implemented in the crystal06 package(Dovesi et al., 2007). Initial structures for these crystals are obtained from the Cambridge Crystallographic Database(CCSD, 2007). Energy convergence was found for a mesh of  $4 \times 4 \times 4$  grid size used for inverse space sampling. Analytical gradients are used to relax the ionic degrees of freedom(Perry, 1978; Bernhard Schlegel, 1984) at different strained states.

An important part of the model used to represent properties and processes in nature lies in the level of accuracy and precision of the employed methods. The most common Gaussian or atom-localized basis sets of current use are the split valence basis sets (Towler, Zupan, & Causà, 1996; Binkley, Pople, & Hehre, 1980; Ditchfield, Hehre, & Pople, 1971). Quality of our basis sets have been validated by a set of calculations on the molecular crystal of urea(Civalleri, Doll, & Zicovich-Wilson, 2006) and other molecular crystal with known binding energy (BE) or sublimation enthalpy. One has to avoid the use of too few functions, which leads to drastic errors in reproducing experimental properties. Another effect to consider is the superposition of basis sets from neighboring atoms (BSSE); this is reduced if a large enough basis is used. We have employed three different type of sets; Ahlrichs' triple-split valence (TZP) basis set(Schafer, Horn, & Ahlrichs, 1992), the 6-21G basis and our modified 6-31G\* basis. For the latter two basis functions, the first digit indicates the number of Gaussian functions that represent core atomic orbitals, and the last two indicate the number of functions used for the valence orbitals. The TZP basis set is the largest one of the three sets employed here.

Full optimization with the different basis sets was performed. The results summarized in Table 1. Energies are reported to the last digit of the imposed tolerance for each self-consistent cycle ( $1 \times 10^{-7}$ ).  $V_0$  stands for the equilibrium unit cell volume in  $\text{\AA}^3$ , as calculated by relaxing all the cell and ionic degrees of freedom. The BE of the urea crystal was estimated to be  $-98.48$  kJ/mol, which compares well with the experimental(Ferro, Barone, Della Gatta, & Piacente, 1987) sublimation enthalpy of  $-94.3$  kJ/mol. From BE values, we see a basis set that reproduces qualitatively the experimental result. The BSSE lies between that of a contracted 6-21G\* basis, and the more expensive Ahlrichs basis set.

For calculations with localized basis sets, the effective pressure values corresponding to each compression value is obtained by fitting the results to a widely used Birch-Murnaghan (BM) equation of state (Birch, 1978). The fourth order BM equation of state has the following form;

$$P/B_0 = 3f(1+2f)^{\frac{5}{2}} \left[ 1 - \frac{1}{2} \left( \frac{\delta_3}{\delta_2} \right) f + \frac{1}{6} \left( \frac{\delta_4}{\delta_2} \right) f^2 + \dots \right] \quad (1)$$

Where;

$$V/V_0 = (1+2f)^{\frac{3}{2}} \quad (2)$$

And;

$$\frac{\delta_3}{\delta_2} = 12 - 3B'_0 \quad (3)$$

$$\frac{\delta_4}{\delta_2} = 9B_0 B''_0 + 9(B_0)^2 - 63B'_0 + 143 \quad (4)$$

This equation of state allows for larger range of volumes, pressures and other thermodynamic properties to be correctly predicted. Here,  $V$  is the unit cell volume at a given thermodynamic state,  $B_0$  stands for the equilibrium bulk modulus at zero pressure, while  $B'_0$  and  $B''_0$  represents the first and second derivative of the bulk modulus.

In order to obtain the anisotropic mechanical properties (namely the second order elastic constants) for NM and PETN, we use the finite strain method. By applying finite strains to the crystallographic unit cell, a new cell structure (representing the strained form) is obtained. The difference in energy (strain energy) can then be computed in terms of a polynomial expansion in strain tensor (Wallace, 1972);

$$E - E_0 = V_0 s_{ij} e_{ij} + \frac{V_0}{2} c_{ijkl} e_{ij} e_{kl} + \dots \quad (5)$$

In this case,  $E_0$  is the reference ground state energy, or the energy of zero-strain state;  $e_{ij}$  and  $e_{jk}$  are the Cartesian strain tensor components. The stress tensor components are  $s_{ij}$ , and  $c_{ijkl}$  is the elastic constants tensor. The first term vanishes in a zero-strain state. We can determine the corresponding elastic constants  $c_{ijkl}$ , by applying specific strain states to the reference system. Owing to the symmetry of the elasticity tensor, and to simplify, we employ

**Table 1**

Formation energy of urea, as calculated from different basis sets. Total energy reported in atomic units (A.U.).

Basis set	Energy/A.U.	$V_0/\text{\AA}^3$	BSSE/KJ/mol	BE/KJ/mol
6-21G*	-449.7130153	136.345	97.05	-96.94
6-31G*M	-450.2513153	145.137	41.00	-98.48
Ahlrichs	-450.0698772	156.486	7.94	-88.38

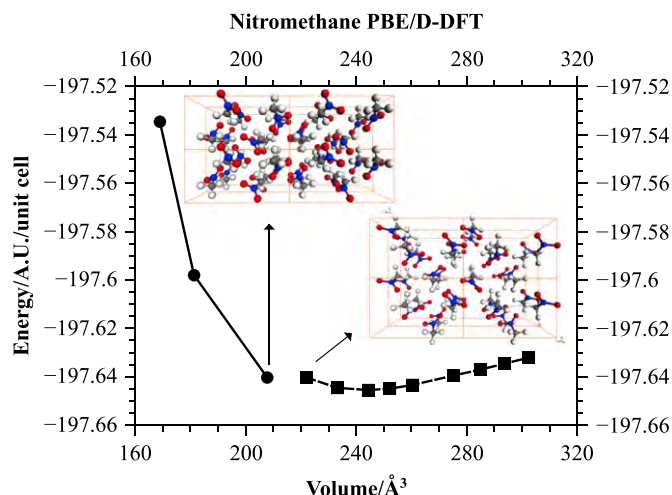


**Fig. 1.** Energy vs. Volume curve for NM. We observe a discontinuity in the calculated equation of state. The symmetry of the unit cell changes from  $P_{212121}$  (supercell on the right) to  $P_{21}$  (supercell on the left) at a volume close to  $220 \text{ Å}^3$ .

the contracted “Voigt” notation; replacing the Cartesian tensor indices by Voigt indices: 11 = 1, 22 = 2, 33 = 3, 23 = 4, 31 = 5, and 12 = 6, for stress, strain and elastic constants. The second order elastic constants,  $C_{ij}$  are then given by the second derivative of the strain energy with respect to the total energy as:

$$C_{ij} = \frac{1}{V_0} \frac{\delta^2 E}{\delta \eta_i \delta \eta_j} \quad (6)$$

In this expression the symmetric finite strain tensor components are now replaced by the 6-dimensional vectors:  $\eta_i$  and  $\eta_j$ . Fitting the strain energy calculated for each applied strain to a second or higher order polynomial then enables us to obtain the corresponding second order elastic constants. The number of independent elastic constants is determined by the symmetry of the crystallographic system. The resulting elastic constants represent the anisotropic response of the crystal to mechanical stimuli. We obtain them by using a total of 6 equally spaced strain values, in addition to the reference or ‘unstrained’ state, and up to a value of 3% of maximum tensile and compressive strain. For the case of empirical corrections to the DFT energy we employed an estimation of dispersion or ‘C6’ coefficients through a parametrization based on atomic polarizabilities (D-DFT). We refer the reader to specialized literature (Grimme, Antony, Schwabe, & Muck-Lichtenfeld,

2007; LeSar, 1984; Marcus, Pavel, Thomas, Sandor, & Efthimios, 2001; Thonhauser et al., 2007; Kohn, Meir, & Makarov, 1998).

Additionally, MD calculations have also been performed. Whenever force field assigned atomic charges were not available, the charges are determined from the Charge Equilibration (QE) method (Rappe & Goddard, 1991). For these simulations with the Isothermal Isobaric ensemble (NPT), the codes LAMMPS (Plimpton, 1995), Cerius2, and Materials Studio have been used. An equilibration time of at least 400 ps (ps) is required for all the runs, with the averages taken over 200 ps long samples of an MD simulation with an integration step size of 1 fs (fs). Nosé-Hoover thermostats and barostats are employed (Martyna, Tobias, & Klein, 1994; Parrinello & Rahman, 1981). Information at the different simulation scales approached here will be correlated with experimental data, when available.

### 3. Results

#### 3.1. Mechanical properties

Here, we analyze in detail the energy vs. volume behavior of primitive unit cells of NM and PETN, composed of 4 and 2 molecules, correspondingly. A discontinuity in the energy-volume curve of NM is observed in the corresponding pressure value of 3.5 GPa, or  $220 \text{ Å}^3$ , see Fig. 1. Upon transition to this state, there is a change in volume close to  $20 \text{ Å}^3$  or 10% reduction. Additionally, a change in the point group symmetry to  $P_{21}$  (Table #4) from  $P_{212121}$ , after the transition at 3.4 GPa is found. The pressure behavior of the elastic coefficients was obtained. We still observe a transition with a larger inverse space integration grid of  $6 \times 6 \times 6$  rather than the earlier  $4 \times 4 \times 4$  grid. The discontinuity is found close to a hydrostatic pressure value of 3 GPa (Fig. 2). The predicted bulk modulus and equilibrium volume for NM, as obtained from localized basis set calculations, are found to be  $288.6 \text{ Å}^3$  and 9.95 GPa. They compare to the experimental values (Winey & Gupta, 2001) of  $285 \text{ Å}^3$  and 10 GPa.

The bulk modulus of PETN is in agreement with the ones found experimentally by Ollinger and Cady (Ollinger, Halleck, & Cady, 1975), with values of 11.36 GPa vs. 9.4 GPa. We found good agreement with their calculated values, as well as in the  $V_0$  ( $592.73 \text{ Å}^3$  vs.  $574.64 \text{ Å}^3$ ).

As opposed to NM, PETN does not show any mechanical instability, as observed from its behavior for compressions up to 6 GPa. This is shown in Fig. 3. Considering, the typical impact tests pressures in the 1 GPa range, and shock or flyer plate test experiment pressures of 3–7 GPa, the discontinuity would be observed close to a shock compression. The bulk modulus as obtained from the Voigt

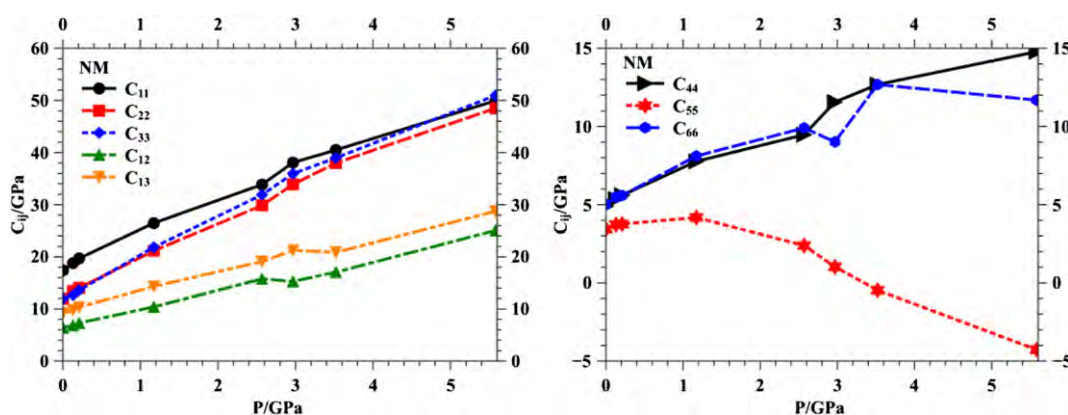


**Fig. 2.** Elastic stiffness coefficients of NM. The observed discontinuity ca. 3 GPa can be observed in elements  $C_{11}$ – $C_{13}$  (left), as well as in the shear constants  $C_{44}$ ,  $C_{55}$ ,  $C_{66}$  (right).

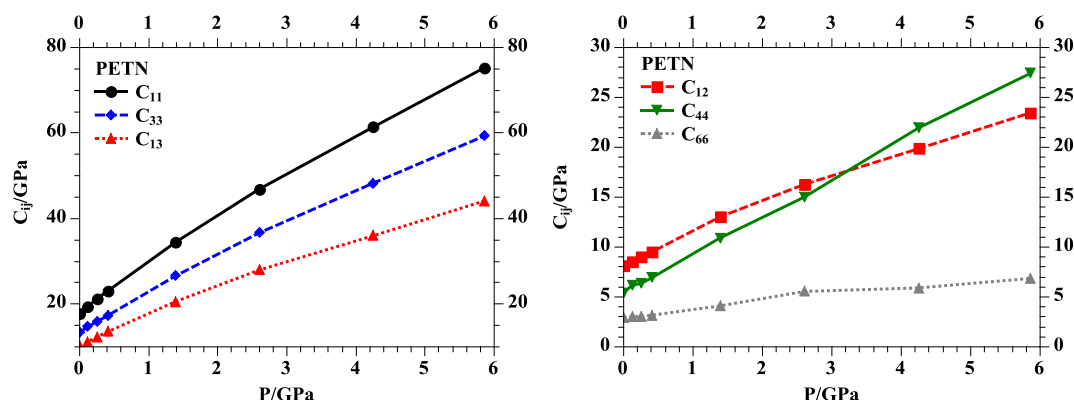


Fig. 3. Changes in the calculated elastic stiffness coefficients of PETN.

average of the individual anisotropic elastic coefficients (11.79 GPa) in very close agreement with the one obtained from our 4th order BM equation of state (11.36 GPa).

### 3.2. Uniaxial compression, ground state

Localization of energy and the corresponding formation of hot spots by compression along particular crystallographic planes can be estimated by the changes in energy observed under uniaxial compressions. This can be represented, for example, through the use of a Gruneisen type of equation (Zel'Dovich, 1968). The deviation from a continuous or monotonic change indicates a highly anharmonic behavior. These results can be observed in molecular crystals, since molecular packing and geometry changes are possible through changes in bonding, torsion and dihedral angles for attaining the lowest enthalpy state of the crystal under applied pressure/stress unlike other materials like metals or ceramics.

For both systems, we found a drastic change in the energy of the system when compressed to 25% of its original volume. Notice the anisotropy found by comparing energy difference at the maximum strain values in Fig. 4 and Fig. 5, we observe the uniaxial compression of NM and PETN, within quantum level DFT calculations. For both systems, there is a region of steep energy change, below 1% strain values. After this, different planes behave differently, in terms of the energy required for compression. This is also an indication of the energy that will be released when a relaxation to initial conditions occur.

At the highest strain value studied here, for NM (Fig. 4), the <001> and <100> show the largest energy change, by almost 10 meV per atom, when compared to the other planes. Below 9%

strain, the <111>, <110> and <101> directions show higher energy differences when compared to the other planes. For this strain level the largest energy differences found between the [100] plane and the [010] plane, which is now smaller than 2 meV/atom. For PETN (Fig. 5), the [010] plane has a higher energy difference of ca. 50 meV/atom as compared to the [001] plane. In contrast, at a compression value close to 8%, the <110> and <001> uniaxial compressions energy differences are below ca. 1 meV/atom, as compared to the rest of the high symmetry directions.

### 3.3. Charge behavior

Since it is commonly assumed that the first step in the initiation of the nitro aliphatic and ester nitrates through the bond breaking (homolytic) of the R-NO and RO-NO<sub>2</sub> groups, we investigate the changes in formal charges measured from Mulliken charges using overpopulation analysis.

The formal charge, as obtained from the atomic number minus the overpopulation in the particular atom, is calculated for the systems under consideration (Fig. 6, Fig. 7). We observe that the behavior is highly anisotropic, with the values of initial charges differing in the highest compressed state.

For the nitro group of the PETN crystal, the largest change in polarization can be observed for <111>, at the maximum strain value of 30%. The polarization for this family of planes is also observed from the ester oxygen atom and the ester carbon atom, with a maximum close to 20% strain.

For NM, we observe an interesting behavior for the charge of the nitro groups, as the crystal is strained along the [111] direction (Fig. 7). In this case, the maximum occurs at strain values close to

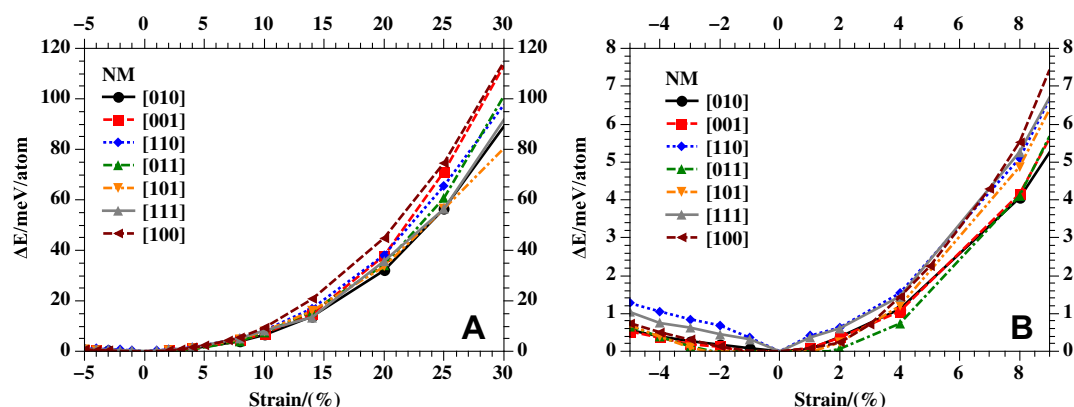


Fig. 4. Uniaxial compression of NM. Complete range of anisotropic strains studied (A). Results of strain comparable to values smaller than 10 GPa (B).

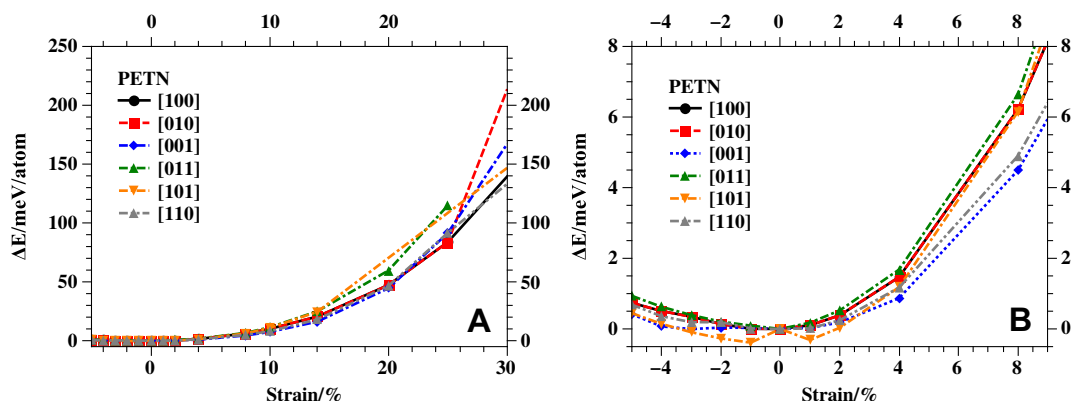


Fig. 5. Uniaxial compression of PETN. Complete range of anisotropic strains studied, (A). Results of strain comparable to values smaller than 10 GPa, (B).

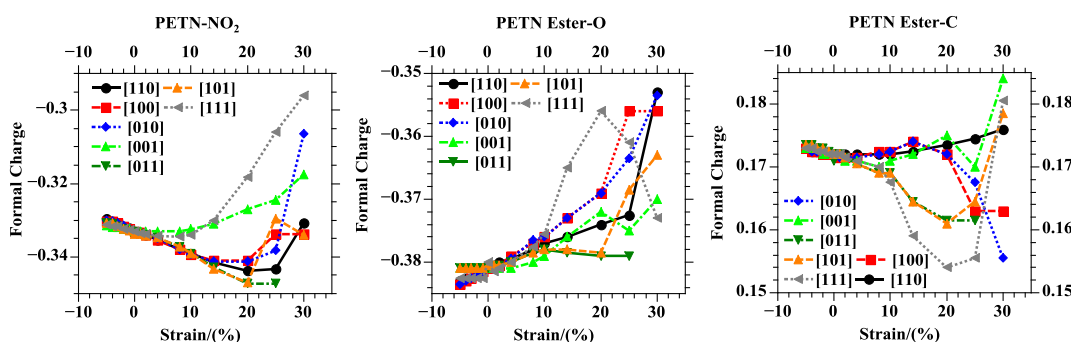


Fig. 6. Change in formal charge for the nitro group in PETN (Top-left), and for the ester oxygen (center). Change in formal charge for the ester carbon (right).

15%. The charge of the nitrogen atom, shows the largest change in formal charge, when compressed along the [001] plane, for values larger than 25% strain.

### 3.4. Effects of temperature and pressure

At elevated temperatures, we have mapped out the stress-strain behavior of the energetic material PETN (for which a phase change ca. 8 GPa has been reported). This is done by generating data on a multidimensional grid of stress values along unique strain directions, based on crystal symmetries. Starting from a slow heating of a  $4 \times 4 \times 6$  supercell from 50 K to 300 K, where we equilibrated the system for over 10 ns. The Molecular Dynamics simulations show curves that differ drastically from an expected uniform/isotropic behavior. From finite temperature evaluation of the equilibrium volumes, we obtain a unit cell of  $289.90 \text{ \AA}^3$  at 150 K for NM, and a value of  $657 \text{ \AA}^3$  at 300 K for PETN. Although our

model over-estimates  $V_0$  for both NM and PETN, they are comparable to reported values ca.  $285 \text{ \AA}^3$  and  $630 \text{ \AA}^3$  correspondingly (Booth & Llewellyn, 1947; Trotter, 1963).

In Fig. 8, we present the changes in enthalpy and internal energy, at different applied external stresses for the studied systems. In both cases we see a change in the slope of the energy change, along particular directions. For the case of PETN, we observe that the  $\langle 001 \rangle$  direction shows an interesting behaviour since it reaches a plateau after 0.4 GPa, in which there is a small change in energy up to 1 GPa. In contrast, the changes in energy in the  $\langle 010 \rangle$  and  $\langle 110 \rangle$  directions show a change in curvature after the value of 0.4 GPa. A changes in the structure of the PETN molecules along this crystallographic plane is expected. For NM, this occurs near pressures of 2 GPa, while for PETN this occurs for pressures close to 1 GPa and smaller. For NM, the most dramatic changes in enthalpy occur for the  $\langle 111 \rangle$  and  $\langle 001 \rangle$  directions. In addition to this, there is a discontinuity, in both enthalpy behavior

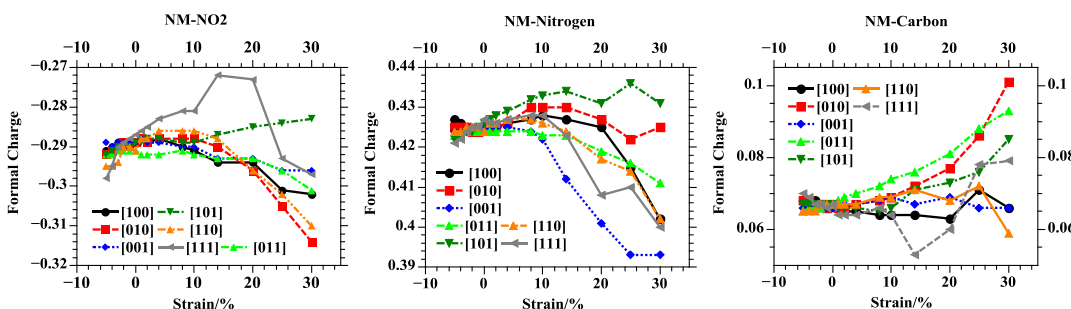


Fig. 7. Change in formal charge for the  $\text{NO}_2$  group (left), nitrogen (center) and carbon (right) of NM.



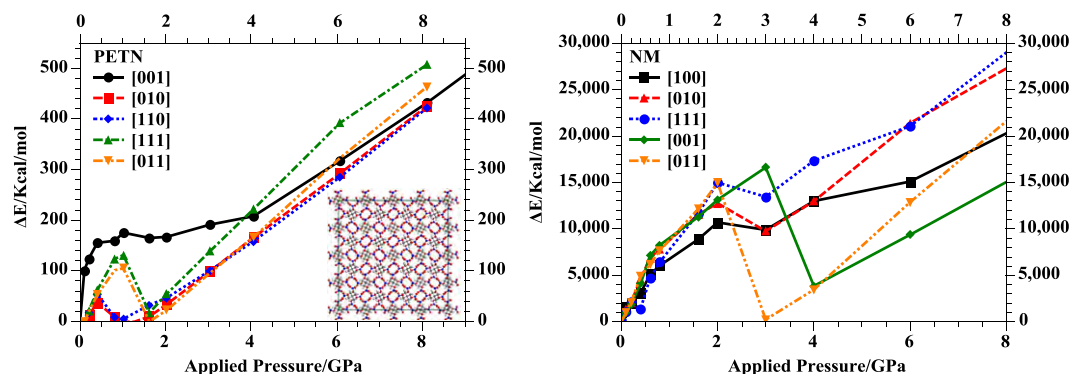


Fig. 8. Changes in the total energy for the PETN supercell (inset, left). Enthalpy changes for NM (right).

and lattice parameters upon compression for the  $\langle 111 \rangle$  direction (Fig. 9). Volume change is larger for this uniaxial compression.

Applied uniaxial stresses could lead to localization of stress, in the form of shear stresses that develop upon compression for the PETN system (Fig. 10). The  $\langle 111 \rangle$  direction shows no increase in shear stresses upon application of uniaxial loads in this compression direction, for PETN. We notice that for this insensitive 111-direction, there is almost no stress increase. In the case of  $\langle 010 \rangle$  this strain is not symmetric, indicating that the original point group of the system is not favored upon compression. There are tensile shear stresses in  $\langle 010 \rangle$  and  $\langle 110 \rangle$  directions. The total increase of stress is larger along 'c' axis when the system is compress in the sensitive [110] plane. For NM, asymmetric buildup of shear stress is found for [001] and [100] planes, which also show the largest change in enthalpy upon axial compression (Fig. 11). We find shear components in XX, and YY for the case of  $\langle 001 \rangle$ , and components in XX, YY and ZZ for  $\langle 100 \rangle$ . Interestingly enough, there is almost no shear buildup for the system when is uniaxially compressed in the [111] direction. The fact that the system undergoes mechanical instabilities after 3 GPa could indicate a difference in the mechanism for the impact and shock sensitivities in NM.

#### 4. Discussion

Cortecuisse (Cortecuisse, Cansell, Fabre, & Petit, 1995) proposed four solid phase transformations in NM up to 25 GPa. Citroni (Citroni et al., 2008) found a phase change after 6.5 GPa, where he cited an increased hydrogen bonding interactions, and

a predominant eclipsed conformation of the nitro group with respect to the methyl group. From our calculations, changes in both symmetry and elastic coefficients indicate that for pressures below 5 GPa, there is phase transformation. This can also be supported by the observed changes in the lattice parameters at elevated temperatures. From a closer inspection of the structure before and after the transition, we find a change in the oxygen interaction of the nitro group with the adjacent molecular hydrogen.

We observed a discontinuity from the pressure dependence behavior of the elastic properties above 3 GPa. Nonetheless noted for the uniaxial compression in the [111] plane direction (Conroy, Oleynik, Zybin, & White, 2009), and in earlier diamond anvil-cell (DAC) studies (Cromer, Ryan, & Schiferl, 1985), this type of behavior has not been reported in other MD simulations or hydrostatic compression studies. Departing from normal conditions, we observe that there is a discontinuity in the enthalpy pressure curves for NM, a system that is sensitive to shocks but insensitive to impact. Dick (Dick, 1993) has proposed the [001] direction is the most sensitive, although no uniaxial DAC was possible. Piermani (Piermarini, Block, & Miller, 1989) reported sensitivities at 3 GPa with the  $\langle 111 \rangle$ ,  $\langle 100 \rangle$  and  $\langle 001 \rangle$  directions. White (Conroy et al., 2009) found greater shear stresses in the  $\langle 111 \rangle$ ,  $\langle 001 \rangle$  and  $\langle 011 \rangle$  directions. Although indications of sensitivity for the [100], [111] and [001] planes for NM have already been reported (Citroni et al., 2008; Conroy et al., 2009; Cromer et al., 1985; Reilly, Habershon, Morrison, & Rankin, 2010; Hervouet, Desbiens, Bourasseau, & Maillat, 2008), our results give insight as to what is the mechanism for sensitivity for each crystallographic direction. Although no available data on the elastic constants were available, the higher sensitivity along the [001] direction (Dick, 1993), is supported by the changes in enthalpy observed from the uniaxial compression runs at 150 K, and from the larger change in total energy from calculations in the limit of 0 K. As expected, due to its low impact sensitivity, the NM system can undergo a monotonic change in enthalpy at low pressures/compressive uniaxial strains. At higher pressures, the shock sensitivity can be observed by the drastic change in enthalpy for the [111] direction, and increase shear pressure for the  $\langle 001 \rangle$  direction, below 4 GPa. Furthermore, the changes in mechanical properties and phase transition, could explain the difference observed between shock and impact sensitivities found from different studies.

For PETN, Soulard (Soulard & Bauer, 1989) observed reactive wave profiles in  $\langle 001 \rangle$  and  $\langle 111 \rangle$  crystals up to 5 and 11 GPa. Dick (Dick, 1984) Classified the  $\langle 001 \rangle$  and  $\langle 110 \rangle$  as sensitive based on wedge experiments. At higher compressions, we see a change in the electronic structure, as measured from the formal charges of the atoms involved in the initiation step for homolytic

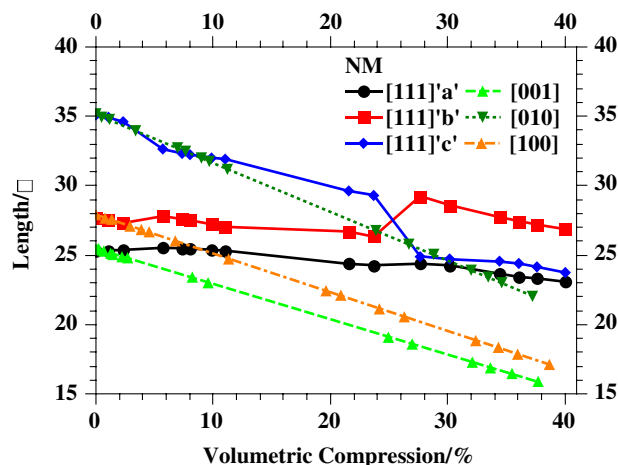


Fig. 9. Changes in lattice parameters for NM.



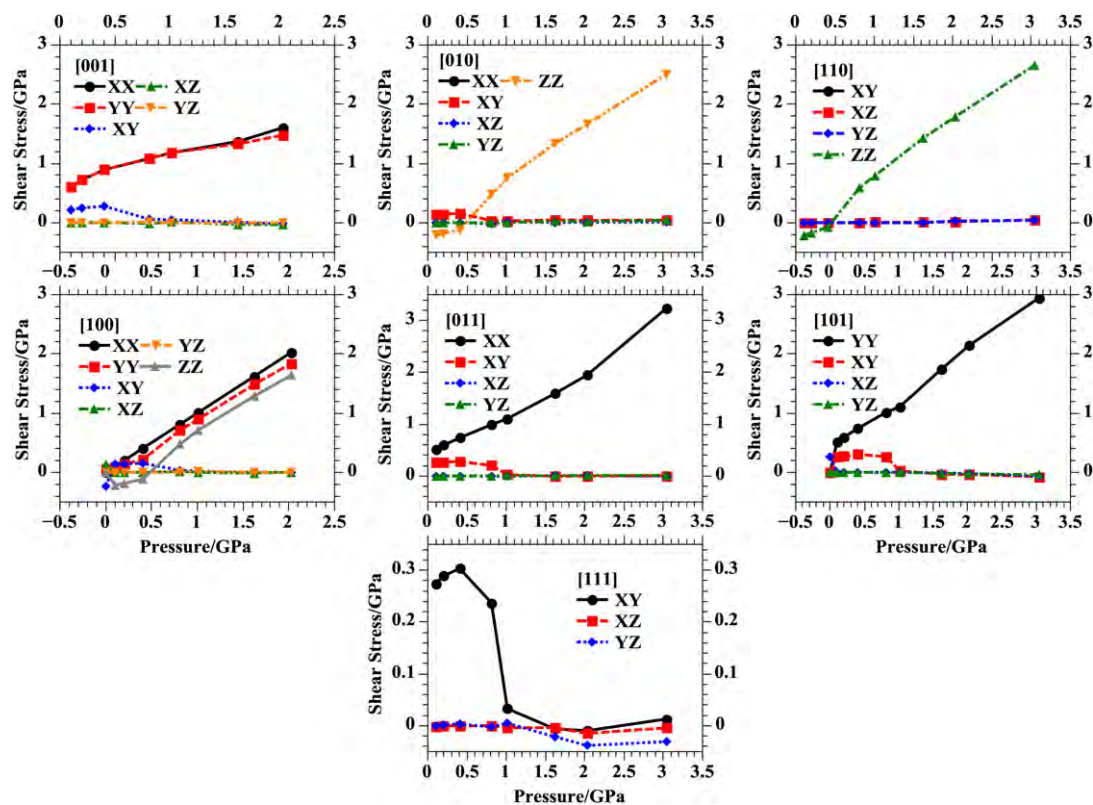


Fig. 10. Shear stress for different applied uniaxial compressions. Values up to 3 GPa, PETN system.

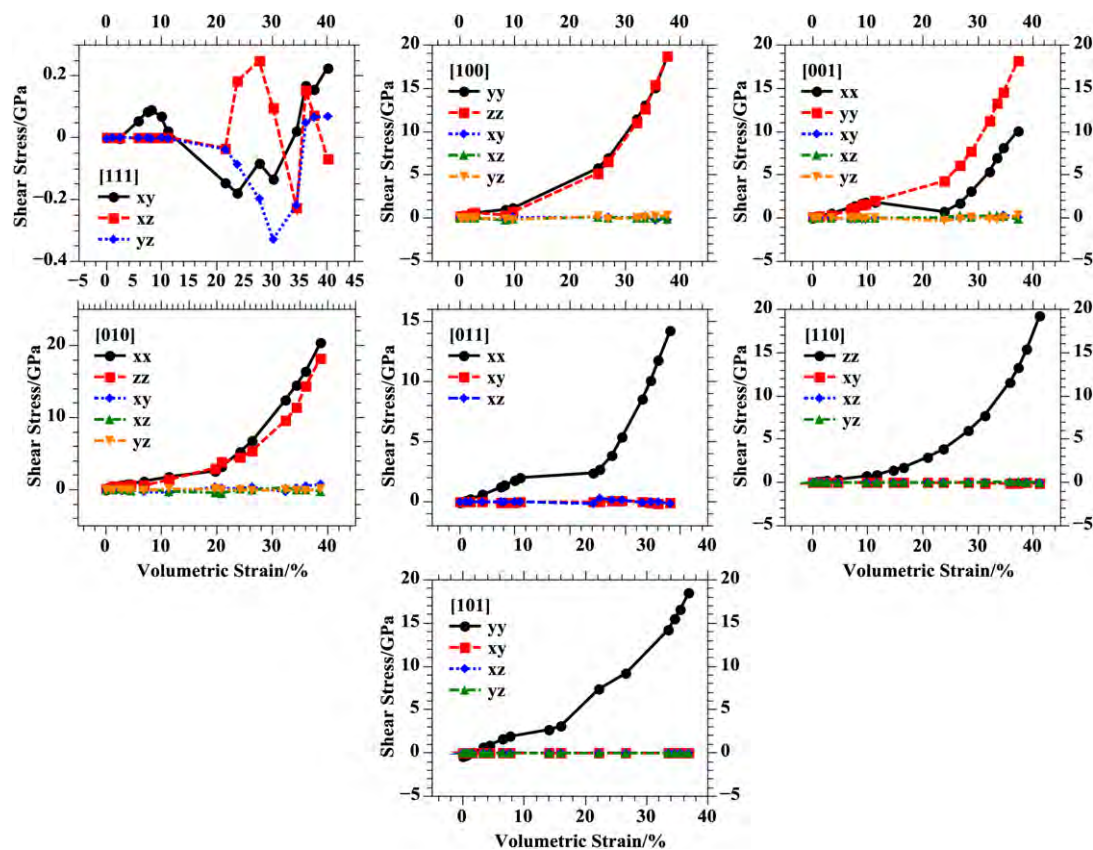


Fig. 11. Shear stresses for different applied uniaxial compression for the system: NM.

bond rupture. The formal charge of the nitro group and carbon atoms varies dramatically for the highest compressed state. This indicates that for the extreme compressed states, initiation can be more easily achieved in preferential directions.

DFT calculations of uniaxial compression along the [010] direction showed the largest energy difference, in the highest strain values studied here. When the effects of temperature are considered, this plane and the [001] plane has displayed non-monotonic behavior. In spite of the anisotropic behavior with the applied external stress, the mechanical properties of PETN show no discontinuity or a drop to negative values up to pressures ca. 6 GPa. In comparison with NM, we can expect a PETN system to be mechanically stable after the pressure of 4 GPa is reached, either by processing or in a controlled application, whilst NM will not. Planes along [111] and [011] showed an inflexion at pressures as small as 1 GPa, which is in line with the observed impact sensitivity. As expected for both cases there are a larger polarization in initiation bonds, at different pressures, and directions. Changes in the formal charge can be observed for different values of uniaxial strain, which indicates that at different compressions (impact, vs. shock) the chemical environment of the strained system is highly anisotropic.

## 5. Concluding remarks

In addition to the reduction of associated cost and safety issues on particular processes that are difficult to study experimentally, we present computational methods that can be used to predict the behavior of materials exposed to extreme conditions. Here we claim that these methods can give an intrinsic advantage, when effort for appropriate parameters and accuracy are met.

We have observed that NM, which shows a crystallographic phase transformation and a drastic behavior of its elastic coefficients, as opposed to PETN, which is observed to be mechanically stable in the studied pressure range. Nonetheless, the effect of elevated temperatures and pressures might provide more insight into their behavior under compression. These studies further have revealed the anisotropic behavior of the studied systems. Further studies that gather information at the chemical, mechanical and thermodynamic level can be applied to the understanding of other type of systems, of lower sensitivity, or even materials, for which unknown sensitivities are of concern.

## Acknowledgments

The research here supported by ARO-MURI: Insensitive Munitions. O.U.O. acknowledges gratefully CONACYT for its kind support for earlier part of his doctoral work. The authors would like to thank the support of the Laboratory for Molecular Simulation and the Supercomputing Centers at Texas A&M College Station and Texas A&M Qatar.

## References

Arman, B., An, Q., Luo, S. N., Tonks, D. L., Cagin, T., Goddard, I. W. A., et al. (2011). Dynamic response of phenolic resin and its carbon-nanotube composites to shock wave loading. *Journal of Applied Physics*, 109.

Badders, N. R., Wei, C., Aldeeb, A. A., Rogers, W. J., & Mannan, M. S. (2006). Predicting the impact sensitivities of polynitro compounds using quantum chemical descriptors. *Journal of Energetic Materials*, 24, 17–33.

Bernhard Schlegel, H. (1984). Estimating the hessian for gradient-type geometry optimizations. *Theoretica Chimica Acta*, 66, 333–340.

Binkley, J. S., Pople, J. A., & Hehre, W. J. (1980). Self-consistent molecular orbital methods. 21. Small split-valence basis sets for first-row elements. *Journal of the American Chemical Society*, 102, 939–947.

Birch, F. (1978). Finite strain isotherm and velocities for single-crystal and polycrystalline NaCl at high pressures and 300° K. *Journal of Geophysical Research*, 83, 1257–1268.

Booth, A. D., & Llewellyn, F. J. (1947). The crystal structure of pentaerythritol tetranitrate. *Journal of the Chemical Society*, 837–846.

Brill, T. B., & James, K. J. (1993). Thermal decomposition of energetic materials. 61. Perfidy in the amino-2,4,6-trinitrobenzene series of explosives. *Journal of Physical Chemistry*, 97, 8752–8758.

Byrd, E. F. C., & Rice, B. M. (2006). Improved prediction of heats of formation of energetic materials using quantum mechanical calculations. *Journal of Physical Chemistry. A*, 110, 1005–1013.

Byrd, E. F. C., & Rice, B. M. (2007). Ab initio study of compressed 1,3,5,7-Tetranitro-1,3,5,7-tetraazacyclooctane (HMX), Cyclotrimethylenetrinitramine (RDX), 2,4,6,8,10,12-Hexanitrohexaazaisowurztane (CL-20), 2,4,6-Trinitro-1,3,5-benzenetriamine (TATB), and pentaerythritol tetranitrate (PETN). *Journal of Physical Chemistry. C*, 111, 2787–2796.

C.S. Database. (2007). CCSD.

Citroni, M., Datchi, F., Bini, R., DiVaira, M., Pruzan, P., Canny, B., et al. (2008). Crystal structure of nitromethane up to the reaction threshold pressure. *Journal of Physical Chemistry. B*, 112, 1095–1103.

Civalleri, B., Doll, K., & Zicovich-Wilson, C. M. (2006). Ab initio investigation of structure and cohesive energy of crystalline urea. *Journal of Physical Chemistry. B*, 111, 26–33.

Conroy, M. W., Oleynik, I. I., Zybin, S. V., & White, C. T. (2009). Density Functional Theory Calculations of Solid Nitromethane under Hydrostatic and Uniaxial Compressions with Empirical van der Waals Correction. *Journal of Physical Chemistry. A*, 113, 3610–3614.

Courteuisse, S., Cansell, F., Fabre, D., & Petit, J. P. (1995). Phase transitions and chemical transformations of nitromethane up to 350 °C and 35 GPa. *Journal of Chemical Physics*, 102, 968–974.

Cromer, D. T., Ryan, R. R., & Schiferl, D. (1985). The structure of nitromethane at pressures of 0.3 to 6.0 GPa. *Journal of Physical Chemistry*, 89, 2315–2318.

Dick, J. J. (1984). Effect of crystal orientation on shock initiation sensitivity of pentaerythritol tetranitrate explosive. *Applied Physics Letters*, 44, 859–861.

Dick, J. J. (1993). Orientation-dependent explosion sensitivity of solid nitromethane. *Journal of Physical Chemistry*, 97, 6193–6196.

Dick, J. J. (1997). Anomalous shock initiation of detonation in pentaerythritol tetranitrate crystals. *Journal of Applied Physics*, 81, 601–612.

Ditchfield, R., Hehre, W. J., & Pople, J. A. (1971). Self-Consistent molecular-orbital methods. IX. An extended Gaussian-type basis for molecular-orbital studies of organic molecules. *Journal of Chemical Physics*, 54, 724–728.

Dovesi, R., Saunders, V. R., Roetti, C., Orlando, R., Zicovich-Wilson, C. M., Pascale, F., et al. (2007). *Crystal06*. [www.crystal.unito.it/](http://www.crystal.unito.it/).

Ferro, D., Barone, G., Della Gatta, G., & Piacente, V. (1987). Vapour pressures and sublimation enthalpies of urea and some of its derivatives. *The Journal of Chemical Thermodynamics*, 19, 915–923.

Gatti, C., Saunders, V. R., & Roetti, C. (1994). Crystal field effects on the topological properties of the electron density in molecular crystals: the case of urea. *Journal of Chemical Physics*, 101, 10686–10696.

Gibbs, T. R., Popolatto, A., & Baytos, J. F. (1980). *LASL explosive property data*. Berkeley: University of California Press.

Grimme, S., Antony, J., Schwabe, T., & Muck-Lichtenfeld, C. (2007). Density functional theory with dispersion corrections for supramolecular structures, aggregates, and complexes of (bio)organic molecules. *Organic & Biomolecular Chemistry*, 5, 741–758.

Hervouet, A., Desbiens, N., Bourasseau, E., & Maillet, J. B. (2008). Microscopic Approaches to Liquid nitromethane detonation properties. *Journal of Physical Chemistry. B*, 112, 5070–5078.

Hu, W.-F., He, T.-J., Chen, D.-M., & Liu, F.-C. (2002). Theoretical study of the CH<sub>3</sub>NO<sub>2</sub> unimolecular decomposition potential energy surface. *Journal of Physical Chemistry. A*, 106, 7294–7303.

Kohn, W., & Sham, L. J. (1965). Self-consistent equations including exchange and correlation effects. *Physical Review*, 140, A1133.

Kohn, W., Meir, Y., & Makarov, D. E. (1998). van der Waals Energies in density functional theory. *Physical Review Letters*, 80, 4153.

Kuklja, M. M., & Kunz, A. B. (1999). Ab initio simulation of defects in energetic materials: hydrostatic compression of. *Journal of Applied Physics*, 86, 4428.

LeSar, R. (1984). Electron-gas plus damped-dispersion model for intermolecular forces. The rare-gas and hydrogen–helium, hydrogen–neon, and hydrogen–argon potentials. *Journal of Physical Chemistry*, 88, 4272–4278.

Li, J. S., Huang, Y. G., & Dong, H. S. (2005). A theoretical study of polynitropyridines and their N-oxides. *Journal of Energetic Materials*, 23, 133–149.

Manaa, M. R., & Fried, L. E. (1998). DFT and ab initio study of the unimolecular decomposition of the lowest singlet and triplet states of nitromethane. *Journal of Physical Chemistry. A*, 102, 9884–9889.

Manelis, G. B. (2003). *Thermal decomposition and combustion of explosives and propellants*. London: Taylor & Francis.

Marcus, E., Pavel, H., Thomas, F., Sander, S., & Efthimios, K. (2001). Hydrogen bonding and stacking interactions of nucleic acid base pairs: a density-functional-theory based treatment. *Journal of Chemical Physics*, 114, 5149–5155.

Martyna, G. J., Tobias, D. J., & Klein, M. L. (1994). Constant-pressure molecular dynamics algorithms. *Journal of Chemical Physics*, 101, 4177–4189.

Olinger, B., Halleck, P. M., & Cady, H. H. (1975). The isothermal linear and volume compression of pentaerythritol tetranitrate (PETN) to 10 GPa (100 kbar) and the calculated shock compression. *Journal of Chemical Physics*, 62, 4480–4483.

Parrinello, M., & Rahman, A. (1981). Polymorphic transitions in single crystals – a new molecular dynamics method. *Journal of Applied Physics*, 52, 7182–7190.

- Perdew, J. P., Burke, K., & Ernzerhof, M. (1996). Generalized gradient approximation made simple. *Physical Review Letters*, 77, 3865.
- Perry, A. (1978). A modified conjugate gradient algorithm. *Operations Research*, 26, 1073–1078.
- Piermarini, G. J., Block, S., & Miller, P. J. (1989). Effects of pressure on the thermal decomposition kinetics and chemical reactivity of nitromethane. *Journal of Physical Chemistry*, 93, 457–462.
- Plimpton, S. (1995). Fast parallel algorithms for short-range molecular dynamics. *Journal of Computational Physics*, 117, 1–19.
- Rappe, A. K., & Goddard, W. A. (1991). Charge equilibration for molecular dynamics simulations. *Journal of Physical Chemistry*, 95, 3358–3363.
- Reilly, A. M., Habershon, S., Morrison, C. A., & Rankin, D. W. H. (2010). Determination of the experimental equilibrium structure of solid nitromethane using path-integral molecular dynamics simulations. *Journal of Chemical Physics*, 132, 094502–094510.
- Schafer, A., Horn, H., & Ahlrichs, R. (1992). Fully optimized contracted Gaussian basis sets for atoms Li to Kr. *Journal of Chemical Physics*, 97, 2571–2577.
- Sewell, T. D., Menikoff, R., Bedrov, D., & Smith, G. D. (2003). A molecular dynamics simulation study of elastic properties of HMX. *Journal of Chemical Physics*, 119, 7417–7426.
- Shaw, R. (1973). Heats of formation and kinetics of decomposition of nitroalkanes. *International Journal of Chemical Kinetics*, 5, 261–269.
- Sorescu, D. C., Rice, B. M., & Thompson, D. L. (1999). Theoretical studies of the hydrostatic compression of RDX, HMX, HNIW, and PETN crystals. *Journal of Physical Chemistry. B*, 103, 6783–6790.
- Soulard, L., & Bauer, F. (1989). In S. C. Schmidt, J. N. Johnson, & L. W. Davidson (Eds.), *Shock compression of condensed matter*. Albuquerque, NM: Elsevier.
- Thonhauser, T., Cooper, V. R., Li, S., Puzder, A., Hyldgaard, P., & Langreth, D. C. (2007). Van der Waals density functional: self-consistent potential and the nature of the van der Waals bond. *Physical Review. B*, 76, 125111–125112.
- Towler, M. D., Zupan, A., & Causà, M. (1996). Density functional theory in periodic systems using local Gaussian basis sets. *Computer Physics Communications*, 98, 181–205.
- Trotter, J. (1963). Bond lengths and angles in pentaerythritol tetranitrate. *Acta Crystallographica*, 16, 698–699.
- Wallace, D. C. (1972). *Thermodynamics of crystals*. New York: Dover.
- Winey, J. M., & Gupta, Y. M. (2001). Second-order elastic constants for pentaerythritol tetranitrate single crystals. *Journal of Applied Physics*, 90, 1669–1671.
- Woodward, J. L., & Ketchum, D. E. (2001). Investigation and modeling of an explosion in a propane absorption column. *Journal of Loss Prevention in the Process Industries*, 14, 251–260.
- Yuan, L., & Smith, A. C. (2009). CFD modeling of spontaneous heating in a large-scale coal chamber. *Journal of Loss Prevention in the Process Industries*, 22, 426–433.
- Zel'Dovich, Y. B. (1968). *Physics of shock waves and high-temperature hydrodynamic phenomena*, Vol. 1. Academic Press. S.I.
- Zeman, S. (1995). New application of kinetic data of the low-temperature thermolysis of nitroparaffins. *Theoretica Chimica Acta*, 261, 195–207.
- Zhang, C., Shu, Y., Huang, Y., Zhao, X., & Dong, H. (2005). Investigation of correlation between impact sensitivities and nitro group charges in nitro compounds. *Journal of Physical Chemistry. B*, 109, 8978–8982.
- Zhang, C. Y., Shu, Y. J., Zhao, X. D., Dong, H. S., & Wang, X. F. (2005). Computational investigation on HEDM of azoic and azoxy derivatives of DAF, FOX-7, TATB, ANPZ and LLM-105. *Journal of Molecular Structure THEOCHEM*, 728, 129–134.

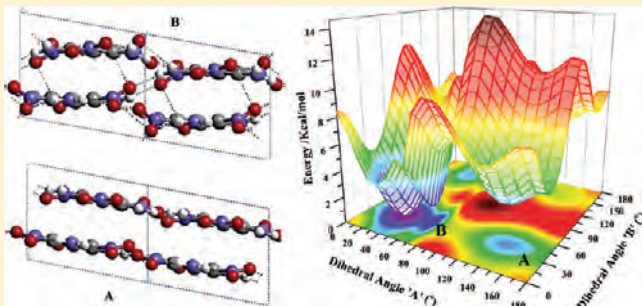


# Hydrogen Bonding and Molecular Rearrangement in 1,3,5-Triamino-2,4,6-trinitrobenzene under Compression

Oscar U. Ojeda and Tahir Çağın\*

Laboratory of Computational Engineering of Nanomaterials, Artie McFerrin Department of Chemical Engineering, Texas A&M University, College Station, Texas 77843-3122, United States

**ABSTRACT:** We studied the structural behavior and properties of 1,3,5-triamino-2,4,6-trinitrobenzene (TATB) under hydrostatic compression using atomistic and electronic (ab initio) level computations. We observed a marked change in the intermolecular hydrogen-bonding network upon compression of the crystal without change in crystal symmetry. The changes in molecular arrangement are found to have a profound impact on various observable properties: energetic, vibrational spectra, structural, and elastic properties. From the analysis of vibrational modes, we observed that the changes are mainly due to the nitro and amino groups. An increase in the number of hydrogen bonding interactions along the *c*-axis of the crystals results in providing the extra stabilization energy. In addition to analyze the isolated molecule and dimer, this molecular rearrangement is systematically studied and characterized in the condensed phase. From higher-level ab initio calculations, the potential energy surface of the dimer indicates the presence of a region with two local minima within 3.42 kcal/mol difference in energy. Since this behavior is not associated with a change of symmetry of the crystal unit cell, the possible coexistence of two molecular arrangements might lead to the loss of a definitive inversion center for bulk. The calculated elastic constants of the crystal dramatically reveal the changes via large increases in certain components. Implications on the observed pressure-induced rearrangement behavior on the mechanical, optical, and thermodynamic properties of TATB are further discussed, and correlations with experimental spectroscopic data are provided.



## 1. INTRODUCTION

TATB, 1,3,5-triamino-2,4,6-trinitrobenzene, is known as an insensitive secondary energetic material (EM).<sup>1–3</sup> This arene-substituted molecule has both electron-withdrawing and -donor groups<sup>4</sup> and favors packing in a lamellar arrangement. Experiments conducted by various researchers provide evidence of changes in its nonlinear optical response<sup>5</sup> and changes in the microstructure and other properties under thermal or mechanical treatment,<sup>6</sup> including an irreversible thermal expansion.<sup>7,8</sup> Besides a general interest in TATB as an energetic material,<sup>9–21</sup> a detailed molecular level investigation of these changes in the solid phase is of significant relevance. Subtle structural differences can have implications in the stability and properties of the molecules as subjected to external stimuli, such as heat<sup>22</sup> or in particular under compression.<sup>23</sup> Therefore, related molecular and atomistic level information<sup>8,24</sup> and its behavior as compared<sup>12</sup> to other type of EM's<sup>25</sup> could also provide hints to the unusual properties<sup>26–28</sup> of this material. At ambient conditions, the experimental crystal structure reported by Cady and Larson<sup>29</sup> has (P-1) symmetry. The unit cell contains two molecules for a total of 48 atoms. Later reports of the structure of TATB from X-ray diffraction studies (XRD) indicated a lack of phase transition when the crystal is subjected to compression.<sup>30</sup> In line with this observation, some atomistic models,<sup>31,32</sup> and other theoretical and ab initio calculations,<sup>33,34</sup> have also reported stable planar molecular conformations, with no phase changes in crystal structure. Still, the molecular behavior of the system under

pressure has been the subject of debate since earlier studies,<sup>35</sup> which have implied the presence of polymorphism.<sup>36</sup> Catalano and Rolon discussed the difficulties in settling the existence of TATB polymorphs and reported the presence of a number of solid state products prior to its decomposition,<sup>37</sup> while Foltz reported an irreversible change in optical properties of TATB upon compression<sup>38</sup> in a diamond-anvil cell (DAC) experiment. More recently, experimental vibrational properties of the system under hydrostatic compression have been reported by Pravica et al.<sup>3,39</sup>

To clarify if any such crystal or molecular transformation upon compression exists, we have performed a systematic study of the crystalline TATB system applying external pressures up to 30 GPa. In the following, we will present the results of our extensive studies on the changes in molecular structure and rearrangements within this triclinic unit cell under compression. Not only will we demonstrate the observed molecular rearrangements, but also we will demonstrate the effect of these structural changes at a molecular level on macroscopic properties, mechanical properties, vibrational spectra, and diffraction patterns. After a brief introduction of the methods employed, we will first describe the observed structural changes. To show how its influence on the vibrational spectra is revealed, we calculate the vibrational spectra

Received: January 25, 2011

Revised: September 14, 2011

as a function of pressure. To relate this observation to experiments, we also present calculated X-ray diffraction patterns before and after molecular rearrangement. To provide the energetic basis for a simple statistical two-state model, we performed extensive potential energy surface calculations using ab initio quantum chemistry and density functional theory (DFT) methods. To demonstrate the influence on the mechanical properties of the system we have calculated the elastic stiffness tensor and its variation as a function of pressure. We will then conclude by discussing the implications of our findings and its relation to the behavior of TATB.

## 2. METHODS

To understand the potential energy landscape of the system under consideration, we have performed ab initio quantum chemistry calculations using localized basis sets<sup>41,42</sup> on a single TATB molecule and TATB dimer. In these calculations, the Hartree–Fock approximation (HF) and the Möller–Plesset perturbation (MP2) have been employed.<sup>43,44</sup> DFT<sup>6,45</sup> calculations with 3-dimensional periodic boundary conditions (PBC) have also been carried out on the TATB single crystal. In this case, the Perdew–Burke–Ernzerhof (PBE) exchange correlation functional<sup>46–49</sup> and the projector-augmented-wave (PAW) type potentials are used.<sup>50,51</sup> For securing accuracy of the results, an appropriate energy cutoff and inverse space integration scheme<sup>52</sup> with a tolerance for convergence of 0.2 meV per atom were chosen. Furthermore, a tolerance on the convergence of the self-consistent wave function optimization cycle is set to  $1 \times 10^{-7}$  eV. Optimization of the cell parameters and fractional coordinates at each applied external stress value is performed without imposing any restriction on the symmetry of the unit cell. In the calculation of elastic properties, we only used the “Born” term. This is the second derivative of the potential energy with respect to the strain tensor. The strain derivatives are calculated analytically from the interaction force-fields for organic materials.<sup>53</sup> More specifically, we use the “Dreiding exponential-6” (DREX6) force-field,<sup>54</sup> which is a well-parametrized valence force-field for the main group elements with an explicit H-bonding term. The force-field has been found to be particularly well-suited for the study of molecular systems made up of main group elements. Atomic charges are determined by the use of the QEq method,<sup>55,56</sup> which reliably accounts for the charges as a function of configuration and ionization energies of the particular element. For the calculation X-ray diffraction spectra, we have simulated the diffraction pattern for an incident radiation of wavelength 1.54178 Å using the diffraction module of the Cerius2 program.

## 3. RESULTS

**Structural Rearrangement as a Function of Pressure.** In Figure 1, we present the variation of unit cell parameters of single crystal TATB as a function of applied pressure with the values ranging from 0 to 5 GPa. TATB displays a reduction in volume and in three lattice constants ( $a$ ,  $b$ ,  $c$ ), as shown in Figure 1. From 0 GPa to approximately 1.5 GPa, all three lattice constants ( $a$ ,  $b$ , and  $c$ ) decrease with slight differences as expected from the anisotropic elastic response of the crystalline material. However, upon further compression, the molecules slightly move from a perfect alignment perpendicular to the  $c$ -axis, hence reducing the electrostatic repulsion caused by the conjugated  $\pi$  system. This causes a distinct variation in the unit cell parameters; we observe

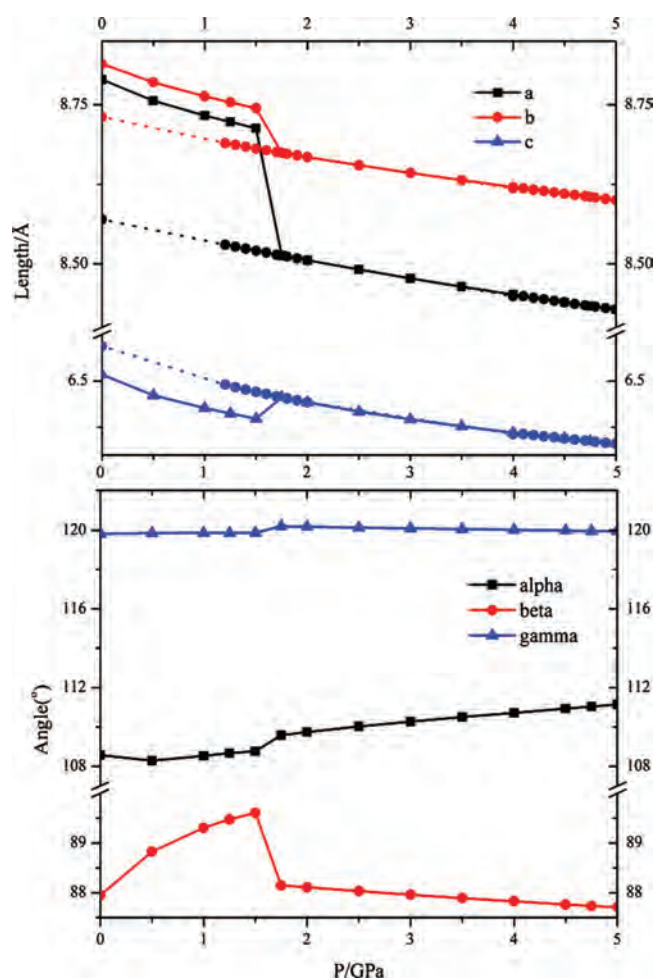


**Figure 1.** Change in lattice parameters upon compression, compressive loading run (solid line); pressure release run (dotted line).

a sharp increase in the  $c$ -axis while  $a$ - and  $b$ -axes drastically decrease, still leading to a decrease in volume. When the structure before and after this “transformation” is analyzed, before the transition, in-plane (perpendicular to the  $c$ -axis) hydrogen bonding and in-plane molecular interactions are dominant. As the pressure increased beyond 1.5 GPa, however, the system responds through a rearrangement by increasing out-of-plane interactions by establishing a new network of hydrogen bonding (we will further characterize this below). Hence, compared with the reported ambient pressure structure, there is a “transformation” in the form of a structural rearrangement at approximately 1.5 GPa. The molecular layers, originally shifted off the axis, align closer one on top of the other. The net result is a lengthening of the  $c$ -axis. This is accompanied by reductions in  $a$ - and  $b$ -axis lengths, and the total volume of the relaxed unit cell after the transition at a pressure ca. 2 GPa is smaller by  $5.1 \text{ Å}^3$ .

**Vibrational Spectra as a Function of Pressure.** To further characterize molecular rearrangement as a function of pressure, we have calculated the vibrational spectra before and after molecular arrangement (focusing between 1.4 and 1.6 GPa). We have evaluated the vibrational frequencies and modes from the Hessian matrix.

The full vibrational spectra of the system under study are displayed in Figure 2 for three pressure values (0, 1.4, and 1.6 GPa). In the full frequency range shown here, we observe notable



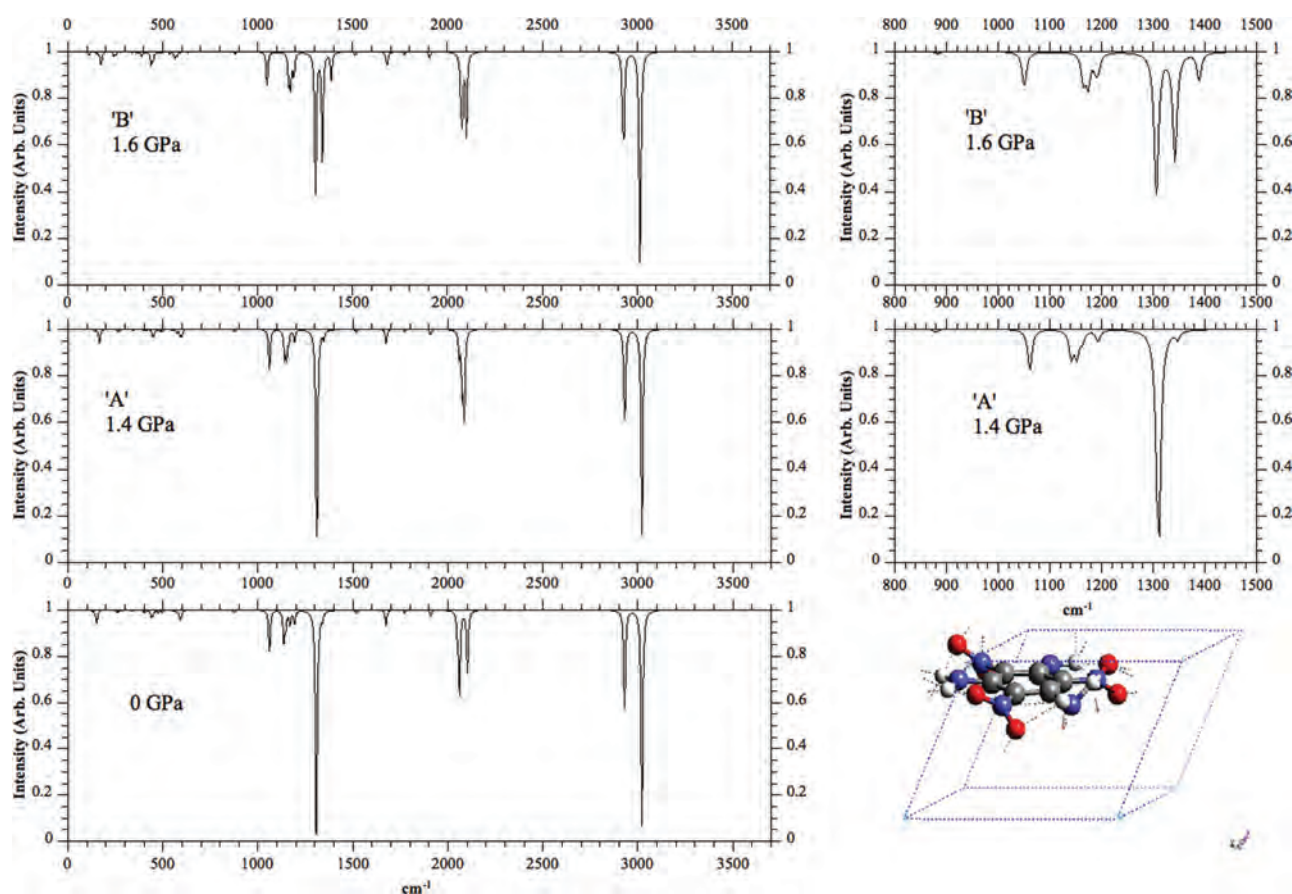


**Figure 2.** Vibrational spectra at different pressures. The frequency range ( $800\text{--}1500\text{ cm}^{-1}$ ) is displayed on the right. Spectra at ambient pressure are labeled as “0 GPa”. Spectra at  $P = 1.4\text{ GPa}$  are labeled “A”, while the spectra obtained at a pressure value close to  $1.6\text{ GPa}$  are labeled as “B”. The bottom right figure depicts the vibrational mode at  $1324\text{ cm}^{-1}$ .

differences between the 0 and  $1.4\text{ GPa}$  pressure range and  $1.6\text{ GPa}$ . There are more striking changes close to the region of  $2000\text{ cm}^{-1}$  and in the region between  $800$  and  $1500\text{ cm}^{-1}$  (shown on the right panel of Figure 2). At higher frequencies, we observe the splitting of the degenerate mode ca.  $2100\text{--}2099\text{ cm}^{-1}$  and  $2101.5\text{ cm}^{-1}$ . This split is caused by the change in the interplanar hydrogen bonds due to rotation of  $\text{NH}_2$ . In the frequency range from  $800$  to  $1500\text{ cm}^{-1}$ , in addition to the appearance of additional vibrational maxima appearing, there is clearly a splitting of the peak near  $1320\text{ cm}^{-1}$ . From the analysis of the vibrational eigenmode at  $1324\text{ cm}^{-1}$  at  $0\text{ GPa}$  pressure, this mode is related to the bonding environment of the amino and nitro groups. In Figure 2, at the bottom right, one of the molecules is displayed within the unit cell to show the orientation of nitro and amino groups (for the purpose of clarity, the inversion symmetry image is not displayed).

The peak near  $1320\text{ cm}^{-1}$  changes into two peaks centered at  $1342$  and  $1336\text{ cm}^{-1}$ , with a further shift to high frequency due to increased pressure. This is mainly caused by the changes in intralayer hydrogen bonding and the emergence of interlayer hydrogen bonding, in which nitrogen-bearing substituents are involved. Lower frequency modes are as well influenced by the changes in molecular orientation within the unit cell. More specifically, the vibrations related to the changes in conformation of the aromatic ring, ring breathing, and modes involving both the ring and its substituents can be observed. We show the results of the frequency region between  $100$  and  $700\text{ cm}^{-1}$  in Figure 3 with more

detail. Here, we have determined the variation of frequency spectra at pressures of  $0, 0.4, 0.8, 1.2, 1.8,$  and  $2.4\text{ GPa}$ . We have displayed both loading and unloading conditions.

**Simulated X-ray Diffraction Patterns.** We have also calculated the associated X-ray diffraction patterns of the structure before and after the observed molecular rearrangement using the crystal diffraction module of the Cerius2 program. Changes in the interplanar spacing for the  $(002)$ ,  $(110)$ , and  $(1\text{--}1\text{--}1)$  directions can be seen in Figure 4. The dramatic change in the structure and unit cell parameters is revealed through the discontinuity in  $d$ -spacing, near the observed “transformation” above  $1.5\text{ GPa}$ .

**Analysis of H-Bond Network.** To understand the changes in the chemical environment of the system, we have closely analyzed the conformations of the amino and nitro substituents, before and after the observed transition. From a close inspection of the structure before and after the transition, we see that the oxygen atoms from the nitro groups, which were aligned in plane in the ambient pressure structure, have rotated out-of-plane to increase their interaction with molecules above and below the original plane. In the ambient pressure structure, there were three hydrogen bonds per amino hydrogen. Two of them bonded within the same molecule, to adjacent nitrogen and oxygen atoms. The other bond is formed with the neighboring molecule's nitro group oxygen. The longest hydrogen bond is  $2.501\text{ \AA}$ . After the transition, adjacent molecules within the crystal field now allow for up to four hydrogen bonds per terminal hydrogen in the

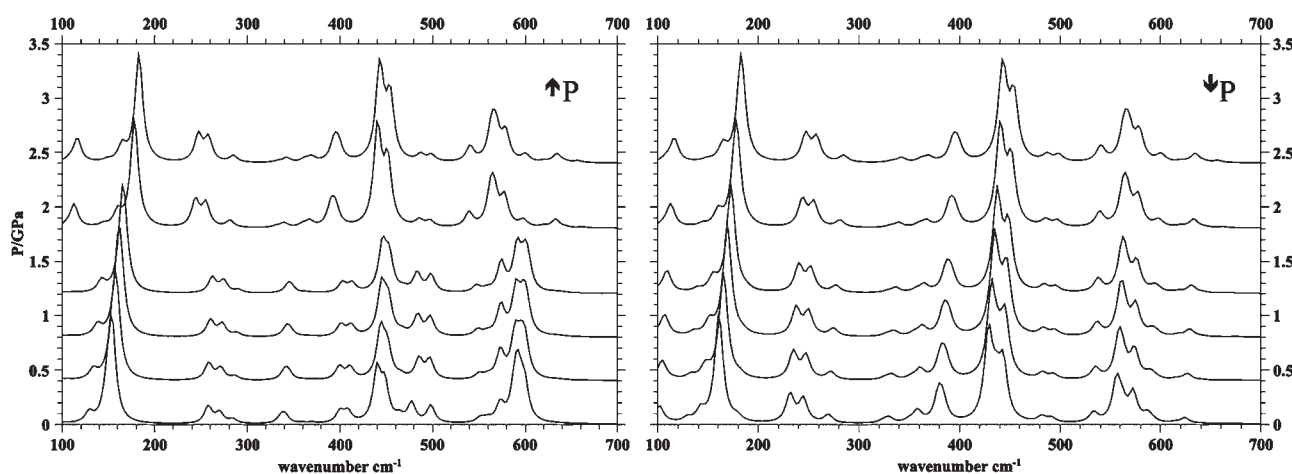


**Figure 3.** Far-infrared section of the spectra for pressures of 0, 0.4, 0.8, 1.2, 1.8, and 2.4 GPa. Data were evaluated over the structures obtained from compression runs, 0 to 5 GPa (left). Notice the irreversible change of different modes, after 1.6 GPa. Results are shown from the structures using states from the release runs: 5 to 0 GPa (right). The pressure variation during the simulation is depicted as  $\uparrow P$  and  $\downarrow P$ , correspondingly.

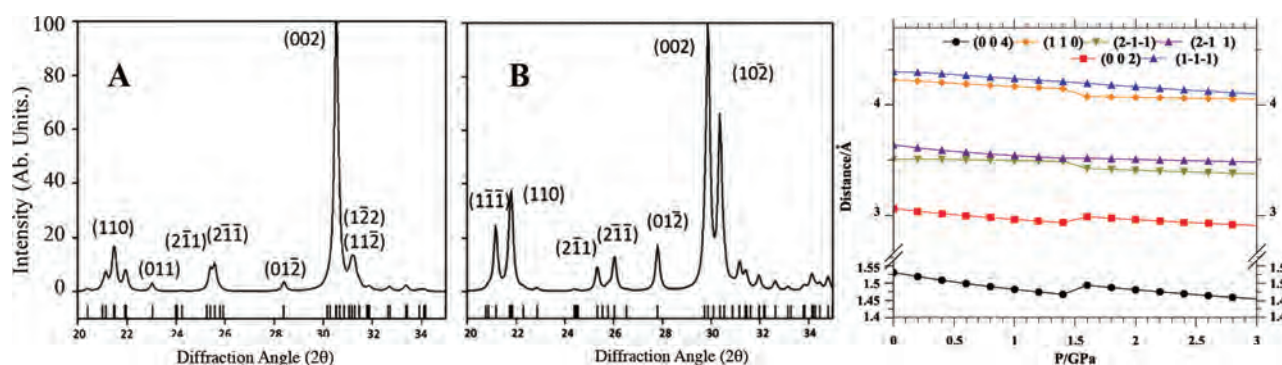


**Figure 4.** Changes in the XRD spectra of the TATB molecule, at 1.5 GPa (A) and 1.55 GPa (B) and changes in  $d$  spacing for the selected planes (right). An abrupt change after 1.5 GPa can be clearly identified, for the spacing of the selected planes.

amino group. The longest interlayer hydrogen bond has a distance of 2.483 Å. The amino group closer to the inversion center has interactions via two intramolecular bonds and two intermolecular bonds; one of them is within the same layer and the other one with a neighboring layer. The total number of hydrogen bonds with neighboring layers along the  $C$ -axis changes from 0 to 8, after 1.6 GPa. All of the amino group hydrogens are bonded to at least one other molecule (Figure 5).

Even though there are no restrictions throughout the calculations, the system retains the symmetry of the initially minimized unit cell even after the observed transition, P-1. As expected from analyzing the changes in the hydrogen-bonding network, its stabilizing contribution to the total energy of the system increases from  $-4$  kcal/mol to more than  $-10$  kcal/mol.

**Two-State Model.** To assess the thermal accessibility of the new state, we use a simple two-state model by calculating the energetics of each state and compare the kinetic energy required for the conformation “A”, or flat dihedral angles, as compared to the “bent” conformation, or conformation “B”. The energy difference from one state to the other can be found from a calculation of the total energy of the each structure using the DFT method with 3-D periodic boundary conditions. From two total energy calculations, we obtain the energy difference from the structure under pressure; at volumes of  $388.15 \text{ Å}^3$  from the pressure loading

run, and at  $389.01 \text{ Å}^3$ , from the pressure release run. The energy difference in this case is ca. 11.48 meV/atom or  $1.83 \times 10^{-21} \text{ J}$  (Figure 6). Using the following expression for a two-state model system

$$P_B = \frac{e^{-\Delta E_B/k_B T}}{e^{-\Delta E_A/k_B T} + e^{-\Delta E_B/k_B T}} \quad (1)$$

the probability of finding the system in state “B” at 300 K can be estimated. A simple calculation with this energy difference would yield a 30% population probability for state B at 300 K.

**Potential Energy Surface.** To further investigate the energy cost associated with the changes in conformation observed here, we have performed accurate quantum level calculations to study the potential energy surface of the TATB molecule and TATB dimer. Indications of possible local minima with bent dihedral angles within substitutional groups can already be seen from the potential energy surface (PES) of the single molecule. We note that the potential barrier is not symmetric around  $90^\circ$ . The second barrier, with the nitro group lying flat, has a barrier of 4.12 kcal/mol.

We also obtained the potential energy surface for a dimer, starting from the initial configuration, with all of the nitro dihedral angles set at ca.  $29^\circ$ . We see a transition into a local configuration



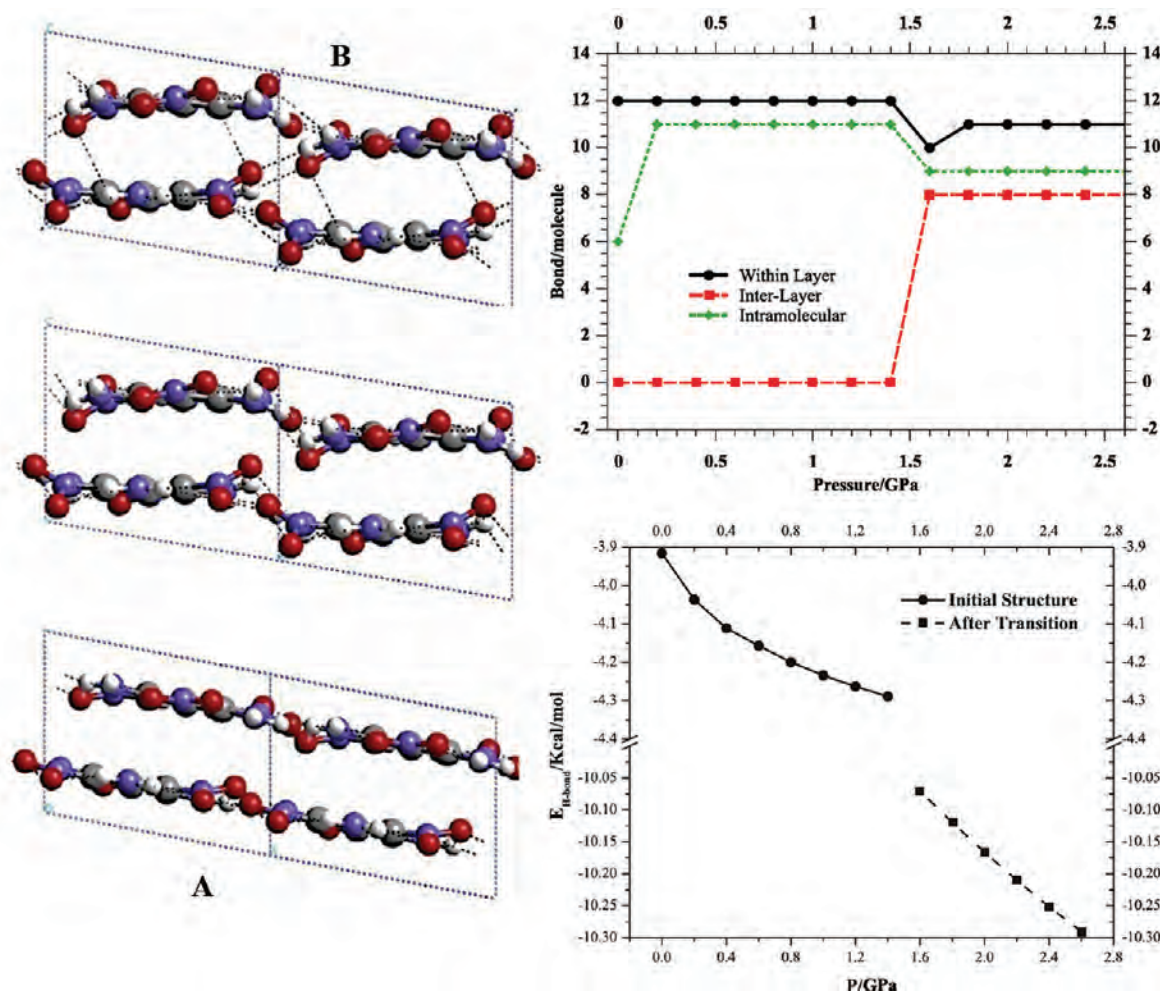


**Figure 5.** Structural rearrangements of the TATB unit cell upon compression: view from the [010] plane of the TATB structure labeled “A”, at 1.5 GPa (left); view at 1.55 GPa in the middle and after the transition, at 1.625 GPa (“B”). Internal and within-layer hydrogen bonding is also rearranged (top, right). The total energy contribution from hydrogen bond energy at different applied pressures is shown (right, bottom).

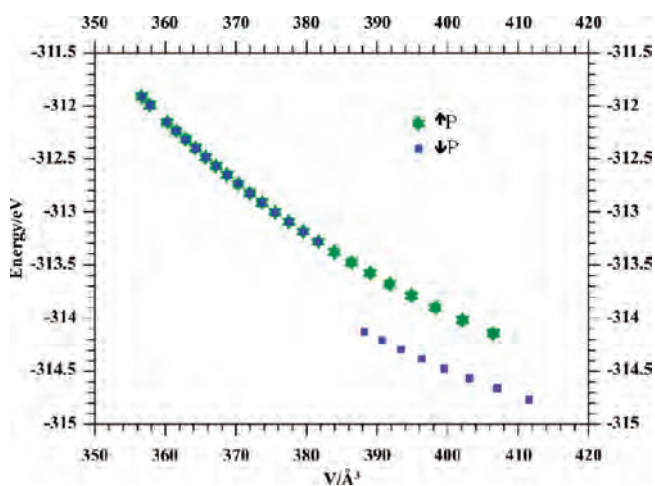


**Figure 6.** Total energy behavior of the TATB crystal structure, as calculated at the DFT/PBE level of theory. The energy difference observed from the initial compression run (green star) and the structure after it recovers its volume upon pressure release (blue square) can be attributed to the structural changes of the unit cell.

minimum, in which the system has one of the nitro dihedral angles rotated to  $-38^\circ$  (Figure 7).

**Effect of Pressure on Elastic Constants.** To determine the anisotropic elastic response behavior of the system, we have proceeded to calculate the elastic stiffness coefficients as a function of increasing pressure. We see an abrupt change in the elastic coefficients of the TATB at around the same pressure (at ca. 1.5 GPa) as the molecular rearrangements occur (Figure 8). This is most notable in  $C_{11}$  and is less pronounced for the  $C_{22}$  element. In the case of  $C_{11}$ , the magnitude of increase is more than 50 GPa by virtue of increased hydrogen-bonding interactions.

Similar noticeable change behavior is also noted in off-diagonal elements of the elastic constant tensor. This is the manifestation of the changes in hydrogen bonding network, hence resulting in a drastic increase in the stiffness of material in directions in accord with the new arrangement of the nitro and amine groups increasing the hydrogen bonding between layers and adding strength to material. As expected by the changes in molecular structure, the coefficient that directly probes the stress–strain relation between the  $a$  and  $c$ -axis undergoes the largest percent increase, as the  $C_{13}$  constant changes from less than 10 GPa to more than 20 GPa after the transition. This interaction is also reflected in the shear elastic constants,  $C_{44}$ ,  $C_{55}$ , and  $C_{66}$ .

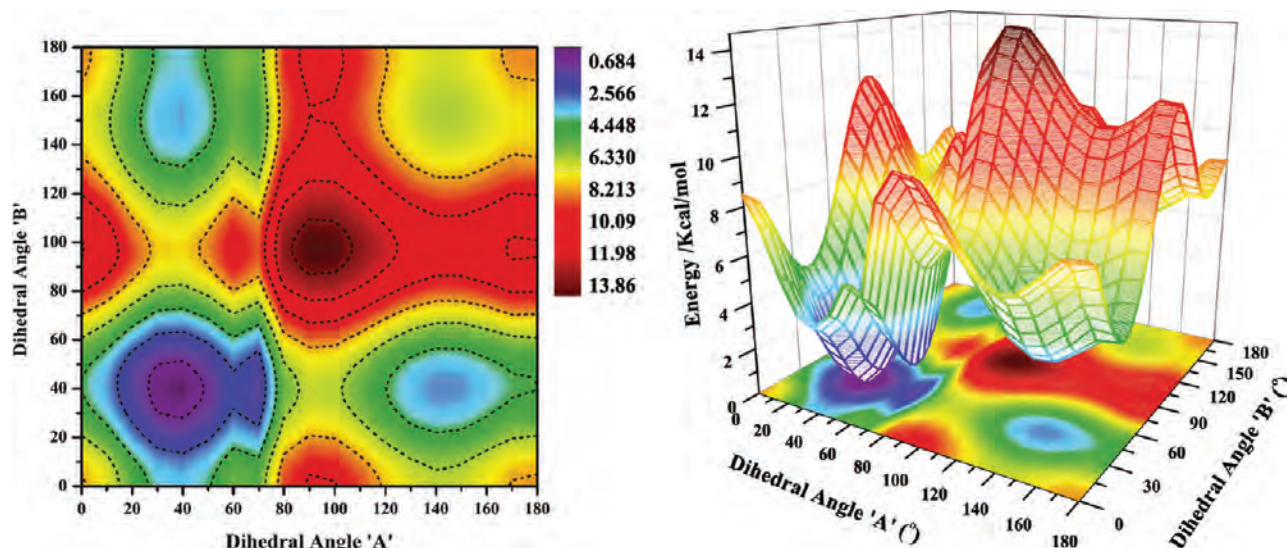


Figure 7. Potential energy surface of the TATB dimer. Calculations were performed at the MP2/6-311++G level of the theory with an angle scan step of  $5^\circ$ . A local energy minima ca.  $40^\circ$  and  $150^\circ$  rotation can be located. The latter is located 3.32 kcal/mol above the one at the intersection of  $40^\circ$ .

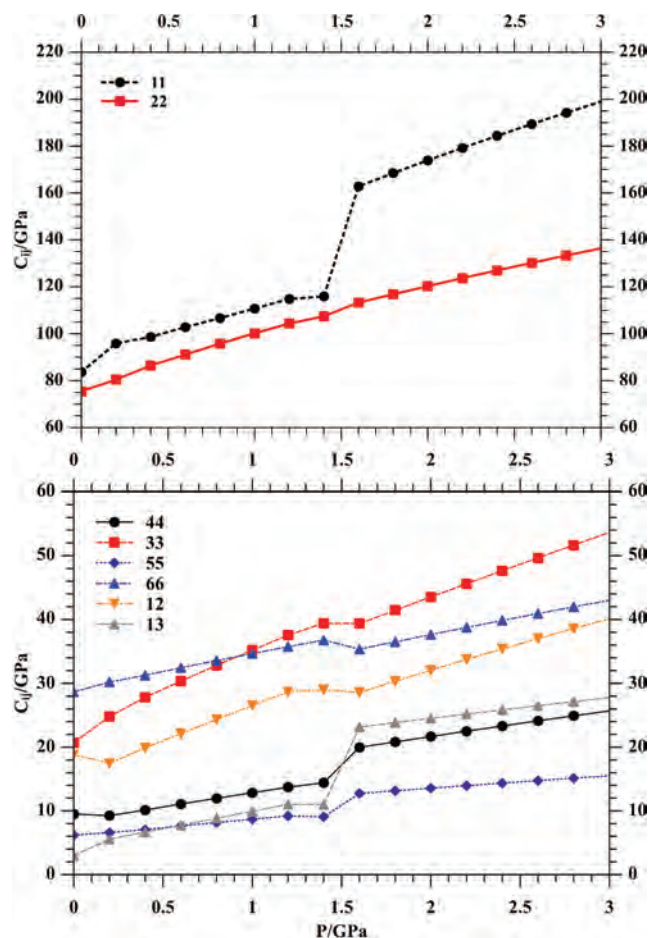


Figure 8. Variation of the anisotropic elastic stiffness tensor components, at different applied pressures.

spectra, energetics, and the mechanical response of the crystal. We have described these changes through calculation of energetic, vibrational spectra, diffraction patterns, and elastic properties of structure before and after “transformation”. To further understand this behavior, in what follows, we present a discussion to compare and contrast our results with other experimental findings.

#### 4. DISCUSSION

**Vibrational Spectra.** Changes in the vibrational spectra and periodic arrangement of the TATB system have been the subject of numerous studies. For example, a gradual loss of transparency of TATB single crystals and the presence of nonlinear optical behavior, through the use of sum-frequency generation spectroscopy (SFG), have been reported after thermal treatment up to  $320^\circ\text{C}$ . Interestingly enough there was also an indication of changes in the microstructure of thermally treated<sup>5,37</sup> TATB. A loss of the  $-\text{NH}$  stretching vibration with temperature and a peak increasing at  $2320\text{--}2340\text{ cm}^{-1}$  were observed in earlier studies.<sup>57</sup> More recently, Holey<sup>58</sup> has studied the effect of compression in the low frequency Raman spectra of TATB pellets up to 180 MPa and noticed an increase in the hydrogen-bonding strength of the material. Assuming a  $D3h$  point group symmetry, Deopura and Gupta rationalized the splitting of the degenerate  $\nu\text{NO}_2$  observed in its neutron diffraction studies<sup>59</sup> as caused by a lowering of the point group symmetry due to the crystal environment. Later, Towns assigned the modes<sup>60</sup> as  $\nu\text{NH}_2$  while comparing the electron-withdrawing and electron-releasing properties of related compounds. Although the assignment from experimental data can be complicated by the presence of mixed modes and intermodal coupling,<sup>61</sup> we can compare each normal mode to reported data. At 0 GPa, the calculated frequency of  $1308.9\text{ cm}^{-1}$  compares to the previously reported values of  $1229\text{ cm}^{-1}$ , obtained by neutron diffraction;  $1221\text{ cm}^{-1}$  from FTIR, and at  $1219\text{ cm}^{-1}$  from Raman scattering<sup>62</sup> experiments.

Recent work in the far-infrared region at different applied pressures pointed out a strong coupling of the  $\text{NO}_2$   $\text{NH}_2$  modes with pressure.<sup>3</sup> An irreversible transition was revealed after release to ambient pressure,<sup>39</sup> as seen from the line at  $290\text{ cm}^{-1}$ , assigned as

In summary, we have found a peculiar change in the hydrogen-bonding network and chemical environment of TATB, that manifests itself a set of observable changes in structure, vibrational



a ring twist mode. The observed changes were rationalized as mixing and shifting of modes that translated with modes of lower pressures.

In our simulated spectra, this vibration shows a shift to lower frequencies, after the system is subjected to a pressure of ca. 1.5 GPa. Upon release of the applied pressure, there is a noticeable change in both the intensity and the maximum positions of the simulated spectra. This can be noted in the increase in the maxima near  $380\text{ cm}^{-1}$ , which involves the oscillation of the  $\text{NH}_2$ ,  $\text{NO}_2$ , and aromatic ring atoms. This represents a change in the molecular orientation of the system, as observed from this low frequency region. Changes in the crystalline structure can be also understood from characterization through diffraction studies.

**Diffraction Studies.** In relation to diffraction studies, Olinger and Cady observed the reduction in the number of diffraction peaks at high pressures,<sup>63</sup> while the group of Dattelbaum<sup>64</sup> studied the hydrostatic equation of state for TATB up to 13 GPa. They observed some reflections that could not be correctly assigned through the whole pressure range and attributed this to the anisotropy of the crystal and its preferred orientation within the cell chamber. Besides the general agreement found at low pressures (below 2 GPa) with other studies, they found a “cusp” in their  $P$ – $V$  curve. Based on previous experimental results on TNT and graphite, they postulate a possible phase transition ca. 8 GPa, caused by a dimerization of the TATB molecule. Although we found no dimerization, results from our simulated data show that most noticeable changes occur in the region close to the (002) plane. The interplanar spacing, as obtained from Bragg's equation, shows a reduction in the distance of adjacent planes after the transition is observed. A close scrutiny of the chemical and structural environment was then conducted.

**Molecular Structure.** In relation to the molecular structure of TATB, we note that its nitro groups show a libration angle of ca.  $12^\circ$  that can be deduced from the Debye Weller factors of the reported diffraction pattern.<sup>29</sup> Based on high-level *ab initio* and DFT method calculations, its molecular structure has been conjectured not to be coplanar<sup>65,66</sup> to the central ring. Manaa et al.<sup>67</sup> found previously a rotation barrier of 5.6 kcal/mol. Additionally, other studies have argued for the ease of libration up to  $30^\circ$  in favor of hydrogen-bonding interactions<sup>4</sup>

We studied both the single molecule TATB and its dimer and found a value of 7.6 kcal/mol for a calculation at the HF/6-311++G//MP2/6-311++G level without any symmetry constraints. We note that the optimized isolated molecule structure has the nitro groups not planar with respect to the aromatic ring, but at a small rotation angle of ca.  $15^\circ$ . For the dimer system, we have found a local minimum that is located with the nitro group rotated to more than  $30^\circ$ . The structure of the dimer in this configuration is similar to the one found for the crystal after rearrangement while at high pressure. The energy barrier to reach the new plateau as measured from our calculations is ca. 6.73 kcal/mol and 3.64 kcal/mol, comparable to the internal rotation barriers of other resonance-assisted hydrogen bonded molecular crystals.<sup>68</sup> That is, there is a stabilization effect, caused by the crystal field, observed from the adiabatic angle rotation. The importance of hydrogen bonding in the series of amino-trinitrobenzene family of series has been acknowledged before.<sup>12</sup> Ledoux et al. hypothesized the absence of inversion symmetry due to a rotation of the TATB molecule around its aromatic center.<sup>41</sup> Furthermore, the presence of sheet–sheet interactions and the breaking of an inversion centered caused by this interactions and defects has been conjectured previously.<sup>35</sup> Our model findings support the

**Table 1. Voigt–Reuss–Hill Polycrystalline Averages before and after the Transition Observed in the TATB Unit Cell<sup>a</sup>**

	before	after	$\Delta/\%$
$K_V$	42.99	54.17	26.00
$\mu_V$	25.43	35.70	40.42
$E_V$	63.72	87.82	37.83
$K_V$	0.0323	0.0294	–8.78
$\mu_V$	0.1545	0.1164	–24.64
$E_V$	0.0551	0.0421	–23.61
$K_{VRH}$	36.99	44.06	19.14
$\mu_{VRH}$	15.95	22.15	38.86
$E_{VRH}$	40.94	55.79	36.29

<sup>a</sup> Values in GPa (Voigt, Hill) and  $\text{GPa}^{-1}$  (Reuss). Here “ $\Delta$ ” represents the difference in percent of before and after values.

hypothesis of a structural rearrangement induced by pressure that involves not a crystalline symmetry change, but changes in the hydrogen-bonding network of the 2D layers to a 3D structure. We can envision systems with the overall center of symmetry lost in regions interfacing planar and bent molecules, caused by local effects. This could explain how compressed samples with an increased SHG signature have been reported,<sup>69</sup> with no apparent change in chemical make-up, stoichiometry, and crystal symmetry of the used samples. The observed reordering will have a direct effect in the thermodynamic responses; as we have observed, there is a drastic change in the form of strain–stress relations or elastic stiffness constants. The effect of the increased stiffness in the velocity of propagation of a compression wave may be better understood as changes in the sound velocity through the bulk system, as we will show next.

**Mechanical Properties.** Molecular rearrangements within the crystal are known to have a direct effect on the elastic properties of solids. The importance of anisotropic properties and elastic coefficients for molecular crystals has been highlighted before.<sup>24,70–73</sup> Approximations for understanding the elastic behavior of polycrystalline materials can be done through the use of the Voigt–Reuss–Hill relationships.<sup>74</sup> The values of the system before and after the transition can be considered to be the upper and lower limits of the elastic behavior of a polycrystalline system.<sup>4</sup> Here, the subscript V, R, and VRH are used to discern among the last names of the authors developing the polycrystalline elasticity approximation.

The Voigt–Reuss–Hill average shows an increase in the observed stiffness of the materials, particularly in the shear constant (Table 1). As observed from the difference in the barrier depth of the single molecule TATB obtained from the DREX6 force field and the *ab initio* single molecule and dimer studies, the transition in the real material could be expected to be at a different pressure. As opposed to the behavior of other energetic materials and molecular crystals, in which crystalline phase transitions and mechanical instabilities with increased pressure arises, changes in structure through molecular rearrangement of TATB, which do not involve a change in the cell symmetry, may help explain the observed experimental behavior and physical properties. Experimentally, one can further try to characterize the elastic response of the system, or more specifically the  $C_{11}$  constant to understand the effect of structural changes, preferably at pressure ranges under 5 GPa.



## 5. CONCLUDING REMARKS

We have reported the molecular and hydrogen-bonding rearrangement as induced by pressure for the insensitive solid energetic material: TATB. We have analyzed the structure, configuration, and conformational changes as a function of applied pressure using molecular and electronic structure methods. We have determined the variation of structure not only from direct methods by also simulating diffraction patterns at different pressures. We have analyzed the variation of vibrational spectra as a function of pressure and correlated the results to changes in the conformations of the pendant groups ( $\text{NH}_2$  and  $\text{NO}_2$ ) within the unit cell. These findings are confirmed by calculations at different levels of theory. A systematic study through accurate ab initio methods indicates the presence of local minima for monomers and dimers of TATB at this high-pressure configuration. Among the different thermodynamic, mechanical, and chemical characterization required in understanding a material's response, elasticity theory is used as a key tool in understanding the response to mechanical loading. We have shown that, in the static and long wave range limit, the second derivative of the system's energy with respect to strain can itself be used as guidance to understand the thermodynamic changes that a known insensitive system (TATB) may show. This type of elasticity-driven study can further be pursued for other systems, for example, NM, Fox-7, PETN, HMX, and other molecular crystals, to gain insight for the relevance of intra- and intermolecular interactions. The changes in bonding and structure, which should manifest additionally as changes in the observed elastic properties, could indicate the necessary chemical characteristics and design principles for other energetic materials.

## AUTHOR INFORMATION

## Corresponding Author

\*Telephone: (979) 862-1449. Fax no.: (979) 845-6446. E-mail: tcagin@che.tamu.edu.

## ACKNOWLEDGMENT

The research here was supported by ARO-MURI: Insensitive Munitions. The authors would also like to thank CONACYT for its kind support. We would like to thank the Laboratory for Molecular Simulation at Texas A&M University and the Supercomputing Centers of Texas A&M College Station and Texas A&M Qatar for providing support and computer time.

## REFERENCES

(1) Dobratz, B. M. *The insensitive high explosive triaminotrinitrobenzene (TATB): Development and characterization, 1888 to 1994*; Los Alamos Scientific Laboratory: Los Alamos, NM, 2008.

(2) Kamlet, M. J.; Adolph, H. G. *Propellants, Explos., Pyrotech.* **1979**, *4*, 30.

(3) Pravica, M.; Yulga, B.; Liu, Z.; Tschauner, O. *Phys. Rev. B* **2007**, *76*, 064102.

(4) Baldrige, K. K.; Siegel, J. S. *J. Am. Chem. Soc.* **1993**, *115*, 10782.

(5) Son, S. F.; Asay, B. W.; Henson, B. F.; Sander, R. K.; Ali, A. N.; Zielinski, P. M.; Phillips, D. S.; Schwarz, R. B.; Skidmore, C. B. *J. Phys. Chem. B* **1999**, *103*, 5434.

(6) Yang, G.; Nie, F.; Huang, H.; Zhao, L.; Pang, W. *Propellants, Explos., Pyrotech.* **2006**, *31*, 390.

(7) Zhang, C.; Yuanjie, S.; Xiadong, Z.; Dong, H. *Cent. Eur. J. Energ. Mater.* **2004**, *1*, 43.

(8) Gee, R. H.; Maiti, A.; Fried, L. E. *Appl. Phys. Lett.* **2007**, *90*, 254105.

(9) Zhang, C. *J. Phys. Chem. B* **2007**, *111*, 14295.

(10) Tu, Y.; Luo, Y.; Agren, H. *J. Phys. Chem. B* **2005**, *109*, 16730.

(11) Balu, R.; Byrd, E. F. C.; Rice, B. M. *J. Phys. Chem. B* **2011**, *115*, 803.

(12) Brill, T. B.; James, K. J. *J. Phys. Chem.* **1993**, *97*, 8752.

(13) Liu, K.; Wang, Y.; Tu, Y.; Agren, H.; Luo, Y. *J. Phys. Chem. B* **2008**, *112*, 4387.

(14) Oxley, J. C.; Smith, J. L.; Ye, H.; McKenney, R. L.; Bolduc, P. R. *J. Phys. Chem.* **1995**, *99*, 9593.

(15) Satija, S. K.; Swanson, B.; Eckert, J.; Goldstone, J. A. *J. Phys. Chem.* **1991**, *95*, 10103.

(16) Sharma, J.; Beard, B. C.; Chaykovsky, M. *J. Phys. Chem.* **1991**, *95*, 1209.

(17) Sharma, J.; Forbes, J. W.; Coffey, C. S.; Liddiard, T. P. *J. Phys. Chem.* **1987**, *91*, 5139.

(18) Sharma, J.; Garrett, W. L.; Owens, F. J.; Vogel, V. L. *J. Phys. Chem.* **1982**, *86*, 1657.

(19) Sorescu, D. C.; Rice, B. M. *J. Phys. Chem. C* **2010**, *114*, 6734.

(20) Trott, W. M.; Renlund, A. M. *J. Phys. Chem.* **1988**, *92*, 5921.

(21) Manaa, M. R.; Schmidt, R. D.; Overturf, G. E.; Watkins, B. E.; Fried, L. E.; Kolb, J. R. *Thermochim. Acta* **2002**, *384*, 85.

(22) Brill, T. B.; James, K. J. *Chem. Rev.* **1993**, *93*, 2667.

(23) Millar, D. I. A.; Marshall, W. G.; Oswald, I. D. H.; Pulham, C. R. *Crystallogr. Rev.* **2010**, *16*, 115.

(24) Politzer, P.; Boyd, S. *Struct. Chem.* **2002**, *13*, 105.

(25) Ojeda, O. U.; Cagin, T. *J. Comput. Med. Commun.* **2010**, *16*, 127.

(26) Lee, E. L.; Tarver, C. M. *Phys. Fluids* **1980**, *23*, 2362.

(27) Tarver, C. M. *J. Phys. Chem. A* **2010**, *114*, 2727.

(28) Manaa, M. R.; Reed, E. J.; Fried, L. E.; Goldman, N. *J. Am. Chem. Soc.* **2009**, *131*, 5483.

(29) Cady, H. H.; Larson, A. C. *Acta Crystallogr.* **1965**, *18*, 485.

(30) Saw, C. K.; Zaug, J. M.; Farber, D. L.; Weeks, B. L.; Aracne, C. M. *AIP Conf. Proc.* **2002**, *620*, 856.

(31) Gee, R. H.; Roszak, S.; Balasubramanian, K.; Fried, L. E. *J. Chem. Phys.* **2004**, *120*, 7059.

(32) Pastine, D. J.; Bernecker, R. R. *J. Appl. Phys.* **1974**, *45*, 4458.

(33) Byrd, E. F. C.; Rice, B. M. *J. Phys. Chem. C* **2007**, *111*, 2787.

(34) *An ab initio study of nitromethane, HMX, RDX, CL-20, PETN, and TATB*; Byrd, E. F. C.; Chabalowski, C. F.; Rice, B. M., Eds.; Science Press Beijing: Beijing, 2007.

(35) Phillips, D. S.; Schwarz, R. B.; Skidmore, C. B.; Hiskey, M. A.; Son, S. F. *AIP Conf. Proc.* **2000**, *505*, 707.

(36) Kolb, J. R.; Rizzo, H. F. *Propellants, Explos., Pyrotech.* **1979**, *4*, 10.

(37) Catalano, E.; Rolon, C. E. *Thermochim. Acta* **1983**, *61*, 53.

(38) Foltz, M. F. In *13th International Symposium on Detonation*, Norfolk, VA, 2006; p 997.

(39) Pravica, M.; Yulga, B.; Tkachev, S.; Liu, Z. *J. Phys. Chem. A* **2009**, *113*, 9133.

(40) Su-Hong, G.; Xin-Lu, C.; Li-Sha, W.; Xiang-Dong, Y. *J. Mol. Struct.: THEOCHEM* **2007**, *809*, 55.

(41) Ledoux, I.; Zyss, J.; Siegel, J. S.; Brienne, J.; Lehn, J. M. *Chem. Phys. Lett.* **1990**, *172*, 440.

(42) Dunning, J. T. H. *J. Chem. Phys.* **1989**, *90*, 1007.

(43) Boddu, V. M.; Viswanath, D. S.; Ghosh, T. K.; Damavarapu, R. *J. Hazard. Mater.* **2010**, *181*, 1.

(44) Goodson, D. Z. *J. Chem. Phys.* **2002**, *116*, 6948.

(45) Kohn, W.; Sham, L. *J. Phys. Rev.* **1965**, *140*, A1133.

(46) Perdew, J. P.; Burke, K.; Ernzerhof, M. *Phys. Rev. Lett.* **1996**, *77*, 3865.

(47) Kresse, G.; Hafner, J. *Phys. Rev. B* **1993**, *47*, 558.

(48) Kresse, G.; Furthmüller, J. *Phys. Rev. B* **1996**, *54*, 11169.

(49) Kresse, G.; Furthmüller, J. *Comput. Mater. Sci.* **1996**, *6*, 15.

(50) Kresse, G.; Joubert, J. *Phys. Rev. B* **1999**, *59*, 1758.

(51) Kresse, G.; Hafner, J. *J. Phys.: Condens. Matter* **1994**, *6*, 8245.

(52) Monkhorst, H. J.; Pack, J. D. *Phys. Rev. B* **1976**, *13*, 5188.

(53) Cagin, T.; Pettitt, B. M. *Phys. Rev. B* **1989**, *39*, 12484.

(54) Mayo, S. L.; Olafson, B. D.; Goddard, W. A. *J. Phys. Chem.* **1990**, *94*, 8897.

- (55) Rappe, A. K.; Casewit, C. J.; Colwell, K. S.; Goddard, W. A.; Skiff, W. M. *J. Am. Chem. Soc.* **1992**, *114*, 10024.
- (56) Rappe, A. K.; Goddard, W. A. *J. Phys. Chem.* **1991**, *95*, 3358.
- (57) Makashir, P. S.; Kurian, E. M. *J. Therm. Anal. Calorim.* **1996**, *46*, 225.
- (58) Holey, J. A. *J. Phys. Chem. B* **2008**, *112*, 7489.
- (59) Deopura, B. L.; Gupta, V. D. *J. Chem. Phys.* **1971**, *54*, 4013.
- (60) Towns, T. G. *Spectrochim. Acta, Part A* **1983**, *39*, 801.
- (61) Brill, T. B.; Royce, W. B. *Appl. Spectrosc.* **2005**, *59*, 1194.
- (62) McGrane, S. D.; Shreve, A. P. *J. Chem. Phys.* **2003**, *119*, 5834.
- (63) Cady, H.; Olinger, B. In *6th International Symposium on Detonation*, Coronado, CA, 1976; p 700.
- (64) Stevens, L. L.; V., N.; Hooks, D. E.; Dattelbaum, D. M. *Propellants, Explos., Pyrotech.* **2008**, *33*, 286.
- (65) Roszak, S.; Gee, R. H.; Balasubramanian, K.; Fried, L. E. *Chem. Phys. Lett.* **2003**, *374*, 286.
- (66) Manaa, M. R.; Fried, L. E. *J. Phys. Chem. A* **2001**, *105*, 6765.
- (67) Manaa, M. R.; Gee, R. H.; Fried, L. E. *J. Phys. Chem. A* **2002**, *106*, 8806.
- (68) Borisenko, K. B.; Hargittai, I. N. *J. Mol. Struct.* **1996**, *382*, 171.
- (69) Kennedy, J. E.; Lee, K.-Y.; Son, S. F.; Martin, E. S.; Asay, B. W.; Skidmore, C. B. *Proceedings of the Conference of the American Physical Society Topical Group on Shock Compression of Condensed Matter*, 1st ed.; Furnish, M. D., Chhabildas, L. C., Hixson, R. S., Eds.; AIP: Snowbird, UT, 2000; Vol. 505, p 711.
- (70) Stevens, L. L.; Eckhardt, C. J. *J. Chem. Phys.* **2005**, *122*, 174701.
- (71) Day, G. M.; Price, S. L.; Leslie, M. *Cryst. Growth Des.* **2001**, *1*, 13.
- (72) Sewell, T. D.; Menikoff, R.; Bedrov, D.; Smith, G. D. *J. Chem. Phys.* **2003**, *119*, 7417.
- (73) Gan, C. K.; Sewell, T. D.; Challacomb, M. *Phys. Rev. B* **2004**, *69*.
- (74) Hill, R. *Math. Proc. Cambridge Philos. Soc.* **1975**, *77*, 225.